ORNL-5850

ornl

OAK
RIDGE
NATIONAL
LABORATORY

UNION
CARBIDE

SOLID STATE DIVISION

PROGRESS REPORT
Period Ending September 30 ,1981

OPERATED BY
UNION CARBIDE CORPORATION
FOR THE UNITED STATES
DEPARTMENT OF ENERGY

DISCLAIMER

Printed in the United States of America. Available from
National Technical Information Service
U.S. Department of Commerce
5285 Port Royal Road, Springfield, Virginia 22161
NTIS price codes—Printed Copy: A16 Microfiche A01

ORNL-5850
Special Distribution

Contract No. W-7405-eng-26

ORNL--5850

DE82 013254

SOLID STATE DIVISION PROGRESS REPORT for Period Ending September 30, 1981

M. K. Wilkinson, Director
F. W. Young, Jr., Associate Director
B. R. Appleton, Section Head
J. F. Cooke, Section Head
L. H. Jenkins, Section Head
R. M. Moon, Section Head

Date Published - April 1982

OAK RIDGE NATIONAL LABORATORY
Oak Ridge, Tennessee 37830
operated by
UNION CARBIDE CORPORATION
for the
DEPARTMENT OF ENERGY

Reports previously issued in this series are as follows:

ORNL-1095	Period Ending April 30, 1951
ORNL-1128	Period Ending July 31, 1951
ORNL-1214	Period Ending October 31, 1951
ORNL-1261	Period Ending January 31, 1952
ORNL-1301	Period Ending May 10, 1952
ORNL-1359	Period Ending August 10, 1952
ORNL-1429	Period Ending November 10, 1952
ORNL-1506	Period Ending February 10, 1953
ORNL-1606	Period Ending August 30, 1953
ORNL-1677	Period Ending February 28, 1954
ORNL-1762	Period Ending August 31, 1954
ORNL-1851	Period Ending February 28, 1955
ORNL-1852	Period Ending February 28, 1955
ORNL-1944	Period Ending August 31, 1955
ORNL-1945	Period Ending August 31, 1955
ORNL-2051	Period Ending February 29, 1956
ORNL-2052	Period Ending February 29, 1956
ORNL-2188	Period Ending August 31, 1956
ORNL-2189	Period Ending August 31, 1956
ORNL-2413	Period Ending August 31, 1957
ORNL-2414	Period Ending August 31, 1957
ORNL-2614	Period Ending August 31, 1958
ORNL-2829	Period Ending August 31, 1959
ORNL-3017	Period Ending August 31, 1960
ORNL-3213	Period Ending August 31, 1961
ORNL-3364	Period Ending August 31, 1962
ORNL-3480	Period Ending May 31, 1963
ORNL-3676	Period Ending May 31, 1964
ORNL-3841	Period Ending May 31, 1965
ORNL-3935	Period Ending December 31, 1965
ORNL-4098	Period Ending December 31, 1966
ORNL-4250	Period Ending December 31, 1967
ORNL-4408	Period Ending December 31, 1968
ORNL-4526	Period Ending December 31, 1969
ORNL-4669	Period Ending December 31, 1970
ORNL-4779	Period Ending December 31, 1971
ORNL-4861	Period Ending December 31, 1972
ORNL-4952	Period Ending December 31, 1973
ORNL-5028	Period Ending December 31, 1974
ORNL-5135	Period Ending December 31, 1975
ORNL-5328	Period Ending April 30, 1977
ORNL-5486	Period Ending September 30, 1978
ORNL-5640	Period Ending February 29, 1980

Special Dedication

This issue of the Solid State Division Progress Report is dedicated to the memory of a valuable Division member who died during the past year.

John Fletcher, a scientist in the research group investigating crystal defects and defect structures by electron microscopic techniques, was killed in an automobile accident on June 20, 1981. Although he had been at the Oak Ridge National Laboratory for only about fifteen months, he had made significant contributions to a broad range of research programs. His skills and his close associations with Division members are greatly missed.

THIS PAGE

WAS INTENTIONALLY

LEFT BLANK

Contents

LASER ANNEALING

2. SURFACE AND NEAR-SURFACE PROPERTIES OF SOLIDS

SURFACE PHYSICS

PLASMA MATERIALS INTERACTIONS

ION-SOLID INTERACTIONS

PULSED-LASER ANNEALING

SEMICONDUCTOR PHYSICS AND PHOTOVOLTAIC CONVERSION

3. DEFECTS IN SOLIDS

RADIATION EFFECTS

FRACTURE

DEFECTS AND IMPURITIES IN INSULATING CRYSTALS

4. TRANSPORT PROPERTIES OF SOLIDS

FAST-ION CONDUCTORS

SUPERCONDUCTIVITY

PHYSICAL PROPERTIES OF INSULATING MATERIALS

5. NEUTRON SCATTERING

SMALL-ANGLE SCATTERING

LATTICE DYNAMICS

MAGNETIC PROPERTIES

6. CRYSTAL GROWTH AND CHARACTERIZATION

NUCLEAR WASTE FORMS

FERROELECTRIC MATERIALS

HIGH-TEMPERATURE MATERIALS

SPECIAL MATERIALS

7. ISOTOPE RESEARCH MATERIALS

Acronyms, Abbreviations, and Initialisms

aBR—anti-Beevers Ross
AES—Auger electron spectroscopy
APD—avalanche photodiode
BCA—binary collision approximation
bcc—body-centered cubic
BCS—Bilby-Cottrell-Swinden
BR—Beevers Ross
BSA—bovine serum albumin
BSF—back surface field
CBD—convergent beam diffraction
CCDW—commensurate charge density wave
CEN—Centre d'Etudes Nucléaires
CFM—charge fluctuation model
CHESS—Cornell High Energy Synchrotron Source
CMA—compositionally modulated alloy
CMA—cylindrical mirror analyzer
CPA—coherent potential approximation
CRBR—Clinch River Breeder Reactor
CVD—chemical vapor deposition
cw—continuous wave
Cz—Czochralski
DCF—dipolar charge fluctuation
DFZ—dislocation-free zone
DOE—Department of Energy
EBIC—electron-beam-induced current
EEL—electron energy loss
EELS—electron energy loss spectroscopy
ENDOR—electron nuclear double resonance
EPR—electron paramagnetic resonance
ER—electroreflectance
fcc—face-centered cubic
FED—Fusion Engineering Device
FF fill factor
FFTF—Fast Flux Test Facility
FLL—flux-line lattice
FWHM—full width at half maximum
Fz—float zone
gff—glass fabric filled
HEDL—Hanford Engineering Development Laboratory
HF—hydrofluoric
HFIR—High Flux Isotope Reactor
HOLZ—higher order Laue zone
ICDW—incommensurate charge density wave
ILL—Institut Laue-Langevin
IR—infrared
IRML—Isotope Research Materials Laboratory
KFA—Kernforschungsanlage
KKR—Korringa-Kohn-Rostoker
LDA—local density approximation
LEED—low-energy electron diffraction
LEIS—low-energy ion scattering study
LiDS—lithium dodecyl sulfate
LIF—laser-induced fluorescence
LLNL—Lawrence Livermore National Laboratory
LP—Lifshitz point
LRO—long-range order
LSS—Lindhard, Scharff, Schiøtt
LTIF—low-temperature irradiation facility
MCD—magnetic circular dichroism
MCDL—minority carrier diffusion length
MHD—magnetohydrodynamic
NCSASR—National Center for Small-Angle Scattering Research
NMR—nuclear magnetic resonance
NTD—neutron transmutation doped
OFHC—oxygen-free high conductivity
ORNL—Oak Ridge National Laboratory
ORR Oak Ridge Research Reactor
PES—photoelectron spectroscopy
PIXE—proton-induced x-ray excitation
PLA—pulsed-laser annealing
PME—polarization modulation ellipsometer
PRF—prototype fast reactor
QFD—quasistationary finite difference
QNS—quasielastic neutron scattering
RBS—Rutherford backscattering
RFS renormalized forward scattering
RTNS—Rotating Target Neutron Source
SANS—small-angle neutron scattering
SAXS—small-angle x-ray scattering
SCE—saturated calomel electrode
SDS—sodium dodecyl sulfate
SEM—scanning electron microscopy
SIMS—secondary ion mass spectroscopy

SLS—scanning laser spot
SNS—Spallation Neutron Source
SPE—solid-phase epitaxial
SRW—Savannah River wastes
SSM—spherical solid model
TEM—transmission electron microscopy
TFA—truncated free-atom (potential)
TRR—time-resolved reflectivity
TRT—time-resolved transmission
TSDC—thermally stimulated depolarization currents
UADA—uniaxial double alignment
UHV—ultrahigh vacuum
VDAE—velocity-dependent activation energy
VSM—vibrating sample magnetometer
WNR—Weapons Neutron Research facility
XES—x-ray energy spectroscopy
XPS—x-ray photoelectron spectroscopy

Introduction

The reporting period covered by this progress report of the Solid State Division includes the 19 months from March 1, 1980, through September 30, 1981. During this period the research emphasis within the Division has been relatively stable compared to that during the previous five-year period. The large changes that occurred in earlier years, of course, were required when the Atomic Energy Commission was replaced first by the Energy Research and Development Administration (ERDA) and later by the Department of Energy (DOE). The broad missions of ERDA and DOE in the development of new energy systems required many new types of investigations in the materials sciences to help find solutions for the severe materials problems in all advanced energy technologies. In adjusting to this requirement, the Solid State Division redirected many programs into new research areas, particularly into areas closely related to the nonnuclear energy technologies. The transition was exceptionally smooth, and these new programs are now providing very interesting and important fundamental information, which is necessary in the prediction and development of new materials with special properties.

Throughout this reporting period, considerable effort has been directed toward the development of users' programs in the Solid State Division, whereby scientists outside ORNL can conduct research with unique facilities located at the Laboratory. Although informal arrangements for users have existed for many years, specific users' programs are being established to ensure the most effective utilization of these facilities for the best possible research. The National Center for Small-Angle Scattering Research (NCSASR), which was initiated at ORNL in 1978 through a joint interagency agreement between the Department of Energy and the National Science Foundation (NSF), operates exclusively in the users' mode. This Center provides state-of-the-art instrumentation for scientists who wish to perform small-angle neutron scattering investigations and/or small-angle x-ray scattering investigations. The major neutron scattering facility is a sophisticated 30-m small-angle scattering instrument, which was constructed at the HFIR with funds obtained from NSF; the major x-ray scattering facility is a unique 10-m small-angle scattering camera that was built for DOE programs and is available to the Center on a part-time basis. During the past two years about 100 research investigations have been performed on these instruments. A users' program has also been established for the other neutron scattering facilities at the HFIR, and these facilities are available to scientists outside the Laboratory for as much time as possible consistent with the programmatic requirements of DOE. In response to a questionnaire that was circulated to the scientific community, over 200 scientists have indicated specific interests in using these excellent neutron scattering facilities. Although the existing users' programs involve only the neutron scattering facilities, careful consideration is being given to users' programs for other unique facilities, such as the accelerators for ion implantation, scattering, and channeling investigations and the lasers for materials processing. These facilities are already

used informally by many scientists from industrial and university laboratories, but specific programs would undoubtedly increase the user participation.

In addition to the users' programs, there are two cooperative programs that involve the ORNL neutron scattering facilities. Already in existence is a cooperative program with scientists of Ames Laboratory. When the Ames Laboratory Research Reactor was shut down, three neutron scattering instruments were moved from that reactor to the ORR; this equipment and the ORNL equipment at the HFIR and ORR are available to scientists of both laboratories. Another cooperative program in neutron scattering is in the final stages of negotiation with the Japanese Science and Technology Agency and the Japanese Ministry of Education. This program is being initiated by DOE under the umbrella of the U.S.-Japan Non-Energy Research Agreement that was signed by representatives of the two governments on May 1, 1980. The program in neutron scattering would involve the development and construction of a unique wide-angle diffractometer and considerable auxiliary equipment at the HFIR with funds provided by the Japanese organizations. The main collaboration would be centered on the use of this new equipment, but the Japanese scientists would also be permitted modest use of the HFIR neutron scattering facilities. Although the primary objective of cooperative programs and users' programs is to ensure effective use of the unique ORNL facilities, they also serve another important purpose; these programs produce very strong interactions between members of the Solid State Division and scientists from other organizations.

The arrangement of this progress report has been chosen to emphasize the major areas of solid-state science in which the Solid State Division conducted research during the reporting period. The areas are Theoretical Solid State Physics, Surface and Near-Surface Properties of Solids, Defects in Solids, Transport Properties of Solids, Neutron Scattering, Crystal Growth and Characterization, and Isotope Research Materials. Each constitutes a section of the report, and additional subdivisions are included within the sections. A short introduction precedes each of the seven sections to indicate the scope and goals of the research and to give a few highlights of recent investigations. These introductions reflect many of the changes that have occurred in the programs of the Division during the past several years. It is also their intent to give a clearer picture of the manner in which the individual programs are interrelated and to indicate how research activities of the Solid State Division contribute to various programs of ORNL and DOE.

Because of the very close interactions among programs within the Division, many research summaries do not fit uniquely into only one subsection of the report. A particularly good illustration is the neutron scattering research on superconducting flux-line lattices; these summaries have been included in the subsection on superconductivity, but obviously they would have fit equally well under small-angle neutron scattering. The situation becomes even more confused in research investigations concerned with ion implantation and laser annealing, particularly when the work involves photovoltaic materials for solar energy conversion. The development of unique materials by these techniques and the understanding of the physical properties of the materials have required the skills and experimental facilities of many Division members. Consequently, a number of research summaries concerned with this exciting new research could have been placed in several subsections. Of course, there is also very close coupling of almost all experimental programs with ongoing theoretical research and with programs

concerned with materials preparation and characterization. In placing certain research summaries into one of the appropriate subsections, the choice has been somewhat arbitrary. It is hoped that the arrangement of the report minimizes difficulties for the reader in finding those summaries of interest.

1. Theoretical Solid State Physics

The primary role of theoretical research in the Solid State Division is to complement the experimental programs. The close collaboration which has existed over the years between the theoretical and experimental programs has naturally resulted in the development and extension of expertise in a wide variety of theoretical disciplines. Specific research activities generally include state-of-the-art investigations, including relevant extensions, of existing theories as well as the development of new concepts, theories, and procedures when appropriate. Of equal importance is the development and use of numerical procedures (e.g., computer programs, mathematical techniques, etc.) for generating accurate predictions from these complex theories of condensed matter for materials relevant to the mission of DOE. For purposes of clarity, the work presented in this section of the progress report is loosely grouped into four categories: Surfaces, Electronic and Magnetic Properties, Particle-Solid Interactions, and Laser Annealing.

Research in the area of surface physics has continued to expand into new areas during the period covered by this report. For example, new techniques have been developed for generating more realistic pair potentials at metallic surfaces. Results from numerical calculations for aluminum and sodium have clearly established that the traditional method of using bulk pair potentials cannot yield reliable results for lattice vibrations or relaxation at surfaces when reduced screening is important. Arguments based on differences between bulk and surface pair potentials, together with the corresponding conduction-electron redistribution, have also indicated that multilayer relaxation must be considered in any surface structure analysis. To investigate the possibility of multilayer relaxation, LEED I-V profile data for Cu(100) were reanalyzed. Strong evidence for relaxations of two (and possibly three) layers was found. In addition, this analysis revealed the unusual result that the spacing between the second and third layer was expanded more than the contraction between the first and second layer. The investigation of the band structure of metallic surfaces also represents a new area of research. A calculation of the electronic structure of Ag(100) has revealed two bands of surface states. Electronic excitations from bulk band states to these surface states have been correlated with two absorption features of Ag(100), which have been observed using the electroreflectance technique. This correlation may prove to be a useful tool to probe the potential distribution at metallic surfaces.

Work on electronic and magnetic properties of solids continues on a wide variety of problems of both current and future interest. The introduction of new high-flux spallation neutron sources in the near future will make it possible to perform neutron scattering experiments with energy transfer in the eV range. It has been suggested that experiments of this type could be a useful tool for the experimental determination of electronic band structures. As an aid to assess the feasibility of such experiments for semiconductors, an extensive series of calculations of the total magnetic scattering cross section has been carried out. The relatively small cross sections obtained from these calculations indicate that the

experiments are going to be difficult. However, if these small cross sections can be measured, important information about the band structure of semiconductors could be provided which cannot, at present, be obtained from any other source. Work on the itinerant theory of magnetism has continued to yield important results. A calculation of the spin part of the magnetic form factor for nickel, which was based on a partial parameterization of the spin-polarized band structure, has established that most of the temperature dependence observed in the corresponding form factor measurement results from Fermi surface smearing and not from any significant change in the spin-splitting energy Δ with temperature. A first-principles calculation of Δ for nickel, which was based on the local density approximation that includes the lowest-order nonlocal, or gradient, contribution, has also been completed. It was found that even though the nonlocal term significantly affected the exchange potential, it had very little effect on Δ and, therefore, could not be the source of the large discrepancy which exists between Δ obtained from the local density theory and from experiment. Several important aspects of the general problem of hydrogen in metals have been studied. A spherical solid model was used to obtain reasonable estimates of lattice relaxation effects, heat of solution, and zero-point energy. A method based on the augmented space formalism has been developed for obtaining the electronic properties of random alloys with various degrees of short-range order. This method is treatable, self-consistent, and provides a useful description of short-range order over a wide range of concentrations.

Research on particle-solid interactions has traditionally been associated with channeling, damage produced in solids by particle beams, and related phenomena. Numerical techniques which have been developed to study these types of problems have recently been used to examine displacement damage production in monazite and related minerals. These materials are important because of the observation that monazites containing radioactive impurities are crystalline, which is in contrast to the majority of radioactive minerals; therefore, monazites may have suitable phases in which long-lived radioactive nuclear waste can be isolated. Computer simulations of channeling in InAs-GaSb superlattices have been carried out to investigate the origin of some unusual features observed in ion dechanneling measurements. Results from this study indicate that these features are most likely generated by a series of multilayer relaxations in the planar spacing at each interface in the superlattices. Work has also continued on the use of an analytical model to describe enhanced Rutherford backscattering yields from disordered solids.

Laser annealing and its applicability to the preparation of semiconductor device materials are areas of intense interest and study within the Division and the Theory Section. Over the past few years theoretical research based on the one-dimensional dopant diffusion model has established rather conclusively that the near-surface region of a sample melts and then regrows epitaxially when irradiated with a sufficiently intense laser pulse. Results from recent calculations for silicon and GaAs based on this melting model have been shown to be consistent with a wide variety of experimental data. The only significant disagreement relates to the surface temperature of unimplanted silicon during and shortly after irradiation. In experiments performed at another laboratory, the temperature inferred from the Stokes-to-antiStokes Raman intensities was found to be significantly below the melting temperature. It is not clear, however, that this is a reliable measure of the temperature of a sample undergoing pulsed-laser annealing because of possible large temperature gradients. This particular problem is currently under investigation.

SURFACES

Cu(100) MULTILAYER RELAXATION[1]

H. L. Davis J. R. Noonan

Metallic crystal termination by a surface affects both the atomic coordination and the conduction-electron distribution. Changes in both can influence the surface crystallography and cause it to differ from that of the truncated bulk crystal. One simple type of difference is a relaxation normal to the surface in which distances between atomic layers deviate from bulk values. Since pair potentials were constructed in a manner to mimic bulk properties, early attempts to calculate the amount of layer relaxation were based only on the change of atomic coordination. Such attempts then produced the almost universal prediction that the distance between the first two layers d_{12} in a metallic surface should be *larger than* the bulk value. However, this prediction was in stark contradiction to the results of LEED analyses of low-indexed metallic surfaces, which indicated that d_{12} is usually *less than* the bulk value in most cases.

The above dilemma between theoretical predictions and experimental results was resolved, at least in principle, when consideration was directed toward the surface-region modification of the conduction-electron distribution. Finnis and Heine (FH)[2] have shown that a heuristic redistribution of the truncated bulk electronic density will produce electrostatic forces on ionic cores in the outermost surface layer, which could result in a d_{12} *less than* the bulk value. Subsequent work of Landman, Hill, and Mostoller (LHM)[3] has considered three distinct models for the surface-region electronic charge density and, importantly, allowed for the participation of several atomic layers in the relaxation process. Although LHM's results showed some sensitivity to the model used for the charge density, their results were generally consistent with those available from LEED analyses. Further, LHM's results illustrated the importance of multilayer relaxation mechanisms, which implies that multilayer relaxation must be considered when performing surface crystallography.

Motivated by LHM's results, we decided to investigate the possibility of multilayer relaxation in some relatively simple metallic surfaces using modern LEED analysis. Results of such an investigation for Cu(100), where existing[4] I-V profile data were reanalyzed, are reported here. The results obtained from the new analysis of Cu(100) clearly provide evidence for multilayer relaxation.

Sets of calculations were performed with 63 different pairs of values for the relative change of the first interlayer spacing from the bulk spacing Δd_{12} and the relative change of the second interlayer spacing Δd_{23}. In these calculations Δd_{12} was varied from -3.25 to $+1.25\%$ and Δd_{23} from -1.75 to $+4.25\%$, with Δd_{ij} incremented in steps of 0.75%. The results of these calculations were compared with the experimental I-V profiles using three distinct reliability factors (R factors). These were R_{ZJ} as defined by Zanazzi and Jona,[5] and R_2 and R_5 as defined by Van Hove, Tong, and Elconin.[6] The factor R_{ZJ} was designed in an attempt to weigh those features that experienced investigators use in a visual comparison of profiles. The R_2 is a measure of the mean-square difference between experimental and calculated profiles, while R_5 indicates the mean-square difference between the profiles' slopes.

Contour maps of optimal values of the four-beam R factors are given in Fig. 1.1. The respective minima in Fig. 1.1 were found for Δd_{12} in the range -1.45 to -0.60% and for Δd_{23} in the range $+1.95$ to $+2.25\%$. Since a 1.0% variation in bulk d_{ij} corresponds to 0.018 Å and the three R factors

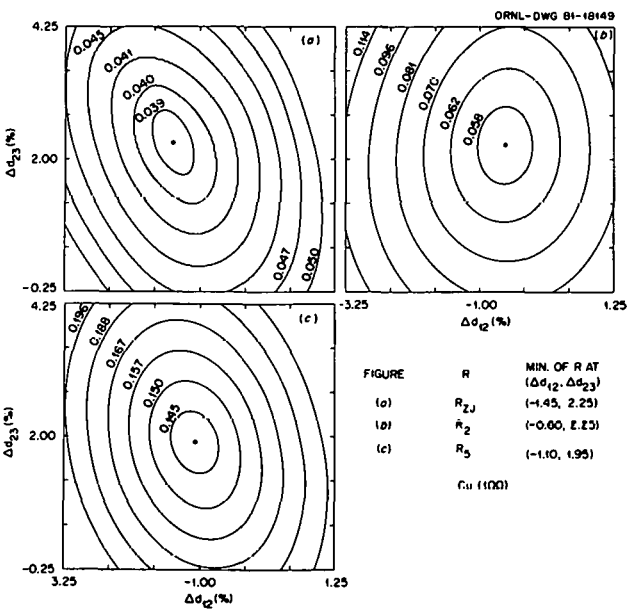

Fig. 1.1. Contour maps of optimal values of four-beam *R* factors.

weigh different features of I-V profiles, the consistency in the Δ_{ij}, giving the minima R factors of Fig. 1.1, is very good for the results of a LEED analysis. Therefore, this consistency can be taken as evidence that the indicated multilayer relaxation is a valid characterization of the crystallography of the Cu(100) surface and not an artifact of the analysis. This statement is made even though the minima placements of Fig. 1.1 indicate what most would believe to be an unusual physical result, namely, that d_{23} is expanded from the bulk value more than d_{12} is contracted.

In previous work[7] on Cu(100) where only relaxation of Δd_{12} was considered, a minimum R_{ZJ} value was obtained for $\Delta d_{12} = -0.9\%$. The R_{ZJ} minimum of Fig. 1.1(a) is for $\Delta d_{12} = -1.45\%$. These different results for Δd_{12} are a consequence of the major axes of the "ellipses" of Fig. 1.1(a) being tilted to the left as Δd_{23} increases. Such a tilt implies that Δd_{12} and Δd_{23} must be self-consistently varied in LEED analyses concerned with multilayer relaxation; that is, Δd_{12} cannot be determined by choosing $\Delta d_{23} = 0$ and then be expected to stay constant as Δd_{23} is varied.

Figure 1.2 contains plots of experimental and calculated I-V profiles. The bottom curves of the subfigures of Fig. 1.2 are the averaged experimental profiles. The top profiles are those calculated[7]

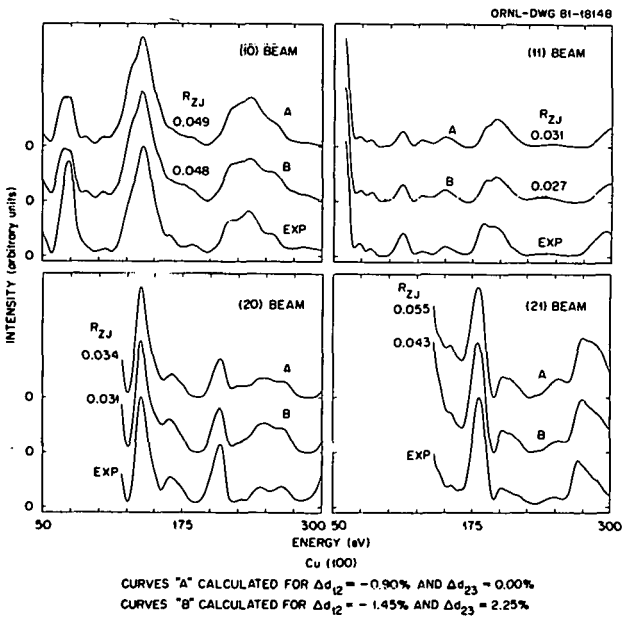

Fig. 1.2. Calculated and experimental profiles for Cu(100).

for the quantities producing the minimum four-beam R_{ZJ} when only Δd_{12} was allowed to deviate from the bulk value, so that these were calculated for $\Delta d_{12} = 0.90\%$ and $\Delta d_{23} = 0\%$. The middle curves were calculated for the quantities producing the minimum R_{ZJ} of Fig. 1.1(a); thus, these were calculated for $\Delta d_{12} = -1.45\%$ and $\Delta d_{23} = +2.25\%$. Associated with each of the calculated profiles of Fig. 1.2 is the single-beam R_{ZJ} for comparison of that profile with the corresponding experimental profile. It is noted that for all four considered beams d_{23} relaxation produces a reduction in R_{ZJ}, with the reduction being about 10% or more for three of the beams. This consistency in reduction of single-beam R_{ZJ} adds reinforcement to the conclusion that the indicated multilayer relaxation is a valid characterization of Cu(100)'s crystallography.

Even though the indicated changes are only a few hundredths of an angstrom and some undoubtedly will question whether our analysis has exceeded the precision that can be expected from a LEED analysis, the analysis has furnished considerable evidence that multilayer relaxation measurably exists for Cu(100) with $|\Delta d_{23}| > |\Delta d_{12}|$. Also, further calculations have been performed where variation was considered in Δd_{34}, the relative change in the spacing between layers 3 and 4 of the surface region. In these calculations only fixed values of $\Delta d_{12} = -1.45\%$ and $\Delta d_{23} = +2.25\%$ were used. When the calculated I-V profiles were compared with the averaged experimental profiles, the four-beam R_{ZJ} had a minimum value slightly less than 0.037 for Δd_{34} between +1 and +2%. In addition, expansion of Δd_{34} reduced all the single-beam R_{ZJ} values from those for the B profiles of Fig. 1.2. We consider both the reduction in four-beam R_{ZJ} and the consistency in reduction of single-beam R_{ZJ} to be reasonable evidence that Δd_{34} is probably expanded by more than 1%. Calculations are now in progress to determine whether this conclusion is stable with variations in Δd_{12}, Δd_{23}, specific R factors, and nonstructural parameters.

---

1. Summary of paper to be published.
2. M. W. Finnis and V. Heine, *J. Phys. F* **4**, L37 (1974).
3. U. Landman, R. N. Hill, and M. Mostoller, *Phys. Rev. B* **21**, 448 (1980).
4. J. R. Noonan and H. L. Davis, *J. Vac. Sci. Technol.* **17**, 194 (1980).

5. E. Zanazzi and F. Jona, *Surf. Sci.* **62,** 61 (1977).
6. M. A. Van Hove, S. Y. Tong, and M. H. Elconin, *Surf. Sci.* **64,** 85 (1977).
7. H. L. Davis and J. R. Noonan, *Proceedings of Conference on Determination of Surface Structure by LEED,* Plenum Press, New York (in press).

CALCULATIONAL DEMONSTRATION THAT AVERAGING ENHANCES DATA FOR USE IN A LEED ANALYSIS

H. L. Davis J. R. Noonan

During the past few years a program has evolved at ORNL for the collection and analysis of LEED data to obtain, as precisely as possible, information concerning the crystallography of surfaces. Thus, some effort is concerned with attempts to improve technique, and the success of one such attempt is described here. A LEED analysis involves a trial-and-error procedure in which experimental I-V profiles are compared with those calculated for various geometric models of a surface. Then, the surface structure determined by a given LEED analysis is the assumed structural model which leads to the "best" agreement between the experimental and calculated I-V profiles. Since the best agreement is never "perfect," questions always remain concerning the accuracy and sensitivity of the analysis. Therefore, an improvement in technique for LEED usually would involve some procedures which result in enhanced agreement between calculated and experimental I-V profiles.

During the LEED investigation of the Cu(100)[1] and Ag(110)[2] surfaces, it was observed that the agreement between calculated and experimental profiles was improved by the application of a relatively simple procedure. This procedure entailed collecting data with the electron beam at normal incidence and then using averaged experimental profiles obtained from the raw data in the analysis. This averaging process is explained below, and some calculational results are described which demonstrate that the averaging process does eliminate some effects of errors that are present in the individual as-measured profiles. In fact, the calculational results show that the averaging process serves to eliminate more than the effects of random errors.

Although several inequivalent I-V profiles form the data base for a LEED analysis, the averaging process can be explained adequately using data for the {10} beams from Cu(100). Such data are illustrated by Fig. 1.3, where the as-measured {10} I-V profiles are the top four curves. Since Cu(100) has fourfold symmetry, the four {10} profiles should be identical. The as-measured profiles are quite similar to each other; however, there are some differences which we believe are due to residual electromagnetic fields, minor detector misalignment, electron-beam divergence, surface topography, etc. The differences between the {10} profiles can be specified quantitatively by use of an R factor. For example, if the Zanazzi and Jona[3] R_{ZJ} is used to compare the (10) profile of Fig. 1.3 with the $(0\bar{1})$, a value of 0.061 results. This R_{ZJ} value is larger than the value that results when calculated profiles are compared[1] with the averaged profile, which is at the bottom of Fig. 1.3.

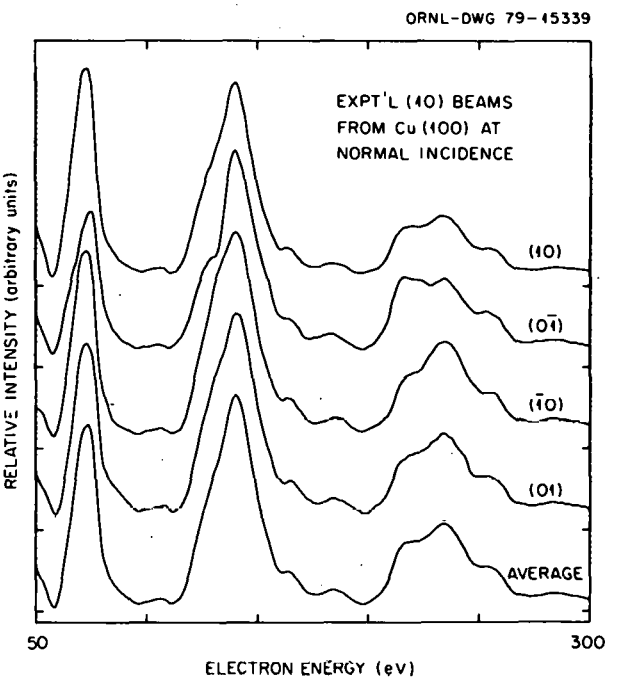

Fig. 1.3. As-measured {10} I-V profiles from Cu(100) and their average.

The differences between as-measured profiles that should be symmetrically identical can influence the final result of a LEED analysis (e.g., the structural conclusion could be different depending upon which one of the four top curves of Fig. 1.3 was employed in an analysis). Therefore, in a pragmatic attempt to reduce the influence of the

differences in as-measured profiles, we decided to average profiles that should be symmetrically equivalent. When such averaging procedures were used, it was found that much better agreement was achieved between calculated and averaged experimental profiles than between calculated and as-measured experimental profiles. Thus, in our analyses of Cu(100) and Ag(110), we "enhanced" the data by collecting, for each individual $\{ij\}$ set of beams, all the profiles that should be symmetrically equivalent and then computed their mean to obtain an averaged experimental profile to represent the (ij) beam in the analysis.

Since the above averaging procedure has been shown to lead to significant improvements in LEED analysis, it can be defended on a strictly empirical basis. However, the procedure can be strengthened further by calculational arguments, which show that the improvement is due to more than the fortuitous cancellation of random errors. Rather, the effects of systematic errors are greatly reduced. This can be illustrated by a study of the effects of averaging over I-V profiles calculated for the case of a misaligned incident beam. For example, the four top curves of Fig. 1.4 are calculated {10} profiles for Cu(100) with the incident beam aligned at 1° away from the surface normal. The curve labeled "average" in Fig. 1.4 is the mean of the top four, and the bottom one labeled "normal" is a (10) profile calculated for the incident beam exactly normal to the surface. First, note that the differences between the top four profiles of Fig. 1.4 are of the same order as the differences between the as-measured profiles of Fig. 1.3. Associated with each of the top five profiles of Fig. 1.4 are single-beam R_{ZJ} (ref. 3) that resulted when the respective profile was compared with the bottom profile (i.e., the one calculated for normal incidence). Since the R_{ZJ} for the average profile is very small and the visual agreement between the bottom two profiles of Fig. 1.4 is very good, it is evident that the process of obtaining the mean of the top four profiles has greatly reduced the effects of systematic errors caused by a 1° misalignment of the incident beam.

Besides those profiles represented by Fig. 1.4, other $\{ij\}$ sets of profiles and other cases of alignment close to the surface normal have been investigated for both Cu(100) and Ag(110). An example for Ag(110) is provided by Fig. 1.5. The results from the totality of calculations give the identical

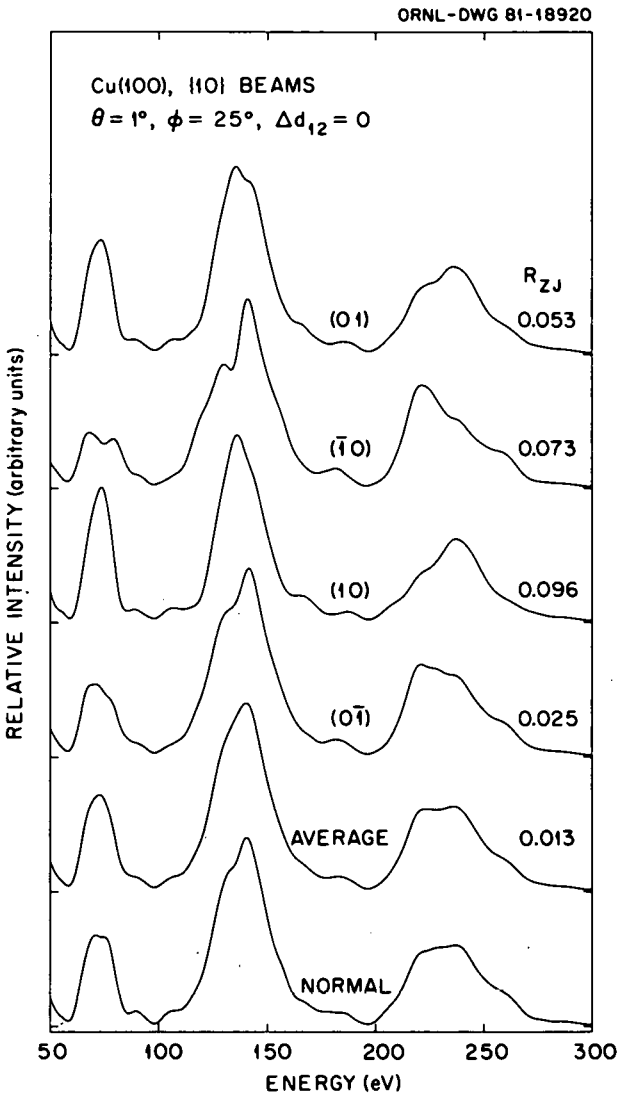

Fig. 1.4. Calculated {10} profiles for Cu(100). The four top profiles were calculated for the incident beam aligned at 1° away from the surface normal and in an azimuth 25° from the azimuth containing the (10) beam. The second profile from the bottom is the mean of the top four, and the bottom profile was calculated for exactly normal incidence.

conclusion as that inferred from the results of Fig. 1.4; that is, obtaining the mean of a set of as-measured $\{ij\}$ profiles serves to reduce greatly the effects of errors caused by minor misalignment. It is inferred then that by using the averaged experimental profiles in a LEED analysis, the effects of those errors caused by beam divergence, beam

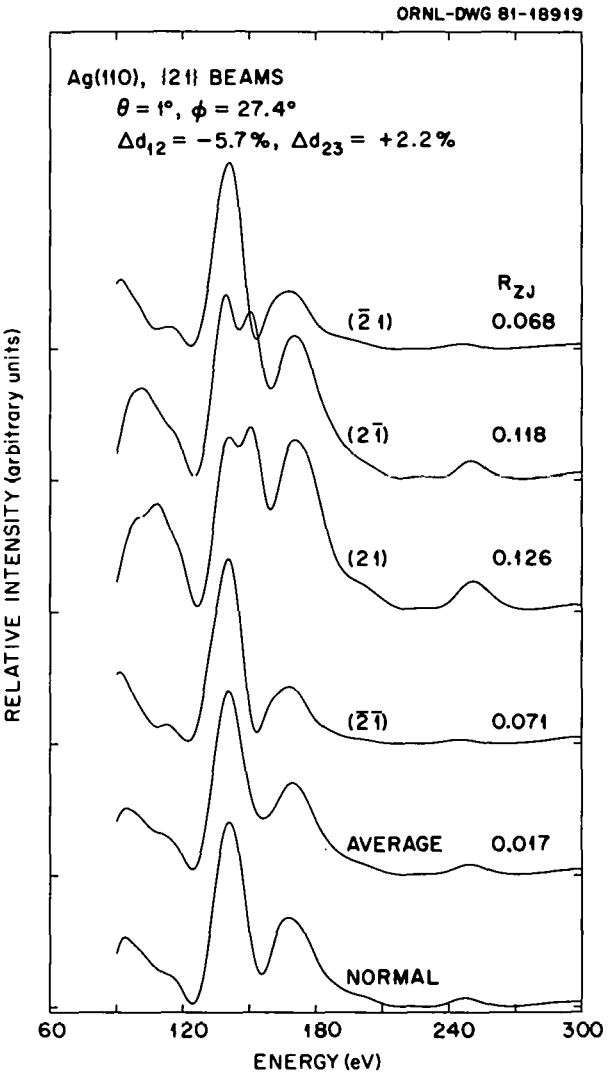

Fig. 1.5. Calculated {21} profiles for Ag(110). The four top profiles were calculated for the incident beam aligned at 1° away from the surface normal and in an azimuth 27.4° from the azimuth containing the (10) beam. The second profile from the bottom is the mean of the top four, and the bottom profile was calculated for exactly normal incidence.

misalignment, and some variations in surface topography are reduced.

1. H. L. Davis and J. R. Noonan, "Cu(100) Multilayer Relaxation," this report.
2. J. R. Noonan and H. L. Davis, "Surface-Induced Multilayer Relaxation of Ag(110)," this report.
3. E. Zanazzi and F. Jona, *Surf. Sci.* **62,** 61 (1977).

SURFACE STATES ON Ag(100)[1]

S. H. Liu

In collaboration with K.-M. Ho of Ames Laboratory, we have studied the electronic structure of the (100) surface of Ag and discovered two bands of surface states. In the meantime, D. M. Kolb of the Fritz-Haber Institute, Berlin, West Germany, has observed two absorption features on Ag(100) by using the electroreflectance (ER) technique in the infrared and visible frequency ranges. We have identified these features as excitations from the occupied bulk band states into the surface states when the latter are unoccupied. There is good agreement between theory and experiment both in the energetic positions of the absorption features and in their dependence on the bias potential.

In situ reflectance spectroscopy in the visible frequency range has been a valuable tool for detecting adsorbed species on the surface of metal electrodes. By applying a moderate bias potential (~1 V) on the electrode, it is possible to obtain an exceedingly high electric field ($\sim 10^7$ V/cm) which is concentrated near the metal surface. Inside the metal the field is screened out within a Thomas-Fermi screening length. Therefore, only the surface electronic states are affected by this field. The ER experiment, which measures the relative reflectance change of the electrode surface as a function of the potential, should be a very effective method to investigate the surface states of the metal. The energies of the surface states are very sensitive to the bias potential, and a study of their Stark shifts gives information on the spatial dependence of the electric field in the electrolyte immediately adjacent to the metal surface.

In calculating the energies of the surface states of Ag(100), we have used the self-consistent, first-principles pseudopotential method that has been found to be reliable in many surface calculations. The Ag(100) surface was investigated by setting up a periodic structure of metal slabs, each seven layers thick, separated by a 12-Å-thick vacuum region. Only the *s*- and *p*-band electrons are iterated to self-consistency. No surface reconstruction or surface relaxation has been observed for the Ag(100), and neither was included in the calculation. For the charged surface we modeled the external potential by a long-wavelength periodic potential. Upon reaching self-consistency, the potential is rapidly screened out inside the metal

by an induced charge on the surface layer. Contact was made with the experiments by relating the induced charge to the actual electrode potential through the differential capacitance.

Figure 1.6 illustrates the surface band structure of the uncharged Ag(100) surface. The corresponding bias potential is the potential of zero charge (pzc), which is −0.9 V. The band energies are measured from the Fermi level E_F. The large band gap at point L in the bulk band structure appears at point $\bar{X}$ of the surface Brillouin zone. In this gap we find two bands of surface states, labeled *A* and *B*, respectively. The empty band *A* has *s* symmetry, and optical absorption can take place by exciting electrons into it from the top of the filled bands, which have *p* symmetry. This results in an absorption feature in the ER spectrum around 3 eV, which is distinct from the bulk interband edge. The surface band *B* is mostly occupied at pzc and does not contribute to absorption.

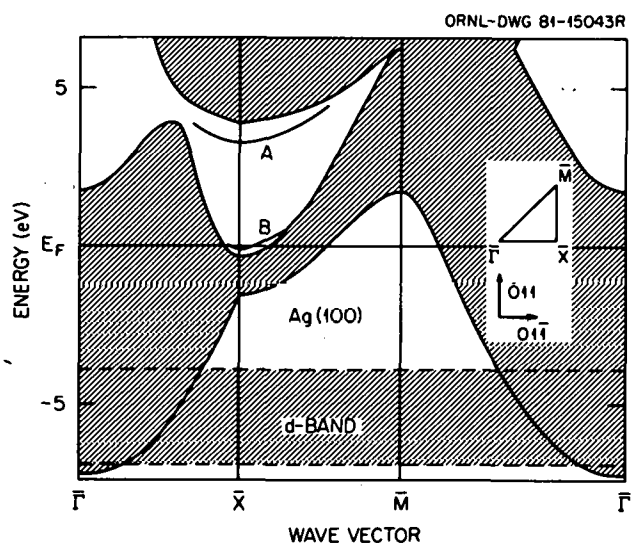

Fig. 1.6. The Ag(100) projected band structure together with surface states (marked A and B). Inset shows the orientation of the surface Brillouin zone with respect to the cubic crystal axes.

When the surface is biased positively, both surface bands *A* and *B* move upward relative to the bulk bands. At −0.5 V of bias the calculated band *A* merges into the continuum and the ER signal is seen to disappear. The bottom of band *B* is found to move above the Fermi level at −0.6 V, and at this point the entire band contributes to the absorption. Experimentally, no ER signal is detectable at −0.7 V, but a distinct signal is seen at −0.6 V. However, for band *B* the energy of the absorption maximum is not simply the energy separation between the surface band and the edge of the bulk band. These two states have the same *p* symmetry, so that an optical transition between them is forbidden. The initial state must be located by an explicit calculation of the optical matrix elements between the bulk and the surface states. In this manner the onset of optical absorption of band *B* is found to occur at 0.73 eV, in agreement with the observed value 0.72 eV. In Fig. 1.7, we show the agreement between the calculated and the observed values of the transition energy for a number of bias potentials. The upper curve is for band *A*, and the lower curve is for band *B*.

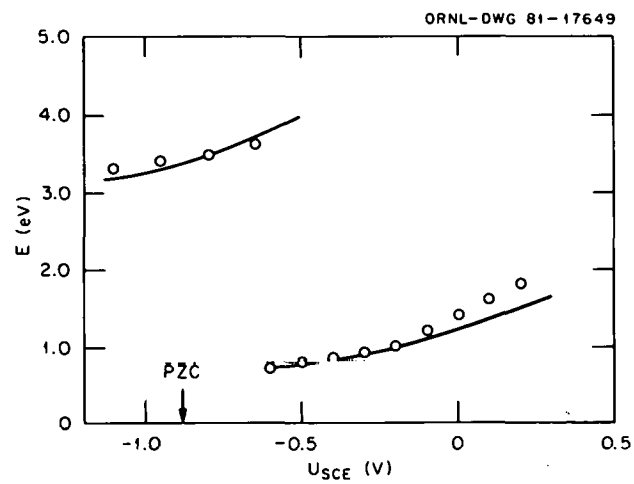

Fig. 1.7. Shift in transition energies *E* with bias potential U_{sce} for excitation into surface bands. (o o o) Experimental data; (——) theoretical data.

For both bands of surface states, the rate of energy shift with the bias potential is nearly unity. This implies that the potential relative to the bulk metal at the position of the surface state is comparable to the total potential drop across the double layer. This is totally unexpected from the classical theory of electrolyte structure, which describes a monotonic drop of potential from the metal surface to the bulk of the electrolyte. Since the surface state is only a small distance $x \sim 1$ Å away from the position of the surface atoms, it should experience only the fraction x/d of the total

potential drop, where d is the mean thickness of the compact double layer (d should be of the order of 3 Å for conditions chosen in the experiments). We contend that the unusually large Stark shift of the surface states must have its origin in the molecular structure of the electrolyte. Carnie and Chen[2] have shown that, at the interface of a metal and a dilute electrolyte, the potential near the metal oscillates around the classical value because the water molecules, which possess large dipole moments and are very effective in electrostatic screening, form alternating layers of overscreened and underscreened regions. In concentrated electrolytes such as those used in the experiment, the oscillation should be rapidly damped out due to ion screening and only an initial overshooting of the potential remains. In the overshooting region where the surface state resides, the local potential can be comparable to the bias potential and the local electric field can be two to three times as high as the average field. We therefore conclude that the electric-field distribution in the compact double layer has a far more complex structure than has so far been generally recognized, and we have demonstrated the effective use of surface studies to probe this potential distribution.

1. Summary of paper to be published.
2. S. L. Carnie and D. Y. C. Chen, *J. Chem. Phys.* **73**, 2949 (1980).

SOME EXACTLY SOLUBLE MODELS FOR SURFACES AND INTERFACES

Mark Mostoller A. K. Rajagopal[1]

A number of three-dimensional problems can be mapped, by appropriate transformations, onto a linear chain. The recursion method[2] does this for three-dimensional density of states calculations, for example. For surfaces and interfaces which preserve a two-dimensional periodicity, the surface wave-vector transform of the Hamiltonian is a linear-chain Hamiltonian for the following: electrons described by a tight-binding model, phonons in a Born–von Kármán model, and magnons in the Heisenberg model. The resulting block-tridiagonal Hamiltonians can be treated by matrix-continued-fraction techniques.[3] The mappings just discussed are exact. In addition, quite simple models can still be used to explore qualitative features of problems like the electronic structure of grain boundaries[4] or lattice vibrations at surfaces and interfaces.[5]

Most applications of linear-chain mappings have involved reductions to linear chains with nearest-neighbor interactions only, because analytic solutions are available for this case. We have derived analytic solutions for the Green's functions for several linear-chain Hamiltonians involving further neighbor interactions; these can be used as numerical checks for more elaborate calculations[3] or for direct application when appropriate. Figure 1.8 provides an example of the latter. It shows spin-wave densities of states at the fcc (110) face

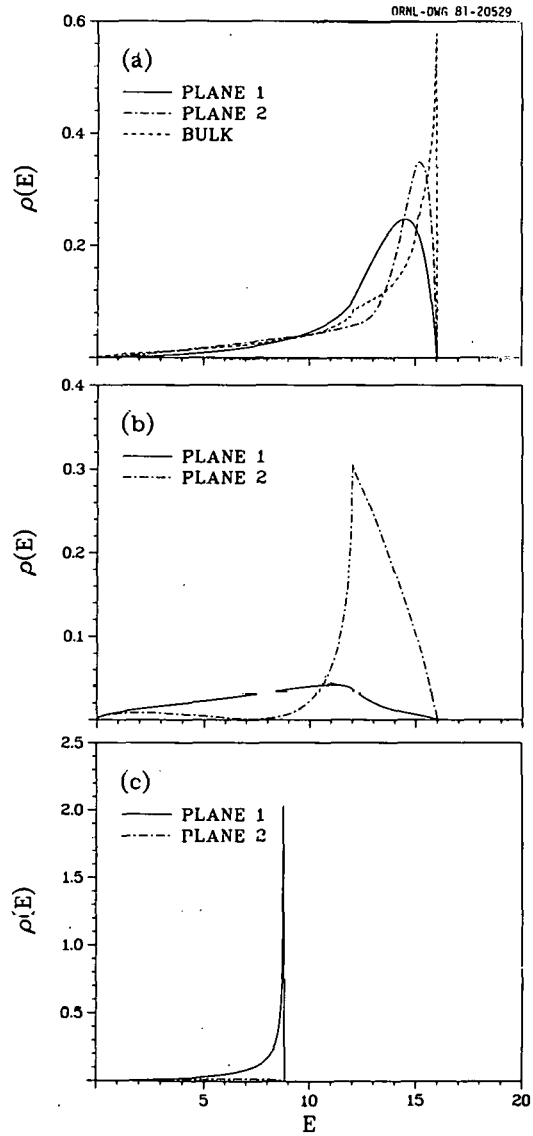

Fig. 1.8. Surface spin-wave densities of states for the fcc (110) face of a Heisenberg ferromagnet: (a) truncated bulk (Goldstone rule violated) and bulk band states, (b) surface band states (Goldstone rule satisfied), and (c) surface states.

of a Heisenberg ferromagnet with first-neighbor interactions. The results given are for $T = 0$ in the random phase approximation, with no changes in the exchange interactions at the surface save for truncation. The surface-wave-vector transform for this problem maps it onto a linear chain with first- and second-neighbor interactions, which we solve analytically and sum over surface-wave vectors to obtain the spin-wave densities of states.

---

1. Consultant from Louisiana State University, Baton Rouge, La.

2. R. Haydock, V. Heine, and M. J. Kelly, *J. Phys. C* **5**, 2845 (1972).

3. M. Mostoller and T. Kaplan, *Phys. Rev. B* **19**, 552 (1979).

4. C. E. T. Goncalves da Silva, *Solid State Commun.* **35**, 611 (1980).

5. V. R. Velasco and F. Yndurain, *Surf. Sci.* **85**, 107 (1979).

PAIR POTENTIALS AND LATTICE VIBRATIONS AT SIMPLE METAL SURFACES[1]

M. Rasolt Mark Mostoller

When a crystal is cleaved, the interactions between atoms close to or on the surface are modified. These changes are dominated by the bond rupture and the electronic redistribution at the surface, accompanied by atomic relaxation and, in some cases, by geometric rearrangement. In simple metals like Al or Na, the electronic redistribution at the surface gives rise to two kinds of effects on the ions. The first involves the static configuration of the relaxed surface and corresponds to the volume-dependent terms that make by far the largest contributions to the bulk potential energy. The large electronic density variations at the surface make a linear-response treatment (or equivalently, a pair-potential description) inadequate to determine the relaxation. Other approaches have to be used; short of surface total energy calculations, some of the more important considerations have been discussed by Finnis and Heine[2] and by Landman, Hill, and Mostoller.[3]

The second effect of the electronic redistribution involves small displacements of the ions around their relaxed, static configuration in the surface region, which is what is needed to describe surface vibrations. Here it is appropriate to use a linear-response approach, just as in the bulk, but with the electronic response function changed to reflect the presence of the surface. In this framework, the relaxation can be treated as externally given and taken either from experiment or from other calculations. We have examined the linear-response effects by approximating the electrons by the semiclassical infinite barrier model and by determining the screened potential between point ionic charges within this model. For small displacements in the bulk, we retrieve the well-known semiclassical, or Thomas-Fermi, pair potentials. In the surface region, the electronic screening is reduced, and the pair potentials change. Since both the surface and bulk pair potentials are treated in the same semiclassical approximation, we should be able to estimate the magnitude and range of the surface screening effects relative to the bulk pair potentials. The model is not intended to give quantitatively reliable surface or bulk pair potentials but rather to investigate trends in surface screening effects.

Our calculations suggest that for an electron density corresponding to Al, differences from bulk screening are negligible at distances greater than ~ 2.5 Bohr radii from the barrier and, for the lower electron density of Na, at distances greater than $\sim 3.5\ a_0$. In Al, this means that surface screening effects are significant for the (110) surface, for which $z = 1.35\ a_0$ is the unrelaxed position of the first plane of atoms relative to the barrier, but that reductions in the screening are relatively unimportant for the (001) and (111) faces. For the bcc metal Na, differences from the bulk potential appear to be large for the (111) surface and still appreciable for the first plane in the (001) surface.

Lattice vibrations at surfaces differ from those in the bulk, because atoms in the surface region have missing neighbors and because the interactions between pairs of atoms near the surface change. For our purposes, these changes arise from two sources. The first, which will be referred to as relaxation, comes from taking a model for the interatomic forces in the bulk (pair potentials here) and from including the effects of contraction or expansion in interlayer spacing in the surface region within this model. The second arises from changes in the electronic response near the surface and will be referred to as screening. From our semiclassical model, we can estimate the contributions of both effects to force constant changes in the surface region and thence to the densities of

states for surface vibrations. The changes in force constants due to relaxation are computed simply by decreasing the interatomic distances in the bulk Thomas-Fermi potentials and are wholly interlayer in nature. Screening changes are primarily intralayer, although there are also nonnegligible interlayer effects for surfaces like Al(110) and Na(111).

Figure 1.9 shows model densities of vibrational states for the first plane in the Al(110) surface, assuming a 10% inward relaxation of the first layer. For this example, cleavage, relaxation, and screening each have a significant impact. Cleavage and screening produce a large shift of spectral densities to lower frequencies relative to the bulk, while inward relaxation stiffens the first-second and first-third layer interactions, thereby opposing this downward shift. Screening and relaxation both give force constant changes of as much as 40–50%. It is clear that any approach based solely on bulk pair potential forms cannot give reliable results for lattice vibrations or relaxation at surfaces where the reduced screening is significant.

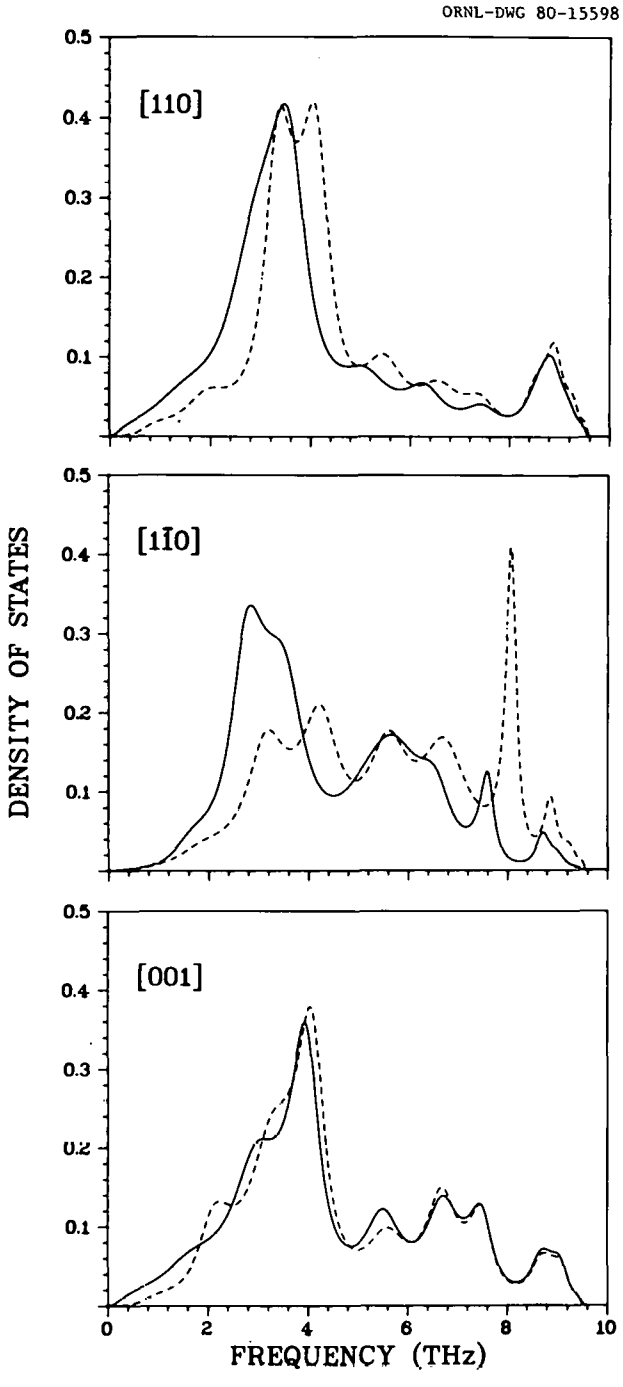

Fig. 1.9. Normalized densities of states for vibrations along the [110], [1$\bar{1}$0], and [001] directions in the first plane at the Al(110) surface. An inward relaxation of 10% by the first plane is assumed. The dashed curves give results including only cleavage and relaxation. The full curves include the screening contributions as well.

1. Summary of paper: *Phys. Rev. B* **23**, 3774 (1981).
2. M. W. Finnis and V. Heine, *J. Phys. F* **4**, L37 (1974).
3. U. Landman, R. N. Hill, and M. Mostoller, *Phys. Rev. B* **21**, 448 (1970).

ELECTRONIC AND MAGNETIC PROPERTIES

CALCULATION OF NEUTRON CROSS SECTIONS FOR INTERBAND TRANSITIONS IN SEMICONDUCTORS[1]

J. F. Cooke J. A. Blackman[2]

The introduction of the new high-flux neutron sources, such as SNS at the Rutherford and Appleton Laboratories, England, and the WNR facility at Los Alamos National Laboratory, in the next few years will make it possible to perform experiments that cannot be carried out at present. One such experiment that has been proposed is the

single-particle excitation of electrons across the band gap in a semiconductor. This is an inelastic scattering experiment in which energy and momentum transfers would be measured, but, unlike previous inelastic measurements, the energy transfer would be in the eV range. Some considerations about the spectrometry for an experiment of this type have already been made by Allen, Mitchell, and Sinclair.[3] If such an experiment proves feasible, one would hope that it would be a useful tool in the experimental determination of band structure.

We have carried out an extensive series of calculations of the total magnetic scattering cross section for electronic excitations in semiconductors to aid in an assessment of the feasibility of the experiment. The interaction of the neutrons with the electrons is the familiar magnetic one in which the cross section comprises spin and orbital parts:

$$\frac{d^2\sigma}{d\Omega dE} = \frac{d^2\sigma}{d\Omega dE}\bigg|_{\text{spin}} + \frac{d^2\sigma}{d\Omega dE}\bigg|_{\text{orbit}}, \qquad (1)$$

$$\frac{d^2\sigma}{d\Omega dE}\bigg|_{\substack{\text{spin}\\\text{orbit}}} = 290\left|\frac{\mathbf{k}_f}{\mathbf{k}_i}\right| \times \sum_{\substack{nm\\\mathbf{k}}} |F_{nm}^{(s)}(\mathbf{k},\mathbf{Q})|^2 (f_{n\mathbf{k}} - f_{m\mathbf{k}+\mathbf{Q}}) \times \delta[E + E(n\mathbf{k}) - E(m\mathbf{k}+\mathbf{Q})]\,\text{mb/sr-eV}, \qquad (2)$$

where $\mathbf{Q} = \mathbf{k}_f - \mathbf{k}_i$ is the momentum transfer in units of $\hbar$, E is the energy transfer, $E(n\mathbf{k})$ is the electronic energy for band n and wave vector $\mathbf{k}$, and $f_{n\mathbf{k}}$ is the Fermi occupation number. $F^{(s)}$ and $F^{(o)}$ are the spin and orbit form factors, respectively.

Results for the inelastic neutron scattering cross section for Si and Ge have been obtained for $\mathbf{Q}$ along [100], [111], and [110] and have been restricted to the first Brillouin zone. The calculations incorporate the full-band structure (obtained from an empirical pseudopotential method) for the four valence and four lowest energy conduction bands, with higher energy bands being neglected. This should ensure that we obtain the total scattering for energies on the order of 10 eV or less, which is sufficient for our needs. It should be emphasized that one of the main purposes of these calculations is to obtain the magnitude of the cross sections in absolute units (mb/sr-eV). All factors in Eq. (2) have been included apart from the ratio $|\mathbf{k}_f|/|\mathbf{k}_i|$, which depends on the experimental configuration. The neutron scattering cross section was obtained by numerically solving the pseudopotential band structure equations and evaluating the Brillouin zone sums using the tetrahedron method.

A comparison of the spin and orbital scattering cross sections for $\mathbf{Q} = (0.4375, 0.0, 0.0)$ is shown in Fig. 1.10 for Si and in Fig. 1.11 for Ge. The total scattering is the sum of these two contributions. Notice that there is a considerable amount of structure in both components of the scattering and that the orbital part is significantly larger than the spin part. The dominance of the orbital part occurred at all values of $\mathbf{Q}$ examined but was less for large $\mathbf{Q}$. Another important feature of these results is that there is not a dramatic rise in the scattering intensity for E near the indirect gap energy (which in our pseudopotential parameterization is about 0.9 eV for Si and 0.8 eV for Ge), as one might expect. It is clear, therefore, that no direct information about the band gap can be determined from inelastic neutron scattering experiments.

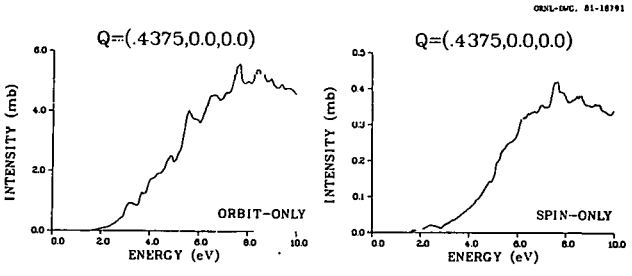

Fig. 1.10. Comparison of spin and orbital scattering cross sections for Si. Notice difference in scales.

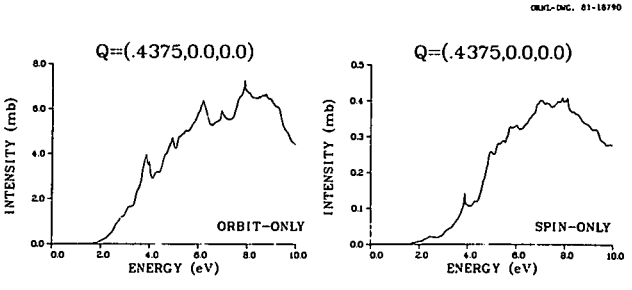

Fig. 1.11. Comparison of spin and orbital scattering cross sections for Ge. Notice difference in scales.

Fortunately, however, it appears from calculations at various values of Q along [100], [110], and [111] that the cross sections have sufficient structure and variation with Q that the band structure, and thus the wave-vector-dependent band gap, could in principle be determined indirectly. This could be accomplished by varying the pseudopotential parameters to provide the best overall agreement between theory and experiment. This procedure could also provide an indirect check on the validity of the pseudopotential theory.

Finally, we indicate the considerations that should be made in assessing the instrumental requirements necessary if neutron scattering is to be a useful technique in band structure determination. Clearly, there are questions of both intensity and resolution. As can be seen in Figs. 1.10 and 1.11, the overall intensities are very small. Intensities at other values of $Q = |\mathbf{Q}|$ can be roughly estimated by assuming a variation like Q^{-2}. Thus, ideally, one should attempt to make Q as small as possible. Also note that, although the band gaps in Si and Ge are of the order of 1 eV, the intensity remains negligible until the energy transfer is about 3 eV. To get a significant amount of useful information, it would be desirable to measure cross sections up to values of E equal to 7 or 8 eV.

The problem of determining band structure parameters precisely is similar to the one of distinguishing between the cross sections for the two similar band structures of Si and Ge. Model calculations of the type we have carried out will not only indicate the regions of energy and momentum transfer that can be studied optimally but also should help in the assessment of the resolution of E and Q required to make the proposed experiments useful. It appears from the results we have obtained that the experiment proposed by Allen, Mitchell, and Sinclair[3] is going to be a difficult one to perform. The successful measurements of these relatively small cross sections would, however, provide important information about the conduction bands in semiconductors which cannot, at present, be obtained from any other source.

1. Summary of paper to be published.

2. Guest scientist from University of Reading, Reading, England.

3. D. R. Allen, E. W. J. Mitchell, and R. N. Sinclair, *J. Phys. E.* **13** 639 (1980).

CALCULATION OF THE TEMPERATURE-DEPENDENT MAGNETIC FORM FACTOR FOR NICKEL

J. F. Cooke

Recent polarized-neutron diffraction experiments have revealed a relatively strong temperature dependence of the magnetic form factor or, equivalently, the unpaired-spin density in ferromagnetic nickel.[1] Results from these measurements have also established unambiguously that the symmetry character of the moment changes with temperature. For example, it was found that the fraction of unpaired-spin electrons with e_g symmetry increased by about 40% over the temperature range from zero to T_c.

These unusual temperature-dependent effects can be understood, at least qualitatively, in terms of the itinerant theory of magnetism. According to the simplest approximation of this theory, the electrons which are responsible for the unpaired-spin distribution occupy spin-split energy bands. At low temperatures, results from numerical calculations of the dynamic susceptibility for nickel based on this theory have been shown to be in excellent agreement with the spin dynamics obtained from inelastic neutron scattering experiments and with band structure information from ARPES.[2] A simple extrapolation of the low-temperature theory to high temperatures suggests that the temperature dependence of the magnetic form factor could result from the explicit temperature dependence of the Fermi occupation function (i.e., Fermi surface smearing and/or a weak intrinsic temperature dependence of the spin-splitting energy Δ). Results from calculations of the dynamic susceptibility have already shown that Fermi surface smearing is important and that Δ may indeed be slightly temperature dependent.

To assess the importance of these two effects on the magnetic form factor, numerical calculations of

the symmetry components of the total moment as a function of temperature have been initiated for nickel. The symmetry decomposition of the total moment follows from the expansion of the wave function in terms of symmetry orbitals $\phi_\mu(\mathbf{r})$,

$$\psi_{n\mathbf{k}\sigma}(\mathbf{r}) = \sum_\mu a_{n\mu\sigma}(\mathbf{k})\phi_\mu(\mathbf{r}) \ , \qquad (1)$$

where the $\{a_{n\mu\sigma}(\mathbf{k})\}$ are expansion coefficients; $(n\mathbf{k}\sigma)$ refers to band, wave vector, and spin indices, respectively; and μ is the symmetry index. The number of unpaired-spin electrons with symmetry $\mu(N_\mu)$ is defined by

$$N_\mu(T) = \frac{1}{N} \times \sum_{n\mathbf{k}} \{|a_{n\mu\uparrow}(\mathbf{k})|^2 f_{n\mathbf{k}\uparrow} - |a_{n\mu\downarrow}(\mathbf{k})|^2 f_{n\mathbf{k}\downarrow}\} \ , \qquad (2)$$

where $f_{n\mathbf{k}\sigma}$ is the Fermi occupation function. The band structure (and wave functions) which was used in these calculations is the same one that was used in the earlier susceptibility calculations.[2] The $N_\mu(T)$ were evaluated first by generating the symmetry-projected density of states:

$$\rho_{\mu\sigma}(E) = \frac{1}{N}\sum_{n\mathbf{k}} |a_{n\mu\sigma}(\mathbf{k})|^2 \delta[E - E(n\mathbf{k}\sigma)] \ , \qquad (3)$$

where $\delta(x)$ is the Dirac delta function, and then by using

$$N_\mu(T) = \int_0^{E_f} \frac{\rho_{\mu\uparrow}(E) - \rho_{\mu\downarrow}(E)}{e^{(E-E_f)/k_BT} + 1} dE \ . \qquad (4)$$

In Eq. (4), E_f is the Fermi energy and k_B is the Boltzmann constant. The tetrahedron method was used to evaluate the Brillouin zone sum in Eq. (3).

Let us consider first only the explicit temperature dependence of the Fermi function. A comparison between theory and experiment of $N_{e_g}(T/T_c)/N_{e_g}(o)$, the relative number of unpaired-spin e_g electrons, as a function of temperature is shown in Fig. 1.12. Clearly, Fermi surface smearing is an important effect which can account for most, but probably not all, of the temperature dependence. Agreement between theory and experiment can be achieved by forcing the spin-splitting energy to decrease slightly with increasing temperature (<5% at 0.8 T_c). This is consistent with results obtained from calculations of the spin dynamics.[3]

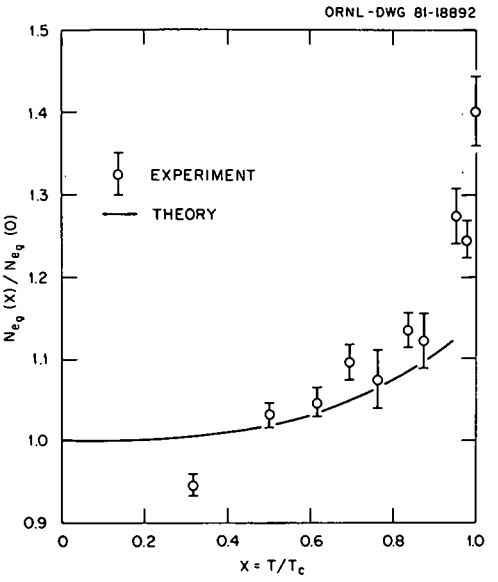

Fig. 1.12. Comparison of theoretical and experimental results for a relative number of e_g-symmetry electrons as a function of the reduced temperature x. Theoretical curve includes Fermi surface smearing only.

Unfortunately, at present there does not exist a tractable systematic approach for calculating the spin-polarized band structure as a function of temperature. It is possible, however, to carry out a consistency check of this temperature-extrapolated approach by determining the two d-symmetry band structure parameters, which are defined in ref. 2, to yield the correct moment and symmetry character of the moment at each temperature. This procedure would uniquely determine the band structure (and spin-splitting energy) at each temperature, which in turn could be used to calculate uniquely the spin dynamics. A comparison of the calculated spin dynamics with inelastic neutron scattering results would provide the consistency check. This study is currently under way. In view of the results obtained so far, it appears that the temperature dependence of the unpaired-spin density for nickel can be described reasonably well in terms of a temperature-extrapolated itinerant electron model which incorporates Fermi surface smearing and a slight decrease in the spin-splitting energy (<5% at T_c) with increasing temperature.

1. J. W. Cable, *Phys. Rev. B* **23**, 6168 (1981).

2. J. F. Cooke, J. W. Lynn, and H. L. Davis, *Phys. Rev. B* **21**, 4118 (1980).
3. J. F. Cooke, *J. Appl. Phys.* **52**, 1640 (1981).

EXCHANGE SPLITTING OF FERROMAGNETIC Ni WITHIN THE LOCAL POTENTIAL APPROXIMATION [1]

M. Rasolt H. L. Davis

The quasiparticle excitation spectrum of a many fermion system is given by locating the poles of a single-particle propagator.[2,3] Equivalently, the self energy $\Sigma_{i,j}(\mathbf{r}, \mathbf{r}', E)$ generates these excitations as solutions of the well-known Dyson equation.[2,3] This self energy is a nonlocal operator in space coordinates $\mathbf{r}$ and $\mathbf{r}'$ and spin coordinates i and j; and it is, in general, complex in the energy E of the quasiparticle. In principle, it contains contributions from all the collective excitations. For example, for an itinerant ferromagnet it should include both charge (plasmon) as well as magnetic (magnon) fluctuations.

At present, the most widely used approximation for $\Sigma_{i,j}(\mathbf{r}, \mathbf{r}', E)$ is the local density approximation (LDA).[4] It involves replacing $\Sigma_{i,j}(\mathbf{r}, \mathbf{r}', E)$ by an energy-independent form which is diagonal in $\mathbf{r}$ and $\mathbf{r}'$. In this form, it is the same exchange-correlation potential $v_{i,j}^{xc}(\mathbf{r})$ which is used in the calculation of the ground state properties of a nonuniform spin-polarized system. It is also important to note that $v_{i,j}^{xc}(\mathbf{r})$ can be further approximated by only considering the first term in a gradient expansion.[4–6]

Ferromagnetic Ni is one example where discrepancies exist between many features of its calculated LDA band structure (i.e., quasiparticle spectra) and the results of experimental measurements. A specific discrepancy with Ni concerns the magnetic exchange splitting between bands of different spin. Calculated values for this splitting have always been about twice the value inferred from experiment (see, e.g., refs. 7–9). Recognizing that $v_{i,j}^{xc}(\mathbf{r})$ employed in the band structure calculations could be inappropriate, we have focused some recent attempts on calculating $\Sigma_{i,j}(\mathbf{r}, \mathbf{r}', E)$ from band structures generated in the LDA.[10] Such nonlocal Σ_{ij} have been shown to make major modifications in the LDA band structure of both simple[11,12] as well as nonsimple metals[10] and semiconductors.[13]

Discrepancies could also originate from the low-order treatment of $v_{i,j}^{xc}(\mathbf{r})$ (especially in a nonsimple metal like Ni). To investigate this possibility, we have calculated the lowest order inhomogeneity corrections to $v_i^{xc}(\mathbf{r}) = v_{ii}^{xc}(\mathbf{r})$, which may be written schematically as

$$v_i^{xc}(\mathbf{r}) = \epsilon_{xc}[n_1(\mathbf{r}), n_2(\mathbf{r})] + [n_1(\mathbf{r}) + n_2(\mathbf{r})] \times \frac{\partial}{\partial n_i(\mathbf{r})} \epsilon_{xc}[n_1(\mathbf{r}), n_2(\mathbf{r})] + \text{gradients of } n_i(\mathbf{r}) \quad (1)$$

The $n_i(\mathbf{r})$ corresponds to the spin-up and spin-down densities.

We have performed two distinct KKR band structure calculations for ferromagnetic Ni. The first used for $v_i^{xc}(\mathbf{r})$ only the first two terms in Eq. (1), with $\epsilon_{xc}[n_1(\mathbf{r}), n_2(\mathbf{r})]$ being the form evaluated in ref. 5. The second calculation used all of Eq. (1), including the gradient corrections. In the first calculation excellent agreement was obtained with the band structure of ref. 14. In the second calculation we found that the gradient contributions added significant corrections to $v_i^{xc}(\mathbf{r})$. More precisely, the difference in the magnitude of $v_1^{xc}(\mathbf{r}) - v_2^{xc}(\mathbf{r})$ is of the order of the exchange splitting. However, these corrections were both positive and negative as $\mathbf{r}$ increased from zero to the muffin tin radius, with the result that the final effect on the band structure was negligible. For example, the exchange splitting was essentially the same in both calculations. We must then conclude that the discrepancies between calculated band structures and experimental results for Ni are more likely to originate in the local treatment of $\Sigma_{ii}(\mathbf{r}, \mathbf{r}', E)$ rather than in a poor representation of the ground state potential $v_i^{xc}(\mathbf{r})$ as derived from electron-gas forms. In fact, this conclusion is in agreement with the strong $\mathbf{k}$ dependence of the exchange splitting found in the work of Cooke, Lynn, and Davis.[15] Of course, the gradients have been evaluated in the high-density limit,[6] and the convergence of the gradient expansion has not as yet been completely assessed. However, for the purpose of trends and order-of-magnitude estimates, the above calculation is likely to be sufficient.

---

1. Summary of paper: *Physics Letters A* (in press).

2. L. Hedin and S. Lundquist, *Solid State Physics*, vol. 23, ed. by H. Ehrenreich, F. Seitz, and D. Turnbull, Academic Press, New York, 1969.
3. L. J. Sham and W. Kohn, *Phys. Rev.* **145**, 561 (1966).

4. W. Kohn and L. J. Sham, *Phys. Rev.* **140,** A1133 (1965).
5. U. von Barth and L. Hedin, *J. Phys. C* **5,** 1629 (1972).
6. M. Rasolt, *Phys. Rev. B* **16,** 3234 (1977).
7. L. Kleinman, *Comments Solid State Phys.* **10,** 29 (1981).
8. F. J. Himpsel, J. A. Knapp, and D. E. Eastman, *Phys. Rev. B* **19,** 2919 (1979).
9. C. S. Wang and J. Callaway, *Phys. Rev. B* **15,** 298 (1977).
10. L. Kleinman and K. Mednick, 1981 preprint; *Bull. Am. Phys. Soc.* **26,** 206 (1981).
11. For example, see M. Rasolt and S. H. Vosko, *Phys. Rev. B* **10,** 4195 (1974); M. Rasolt, S. B. Nickerson, and S. H. Vosko, *Solid State Commun.* **16,** 827 (1975).
12. A. H. MacDonald, *J. Phys. F* **10,** 1737 (1980).
13. For example, see E. O. Kane, *Phys. Rev. B* **4,** 1493 (1971).
14. V. L. Moruzzi, J. F. Janak, and A. R. Williams, p. 180 in *Calculated Electronic Properties of Metals,* Pergamon Press, New York, 1978.
15. J. F. Cooke, J. W. Lynn, and H. L. Davis, *Phys. Rev. B* **21,** 4118 (1980).

EXCHANGE AND CORRELATION ENERGY OF NONUNIFORM ELECTRONIC SYSTEMS

M. Rasolt D. J. W. Geldart[1]

Statistical forms for the ground state exchange and correlation energy[2] are essential for attempts to calculate various atomic, bulk, and surface properties of nonuniform electron systems. Even though such forms have been widely applied, their accuracy has not been fully examined until recently.[3,4] We have initiated such a study for widely different systems, such as metal surfaces, metallic bulk, and atoms.

The general form for the exchange and correlation energy E_{xc} can be written as[3,4]

$$E_{xc} = N \int \frac{d^3q}{(2\pi)^3} E_{xc}(\mathbf{q})$$

$$= \frac{N}{2} \int \frac{d^3q}{(2\pi)^3} v(q) \int_0^1 d\lambda [S_\lambda(\mathbf{q},\mathbf{q}) - 1] \ , \quad (1)$$

with

$$S_\lambda(\mathbf{q},\mathbf{q}) = \int d^3r \int d^3r' e^{-i\mathbf{q}\cdot\mathbf{r}} e^{i\mathbf{q}\cdot\mathbf{r}'} S_\lambda(\mathbf{r},\mathbf{r}') \ , \quad (2)$$

where $v(q) = 4\pi e^2/q^2$ and λ is the usual coupling constant.

Statistical approximations (such as the LDA) are based on forms structured around the local electronic density variation. For example, the LDA is given by

$$E_{xc}^{LD} = \int d^3r \, n(\mathbf{r}) E_{xc}[n(\mathbf{r})] \ , \quad (3)$$

where $E_{xc}[n(\mathbf{r})]$ is the exchange-correlation energy per electron of a homogeneous electron gas of density $n(\mathbf{r})$. Additional gradient corrections are also given by the local behavior of the density $n(\mathbf{r})$; that is,

$$E_{xc}^{g} = \int d^3r \, B_{xc}[n(\mathbf{r})] |\nabla n(\mathbf{r})|^2 \ . \quad (4)$$

Equation (3) can be expressed in terms of the individual wave-vector components $\mathbf{q}$ of the interparticle interaction $v(q)$; i.e,

$$E_{xc}^{LD} = \frac{1}{2} \int \frac{d^3q}{(2\pi)^3} \int d^3r \times \int_0^1 d\lambda \, v(q) n(\mathbf{r}) \{S_\lambda^h[\mathbf{q}, n(\mathbf{r})] - 1\} \ , \quad (5)$$

where $S_\lambda^h[\mathbf{q}, n(\mathbf{r})]$ is the structure factor of the homogeneous electron gas with local density $n(\mathbf{r})$. Similarly, by expanding Eq. (1) to second order in an arbitrary external potential, E_{xc} of Eq. (4) can be expressed in terms of the individual $\mathbf{q}$ components. If Eqs. (1) and (5) are compared, it is expected, on physical grounds, that as $\mathbf{q}$ gets smaller, more and more of the global behavior of $S_\lambda(\mathbf{r}, \mathbf{r}')$ gets sampled and the local-like approximations of Eqs. (3) and (4) become less valid. This is demonstrated schematically for atomic systems by Fig. 1.13, where the results of the $\mathbf{q}$ decomposition of Eq. (4) are sketched for atomic-like density profiles. For microscopic size systems (e.g., atoms), the structure factor $S_\lambda(\mathbf{r}, \mathbf{r}')$ must be localized within a finite region (i.e., the size of the system), and it follows from the conservation of particles that $\lim_{\mathbf{q}\to 0} [(S_\lambda(\mathbf{q}, \mathbf{q}) - 1]$ must go to zero. From Eq. (1), $E_{xc}(q)$ must go to zero, as well, when $q \to 0$.

The solid curve in Fig. 1.13 is indicative of the behavior of $E_{xc}^{g}(q)$ [as given by Eq. (4)]. Notice that the $q \to 0$ limit tends to be a constant. The dashed curves are the expected behavior at small q for the exact $E_{xc}(q)$ [Eq. (1)] for two sys-

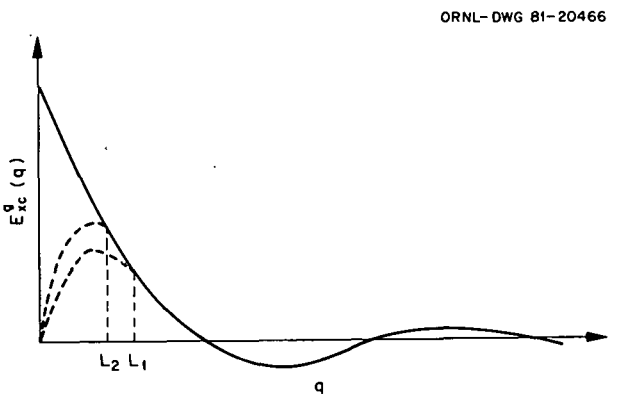

Fig. 1.13. The decomposition of the gradient contribution $E^q_{xc}(q)$ in Eq. (4) as a function of wave vector q. The solid curve is the decomposition following Eq. (4), and the two dashed curves are the expected small q behavior of the exact form [Eq. (1)] for two microscopic systems of size L_1 and L_2.

tems of size L_1 and L_2. We conclude, therefore, that Eq. (4) must overestimate (and perhaps even give the wrong sign) the magnitude of E^g_{xc} in atomic systems. This result was first observed by Ma and Brueckner,[5] and our results provide a clear explanation for this behavior. The uniform electron gas, therefore, might not provide a universal structure for $E_{xc}[n(\mathbf{r})]$ which can be used blindly in arbitrary systems.

1. Guest scientist from Dalhousie University, Halifax, Nova Scotia, Canada.

2. J. C. Slater, *Phys. Rev.* **81,** 385 (1951); P. Hohenberg and W. Kohn, *Phys. Rev.* **136,** 864 (1964).

3. J. Harris and R. O. Jones, *J. Phys. F* **4,** 1170 (1974); E. Wikborg and J. E. Inglesfield, *Solid State Commun.* **16,** 335 (1975).

4. M. Rasolt, G. Malmstrom, and D. J. W. Geldart, *Phys. Rev. B* **20,** 3012 (1979); M. Rasolt and D. J. W. Geldart, *Phys. Rev. B* **21,** 3158 (1980).

5. S. K. Ma and K. Brueckner, *Phys. Rev.* **165,** 18 (1968).

LATTICE RELAXATION AROUND AN H IMPURITY IN AN Al METAL HOST

F. Perrot[1] M. Rasolt

Since nonlinear screening effects occur when H is placed in Al, the pair-potential description for the H-Al interaction is inadequate. Thus, the usual simplifications provided by the lattice static method are no longer appropriate. Therefore, a calculation for the relaxation of the Al ions around an H impurity was performed within the spherical solid model (SSM).

The relaxation energy ΔH^{re} is defined by

$$\Delta H^{re} = H_1\{\mathbf{R}_i\} - H_1\{\mathbf{R}_{io}\} \ , \qquad (1)$$

where $\mathbf{R}_{io}$ are the positions of the Al ions in the perfect lattice and $\mathbf{R}_i = \mathbf{R}_{io} + \delta_i$, with δ_i being the lattice relaxations. $H_1\{\mathbf{R}_{io}\}$ and $H_1\{\mathbf{R}_i\}$ are the energies of the unrelaxed and relaxed lattice, respectively, in the presence of the proton impurity. $H_1\{\mathbf{R}_i\}$ contains the charge response relaxation due to the electrostatic, kinetic, exchange and correlation, and Madelung energies.

It is as yet virtually impossible to evaluate Eq. (1) exactly for relaxations in the presence of a strong scatterer like H. Therefore, Eq. (1) has been evaluated within the SSM. However, simply to take Eq. (1) and approximate it within the SSM by

$$\Delta H^{re} = (H_1\{\mathbf{R}_i\} - H_1\{\mathbf{R}_{io}\})_{\mathrm{SSM}} \ , \qquad (2)$$

is incorrect, since such an approximation would obviously produce artificial lattice displacements at distances significantly removed from the H sites. The correct procedure is to write Eq. (1) as

$$\Delta H^{re} = (H_1\{\mathbf{R}_i\} - H_1\{\mathbf{R}_{io}\})_{\mathrm{SSM}} - (H_0\{\mathbf{R}_i\} - H_0\{\mathbf{R}_{io}\})_{\mathrm{SSM}} + H_0\{\mathbf{R}_i\} - H_0\{\mathbf{R}_{io}\} \ . \qquad (3)$$

Equation (3) is obtained from Eq. (2) by formally adding and subtracting the quantity $H_0\{\mathbf{R}_i\} - H_0\{\mathbf{R}_{io}\}$ where $H_0\{\mathbf{R}_i\}$ is the energy of the perfect lattice displaced by the *same* δ_i's. When Eq. (3) is used, *only* differences relative to the perfect and nonperfect lattice are evaluated within the SSM. The last term in Eq. (3) is then evaluated via the usual form factors and structure factors for the perfect lattice (in the pair-potential approximation)[2] *without* making the SSM approximation. Since the δ_i's are expected to be small, ΔH^{re} can be expanded to second order in δ_i and then minimized with respect to the displacements to yield a set of linear equations for the relaxations.

Of the four terms entering $H_1\{\mathbf{R}_i\}$ in Eq. (3), the most difficult to treat are the changes in the kinetic and electrostatic energies upon relaxation.

These were treated by calculating response functions appropriate to the electron density surrounding the proton in the unrelaxed Al lattice, using a statistical representation (Thomas-Fermi-like) for the kinetic energy.[3] Results are listed in Table 1.1. Detailed experimental results are not yet available for H in Al. A theoretical and experimental comparison[4] should, however, be possible in the near future.

1. Commissariat a l'Energie Atomique, Saint Georges, France.
2. W. A. Harrison, *Pseudopotentials in the Theory of Metals,* Benjamin, New York, 1966.
3. L. M. Kahn, F. Perrot, and M. Rasolt, *Phys. Rev. B* **21,** 5594 (1980).
4. J. Chappernt, CENG, Grenoble, France, private communication.

THE POTENTIAL SURFACE OF H IN Al

L. M. Kahn[1] F. Perrot[2] M. Rasolt

A proton placed in a metallic host creates, in its vicinity, both a polarization of the metal's electronic charge distribution as well as a relaxation of the positions of the host atoms. These two effects are responsible for the important differences which exist for H absorption in a variety of metallic hosts. Here we consider the detailed potential surface for H placed in an unrelaxed Al host.

The calculation of the potential surface was complicated by the fact that the proton is a very strong scatterer, and, consequently, it creates a large polarization in the surrounding electronic distribution. Thus, the usual simplifications provided by linear screening are inappropriate, so that the full nonlinear solution for the charge density distribution around H was required. The calculations were done within the SSM, where the coordinate system was centered at the proton site. The potential of the Al lattice around the proton was approximated by only its spherical component. That is, let

$$V(\mathbf{r}) = \sum_i V_{\mathrm{Al}}(\mathbf{r} + \tau - \mathbf{R}_i) = \sum_{l,m} V_{l,m}(\mathbf{r}) Y_{l,m}(\theta, \phi) \ , \quad (1)$$

where τ is the position of the proton (in the unit cell) and the $\mathbf{R}_i$ are the positions of the Al ions. Use was made of only the $l = 0$ component in Eq. (1). The spherical charge density $n(r)$ was then calculated via a self-consistent Hartree-like set of equations. The response of the electrons to the nonspherical components of the Al potential [i.e., $V_{l\neq 0,m}(r)Y_{l,m}(\theta, \phi)$] was obtained in an approximate fashion by developing polarization functions appropriate to the spherical charge density $n(r)$ surrounding the proton.[3] In Fig. 1.14 the potential surface of H in an unrelaxed Al lattice is illustrated schematically. From Fig. 1.14 it is noted that a slight preference exists for the octahedral site, for which a heat of solution of 0.59 eV and an activation energy of 0.5 eV are obtained. From the curvature of the potential surface around the octahedral site, it is estimated that the zero-point

Table 1.1. Lattice relaxation δ_i for *H* in Al

The two series (separated by double lines) of results refer to *H* in the octahedral position and in a vacancy, respectively. In each case, the convergence may be appreciated by comparing the results of two calculations, one with three and the other with five shells. The last row gives the results obtained with linear screening of the proton in the octahedral site

Shell	100	111	210	221	300	ΔH^{re} eV
$\delta_i \times 10^2$	2.24	−0.24	0.25			−0.059
$\delta_i \times 10^2$	2.24	−0.25	0.26	0.01	0.06	−0.060
Shell	**110**	**200**	**211**	**220**	**310**	ΔH^{re} eV
$\delta_i \times 10^2$	−2.30	−0.30	−0.18			−0.138
$\delta_i \times 10^2$	−2.55	−0.35	−0.20	−0.41	−0.05	−0.155
$\delta_i \times 10^2$	3.52	0.03	0.34	0.03	0.08	−0.168

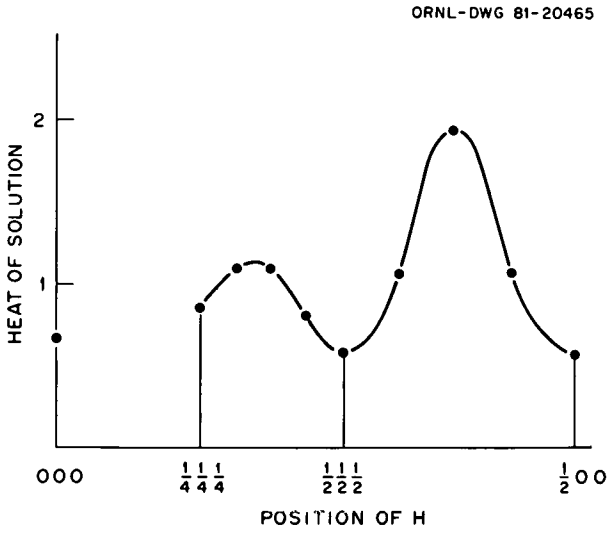

Fig. 1.14. Variation of the heat of solution with the position of H in the fcc lattice of Al.

energy is 0.147 eV. These results are in good agreement with recent experimental measurements.[4]

1. University of Virginia, Charlottesville, Va.
2. Commissariat a l'Energie Atomique, Saint Georges, France.
3. L. M. Kahn, F. Perrot, and M. Rasolt, *Phys. Rev. B* **21**, 5594 (1980).
4. S. Matsuo and T. Hirata, *Trans. Natl. Res. Inst. Met.* (JPN) **11**, 22 (1969).

RANDOM ALLOYS WITH SHORT-RANGE ORDER[1]

Theodore Kaplan L. J. Gray[2]

Some years ago, a major advance in the theory of alloys was made with the introduction of the coherent potential approximation (CPA).[3,4] As originally presented, the CPA was a single-site, mean-field theory for diagonal disorder only (that is, random-site diagonal energies for electrons and random masses for phonons). Recently the CPA has been generalized by Kaplan et al.[5] to a form which is applicable to Hamiltonians with any type of disorder (diagonal, off-diagonal, and environmental). It can include cluster rather than just single-site averages and can yield a configurationally averaged analytic Green's function which has the proper translational symmetry. The only restriction on this theory was that it could not be applied to random alloys with short-range order.

We have developed a method for approximating the averaged Green's function for random alloys with short-range order by using the self-consistent approximation[5] and the augmented space formalism.[6,7] In this approximation the Green's function for the short-range order problem is expanded in terms of the self-consistent solutions. The coefficients in this expansion systematically include the appropriate short-range order probabilities. Once the self-consistent solutions have been evaluated, it is computationally quite simple to evaluate the averaged Green's function for any type of short-range order. The only limitation on this approximation occurs because we use only a finite set of terms from the expansion. As a result, the accuracy of the solution depends on how quickly the expansion converges for the particular choice of parameters.

To understand the approximation better, we have examined the Markov chain, a system which we could solve exactly by other means. We calculated the density of states for an s-state tight-binding binary alloy with nearest-neighbor interaction and diagonal disorder. The Hamiltonian is

$$H_{ij} = e(s_i)\delta_{ij} + W_{ij} \ ,$$

where $W_{ij} \neq 0$ for i and j nearest neighbors and $s_i = A$ or B depending on whether an A or B atom is at site i with probability c_A or c_B. For simplicity we used the lowest order approximation which included information about short-range order, the nearest-neighbor pair approximation. For this case we used only c_A and P_{AB} (the probability that A and B are nearest neighbors).

In the first column of Figs. 1.15(a)–(e), we have plotted the densities of states of the Markov chain, as it changes from the case where the sites are uncorrelated ($P_{AB} = 0.25$) at the top to the case of the almost segregated crystal, when A and B atoms separate into two nearly distinct crystals ($P_{AB} = 0.05$), at the bottom. In the second column, Figs. 1.15(f)–(j), the changes from the uncorrelated case toward the almost perfect alternating crystal $P_{AB} = 0.45$ are plotted. The first column shows an increase near the band edges and a corresponding decrease at the center as P_{AB} decreases. The second column shows the opposite behavior as P_{AB} increases. The approximation gives relatively good agreement with the exact results (histogram) in the range from $P_{AB} = 0.15$ to 0.35. The approximation does not pick up the extremely peaked behavior, but it does show good overall

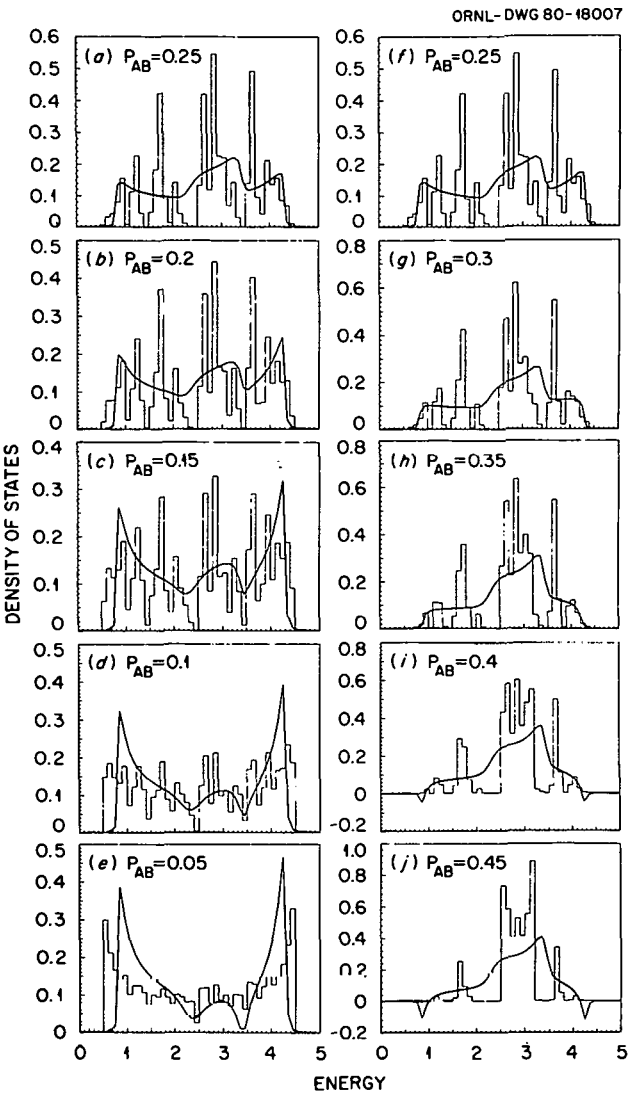

Fig. 1.15. Density of states for electrons in a Markov chain with $e(A) = -e(B) = -2.5$, $W = 1.0$, $c_A = 0.5$, and $P_{AB} = 0.05$–0.45. Comparison of the exact results (histogram) with the nearest-neighbor pair approximations.

agreement with major structure in the density of states. Such agreement in one dimension indicates far superior results in three dimensions.

In the regime of stronger short-range order, where P_{AB} is very large or very small, the match with exact results is not as good. In fact, by a simple analysis of the expansion coefficients, we can determine the range over which the approximation is valid. For the example considered in Fig. 1.15, we find that we get adequate convergence only for $0.125 \leqslant P_{AB} \leqslant 0.375$. Therefore, we see that the approximation can give a useful description of short-range order, provided it is used within its proper region of convergence.

---

1. Summary of paper: *Physical Review* (in press).
2. Computer Sciences Division, UCC-ND.
3. P. Soven, *Phys. Rev.* **156,** 809 (1967).
4. D. W. Taylor, *Phys. Rev.* **156,** 1017 (1967).
5. T. Kaplan et al., *Phys. Rev. B* **21,** 4230 (1980).
6. A. Mookerjee, *J. Phys. C* **6,** 2205 (1973); **6,** 1340 (1973).
7. T. Kaplan and L. J. Gray, *Phys. Rev. B* **14,** 3462 (1976); *J. Phys. C* **9,** L303 (1976).

ON THE CHARGE COMPENSATION MECHANISM IN β-ALUMINA[1]

J. C. Wang

In β-aluminas there exist about 15 to 40% extra M^+ ions compared to the ideal formula $M_2O \cdot 11Al_2O_3$, where M represents monovalent conducting cations such as Ag, Na, K, Rb, Tl, etc. These extra M^+ ions are believed to be closely related to the high ionic conductivities of the materials.[2] An interesting question is how the charges of these extra ions are compensated. In this work the problem was studied by making potential energy calculations for various ionic arrangements. Coulomb, short-range repulsive, and polarization energy terms were used.

For the ideal structure of Naβ-alumina, the Coulomb potentials at all ions in a unit cell were first calculated. It was found that the potentials at Al^{3+} ions in the spinel block are about 20 eV lower than those at the Na^+ sites in the conduction plane. This implies that it is unlikely that the charges of extra Na^+ ions in the conduction plane of actual crystals are compensated by replacing Al^{3+} ions in the spinel block with particles of less positive charge, because that will require a transfer of charge against a large electrostatic potential difference. This was further verified by the calculation of energies needed to (1) transfer artificially charge from the Al^{3+} ions to the Na^+ ions, (2) replace an Al(1) or Al(2) ion with three extra Na^+ ions in the conduction plane, and (3) replace an Al^{3+} ion with a divalent cation and add an extra Na^+ ion in the conduction plane.

Roth, Reidinger, and LaPlaca[3] proposed a model in which the excess Na^+ ions are compensated by extra O^{2-} ions in the conduction plane. Each of

these extra O^{2-} ions is assumed to be located at an mO position and bound to two Al^{3+} ions which move from their octahedral sites [Al(1)] to interstitial positions closer to the extra O^{2-} ion [Al(3)]. Together these ions form a V_{Al}-Al-O-Al-V_{Al} defect. Four calculated equilibrium configurations for this V_{Al}-Al-O-Al-V_{Al} defect are shown in Fig. 1.16, where Fig. 1.16(a) corresponds to the arrangement proposed by Roth. The energies needed to reach these equilibrium configurations are shown in Table 1.2. These results suggest that the model proposed by Roth, Reidinger, and LaPlaca[3] is energetically possible.

Table 1.2. Changes of potential energies in eV when an O^{2-} ion and two Na^+ ions are brought into Na β-alumina

ΔV_r is from the short-range repulsive potential, ΔV_e is from the Coulombic, polarization, and van der Waals terms, and ΔV_t is the sum of the two. The ionic configurations are shown in Fig. 1.16

Configuration	(A)	(B)	(C)	(D)
ΔV_r	8.50	8.50	8.01	7.95
ΔV_e	−47.57	−47.65	−47.08	−47.28
ΔV_t	−39.07	−39.15	−39.07	−39.33

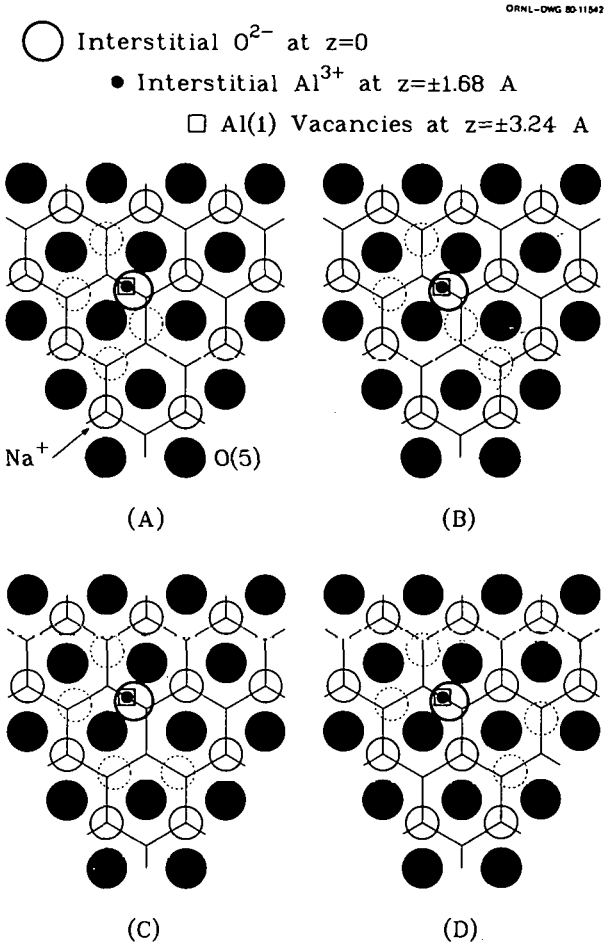

Fig. 1.16. Calculated equilibrium configurations for a V_{Al}-Al-O-Al-V_{Al} compensating defect plus two extra Na^+ ions in the conduction plane. The major differences between (A), (B), (C), and (D) are the arrangements of the Na^+ ions which were treated as mobile in the calculation (dashed circles). (A) corresponds to the arrangement proposed by Roth et al.

It is interesting to see how the potential energy of the system varies when the distance of the two interstitial Al^{3+} ions from the conduction plane is changed. To simplify the calculation, we fixed all other ions in Fig. 1.16(b) during the process. The result is shown by the dashed line in Fig. 1.17. The deep minimum near the Al(3) layer suggests that the two interstitial Al^{3+} ions are tightly bound to the interstitial O^{2-} ion. We made the same calculation for the ideal structure, where the interstitial

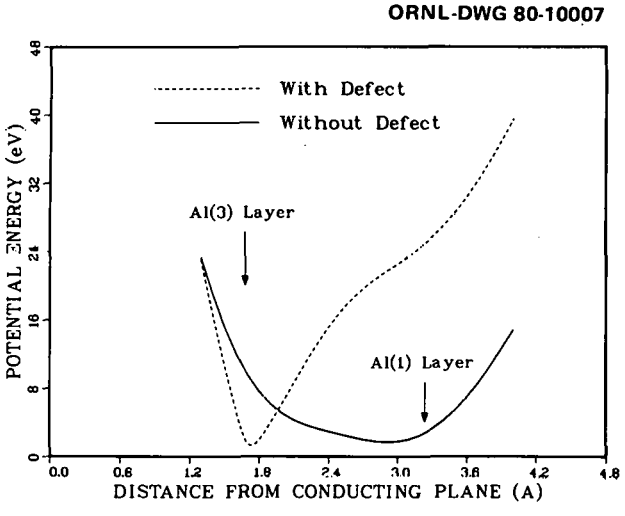

Fig. 1.17. Potential energy of the system when two Al(1) ions (one above and one below a *m*O site) are moved toward the conduction plane. The solid line demonstrates that for the ideal structure the Al(1) ions tend to stay at their regular sites [Al(1) layers]. The dashed line indicates that for the configuration (B) shown in Fig. 1.16, because of the presence of the interstitial O^{2-} ion near the *m*O site, the two Al(1) ions tend to move toward the conduction plane to the Al(3) layers.

O^{2-} ion and the two extra Na^+ ions were not present. The result is shown by the solid line in Fig. 1.17, where now the minimum is close to the Al(1) layer. This demonstrates that when the extra Na_2O is removed, the two interstitial Al^{3+} ions associated with it will return to the Al(1) vacancies. Since Na_2O is often one of the starting materials for growing Naβ-alumina, it seems reasonable that an O^{2-} ion and two Na^+ ions will enter or leave the conduction plane together as a unit. This combined action will also maintain the neutrality of the crystal. Figure 1.17 demonstrates that the creation of two Al Frenkel pairs is a natural result of the presence of an extra unit of Na_2O and that, when the Na_2O is removed from the crystal, the two interstitial Al^{3+} ions will recombine with the two Al(1) vacancies. This is consistent with the result that V_{Al}-Al-O-Al-V_{Al} defects proposed by Roth, Reidinger, and LaPlaca disappear in stoichiometric β-alumina.[4]

1. Summary of paper: *J. Chem. Phys.* **73,** 5786 (1980).

2. J. C. Wang, M. Gaffari, and Sang-il Choi, *J. Chem. Phys.* **63,** 772 (1975).

3. W. L. Roth, F. Reidinger, and S. LaPlaca, p. 223 in *Superionic Conductors,* ed. by G. D. Mahan and W. L. Roth, Plenum Press, New York, 1976.

4. Ph. Colomban and G. Lucazeau, *J. Chem. Phys.* **72,** 1213 (1980).

PARTICLE-SOLID INTERACTIONS

DISPLACEMENT CASCADES IN MINERAL CRYSTALS

M. T. Robinson

It has recently been proposed[1] that certain synthetic minerals, in particular the monoclinic rare-earth phosphate monazite, may have suitable phases in which to isolate long-lived radioactive nuclear wastes. The proposal is based in part on the observation that thorium- and uranium-containing monazites in nature are crystalline, in contrast to the majority of radioactive minerals. The latter are found typically in the more-or-less amorphous condition described by geologists as *metamict.*[2] The reasons why monazite behaves differently from many other minerals are unknown, but recent experiments[3] suggest that this may be the result of an unusual low-temperature annealing process. Whether or not this idea is correct, it seems desirable to examine displacement damage production in monazite and related minerals, using the computer simulation method which has been developed for studies of radiation effects in metals.[4]

The computer program MARLOWE constructs the trajectories of energetic particles slowing down in a crystalline solid in the binary collision approximation (BCA). It was necessary to make extensive modifications in the program to enable it to deal with mineral crystals, many of which are monoclinic or triclinic. At the same time, an improved scheme of describing a crystal was developed. A small number of preliminary calculations has been carried out with the modified code (designated as Version 11.6), and these are described briefly here.

It was desired to understand the effects of the crystal structure itself on cascades generated in monazite, without the complications of differing atomic masses, interatomic potential parameters, and so forth. Therefore, a monazite lattice was set up but was entirely populated with Cu atoms. The lattice parameters of the structure were adjusted so that the density of "monazite Cu" was the same as that of ordinary fcc Cu. The parameters used are given in Table 1.3. The structure used is one given by Wyckoff[5] and differs somewhat from the more recent work of Beall et al.[6] Other parameters needed in the calculation are given in Table 1.4. The computations for the "monazite Cu" take only slightly longer than those for fcc Cu.

Table 1.3. Parameters describing "monazite Cu" $a_0 = 0.66585$ nm; $b_0 = 0.68949$ nm; $c_0 = 0.63531$ nm; $\beta = 103.633$ deg. Space group $P2_1/n$ with all atoms in fourfold general positions:

$\pm(x,y,z;\ x + \frac{1}{2},\ \frac{1}{2} - y,\ z + \frac{1}{2})$, with

Site	x	y	z
Ce	0.292	0.156	0.083
P	0.292	0.156	0.581
O(1)	0.211	−0.010	0.423
O(2)	0.374	0.323	0.464
O(3)	0.467	0.070	0.765
O(4)	0.116	0.235	0.680

Table 1.4. Parameters used in cascade calculations

Lattice constant of fcc Cu: a = 0.36150 nm
Moliére potential parameter: a_{12} = 7.38 pm
Maximum impact parameter: p_c/a = 0.62
Nonlocal inelastic losses normalized to the LSS theory

This indicates that cascade calculations for complex mineral crystals will not be prohibitive in computational costs.

Comparisons have been made of cascades generated by 1-keV Cu atoms recoiling from the "Ce" site of the monazite structure and of those generated by similar recoils in ordinary fcc Cu. The vector range distributions obtained in the two cases are compared in Fig. 1.18. Note that both histograms are expressed in terms of the lattice constant of fcc Cu. At 1 keV, very little (if any) channeling is displayed by recoiling atoms in the fcc structure. The range distribution is relatively symmetrical and has only a small extension on the penetrating side. In contrast, the range distribution in the monazite case shows a pronounced penetrating tail, involving perhaps 15% of the particles. This tail is apparently a result of the relative ease of channeling in the rather open monazite structure. The direction(s) of the channeled particles has not been determined, but examination of a model suggests the [001] direction as probable.

In addition to increased channeling, another important difference between the two structures is the absence of replacement sequences from the monazite cascades. In fcc crystals, an important feature of the development of cascades is the propagation of sequences of replacements along ⟨011⟩, ⟨001⟩, ⟨111⟩, and (to a much lesser extent) other directions. These sequences are responsible for the survival of a considerable fraction of the interstitial atoms produced in the cascades, since they provide a mechanism for transporting them far away from their vacancies. Such sequences do not occur at all in monazite. Consequently, the monazite cascades are generally more compact than those in fcc metals. Figure 1.19 shows this effect quantitatively for 1-keV cascades in the two crystals and shows the average number of Frenkel pairs in each cascade with separations which exceed a specified minimum. It is clear that the role of replacement sequences in separating interstitials and vacancies

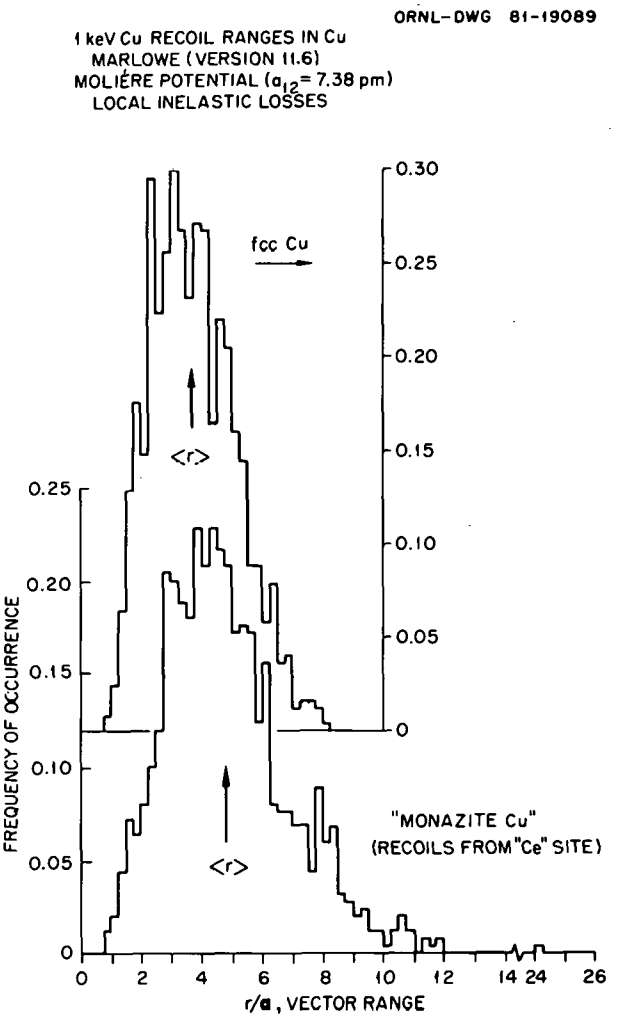

Fig. 1.18. Vector range distributions calculated for 1-keV Cu atoms recoiling from lattice sites in fcc Cu and in "monazite Cu."

outweighs their role in dissipating energy in the fcc crystal. Thus, one may expect somewhat less damage in the lower symmetry monazite crystal than would be anticipated from calculations on metals.

These calculations are being extended to monazite crystals of the correct compositions. An objective is to calculate the apparent cross sections for damaging these crystals as an aid to understanding experiments involving them.

1. L. A. Boatner et al., *Solid State Div. Prog. Rep., Feb. 29, 1980,* ORNL-5640, p. 215.

2. R. C. Ewing, p. 81 in *Alternate Nuclear Waste Forms and Interactions in Geologic Media,* ed. by L. A.

Boatner and G. C. Battle, Jr., U.S. Department of Energy CONF-8005107, Washington, D.C., 1981.

3. F. G. Karioris, K. Appaji Gowda, and L. Cartz, *Radiat. Eff. Lett.* **58,** 1 (1981).

4. M. T. Robinson, p. 73 in *Sputtering by Ion Bombardment I, Topics in Applied Physics,* vol. 47, ed. by R. Behrisch, Springer-Verlag, Berlin, 1981.

5. R. W. G. Wyckoff, p. 33 in *Crystal Structures,* vol. 3, Interscience, New York, 1965.

6. G. W. Beall et al., *J. Inorg. Nucl. Chem.* **43,** 101 (1981).

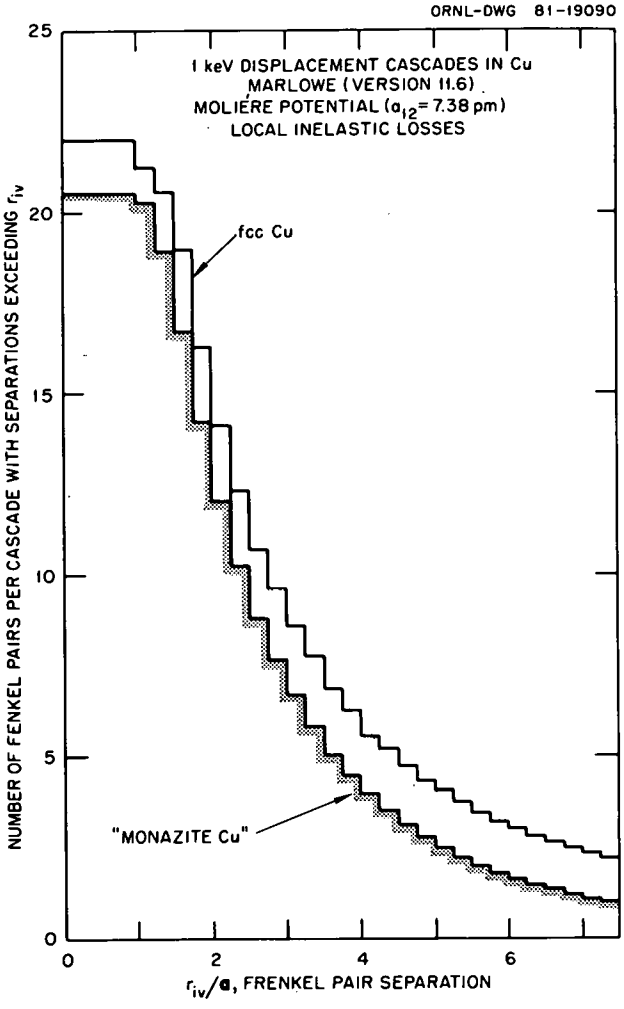

Fig. 1.19. The distributions of Frenkel pair separation distances calculated for displacement cascades generated by 1-keV Cu atoms recoiling from lattice sites in fcc Cu and in "monazite Cu."

MECHANISM OF ION DECHANNELING IN III-V SEMICONDUCTOR SUPERLATTICES[1]

J. H. Barrett

Computer simulations of channeling have been used to evaluate a model proposed by Saris et al.[2] to explain some of their ion dechanneling measurements in InAs-GaSb superlattices. They observed that ions remain channeled to considerable depths for beams incident along [100], the surface normal and crystal growth direction, but that ions are dechanneled very near the surface for beams incident along directions such as [110] that are inclined to the normal. To explain this second result, they proposed a model in which slight alterations in bond lengths at the interfaces between layers cause the atomic rows parallel to inclined directions to be offset slightly at each interface. Their suggestion was that at an interface with Ga-As bonds, the bond lengths are about 7% shorter than average, while at an interface with In-Sb bonds they are about 7% longer. For rows inclined to the surface normal, the result in either case is to offset the rows slightly at each interface. For [110], a 7% difference in bond lengths causes an offset of 0.021 nm. Some quantitative estimates for their model have been made by computer simulation of channeling and are presented here. These estimates indicate that the effects due to the small offsets in their model are much too weak to cause the observed dechanneling and that much stronger perturbations at each interface are required to explain their result.

In using computer simulation of ion trajectories in the present case, an electronic stopping power of 310 eV/nm was used,[3] and the associated multiple scattering was calculated as

$$\langle \psi^2 \rangle = 1/2(m_{el}/M_{ion}) \cdot (\Delta E/E) \ .$$

The best measured value for the thermal vibration amplitude appears to be Kyutt's result[4] of $u_1 = \langle x^2 \rangle^{1/2} = 0.0108$ nm for GaSb. With these parameters, the calculated dechanneling rate in pure GaSb was found to be too small. Results of subsequent calculations based on a value of 0.0156 nm for u_1 were found to be very close to the observed dechanneling rate in GaSb. Consequently,

computer simulation studies were carried out for each of these values of u_1.

The main results of the simulations are shown in Fig. 1.20. Consider first the results for the single-step offsets. With either u_1, the distance calculated for half dechanneling for the proposed row offset of 0.021 nm is only slightly less than for no offset and is far larger than the observed[2] value of 0.6 μm. It seemed natural to extend the model of Saris et al. to larger offsets, which would displace the rows at each interface to regions of higher ion flux. For u_1 = 0.0108 nm, even the largest offset fails to give the observed amount of dechanneling, which may be related to the weaker calculated dechanneling in the substrate for this thermal vibration amplitude. For u_1 = 0.0156 nm, an offset of about 0.086 nm gives the observed half distance for dechanneling. This offset corresponds to a change of $\pm$0.122 nm in the standard (100) planar spacing of 0.152 nm. It would seem very unlikely that a large alteration in planar spacing could occur without some alteration in adjacent spacings. Consequently, a calculation was done at each value of u_1 for a multistep row offset. The particular set of offsets used was 0.001, 0.004, 0.010, 0.017, 0.022, 0.017, 0.010, 0.004, and 0.001 nm, which total 0.086 nm. The results, also shown in Fig. 1.20, each lie above the curve through the corresponding single-step values. The particular set of multistep offsets used appears to be equivalent to a single-step offset about 70% as large as the total for all steps. This reduction in effectiveness is most likely due to a steering or shielding effect of each atom in the offset pattern in relation to atoms further along the row. Two additional multistep calculations were done for u_1 = 0.0156 nm with steps in the same proportions as above but with larger total values. The results are also shown in Fig. 1.20 and bracket the observed distance for half dechanneling.

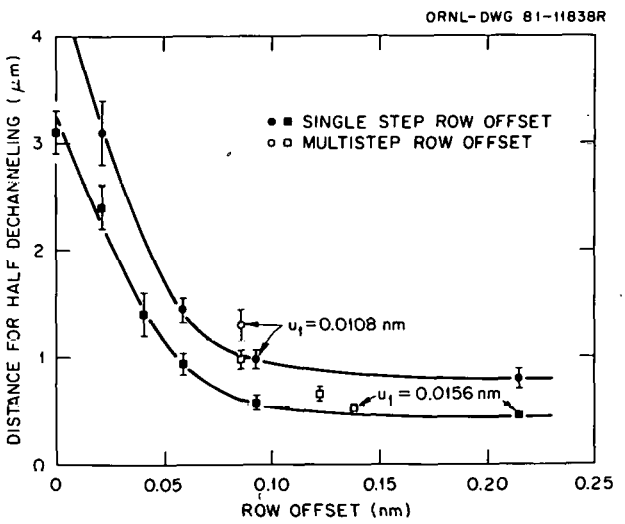

Fig. 1.20. Dechanneling distance along [110] as a function of row offset for 2.225-MeV He in InAs-GaSb superlattices. The layers were 50 nm thick, and the distance through each layer along [110] was 70.7 nm. The row offset values shown for the multistep cases are the total of all offset steps at an interface.

Dislocations or stacking faults as alternate dechanneling mechanisms seem incapable of explaining the observed behavior inasmuch as they would be expected to produce substantial dechanneling along [100] as well as along [110] and other directions inclined to the surface normal. In addition, dislocations should produce a dependence of the dechanneling rate on ion energy, whereas Saris et al. found the dechanneling rate to be energy independent.

The conclusions drawn concerning the observed dechanneling behavior are the following. The only mechanism that appears capable of obstructing channels inclined to the surface normal while not obstructing those parallel to the normal is a series of relaxations (contractions or expansions) in planar spacing at each interface in the superlattice. The relaxation is probably distributed over several layers at an interface, and the resulting distributed set of row offsets is less effective than is a single offset equal to the total of the distributed offsets. The adjustment of u_1 to produce the amount of dechanneling observed in the bulk for GaSb introduces uncertainty into making quantitative estimates. However, from the simulation results, there should be a total offset of at least 0.08 nm and a total relaxation of at least 0.11 nm at each interface.

---

1. Summary of paper to be published.
2. F. W. Saris et al., *Appl. Phys. Lett.* **37**, 931 (1980); *J. Appl. Phys.* (to be published).
3. Obtained by application of Bragg's Rule to data from J. F. Ziegler, *Helium Stopping Powers and Ranges in All Elemental Matter*, Pergamon Press, New York, 1977.
4. R. N. Kyutt, *Fiz. Tverd. Tela* **20**, 395 (1978) [*Sov. Phys. Solid State* **20**, 227 (1978)].

THE TWO-ATOM MODEL IN ENHANCED ION BACKSCATTERING NEAR 180° SCATTERING ANGLES[1]

O. S. Oen

An analytical two-atom scattering model has been developed to treat the recent discovery[2] of the enhancement near 180° of Rutherford backscattering yields from disordered solids. In contrast to conventional calculations of Rutherford backscattering that treat scattering from a single atom only (the backscattering atom), the present model includes the interaction of a second atom lying between the target surface and the backscattering plane. The projectile ion makes a glancing collision with this second atom both before and after it is backscattered. Let the backscattering atom be located at some fixed position B, a distance D below the surface. Consider a second atom A at some arbitrary position in a plane at distance l above B, such that the pair of atoms is inclined at a small angle θ with respect to the surface normal (see Fig. 1.21). The differential scattering cross section for a normally incident beam to be focused by atom A toward B (and therefore backscattered) is

$$\frac{1}{l^2}\frac{s}{\theta}\left|\frac{ds}{d\theta}\right| = \frac{s}{[s + l\eta(s)]}\left|\frac{ds}{1 + l\dfrac{d\eta}{ds}}\right| \qquad \theta \geq \theta_c$$

$$= 0 \qquad \theta < \theta_c \,. \tag{1}$$

Here $\theta = (s/l) + \eta(s)$, where s is the impact parameter between the projectile ion and atom A and $\eta(s)$ is the corresponding scattering angle. Since $\eta(s)$, in general, increases with a decrease in s, θ has a minimum value θ_c for $s = s_c$. Because of this extremum, it is only necessary that the trajectories of the backscattered ions lie in the neighborhood of the critical impact parameter s_c in order to emerge at angles close to the surface normal. This tolerance of path is the basic reason, in this model, for the enhancement of the backscattering yield.

The backscattered flux starting toward the surface from atom B is assumed to have angular isotropy, since Rutherford scattering changes little over a few degrees from 180°. Before this flux exits the target surface, it is scattered by atom A. The number of particles scattered per unit solid

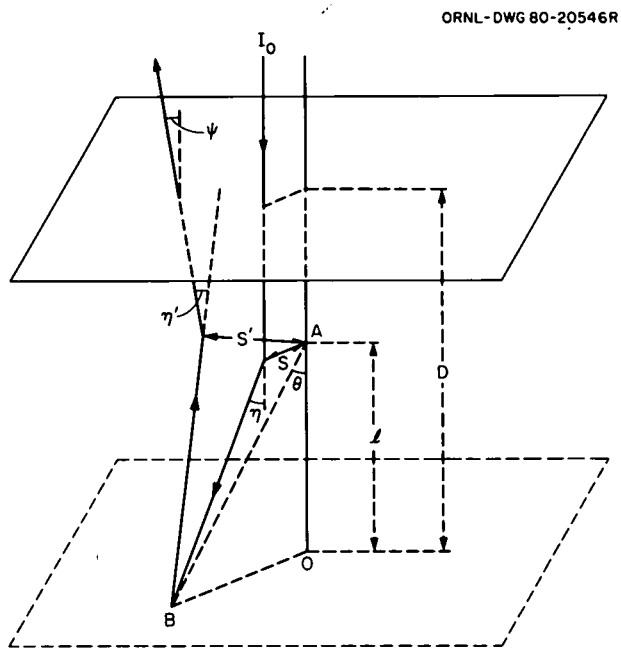

Fig. 1.21. Typical trajectory of an ion in the two-atom model. The ion makes glancing collisions with atom A before and after being backscattered by atom B. The ion exits the solid at an angle ψ, which is measured with respect to the surface normal.

angle at angle θ' (θ' is measured with respect to the axis of the dipole BA) is proportional to

$$\frac{s'}{l^2\theta'}\left|\frac{ds'}{d\theta'}\right| = \frac{s'}{[s' + l\eta(s')]}\left|\frac{ds'}{1 + l\dfrac{d\eta}{ds'}}\right| \qquad \theta' \geq \theta'_c$$

$$= 0 \qquad \theta' < \theta'_c \,, \tag{2}$$

where $\theta' = (s'/l) + \eta(s')$, s' is the impact parameter, and $\eta(s')$ is the scattering angle. The minimum or critical angle θ'_c produces a shadow region behind atom A, as viewed from atom B. Both functions given in Eq. (1) and Eq. (2) are highly peaked near the critical angle and approach unity for large angles.

The two-atom model should be a good approximation in a solid of N atoms per unit volume provided there is only one significant scattering before the ion strikes the backscattering atom. The probability for a single scattering with an impact parameter s is taken to be $\exp(-\pi NDs^2)$. Atom A is assumed to be distributed at random with uniform

probability density above the backscattering atom. Convoluting the incoming [Eq. (1)] and backscattered [Eq. (2)] fluxes, the normalized backscattering yield at small exit angle ψ is

$$\chi(\psi) = \sum \frac{\Delta l}{D} \int_0^\infty \int_0^{2\pi} \frac{s'}{l^2\theta'} \left| \frac{ds'}{d\theta'} \right| \times e^{-\pi N s^2 D} N D s \, d\phi \, ds \quad , \quad (3)$$

where the summation extends over all atomic layers between the backscattering plane and the target surface. The angles θ' and θ are related by $\theta'^2 = \theta^2 + \psi^2 - 2\psi\phi \cos \phi$. Equation (3) is the central result of this paper.

The Molière potential is used to calculate the ion-atom scattering angles. A good approximation for light ions hitting heavy targets is to assume that the ion loses no energy on backscattering; therefore, $\theta_c' = \theta_c$. Numerical methods were used to calculate Eq. (3) because of complexities in the scattering function [Eq. (2)]. As an illustration of the predictions of Eq. (3), the normalized yield vs depth at $\psi = 0.1°$ for various ion energies is shown in Fig. 1.22. It is found that the enhancement region is compensated by a deficit region at larger backscattering angles. In addition to ion energy, the predictions of yield enhancement on the following parameters have been studied: backscattering depth, exit angle, scattering potential, atomic numbers of projectile and target, and atomic density of target. Scaling of some of the results to other systems is possible since the ion atomic number and energy appear only in the ratio Z_1/E.

Overall, it is found that the model reproduces the typical feature of the effect and its dependence on the various physical parameters. The main differences are that it predicts enhancements somewhat too small and at depths somewhat shallower than those found experimentally. The model gives a simple picture of ion-path tolerance near the critical impact parameter as the physical origin of the enhancement in the backscattering yield. It is, to date, the only analytical model that gives an explanation of the enhancement effect. The simplicity and rapidity with which one can do exploratory calculations make it a complementary approach to the detailed computer simulation methods of Barrett, Appleton, and Holland.[3]

1. Summary of paper: *Nuclear Instruments and Methods* (in press).

2. P. P. Pronko et al., *Phys. Rev. Lett.* **43**, 779 (1979).

3. J. H. Barrett, B. R. Appleton, and O. W. Holland, *Phys. Rev. B* **22**, 4180 (1980).

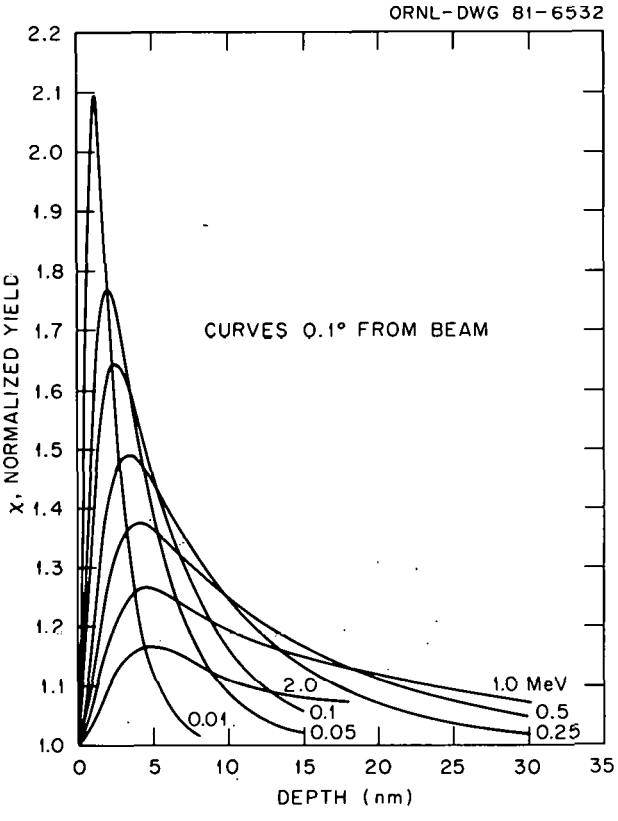

Fig. 1.22. Calculated He ion backscattering yield in amorphous Pt vs depth for different ion energies.

LASER ANNEALING

MACROSCOPIC THEORY OF PULSED-LASER ANNEALING: I. MODEL FOR THERMAL TRANSPORT AND MELTING[1]

R. F. Wood G. E. Giles[2]

It is now well established that nanosecond pulses of radiation from high-power lasers can be used very effectively to anneal the lattice damage caused by ion implantation of semiconductors. Other similar applications include the laser-induced diffusion of thin dopant films deposited on the surface of samples, recrystallization of doped amorphous films deposited on single-crystal substrates, and the removal of precipitates present after con-

ventional high-temperature dopant diffusion. All these processes can be understood in terms of models and calculations based on macroscopic diffusion equations for heat and mass transport, cast in a finite-difference form to allow for the temperature- and spatial-dependence of the thermal conductivity, absorption coefficient, reflectivity, and other quantities. In this paper, which is the first in a series of three, a description of the model used at ORNL for calculations of heat transport during pulsed-laser annealing is given. Results of the modeling are illustrated by a variety of calculations. These results include the effects of pulse duration, shape, and energy density; the effects of assumptions made about the latent heat of amorphous silicon; the effects of substrate heating; the role played by the absorption coefficient in determining melt-front penetration; and the duration of surface melting.

Two basic models were used in most of the calculations described in the paper. In one model, the absorption coefficient k was assumed to have some average, constant value k_c throughout the sample. Such a model is suggested by (a) ion implantation of light ions, such as boron, in silicon where the implanted region is not made completely amorphous and the nature and extent of the damage is not defined very well; (b) multipulse annealing, where it is known that after the first laser pulse the damage in the implanted layer may be completely removed; and (c) laser-induced melting of undoped, crystalline samples. Because of the absence of a well-defined damaged region in these cases, we refer to this as the crystalline or c model. The use of a single value (k_c) for the absorption coefficient in the c model is a rather crude approximation whose validity must be checked as more experimental data are accumulated.[3] In the second model, referred to as the amorphous or a model, a reasonably well-defined amorphous region is assumed to be present. This model is expected to apply to silicon samples implanted with heavy ions in certain ranges of energy and dose and to samples on which an amorphous layer has been deposited by sputtering, e-beam deposition, etc. In the calculations, the absorption coefficient was assigned one value in the damaged region and some other, significantly lower, value in the undamaged, crystalline region.

As an example of the temperature calculations, results for a series of cases in which the sample was either cooled or heated while the laser annealing was carried out are shown in Fig. 1.23. These calculations, which employed the a model, yielded the position of the liquid-solid interface (melt front) as a function of time after the beginning of the laser pulse. Curves like those on Fig. 1.23 are typical of one class of results which the calculations provide for a variety of assumptions about the annealing conditions and mechanisms. The slope of such curves gives the melt-front velocity at any time during the melting and resolidification process. The results shown in Fig. 1.23 suggest that substrate heating may be of interest for several reasons. If, for example, an available laser cannot

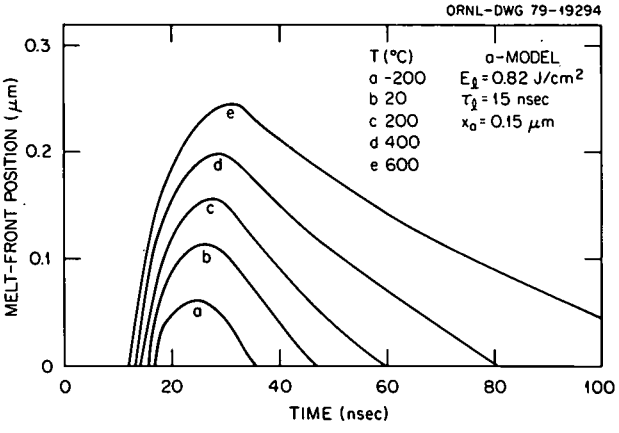

Fig. 1.23. Effects of substrate heating on melt-front profiles for a 15-ns, 0.82-J/cm² pulse.

supply the energy required to melt the near-surface region to a particular depth, sample heating may extend the melting range to that depth. The calculations of Fig. 1.23 were carried out for samples irradiated with single pulses of 0.82 J/cm² and 15-ns duration. The results show that the melt-front penetration depth can be extended by almost a factor of 2 by increasing the sample temperature from 20 to about 500°C. Even if a laser has sufficient power, it may still be advantageous to use substrate heating so that the lowest possible energy density for annealing can be used. In this way, the magnitude of the spatial inhomogeneities in the laser energy can be reduced. Undoubtedly, the most interesting use of substrate heating and cooling at this time is to control the melt-front velocity during resolidification of the melted near-surface region.[4]

Most theories of crystal growth relate the crystallization rate to the temperature of the liquid-solid interface. In practice, this temperature is not well defined and virtually impossible to measure at the melt-front velocities involved in laser annealing. Moreover, in terms of the macroscopic diffusion equations used here, it is the temperature *gradients* at the melt front which are important in determining the melt-front velocity. Table 1.5 shows the gradients obtained from calculations of some typical melt-front profiles; the gradients are very large and explain the high melt-front velocities which play an important role in many laser annealing phenomena. Calculations of temperature gradients, melt-front velocities, etc., are particularly important because they provide information which is difficult, if not impossible, to obtain experimentally.

1. Summary of paper: *Phys. Rev. B* **23**, 2923 (1981).
2. Computer Sciences Division, UCC-ND.
3. D. H. Lowndes, "Time-Resolved Optical Transmission and Reflectivity of Pulsed Ruby Laser-Irradiated Si," this report.
4. R. F. Wood, "Macroscopic Theory of Pulsed-Laser Annealing: III. Nonequilibrium Segregation Effects," this report; C. W. White et al., "Factors Limiting Substitutional Solubilities Achieved by Laser Annealing of Ion-Implanted Si," this report; R. T. Young et al., "Substrate Heating and Emitter Dopant Effects in Laser-Annealed Solar Cells," this report.

MACROSCOPIC THEORY OF PULSED-LASER ANNEALING: II. DOPANT DIFFUSION AND SEGREGATION[1]

R. F. Wood J. R. Kirkpatrick[2]
G. E. Giles[2]

In this, the second paper in this series, we discuss dopant diffusion calculations in detail, with particular emphasis on the incorporation of segregation effects into the modeling. From the forms of the experimental dopant profiles, it is established that pulsed-laser annealing is a nonequilibrium process, but in this paper the interface segregation coefficient is treated as an adjustable parameter and no attempt is made to justify the values obtained. Approximate analytical and finite-difference solutions to the diffusion equation are discussed and compared. It is argued that the excellent fit between theory and experiment is a strong indication of the basic validity of the melting model of pulsed-laser annealing.

Our most complete treatment of the dopant diffusion problem employed the so-called quasi-stationary approximation. In this approximation, the sample is assumed to be divided into N layers, or cells, of various thicknesses. All the material in any one layer melts or solidifies at the same time. The melt front thus advances into the solid and recedes back to the surface in finite jumps, and between jumps it is held stationary while diffusion in the molten material occurs. For example, beginning at the surface layer, the dopant diffusion equation is solved in that layer for some time interval, with the implanted profile as the starting profile. The melt front then jumps to the next layer, where it pauses for a chosen time interval. During this interval, diffusion occurs with the initial profile given by the distribution of impurity in the first layer after the first time interval plus the implanted profile in the second layer. In this way, the diffusion equation is solved in steps as the melt front first penetrates into the sample and then returns to the surface. This problem can be solved analytically by using Green's functions appropriate to slabs of widths determined by the finite steps of the melt front. However, these Green's functions are given as infinite series and are rather cumbersome. We have, therefore, used a quasi-stationary,

Table 1.5. Temperature gradients in units of °C/cm at the melt front for typical melt-front profiles

t(ns)	E_l = 1.75 J/cm²		E_l = 1.25 J/cm²	
	G_{mi}	G_{si}	G_{mi}	G_{si}
25.0	1.79×10^7	1.01×10^6	0.96×10^7	1.33×10^7
37.5	2.04×10^7	0.95×10^7		
50.0	9.63×10^6	1.25×10^7	5.17×10^6	9.0×10^6
75.0			1.33×10^4	6.57×10^6
100.0	7.33×10^4	0.57×10^6	$<1.3 \times 10^4$	5.5×10^6
200.0	$<10^4$	0.37×10^6		

finite-difference (QFD) approach, which is described in some detail in the paper.

Our most extensive use of the QFD has been in fitting the data of White et al.[3] on Si implanted with Sb, Ga, In, and Bi. Unlike the results for B-, P-, and As-implanted laser-annealed Si, the profiles of Ga, In, and Bi in Si after laser annealing show clear evidence of segregation; the case of Sb is not as clear-cut, as we shall see. For Ga-, In-, and Bi-implanted samples, surface segregation spikes are observed, but they are not nearly as large as they would be if equilibrium values (k_i^0) of the interface segregation coefficient k_i were applicable during the recrystallization process. The necessity of choosing $k_i > k_i^0$ to obtain agreement between experimental and calculated profiles and the fact that the equilibrium solubility limit can be greatly exceeded as a result of the laser-annealing process show that the process is a highly nonequilibrium one.

As an example of the type of results which can be obtained with the methods described in this paper and the melt-front data given in the preceding paper[4] of this report, we can briefly consider observed and calculated profiles of Sb. In fitting the profiles of Sb (and Ga) in Si, it was necessary to take into account the measurable loss of dopant that is observed during laser annealing. To investigate this problem, three different assumptions about dopant loss were made. In one set of calculations, all the loss occurred during the initial part of the surface melting when the temperatures in the liquid Si were the highest. A second set of calculations was carried out with the assumption that dopant loss occurred only when the surface concentration exceeded some threshold value. In the third set of calculations, we used the approximation that the loss is proportional to the surface concentration, as one would expect from a simple kinetic rate theory approach. We found that satisfactory fits to both Sb and Ga in Si could be obtained with this method. Although the root-mean-square deviations between experimental and calculated profiles for both dopants were not quite as good as those obtained with the assumption of a threshold concentration for dopant loss, the values of the maximum melt-front penetration needed to obtain the fits were much more in accord with the values given by the heat transfer calculations.[4] Figure 1.24 shows the results for Sb in Si from the third set of calculations. The overall fit is good, but the loss of dopant makes it difficult to obtain a truly satisfactory fit near the surface.

1. Summary of paper: *Phys. Rev. B* **23,** 5555 (1981).
2. Computer Sciences Division, UCC-ND.
3. C. W. White et al., *J. Appl. Phys.* **51,** 738 (1980).
4. R. F. Wood and G. E. Giles, *Phys. Rev. B* **23,** 2923 (1981); "Macroscopic Theory of Pulsed-Laser Annealing: I. Model for Thermal Transport and Melting," this report.

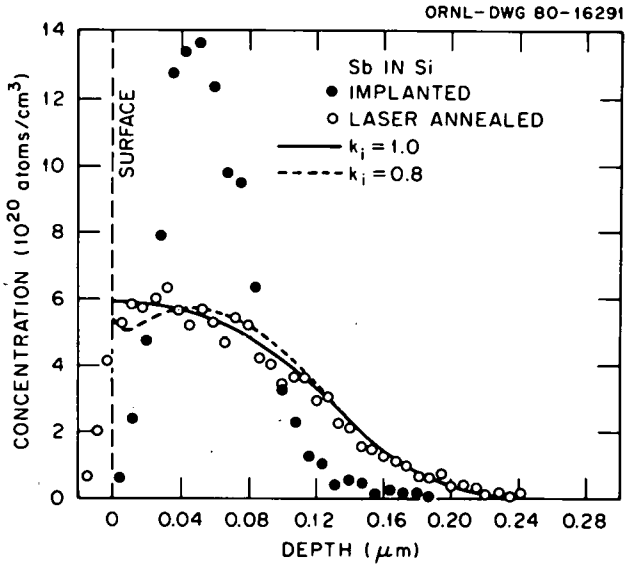

Fig. 1.24. Antimony distribution in Sb-implanted Si before and after laser annealing. There is some loss of Sb from the sample during laser annealing. The solubility limit of Sb in Si is $\sim 7 \times 10^{19}$ atoms/cm.

MACROSCOPIC THEORY OF PULSED-LASER ANNEALING: III. NONEQUILIBRIUM SEGREGATION EFFECTS[1]

R. F. Wood

In the first two papers of this series on the theory of pulsed-laser annealing, the results of heat and mass (dopant) transport calculations based on the melting model were described in considerable detail. It was shown that dopant profiles observed after pulsed-laser annealing could not be fit when values of the interface segregation coefficient k_i^0, appropriate for solidification under nearly thermodynamic equilibrium conditions, were used in the dopant redistribution calculations. In this paper, a model[2] is developed which relates the nonequilibrium interface segregation coefficient k_i to k_i^0 and to the velocity v of the liquid-solid interface during recrystallization of the molten region created by

the laser radiation. The model, which uses an approach based on kinetic rate theory, introduces the concept of a velocity-dependent activation energy for jumps of the dopant atoms from the solid to the liquid. This velocity dependence comes about when the material is solidifying at such a rate that the probability of escape of a dopant atom from the liquid-solid interface region is significantly reduced from the corresponding probability during solidification near equilibrium. The functional dependence of k_i on v cannot be calculated exactly, but simple approximate expressions for this dependence yield results which are in accord with the experimental data presently available. Moreover, using the velocity dependence of k_i, it is shown that the velocity-dependent activation energy (VDAE) model gives satisfactory agreement with the nonequilibrium dopant concentrations which have been observed[3] for an interface velocity of ~4 m/sec.

Using the results of the VDAE model, the theory of Mullins and Sekerka[4] on the stability of a planar liquid-solid interface against cellular formation is reinterpreted. It is shown that if $k_i = k_i(v)$ is used in this theory, there is satisfactory agreement with pulsed-laser annealing experiments but that if k_i^0 is used, there is no agreement whatsoever. An example of these stability calculations is shown in Fig. 1.25 for In in Si. The two heavy solid curves give the demarcation lines between stable and unstable regions of the plots of concentration vs melt-front velocity. The lower curve was calculated with $k_i = k_i^0$; the upper curve, with a form of $k_i = k_i(v)$ obtained from the VDAE model. The dashed curve, which also was calculated with $k_i(v)$, gives the so-called "capillary limit" for which capillary effects completely dominate the effects of constitutional supercooling due to the presence of the dopant atoms. The stability curve for the case in which the effect of constitutional supercooling is completely dominant does not appear on Fig. 1.25, because it lies so close to the ordinate on the velocity scale used. The light horizontal line, labeled $C_s^0(k_i^0 = 0.0004)$, in Fig. 1.25 gives the equilibrium solubility limit ($v \simeq 0$) estimated from data in the literature. The other horizontal line, labeled C_s ($v \simeq 4$ m/s), indicates the approximate nonequilibrium concentration reported by White et al.[3] It should be realized that, because $k_i \rightarrow k_i^0$ as $v \rightarrow 0$, the stability curves for $k_i = k_i(v)$ and $k_i = k_i^0$ must go to the same value as $v \rightarrow 0$.

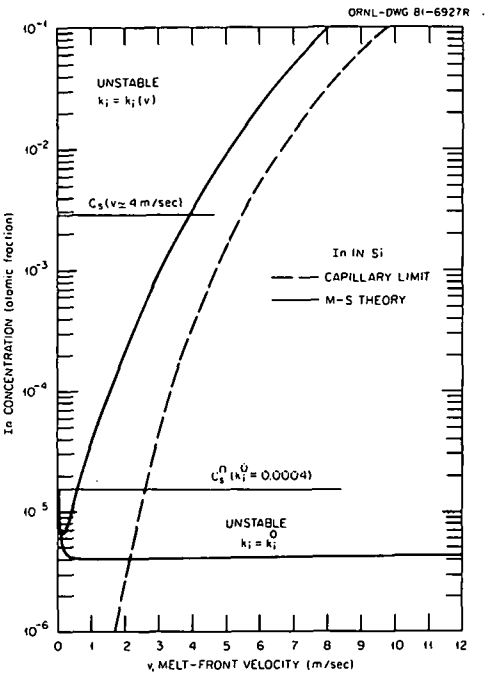

Fig. 1.25. Results of an interface stability calculation for In in Si following the Mullins and Sekerka theory and using values of k_i from the VDAE model.

The curves displayed in Fig. 1.26 give information about the relationship between dopant concentration, cell size, and melt-front velocity. To construct these curves, a melt-front velocity is chosen and the dopant concentration at which a particular cell size appears is determined. For example, in Fig. 1.26 let us suppose that 4 m/s has been chosen for v; then we can determine the cell size for each concentration above the critical concentration for instability. This leads to curve 2 for the In group of curves in Fig. 1.26. The point at the extreme right on each curve corresponds to the cell size and dopant concentrations at the onset of the interfacial instability. It should be noted that if the concentration is held fixed while the melt-front velocity is increased, the cell size *increases* up to a certain maximum value corresponding to that velocity at which the stability curve (Fig. 1.25) is crossed. It is apparent from Fig. 1.26 that for a given concentration, the increase in cell size is very rapid as the velocity approaches that of the stability curve. This means that experimental values of the cell size at the onset of the instability will be difficult to determine accurately. In fact, Mullins and Sekerka cautioned against the use of their theory to predict cell sizes unless the instability is

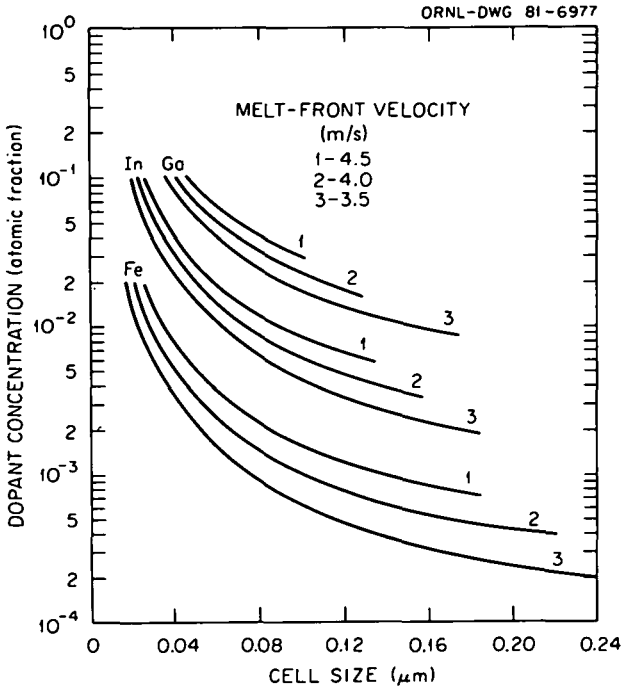

Fig. 1.26. Interrelationship of dopant concentration, melt-front velocity, and cell size. The cell size at the extreme right for a given velocity occurs at the onset of the instability. If the concentration is held fixed, the cell size *increases* as the velocity is increased until, for a given velocity, the interface becomes stable.

known to be weak. However, from the sparse data that are now available, it appears that the predictions of cell size are perhaps more accurate than might be expected. Narayan[5] has reported cell diameters of 0.07 μm, 0.052 μm, and 0.035 μm, respectively, for Ga, In, and Fe in Si after laser annealing with pulses which should have produced melt-front velocities of approximately 4 m/s. The calculated cell sizes for the estimated concentrations involved are in rather good agreement with these values.

Other topics which are covered in the paper include the following. It is shown that the VDAE model satisfies the Baker and Cahn criteria for "solute trapping"; that is, that the change in the chemical potential of a dopant atom in going from the liquid to the solid is positive for values of k_i greater than k_i^0. It is pointed out that the traditional thermodynamic approach of assigning a temperature to the interface region may need modifications when the temperature gradients are very large, as they are in pulsed-laser annealing. The dependence of k_i on the direction of crystal growth is discussed on the basis of a very simple model. Finally, attempts of other authors to obtain expressions for the velocity dependence of k_i are reviewed and compared to the VDAE model.

---

1. Summary of paper: *Phys. Rev. B* (in press).
2. R. F. Wood, *Appl. Phys. Lett.* **37**, 302 (1980).
3. C. W. White et al., *J. Appl. Phys.* **51**, 738 (1980).
4. W. W. Mullins and R. F. Sekerka, *J. Appl. Phys.* **35**, 444 (1964).
5. J. Narayan, *J. Appl. Phys.* **52**, 1289 (1981).

MODEL CALCULATIONS OF PULSED RUBY LASER MELTING OF GaAs

R. F. Wood D. H. Lowndes
G. E. Giles[1]

Methods used previously for calculations of thermal and mass transport[2,3] during pulsed-laser annealing of Si have been applied to similar problems in GaAs. Although the range of temperatures over which the thermal properties have been measured is more limited in GaAs than it is in Si, the thermal properties of the two materials are not greatly different; therefore, the Si data was considered a reliable guide to extrapolations of the GaAs data. On the other hand, the optical properties of the two semiconductors are quite different, since the minimum-band gap is direct in GaAs and indirect in Si. As a consequence, the absorption coefficient in crystalline GaAs at the 0.693-μm wavelength of the ruby laser is approximately an order of magnitude greater than it is in crystalline Si at the same wavelength. Because of this, the differences between the crystalline and amorphous models described in ref. 2 were expected to be less pronounced in GaAs than they are in Si, and the calculations confirmed this expectation. Melt-front profiles, recrystallization velocities, surface melt duration times, etc., were calculated and found to be quite similar to the corresponding properties in Si. The differences that do exist in such quantities are easily understood in terms of the differences in the thermal and optical properties of the two materials. For example, the latent heat of fusion is more than a factor of 3 greater in Si than it is in GaAs, and as a result significantly less energy is required to melt GaAs to a given depth. The calculations also showed that the energy "window" between melting and vaporization is considerably smaller in Si than it is in GaAs.

Generally speaking, the calculated results are in good agreement with the experimental data on time-resolved reflectivity (TRR) reported by Lowndes and Wood.[4] For example, the calculations predict an energy density threshold E_l of $\sim$0.2 J/cm^2 for melting to a depth of $\sim$200 Å; this is in excellent agreement with the observed value of E_l for which the TRR signal just barely reaches the maximum value characteristic of the creation of a fully molten surface layer. The model calculations predict the onset of vaporization of GaAs at about 0.8 J/cm^2 for 15-ns pulses from a ruby laser, and again this seems to be in reasonably good agreement with the experimental results. Finally, good fits between the experimental and calculated dopant profiles for Mg and Zn implanted into GaAs can be obtained, and these fits allow values of D_l (diffusion coefficient in liquid) and k_l (non-equilibrium interface segregation coefficient) to be determined for these dopants.

---

1. Computer Sciences Division, UCC-ND
2. R. F. Wood and G. E. Giles, *Phys. Rev. B* **23**, 2923 (1981); "Macroscopic Theory of Pulsed-Laser Annealing: I. Thermal Transport and Melting," this report.
3. R. F. Wood, J. R. Kirkpatrick, and G. E. Giles, *Phys. Rev. B* **23**, 5555 (1981); "Macroscopic Theory of Pulsed-Laser Annealing: II. Dopant Diffusion and Segregation," this report.
4. D. H. Lowndes and R. F. Wood, *Appl. Phys. Lett.* **38**, 971 (1981).

RAMAN SCATTERING FROM ION-IMPLANTED LASER-ANNEALED Si

R. F. Wood

Compaan and co-workers[1-3] have reported the results of several types of time-resolved Raman scattering experiments on Si samples irradiated with intense laser pulses of nanosecond duration. They concluded that their results were inconsistent with the melting model of pulsed-laser annealing which they, therefore, asserted could not be correct. We have shown by direct calculations that a number of the results, believed by Compaan and co-workers to contradict the melting model, are in fact in satisfactory agreement with that model.

Lo and Compaan[1] used a pulsed-probe beam (λ = 0.405) to measure the ratio of the Stokes-to-anti-Stokes (S/AS) Raman intensities from a laser-irradiated Si sample that was not ion implanted. From the S/AS ratio, they concluded that the near-surface region of the sample did not exceed 300 ± 50°C even at $E_l \simeq 1.0$ J/cm^2. The melting model predicts that the lattice should reach temperatures very near the melting point under the conditions used in ref. 1. Later, Lo and Compaan[2] used essentially the same techniques to measure the recrystallization of Si samples ion implanted with 200 keV As ions to a dose of 10^{15}/cm^2. By monitoring the growth of the Raman signal, they concluded that recrystallization from the amorphous state (created by the ion implantation) was already far advanced at $\sim$30 ns after a laser pulse of E_l = 0.6 J/cm^2. During part of the time that the Raman signal was detectable, the sample was observed to be in the high reflectivity phase, usually associated with melting of the near-surface region. Lo and Compaan contended that this was conclusive proof that the high-reflectivity phase was not indicative of melting. Compaan et al.[3] extended the measurements of ref. 2 to include the measurement of the lattice temperature by the Raman S/AS ratio and reported a temperature of 600 ± 200°C, approximately 60 ns after 0.6 J/cm^2 laser pulses; they again contended that this was inconsistent with the melting model.

Melting model calculations designed to approximate as closely as possible the experimental conditions employed by Compaan et al. in refs. 2 and 3 were carried out. The results for the motion of the melt front showed that the occurrence of a Raman signal at $\sim$30 ns after the end of the 0.6 J/cm^2 heating pulse is not only *not surprising*, as Compaan et al. imply, but also is fully in accord with the predictions of the melting model. In fact, in view of the unavoidable energy inhomogeneities of individual laser pulses, the variations of the energy density from pulse to pulse, and the fact that Compaan et al. employed a statistical counting technique over thousands of laser pulses, it is quite likely that a Raman signal would have been obtained at even shorter delay times had these been used in the experiments. For the same reason, it is hardly surprising that both the high reflectivity phase and Raman scattering were observed at approximately the same delay times and energy densities.

The calculations also gave information about the temperature in the near-surface region after the melt front had returned to the surface (complete recrystallization). Table 1.6 shows the temperature of the near-surface region accessible to the 0.405-μm probe light used in ref. 3 for selected

Table 1.6. Temperatures in °C at various depths and times in an As-implanted Si sample after irradiation with laser pulses of E_l = 0.4, 0.6, and 0.8 J/cm²

Time (ns)	E_l = 0.4 J/cm² depth (μm)				E_l = 0.6 J/cm² depth (μm)				E_l = 0.8 J/cm² depth (μm)			
	0	0.04	0.08	0.12	0	0.04	0.08	0.12	0	0.04	0.06	0.08
50	666	666	665	663	1028	1027	1025	1020	1410	1404	1391	1378
60	596	595	594	593	907	907	905	902	1263	1261	1259	1256
70	541	541	540	539	823	822	821	819	1094	1093	1092	1091
80	498	498	498	497	759	758	757	756	993	993	992	992

times near the 59-ns delay time utilized by Compaan et al. for values of E_l of 0.4, 0.6, and 0.8 J/cm². Clearly, the calculated temperatures at E_l = 0.6 J/cm² are very nearly within the estimated temperature range reported in ref. 3. When it is considered that the calculations, as well as the experiments, have uncertainties associated with them, it is difficult to substantiate the claim that the Raman experiments unambiguously reveal a temperature significantly below that predicted by the melting model. Thus, we conclude that the experimental Raman results for ion-implanted Si published to date are not necessarily inconsistent with the melting model of pulsed-laser annealing.

The temperature of 300 ± 50°C reported in ref. 1 for unimplanted Si is more difficult to explain, and therefore more significant, if indeed it is correct. Obviously, the time-resolved measurements need to be repeated carefully under improved experimental conditions. However, it is interesting to consider whether or not the S/AS ratio is a reliable measure of the temperature of a sample undergoing pulsed-laser annealing. In Brillouin scattering it is known that large temperature *gradients* will make the S/AS ratio completely invalid as a measure of the temperature.[4] The possibility that the large temperature gradients which occur during pulsed-laser annealing may also affect the Raman measurements of temperature is being investigated.

1. H. W. Lo and A. Compaan, *Phys. Rev. Lett.* **44,** 1604 (1980).

2. H. W. Lo and A. Compaan, *Appl. Phys. Lett.* **38,** 179 (1981).

3. A. Compaan et al., p. 13 in *Laser and Electron-Beam Solid Interactions and Materials Processing*, ed. by J. F. Gibbons, L. D. Hess, and T. W. Sigmon, North Holland, New York 1981.

4. A. Griffin, *Can. J. Phys.* **46,** 2843 (1968).

2. Surface and Near-Surface Properties of Solids

During this reporting period the use of ion implantation and/or laser annealing techniques to alter the surface and near-surface properties of solids in a desired manner has increased markedly. A significant portion of the work reported in this section involves materials prepared or processed by one or both of these techniques. Reported here also are the results of the first research performed by members of the Division staff employing synchrotron radiation at other national facilities. Cooperative work with staff in other ORNL divisions has continued to increase, and collaborative research with staff at academic and industrial institutions has grown at an even greater rate. The multiplicity of coauthors listed on a majority of the papers in this section of the report demonstrates the extent of these joint efforts. Much of the experimental work summarized here requires theoretical support. To obtain a more comprehensive view of the total effort, the reader is referred to the first section of this report, which is devoted to theoretical solid state physics.

Research in the Surface Physics Program has continued to emphasize the examination of relaxed and reordered surfaces. The best agreement ever obtained between LEED theory and experiment for a semiconductor surface structure was achieved, and the electronic structure of this surface was determined. Studies of surface-induced multilayer relaxation systems were also emphasized, and investigations of dilute binary alloys and of domain reconstruction and phase transitions on surfaces were initiated. Combined EELS and LEED techniques continued to be used to establish the sequence of events occurring during both adsorption and reaction of molecular species at surfaces.

Work supporting the ORNL Magnetic Fusion Energy Program has been increased by staff in the Plasma Materials Interactions Program, and very interesting and useful information has been obtained. A major effort was made to determine the effects produced by hydrogen recycling in ISX-B, and mechanisms of impurity introduction into the plasma from the limiter and walls were identified. The use of deposition-probe techniques to determine plasma and impurity fluxes was continued, particularly as they relate to the effects of isotopic exchange, neutral beam injection, and gas puffing on plasma edge characteristics. In addition, the development of laser-induced fluorescence as a technique for determining the density and velocity distributions of impurities in the plasma edges was continued, and significant new results using this technique are reported.

Although part of a larger program, reports concerning fundamental processes in ion-solid interactions are separated from other program elements for the reader's convenience. A joint effort has been established with staff in the ORNL Metals and Ceramics Division to study ion-implanted ceramic materials. Results obtained from Cr-doped α-Al_2O_3 have demonstrated that the mechanical properties of ceramic surfaces can be controlled by selective implantations and thermal annealing. The research effort on enhanced scattering yields near 180°C has continued; understanding of the physical processes leading to enhancement has

been increased; and it was established that double-alignment measurements and their normalization are matters of considerable concern. Also, work on lattice site location by proton-induced x-ray excitation was continued, as were examinations of implantation-induced lattice damage and solid-phase epitaxial crystal growth.

The pulsed-laser annealing (PLA) studies reported here involved cooperative efforts of a large number of people both within and without ORNL. The principal areas addressed by PLA research were: the question of melting of pure and ion-implanted Si, an examination of the kinetic and thermodynamic limitations on solute trapping during epitaxial regrowth, studies of the factors contributing to interfacial instabilities and cell formation, and the characterization of defects associated with the annealing process. The effects of PLA on the properties of some superconducting materials are also reported here. One of the more interesting results from this body of work was the demonstration by synchrotron x-ray diffraction studies and related work that, during PLA, the melting model is very probably correct for Si and a number of its alloys. The synchrotron experiments were particularly important, because they showed for the first time that structural information could be obtained with a single synchrotron pulse.

In studies of the photovoltaic conversion of solar energy, the continuing development of laser annealing techniques has resulted in the routine laboratory production of single-crystal Si solar cells of very high efficiency. Reported here are results obtained from amorphous, single-crystal, and polycrystalline Si and crystalline and amorphous GaAs. Optical and electrical property measurements and determinations of changes in these properties resulting from PLA were emphasized. Time-resolved optical reflectivity and transmission of Si while it was subjected to pulses of laser light provided evidence confirming the melting model for PLA. Studies of grain boundary effects have emphasized the careful characterization of the boundaries and the correlation of electrical activity with the type of boundary. Also, the electrical passivation of the boundaries by Li was shown to be a promising technique.

SURFACE PHYSICS

ATOMIC STRUCTURE OF LASER-ANNEALED Si(111)-(1×1)[1]

D. M. Zehner H. L. Davis
J. R. Noonan C. W. White

The results of recent experiments in which single-crystal semiconductors are irradiated with the output of a pulsed laser in a UHV environment demonstrate that the expitaxial regrowth process extends to the outermost surface layers and that clean, well-defined surface structures are produced.[2,3] In particular, the LEED spot patterns obtained from surfaces of Si(111)- and Ge(111)-oriented single crystals indicate that metastable (1×1) structures can be produced with this process.[3] These observations are to be contrasted with the reconstructed surface arrangements present after other preparation techniques, such as cleavage or sputtering followed by thermal annealing, are used. Although extensively investigated,[4] the successes achieved in the structural determinations of the reconstructed surfaces have been quite limited. Some attempts to avoid the difficulties arising from reconstruction have been explored, such as using impurities (<5% of a monolayer of Te) to stabilize a (1×1) structure, for which a conventional LEED analysis has been performed.[5] However, it is difficult to assess the effects due to the presence of impurities and to compare results of this investigation with predictions of various model calculations. Thus, since the (1×1) surface structures obtained by laser irradiation are also observed to be atomically clean,[2] we have performed a detailed LEED analysis of the Si(111)-(1×1) surface, and the results are presented here.

All measurements were made in a conventionally equipped UHV surface analysis facility. The pro-

cedures for obtaining an atomically clean Si(111)-(1×1) surface using the light from a Q-switched ruby laser have been discussed previously.[2] The intensities of the diffracted electron beams were measured with a Faraday cup operated as a retarding field analyzer. By equalizing the intensities and diffraction angles of intense diffraction peaks in symmetrically related beams, the surface normal was aligned to within ±0.1° of the incident beam direction. Symmetrically equivalent beams were averaged to produce a data base which contained the mean profiles. These profiles were compared with those obtained from fully dynamical LEED calculations, which have been based on assumed structural models that have allowed only for relaxations in the interlayer spacings of the bulk termination. Since alternate interlayer spacings of the (111) truncation of the diamond lattice are quite small (0.78 Å for Si), the effects of both intralayer and interlayer multiple scattering were treated using the angular momentum (or L) representation. Tests were performed to determine that the calculations were both convergent numerically and employed reasonable values of the nonstructural parameters. It was determined that adequate convergence was obtained when calculations were performed using seven phase shifts and ten atomic layers. The phase shifts used were obtained from a truncated free-atom potential (TFA), which was constructed with full-Slater exchange. In addition, a surface-region Debye temperature of 550 K and a constant imaginary component of the optical potential equal to 4.5 eV were employed. The real component of the optical potential was selected by shifting the computed profiles until the best overall agreement with the total experimental data base was obtained.

Intensity-vs-voltage (I-V) profiles were obtained for all the {10}, {01}, {20}, and {02} beams and three of each of the {11} and {21} beams. The indexing is such that the (10) and (01) beams lie in the [10$\bar{1}$] and [$\bar{1}$2$\bar{1}$] azimuths, respectively. Calculations were performed in which both the first and second interlayer spacings, d_{12} (bulk value = 0.78 Å) and d_{23} (bulk value = 2.35 Å), were varied over reasonable ranges. Results of the calculations can be presented conveniently using the optimal R factor,[6] which is the minimum value of R obtained for variation of the real component of the optical potential for a given d_{12} and d_{23}. The changes in the six-beam optimal R factor with these variations are illustrated by the contour map shown in Fig. 2.1. The results suggest that d_{12} is contracted by 25.5 ± 2.5% and d_{23} is expanded by 3.2 ± 1.5%. Profiles calculated using these values are shown in Fig. 2.2, which also contains the corresponding

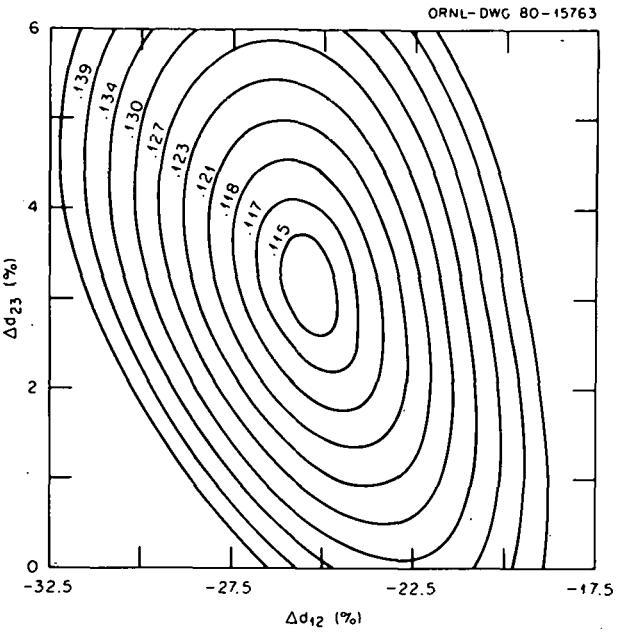

Fig. 2.1. Six-beam optimal R-factor contour map illustrating the effects of variation of the second interlayer spacing d_{23} with variation of the first interlayer spacing d_{12}.

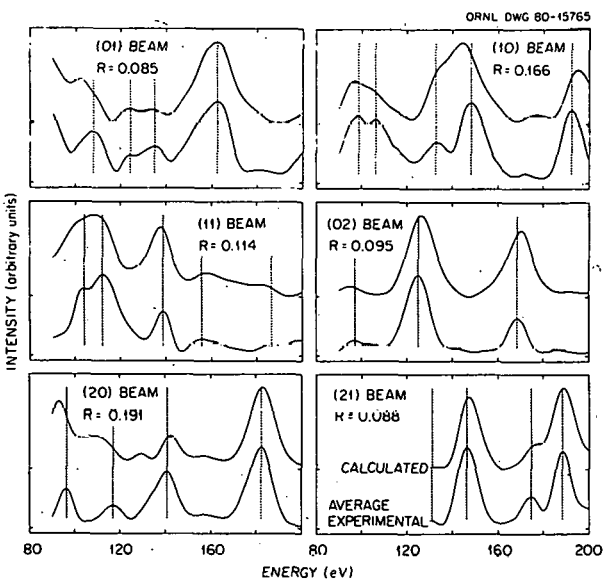

Fig. 2.2. A comparison of the averaged experimental I-V profiles with calculational results for $\Delta d_{12} = -25.5\%$ and $\Delta d_{23} = 3.2\%$.

experimental profiles and single-beam R factors determined for each comparison. The six-beam R factor, corresponding to Fig. 2.2 and determined as the minimum of Fig. 2.1, is 0.115. The changes in interlayer spacings determined from this analysis correspond to nearest-neighbor bond-length changes of -0.058 and 0.075 Å.

Although only ordered structural models were tested in this analysis, the quality of agreement as determined by the value of the R factor, when compared with similar analyses for other surfaces, suggests a highly probable structural determination. Also, the R value obtained in this analysis is the smallest ever obtained in a LEED analysis of a semiconductor surface. This may in part be due to the fact that the structural model proposed as a result of this investigation is one which involves interplanar spacing changes, relaxation without reconstruction, and is obviously much simpler to treat in a calculational sense. It should also be noted that the size of contraction in the first interplanar spacing determined in this analysis is almost the same in magnitude as that predicted by total energy calculations.[7] Although the first-to-second interlayer spacing determined for the Te-stabilized (1×1) structure is similar to that obtained in this investigation, it is not obvious that identical surface structures are present following the two different surface preparations.

Heating to ~800 K subsequent to laser annealing converts the (1×1) to a (7×7) structure. It appears reasonable that, under the combined time and temperature conditions present during the laser annealing process, the atoms in the outermost layers are not able to diffuse into the ordered geometric arrangements corresponding to a reconstructed surface[3] after the regrowth of the molten region (~5000 Å). However, it may be that some type of defect remains in the surface layer after laser irradiation which effectively inhibits the reconstruction. Although impurities such as Te have been used as the stabilizing component,[5] the laser-irradiated surface is atomically clean;[2] therefore, this type of defect can be eliminated. The question of order and the extent of defects can be examined by comparing the intensity of diffuse scattering for both the (1×1) and (7×7) surface structures, and such work is in progress.

1. Summary of paper: *J. Vac. Sci. Technol.* **18,** 852 (1981).

2. D. M. Zehner, C. W. White, and G. W. Ownby *Appl. Phys. Lett.* **36,** 56 (1980).
3. D. M. Zehner, C. W. White, and G. W. Ownby, *Appl. Phys. Lett.* **37,** 456 (1980).
4. D. E. Eastman, *J. Vac. Sci. Technol.* **17,** 492 (1980).
5. H. D. Shih et al., *Phys. Rev. Lett.* **37,** 1622 (1976).
6. E. Zanazzi and F. Jona, *Surf. Sci.* **62,** 61 (1977).
7. J. Ihm and M. L. Cohen, *Phys. Rev. B* **21,** 1527 (1980).

ELECTRONIC STRUCTURE OF THE ANNEALED Ge(111) AND Si(111) SURFACES: SIMILARITIES IN LOCAL BONDING[1]

D. M. Zehner B. Reihl[2]
C. W. White F. J. Himpsel[2]
P. Heimann[2] D. E. Eastman[2]

The annealed (111) surfaces of Ge and Si are observed to reconstruct in different ways: a (1×1) LEED pattern is obtained from the laser-annealed Ge(111) and Si(111) surfaces, a (2×8) pattern from the thermally annealed Ge(111), and a (7×7) pattern from the thermally annealed Si(111). Despite these differences, similar types of geometries have been proposed for all thermally annealed surfaces, for example, buckling models, island-type microdomains, or (2×2) building blocks centered around vacancies. Each of these models has a characteristic short-range order, or local bonding, and can accommodate different types of long-range order for different surfaces as seen in LEED observations. In addition, results of a recent dynamical LEED analysis of the laser-annealed Si(111)-(1×1) surface are in good agreement with a model in which the outermost atomic layer is relaxed inwards by ~0.20 Å and the distance between the second and third layers is expanded by ~0.07 Å relative to the ideal (1×1) geometry, with no lateral displacements.[3] Theoretical band calculations predict that such a surface would be metallic, with a half-filled band of dangling-bond states at the Fermi energy E_F, and would be very different from the annealed Si(111)-(7×7) surface. Photoelectron spectroscopy (PES) yields information directly about the local bonding but is less sensitive to the long-range order than LEED. Therefore, we have used PES to determine the electronic surface states and surface core levels associated with different Ge(111) and Si(111) surfaces.

A display-type spectrometer at the synchrotron radiation source, Tantalus I, was used to determine the extent of the surface states in $\bar{k}$ space, their symmetries, and binding energies and to obtain the number of special surface atoms which exhibit shifted core levels.[4] The procedure used for preparing each of the surface structures using laser annealing and thermal annealing has been described previously.[5]

Figure 2.3 shows angle-integrated (1.8 sr) photoelectron spectra for clean (laser-annealed and thermally annealed) and H-covered Ge(111) and Si(111) surfaces. Note that all four clean surfaces have a doublet of states near the top of the valence band E_V, which are quenched by H exposure (about one monolayer of H). Relative to E_V, these states lie at -0.4 and -1.3 eV for the two Si(111) surfaces and at -0.7 and -1.3 eV for the two Ge(111) surfaces. The width of these surface states is $\sim$0.5 eV (FWHM), and no dispersion is observed when $\bar{k}_{\parallel}$ is changed (detection limit $\sim$0.1 eV). The absence of any emission in the gap at E_F for the Si(111)-(1×1) surface is not in accord with predictions of one-electron band calculations for an unreconstructed surface and, therefore, appears to be inconsistent with the structural model for this surface determined in the LEED analysis.[3]

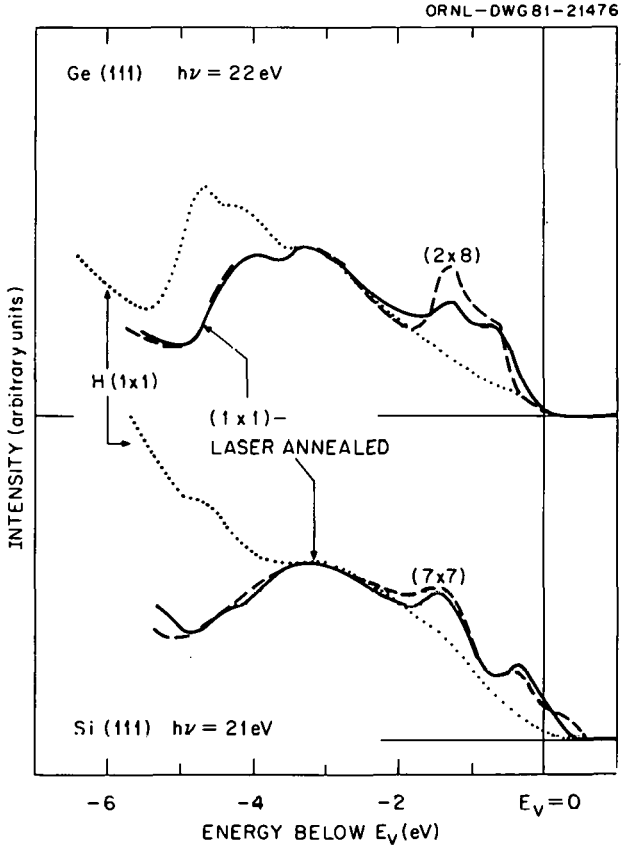

Fig. 2.3. Angle-integrated photoelectron spectra for the annealed Ge(111) and Si(111) surfaces showing emission from two surface states near the top of the valence band which is quenched by H exposure (dotted lines).

Using angle-resolved polarization-dependent PES, we find that the surface states have distributions in momentum $k_{\parallel}$ space and symmetries which are similar for all four surfaces. Remarkably, these predominant surface states match the (1×1) surface Brillouin zone and show no indication of the small reciprocal (2×8) or (7×7) unit cells. This may be taken as a confirmation that we indeed observe the short-range order [given by the larger (1×1) unit cell in $k_{\parallel}$ space]. There is one exception for the Si(111)-(1×1) surface: we find a weak third surface state near the Fermi level (Fig. 2.3) which makes the Si(111)-(7×7) surface metallic, in contrast to the other three surfaces. This state exhibits a well-defined hexagonal angular emission distribution that is peaked at the Brillouin-zone boundary of a (2×2) surface unit cell and is sensitive to the long-range (7×7) order. This observation is consistent with a band picture wherein the Si(111)-(7×7) surface must be metallic, because there is an odd number of electrons in the (7×7) unit cell. Each band holds two electrons, which leaves a partially filled band.

Complementary information about the surface geometry is given by the shifts of core levels[6] for specific surface atoms. Figure 2.4 depicts surface-sensitive angle-integrated photoelectron spectra for Ge $3d$ and Si $2p_{3/2}$ core levels. By comparing spectra for the clean surfaces (full lines) with the H-covered surface spectra (dotted lines), it is clear that there are core levels at lower binding energies which are characteristic of the clean surfaces. A least-squares fit to the data has been performed using bulk and surface core levels and their spin-orbit partners. The results of this analysis are given in Table 2.1. All the annealed Ge(111) and Si(111) surfaces have roughly 1/4 monolayer of surface atoms with a large core level shift (0.6–0.8 eV) toward lower binding energy.

The strong similarity in the valence-band surface states and in the surface core-level spectra for the Si(111)-(7×7) and Ge(111)-(2×8) surfaces appears to be the first measurements which conclusively demonstrate the similarity in the

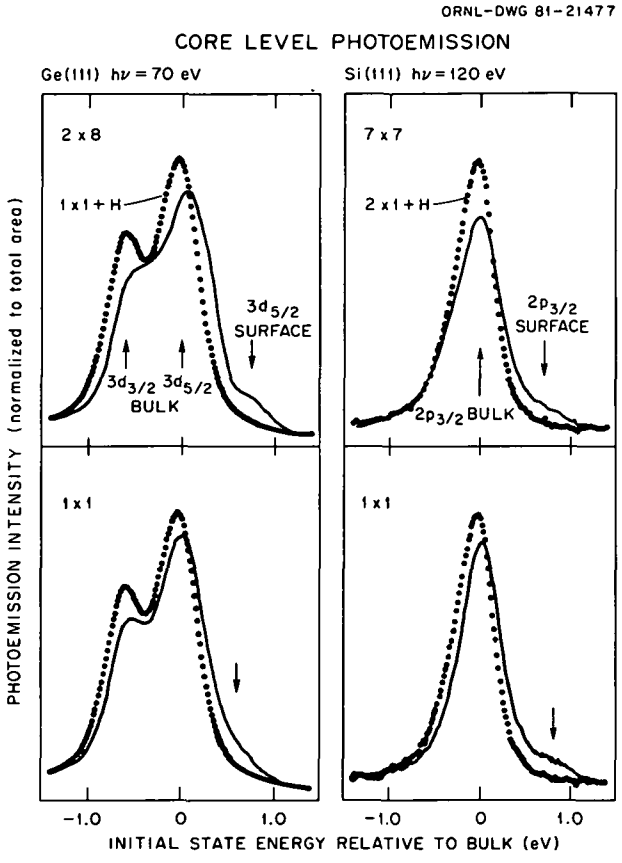

Fig. 2.4. Surface-sensitive core level spectra for the annealed Ge(111) and Si(111) surfaces showing shifted core levels for special surface atoms. The Ge data consist of spin-orbit split $3d_{3/2}$ and $3d_{5/2}$ levels, whereas in the Si data the $2p_{1/2}$ levels have been removed by spin-orbit deconvolution. Dotted lines are for H-covered surfaces [Ge(111)-(1×1) + H and Si(111)-(2×1) + H, respectively], wherein the surface core levels at lower binding energies become removed.

short-range order for these surfaces. Within a band picture, either a suitable distorted (2×2)-vacancy model or buckled-surface models, which have both sufficient distortions to create strong back bonds and weaker long-range order [(2×8) and (7×7)], could be consistent with these findings.

Furthermore, the similarities in the spectra for the laser-annealed Si(111)-(1×1) and thermally annealed Si(111)-(7×7) surfaces indicate that these surfaces have very similar local-bonding geometries and differ mainly in long-range order involving geometrical arrangements that are only a perturbation on the average local-bonding geometry. An interesting question then is why the LEED analysis[3] of the laser-annealed surface yields such good agreement with data using a model (1×1) geometry which appears to be different from that needed to describe the surface electronic structure. One possible explanation is that LEED is not particularly sensitive to long-range disorder, if it is present, on the (1×1) surface. Another explanation is that photoemission can rule out the relaxed ordered (1×1) geometry only if the surface states are bandlike as assumed in one-electron band calculations. However, correlation effects may be very important for these narrow surface levels. Recent theoretical studies[7,8] of the Si(111)-(1×1) surface have shown that the photoemission data are not inconsistent with the unreconstructed relaxed surface structure predicted by LEED analysis when correlation effects are considered. In these models it is assumed that strong correlations dominate the surface-state band structure. Both theories predict a low-temperature antiferromagnetic ground state and a downward

Table 2.1. Special surface atoms for the annealed Ge(111) and Si(111) surfaces

	Core level shift (toward lower binding energy, ±0.1 eV)	Number of atoms involved (±0.05 layer)
Ge(111)-(2×8)	0.75 eV	0.28 Layer
Ge(111)-(1×1)	0.60 eV	0.37 Layer
Si(111)-(7×7)	0.70 eV	0.16 Layer
Si(111)-(1×1)	0.80 eV	0.23 Layer

dispersion of the dangling bond along Γ-J at low temperatures. These theories should be tested experimentally.

1. Summary of two papers: *Physical Review B* (in press).
2. IBM T. J. Watson Research Center, Yorktown Heights, N.Y.
3. D. M. Zehner et al., *J. Vac. Sci. Technol.* **18,** 852 (1981).
4. D. E. Eastman et al., *Nucl. Instrum. Methods* **172,** 327 (1980).
5. D. M. Zehner, C. W. White, and G. W. Ownby, *Appl. Phys. Lett.* **37,** 456 (1980).
6. F. J. Himpsel et al., *Phys. Rev. Lett.* **45,** 1112 (1980).
7. C. B. Duke and W. K. Ford, *Surface Science Letters* (in press).
8. R. Del Sole and D. J. Chadi (to be published).

ELECTRONIC PROPERTIES[1] OF LASER-ANNEALED (111)-(1×1) SURFACES OF HIGHLY DOPED SILICON[1]

D. E. Eastman[2] B. Reihl[2]
P. Heimann[2] D. M. Zehner
F. J. Himpsel[2] C. W. White

The observation that laser annealing can be combined with ion implantation to provide semiconductor surface regions which contain novel doping concentrations (supersaturated alloys) suggests that these techniques may be used to alter or tailor the electronic structure in this region. To examine the possibility, photoemission techniques using synchrotron radiation and laser annealing with a Q-switched ruby laser have been employed to investigate highly degenerate n-type Si(111)-(1×1) surfaces as a function of As concentration up to 5×10^{21} cm^{-3} (10 at. %) and degenerate p-type Si(111)-(1×1) as a function of B concentration up to 1×10^{21} cm^{-3} (2 at. %). The samples were prepared by ion implanting ^{75}As (100 keV, 7×10^{16} cm^{-2} and 1×10^{16} cm^{-2}) and ^{11}B (35 keV, 2×10^{16} cm^{-2}) and then by laser annealing in situ. The maximum doping concentrations are about ten and three times the concentrations of electrically active As and B achievable by conventional techniques, respectively.

Angle-integrated photoemission spectra for the valence bands and 2p core levels are shown in Figs. 2.5 and 2.6 for intrinsic Si(111)-(1×1), degenerate

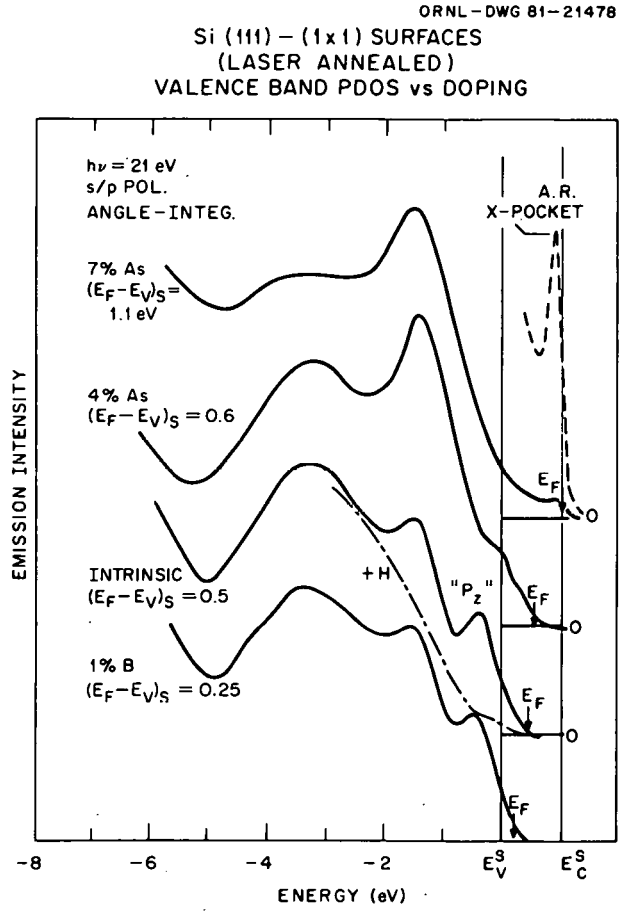

Fig. 2.5. Photoemission spectra for the valence bands of laser-annealed (111)-(1×1) surfaces of intrinsic and highly doped Si. The levels near −0.4 and −1.3 eV are due to surface states. E_V^s, E_C^s, and E_F denote the valence-band maximum, conduction-band minimum, and Fermi-level positions at the surfaces, respectively.

n-type As-doped (4 and 7 at. %) Si(111)-(1×1), and degenerate p-type B-doped (1 at. %) Si(111)-(1×1) surfaces. In Fig. 2.5, spectra are normalized to constant total emission within 5 eV of E_F, and energies are given relative to the valence-band maximum at the surface E_V^s. The Fermi-level position relative to the valence-band maximum at the surface $(E_F - E_v)s$ for intrinsic Si(111)-(1×1) was previously determined to be 0.5 eV.[3] E_F is seen to shift markedly with doping (i.e., from 0.25 eV above E_V^s for the B-doped sample to the conduction-band minimum $E_C^s = 1.1$ eV for the 7% As-doped sample). For intrinsic Si(111)-(1×1) in Fig. 2.5, the dash-dot line shows the effect of an adsorbed monolayer of H, which is

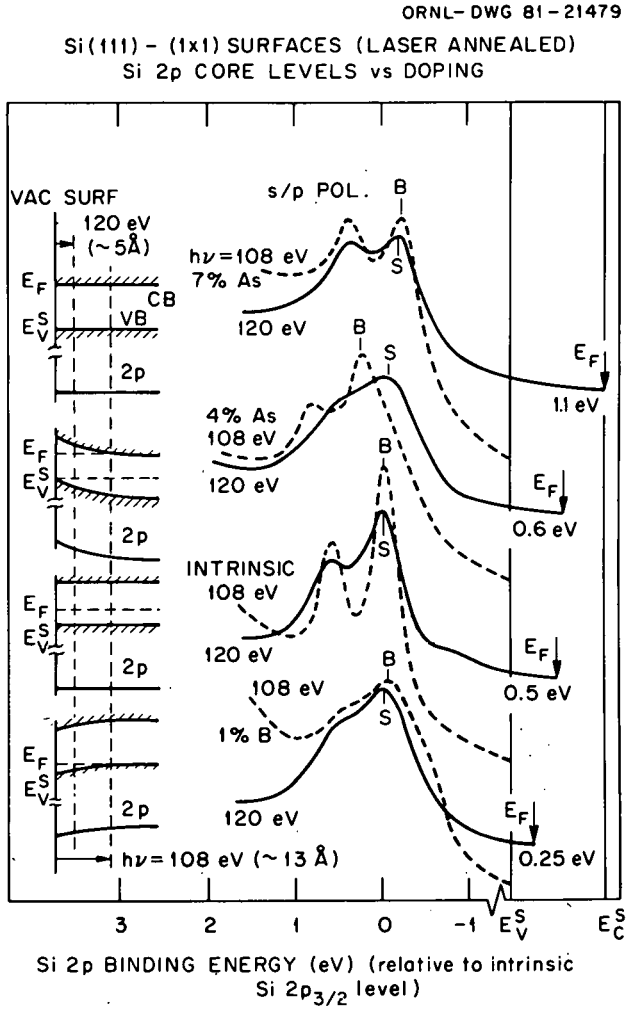

Fig. 2.6. Angle-integrated photoemission spectra for the Si 2*p* core levels of the four Si surfaces depicted in Fig. 2.5. The binding energy at zero corresponds to the Si $2p_{3/2}$ level for bulk Si(111)-(1×1). The schematic diagrams on the left depict band bendings and energy-level positions; escape depths are $l \sim 5$ Å for $h\nu = 120$ eV and ~13 Å for $h\nu = 108$ eV.

to remove the two predominant surface-state levels at 0.4 and 1.3 eV below E_V^s. Relative to intrinsic Si, for highly degenerate (1 at. %) B doping, the two states are unaltered and the principal changes are that E_F moves down by 0.25 eV and the surface becomes metallic.

More dramatic effects are seen with As doping. At 4 at. % As doping, the surface states have become significantly altered, while E_F has increased by 0.1 eV relative to the intrinsic Si. Namely, the upper "Sp_z-like" dangling bond state has become much weaker and shifted upward in energy by 0.3 eV, the lower −1.4 eV state has increased significantly in intensity but is unshifted, and the surface has become metallic with new states near E_F. As the doping is further increased from 4 to 7 at. %, E_F rapidly shifts and becomes pinned at the E_C^s. Also, the intensity from the upper Sp_z-like surface state continues to diminish so that it is nearly imperceptible by 7 at. % doping, and the lower surface state becomes extremely intense. The conduction-band minima Δ_{min} near X become occupied, and emissions from these minima are observed as intense elliptical lobes in angle-resolved photoemission spectra (dotted line labeled AR in Fig. 2.5).

The Si 2*p* core-level spectra shown in Fig. 2.6 were obtained using $h\nu = 108$ eV (dashed lines) and $h\nu = 120$ eV (solid lines), which provide "bulk-sensitive" and "surface-sensitive" spectra, respectively.[4] *S* and *B* denote surface and bulk 2*p* levels. For intrinsic Si and 7 at. % As-doped Si surfaces, the 2*p* levels are the same for both $h\nu = 108$ and $h\nu = 120$ eV (i.e., the "surface" *S* and "bulk" *B* $2p_{3/2}$ levels coincide in binding energy). This is an indication of the "flat-band" condition at the surface, as shown by the schematic diagrams on the left of Fig. 2.6. *CB* and *VB* denote the conduction-band and valence-band edges. A finding of significant interest is that at an As-doping level of 7% or greater, E_F has shifted across the entire gap from 0.5 eV for an intrinsic Si-(1×1) surface to the E_C^s at 1.1 eV. By depositing a thin Au film on this surface, it was possible to determine via Si 2*p* core-level measurements (not shown in Fig. 2.6) that E_F remained unchanged (within ~ 5.0 meV). Thus, a "zero-barrier-height" Schottky barrier was formed, although for electrical purposes the AuSi interface is undoubtedly shorted due to the extreme degenerate *n*-type doping, (i.e., short Debye screening length). For 4 at. % As- and 1 at. % B-doping levels, the bands are bent upward and downward in the surface region, respectively. The broadening and smearing of the spectra, when compared to that obtained for intrinsic Si, reflect the distribution in energy of the 2*p* core levels in the sampled region.

It is observed that the binding energy of the $2p_{3/2}$ peak B relative to the valence-band maximum monotonically decreases with increased As doping; for 7 at. % As doping there is a reduction in binding energy of 0.2 ± 0.5 eV (Fig. 2.6). This effect, which appears to be observed for the first time, i

attributed to an initial-state shift due to the change in potential caused by the itinerant As-derived conduction electrons as well as possibly to more effective final-state screening by these conduction electrons.

1. Summary of paper: *Physical Review B* (in press).
2. IBM T. J. Watson Research Center, Yorktown Heights, N.Y.
3. D. M. Zehner et al., *Physical Review B* (in press).
4. F. J. Himpsel et al., *Phys. Rev. Lett.* **45,** 1112 (1980).

OXYGEN-INDUCED RECONSTRUCTION OF THE Cu(110) SURFACE[1]

J. R. Noonan H. L. Davis

Experience has shown that the chemisorption of O on open-faced surfaces of metals is a complex process. For example, a LEED study of O on Ni(110) has indicated that the O atoms position themselves between Ni atoms in the ⟨110⟩ direction.[2] However, results of a more recent ion-scattering study imply that the O replaces each Ni atom in every other (100) chain.[3] Establishing the O adsorption site on the Ag(110) experimentally is equally difficult.[4] Therefore, it is not surprising that our initial attempts to determine the site of O adsorbed on Cu(110) presented difficulties. Recently, however, significant progress has been made in determining the lattice location of O in the Cu(110)-(2×1)O surface. The exact structure has not yet been completely established, but the solution of the problem appears from our LEED analysis to be related to reconstruction by Cu to a ripple surface due to the O atoms being below the surface.

The Cu(110)-(2×1)O system appears from LEED patterns to be relatively simple. For room-temperature exposures as low as 0.05 L and up to 2000 L (1 L = 10^{-6} Torr exposure of gas for 1 s), a (2×1) superlattice LEED spot pattern was observed [i.e., the surface unit cell was twice that of the Cu substrate's ($\bar{1}10$) intraplanar spacing and the same as that of the substrate in the (001) intraplanar spacing]. Annealing at temperatures to 200°C only improved the order of the surface, and no new superlattice beams were detected.

The O-saturated Cu(110)-(2×1)O surface was studied at ORNL by a LEED analysis.[5] The Cu(110) sample was cleaned and annealed until a surface was prepared which was well ordered and free from contamination, as measured using the retarding field analyzer for AES. The crystal was exposed to 20 L of O by backfilling the UHV chamber to 10^{-7} Torr of O for 200 s to produce a (2×1) LEED pattern with streaking in the ⟨110⟩ directions. Well-ordered superlattice diffraction beams were observed after anneals to 185°C for 30 min. The sample was then aligned normal to the incident electron beam, and experimental I-V profiles were measured for 15 nonequivalent, nonspecular LEED beams.

The measured I-V profiles were compared with the results of extensive sets of dynamical LEED calculations. These calculations used computer codes, based on the layer KKR formalism and renormalized forward scattering (RFS) perturbation theory,[6,7] which were developed at ORNL to treat surfaces with a simple overlayer selvedge. Several electron scattering potentials were used for the Cu and O atoms in an attempt to find an optimal potential. Atomic vibrations in the surface region were important in the analysis. Therefore, different values of the isotropic Debye temperature θ_D were used, and it was found that the Cu and O sublattices have different θ_D values. Several model forms of the complex electron optical potential were tested to find one which would give the best agreement with experimental data. Structural models in which the O was above, below, and within the outermost surface plane of the Cu lattice were tested; models which would create reconstruction of the Cu atoms were also included.

Comparing experimental LEED spectra with computed spectra for surface models initially produced unsatisfactory agreement, a result similar to that of others studying O on Ni and Ag. Several model overlayer sites were tested, including the "short bridge," "two-fold hollow," and "on-top" models. None of the simple overlayer models produced satisfactory agreement [Table 2.2(a)-(c)]. During this testing period, De Wit et al.[8] reported a low-energy ion-scattering study (LEIS) of Cu(110)-(2×1)O. They predicted a structure which had two salient features. First, the O atom was located at the long-bridge site but below the Cu surface layer by 0.6 Å. Second, the Cu atoms in the surface were located within 4% at bulk lattice sites. Recently, a He molecular beam scattering study of Cu(110)-(2×1)O has reported results which agree with the LEIS model.[9] Unfortunately, when used in our LEED analysis, this

Table 2.2. Comparison of O lattice position and model parameters for the Cu(110)-(2×1)O structure

Oxygen atomic geometry	Distance from surface layer (Å)	V_{0i} (eV)	D^{Cu} (K)	D^{O} (K)	R_{ZJ}[a]
a Short bridge	+1.3	$-0.85^{1/3}$	250	250	0.525
b 2-fold hollow	+1.8	$-0.85^{1/3}$	250	250	0.367
c Long bridge	+0.4	$-0.85^{1/3}$	250	250	0.574
d Long bridge (De Wit)	−0.6	$-0.85^{1/3}$	250	250	0.422
e Long bridge, Cu rippl	−0.6	$-0.85^{1/3}$	250	250	0.328
f 2-fold hollow	1.8	−6 eV	330	850	0.242
g Long bridge	+0.4	−6 eV	330	850	0.308
h Long bridge (De Wit)	−0.6	−6 eV	330	850	0.249
i Long bridge, Cu ripple	−0.6	−6 eV	340	700	0.217

[a]Zanazzi-Jona reliability factor[10] was used as a measure of agreement between theory and experiment.

model did not produce good agreement between calculations and experiment [Table 2.2(d)].

A serious problem with the De Wit model is that the Cu-O bond length between O and the first layer Cu nearest neighbors is much shorter than Cu-O bond lengths in Cu oxides, which have values between 1.85 and 1.95 Å. To overcome this problem, consider a model in which the O lattice site satisfies three conditions. The O is located at the long-bridge site below the surface; the O placement satisfies the (2×1) superlattice (i.e., an O atom is found at every long-bridge site in the $\langle\bar{1}10\rangle$ direction, but only at every other bridge site in the $\langle 001\rangle$ direction); and finally, the Cu atoms adjust to accommodate a more desirable Cu-O bond length. An immediate consequence of the three criteria, especially considering the bond lengths, is that the Cu atoms in the first layer nearest the O move up to form a ripple-type reconstruction (Fig. 2.7). When this model was tested, the results of our LEED analysis improved significantly over other models tested [Table 2.2(e)].

Following improvement in the LEED analysis due to structural modifications, further refinements of the model were tested. As seen from Table 2.2(i), agreement can be improved even more by consideration of the nonstructural parameters in the analysis. It was found that the O sublattice is considerably stiffer to thermal motion than are the Cu atoms in the surface. In addition, agreement was improved when the imaginary part of the inner potential, V_{0i}, was maintained constant at −6 eV

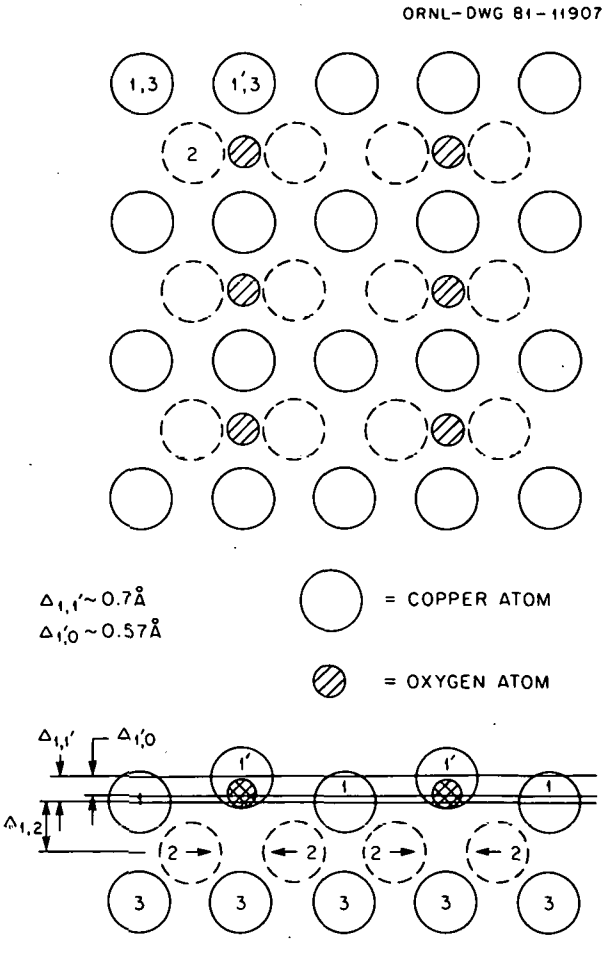

Fig. 2.7. Illustration of the surface atomic structure for the O-induced reconstruction of the Cu(110)-(2×1)O.

in the calculations. Our best LEED analysis to date was obtained using the nonstructural parameters given in Table 2.2. The best model structure obtained to date is that shown in Fig. 2.7. The O atoms are at the long-bridge site with the Cu-O interlayer distance, $\Delta_{1,0}$ = 0.57 Å; the Cu-Cu ripple spacing, $\Delta_{1,1}$ = 0.7 Å; and the second interlayer spacing, $\Delta_{1,2}$, at the spacing and position for bulk Cu. In addition, since the agreement is improved when the second layer Cu atoms, which form a short-bridge bonding to the Cu, contract toward the O by 5%, there is at least a suggestion of subsurface displacement as well.

As a further test to illustrate that the reconstructed surface model produces the best agreement to date, a LEED analysis using the other models was recomputed using the "optimal" nonstructural parameters. As can be seen [Table 2.2(f)-(h)], although the agreement improves with the parameter changes, use of the other models, including the De Wit model, does not produce as good an agreement with experiment as does the reconstructed surface.

Although the agreement between theory and experiment is approaching an acceptable level, as illustrated by a Zanazzi-Jona[10] R factor of 0.217, the conclusions derived in this LEED structure analysis are to be considered as preliminary in nature. The important and novel feature which is reported is that the O atoms located below the surface Cu atoms induce every other (100) row of Cu atoms to move outward, inducing a ripple-type reconstruction in doing so. There are several substantiating observations which support this conclusion. First, the superlattice LEED beams are as strong as the integral order beams, and there is a considerable change of the integral order beam I-V spectra from that of clean Cu. Since O is a weaker scatterer than Cu, the large change in intensities observed is more consistent with the Cu ripple model than with a simple O "on-top" overlayer model. Furthermore, x-ray diffraction analysis of thin epitaxial Cu_2O films on Cu found large strains and vertical displacements in the oxide film.[11] Of course, the O here is in a chemisorbed state, but it is reasonable to extrapolate the concept of large induced strains in the rippled surface as the precursor of the strain in thin oxide films. Further studies of the Cu(111)-(2×1)O surface, which are attempting to refine the prediction of the O and Cu lattice positions, are in progress.

1. Summary of paper to be published.

2. J. E. Demuth, *J. Colloid Interface Sci.* **58,** 184 (1977).

3. R. G. Smenk, R. M. Tromp, and F. W. Saris, *Surf. Sci.* **107,** 429 (1981).

4. E. Zanazzi et al., p. 2447 in *Proc. 7th Int. Vac. Congr. and 3rd Int. Conf. on Solid Surfaces, Vienna, 1977.* ed. by R. Dobrozemsky et al., F. Verger and Sohne, Vienna, Austria, 1977.

5. H. L. Davis, J. R. Noonan, and L. H. Jenkins, *Surf. Sci.* **83,** 559 (1979).

6. D. W. Jepsen, P. M. Marcus, and F. Jona, *Phys. Rev. B* **5,** 3933 (1975).

7. J. B. Pendry, *J. Phys. C* **4,** 3095 (1971).

8. A. G. J. De Wit, R. P. N. Bronckers, and J. M. Fluit, *Surf. Sci.* **82,** 177 (1979).

9. J. Lapajoulade et al., *Phys. Rev. B* **22,** 5740 (1980).

10. E. Zanazzi and F. Jona, *Surf. Sci.* **62,** 61 (1977).

11. B. Borie, C. J. Sparks, Jr., and J. V. Cathcart, *Acta. Met.* **10,** 691 (1962).

SURFACE-INDUCED MULTILAYER RELAXATION OF Ag(110)[1]

J. R. Noonan H. L. Davis

The termination of a solid, creating a surface, may result in the modification of both the atomic and electronic structure in this region. Recently, theoretical studies of surfaces have shown that the atomic and electronic structures can adjust self-consistently to produce multilayer relaxations between atomic planes at the surface.[2] Also, a LEED structural analysis of Cu(100) has provided evidence that at least the first two, and probably three, atom layers at the surface are relaxed from their bulk positions;[3] however, differences exist between the theoretical calculations and the experimental LEED results. These differences are not surprising because the electron distribution used in the theoretical work was free-electron-like, whereas Cu does not behave as a free-electron-type metal. Further studies need to be performed to provide more information about multilayer relaxations at surfaces. Thus, our existing LEED data for the Ag(110) surface have been reanalyzed to determine if this surface also exhibits multilayer relaxation.

The LEED analysis of the Cu(100) surface has shown that in order to determine multilayer relaxations accurately, the experimental data must be of the highest possible quality. For the Cu study all

symmetrically equivalent LEED I-V spectra were measured and then averaged to produce refined spectra to compare with theoretical LEED calculations. The Ag(110) is the only other metal surface for which we have obtained the data necessary to permit averaging of spectra. Therefore, the Ag(110) surface has been restudied to determine if it also exhibits multilayer relaxations.

The Ag (110) sample was cut from a single-crystal boule, lapped, and electropolished. It was then cleaned repetitively by bombarding with 500-eV Ar^+ ions and annealing at 700 K in a UHV chamber until a well-ordered, sharp, LEED pattern with low diffuse scatter was observed and no contaminants could be detected by Auger electron spectrometry. The sample was aligned with procedures developed during the Cu(100) study[3] so that the Ag surface was normal to the electron beam. I-V spectra were collected for all symmetrically equivalent LEED beams in the {01}, {10}, {11}, {02}, {20}, {12}, and {21} data sets using a movable Faraday cup as a retarding field analyzer. Spectra related by symmetry were averaged to obtain refined I-V profiles, which served as the data base for analysis.

Extensive sets of dynamical LEED calculations were performed in which effects of structural changes and nonstructural model parameters were studied. In addition, three different reliability factors (R factors)[4,5] were determined in order to compare experimental and calculated profiles. Since the LEED patterns showed no indication of a superlattice, the only structural changes investigated were displacements of the atomic layers from their bulk positions. Changes in the nonstructural parameters were investigated to identify their optimal values and forms. For example, several forms for the atomic scattering potential, including those of a truncated free atom and of band structure origin, were investigated. One of the band structures provided the best agreement.[6] Several models of the imaginary part of the optical potential also were studied. The form giving the best agreement was one in which the electron amplitude attenuation λ_{ee} was assigned a constant value of 7.5 Å. As was the case for the Cu(100) surface, the nonstructural parameters affected the quality of the agreement between theory and experiment; however, the structural conclusions were not changed significantly by a wide range of variations in model parameters.

A topograph giving values of the seven-beam R_{ZJ} (the Zanazzi-Jona R factor) value for percent changes of the first and second interlayer spacings Δd_{12} and Δd_{23}, respectively, clearly indicates multilayer relaxation for the Ag(110) surface (Fig. 2.8). A Δd_{12} contraction of 5.7% and a Δd_{23}

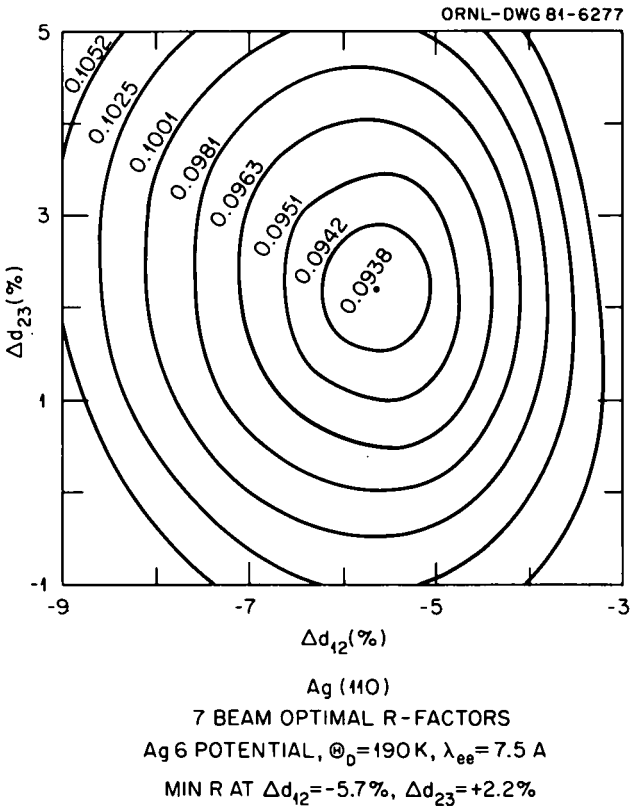

Fig. 2.8. Seven-beam R_{ZJ} topograph as a function of the first interlayer spacing change Δd_{12} and the second interlayer spacing change Δd_{23}. The optimal R_{ZJ}, 0.0938, occurs for $\Delta d_{12} = -5.7\%$, $\Delta d_{23} = +2.2\%$.

expansion of 2.2% give the best agreement between theory and experiment. There are several features of the analysis which reinforce the indicated displacement of the second layer. First, the change in the calculated I-V profiles improves the agreement between theory and averaged experimental data as seen by the change of the R-factor value from 0.098 for only first layer displacement to 0.094 for displacement of the first two layers. Second, analyses of all seven single averaged beams indicate that the second layer is expanded away from the third (determined values of 1–4%). The scatter between the predicted values is quite small and of the order of 2% or less (Fig. 2.9).

The analysis of the Ag(110) LEED data has provided another illustration that by taking special

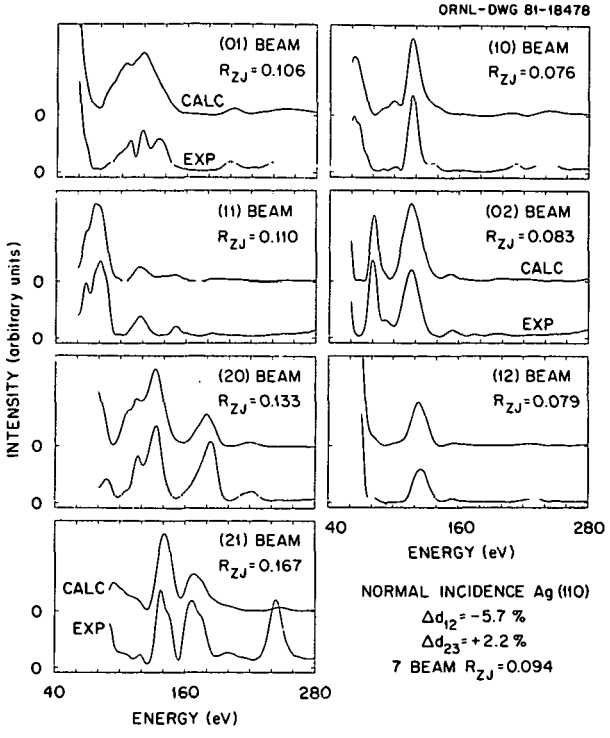

Fig. 2.9. Comparison of theoretical (top) and experimental (bottom) LEED I-V spectra for the seven lowest order nonspecular beams from Ag(110). The calculated profiles are those giving the best agreement with the experimental profiles. The single-beam R factor R_{ZJ} for each pair of profiles is given for each beam. The experimental profiles are the mean profile derived for each equivalent set of LEED beams.

care in measuring the I-V spectra, by collecting symmetrically equivalent beams and determining the mean profile, and by examining extensive sets of calculated profiles (derived using many test values of nonstructural parameters), detailed and very sensitive analyses of surface structures are possible. The first interlayer spacing of the Ag(110) is contracted by 5.7 ± 1.5% from the bulk value, while the second interlayer spacing is expanded by 2.2 ± 2%. Further refinement of the electron mean-free-path model is expected to produce additional improvement in the R-factor agreement, but it should not affect significantly the structural conclusions.

1. Summary of paper to be published.

2. U. Landman, R. N. Hill, and M. Mostoller, *Phys. Rev. B* **21**, 448 (1980).

3. H. L. Davis and J. R. Noonan, *Journal of Vacuum Science and Technology* (to be published); H. L. Davis and J. R. Noonan, "Cu(100) Multilayer Relaxation," this report.

4. E. Zanazzi and F. Jona, *Surf. Sci.* **62**, 61 (1977).

5. M. A. Van Hove, S. Y. Tong, and M. H. Elconin, *Surf. Sci.* **64**, 85 (1977).

6. H. L. Davis, p. 123 in *Proceedings of the International Conference on High Pressure Properties of Solids*, ed. by D. Bloch, Centre National de la Recherche Scientifique, Paris, France, 1970.

ELECTRON SPIN POLARIZATION IN ENERGY- AND ANGLE-RESOLVED PHOTOEMISSION FROM W(001): EXPERIMENT AND THEORY[1]

J. Kirschner[2] R. Feder[3]
J. F. Wendelken[4]

The first observation of spin-polarized photoemission from nonmagnetic crystals by unpolarized light is reported. Two causes have been reported in the past for spin-polarized photoemission, initial-state effects in photoemission from ferromagnets,[5] and matrix-element effects involving circularly polarized light and spin-orbit coupling.[6] A third cause, which is reported here, is a final-state effect in which initially unpolarized photoelectrons may acquire spin polarization as they pass from the solid to the detector located in vacuum outside the solid.

Final-state spin-polarized photoemission is similar to spin-polarized LEED except that the "primary" electrons in photoemission may occupy different Bloch states with the same energy. Also, the source and detector lie on different sides of the crystal-vacuum interface. A common feature is the strong wave-vector dependence of electron spin polarization. Thus, an energy-, angle-, and spin-resolved photoemission experiment is required. To avoid confusion with initial state and matrix element effects, observation of final-state polarization requires the use of nonmagnetic target crystals and unpolarized light.

The experimental apparatus which meets these requirements is shown in Fig. 2.10. Unpolarized light from a commercial discharge lamp (H, L_{ya}) is normally incident onto a W(001) single-crystal surface. The polar angle θ, which must be nonzero for symmetry reasons, was set at 70° due to geometrical constraints. Photoelectrons leaving the surface are accelerated and focused by a four-

ORNL-DWG-81-19005

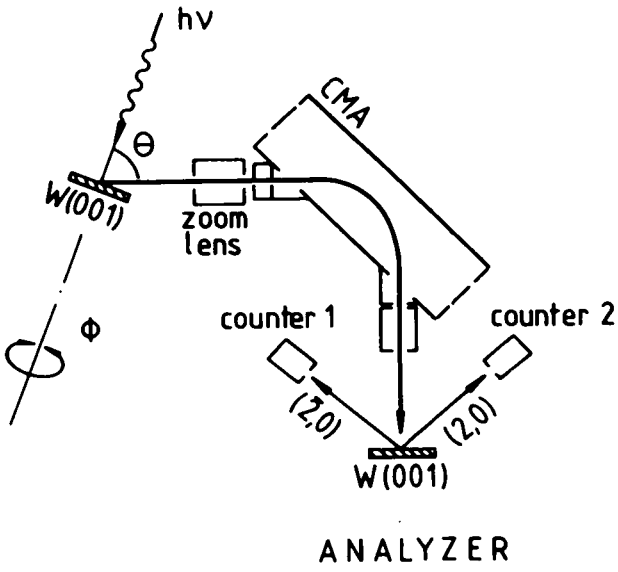

Fig. 2.10. Schematic representation of experimental apparatus used to measure energy- and angle-resolved spin-polarized photoemission.

ORNL-DWG-81-19004

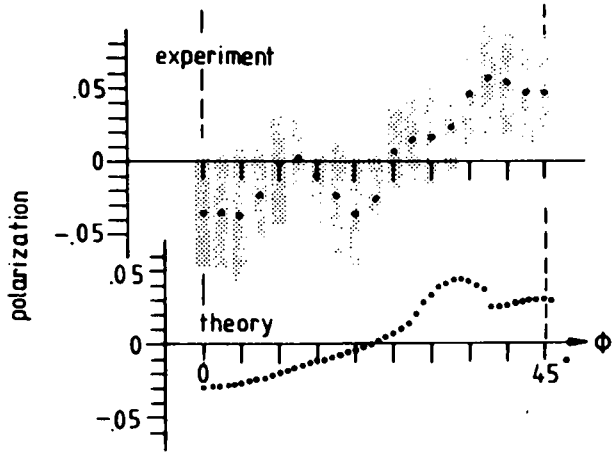

Fig. 2.11. Experimental and theoretical polarization rotation diagrams which show the existence of final-state spin-polarization effects in photoemission from nonmagnetic solids by unpolarized light.

element zoom lens into the energy analyzer, which is a section of a cylindrical mirror analyzer (CMA) operating with a constant-pass energy giving an energy resolution of 0.3 eV. To reduce the contributions from secondary electrons and inelastically scattered photoelectrons, the energy window was set closely below the Fermi energy as measured from intensity spectra. After passing the CMA, the electrons are accelerated onto the second W(001) crystal (normal incidence), and the intensity asymmetry in the two detectors is a measure of the component of the polarization vector normal to the plane of Fig. 2.10. The final stage of this analyzer is identical to the spin analyzer used for previously reported electron double diffraction experiments,[7] where its sensitivity and efficiency have been characterized.

The experimental data are shown in Fig. 2.11 in the form of azimuthal rotation diagrams at a fixed photon energy $h\nu = 10.2$ eV and an electron kinetic energy $E \simeq E_F - 0.5$ eV. In the absence of final-state effects, a constant-zero polarization is expected. The structure observed in the data, which is directly connected with the crystal symmetries, is direct proof of the existence of final-state spin-polarization effects. Results of a theoretical calculation are also shown in the lower portion of Fig. 2.11, and good agreement with the data is observed. In this calculation, unpolarized Bloch electrons, incident from the interior of the crystal, are diffracted at the surface. Spin-orbit interaction may then result in plane-wave electrons (beams) going out into the vacuum, where a particular beam is observed with the detector.

There are several key results of this experiment. First, the feasibility of using the LEED spin-polarization detector for energy-, angle-, and spin-resolved photoemission has been demonstrated. Second, as spin polarization in electron diffraction is known to be sensitive to structural parameters,[8] its analysis may add a further dimension to structure determination via photoelectron diffraction. The main constraint faced in the present experiment, low uv light intensities, should be much relaxed by the future use of synchrotron light. Third, final-state polarization effects must be taken into account in all energy- and angle-resolved photoemission experiments where spin-orbit interaction is present.

---

1. Summary of paper: *Phys. Rev. Lett.* **47**, 614 (1981).

2. Institut für Grenzflächenforschung und Vakuumphysik, Kernforschungsanlage, Jülich, Federal Republic of Germany.

3. Universität Duisburg GH, Duisburg, Federal Republic of Germany.

4. This research conducted while the author was on foreign assignment at the Institüt fur Grenzflächenforschung und Vakuumphysik, Kernforschungsanlage, Jülich, Federal Republic of Germany.

5. S. F. Alvarado, *Z. Phys.* **33**, 51 (1979).

6. M. Wohlecke and G. Borstel, *Phys. Rev. B* **23**, 980 (1981).

7. J. Kirschner and R. Feder, *Phys. Rev. Lett.* **42**, 1008 (1979).

8. R. Feder and J. Kirschner, *Surf. Sci.* **103**, 75 (1981); J. F. Wendelken and J. Kirschner, *Surface Science* (in press).

RECONSTRUCTED DOMAINS ON A STEPPED W(100) SURFACE

G.-C. Wang T.-M. Lü[1]

Previous LEED patterns from a reconstructed, stepped W(100) surface showed extra spots located at (1/2,1/2) beam positions for temperatures less than 370 K.[2] Although the integral-order beams were split at certain electron energies due to the existence of steps on the surface, the half-order beams were never split at any energy. Debe and King[2,3] (DK) estimated that the average terrace width was 85 Å from the angular separation of the splitting of the integral-order beams. They attributed the nonsplitting of the half-order beams to result from the finite "transfer width" (which was estimated to be 45 Å) of the instrument and deduced that a step must inhibit the reconstruction up to 20 Å from the step edge (i.e., the reconstructed domains cannot be nucleated at a terrace smaller than 40 Å). Also, the lateral atomic displacements in the reconstructed domains have been determined to be along the ⟨11⟩ directions.[3]

The "transfer width" (or "coherence width") approach, in our opinion, is too crude and cannot explain the nonsplitting phenomenon of the half-order beams. In the DK experiment, the instrument was able to resolve the stepped surface with an 85-Å terrace width, and the angular separation of the splitting of an integral-order beam reflected the periodicity of the occurrence of steps. This implies that the same instrument (with perhaps slightly different conditions) should be able to resolve domains separated by 85 Å, which have the same periodicity as the steps. This conclusion is independent of domain size. We proposed that the nonsplitting phenomenon is not due to the limitation of the instrument-resolving capability. Instead, we showed[4] that (1) the angular profile of a superlattice beam obtained from LEED from randomly nucleated reconstructed domains on a stepped surface does not split or broaden in an oscillatory manner when the incident electron energy is changed and that (2) the width of the angular profile is inversely proportional to a measure of the domain size.

To test the conclusion that the growth of the reconstructed domains on a W(100) surface is inhibited by step edges up to a distance of 20 Å from a step edge, we prepared a stepped W(100) surface which was 3.5° ± 0.2° off the (100) orientation along the [110] direction and which should have a terrace width 26 Å ± 2 Å along this direction. If the 20-Å inhibition range is true, the reconstruction should not occur on the stepped surface that we prepared.

Extensive oxygen treatments were used to clean the surface until Auger spectra showed no trace of impurities, and a (1×1)-LEED pattern with integral-order beams split at certain characteristic voltages was obtained from the stepped surface at room temperature. An example is shown in Fig. 2.12(a), where all the (11) beams split along the [110] direction at $E = 112$ eV for near normal incidence. These well-resolved splittings in the integral-order beams indicate that the terrace-width distribution is a narrow function centered around an average terrace width. We scanned across the (11) beam with a Faraday cup; from the angular separation of the splitting intensity maxima, we determined the average-terrace width to be 27 Å ± 2 Å. This result is in good agreement with the result obtained using x-ray Laue diffraction. From the characteristic energies where nonsplitting of integral-order beams occurs, we calculated the step heights and obtained single atomic heights.

As the crystal was cooled below room temperature, the integral-order beam splittings remained the same, but the intensities were larger due to the Debye-Waller factor. However, extra nonsplitting half-order beams were seen for a wide range of incident electron energies. An example is shown in Fig. 2.12(b), where half-order beams from two orthogonally oriented domains are observed. The appearance of the extra half-order beams from this stepped W(100) surface strongly suggests that the inhibition range (if it exists at all) is less than 20 Å.

We are in the process of measuring the angular width of the extra half-order beams from which the size of the reconstructed domain can be calculated. Knowing the terrace width and the size of

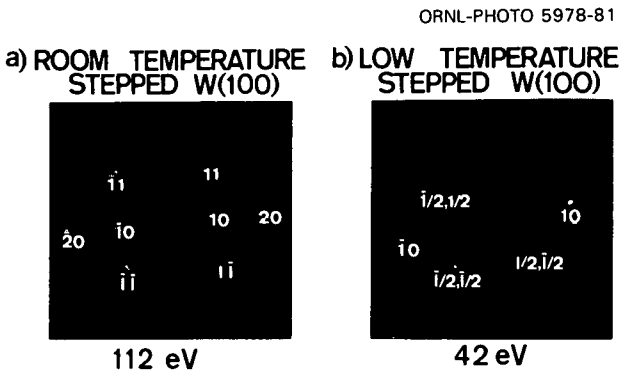

Fig. 2.12. LEED pattern from a stepped W(100) surface (a) at $E = 112$ eV, $\partial_0 = 0°$, $T = 300$ K and (b) at $E = 42$ eV, $\partial_0 = 0°$, $T = 150$ K.

the reconstructed domain, the inhibition range due to the step edge can be determined quantitatively. This knowledge will play an important role in understanding the mechanism of metal surface reconstruction.

1. University of Wisconsin, Madison, Wis.

2. M. K. Debe and D. A. King, *Surf. Sci.* **81,** 193 (1979).

3. M. K. Debe and D. A. King, *Phys. Rev. Lett.* **39,** 708 (1977).

4. T.-M. Lu and G.-C. Wang, *Surf. Sci.* **107,** 139 (1981).

THE EFFECT OF INSTRUMENTAL BROADENING ON LEED INTENSITY-ENERGY PROFILES[1]

T.-M. Lu[2] M. G. Lagally[2]
G.-C. Wang

LEED is the major technique used for surface structure determinations. Considerable effort has been expended during the last ten or more years in developing dynamical theories to extract equilibrium positions of surface or overlayer atoms from experimental intensity-versus-energy (J-vs-E) profiles. The limitations of LEED for such structure determinations, as well as the reliability of the predictions of a particular structure for a particular surface or overlayer, continue to be of concern[3] and were a major topic at a recent conference.[4] There are two types of limitations to the reliability of a structure determination, one introduced by the approximations made in the calculations and the other by uncertainties in the data. A manifestation of the latter is that frequently differences exist between data taken on the same surface in different laboratories. Several factors may be responsible for these differences, including surface imperfections and the instrumental broadening inherent in the LEED instrument. In this report we will summarize the effect of instrumental broadening on the measurements of J-vs-E profiles and suggest a simple method to extract from the measurements the scattering strength, the quantity calculated in dynamic theories.

It has been recognized for some years that instrumental effects can distort J-vs-E spectra.[5,6] However, it has never been shown quantitatively how instrumental broadening affects the measured intensity. We show that in most circumstances the instrumental broadening can be corrected to good approximation for J-vs-E data by measuring both the peak intensity and the FWHM of the intensity distribution in the diffracted beam under consideration, rather than only the maximum intensity, which for different electron optics, different detector apertures, and frequently different laboratories will have different values. This measured intensity $J(\partial, E)$ always includes instrumental effects (e.g., the spreading of the incident beam in energy and angle, the finite beam width, and the detector width).[6] $J(\partial, E)$ can be represented by a convolution of the "true" intensity $I(\partial, E)$ and an instrumental response function[6] $T(\partial, E)$,

$$J(\partial,E) = I(\partial,E) * T(\partial,E) \ . \qquad (1)$$

$T(\partial, E)$ can be thought of as a "shape function," whose integral is equal to one, that distributes the intensity in $I(\partial, E)$ over a range of angles in reciprocal space. Generally, $T(\partial, E)$ is broader at low energies than at high energies, but it is usually smoothly varying with energy.[6] In structure determinations the integrated Bragg intensity (i.e., the integral of $I_{\text{Bragg}}[\partial, E]$), is of interest and not its angular distribution. Because the integral of $T(\partial, E)$ is by definition equal to one, the integral of $I_{\text{Bragg}}(\partial, E)$ is obtained simply by integrating $J_{\text{Bragg}}(\partial, E)$ over a Brillouin zone.

We now consider a plane wave incident on a defect-free, infinitely periodic surface. In this case, there is no spreading in the angular profile of a

diffracted beam, and the Bragg intensity can be represented by a delta function,

$$I_{\text{Bragg}}(\partial,E)=I_0(E)\delta[\partial-\partial_B(E)]\,, \qquad (2)$$

where E is the incident-electron energy and $\partial_B(E)$ is the diffraction angle satisfying the two-dimensional Bragg condition $S_\parallel = G_\parallel$ (i.e., the parallel component of momentum transfer falls on a reciprocal-lattice rod). $I_0(E)$ is the area under the delta function and is the value commonly obtained in dynamic calculations. This area represents the scattering strength. It is this value that needs to be extracted from experimental data for comparison with the results of dynamical calculations. Note that a true "peak" intensity is not an observable quantity. Only the value of the measured intensity can be defined.

We assume that the effect of $T(\partial, E)$ on $I_0(E)$ is negligible. Then, from Eqs. (1) and (2), the scattering strength can be obtained simply by integrating the measured intensity profile $J(\partial, E)$, if there are no contributions to $J(\partial, E)$ other than the Bragg intensity. This condition is generally approximated experimentally only at very low temperatures.

In a particular case of a Gaussian Bragg intensity profile, it is commonly observed that[6]

$$J_{\text{Bragg}}(\partial,E) = A(E)\exp-\left\{\frac{4\log^2[\partial-\partial_B(E)]^2}{[b(E)]^2}\right\}\,, \qquad (3)$$

where $A(E)$ is the measured peak intensity and $b(E)$ is the measured FWHM of the angular profile. If the shape remains Gaussian for all energies and angles, integration gives

$$I_0(E)=\int_{BZ} J_{\text{Bragg}}(\partial,E)\,d\partial = \frac{\pi^{1/2}}{2(\log 2)^{1/2}}\,A(E)b(E)\,. \qquad (4)$$

This result shows that it is necessary only to measure the peak intensity and FWHM of the profile in order to specify its integral, if the profile is Gaussian. Other analytical forms give similarly simple relations for the integral. The result of Eq. (4) is independent of the size of the detector. The reliability of the scattering strength extracted from measurements depends on the accuracy of the experimental determination of both the peak value $A(E)$ and the width $b(E)$ of the measured profile.

It is now worthwhile to ask how important these effects are on structure determinations using typical experimental data. We discuss first the perfect surface. This will produce a delta-function intensity that is spread by $T(\partial, E)$. $T(\partial, E)$ is generally smoothly varying with ∂ and E, and thus any peak intensity measurement that is interpreted as the integrated Bragg intensity will cause similarly varying errors in the extracted scattering strength. This may appear in the comparison of theoretical calculations and experiment as an incorrect Debye-Waller factor or as a ratio of inelastic-to-elastic scattering. Because the changes are smooth, however, peaks next to each other in a J-vs-E curve for a particular beam will not show large changes for a perfect surface. Of course, the relative scattering strengths in different beams may still be incorrect. These effects may not prevent the determination of a surface structure, although they may significantly affect the R factor of a given determination.

More serious problems arise if the surface is not perfect, as will most likely be the case for all sputter-cleaned surfaces as well as most adsorption systems. If surface imperfections exist, $I_{\text{Bragg}}(\partial, E)$ is not a delta function but has a finite width. This width generally will not be smoothly varying with energy or angle. This fluctuating beam width can cause large changes in the maximum intensity observed with a fixed detector. If this maximum intensity is interpreted as the integrated Bragg intensity, significant errors can be made in the intensity of peaks lying close to each other in energy in J-vs-E curves. Such errors can significantly affect structure determinations. In such cases it becomes imperative to measure $b(E)$ as well as $A(E)$.

---

1. Summary of paper: *Surf. Sci.* **104,** L229 (1981).
2. University of Wisconsin, Madison, Wis.
3. See, for example, W. N. Unertl, *J. Vac. Sci. Technol.* **17,** 186 (1980).
4. *Proceedings of the Conference on Determination of Surface Structures by LEED,* ed. by P. Marcus and F. Jona, Plenum Press, New York (to be published).

5. See, for example, M. B. Webb and M. G. Lagally, *Solid State Phys.* **28**, 301 (1974).

6. R. L. Park, J. E. Houston, and D. G. Schreiner, *Rev. Sci. Instrum.* **42**, 60 (1971).

STUDIES OF SURFACE COMPOSITION AND PHASE TRANSITION OF Mo-5%Re(100)[1]

G.-C. Wang D. M. Zehner
H. C. Eaton[2]

The reconstruction of a clean W(100) surface from a (1×1) to a ($\sqrt{2}\times\sqrt{2}$) R45° structure has been observed at temperatures below 370 K by LEED.[3,4] A phase transition has also been observed for a clean Mo(100) surface, as indicated by the appearance of a quartet of spots located at half-order beam positions in the LEED pattern obtained at ~160 K.[4]

Several different models of the driving force for the transitions have been suggested.[5] In one model, a surface state or strong resonance very near E_f drives the transition via a surface phonon softening and gapping of the two-dimensional Fermi surface.[4] Other models assume that the transition is not due to the temperature dependence of the Fermi distribution, as in a charge density wave, but is a consequence of the surface atoms being unstable.[6]

Recent experiments show that a very low coverage (~2% of a monolayer) of chemisorbed nitrogen may inhibit surface reconstruction. The inhibition range can be estimated to be about 20 Å for nitrogen on a W(100) surface.[7] This inhibition range is an indication of the existence of a substrate-mediated long-range interaction induced by a chemisorbed atom.

In order to test the effect of a substitutional impurity atom on surface reconstruction and to provide additional information for use in determining the driving force, we chose to study a Mo-5%Re(100) surface. The 5%Re refers to a bulk quantity; there could be surface segregation. Thus, first we quantify the surface composition by both Auger electron spectroscopy (AES) and x-ray photoelectron spectroscopy (XPS), and then we present the LEED observations.

(a) *AES.* The major Re-Auger peaks at low energy overlap with the major Mo-Auger peaks. Therefore, we used the clearly separated high energy Re-$M_5N_{6,7}N_{6,7}$ peak at 1799 eV and the Mo-$L_3M_{4,5}M_{4,5}$ peak at 2044 eV for the composition study. The signal-averaged Auger spectrum (16 repetitive spectra) for the Re peak (1799 eV) and for the Mo peak (2044 eV) using a 5-KeV primary-beam energy is shown in Fig. 2.13. By

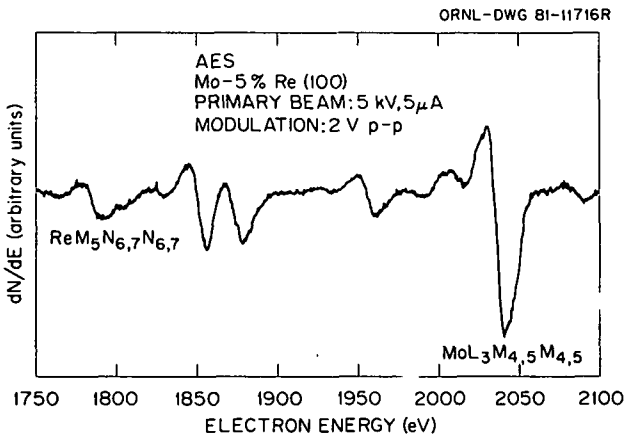

Fig. 2.13. A signal-averaged AES spectrum from a Mo-5%Re(100) surface. The data consist of 16 repetitive spectra.

using the values of the peak heights P'_{MNN} and P'_{LMM} in the unknown sample measured at room temperature and shown in Fig. 2.13 and the ratio of the measured relative sensitivity factors,[8] the surface concentration of Re (C_{Re}) is calculated to be 7.4 ± 0.5%. The measurements have been repeated at 120 K, and the results are approximately the same, within experimental uncertainty.

(b) *XPS.* The Mo-$3d_{5/2}$ peak and the Re-$4f_{7/2}$ peak were used for composition studies. The XPS spectra from the single-crystal Mo-5%Re(100) and a pure Mo foil in two different binding-energy ranges are shown as lower and upper curves in Fig. 2.14. Within the binding-energy range 46–30 eV, two extra peaks near 43 and 40.6 eV are observed in the lower right scan, which is from the Mo-5%Re(100) surface, but they do not appear in the scan from the pure Mo foil (upper right scan). These two extra peaks are from the Re-$4f_{7/2}$ and Re-$4f_{5/2}$ core levels. The ratio of our measured peak heights Mo-$3d_{5/2}$/Mo-$3d_{3/2}$ from Mo-5%Re is 0.68, a value which corresponds to that obtained from a pure Mo sample.[8] This agreement implies that the Mo peak heights are not affected by the presence of a few percent of Re. Also, there are no

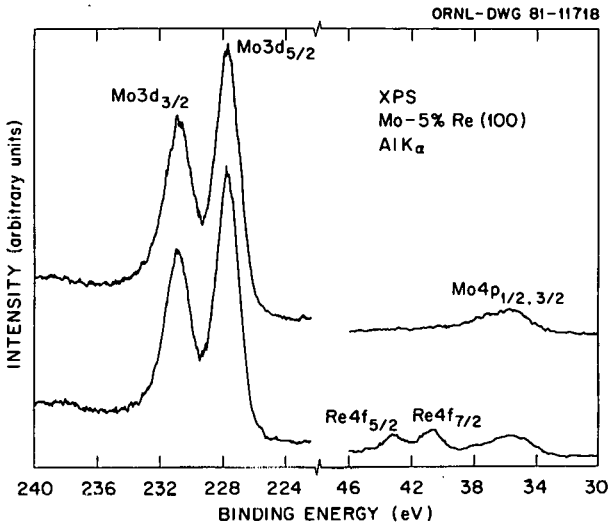

Fig. 2.14. XPS spectra obtained from a pure Mo thin foil (upper curves) and a Mo-5%Re(100) surface (lower curves).

energy shifts of Re peaks detected under the experimental energy resolution. The value of C_{Re} is obtained by using a standard formula.[8] The C_{Re} value thus obtained by evaluating areas under Re-$4f_{7/2}$ and Mo-$3d_{5/2}$ peaks is 8.2 ± 0.5%. If the peak heights are used instead of peak areas, the value of C_{Re} is 7.5 ± 0.5%.

(c) *LEED Observations.* The clean surface at room temperature gives a (1×1) pattern as shown in Fig. 2.15(a). For temperatures near 160 K, no extra quartets of spots were observed at the (1/2,1/2) beam positions, as shown in Fig. 2.15(b), an observation in contrast to that for a pure Mo(100) surface.

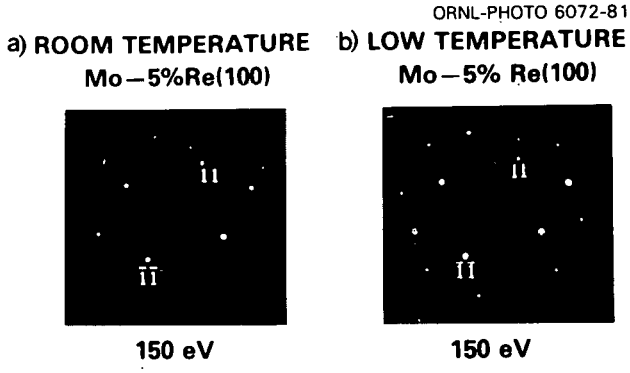

Fig. 2.15. The (1×1) LEED pattern from the Mo-5%Re(100) surface at (a) room temperature and (b) 160 K. Here, E = 150 eV, $\partial_0 \sim 0°$.

The results of a surface composition determination of the Mo-5%Re(100) by AES and XPS are consistent. Both indicate a slight enrichment of Re within a 30-Å escape depth of the surface. The slight enrichment of Re near the surface implies that the heat of segregation, which is defined as the change in enthalpy that occurs when a solute atom (Re atom) is exchanged between a bulk and surface site, is negative. Recently a graphical prediction of segregation has been proposed by Hamilton.[9] This method is based on the extensive work of Miedema and co-workers[10] on the heats of solution of binary alloys. This graphical prediction indicates surface segregation of Re in a MoRe alloy and is in agreement with our experimental results.

A (1×1)-LEED pattern from Mo-5%Re(100) similar to a pure Mo(100) is observed at room temperature. This implies that the Re atoms replace Mo atoms substitutionally, which is consistent with the neutron scattering result.[11] No structural change was observed at temperatures near 160 K. This result implies that the substitutional Re atoms inhibit the formation of a periodic lattice distortion at this low temperature.

The range of inhibition can be estimated to be at least 5 Å. The inhibition due to substitutional impurities is similar to inhibition by chemisorption. However, this result cannot be used to distinguish between two proposed models. The presence of randomly substituted Re destroys the long-range order required in both.

---

1. Summary of paper to be published.
2. Louisiana State University, Baton Rouge, La.
3. M. K. Debe and D. A. King, *Phys. Rev. Lett.* **39,** 708 (1977); M. K. Debe and D. A. King, *J. Phys. C* **10,** L303 (1977).
4. T. E. Felter, R. A. Barker, and P. J. Estrup, *Phys. Rev. Lett.* **38,** 1138 (1977).
5. See, for example, E. Tosatti, *Solid State Commun.* **25,** 881 (1978).
6. J. E. Inglesfield, *J. Phys. C* **11,** L69 (1978); *J. Phys. C* **12,** 149 (1979).
7. K. Griffiths and D. A. King, *J. Phys. C* **12,** L755 (1979).
8. *Handbook of Auger Electron Spectroscopy*, ed. by P. W. Palmberg et al., Physical Electronics Industries, Inc., Edina, Minn., 1972.
9. J. C. Hamilton, *Phys. Rev. Lett.* **42,** 989 (1979).
10. A. R. Miedema, *Philips Tech. Rev.* **36,** 217 (1976); R. Boom, F. R. DeBoer, and A. R. Miedema, *J. Less-Common Met.* **46,** 271 (1976).

11. H. G. Smith, N. Wakabayashi, and M. E. Mostoller, p. 223 in *Superconductivity in d- and f-band Metals,* ed. by D. H. Douglass, Plenum Press, New York, 1976.

EELS STUDY OF NITRIC OXIDE ADSORPTION ON Cu(100) AND Cu(111) SURFACES[1]

J. F. Wendelken

In recent XPS[2] and EELS[3,4] studies, the adsorption of NO on Cu surfaces has been shown to be highly complex at low temperatures. In the XPS study of NO adsorption on Cu(100) and Cu(111), evidence was found for the existence of N_2O(ad), bent and linear forms of NO(ad), and O(ad) on both surfaces. Very different behavior has been observed via EELS for NO adsorption on Cu(110), where only a bent predissociative NO molecular form may exist at low coverages. In this work, the EELS study of NO adsorption on Cu has been extended to the Cu(100) and Cu(111) surfaces. The data were obtained in a single system containing EEL[5] and quadrupole spectrometers.

For Cu(100), two vibrational loss peaks were observed to develop initially at 96.5 and 153 meV following a 1.0-L exposure to ^{14}NO as shown in Fig. 2.16. A shoulder on the elastic peak became a distinct peak at 43 meV, with a 1.6-L exposure. When exposures of ^{15}NO were used instead of ^{14}NO, the peak at 43 meV was unaffected, but the other two peaks were reduced in energy by 1.5 meV. The 43-meV peak may be assigned to O(ad) on the basis of its energy,[6] its insensitivity to isotopic substitution, and its stability at higher temperatures where the other peaks have vanished. The observed energies and isotopic shifts of the other two peaks are consistent with gas-phase energies of either N_2O(ad) or NO_2(ad).[3] When the crystal was heated to 110–120 K following the 1.6-L NO exposure, only N_2O was observed to desorb; hence, that is the preferred assignment which is consistent with the presence of the remaining O(ad).

Following an exposure of 2.3 L, an additional loss peak was observed at 190 meV for ^{14}NO and 186 meV for ^{15}NO. The energy and isotopic shifts of this new loss peak are consistent with a bridge-bonded NO(ad) molecular stretching mode. When

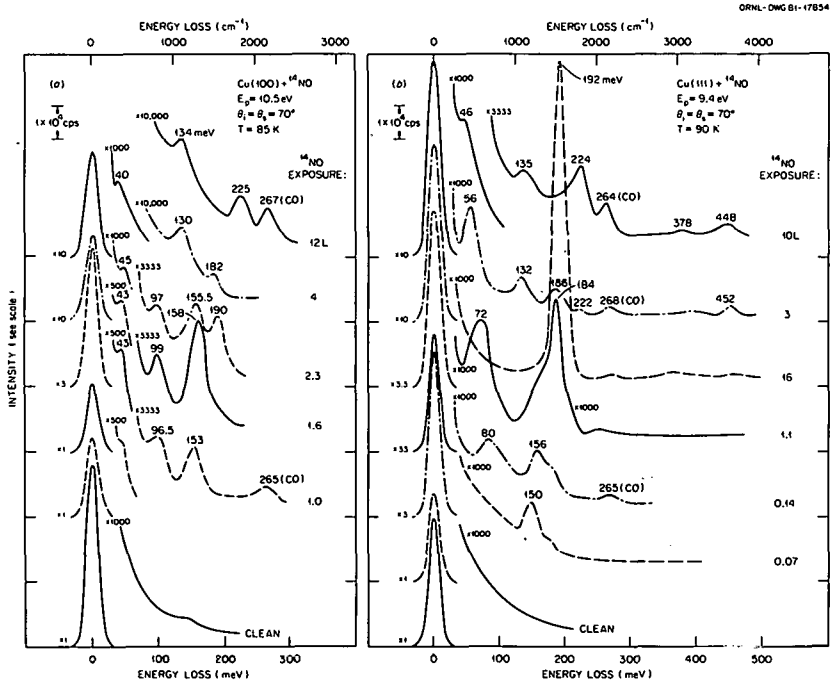

Fig. 2.16. EEL spectra for (a) Cu(100) at 85 K and (b) Cu(111) at 90 K following various exposures to ^{14}NO. The indicated CO stretching mode peaks are a result of adsorption from background and displacement of CO from chamber walls during exposures of NO which were made by backfilling.

the crystal was heated to 120 K, both the peaks at 190 and 97 meV were strongly reduced, suggesting that the 97-meV peak is in part an NO bending mode and hence the molecule is bent on this surface, although not as strongly as on the Cu(110) surface.[3] Thermal desorption of NO was not observed under these conditions, but growth of the 43-meV peak indicates dissociation.

With higher exposures, the N_2O peaks vanished, the bridge-bonded NO peak shifted down in energy, and new peaks appeared independently near 130 and 225 meV. The latter peak may also be attributed to NO but in a linear, atop site. Upon heating the crystal, NO desorption was observed over a wide temperature range 120–243 K, indicating that the atop NO is a predesorptive state. Significant amounts of N_2O were desorbed up to 210 K, and an N_2 peak was observed over a narrow temperature range near 120 K. The presence of N_2 has not been identified in the vibrational spectrum, and it is possible that the N_2 forms and desorbs immediately only after heating the crystal. The assignment of the peak near 130 meV is not as clear as that for a similar peak from Cu(111) discussed below.

The vibrational data for Cu(111) exposed to NO show similarities to the data for Cu(100) but also pronounced differences. At very low exposures, the first two peaks observed are very close in energy and isotopic shifts to the peaks observed for a low coverage of N_2O on Cu(100). However, no thermally desorbed N_2O could be detected following these very low exposures. Vibrational peaks, which developed with exposure, at 184 and 72 meV may be assigned to the stretching and bending modes of a bent, bridge-bonded NO molecule. The subsequent disappearance of the bending mode, upward shift in NO stretching-mode energy and intensity, and increase in elastic intensity are all indications that the molecule straightens up with coverage, although it is still bridge bonded. Thermal desorption observations following an exposure in which only NO is observed in the vibrational spectrum are surprising. At 110 K, both N_2 and N_2O were observed to desorb and reach a maximum desorption rate at 135 K. No NO desorption was noted until near 135 K. Above 135 K, NO became the dominant species desorbing with sharp reductions in the N_2 and N_2O desorption rates. It is unlikely that there could have been substantial quantities of N_2 and N_2O on the surface undetected by EELS. The probable explanation is that the bridge-bonded NO, as on the Cu(110)[3] and Cu(100) surfaces, is a predissociative species. When it dissociates, the N atoms may then migrate and bond to other N atoms or NO molecules to create N_2 and N_2O which desorb above 110 K. This may also explain the apparent N_2 desorption from Cu(100) when neither EELS nor XPS[2] indicates its presence on the surface.

For higher exposures the bridge-bonded NO is replaced by linear-bonded NO represented by an NO stretching mode peak at 224 meV as for Cu(100). Thermal desorption indicated that NO begins desorbing at 110 K with smaller quantities of N_2 and N_2O observed than in the lower coverage case, which was dominated by the bridge-bonded NO. Hence, the atop NO molecule desorbs rather than dissociates as it also does in the Cu(111) case. A peak which developed and shifted from 56 to 48 meV is probably O(ad) following the dissociation of bridge-bonded NO. As on Cu(100), there is also a peak near 130 meV at high exposures. In addition, peaks are also present near 450 and 380 meV. The peak near 450 meV was found to be nondipole in character. Hydrogen from the vacuum system residual background could combine with the O(ad) to produce the 135-, 378-, and 448-meV loss peaks. The peak at 135 meV might also be due to atomic hydrogen. Since the photoemission studies indicate that N_2O is a major surface species at the higher coverages on both surfaces, the possibility of a second N_2O(ad) state in which the 130-meV mode is a distorted stretching mode must be considered. Work is continuing on these latter possibilities, and results will be published later.

---

1. Summary of paper to be published.
2. D. W. Johnson, M. H. Matloob, and M. W. Roberts, *J. Chem. Soc. Faraday Trans. I* **75**, 2143 (1979).
3. J. F. Wendelken, *Proceedings of 2nd International Conference on Vibrations at Surfaces,* Plenum Press, New York, 1981; *Applications of Surface Science* (in press).
4. J. F. Wendelken, *Applications of Surface Science* (in press).
5. J. F. Wendelken and F. M. Propst, *Rev. Sci. Instrum.* **47**, 1069 (1976).
6. B. A. Sexton, "A vibrational energy of 41 meV was also observed in this laboratory at low coverages of O(ad). The 2-meV higher energy in the present experiment may result from interaction with another species on the surface," *Surf. Sci.* **88**, 299 (1979).

PLASMA MATERIALS INTERACTIONS

HYDROGEN RECYCLING AND IMPURITIES DURING ISOTOPIC EXCHANGE IN ISX-B[1]

J. B. Roberto L. E. Murray[2]
R. C. Isler[2] J. E. Simpkins[2]
S. Kasai[2] S. P. Withrow
R. A. Zuhr

The interaction of plasma particles with exposed surfaces in tokamaks contributes significantly to fueling and to impurity introduction in existing devices. H-D isotopic exchange experiments, which involve monitoring the plasma composition after switching to one working gas following many discharges in the other, allow direct observation of surface contributions to the plasma isotopic composition and isotope effects in impurity introduction. We report here measurements of working gas composition and edge impurity levels during H-D changeover experiments in the ISX-B tokamak. The results are interpreted in terms of recycling and impurity introduction mechanisms in ISX-B.

Plasma operation was shifted from D to H and from H to D by changing the fill and puffing gases for a sufficient number of discharges to obtain complete (>98%) changeover for each isotope. H/D ratios were monitored during the discharge from relative H_β and D_β spectral intensities and after each discharge by residual gas analysis and nuclear reaction analysis of Si surface probes which were exposed in the plasma edge. Relative O and Fe impurity levels in the edge were determined from O VI and Fe IX spectral intensities. Plasma conditions for the nongettered, ohmic discharges were B_T = 1.3 T, I_p = 135 kA, $T_e(o)$ = 540 eV, and $n_e(o)$ = 6–7 × 10^{13}/cm^3 with a current flattop of 150 ms. ISX-B has type 304 stainless steel walls.

The isotopic changeover in the plasma edge as determined from optical measurements is shown in Fig. 2.17. Plotted in Fig. 2.17 is the fraction of plasma composition made up by the previous isotope as a function of the number of discharges in the new isotope. Data for H → D and D → H changeovers are shown at times varying from 16–145 ms into the discharge. The results indicate that the isotopic exchange in the plasma is ~80% complete after the first 15 ms of the first discharge in the new isotope but requires ~10 discharges to reach 98% completion. There is no evidence of a trend in the isotopic composition as a function of time during the discharge. Residual gas analysis and surface-probe results are consistent with the optical data.

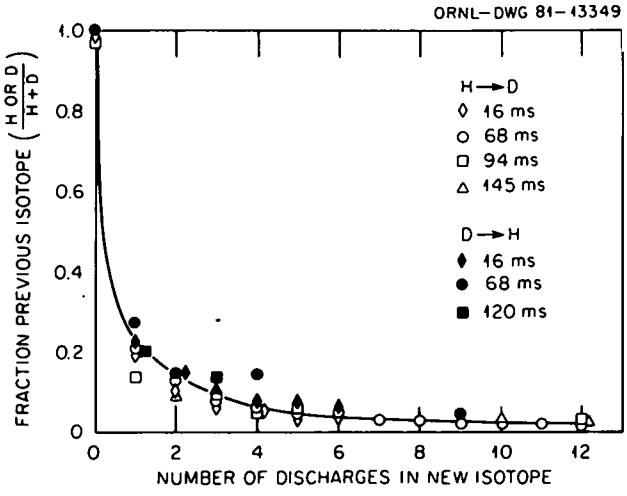

Fig. 2.17. Fractional contributions of the previous isotope to the plasma composition as a function of number of discharges in the new isotope. Data are from relative H_β and D_β spectral intensities and are shown for various times during the discharge for both H → D and D → H changeovers.

The changeover results indicate that plasma isotopic composition for these experimental conditions in ISX-B is determined primarily by the fill gas, with ~20% of the plasma particles originating from exposed surfaces. This surface contribution appears within the first 20 ms of the discharge, after which the plasma composition remains approximately constant. These results suggest that recycling in ISX-B occurs without significant isotopic mixing after the first 20 ms of the discharge. This requires the rapid establishment of an equilibrium between the plasma composition and the interacting surfaces. Isotopic replacement in the walls does not contribute to the recycling, since this process would be continuous throughout the discharge. The isotopic replacement does occur in ~10 discharges by diffusion between discharges and subsequent release.

Fe levels in the plasma edge increase by a factor of ~3 for D as compared to H operation. This result is consistent with the expected D/H sputtering ratio for a Maxwellian distribution of H atoms

on stainless steel near 100 eV. This suggests that charge exchange neutral sputtering of the walls is the dominant heavy impurity introduction mechanism in ISX-B. The importance of the wall as a heavy impurity source is also indicated by the low Ti levels[3] in ISX-B despite operation with a TiC outer limiter. The O levels in the edge are unchanged for D and H operation, consistent with a thermal release mechanism for light impurities.

Overall, the results demonstrate low H inventory and rapid isotopic changeover for tokamak operation with stainless steel walls. The surface-released contribution is ~20% of the plasma composition and appears within the first 20 ms of the discharge. This is associated with wall desorption and fast release processes at the limiter. Ion-induced effects do not contribute to recycling during the steady-state portion of the discharge. The results are consistent with a thermal mechanism for recycling[4] and O release and with H sputtering of the walls for heavy impurity introduction.

1. Summary of paper, *Journal of Nuclear Materials* (in press).

2. Fusion Energy Division, ORNL.

3. R. A. Zuhr, J. B. Roberto, and S. P. Withrow, "Effects of Neutral-Beam Injection and Gas Puffing on Deuterium and Impurity Levels in the Scrapeoff Layer of ISX-B," this report.

4. J. B. Roberto et al., "Minority Hydrogen Isotope Recycling in ISX-B," this report.

MINORITY HYDROGEN ISOTOPE RECYCLING IN ISX-B[1]

J. B. Roberto R. C. Isler[2]
H. C. Howe[2] L. E. Murray[2]

The recycling of H from exposed surfaces controls plasma fueling in present tokamaks and will play a significant role in determining the wall tritium inventory in D-T devices. Recent H/D isotopic exchange experiments[3] for nongettered ohmic discharges in the ISX-B tokamak suggest a fast recycling process, with no significant isotopic mixing after the first 20 ms of the discharge. This result is consistent with an H recycling mechanism for the wall that is not controlled by ion-induced effects. In the present experiment, H/D ratios were monitored in ISX-B plasmas for D_2 discharges during which a short pulse of H_2 was introduced as a minority isotope. The results confirm the previous observations and are consistent with near-unity recycling controlled by a thermally activated process.

In the experiment, a short burst of H_2 was puffed into an established ohmically heated D_2 plasma at 80 ms into the discharge. H/D ratios were determined throughout the discharge from relative H_β/D_β spectral intensities using a high-resolution spectrometer equipped with an oscillating mirror for repetitively scanning a 10-Å region around 4861 Å. The spectrometer viewed the plasma along a major radius ~90° toroidally from the limiter and ~180° toroidally from the H_2 injection port. The narrow H Balmer lines in tokamaks are attributed to excited atoms formed during and following the dissociation of molecular H in the plasma edge and probably reflect molecular fluxes from the wall. Plasma conditions for this experiment were $n_e(o) = 6 \times 10^{13}/cm^3$, $T_e(o) = 720$ eV, $B_T = 1.3$ T, and $I_p = 170$ kA with a current plateau from 80 to 180 ms. ISX-B had nongettered type 304 stainless steel walls at the time of this experiment and was equipped with a TiC outer and stainless steel inner limiter.

Relative H_β/D_β signals for several D_2 discharges with H_2 input are shown in Fig. 2.18. The H_β signal rises rapidly during the puff to one-fourth of the D_β signal, consistent with the ratio of overall

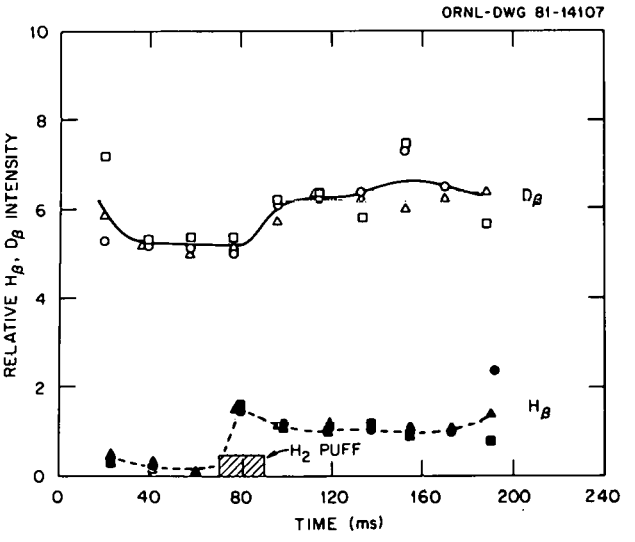

Fig. 2.18. Relative H_β and D_β spectral intensities for three successive D_2 discharges in ISX-B with a short puff of H_2 at 80 ms. The apparent time shift in the relative H_β and D_β increases during the puff probably reflects the time difference in H_β and D_β sampling.

H_2/D_2 gas input (0.24). H_β remains essentially constant during the remainder of the discharge. The H charge exchange neutral flux (measured radially outward at a location well away from both the limiter and the H_2 injection port) shows a comparable rapid increase during the H_2 puff with a plateau from 90 to 170 ms.[4] These results suggest recycle times of $\leqslant$20 ms and coefficients of $\geqslant$0.98 for the minority isotope from a time almost immediately following the H_2 puff until the end of the discharge. The H_β signal at the beginning of the discharge is approximately one-fifth of the steady-state value following the puff, consistent with the previous observation[3] that ~20% of the initial plasma composition for nongettered, ohmic ISX-B discharges is released from exposed surfaces.

For the case of recycling dominated by thermally activated processes, the H outflux for isotope i from the wall can be written

$$\phi_i = k_r C_i (C_i + C_j) \ , \qquad (1)$$

where k_r is the recombination rate constant and $C_{i,j}$ is the near-surface H concentration for isotope i,j. This equation governs the formation of molecular H at the surface which readily desorbs at room temperature. Thermally activated recycling has been observed in plasma simulator experiments with stainless steel walls.[5,6] Equation (1) implies that the minority isotope release will be dominated by recombination with the majority isotope, forming the HD molecule in our case. This requires essentially the same recycling behavior for the minority and majority species and an increase in the majority isotope outflux approximately equal to the minority isotope release. This is consistent with Fig. 2.18, where the D_β signal increases after the H_2 puff by an amount comparable to the H_β increase.

The present results are not easily explained by recycling mechanisms based solely on ion-induced effects such as particle reflection or isotopic replacement in the walls. Reflection coefficients of $\leqslant$0.8 are expected for wall neutrals in ISX-B, and wall neutral fluxes are too low for significant replacement in the bulk to occur during a discharge. Neither mechanism explains the simultaneous rise in the H_β and D_β signals. On the other hand, a thermally activated process based on diffusion and surface recombination is consistent with the observed recycling behavior, although the recycling time is somewhat faster than theoretically expected[5,6] for ISX-B operating conditions. Overall, the present results demonstrate fast ($\leqslant$20 ms), near unity ($\geqslant$0.98) minority species recycling in a nongettered, stainless steel tokamak.

---

1. Summary of paper to be published.
2. Fusion Energy Division, ORNL.
3. J. B. Roberto et al., "Hydrogen Recycling and Impurities during Isotopic Exchange in ISX-B," this report.
4. S. D. Scott, private communication.
5. F. Waelbroeck, J. Winter, and P. Wienhold, *Journal of Nuclear Materials* (to be published).
6. R. E. Clausing, L. C. Emerson, and L. Heatherly, *J. Nucl. Mater.* **76/77**, 267 (1978).

RECYCLING STUDIES IN ISX-B BY HYDROGEN-ALPHA EMISSION

B. Emmoth[1] E. W. Thomas[2]
R. Young[2] T. B. Cook

The recycling of gas atoms from the limiter and walls in a tokamak is as important as magnetic confinement in determining plasma density. In the current generation of fusion energy devices, most of the gas fueling is by recycling with only a small fraction of the plasma particles supplied by active gas puffing.

A useful diagnostic for studying recycling is the monitoring of H-α emission from the plasma edge. This radiation, generated as neutral H is excited as it moves into the plasma, has been shown to be a useful indicator of H flux into the plasma. H-α detectors for the present experiment consist of a collimating lens, an interference filter to isolate the H line, and a photodiode as the receiver. Four such detectors have recently been installed on the ISX-B tokamak, each viewing a 2.5-cm diameter cylinder on a chord through the plasma and intercepting the relevant plasma edge region twice, once on the near side of the plasma and once on the far side.

Although the work is at an early stage, several preliminary observations have been made. We find that there are pronounced toroidal and poloidal variations in H-α emission, with the limiters and the gas puff being strong sources. For ohmic discharges, the detector viewing the gas puff region follows the flow of gas into the vessel; while simultaneously, a detector viewing a region far from the gas puff or limiters shows a smooth increase in signal. For neutral beam injection, the H-α signa'

from the gas puff region increases steadily even with constant puffing, which is suggestive of beam-induced desorption from the hardened energy spectrum of neutrals striking the wall. Several H-α experiments are planned for the near future to investigate particular issues in the recycling problem.

1. Institute of Physics, Stockholm, Sweden.
2. Georgia Institute of Technology, Atlanta, Ga.

EFFECTS OF NEUTRAL-BEAM INJECTION AND GAS PUFFING ON DEUTERIUM AND IMPURITY LEVELS IN THE SCRAPEOFF LAYER OF ISX-B[1]

R. A. Zuhr J. B. Roberto
S. P. Withrow

Si deposition probes have been exposed to a variety of operating conditions in the plasma edge of ISX-B to investigate the effects of neutral beam injection and gas puffing on edge characteristics. The exposures were made using a bellows-sealed sample insertion system that allowed the samples to be positioned at any radius between the limiter and the outer wall. An electrically driven rotating shaft permitted multiple or time-resolved (15 ms) sampling. All measurements were made in the horizontal midplane of the tokamak at a toroidal position $\sim$120° from the limiters in the positive ion current direction. For these experiments, ISX-B was operated with an inner bar limiter of stainless steel and an outer mushroom-shaped limiter of TiC-coated graphite.

Exposures were made for both ohmic and neutral-beam-injected discharges and for discharges in which the fill-gas puffing was programmed to determine its effect on the plasma edge. After exposure, the samples were transferred to the Solid State Division's 2.5-MeV Van de Graaff accelerator, where they were analyzed for impurity deposits using 2-MeV ^{4}He backscattering and for retained D using the D(^{3}He,p)^{4}He nuclear reaction.

The temporal behavior of the principal impurities collected 2.5 cm behind the limiter during 1.1-MW neutral-beam-injected discharges in ISX-B is shown in Fig. 2.19. The 40-keV neutral H beam was co-injected into the D plasma from 80 to 180 ms. Beam power during injection exceeded ohmic heating power by a factor of 4. Oxygen is the most abundant impurity observed, with more

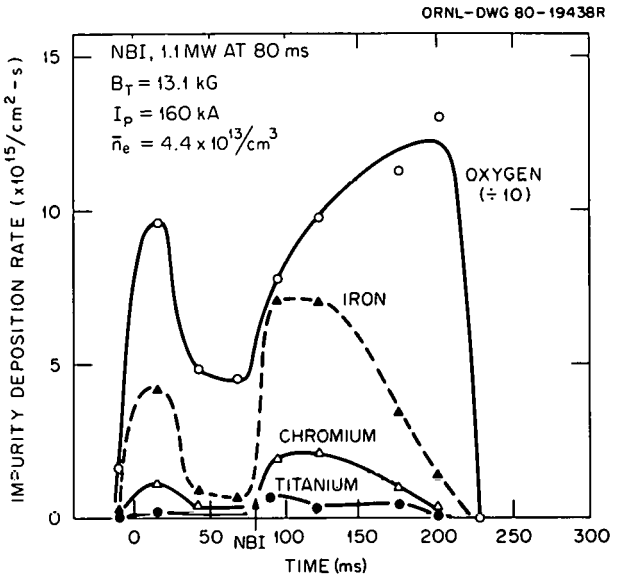

Fig. 2.19. Impurity deposition as a function of time for 1.1 MW neutral-beam-injected D discharges in ISX-B. The arrow indicates the start of 100 ms neutral-beam injection (NBI).

than an order-of-magnitude greater deposition than the most common metallic element, Fe. Cr and Ni (not shown) are present in approximately the same ratio to Fe as they are in type 304 stainless steel, the wall material in ISX-B. The amount of Ti on the probe is an order of magnitude less than Fe. A sharp increase in all impurity levels occurs at the onset of the neutral-beam injection. A similar increase is observed in the measured D flux at the time of injection. Even though these effects may be caused indirectly, such as through variations in plasma position, it is clear that edge impurity fluxes are increased by neutral-beam injection by a factor of 2–3 for O and $\sim$7 for metallic elements. If the metallic impurity fluxes are compared with magnetohydrodynamic (MHD) activity in the plasma, a correlation is found between high fluxes and high levels of MHD activity. Such a correlation has been observed in all previous time-resolved probe data from ISX.[2]

To clarify the effects of gas puffing on both impurity and plasma fluxes in the scrapeoff layer, an experiment was carried out in which a sharp puff of $\sim$0.3 Torr-*l* of D gas was injected at 120 ms into a conventional ohmically heated D plasma. This was in addition to the "normal" puff at $\sim$40 ms as shown in Fig. 2.20. In Fig. 2.20, Si surface damage, which is indicative of incident D flux and

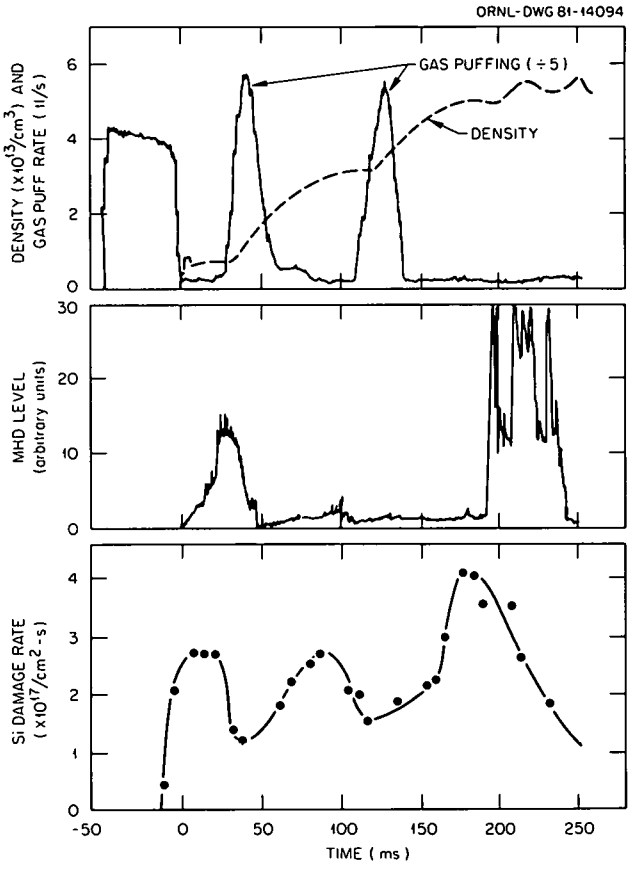

Fig. 2.20. Comparison of single-crystal Si damage rate (indicative of D flux and energy) with MHD activity, plasma density, and gas puff rate for ohmic D discharges in ISX-B with 0.3 Torr-*l* gas puffing at 40 and 120 ms.

energy,[3] is plotted as a function of time during the discharge. Comparisons are made with MHD level, density, and gas puffing rate for these discharges. A significant decrease in damage occurs with each gas puff. Unfortunately, saturation measurements, which can be used to estimate both energy and fluence to the probe, are not compatible with this time-resolved technique. Previous saturation studies on comparable discharges[4] at this same radius have given estimates of D energy of ~100 eV and fluence of $\sim 10^{17}$ D/cm^2 per discharge. In the present work, primarily we collect ions traveling parallel to B_T, and the factor of 2 reduction in incident flux during puffing implies that the ion density has decreased by 2, that the average ion energy has decreased by $\sqrt{2}$, or that a combination of these effects has taken place. In all cases, it is clear that the D flux in the edge has been "cooled" by the gas puffing.

The effect of D puffing on edge impurities is far less dramatic. Oxygen is unaffected, while Fe shows only a small decrease at the time of the second puff. The lack of effect on O is in agreement with the neutral-beam-injected results, while the minimal effect on Fe is probably due to the stable, low MHD operation during this part of the discharge. Note that the slight peaking in Fe flux just prior to 100 ms is also a time of incipient MHD activity. Both effects are eliminated during the second D puff. It would appear that gas puffing can minimize edge metallic impurity levels only to the extent that it can maintain a stable, low MHD plasma.

The impurities found in the plasma edge of ISX-B were O from the wall and residual gases, stainless steel (Fe, Cr, and Ni) from the vacuum vessel, and Ti from the TiC limiter. The relative amounts of Fe and Ti indicate that the wall, and not the limiter, is the principal source of metallic impurities. Spectroscopic[5] and isotopic exchange[6] experiments that suggest charge exchange neutral sputtering of the wall may be the principal introduction mechanism for metals are consistent with the present data. Impurity levels in the edge were found to correlate well with both MHD activity and instabilities in plasma position, reaching levels 2 to 5 times higher during breakdown and the disruptive end of a discharge than during the steady-state portion. Finally, it was observed that gas puffing effectively can cool the plasma edge and, by minimizing instabilities, lower the level of impurities.

---

1. Summary of paper: *Journal of Nuclear Materials* (in press).
2. R. A. Zuhr et al., *J. Nucl. Mater.* **85/86,** 979 (1979).
3. S. P. Withrow et al., *J. Nucl. Mater.* **98,** 231 (1981).
4. R. A. Zuhr, S. P. Withrow, and J. B. Roberto, *J. Nucl. Mater.* **93/94,** 127 (1980).
5. R. C. Isler et al., *Physical Review Letters* (in press).
6. J. B. Roberto et al., "Hydrogen Recycling and Impurities during Isotopic Exchange in ISX-B," this report.

DEPOSITION PROBE MEASUREMENTS OF IMPURITY AND PLASMA FLUXES NEAR THE WALL IN ISX-B[1]

R. A. Zuhr J. B. Roberto
S. P. Withrow

Deposition probe techniques have been used previously to study the fluxes of impurities and plasma particles incident upon limiter-like probes in the scrapeoff layer of the ISX-B tokamak.[2] In the present work, surface probes were used to measure impurity and plasma fluxes perpendicular to the toroidal field, both at and beyond the radius of the vacuum vessel wall. A comparison of material collected on these wall position samples with the earlier measurements of fluxes parallel to the toroidal field shows that the wall fluxes are far lower for both impurities and plasma particles. In addition, the wall at a location away from the limiters is shown to be a source, rather than a sink, of metallic impurities.

The ISX-B vacuum vessel is constructed of type 304 stainless steel and was not gettered for these experiments. Operating conditions for the wall position exposures were $B_T = 1.3$ T, $I_p = 170$ kA, and $\bar{n}_e = 5 \times 10^{13}/\text{cm}^3$; while for the limiter-like measurements, they were $B_T = 1.5$ T, $I_p = 120$ kA, and $\bar{n}_e = 2 \times 10^{13}/\text{cm}^3$. An outer mushroom limiter of TiC-coated graphite and an inner stainless steel bar limiter were in use during all the exposures reported.

A comparison of Fe and D deposition for typical ohmic discharges in ISX-B for samples exposed at-wall position, behind-wall position, and at a limiter-like position is given in Table 2.3. Retained D levels at the wall are an order of magnitude lower, while the Fe is 3000× lower. The neutral metallic impurity flux at the wall is clearly much smaller than the ionized metallic flux circulating along magnetic field lines in the plasma edge. The values given for Fe at the wall locations are upper limits taken from the samples with the greatest accumulation. Many of the samples show no detectable Fe. This variation in retained Fe suggests that most of the Fe may be deposited during disruptive behavior and that the steady-state flux to the walls is lower than indicated.

The quantity of D retained as a function of exposure for the different probe locations is shown in Fig. 2.21. The upper curve, which shows the amount of retained D on samples exposed perpendicular to the toroidal field at a radius 2 cm outside the limiter, has been fitted to trapping-vs-fluence curves.[3] If an isotropic Maxwellian energy distribution is assumed, this fit results in estimates

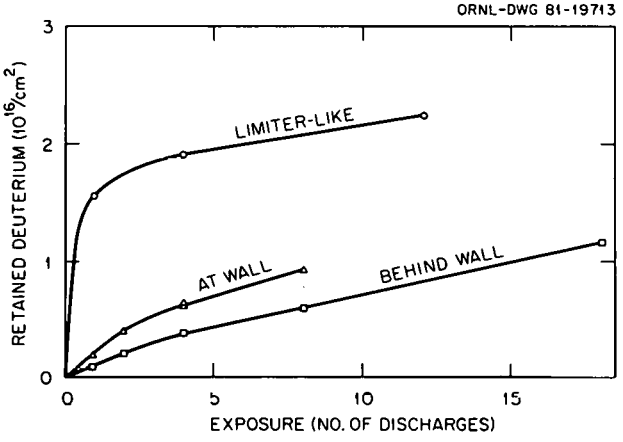

Fig. 2.21. Deuterium retained in α-Si probes vs exposure for ohmic discharges in ISX-B. ○ = limiter-like, 2 cm outside limiter radius; △ = at wall; and □ = 7 cm behind wall.

Table 2.3. D and Fe deposition for samples exposed at the wall position, 7 cm behind the wall, and 2 cm outside the limiter radius in ISX-B

The at-wall and behind-wall samples were positioned parallel to the wall along a major radius of ISX-B, and the limiter-like samples were oriented facing the toroidal field

Deposition rate	At wall	Behind wall (7 cm)	Limiter (2 cm)
D (atoms/cm^2-disch.)	1.9×10^{15}	9.4×10^{14}	1.6×10^{16}
Fe (atoms/cm^2-disch.)	$<3 \times 10^{11}$	$<2 \times 10^{11}$	1×10^{15}

of fluence and energy of 2×10^{17}D/cm^2-disch. at 50 eV. If such a technique is applied to the wall-position samples, we find that the amounts retained are in a region ($\sim 10^{15}$D/cm^2) where retention (for $E \geq 50$ eV) vs incident fluence is linear and an estimate of energy cannot be made. The shape of the experimental curves (Fig. 2.21) indicates that the energy distribution of the incident particles is neither monoenergetic nor a simple Maxwellian. The data would be consistent with a bimodal distribution having a low-energy component ($\sim$30 eV) that saturates at $\sim 5 \times 10^{15}$D/cm^2 and with a high-energy tail that remains unsaturated at 18 discharges. It is clear from charge exchange neutral data[4] that such a high-energy tail exists, but there are no other diagnostics that are capable of corroborating the low-energy flux. The linear portion of the data can still be used to estimate the incident fluence. Results for the at-wall and behind-wall cases are approximately 1.1×10^{16} and 6×10^{15}D/cm^2-disch. The difference in these two values is explained completely by the change in exposure geometry. Measurements of damage to single-crystal Si samples exposed at the wall position give a surface-peak yield of 3×10^{16}D/cm^2 after eight discharges. Such a yield is consistent[5] with a monoenergetic dose of $\sim 7 \times 10^{15}$D/cm^2-disch. at 50 eV, and thus it confirms the above estimates.

If the primary source of metallic impurities in the plasma is charge exchange neutral sputtering of the wall, as has recently been suggested,[6] then such a model should be consistent with the present data. If we use our estimated D flux to the wall and assume a sputtering coefficient of 1×10^{-3} ($D_\perp$ on Si at $\sim$60 eV), the Fe sputtered from the walls is 1×10^{18} atoms/disch. (This figure would correspond to an erosion rate of 0.02 mm/year in a tokamak operating at a 10% duty cycle.) The Fe deposited on the limiter-like probe 2 cm behind the plasma edge, when integrated over the area where such flux is present, is equivalent to 5×10^{17} atoms/disch. Considering the uncertainties involved in the above estimates, this is in reasonable agreement with the estimated total Fe input. If a substantial fraction of the Fe were being redeposited on the wall uniformly around the torus, it would have been detected on our wall-position probes. Thus, our data are consistent with a model in which most of the metallic impurities are introduced by charge exchange neutral sputtering of the wall and are removed by impact with primary and secondary limiters.

In summary, we have shown that metallic impurity fluxes to the wall in ISX-B are far lower (by a factor $\geq$3000) than those to limiter-like probes located 2 cm outside the limiter radius. Deuterium fluxes are also lower (by a factor of $\sim$10) at the wall position and are in reasonable agreement with single-crystal Si damage data. Finally, both wall and limiter position data are consistent with an impurity introduction model in which charge exchange neutral sputtering of the wall is the dominant introduction mechanism.

---

1. Summary of paper: *Journal of Vacuum Science and Technology* (in press).
2. R. A. Zuhr, S. P. Withrow, and J. B. Roberto, *J. Nucl. Mater.* **93/94,** 127 (1980).
3. S. A. Cohen and G. M. McCracken, *Princeton Plasma Physics Laboratory Report No. 1,* PPPL-1529 (1979).
4. S. D. Scott, private communication.
5. S. P. Withrow, R. A. Zuhr, and J. Roth, "Lattice Damage in Si from Low-Energy Deuterium Bombardment: Evaluation and Application to Plasma Edge Studies," this report.
6. R. C. Isler et al., *Physical Review Letters* (in press).

LATTICE DAMAGE IN Si FROM LOW-ENERGY DEUTERIUM BOMBARDMENT: EVALUATION AND APPLICATION TO PLASMA EDGE STUDIES[1]

S. P. Withrow R. A. Zuhr
J. Roth[2]

Rutherford backscattering (RBS) spectra taken in a channeling geometry from single-crystal samples are sensitive to lateral displacements of near-surface atoms from their lattice sites. Such displacement damage has been observed for Si probes exposed in the plasma edge of tokamaks due to the incident plasma particle flux.[3-5] RBS measurements of the amount and depth of particle-induced damage can be used to obtain estimates of both incident energies and fluences by comparison to laboratory simulations and theoretical predictions. We report here laboratory measurements to correlate the amount of damage induced in Si samples with the energy and fluence of incident low-energy D ions. The results are used to estimate incident

plasma parameters for probe samples exposed in ISX-B.

The laboratory simulation measurements were made on single-crystal Si(100) samples implanted at normal incidence with D^{3+} at energies between 50 and 500 eV per nucleon and doses between 10^{13} and 10^{18} D/cm^2. The surface peak in 1-MeV ^{4}He backscattering spectra obtained in a ⟨110⟩ axis channeling geometry was used to measure the amount of lattice damage resulting from D implantation. The surface-peak yield from an unexposed single-crystal Si(100) sample was used as an undamaged control. The data indicate that for energies ≤500 eV, fluences >10^{15}/cm^2 are required to produce lattice damage observable by RBS. In Table 2.4 surface-peak yields are given for the highest dose implants made at 50, 250, and 500 eV, as well as for the control sample. For sufficiently high doses at any energy, the Si crystal should become amorphous to the depth that the incident ions penetrate. Under these conditions the surface-peak yield will saturate, and the RBS results will resemble a spectrum taken from an amorphous sample. The values listed in Table 2.4 are near saturation.

Table 2.4. Near saturation surface-peak yields for D implants in Si at 50–500 eV

Energy (eV)	Dose (× 10^{17}/cm^2)	Surface-peak yield (× 10^{16}/cm^2)[a]
50	10	2.8
250	1	11.3
500	0.5	20.6
Control		1.5

[a]Units reflect number of Si atoms detected per cm^2.

Particle energies of ~150 eV have been estimated[5] in previous plasma edge studies in ISX-B by comparison of retained D concentrations in Si probes to empirical trapping curves. In an experiment in which the saturation behavior of the Si surface peak was monitored as a function of exposure to discharges in ISX-B, a saturation value of 7.7 × 10^{16} Si atoms/cm^2 was measured. This result falls between the surface-peak yields reported in Table 2.4 for 50- and 250-eV incidence and, hence, is in good agreement with the 150-eV estimate determined using trapping curves. These ISX-B data were also analyzed by comparing the widths of the damage profiles (surface peaks) in Si with theoretical TRIM binary collision code calculations. The resulting incident energy estimate was 150–300 eV[6], in good agreement with the trapping and damage saturation results.

These preliminary experiments indicate that damage to the Si lattice is observable for incident D at energies above 50 eV and fluences above 10^{15}/cm^2. Saturation effects are seen at higher fluences in the yield in the surface peak. The near saturation surface-peak yield is more than seven times greater at 500 eV than at 50 eV. For lattice damage above saturation, the yield in the surface peak can be used to estimate incident energies, particularly for monoenergetic or narrow energy distributions. In principle, below damage saturation exposures, combined measurements of the surface-peak yield and width (damage depth) should allow estimates of both energy and fluence. Energy estimates using this damage technique for samples exposed in the ISX-B tokamak are seen to agree with energy results obtained using the D trapping-vs-fluence technique.

1. Summary of paper to be published.
2. Max-Planck-Institut für Plasmaphysik, Garching bei München, Federal Republic of Germany.
3. S. A. Cohen et al., *J. Nucl. Mater.* **76/77,** 459 (1978).
4. S. A. Cohen and G. M. McCracken, *J. Nucl. Mater.* **84,** 157 (1979).
5. R. A. Zuhr, S. P. Withrow, and J. B. Roberto, *J. Nucl. Mater.* **93/94,** 127 (1980).
6. S. P. Withrow et al., *J. Nucl. Mater.* **98,** 231 (1981).

CONTINUOUS WAVE LASER-INDUCED FLUORESCENCE MEASUREMENTS IN ISX-B

T. B. Cook C. E. Young[2]
P. W. King[1] W. R. Husinsky[3]
J. B. Roberto

The method of laser-induced fluorescence (LIF) is a powerful diagnostic for detection of trace species in hostile environments and has been demonstrated in studying impurity metal atoms in tokamaks.[4] The transport of such impurities into the tokamak plasma is a serious concern for fusion reactors, because as little as 0.1% contamination by heavy metals can prevent plasma ignition.

The application of LIF to plasma impurity studies has primarily involved pulsed-laser systems.[5] There are, however, two disadvantages to such systems. First, it is difficult to operate a pulsed dye laser at bandwidth sufficiently narrow to allow estimation of thermal Doppler widths. This is significant since the relative importance of sputtering vs thermal evaporation has not yet been fully characterized. Second, pulsed-laser systems provide information at only a few (1–10) submicrosecond intervals during the tokamak discharge. It is thus a time-consuming process to map the impurity evolution during a 200–300 ms shot. To address these two problems of energy spectrum and temporal development better, we have undertaken LIF experiments on ISX-B using a cw dye laser.

The laser system is a tunable, actively stabilized ring dye laser pumped by an argon ion laser. It produces single-frequency radiation with a linewidth of under 1 MHz and, therefore, can be tuned inside a Doppler-broadened transition even for low-temperature thermal distributions. Output power is sufficient to saturate the relevant absorption transitions over an interaction volume of ~1 cm^3.

The first studies have been performed on Cr neutrals in the vicinity of a Cr probe in the plasma edge of ISX-B. The dye laser is operated on one of the components of the atomic resonance line at ~425 nm (producing a power output of 50–150 mW). As indicated in Fig. 2.22, the laser is tuned to the absorption using a variety of devices including a small grating spectrometer for rough tuning and a hollow-cathode lamp (utilizing the optogalvanic effect) for fine tuning. Final adjustment to allow for Zeeman shifts in the ~1-T torodial field is accomplished using a pair of scanning Fabry-Perot etalons. The laser beam is acousto-optically chopped (allowing high-order diffraction spots to be used for the various monitoring functions) and is injected into the tokamak vessel which is located ~8 m from the laser table. Fluorescence from atoms illuminated by the laser just outside the plasma edge are collected, spectrally filtered using a double spectrometer with holographic gratings, and detected with a photomultiplier tube. A computer-controlled data acquisition system operates a gated counter, stores the data for later analysis, and graphically displays the results on a terminal in the laser enclosure.

Only a preliminary analysis of Cr results is available, but a signal due to Cr has been detected and some estimates of Doppler-widths have been performed. Uncertainties in the measurements are large, due principally to extremely high count rates from plasma light scattered into the collection cone of the detector. To provide better rejection of plasma light and to reduce the background due to laser light scattered off vacuum components, efforts are now under way to replace the double spectrometer with an interferometer giving improved transmission with a narrower pass band

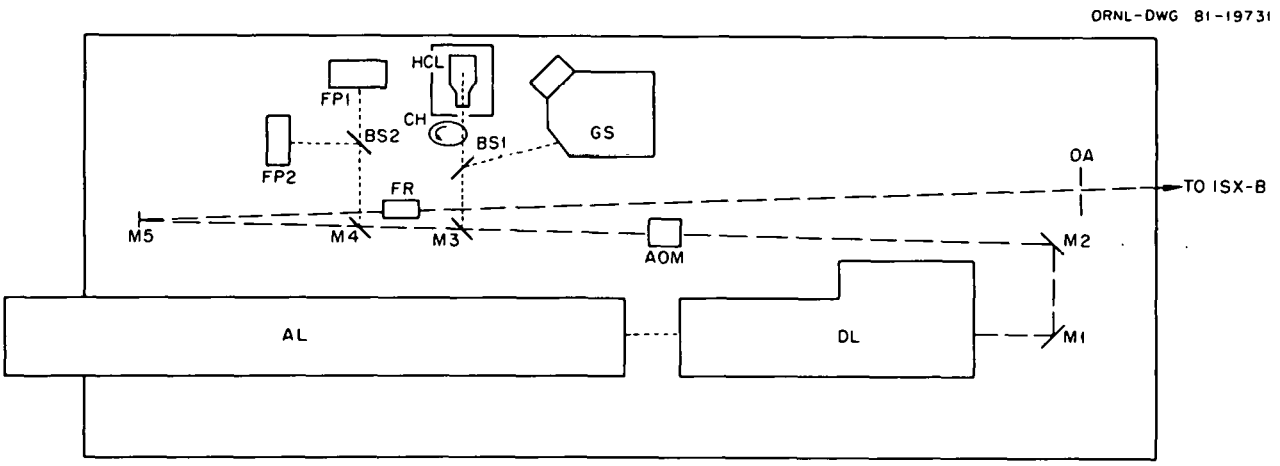

Fig. 2.22. Continuous-wave laser-induced fluorescence system. A ring dye laser (DL) is pumped by an argon ion laser (AL). The output beam is modulated using an acousto-optic modulator (AOM), wavelength-tuned using a grating spectrometer (GS) and hollow cathode lamp (HCL), and wavelength-monitored using two scanning Fabry-Perot etalons (FP1-2). Other optical elements include a Faraday rotator (FR), mirrors (M1-5), beam splitters (BS1-2), a mechanical chopper (CH), and an output aperture (OA).

and to study an off-resonance three-level excitation in Ti, instead of the resonant two-level Cr transition. It is hoped that these measurements will lead to a better understanding of impurity introduction, transport, and ionization lengths in the plasma edge of ISX-B.

1. Fusion Energy Division, ORNL.
2. Guest scientist from Argonne National Laboratory, Argonne, Ill.
3. Guest scientist from Technical University, Vienna, Austria.
4. H.-B. Schweer et al., *J. Nucl. Mater.* **93/94,** 357 (1980).
5. A cw LIF measurement of Zr impurities in the APEX tokamak has recently been reported; C. E. Young et al. (to be published).

MEASUREMENT OF THE DENSITY AND VELOCITY DISTRIBUTION OF SPUTTERED Al ATOMS IN EBT-S BY LASER-INDUCED FLUORESCENCE

E. Dullni[1] J. B. Roberto

The density and velocity distribution of neutral Al atoms have been measured in the vicinity of the outer wall of the EBT-S fusion device by laser-induced fluorescence. EBT-S is a steady-state plasma experiment consisting of 24 mirror sections bent into a torus. Macroscopic erosion rates are observed where magnetic field lines intercept the Al vacuum vessel walls. The mechanism of this erosion has been the subject of considerable speculation and is an important consideration in the design of the next generation EBT-P device. Laser-induced fluorescence[2] provides direct information on the erosion process through measurements of the flux and velocity distribution of the eroded atoms.

The experimental setup is shown in Fig. 2.23. A flashlamp-pumped frequency-doubled dye laser was tuned to the resonance transition of Al at 308.2 nm. The laser-induced fluorescence was detected using a photomultiplier and lens system which optically intercepted the laser beam 5 cm in front of a cavity wall in EBT-S. An Al plate partially covered the access port at the wall position to simulate a continuous wall. Wavelength scanning the dye laser at narrow linewidth (~11 mÅ) allowed measurements of the Doppler-broadened profile of the Al line with a velocity resolution of

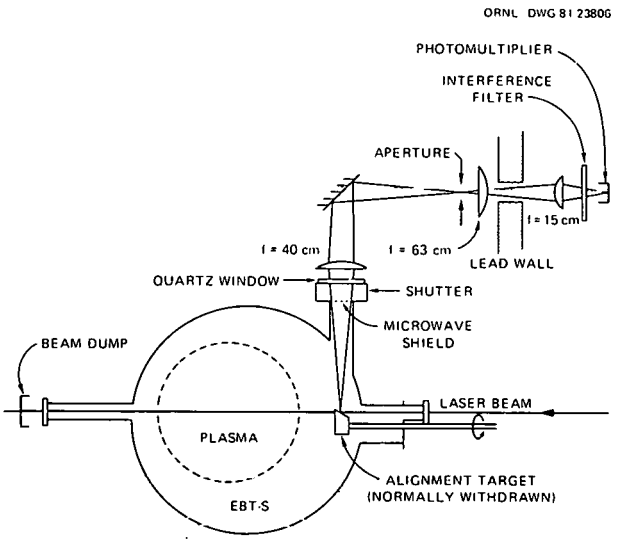

Fig. 2.23. Experimental setup for laser fluorescence measurements in EBT-S.

~10^4 cm/s (~0.1 eV). Plasma parameters for these measurements were: 100-kW microwave power at 28 GHz, $B(0) = 1.4$ T, $n_e(0) = 1.0 \times 10^{12}/\text{cm}^3$, $T_e(0) = 400$ eV, and $T_i(0) = 20$–40 eV.

The Doppler-broadened absorption profile for Al is shown in Fig. 2.24. The integral of this profile corresponds to a neutral Al density of 6.5×10^7 atoms/cm^3. The maximum in the distribution is

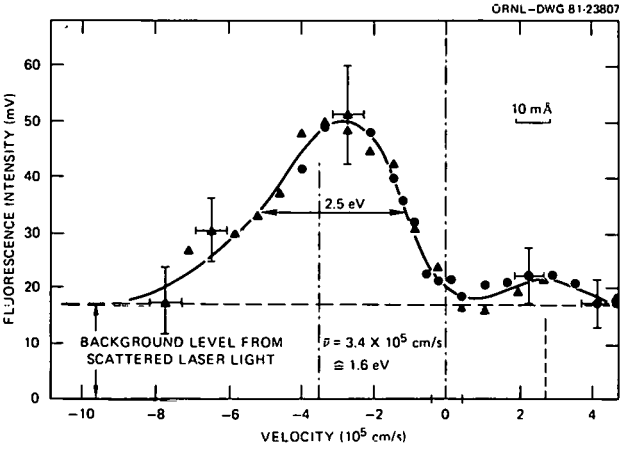

Fig. 2.24. Velocity distribution for neutral Al perpendicular to and 5 cm from an outer cavity wall in EBT-S. Atoms moving away from the wall show a negative velocity shift.

shifted to the left indicating atoms moving away from the wall. The small peak on the right side of the distribution corresponds to atoms originating at the mirror throats which would have an opposite velocity component at the detection volume. The mean energy of the Al atoms released from the wall is 1.6 eV with a Doppler width of 2.5 eV. These energies are typical of sputtering distributions and are much higher than energies expected for other release mechanisms such as arcing or evaporation. Efforts are currently under way to identify the source of the sputtering by measuring Al densities as a function of H vs D operation. Measurements as a function of plasma parameters and along the laser beam at different distances from the wall are also planned.

1. Guest scientist from Ruhr-Universitaet, Bochum, Federal Republic of Germany.
2. E. Hintz, *J. Nucl. Mater.* **93/94,** 86 (1980).

NEUTRAL ATOM IMAGING IN EBT USING A PINHOLE CAMERA

R. A. Zuhr R. K. Richards[1]

Initial exposures have been made using a pinhole camera to image the neutral atom distribution coming from the plasma in a sector of the ELMO Bumpy Torus Scale (EBT-S) fusion device. EBT-S is a microwave-heated steady-state plasma experiment consisting of a series of magnetic mirrors arranged end to end in a toroidal configuration. The angular distribution of neutral impurities and H isotopes gives information on impurity sources and mechanisms, particle transport, and charge exchange processes.

The camera consisted of a 0.76-mm pinhole located 7.5 cm outside the plasma-wall interface on the centerline of the cavity. C and Si deposition samples were placed 12.7 cm behind the pinhole to collect neutral plasma and impurity atoms. After exposure, the samples were removed and analyzed using Rutherford ion backscattering for impurity detection and nuclear reaction analysis with the $D(^3He, p)^4He$ reaction for D detection.

Initial impurity results show the presence of C, O, and Si. It is surprising that Si, which is present in EBT-S in very small quantities, is observed, while Al, from which the vacuum vessel is constructed, is not. The most likely source of the Si appears to be Si-greased O-ring seals. These seals can be heated to the point of failure by the microwave radiation, if they are not perfectly shielded. The absence of Al, which is known to be transported in substantial quantities in EBT-S, can be explained if it is present in ionized form, since the camera is sensitive only to neutral particles.

Geometric data have been taken in a horizontal plane that cuts through the centerline of the torus. Such data represent the neutral density, integrated along chords through the plasma, as a function of position in the cavity. The geometry is such that observations can be made from the narrow region or throat where the coils are located on one end of the cavity to the same location on the other end. It has been proposed that these narrow throats would be regions of high neutral density because of the charge exchange that takes place at such surfaces. This idea is supported by our initial results, which show increased neutral deposition (~50%) of both D and impurities from each of the throat regions.

A more thorough analysis of the data will require modeling of electron and ion densities and temperatures so that the integrated effects of neutralization and ionization along the chords can be calculated. For the present, the initial results show promise for using deposition probe techniques to take "pictures" of neutral distributions in the EBT-S plasma.

1. Fusion Energy Division, ORNL.

ION-SOLID INTERACTIONS

ION IMPLANTATION AND ANNEALING OF α-Al_2O_3 CRYSTALS

H. Naramoto[1] J. M. Williams
C. W. White C. J. McHargue[2]
B. R. Appleton

It is well known that ion implantation can alter the physical properties of the near-surface region of semiconductors and metals in a controlled manner. We have applied this technique to alter the near-surface properties of insulating α-Al_2O_3 crystals, which are expected to play an important role as high-temperature materials. During implantation foreign atoms are introduced into the matrix under nonequilibrium conditions, but this is accompanied by displacement damage in the matrix,

which is especially sensitive for insulating systems. There may be strong interactions between implanted species and induced defects. For our experiments, Cr ions were used as the implanted species, because Cr exhibits total solubility under equilibrium conditions[3] in Al_2O_3. In addition, this combination is ideally suited for studies using Rutherford backscattering and ion channeling techniques.

Prior to implantation, α-Al_2O_3 single crystals with a (0001) orientation were polished using diamond paste and then were annealed at 1200°C for five days in air to remove polishing damage. In this state these crystals exhibited excellent channeling behavior [χ_{min} (Al) ~ 1.8%] indicating that the annealing procedure was very effective in removing polishing damage. Crystals were then implanted with ^{52}Cr (300 keV) to doses up to $10^{17}/cm^2$. Ion-scattering/channeling measurements were used to determine the depth distribution of damage in the crystal and the total and substitutional concentrations of Cr. Comparisons were made for the as-implanted crystals before and after thermal annealing at 800, 1000, 1200, and 1300°C (for 1 h in air). Part of each crystal was masked during implantation, and channeling spectra from the virgin region were taken at each stage of annealing to ascertain that no significant physical change occurred in the virgin material. Mechanical properties such as fracture toughness and indentation hardness were evaluated at each stage of modification and annealing to determine the effect of implantation on the fundamental physical properties.

Figure 2.25 shows backscattered energy spectra from α-Al_2O_3 single crystals implanted with ^{52}Cr (300 keV) to a dose of $10^{17}/cm^2$. The random spectrum was taken in the implanted region, and ⟨0001⟩ aligned spectra were taken from both the implanted and virgin regions. The random spectrum shows a noticeable deficiency of Al in the Al sublattice after Cr implantation. No similar deficiency is discernible in the O sublattice. Following implantation, the ⟨0001⟩ aligned spectra show that the Al and O surface peaks have increased in intensity but have the same FWHM as do those from the virgin region. This shows that surface damage remains after implantation within the depth (energy) resolution of the detector (~200 Å). The ⟨0001⟩ aligned spectra from the implanted region show that implantation caused considerable damage in the near-surface region of both the Al and O sublattices, but it is significant

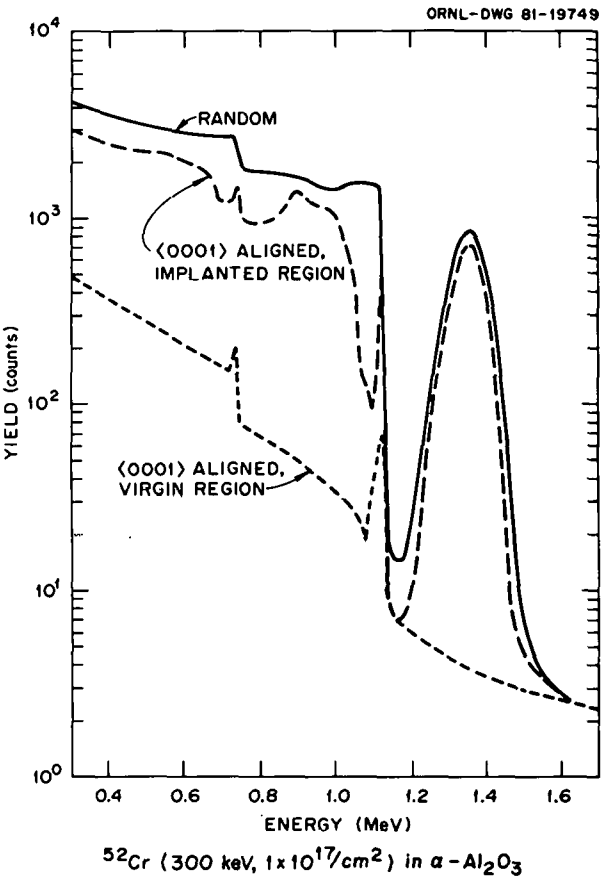

Fig. 2.25. 2-MeV ^4He backscattering spectra for α-Al_2O_3 crystals implanted with ^{52}Cr (300 keV, 1×10^{17} cm^{-2}).

that no region was turned completely amorphous by the implantation of 10^{17} ions/cm^2. (The aligned spectra do not reach the random value.) For semiconductors such as Si, implantation of ~10^{15} atoms/cm^2 would have turned the entire near-surface region completely amorphous. The damage distributions for both the Al and O sublattice show a peak near the end of range for Cr, but the near-surface region is relatively undamaged. Just behind the surface peak, the χ_{min} value in the implanted crystal is ~8% in the Al sublattice, compared with 1.8% in the virgin crystal. Finally, comparison of the aligned and random spectra associated with scattering from the implanted Cr shows that a part of the implanted Cr atoms were incorporated into substitutional lattice sites during implantation, also suggesting that considerable reordering occurs during implantation.

Figure 2.26 shows the annealing behavior of the Cr-implanted α-Al_2O_3 crystal (300 keV, 1×10^{17}

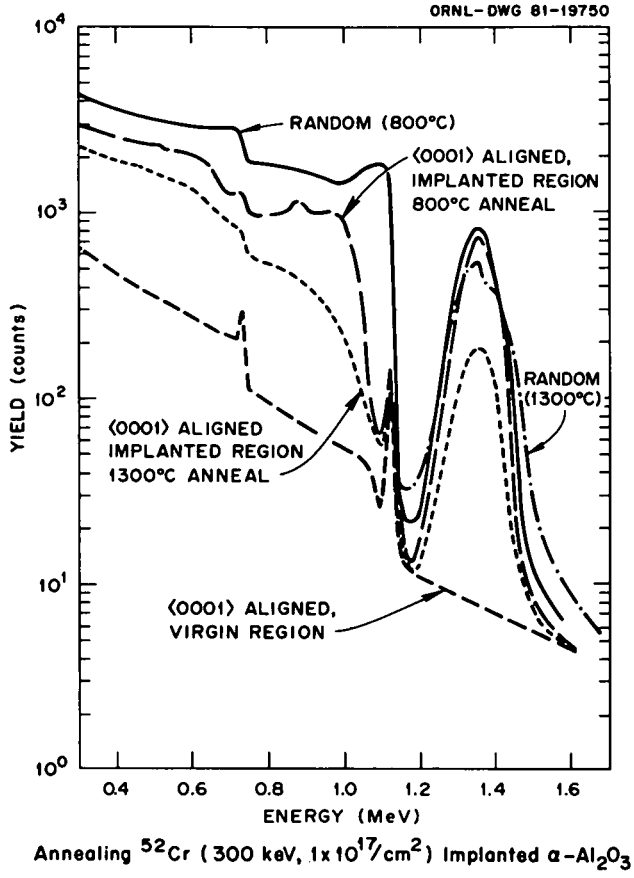

Fig. 2.26. 2-MeV ^4He backscattering spectra for α-Al_2O_3 crystal implanted with ^{52}Cr (300 keV, 1×10^{17} cm^{-2}) and annealed at 800°C and 1300°C in air.

cm^{-2}). Spectra are shown after annealing at 800°C and 1300°C. The random spectra in the Al and O matrices are the same at each annealing stage, and the data points are omitted. As seen by comparison with the spectrum in Fig. 2.25, a selective annealing occurs in the Al matrix without significant change of Cr substitutionality after annealing at 800°C. This may be due to the higher mobility of Al atoms in the α-Al_2O_3 crystal. Annealing at 1200°C causes a big change in the substitutionality of the implanted Cr atoms accompanied by substantial recovery in both the Al and O sublattices. Results obtained after annealing at 1300°C are also indicated in Fig. 2.26. The ⟨0001⟩ aligned spectrum shows that substantial annealing of damage has been achieved, but some defects still remain in the implanted region. In addition, the implanted Cr atoms have undergone some redistribution in depth as a result of the 1300°C annealing. After this annealing, Cr is highly substitutional (>90%), and the substitutionality is highest in the near-surface region.

After every thermal annealing, measurements were done on the fracture toughness and the hardness. The former, which is one measure of the residual stress at the surface, was evaluated from indentation-induced cracking, assuming an isotropically elastic body. These measurements show that residual stress saturates after the implantation for doses in excess of 1×10^{16} cm^{-2} and recovers to the values of the virgin crystal after thermal annealing. From the microhardness and channeling measurements, it is clear that the hardness decreases as the Cr implantation damage anneals, and after annealing at 1200°C, the hardness in the implanted specimen is equal to that in Al_2O_3-Cr_2O_3 alloys with the corresponding Cr concentration which are grown through the melting process.[4]

The microscopic structure analysis by ion scattering and the subsequent evaluation of mechanical properties show that Al_2O_3-Cr_2O_3 alloys can be obtained by thermal annealing after Cr implantation. Measurements are in progress to determine the exact location of incorporated Cr atoms using *a*- and *c*-axes crystals. This work is being extended also through the implantation of other species such as Ti, Ge, and Zr, because these species do not exhibit complete solid solubility at Al_2O_3. These early results are encouraging indications that one can tailor the mechanical properties of these surfaces by such selective implants.

1. Guest scientist from Japan Atomic Energy Research Institute, Tokai-mura, Japan.
2. Metals and Ceramics Division, ORNL.
3. R. C. Bradt, *J. Am. Ceram. Soc.* **50,** 54 (1967).
4. C. J. McHargue et al., *Proceedings of International Conference on the Science of Hard Materials,* to be published.

A STUDY OF NEW ION-SCATTERING EFFECTS IN SOLIDS

O. W. Holland B. R. Appleton
J. H. Barrett

The yields of energetic ions scattered from the near surface of amorphous solids have been shown to be enhanced in a small angular range about 180° by more than 2.5 times that expected for elastically scattered ions.[1-3] It has been demon-

strated that correlations between an ion's incoming and outgoing (after backscattering) paths in the solid due to trajectory reversibility can account for the enhanced scattering yields.[4-6] A detailed study of the ion and target dependencies of this effect has been made and compared with results of computer simulations. Also, the manifestations of the effect in single crystals under both channeling and nonchanneling conditions were explored. These studies in single crystals not only add to the understanding of this new ion-scattering effect but also are critical to the understanding and proper interpretation of uniaxial double-alignment (UADA) channeling experiments.

The effect can be characterized by its dependency upon scattering depth in the solid as well as the angular extent over which it persists. Measurements were accomplished using an array of planar, solid-state detectors which recorded, at various scattering angles near 180°, energy spectra of ions backscattered from the solid. The detector array was able to probe the scattered ion flux to within $\psi = 0.082°$ of 180° with an angular acceptance less than 0.1°. The results of such measurements are shown in Fig. 2.27 for 1.0-MeV $^4He^+$ ions incident upon polycrystalline Pt. The maximum yield enhancement for a given scattering angle ψ (measured from 180°) is seen to decrease rapidly as ψ increases. Also, Fig. 2.27(b) shows that the enhanced yield for a fixed scattering angle $\psi = 0.082°$ increases rapidly from the surface to a maximum, after which it decreases to zero at a somewhat slower rate. Similar results were obtained from a variety of elemental targets with differing atomic numbers and densities probed with both protons and helium ions of energies from 0.5 to 1.5 MeV. As ion and target parameters were

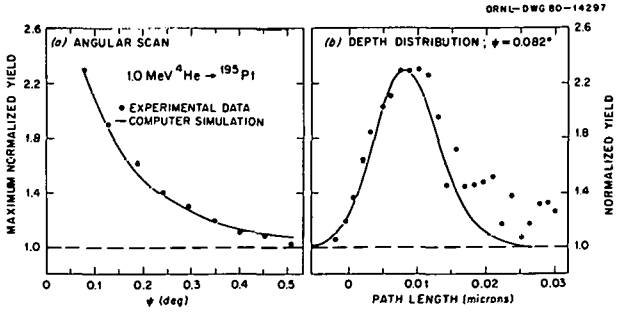

Fig. 2.27. Comparison of computer simulation results with experimental results for 1.0-MeV He on Pt.

changed such that the average scattering of an ion over a unit path length in the solid increased, the extent of the angular distribution narrowed, and the scattering depth over which the enhancement was observed persisted to greater depths.

An invaluable aid in the understanding of the effect has been the use of computer simulation of the ion-solid interaction. When the interaction was modeled such that trajectory reversibility was allowed, the calculated scattering yields were in excellent agreement with those measured, as can be seen in Fig. 2.27. A detailed discussion of the computer model can be found in ref. 3. Additionally, simulations showed that the excess yield near 180° was compensated by a yield deficiency and that two nuclear recoil effects (the recoil of lattice atoms impacted by the incident ion and the energy loss of the ion during backscattering) can have a significant influence upon the effect.

Two aspects of the new ion-scattering effect as manifested in single crystals were investigated. Both have impact upon the interpretation of the results of UADA measurements. Unlike single alignment, in which the crystal is aligned with the incident beam, the detector is additionally aligned in the double-alignment geometry so that only scattered ions that leave the crystal along a major crystallographic direction are detected. The UADA is unique among the double-alignment geometries in that the detector is positioned essentially at 180° so that both it and the incident beam are aligned along the same crystal axis. Previously, it was expected that the yield of scattered ions from the surface layers of a single crystal, those which comprise the characteristic surface peak in the aligned spectra, would be smaller in double alignment than in single. This is because the scattered ions in the double-alignment geometry would be blocked from the detector by the crystal rows. Measurements of the Au(100) single-crystal surface have shown that this is indeed the case for a 90° double-alignment measurement where the beam was incident along [110] and the detector was aligned along [110]. The measured surface yield in this case was 2.26 atoms/row, a reduction of about 15% from that measured in single alignment. If trajectory reversibility effects did not exist, about the same yield reduction would be expected for the UADA. Instead, the surface yield shows an enhancement of 45% to 3.77 atoms/row. This surface-yield enhancement occurs because trajectory reversibility causes ions scattered from sub-

surface atoms to have an enhanced probability of being detected. This raises the possibility that the UADA geometry could increase sensitivity in the use of positive ion scattering as a tool in surface studies.

The second effect involves random reference spectra measured from single-crystal targets in the UADA geometry. It is well known that in a single-alignment scattering geometry, the yield from a continuously rotated single crystal closely approximates that of an amorphous solid. This is an important result since most channeling data require normalization to a random yield. However, in UADA such normalization is made difficult because of the enhancement effect. An additional complication in the UADA geometry was identified when the yield from a rotated crystal was found to differ from that of an amorphous sample. The results of measurements made on an amorphous Ge target and a Ge single crystal are shown in Fig. 2.28 and clearly demonstrate that the

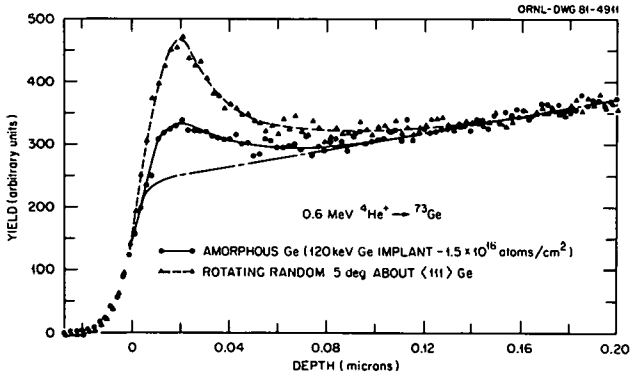

Fig. 2.28. Measured scattering yields for 0.6-MeV He ions on amorphous and rotating single-crystal Ge targets.

rotating crystal procedure leads to a larger yield enhancement which persists to greater depths. This additional enhancement, which arises because of the collective reflections near low-index directions, raises a number of concerns about double-alignment measurements and their normalization.

1. P. P. Pronko et al., *Phys. Rev. Lett.* **43,** 779 (1979).
2. P. P. Pronko et al., *Nucl. Instrum. Methods* **170,** 227 (1980).
3. O. W. Holland, B. R. Appleton, and J. H. Barrett, *IEEE Trans. Nucl. Sci.* **NS-28,** 1824 (1981).
4. O. H. Crawford, *Phys. Rev. Lett.* **44,** 185 (1980).
5. M. M. Jakas and R. A. Baragiola, *Phys. Rev. Lett.* **44,** 424 (1980).
6. J. H. Barrett, B. R. Appleton, and O. W. Holland, *Phys. Rev. B* **22,** 4180 (1980).

COMBINED ANALYTICAL METHODS IN THE ANALYSIS OF Cr-IMPLANTED GaAs[1]

O. W. Holland J. Narayan
B. R. Appleton P. P. Pronko[2]

The behavior of Cr-implanted GaAs was investigated using a combination of analytical techniques. These included transmission electron microscopy (TEM) for analysis of the residual defects in implanted layers after annealing and ion scattering for both defect analysis and location of the implanted impurity in the lattice. A major aspect of this study was the use of MeV proton-induced x-ray excitation (PIXE) in determining the Cr lattice site. Normally, an analysis of the energy spectra of ions backscattered from the sample under both channeling and nonchanneling conditions is used in this determination. However, backscattering techniques are sensitive only to heavy impurities in light substrates and, therefore, were not suitable for the present work. The distinct separation of the Cr characteristic x rays from those of the lattice, as seen in Fig. 2.29, makes possible lattice location studies in this material through the analysis of x-ray spectra that would otherwise be impossible by other ion-scattering techniques.

GaAs(100) specimens were room-temperature implanted at 120 keV to doses of 1×10^{15}, 5×10^{15}, and 5×10^{16} ions cm^{-2}. These samples were capped with a 0.08-μm plasma deposited Si_3N_4 film and annealed in flowing N_2 at 900°C for 15 min. The caps were removed in HF acid before analysis with a 1.0-MeV proton beam. Backscattered proton energy spectra were acquired simultaneously with the x-ray spectra so that the recovery of the damage in the implanted layer after annealing could be studied. Companion samples were examined by TEM.

The ⟨110⟩ aligned, backscattering spectra from the two lower dose implants indicated that a nearly damage-free epitaxial regrowth of the implanted layer had occurred during thermal annealing. This was evidenced by minimum yields in the near surface that were essentially identical to those obtained from virgin crystals. Beyond the near-surface region, the dechanneling rate in both

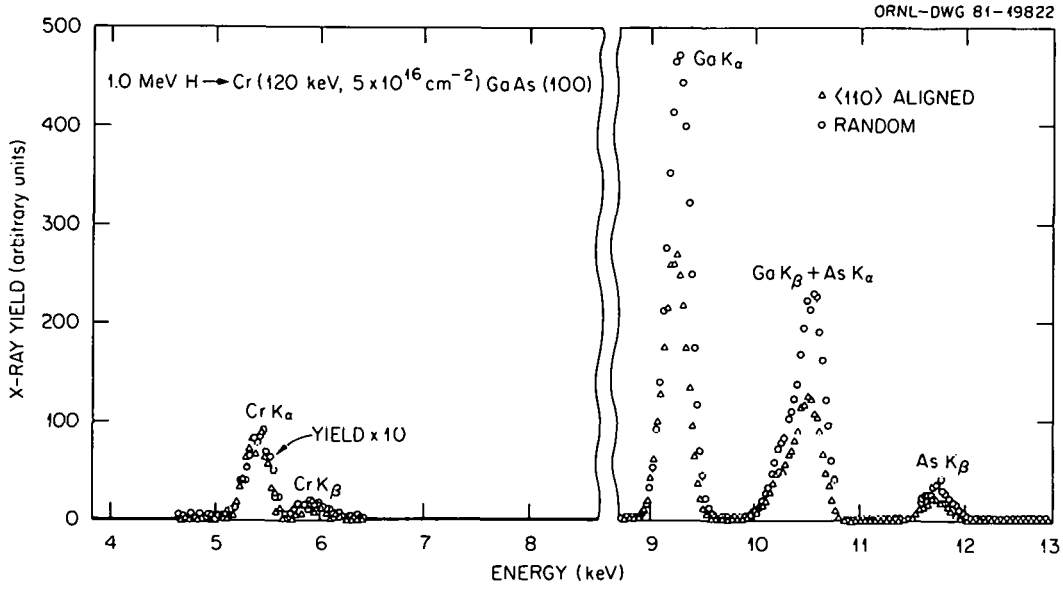

Fig. 2.29. Characteristic x-ray spectra excited by 1.0-MeV H incident on ⟨110⟩ aligned and randomly oriented Cr-implanted GaAs(100).

spectra were only slightly higher than in virgin crystals, indicating the possible presence of some small number of extended defects. This conclusion was corroborated by the TEM results which showed a low density of large dislocation loops. Also, Cr precipitates were observed in the micrographs for the 5×10^{15} cm^{-2} implanted sample, while none were evident in the lowest dose sample. In the high dose 5×10^{16} cm^{-2} implanted sample, the micrographs showed massive Cr precipitates mainly associated with the dislocations in the lattice. The lattice was highly strained and even contained some polycrystalline structure. This agreed well with the backscattering results on this sample, which showed very high minimum yields for the aligned spectrum as well as large dechanneling rates.

The spectrum of characteristic x rays from the 5×10^{16} cm^{-2} implanted crystal aligned along the ⟨110⟩ axis is compared in Fig. 2.29 to that from the randomly oriented crystal. The ratio of aligned yield to random for the Ga and As K_α x rays is approximately 0.54, which is somewhat higher than the virgin ratio of 0.32 and reflects the large amount of residual damage in the implanted layer after annealing. It is clear that there is no reduction in the Cr characteristic x rays. Similar behavior for the two lower dose samples was observed. This indicates that little or no Cr was in substitutional sites in the samples. Additionally, detailed angular scans across the ⟨110⟩ channel were taken for the 5×10^{15} and 5×10^{16} cm^{-2} implanted crystals. The angular scan in the sample implanted with 5×10^{16} cm^{-2} showed a uniform distribution of the Cr x-ray yield as expected from the precipitated nature of the Cr in this sample. However, the structure in the angular scan of the lower dose sample, as seen in Fig. 2.30, suggests that, while some of the Cr had been precipitated, an interstitial site may have been occupied. This is evidenced by the peaking of the yield along the channel center.

Cr is an amphoteric impurity in GaAs and is introduced during growth to compensate both native donor and acceptor impurities and to render GaAs semi-insulating via its deep acceptor levels. Although it is clear from the results that little or no Cr was incorporated into the GaAs lattice by the present techniques, such studies are of technological importance, because not only could Cr be implanted into GaAs to tailor the resistivity selectively, but also to compensate donor and acceptor profiles at selected depths. The combination of the analytical techniques used for the lattice location

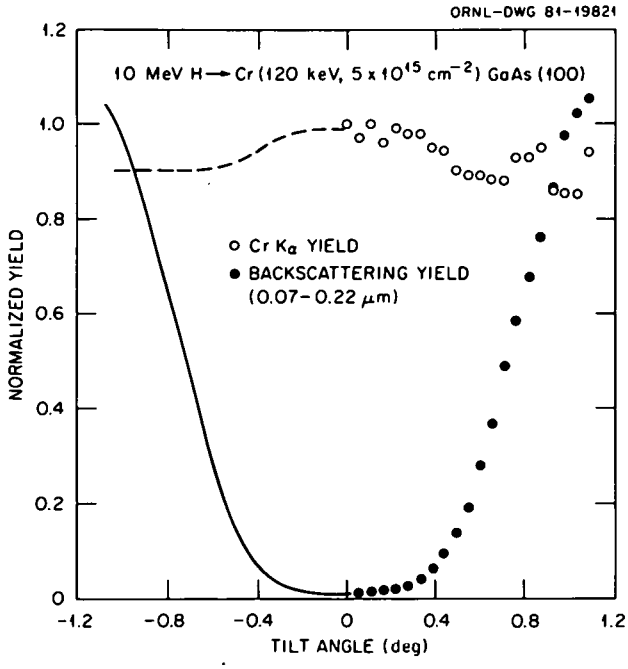

Fig. 2.30. Comparison of the yields of Cr x rays and backscattered ions from the GaAs lattice in an angular scan across the ⟨110⟩ axis in Cr-implanted GaAs(100).

studies and defect analysis was demonstrated to be a viable method to deduce the role of impurities in GaAs.

1. Summary of paper to be published.
2. Universal Energy Systems, Dayton, Ohio.

DEFECTS AND LIMITS OF SOLID SOLUBILITY IN SPE-GROWN Sb^+- AND In^+-IMPLANTED Si[1]

J. Narayan O. W. Holland

Ion implantation in semiconductors at relatively high doses frequently leads to the formation of amorphous layers. The implanted impurities (dopants) do not occupy regular lattice sites and, therefore, are electrically inactive. It is possible to grow defect-free layers epitaxially by either heating the implanted specimen in a furnace (temperature range 450-650°C) or by using cw lasers or electron beams (temperature range 650–1400°C). During SPE growth where underlying substrates act as a seed for crystal growth, the concentrations of dopants in substitutional sites (electrically active) and the residual damage in the implanted region are of particular interest. Pioneering work by Csepregi et al.,[2] using ion backscattering and channeling techniques, showed that amorphous layers on ⟨100⟩ and ⟨110⟩ substrates grew (in the temperature range 450–600°C) into fairly defect-free layers, whereas significant amounts of damage remained in the case of ⟨111⟩ substrates. There was also some evidence for exceeding the solubility limits after furnace annealing below about 600°C.[3] However, the previous studies relied primarily on ion backscattering and channeling techniques, which provide detailed information about the lattice location and dopant concentration of impurities but are less sensitive to the nature of residual damage in the crystals. In the absence of detailed information on the residual damage in the above studies, there was always a question of whether the solubility limits were enhanced by the presence of defects. In the present study, we have combined ion backscattering and channeling techniques with TEM (both plan-view and cross-section) techniques. The TEM techniques are extremely useful for analysis of the nature of residual damage and for accurate determinations of thicknesses of regrown and amorphous layers. Lattice locations and concentrations of dopants as a function of depth can be determined from aligned axial channeling spectra and from detailed angular scans across axial directions. The combination of these analysis techniques has provided a much better understanding of the details of SPE growth, including the limits of solid solubility, the nature of defects, and the interfacial accumulation and redistribution of impurities.

Si single crystals (having ⟨100⟩ and ⟨111⟩ orientations, 2–6 Ω-cm resistivity, ~500 μm thick) were implanted with (200 keV) $^{121}Sb^+$ and (125 keV) $^{115}In^+$ ions with doses ranging from 1.0×10^{14} to 5.0×10^{16} cm^{-2}. The implanted specimens were annealed in a furnace under flowing dry nitrogen at constant temperatures (isothermally) which ranged from 475–600°C. All the specimens were studied by plan-view and cross-section TEM techniques using a Philips EM-400 analytical microscope. Companion specimens were analyzed by ion backscattering and channeling techniques.

Figure 2.31 shows a typical example of cross-section micrographs from Sb-implanted specimens (dose = 4.4×10^{15} cm^{-2}) after annealing at 525°C for various times. The as-implanted specimen contained an amorphous layer 158 nm thick, which was followed by a band of dislocation loops. During thermal annealing, the epitaxial

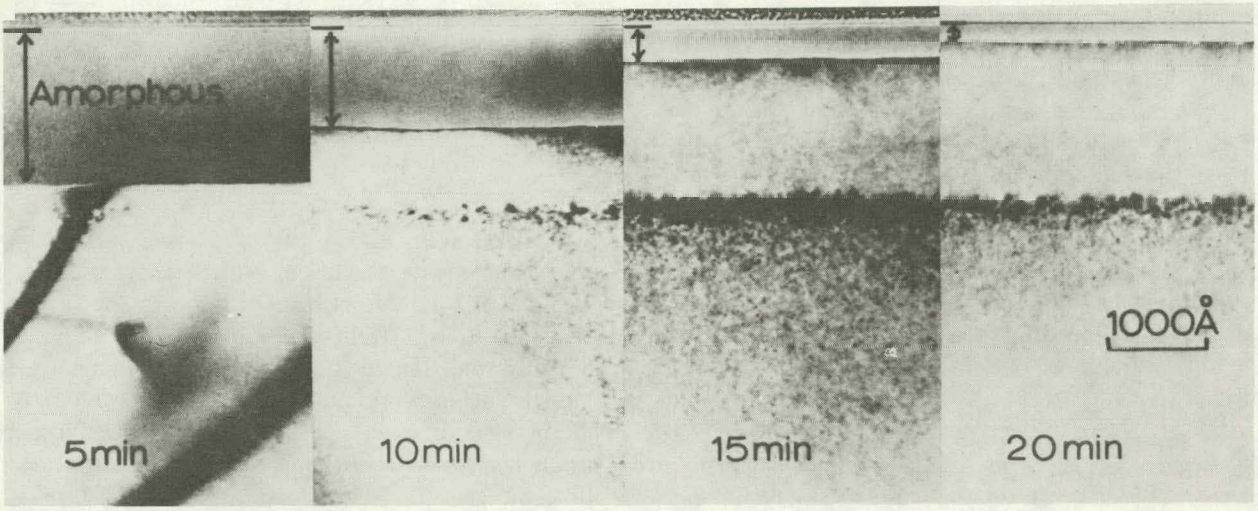

Fig. 2.31. Cross-section TEM micrographs for Sb^+-implanted (100) Si (200 keV, 4.4 × 10^{15} cm^{-2}) annealed at 525°C for 5, 10, 15, and 20 min.

growth started with the substrate acting as a seed for the crystal growth, and the underlying dislocation-loop structure remained largely unaffected at these low temperatures. From the thicknesses of regrown layers as a function of time at 525°C, it was found that the growth rates varied from 0.05 to 0.23 nm s^{-1}, being proportional to the implanted dopant concentration. The effect of the underlying dislocation band was clearly observable in the channeling spectra. Direct large-angle scattering from the defects produced a peak in the scattering yield at a depth that was consistent with location of the dislocation band as determined from the cross-section micrographs. The experiments done using detailed angular scans showed that greater than 99% of the implanted Sb in SPE grown layers was in the substitutional sites. The substitutional and total concentrations of Sb as a function of depth are plotted in Fig. 2.32 showing a complete incorporation of Sb in substitutional sites for 4.4 × 10^{15} and 0.9 × 10^{16} cm^{-2} specimens. For higher dose implants of 2.9 × 10^{16} cm^{-2}, the SPE growth occurred only to about 86 nm above the dislocation band (120 nm from the surface). Further growth in these specimens did not occur even after 17 h of annealing at 525°C, and at higher temperatures the region became polycrystalline. Nearly complete incorporation of Sb occurred in the regrown layer. The substitutional concentration of Sb near the interface was

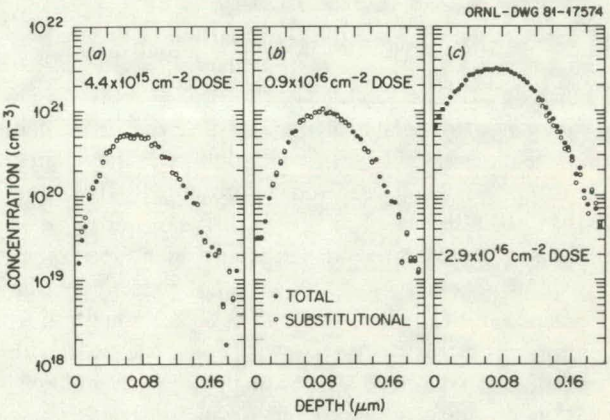

Fig. 2.32. Substitutional and total concentrations of Sb as a function of depth for (a) 4.4 × 10^{15}, (b) 0.9 × 10^{16}, and (c) 2.9 × 10^{16} cm^{-2} Sb^+-implanted specimens after annealing at 525°C.

1.3 × 10^{21} cm^{-3}, which was found to be the maximum substitutional concentration under SPE growth conditions at any temperature below 600°C. The maximum substitutional concentration in the case of In-doped Si was found to be 5.0 × 10^{19} cm^{-3}. These concentrations in Si-Sb and Si-In systems exceed the respective retrograde solubility maxima by factors of 18 and 60. In the case of the Si-In system, substantial redistribution and precipitation of In occurred during SPE growth, whereas for the Si-Sb system the as-implanted distribution

was retained after SPE growth. After subsequent heating, most of the dopants in excess of solubility limits precipitate out (after 1000°C/30 min annealing), but the metastability is not easily destroyed (e.g., after 800°C/30 min annealing of the 0.9×10^{15} cm^{-2} specimen, the substitutional concentration of Sb was 4.0×10^{20} cm^{-3}, which is five times its retrograde maximum). In conclusion, by SPE growth, it is possible to form metastable solid solutions in the absence of any defects, and there seems to be a maximum in the substitutional dopant concentration for each system under SPE growth conditions.

1. Summary of paper to be published.
2. L. Csepregi et al., *J. Appl. Phys.* **49,** 3906 (1978).
3. P. Blood, W. L. Brown, and G. L. Miller, *J. Appl. Phys.* **50,** 173 (1979).

ENHANCED DIFFUSION AND FORMATION OF DEFECTS DURING THERMAL OXIDATION[1]

J. Narayan B. R. Appleton
J. Fletcher W. H. Christie[2]

Enhanced diffusion of dopants and the formation of defects during thermal oxidation of Si have been investigated using electron microscopy, RBS, and SIMS techniques. Enhanced diffusion of B was clearly demonstrated in laser-annealed specimens in which secondary defects were not present. In the presence of secondary defects, such as precipitates, enhanced diffusion of B was not observed. The absence of enhanced diffusion during thermal oxidation was also observed for As in Si. These studies shed light on the mechanisms associated with thermal-oxidation enhanced diffusion.

1. Summary of paper: p. 355 in *Defects in Semiconductors,* ed. by J. Narayan and T. Y. Tan, North Holland, New York, 1981.
2. Analytical Chemistry Division, ORNL.

PULSED-LASER ANNEALING

SYNCHROTRON X-RAY DIFFRACTION STUDY OF Si DURING PULSED-LASER ANNEALING[1]

B. C. Larson T. S. Noggle
C. W. White D. Mills[2]

Time-resolved x-ray diffraction measurements, with nanosecond resolution, have been carried out on Si during pulsed-laser annealing through the use of single pulses from the Cornell High Energy Synchrotron Source (CHESS). These real time measurements represent the first nanosecond resolution structural measurements to be performed using x rays and further represent the first real time measurements to probe below the surface of Si during the annealing process. These measurements provide direct information on the time duration and depth distribution of near-surface lattice strains associated with laser annealing of Si and, when analyzed in terms of thermal expansion, provide the first determination of the lattice temperatures below the crystal surface.

In this study, we have made use of the extended Bragg scattering intensity[3] that is found in the vicinity of Bragg reflections as a result of Bragg-like scattering from near-surface strains. This intensity has been measured in a time-resolved mode following ~1.3-J/cm^2 ruby laser pulses. Figure 2.33 shows schematically the method employed. The nanosecond time resolution utilizes the pulsed nature of synchrotron radiation (~0.1 ns pulse length, 2.5 μs between pulses) and the fact that there are enough photons in a single pulse (25,000 in the A1 beam line at CHESS) to measure x-ray reflectivities in the range 10^{3}–10^{-4}. Pulses from a Q-switched ruby laser (15 ns pulse width, $\lambda = 0.694$ μm) were synchronized with the x-ray pulses using coincidence circuits and variable time delays. The time delay between each laser pulse and the probing x-ray pulse was determined

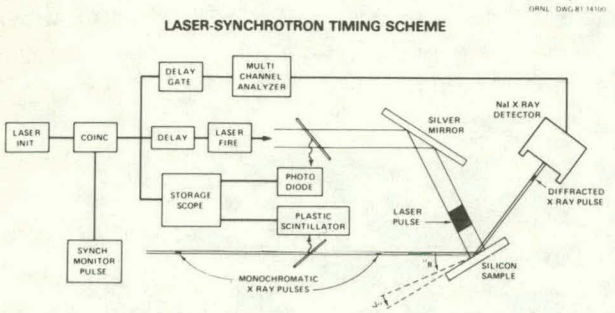

Fig. 2.33. Schematic representation of the time-resolved x-ray diffraction measurement technique.

directly to a precision of 5 ns with a storage oscilloscope. A multichannel pulse height analyzer was gated to accept only the pulse from the NaI x-ray detector corresponding to the x rays scattering from the probing pulse. The actual number of photons detected was determined by comparison with the pulse height generated by a single x ray, since all the photons detected from a single synchrotron burst are in coincidence.

Figure 2.34 shows the measured reflectivities of pure Si near the (400) reflection (100 ns after laser pulsing) as a function of the deviation $\Delta\theta$ from the Bragg reflection angle for unstrained Si; scattering out to $\Delta\theta \simeq -1000$ s is evident. The inset in Fig. 2.34 shows the strain distribution corresponding to the dashed line fit to the measured x-ray reflectivities. This fit was carried out

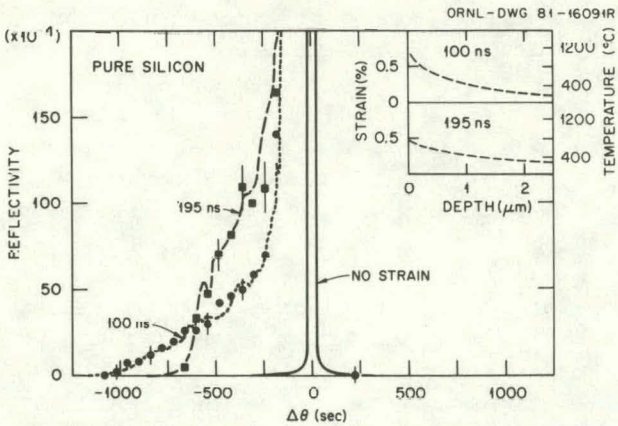

Fig. 2.34. Measured x-ray scattering near the (400) Bragg reflection of pure Si at 100 and 195 ns after laser pulses. The dashed lines are fits to the data corresponding to the strain profiles in the insets.

by iteratively varying the strain profile to obtain a fit to the x-ray data, as was done previously[3] for the analysis of static strain scattering. Figure 2.34 also includes data for a time of 195 ns. These data are similar to those at 100 ns; however, they have a smaller angular shift from the Bragg angle. As shown in the lower inset, the analysis of these 195-ns data indicates lower surface strain values than the 100-ns data but indicates somewhat higher strain values deeper into the crystal.

Transforming these strains into lattice temperatures through the use of temperature-dependent thermal expansion coefficients and assuming one-dimensional strains[3] gives an equivalent temperature scale as shown on the right-hand side of the insets of Fig. 2.34. At 100 ns, surface temperatures of ~1150°C are found, while at 195 ns the surface temperature was 750°C.

These high temperatures are qualitatively in accord with the melting model of laser annealing, and these results are apparently incompatible with experiments suggesting[4] ~300°C lattice temperatures during laser processing; however, the time scale of the annealing process suggested by these results would appear somewhat shorter than anticipated on the basis of published calculations[5] for fully crystalline samples. The question of actual surface melting is addressed elsewhere in this report.[6]

---

1. Summary of paper to be published.
2. Cornell University, Ithaca, N.Y.
3. B. C. Larson and J. F. Barhorst, *J. Appl. Phys.* **51,** 3181 (1980).
4. H. W. Lo and A. Compaan, *Phys. Rev. Lett.* **44,** 1604 (1980).
5. R. F. Wood and G. Giles, *Phys. Rev. B* **23,** 2923 (1981).
6. B. C. Larson et al., "Near-Surface Structure of B-Implanted Si during Laser Annealing," this report.

NEAR-SURFACE STRUCTURE OF B-IMPLANTED Si DURING LASER ANNEALING[1]

B. C. Larson T. S. Noggle
C. W. White D. Mills[2]

Time-resolved synchrotron x-ray diffraction studies have provided real-time measurements of near-surface temperatures in pulsed-laser annealed Si.[3] While these extended Bragg scattering measurements determine the temperature of the crystal

lattice, they are not directly sensitive to melted or amorphous surface layers. This technique can be modified, however, to study surface melting by doping a thin surface layer with B. The lattice contraction induced by substitutional B shifts the surface layer scattering to angles sufficiently different from substrate scattering that the surface layer can be monitored directly. In this experiment, synchrotron x-ray pulses from CHESS have been used to carry out such a time-resolved study of the near-surface structure of B-implanted Si during pulsed-laser annealing. Si samples implanted with 2.5×10^{16} B/cm^2 were chosen for this study, and ruby laser pulses with energy densities of $\sim$1.3 J/cm^2 and time durations of 15 ns were used. The measurements were carried out as described elsewhere[3] in this report.

Figure 2.35 shows the scattering [near the (400) reflection] from the B-doped layer measured with

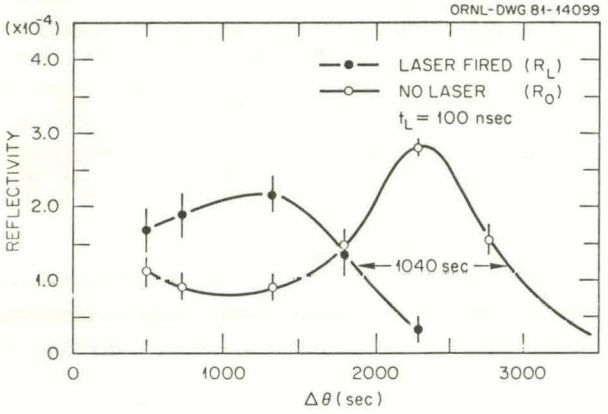

Fig. 2.35. Angular shift of the B-contracted surface layer scattering 100 ns after laser pulses.

no laser pulsing (R_0) and the scattering measured 100 ns after laser pulsing (R_L). The presence of scattering from the B-doped layer at 100 ns after the laser pulse indicates that part (or all) of the B-doped layer was crystalline; however, the 1040-s angular shift in the scattering indicates the average temperature of the B-doped layer ($\sim$0.3 μm) to be $\sim$1100°C at this time. This temperature rise is consistent with, and perhaps even exceeds, the average temperature observed[3] in the pure Si measurements. In order to follow the time evolution of the scattering from this layer more closely, the scattering intensities in the cold peak (2300 s) region and in the shifted peak (600–1100 s) region (Fig. 2.35) were measured as a function of time after laser pulsing. These data are shown in Fig. 2.36 in the form of the ratio R_L/R_0. The lower section shows that the intensity at the cold peak posi-

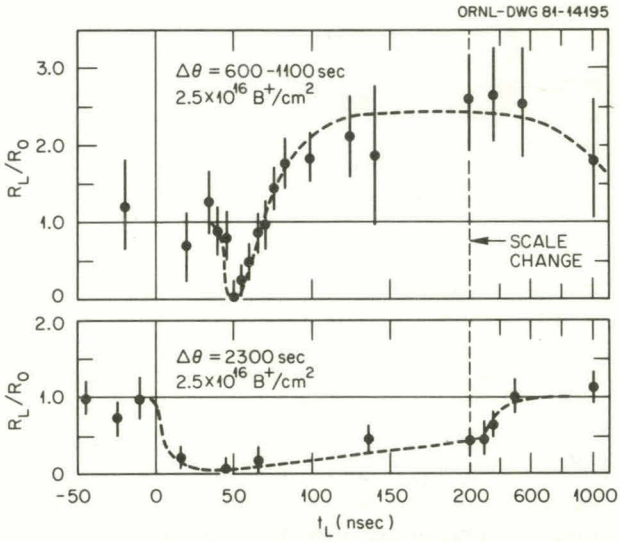

Fig. 2.36. Time evolution of the scattering ratio from the B-contracted layer with (R_L) and without (R_0) laser pulses. See Fig. 2.35 for significance of angular positions.

tion disappears immediately after laser pulsing and returns gradually after >500 ns. On the other hand, the scattering at the shifted peak position appears to be unchanged for a few nanoseconds after the laser pulse and then vanishes during the time interval between 40 and 60 ns after the laser pulse. The recovery of the scattering in the shifted peak region is more rapid than that observed for the intensity in the cold peak region, and the intensity (ratio) in the shifted peak region actually increases to a level of twice the intensity present before laser pulsing. This extra intensity is a result of the doped layer scattering shifting to this region, of course, and this intensity subsides as the surface layer cools.

These results are interpreted in terms of initial heating of the near-surface region (removing the intensity in the cold region), melting of the entire B-doped layer by 50 ns (removing all intensity associated with the B-doped layer), rapid resolidification of the doped layer (restoring intensity in the heated peak region), and finally a cooling of the near-surface region (returning the intensities to the cold measurement values). These measurements support laser annealing models involving high tem-

peratures and near-surface melting, but more importantly they provide a basis for detailed real-time studies of the transient phenomena involved in the laser annealing process.

1. Summary of paper to be published.
2. Cornell University, Ithaca, N.Y.
3. B. C. Larson et al., "Synchrotron X-ray Diffraction Study of Si during Pulsed-Laser Annealing," this report.

FACTORS LIMITING SUBSTITUTIONAL SOLUBILITIES ACHIEVED BY LASER ANNEALING OF ION-IMPLANTED Si[1]

C. W. White H. Naramoto[2]
J. Narayan J. M. Williams
B. R. Appleton S. R. Wilson[3]

Supersaturated alloys of Group III and Group V species in Si can be readily formed by laser annealing of ion-implanted Si.[4] Measured maximum substitutional concentrations following laser annealing exceed equilibrium solubility limits by almost three orders of magnitude in some cases. However, there is a maximum substitutional solubility which can be achieved for a given regrowth velocity, and knowledge of the mechanisms limiting the solubilities which can be achieved by laser annealing is an important consideration for this high-speed non-equilibrium crystal growth process.

The maximum substitutional solubilities which can be achieved by pulsed-laser annealing appear to be limited by three mechanisms. The first of these, which is related to the materials properties of the implanted region, is lattice strain. When B is incorporated substitutionally in the Si lattice during pulsed-laser annealing, the lattice undergoes a one-dimensional contraction in the implanted region in a direction normal to the surface,[5] because the covalent bonding radius of B is significantly smaller than that of the Si atom it replaces. The magnitude of the contraction is proportional to the local B concentration. Contraction gives rise to strain in the implanted region, and when the strain exceeds the fracture strength of Si (~4 at. % B in Si), cracks will develop in the near-surface region. To incorporate more B substitutionally in the Si lattice by laser annealing, it would be necessary to incorporate a dopant which is known to give rise to lattice expansion. Possible candidates include Ga, In, Bi, or Sb.

A second mechanism which limits substitutional solubility achieved by laser annealing is an interfacial instability which develops during regrowth and leads to lateral segregation of the rejected dopant and to the formation of a well-defined cell structure in the near-surface region.[6,7] Figure 2.37 shows both concentration profiles and TEM micrographs for a ⟨100⟩ Si crystal implanted by ^{115}In (125 keV, $1.3 \times 10^{16}/cm^2$) and laser annealed. From the total and substitutional concentration profiles (measured by ion scattering/channeling techniques) up to concentrations of $\sim 1.2\text{–}2.0 \times 10^{20}/cm^3$, almost all of the In is substitutional. However, in the near-surface region where the total concentration extends to $\sim 10^{21}/cm^3$, the substitutional component stays relatively flat at $\sim 1.5 \times 10^{20}/cm^3$. Results from TEM in Fig. 2.37 show that the microstructures in the near-surface region consist of the epitaxial columns of Si (average diameter ~450 Å), surrounded by thin cell walls ~50 Å thick. The electron diffraction pattern obtained from the near-surface region shows the presence of weak extra spots which arise from crystalline In in the cell walls, thus demonstrating nucleation of the second phase during laser annealing. Plan-view TEM results (not shown) indicate that the cell walls penetrate to a depth of ~1200 Å, in good agreement with the concentration profile results which show that the nonsubstitutional In is confined to a depth of ~1200 Å. The substitutional In in the near-surface region is trapped in the interior of the epitaxial columns of Si. The limiting concentration which can be trapped in the columns depends on the growth velocity and not on the implanted dose. If a higher dose had been used than that in Fig. 2.37, the same limiting substitutional concentration would have been incorporated into the epitaxial Si columns, but the cell walls would have penetrated to a greater depth.

In addition to the limitations on substitutional solubility imposed by lattice strain and by interfacial instability during regrowth, there are predicted thermodynamic limits to solute trapping in Si.[7] Basic ideas underlying these predictions are illustrated schematically in Fig. 2.38. On a plot of the Gibbs free energy vs composition at fixed temperature, the solidus and liquidus lines intersect at one point, which is the upper limit for the solid composition that can be formed from the liquid at any composition. Plotting the locus of these points at different temperatures on the equilibrium phase diagram defines the T_0 curve, which is the maximum solid composition that can be formed from

ORNL PHOTO 5179-80

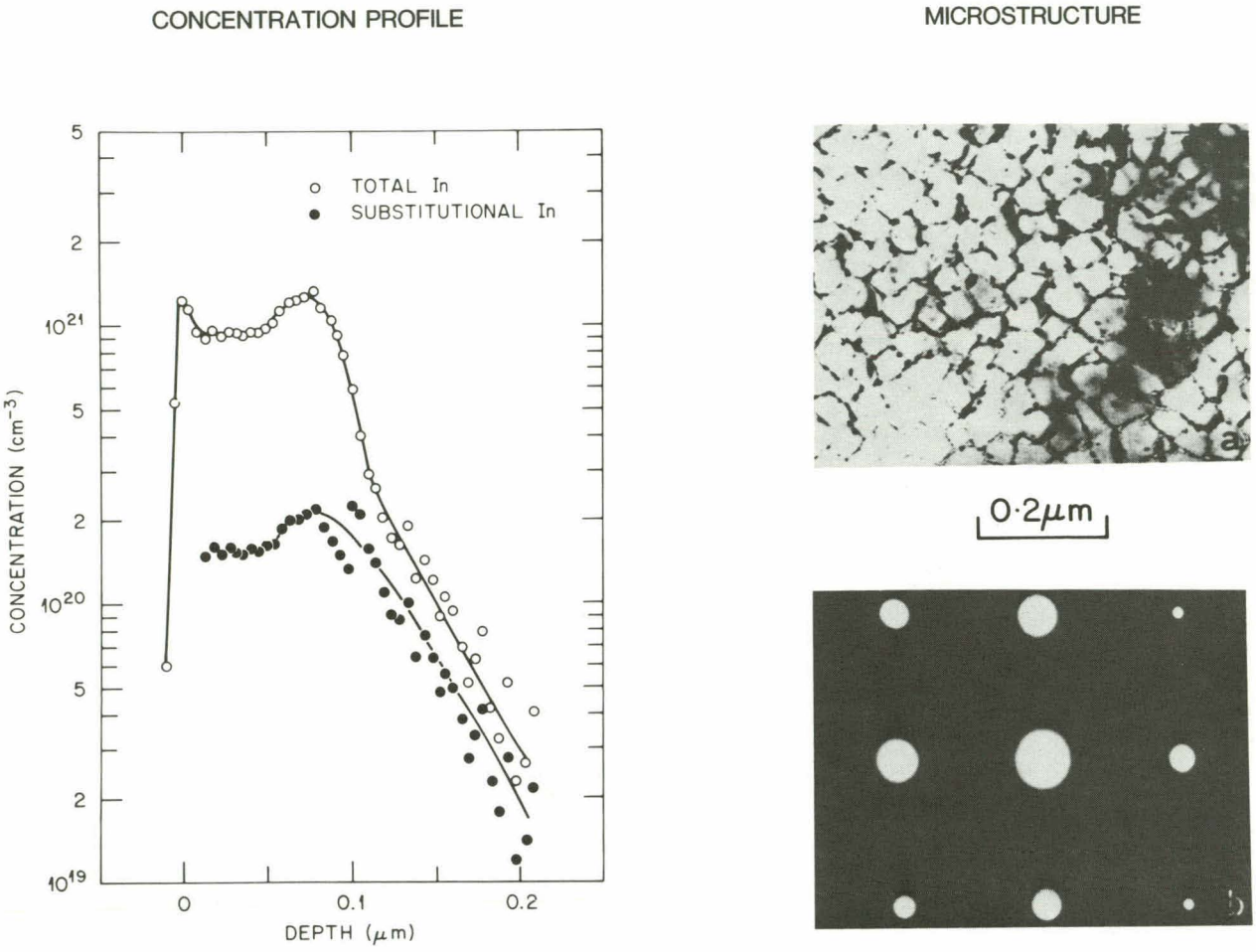

Fig. 2.37. Profiles (left) and microstructure (right) for ^{115}In (125 keV, 1.3 × 10^{16}/cm^2) in ⟨110⟩ Si after laser annealing.

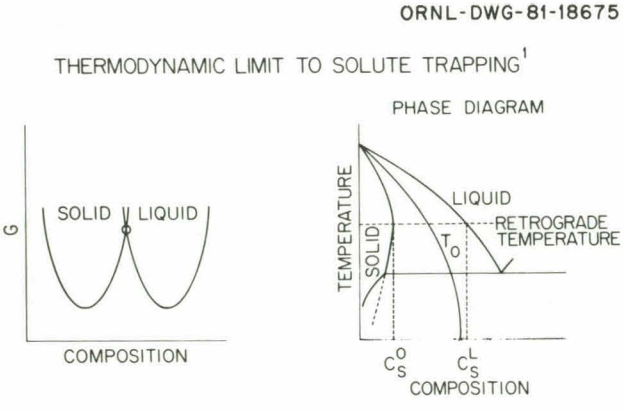

Fig. 2.38. Representation of the method used to determine the thermodynamic limit to solute trapping.

the liquid at any temperature even at infinite growth velocity. The T_0 curve thus defines the thermodynamic limit to diffusionless solidification. For retrograde systems, thermodynamic arguments[7] can be used to obtain a simple estimate for the maximum composition C_s^L on the T_0 curve. This maximum composition on the T_0 curve is the liquidus composition on the equilibrium phase diagram at the retrograde temperature.

Predictions[7] of C_s^L for five dopants in Si are listed in Table 2.5 and are compared with measurements of maximum substitutional solubilities C_s^{max} obtained at a growth velocity of 4.5 m/s. (The equilibrium solubility limits C_s^0 are also indicated in Table 2.5.) Dopants for which the interfa-

Table 2.5. Comparison of equilibrium (C_s^0) and laser annealing (C_s^{max}) solubility limits with predicted thermodynamic limits (C_s^L) to solute trapping in Si

Dopant	C_s^0 (cm^{-3})	C_s^{max}[a] (v = 4.5 m/s) (cm^{-3})	C_s^L (cm^{-3})
As	1.5×10^{21}	6.0×10^{21}	5×10^{21}
Sb	7.9×10^{19}	2.0×10^{21}	3×10^{21}
Ga	4.5×10^{19}	4.5×10^{20}	6×10^{21}
In	8.0×10^{17}	1.5×10^{20}	2×10^{21}
Bi	8.0×10^{17}	4.0×10^{20}	1×10^{21}

[a]Values for C_s^{max} were determined at a growth velocity of 4.5 m/s.

cial distribution coefficient k' is very near to unity (As and Sb) have measured solubilities which are very close to predicted thermodynamic limits. Dopants with relatively lower values for k' (Ga, In) have measured solubilities somewhat lower than predictions but are still within an order of magnitude of thermodynamic limits. Results for Ga, In, Bi, and Sb are still limited by interfacial instability during regrowth.[8] For the case of As in Si, the value for k' is -1.0, which implies that the liquidus and solidus line on the phase diagram are coincident (i.e., the T_0 limit). Consequently the thermodynamic limit for the incorporation of As in Si may have been reached. The fact that the measured value for C_s exceeds the predicted thermodynamic limit is probably due to uncertainties on the equilibrium phase diagram from which the predictions were made.

1. Summary of paper: p. 59 in *Laser and Electron-Beam Solid Interactions and Materials Processing*, ed. by J. F. Gibbons, L. D. Hess, and T. W. Sigmon, North Holland, New York, 1981.

2. Guest scientist from Japan Atomic Energy Research Institute, Tokai-mura, Japan.

3. Motorola, Inc., Phoenix, Ariz.

4. C. W. White et al., *J. Appl. Phys.* **51**, 738 (1980).

5. B. C. Larson, C. W. White, and B. R. Appleton, *Appl. Phys. Lett.* **32**, 801 (1978).

6. See, for example, C. W. White et al., p. 124 in *Laser and Electron Beam Processing of Materials*, ed. by C. W. White and P. S. Peercy, Academic Press, New York, 1980.

7. J. W. Cahn, S. R. Coriell, and W. J. Boettinger, p. 89 in *Laser and Electron Beam Processing of Materials*, ed. by C. W. White and P. S. Peercy, Academic Press, New York, 1980.

8. J. Narayan, *J. Appl. Phys.* **52**, 1289 (1981).

TEST OF PREDICTED THERMODYNAMIC LIMIT TO SOLUTE TRAPPING IN Si[1]

C. W. White, B. R. Appleton, H. Naramoto[2], J. M. Williams, J. Narayan, S. R. Wilson[3]

Previous work[4] has demonstrated that supersaturated alloys of Group III and Group V impurities in Si can readily be formed by ion implantation and laser annealing. In the previous work it was shown that these impurities could be incorporated into the lattice (by solute trapping) up to maximum concentrations C_s^{max} during the high-speed nonequilibrium liquid phase epitaxial regrowth process. Based on these results, Cahn et al.[5] predicted from thermodynamic arguments absolute limits to dopant incorporation into Si even at infinite growth velocity. To test these predictions, we have measured the maximum substitutional solubility obtainable by laser annealing of ion-implanted Si for four different alloy systems at two different growth velocities.

For these experiments, regrowth velocity was changed by changing the substrate temperature during laser annealing (ruby laser, 15×10^{-9} s pulse duration time, ~ 1.4 J/cm^2). Under these laser annealing conditions, regrowth velocities of 4.5 and 6.0 m/s can be obtained at substrate temperatures of 300 and 77 K, respectively. Maximum substitutional solubilities at each growth velocity were determined by comparing the total and substitutional dopant concentrations as a function of depth by using ion scattering/channeling analysis.[4]

Table 2.6 compares the measured C_s^{max} for four Group III and Group V dopants at two different growth velocities (4.5 and 6.0 m/s) with predicted thermodynamic limits C_s^L to dopant incorporation into Si even at infinite growth velocity. The equilibrium solubility limit C_s^0 is given also for comparison. As shown in Table 2.6, at either growth velocity, substitutional concentrations are approaching predicted thermodynamic limits. For Ga, In, and Bi, the substitutional solubilities can be increased by factors of 2–3 at a velocity of 6.0 m/s compared to results at 4.5 m/s. The solubilities for these dopants are limited by interfacial instability during regrowth, and the onset of instability can be delayed to higher concentrations by going to higher growth velocities as discussed elsewhere.[6] For the case of As, however, we observed no increase in the substitutional solubility at the higher growth veloc-

Table 2.6. Comparison of predicted thermodynamic limits C_s^L for solute trapping in Si to measured maximum substitutional solubilities C_s^{max} obtained after laser annealing at regrowth velocities of 4.5 and 6.0 m/s
The equilibrium solubility limit C_s^0 is given also for comparison

Dopant	C_s^0 (cm^{-3})	C_s^{max} (v = 4.5 m/s) (cm^{-3})	C_s^{max} (v = 6.0 m/s) (cm^{-3})	C_s^L (cm^{-3})
As	1.5×10^{21}	6.0×10^{21}	6.0×10^{21}	5×10^{21}
Ga	4.5×10^{19}	4.5×10^{20}	8.8×10^{20}	6×10^{21}
In	8.0×10^{17}	1.5×10^{20}	2.8×10^{20}	2×10^{21}
Bi	8.0×10^{17}	4.0×10^{20}	1.1×10^{21}	1×10^{21}

ity. For As in Si, k' is unity even at a velocity of 4.5 m/s and this indicates[4] that the thermodynamic limit for As incorporation into Si may have been reached. Measurements at even faster regrowth velocities will be required to provide a more stringent test of the predicted thermodynamic limits. This will require the use of picosecond rather than nanosecond laser pulses. Such experiments are currently under way.

1. Summary of paper: p. 59 in *Laser and Electron-Beam Solid Interactions and Materials Processing,* ed. by J. F. Gibbons, L. D. Hess, and T. W. Sigmon, North Holland, New York, 1981.
2. Guest scientist from Japan Atomic Energy Research Institute, Tokai-mura, Japan.
3. Motorola, Inc., Phoenix, Ariz.
4. C. W. White et al., *J. Appl. Phys.* **51,** 738 (1980).
5. J. W. Cahn, S. R. Coriell, and W. J. Boettinger, p. 89 in *Laser and Electron Beam Processing of Materials,* ed. by C. W. White and P. S. Peercy, Academic Press, New York, 1980.
6. C. W. White et al., "Factors Limiting Substitutional Solubilities Achieved by Laser Annealing of Ion-Implanted Si," this report.

THERMAL STABILITY OF ION-IMPLANTED FILMS SUBJECTED TO LASER ANNEALING

S. R. Wilson[1] R. B. Gregory[1]
M. W. Paulson[1] C. W. White
G. Tam[1] B. R. Appleton

Laser annealing (both cw and pulsed) has many potential advantages over conventional thermal annealing of ion-implanted films of single-crystal silicon and polysilicon on dielectrics. Essentially 100% electrical activation of implanted dopants can be achieved after laser annealing, even if impurity concentrations exceed 1×10^{21} cm^{-3}. However, for these films to be useful in integrated circuit fabrication, they must be thermally stable through subsequent processing steps.

Polysilicon films on Si_3N_4 and single-crystal silicon samples have been ion implanted with ^{75}As or ^{31}P to doses ranging between 10^{14} cm^{-2} and 10^{16} cm^{-2}. Samples were annealed with either a pulsed or cw laser to activate the dopant electrically. Then samples were exposed to isothermal anneals in the temperature range 450–1000°C for times varying from minutes to hours. The electrical properties of these layers were examined by four-point probe, Hall effect, and spreading resistance probe measurements. The ^{75}As depth profiles and lattice locations were measured before and after thermal processing using ion backscattering.

Figure 2.39 is a plot of sheet resistance mobility and carrier concentration vs anneal temperature for a 7000-Å polysilicon film on Si_3N_4 implanted to a dose of 2×10^{16} As/cm^2 and laser annealed with a pulsed Nd:YAG laser. After laser annealing, the As is essentially 100% electrically active and the sheet resistance is 20 ohm/square. Ion backscattering shows the impurity concentration to be 7×10^{20} As/cm^3 over the first few thousand angstroms and to fall to nearly zero by 6000 Å. After cumulative anneals up to 700°C, the impurity profile does not change; but the sheet resistance increases by a factor of 5, and the carrier concentration drops by a factor of 5. Above 800°C, diffusion of the As occurs as determined by ion backscattering, and the carrier concentration begins to increase resulting in a decrease in the sheet resistance. The cw laser-annealed polysilicon films have much larger grains than the pulsed Nd:YAG laser-annealed films. When these samples are subjected to the same thermal anneal sequence, the decrease in carrier concentration is considerably smaller.

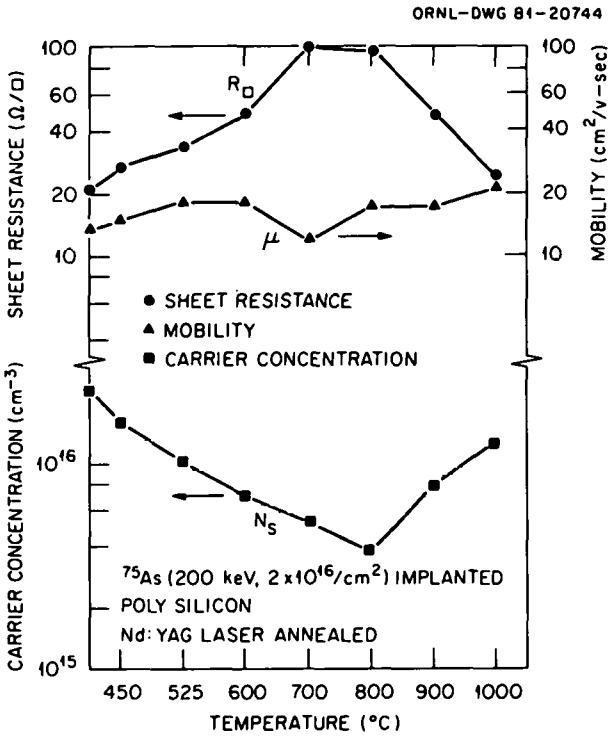

Fig. 2.39. Sheet resistance, sheet carrier concentration, and mobility for As-implanted polysilicon after 1 h anneals at the indicated temperatures.

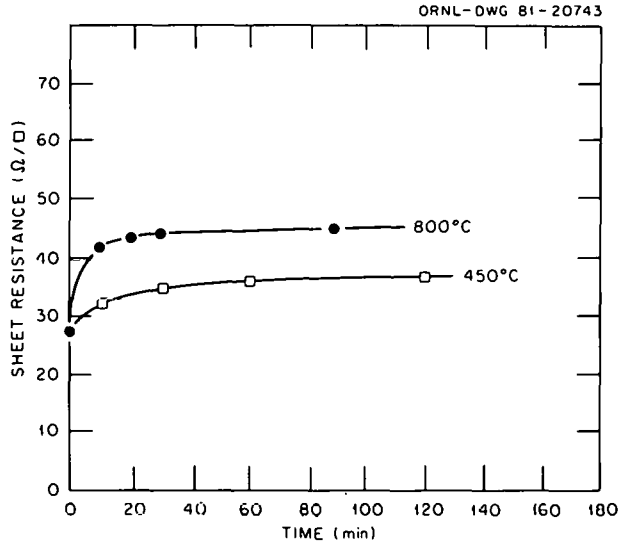

Fig. 2.40. Sheet resistance vs time for single-crystal silicon implanted with 10^{16} cm^{-2} As and annealed at 450 or 800°C.

Single-crystal silicon samples were implanted with ^{75}As to a dose of $10^{16}/cm^2$ and were annealed with a pulsed ruby laser. Figure 2.40 presents sheet resistance vs time for samples annealed at either 450°C or 800°C. The sheet resistance increases rapidly after only 10 min at each temperature and continues to increase for times exceeding 2 h. However, the sheet resistance for the single-crystal samples changed by less than a factor of 2 compared to the factor of 5 increase for the polysilicon samples when annealed at 800°C for 1 h. Ion channeling measurements indicate the ^{75}As is no longer 100% substitutional. This effect can also be observed in single-crystal samples annealed with a cw laser. For samples implanted with ^{31}P at comparable doses, the changes in sheet resistance are not nearly as pronounced.

These results indicate that the high As concentrations produced by laser annealing are unstable and will precipitate out of solution at the times and temperatures encountered in silicon wafer processing. In the case of polysilicon films, the segregation of dopants to grain boundaries is occurring and is most pronounced for small-grained samples.

1. Motorola, Inc., Phoenix, Ariz.

DEVELOPMENT OF MORPHOLOGICAL INSTABILITY AND FORMATION OF CELLS IN Si ALLOYS DURING PULSED-LASER IRRADIATION[1]

J. Narayan C. W. White
H. Naramoto[2]

High-power laser pulses can be used in a controlled way to heat and melt thin layers of semiconductors with heating and cooling rates exceeding 10^8°C s^{-1}. The crystal growth rates associated with laser-melt quenching are of the order of meters per second, and these growth rates can be varied by changing either the laser parameters or the substrate temperature. During solidification of a dilute binary alloy, a planar liquid-solid interface can become morphologically unstable above a certain solute concentration at a given velocity of solidification. We have performed systematic studies on interfacial instability, cell formation, and associated solute concentrations in Si-In, Si-Sb, Si-Ga, Si-Bi, and Si-Fe systems after ion

implantation and laser annealing. The depth of cell formation and the average cell size at the position of onset of instability (OI region) and in the region of well-developed instability (DI region) were determined using plan-view and cross-section TEM. Total and substitutional concentrations of solutes as a function of depth were obtained by Rutherford backscattering-channeling techniques by which it was possible to determine the depth of instability and the solute concentration above which instability sets in.

The average cell sizes, the depths of cell formation, and solute concentrations associated with the interfacial instability were determined as a function of solidification velocity in the range 2–6 ms^{-1}. These results were compared with the calculations of the perturbation theory, originally developed by Mullins and Sekerka.[3] From these calculations, we can obtain the critical concentrations above which instability occurs and the wavelength of instability corresponding to the average cell size. This theory includes constitutional supercooling, surface tension between the solid-liquid interface, and the transport and evolution of latent heat from the interface. Assuming local equilibrium at an isotropic liquid-solid interface during unidirectional freezing of dilute binary alloys, the limiting concentration C_s' is given by[4]

$$C_s' = \frac{D_L k'}{mV\bar{\alpha}(k'-1)}\left[\frac{k_L G_L}{k_L+k_s}\left(\alpha_l - \frac{V}{K_L}\right) + \frac{k_s G_s}{k_s+k_L}\left(\alpha_s + \frac{V}{K_s}\right) + \bar{\alpha}\Gamma T_m \Gamma\omega^2\right]\left[1 + \frac{2k'}{(1+(2D_L\omega/V)^2)^{1/2}-1}\right], \quad (1)$$

with

$$\alpha_L = (V/2K_L) + [(V/2K_L)^2 + \omega^2]^{1/2}$$
$$\alpha_s = -(V/2K_s) + [(V/2K_s)^2 + \omega^2]^{1/2}$$
$$\bar{\alpha} = (k_s\alpha_s + k_L\alpha_l)/(k_s + k_L)$$
$$G_s = (L_v V + k_L G_L)/k_s \ ,$$

where D_L is the impurity diffusion coefficient in the liquid; V is the velocity of solidification; m is the liquidus slope obtained using the procedure described by Thurmond and Kowalchik;[5] k_L and k_s are the thermal conductivities, and K_L and K_s are the thermal diffusivities of the liquid and solid, respectively; G_L and G_s are the thermal gradients in the liquid and solid, respectively; T_m is the melting point of the planar interface in the absence of solute; Γ is the ratio of the solid-liquid surface energy to the latent heat of fusion per unit volume L_v; ω is the spatial frequency associated with the instability; and k' is the interfacial distribution coefficient ($k' = C_s'/C_L'$, where C_s' and C_L' are the interface solubilities in the solid and liquid, respectively). The values of k' used in the calculations were deduced by fitting calculated profiles with the measured dopant profiles.

We have solved $C_s'(\omega)$ as a function of ω for given values of V. The minimum value of $C_s'(\omega)$ gives the stability-instability demarcation. The cell size is $\lambda_{min} = 2\pi/\omega_{min}$, where ω_{min} is the value corresponding to the minimum value of C_s'. The following values of the materials constants were used in the calculations:

k_L = 70 $Jm^{-1}s^{-1}K^{-1}$, k_s = 22 $Jm^{-1}s^{-1}K^{-1}$
D_L = 1.0×10^{-8} m^2s^{-1} and 5.0×10^{-8} m^2s^{-1}
k_0 = 4.0×10^{-4} (equilibrium distribution coefficient of In in Si)
T_m = 1.3×10^{-7} Km
K_L = 3.0×10^{-5} m^2s^{-1}, K_s = 9.4×10^{-6} m^2s^{-1}
G_L = 1.33×10^6 Km^{-1}
m = -509 K (at. fract.)$^{-1}$ for Si-In.

The calculations were performed for Si-In, Si-Sb, Si-Ga, and Si-Bi systems, and the results for the Si-In systems are presented in Figs. 2.41 and 2.42. Figure 2.41 shows plots of C_s'(min) vs V, and the good agreement between the experimental results and the calculations is obtained when the dependence of k' on V is taken into account in the calculations. The original constitutional supercooling (CS) criterion ($mG_c = G_L$, where G_c and G_L are solute and temperature gradients, respectively) gives poor agreement with the experiment, particularly at higher velocities of solidification. At low velocities, Eq. (1) reduces to $mG_c = G_L(k_L/k')$, and it gives better agreement at low velocities compared to the original CS criterion. The results on cell sizes as a function of solidification velocity are shown in Fig. 2.42. The calculations predict a decrease in cell size with increase in V, which is consistent with experimental results (shown as dots). The cell sizes in the OI region were found to be slightly larger than those in the DI region,

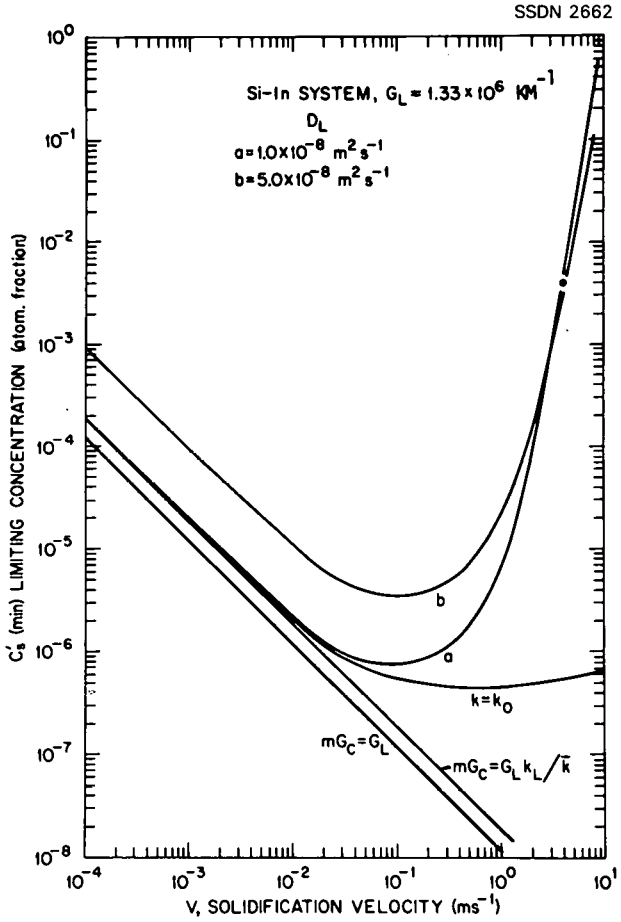

Fig. 2.41. Limiting concentration associated with instability as a function of V: $D_L = 1.0 \times 10^{-8}$ m^2 s^{-1} (curve a), $D_L = 5.0 \times 10^{-8}$ m^2 s^{-1} (curve b), perturbation theory curve with constant k_0, CS criterion ($mG_c = G_L$), and modified CS criterion. The dot represents the experimental point.

which made the agreement between the experimental and theoretical results even closer. The effects of surface tension and the melting points were calculated, because the segregation of In and Sb may decrease the interfacial surface energy as well as the melting point. The solute concentrations, as well as average cell sizes, were found to decrease with decreasing surface tension and melting point. This further improved the agreement between the experimental results and the theory.

1. Summary of paper to be published.
2. Guest scientist from Japan Atomic Energy Research Institute, Tokai-mura, Japan.
3. W. W. Mullins and R. F. Sekerka, *J. Appl. Phys.* **35**, 444 (1964).
4. J. Narayan, *J. Appl. Phys.* **52**, 1289 (1981).
5. C. D. Thurmond and M. Kowalchik, *Bell Sys. Tech. J.* **39**, 169 (1980).

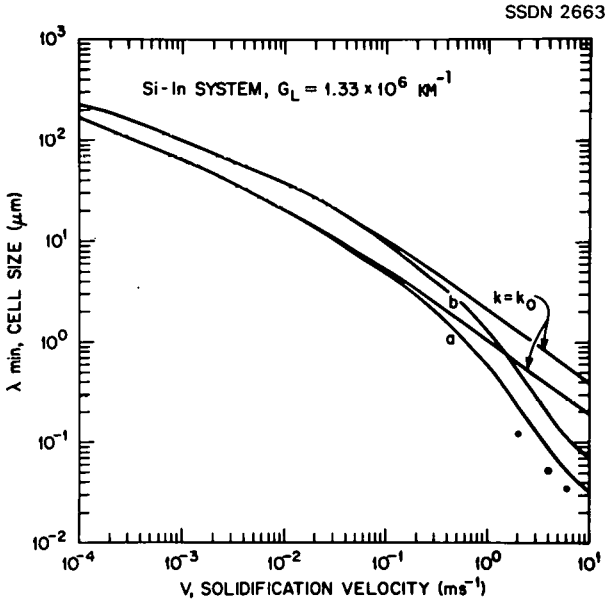

Fig. 2.42. Calculated cell size λ_{min} as a function of V: $D_L = 1.0 \times 10^{-8}$ m^2 s^{-1} (curve a) and $D_L = 5.0 \times 10^{-8}$ m^2 s^{-1} (curve b). The dots represent experimental points.

INTERFACE INSTABILITY AND CELL FORMATION IN ION-IMPLANTED AND LASER-ANNEALED Si[1]

J. Narayan

The phenomenon of solid-liquid interface instability during directional solidification has been studied in In^+-, Ga^+-, Fe^+-, and Sb^+-implanted Si after pulsed-laser annealing. Interface instability results in lateral segregation which leads to the formation of cellular structures. The cellular

structures have been studied using TEM. The critical bulk solute concentration above which instability develops and the wavelength of instability (cell size) as a function of velocity of solidification have been calculated following the perturbation theory originally developed by Mullins and Sekerka.[2] Good agreement between experimental results and the calculations was obtained when the dependence of the interfacial distribution coefficient on the velocity of solidification was taken into account in the calculations.

1. Summary of paper: *J. Appl. Phys.* **52,** 1289 (1981).
2. W. W. Mullins and R. F. Sekerka, *J. Appl. Phys.* **35,** 444 (1964).

MELTING PHENOMENON AND PULSED-LASER ANNEALING IN SEMICONDUCTORS[1]

J. Narayan C. W. White
J. Fletcher W. H. Christie[2]

High-power ruby and Nd:YAG laser pulses have been used to remove displacement damage, dislocation loops, and precipitates in semiconductors. This annealing phenomenon, known as "laser annealing," as well as the effects on dopant profile broadening and on the formation of constitutional supercooling cells, has been successfully interpreted on the basis of a melting model. An alternate explanation has been proposed, whereby laser annealing effects are produced by the presence of an electron-hole plasma with the lattice remaining close to ambient temperature.[3] The basic assumption in the melting model is that the energy from the electronic system can be rapidly ($<10^{-9}$ s) transferred to the lattice and that this energy is then utilized to heat and melt thin (<1 μm) surface layers of the material. According to the plasma model, the energy transfer from the electronic system to the lattice is delayed ($\sim$200 ns) through the screening of phonon emission, and the high concentration of electrons and holes (plasma) produced by pulsed-laser irradiation may cause annealing via enhanced diffusion of point defects and glide and climb of dislocations. At a still higher plasma density ($\sim 8 \times 10^{21}$ cm^{-3}), electrons excited into antibonding states are proposed to undergo a second-order phase transition resulting in softening of the lattice. The crystal would then be in a fluid-like state with energy primarily retained in the electronic system. This energy would be distributed over a much greater depth as carrier diffusion becomes important. As the plasma density declines, the material passes back through the phase transition, leading to recrystallization. The support for the plasma model is derived primarily from the recent experiments on Raman-measured temperatures[4] and optical transmission[5] measurements in Si. They reported a temperature rise of only about 300°C and enhanced transmission for photon energies ($\leq$1.08 eV) in Si after irradiation with dye laser pulses ($\lambda = 0.485$ μm, $\tau = 9$ ns, E $\sim$ 1.0 J cm^{-2}).

To address the controversy between the two models, we have performed a series of collaborative experiments using the dye laser pulses to anneal Compaan's samples (As^+-implanted specimens containing amorphous layers) and a variety of ORNL samples (containing precipitates, dislocations, and dopants leading to the formation of constitutional supercooling cells). Annealing of displacement damage was studied in As^+-implanted specimens (100–200 keV, dose = 1.0–10.0 $\times$ 10^{15} cm^{-2}) using plan-view and cross-section TEM techniques. Figure 2.43 shows typical cross-section micrographs starting from the outer regions and proceeding to the central regions of the laser spots in As^+-implanted specimens. In the central regions of the laser spots [Fig. 2.43(d)], the pulse energy density was high enough that the melt front exceeded the depth of the damage layer, and the specimens grew defect-free with the same perfection as the underlying substrate. In the region immediately surrounding the central region, the melt front could reach only the dislocation band, and the loops intersected by the melt front grew back as two segments of V-shaped dislocations. These directions were characteristic of dislocation directions observed in crystal growth from the melt. In the outer regions of the laser spots where the melt front did not reach the crystalline substrate, polycrystals were observed. The As^+ concentration profiles in the central regions of the spots were determined by SIMS techniques, and a typical example is shown in Fig. 2.44. The observed profiles were fitted to the model calculations, and the value of the impurity diffusion coefficient ($D_L = 3.0 \times 10^{-8}$ m^{-2} s^{-1}) obtained from the fit was in good agreement with the value of the impurity diffusion coefficient in liquid Si. The extent of dopant-profile broadening is directly related to the melt lifetime, which is dependent on the pulse energy density. It was estimated that

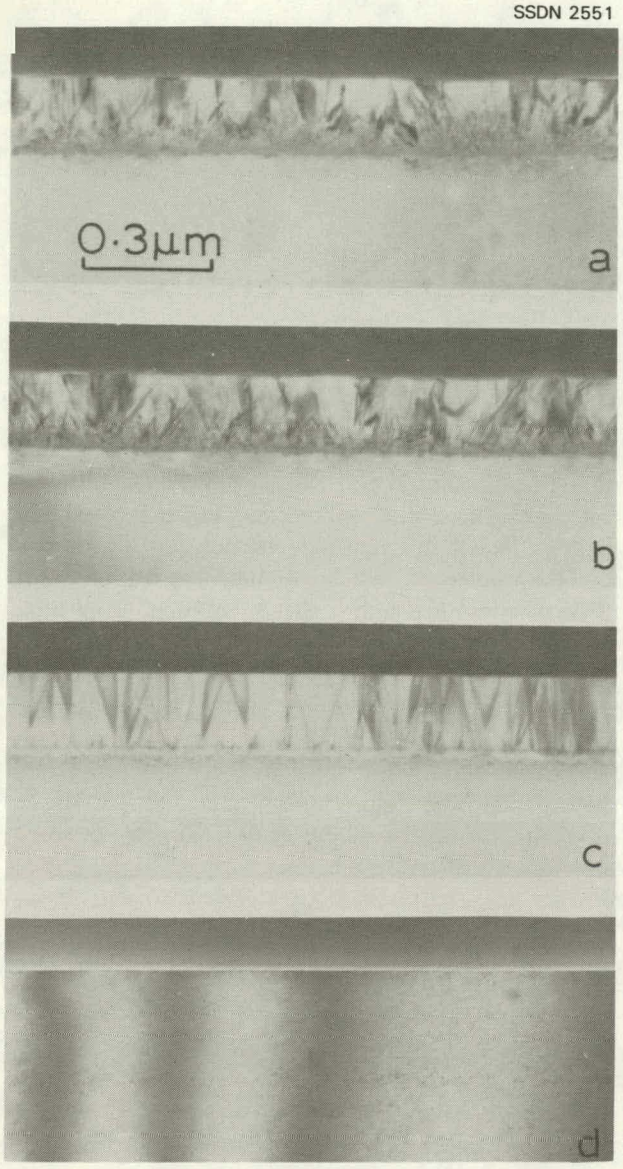

Fig. 2.43. Cross-section electron micrographs showing microstructures (for nominal pulse energy density E = 0.75 J cm^{-2}) from the outer regions to the center of the laser spot (i.e., as a function of increasing pulse energy density) in As$^+$-implanted specimens containing amorphous layers: (a) polycrystalline layer with underlying amorphous layer, (b) polycrystalline layer with no amorphous layer, (c) V-shaped dislocations growing from the dislocation band below the amorphous layer, and (d) nearly a "complete" annealing of defects.

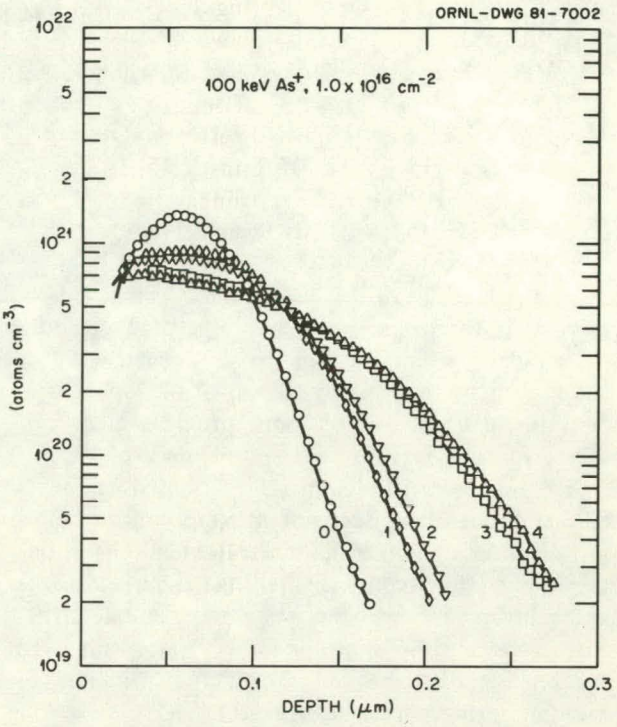

Fig. 2.44. As$^+$ concentration profiles from specimens with nominal pulse energy density E = 1.23 J cm^{-2}: curve labeled 0 shows as-implanted profile; curves 1 to 4 are from four different neighboring laser spots.

more than 60% of the laser spots used for Raman-temperature measurements had varying amounts of profile broadening, indicating a large pulse-to-pulse variation in energy density. The laser pulses similar to those used for Raman-temperature measurements led to the dissolution of B precipitates and to the formation of constitutional supercooling cells. These results provided clear evidence of melting during pulsed-laser irradiation. The low-temperature rise (~300°) in Lo and Compaan's experiments seems to be due to pulse-to-pulse variation in energy density which resulted in melted regions varying from 20–60 μm, while the size of the probe beam (70–100 μm diameter) was larger than the melted regions. The time-resolved transmission measurements,[5] indicating enhanced transmission at λ = 1.152 μm or photon energy = 1.076 eV which is less than the band gap of Si = 1.12 eV, can also be explained by invoking spatial inhomogeneity where the melted and unmelted regions are present simultaneously.

1. Summary of paper to be published.
2. Analytical Chemistry Division, ORNL.
3. J. A. Van Vechten et al., *Phys. Lett. A* **74,** 417 (1979).

4. H. W. Lo and A. Compaan, *Phys. Rev. Lett.* **44,** 1604 (1980).
5. M. C. Lee et al., *Appl. Phys. Lett.* **38,** 499 (1981).

MELTING PHENOMENON AND PROPERTIES OF DEFECTS ASSOCIATED WITH PULSED-LASER IRRADIATION[1]

J. Narayan C. W. White

The phenomenon of melting produced by pulsed-laser irradiation in Si has been studied using electron microscopy. Removal of dopant precipitates, dislocations, or loops provides clear evidence for melting. From the thickness of defect-free regions and the length of reoriented segments of dislocations, the depth of melting can be determined as a function of laser parameters. Using this technique, the depth of melting underneath the oxide layers has been investigated. Cellular structures observed in ion-implanted, laser-annealed specimens also provided convincing evidence of melting during pulsed-laser irradiation.

1. Summary of paper: *Philos. Mag. A* **43,** 1515 (1981).

CHARACTERISTICS OF EMERGENT DISLOCATIONS AFTER LASER MELTING OF Si[1]

J. Narayan R. Bullough[2]
J. R. Willis[3]

Growth directions of dislocations in laser-melted layers have been studied using TEM techniques. The dislocations after laser irradiation normally consisted of two emergent segments which were connected by a segment lying approximately parallel to the surface in the unmelted region. The observed directions of emergent segments were found to be in excellent agreement with the calculated directions that correspond to a minimum in the total elastic energy of the dislocation configurations. TEM experiments, performed on the same area after heat treatments outside the microscope, showed that the above orientations of dislocation segments remained unaffected by the subsequent heat treatment, thus establishing that these directions of dislocations, indeed, correspond to the energy minimum.

1. Summary of paper to be published.
2. Atomic Energy Research Establishment, Harwell, England.
3. University of Bath, Bath, England.

LASER-INDUCED DEFECTS IN V_3Si SINGLE CRYSTALS[1]

B. R. Appleton Y. K. Chang
J. Narayan C. W. White
B. Stritzker[2]

A companion paper in this report clearly shows that the laser-initiated defects in V_3Si films fabricated by pulsed-laser mixing are much more difficult to anneal than ion-induced defects.[3] To evaluate the nature of defects produced in V_3Si, single crystals of (100) and (110) orientation were subjected to pulsed-laser annealing and examined by ion channeling and TEM. The ion channeling analysis of Fig. 2.45 compares the backscattering spectra for 2.5-MeV He ions incident parallel to the ⟨100⟩ axial directions of V_3Si single crystals before and after pulsed-laser annealing in air at 300 K. The unirradiated ⟨100⟩ channeling spec-

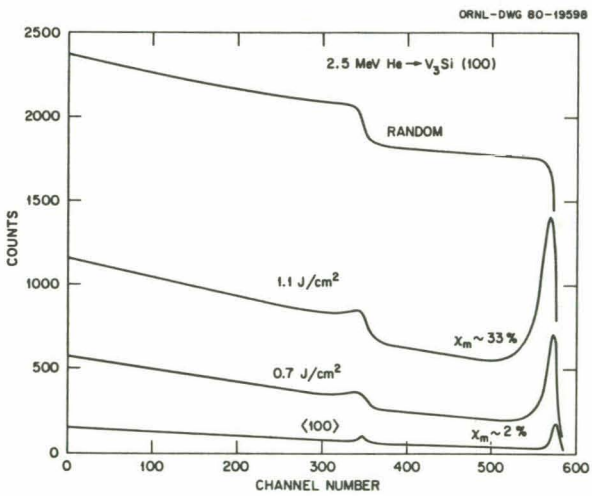

Fig. 2.45. 2.5-MeV He ion channeling analysis of ⟨100⟩ direction of a (100) V_3Si single crystal before and after annealing with pulses of 0.7 and 1.1 J/cm².

trum had a minimum yield of ~2%, indicating that it was a good single crystal. The ⟨100⟩ spectra obtained after 0.7- and 1.1-J/cm^2 laser pulses show that severe damage to the single crystal occurred in the near-surface region and that this damage increased with increasing energy density. Examination by TEM of a companion (100) single crystal exposed to one 1.0-J/cm^2 pulse is shown in Fig. 2.46. This analysis shows that microcracks

SSDN 2646

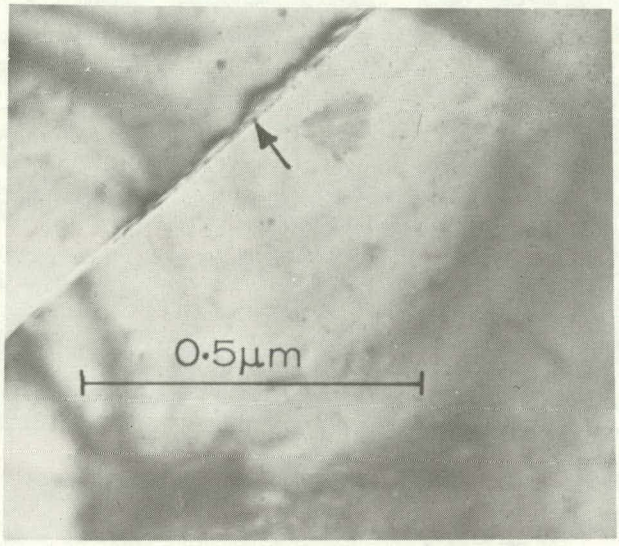

Fig. 2.46. Transmission electron micrograph of a surface crack in a (100) V_3Si single crystal after one 1.0 J/cm^2 pulse from a pulsed ruby laser.

developed in the surface as a consequence of the rapid quenching. More significantly, these cracks did not have plastic zones associated with them. Based on recent studies of the plastic stress-strain behavior of V_3Si between 1200 and 1800°C,[4] it is likely that this absence of plastic zones indicates that the annealed surface region did not remain above 1300°C for sufficient times to generate dislocations in the specimen. In V_3Si, yield stress is greater than the fracture stress for temperatures <1300°C; at higher temperatures yield stress decreases with temperature and plastic deformation can occur.

In related studies, (110) V_3Si single crystals which were predamaged by 300-keV He ion bombardment were pulsed-laser annealed and studied by ion channeling.[5] With increasing energy densities, the channeling yields increased as seen in Fig. 2.45. At an energy density of 1.0 J/cm^2 the channeling effect was no longer measurable and the energy spectra was essentially random. At 1.5 J/cm^2 the surface became heavily damaged and large irregular flakes developed. This type of laser-induced surface damage has been observed in Nb_3Ir and NbN as well.[6]

The microcracks observed in the surface of the laser-annealed (100) V_3Si single crystal and the flaking of the (110) surface appear to be caused by severe mechanical stresses established in the surface by the mechanisms already discussed and are a direct consequence of thermal gradients which develop during laser annealing. It is interesting that, although the temperature dependence of the yield strength of both Si and V_3Si are very similar,[3] pulsed-laser annealing of Si has not been observed to cause cracks. It has been observed, however, that supersaturated alloys of Si fabricated by B implantation and pulsed-laser annealing undergo a unique lattice contraction which causes strain along a direction normal to the surface of the sample.[7,8] This lattice strain increases with increasing substitutional concentrations of B until the fracture strength of Si is exceeded and cracks develop in the implanted region. Since this crack formation limits the practical maximum substitutional concentration of B in Si, it has been suggested that even larger doping levels might be possible through compensating implants to relieve the surface strain.[9] Similarly, the suggestion that deformation processing of V_3Si might be possible at elevated temperatures[4] indicates that some of the surface strain problems in V_3Si might be relieved by several techniques which would reduce the surface temperature gradients during laser annealing.

The contribution these surface cracks make to the surface damage peak and dechanneling observed in the V_3Si channeling spectra of Fig. 2.45 has not been established, because the density of surface cracks has not been determined. However, the dislocation density in the V_3Si single crystal studied by TEM was not sufficient to cause this observed behavior. Neither has it been determined if cracks are formed in the pulsed-laser mixed V-Si samples[3] nor, if they are formed, their effect on T_c. It is known that these and other[6] thin-film superconducting samples deposited on insulating substrates crack and peel at high laser energy densities, but this could be due to substrate problems.

The entire question concerning the nature of the defects in the A15 superconductors with A_3B composition has received much attention in recent years. Ion-induced defects have been studied extensively. X-ray diffraction studies have shown that site-exchange disorder occurs from ion irradiation,[10] and ion channeling studies have concluded that static displacement of V atoms in V_3Si results.[11-14] Recent ion channeling studies on V_3Ge and V_3Si single crystals have also determined that the B atom sites (Ge and Si, respectively) also acquire off-lattice static displacements as a result of ion damage.[14] A similar effort is needed to determine the nature and annealing characteristics of laser-induced defects.

1. Summary of paper: p. 607 in *Laser and Electron-Beam Solid Interactions and Materials Processing,* ed. by J. F. Gibbons, L. D. Hess, and T. W. Sigmon, North Holland, New York, 1981.
2. Guest scientist from Institut für Festkörperforschung, Kernforschungsanlage, Jülich, Federal Republic of Germany.
3. B. R. Appleton et al., "Laser-Induced Defects and Materials Interactions in the V-Si System," this report.
4. S. Mahajan et al., *Appl. Phys. Lett.* **33,** 972 (1978).
5. O. Meyer et al., unpublished data.
6. B. R. Appleton et al., p. 714 in *Laser and Electron Beam Processing of Materials,* ed. by C. W. White and P. S. Peercy, Academic Press, New York, 1980.
7. B. C. Larson, C. W. White, and B. R. Appleton, *Appl. Phys. Lett.* **32,** 801 (1978).
8. B. R. Appleton et al., p. 291 in *Laser-Solid Interactions and Laser Processing—1978,* ed. by S. D. Ferris, H. J. Leamy, and J. M. Poate, AIP Conference Proceedings No. 50, American Institute of Physics, New York, 1979.
9. C. W. White et al., p. 59 in *Laser and Electron-Beam Solid Interactions and Materials Processing,* ed. by J. F. Gibbons, L. D. Hess, and T. W. Sigmon, North Holland, New York, 1981.
10. A. R. Sweedler, D. G. Schweitzer, and G. W. Webb, *Phys. Rev. Lett.* **33,** 168 (1974).
11. R. Kaufmann and O. Meyer, *Radiat. Eff.* **40,** 97 (1979); **40,** 161 (1979).
12. O. Meyer and B. Seeber, *Solid State Commun.* **22,** 603 (1977).
13. L. R. Testardi et al., *Phys. Rev. Lett.* **39,** 716 (1977).
14. O. Meyer et al. (to be published).

LASER-INDUCED DEFECTS AND MATERIALS INTERACTIONS IN THE V-Si SYSTEM[1]

B. R. Appleton J. Narayan
B. Stritzker[2] J. Fletcher
C. W. White O. Meyer[3]
S. S. Lau[4]

Pulsed-laser annealing has been evaluated as a technique for fabricating superconducting V_3Si from multilayer samples. Correlated analyses by ion scattering, ion channeling, T_c measurements, and TEM were used to examine the composition and structure of films subjected to single and multiple pulses from a Q-switched ruby laser.

A typical pulsed-laser mixing result is shown by the 2.5-MeV ion-scattering spectra in Fig. 2.47.

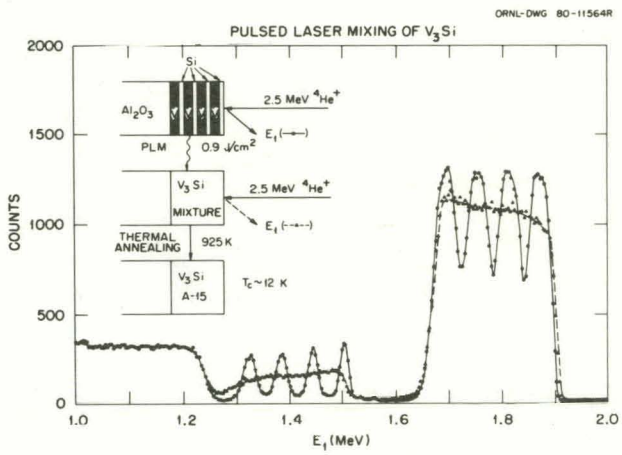

Fig. 2.47. 2.5-MeV He ion scattering analysis of V-Si multilayer samples before (closed circles) and after (closed triangles) pulsed-laser mixing.

Analysis of the as-prepared multilayer sample clearly shows four V layers separated by four Si layers. After a single 0.9-J/cm^2 laser pulse, the films became uniformly mixed with no remaining evidence of the multiple layers. Quantitative analysis showed an average composition of V:Si = 2.8:1. Similar analyses showed that complete mixing occurred for all single laser pulses with energy densities $\gtrsim$0.9 J/cm^2 and that the compositions of the mixed layers were unchanged by higher energy

density pulses, multiple pulses, or thermal annealing.

Measurements of the superconducting transition temperatures of a variety of identical V-Si multilayer samples after pulsed-laser mixing by single laser pulses in air at 300 K are shown in Fig. 2.48

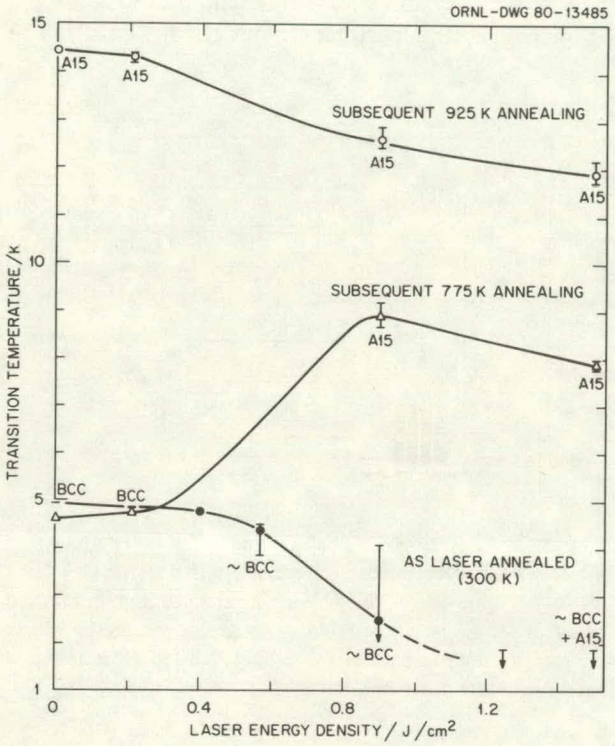

Fig. 2.48. Measured superconducting T_c's and structures of V-Si samples laser processed and thermally annealed.

as a function of laser energy density. The original samples with no thermal anneals had $T_c \sim 5$ K, presumably due to the V layers, and exhibited broad bcc x-ray lines of V. For increasing energy densities, T_c in the as-laser-mixed films decreased, ΔT_c (the width of the transition) increased, and x-ray analysis showed no evidence of any A15 phase until 1.55 J/cm^2. Although all samples receiving >0.9-J/cm^2 processing were uniformly "mixed," as determined from ion scattering, there was no appreciable nucleation of the A15 phase, and the low values of T_c (~1-2 K) were comparable to those which result from neutron,[5] heavy ion,[6,7] and light ion[8,9] irradiation of superconducting V_3Si.

The results of subsequent thermal annealing for 1 h of each of these pulsed-laser mixed samples are also shown in Fig. 2.48. Thermal annealing at 775 K of the 0.9-J/cm^2 sample, which was completely mixed, caused the A15 phase to form out of the defected bcc phase with a $T_c \sim 9$ K. Similarly, x-ray analysis showed that the 1.55 J/cm^2 sample converted completely to the A15 phase even though it had a lower $T_c \sim 8$ K. Additional thermal annealing of these same samples to 925 K for 1 h increased T_c even further. The 0.9 J/cm^2 still showed a higher T_c than the 1.55-J/cm^2 sample; and, surprisingly, the unirradiated multilayer sample showed the highest T_c of all with the unmixed 0.2-J/cm^2 sample the next highest.

Experiments performed to assess the effects of successive 0.9-J/cm^2 laser pulses showed that the first pulse decreased T_c of the initial V films due to intermixing of Si. Five pulses increased T_c to 6.7 K and initiated the formation of an A15 phase. A total of ten pulses improved T_c slightly (to 6.9 K) indicating some increase in long-range order. Subsequent thermal annealing to 925 K for 1 h improved T_c of all samples, with the unirradiated sample showing the highest T_c. These results showed that T_c increased from only 12.6 K for the sample irradiated by one pulse to 12.8 K for the sample irradiated by ten pulses after thermal annealing and that the highest T_c was that for the sample receiving no laser processing. Furthermore, ΔT_c increased with increasing number of pulses, signaling a more inhomogeneous composition.

Additional experiments were performed on samples held at 4 K during laser annealing in the low-temperature vacuum cryostat to determine the effects of increased quenching rates. The overall effects on T_c were similar to those reported above except the magnitude of T_c was always observed to be less and ΔT_c was always larger.

Thermal annealing uniformly improved T_c of all the pulsed-laser mixed films but never to as high values as the films which were not laser mixed before thermal annealing. This indicates that the laser-induced defects are not completely annealed even at temperatures of 925 K which is in contrast to neutron-damaged films[5] where annealing at temperatures $\gtrsim$775 K resulted in complete recovery of the superconducting properties. Similar results have been observed for V_3Si formed by ion-beam mixing.[10] In these experiments multilayer samples of V-Si which were uniformly mixed by bombardment with 4×10^{15}, 300-keV Xe ions/cm^2 and were thermally annealed to only 775 K for 1 h resulted in the formation of the V_3Si, A15 phase with $T_c \sim 15$ K. All these observations show that

the defects formed by pulsed-laser irradiation are much more difficult to anneal than ion-induced defects and are thus probably more complex.

1. Summary of paper: p. 607 in *Laser and Electron-Beam Solid Interactions and Materials Processing,* ed. by J. F. Gibbons, L. D. Hess, and T. W. Sigmon, North Holland, New York. 1981.

2. Guest scientist from Institut für Festkörperforschung, Kernforschungsanlage, Jülich, Federal Republic of Germany.

3. Guest scientist from Nuclear Research Center, Karlsruhe, Federal Republic of Germany.

4. University of California at San Diego, La Jolla, Calif.

5. A. R. Sweedler, D. E. Cox, and S. Moehleche, *J. Nucl. Mater.* **72,** 50 (1978).

6. O. Meyer, H. Mannard, and E. Phrilingose, p. 15 in *Applications of Ion Beams to Metals,* ed. by S. T. Picraux, E. P. EerNisse, and F. L. Vook, Plenum Press, New York, 1974.

7. B. Besslein et al., *Phys. Lett.* **53A.** 49 (1975).

8. J. M. Poate et al., *Phys. Rev. Lett.* **37,** 1308 (1976).

9. O. Meyer and G. Linker, *J. Low Temp. Phys.* **38,** 747 (1980).

10. S. S. Lau et al., p. 511 in *Laser and Electron Beam Processing of Materials,* ed. by C. W. White and P. S. Peercy, Academic Press, New York, 1980.

THE EFFECT OF LASER ANNEALING ON THE CRITICAL CURRENT DENSITY OF Nb_3Ge[1]

A. I. Braginski[2] R. C. Kuznicki[2]
J. R. Gavaler[2] B. R. Appleton
C. W. White

Past attempts to increase the global flux pinning force F_p and, concomitantly, the critical current density J_c in films of A15 Nb-Ge have been based mainly on two ideas: (a) production of the tetragonal Nb_5Ge_3 (σ) phase dispersed as a second phase in the Nb_3Ge and (b) reduction of the average grain size. Only the first has proved successful, but recent structural analyses of laser-annealed Nb-Ge films (>1 μm thick) indicated that a surface layer, approximately 0.1 μm in thickness, melts and recrystallizes to a fine-grained structure during pulsed-laser annealing (PLA) of the film.[3] The present study was, therefore, undertaken to explore the effect of PLA on the J_c of Nb-Ge films. In so doing, it was necessary to distinguish between possible effects due to precipitation (or further precipitation) of Nb_5Ge_3 and effects due to grain size refinement.

Our experimental samples may be classified by thickness into two sets, one of ~4 μm thickness (thick) and the other of ~0.2 μm thickness (thin). Pulses from the Q-switched ruby laser (2 J/cm^2 energy density) melt thin samples more than halfway through but melt only a thin layer (<0.2 μm thickness) on a thick sample.

Figure 2.49 shows the effect of PLA on J_c for thick Nb_xGe_y films of three compositions (x/y), together with pertinent numerical data. The

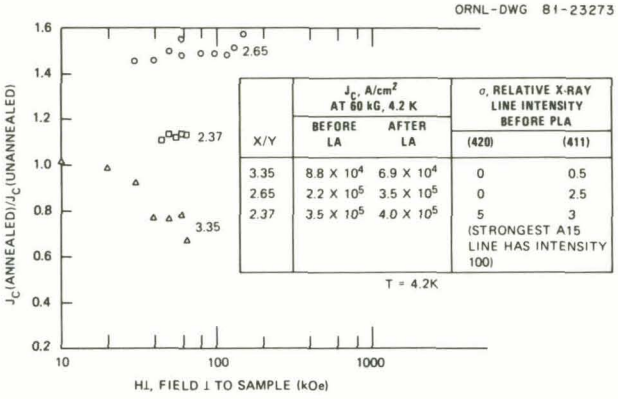

Fig. 2.49. Ratio of J_c before and after laser annealing (2 J/cm^2) vs perpendicular field strength for Nb_xGe_y films of x/y values 3.35, 2.65, and 2.37. For the numerical data in the inset, the relative intensities of the x-ray reflections increase with increasing Nb_5Ge_3 fraction and pertain before laser annealing only.

greatest improvement was in the sample of intermediate composition (x/y = 2.65). The sample that had the most Ge showed little improvement, and the one with the least Ge showed a decrease in J_c over most of the range in the applied field. These results are not readily explained by the expected flux pinning on grain boundaries. This effect should have caused an increase in J_c for all compositions, in the absence of overriding effects due to composition changes in the A15 phase. This latter effect is not probable, because even the sample that was poorest in Ge contained enough Ge to saturate the A15 phase at its highest possible Ge concentration. Even if the concentration of the A15 (that existed after PLA) had varied with composition of the film, the effect of the grain-boundary pinning should have been to increase J_c for all compositions. Additional flux pinning due to further precipitation of the σ phase in the unmelted material is more strongly indicated as an explanation of the improvements that were observed

Presumably, the sample that is poorest in Ge has little potential for pinning by this mechanism; whereas appreciable Nb_5Ge_3 has already been nucleated before PLA in the material that is richest in Ge (see Fig. 1), causing a high critical current for this composition.

Laser annealing of thin samples indicated that melting and resolidification, in itself, was probably deleterious. The J_c's of this latter set fell to zero or nearly zero because of PLA. RBS indicated that the material had not evaporated to a significant extent and x-ray analysis indicated that the resolidified layer was amorphous. Thermal annealing at 750°C, which should have restored the A15 structure, did indeed restore J_c to near its original value.

It was concluded that J_c increases in the thicker films probably resulted from further precipitation of Nb_5Ge_3 in the material that was heated, but remained solid, behind the laser-melted zone. Furthermore, since the average precipitate size that is optimal for pinning should be near the Ginsburg-Landau coherence length (ξ_{GL} = 30–50 Å for Nb_3Ge at T well below T_c), it was concluded that the dominant effect of PLA was to cause nucleation of new precipitates rather than growth of existing ones. This is because the mean size of precipitates that existed in the films before PLA was already so large that further growth would presumably have been deleterious.

1. Summary of paper: *Appl. Phys. Lett.* **39,** 277 (1981).

2. Westinghouse Research and Development Center, Pittsburgh, Pa.

3. B. R. Appleton et al., p. 714 in *Laser and Electron Beam Processing of Materials,* ed. by C. W. White and P. S. Peercy, Academic Press, New York, 1980.

ANALYSIS OF DEFECTS IN LASER-ANNEALED GaAs[1]

J. Fletcher J. Narayan
D. H. Lowndes

Good electrical activation in ion-implanted GaAs usually requires annealing temperatures above 800°C. It is then necessary to use some form of encapsulation to prevent evaporation of As and degradation of the surface of the wafers. However, during furnace annealing none of the presently available encapsulants give good electrical reproducibility. Since nanosecond laser pulses have been successfully used to anneal displacement damage in ion-implanted Si, the possibility of pulsed-laser annealing of GaAs without using an encapsulant was examined in view of the short duration for which the annealed region remains at high temperature during pulsed annealing. In this report we present a summary of systematic studies on residual damage in laser-annealed Zn^+-, Se^+-, Cr^+-, and Mg^+-implanted GaAs. Companion specimens were used for electrical activation and SIMS measurements.

Single-crystal (100) semiconducting GaAs wafers were implanted with either 150-keV Zn^+, 160-keV Se^+, 35-keV Mg^+, or 80-keV Cr^+ ions. The implanted doses ranged from 1–5 × 10^{15} cm^{-2}, and the laser annealing was performed with single pulses from a ruby laser (λ = 0.694 μm, τ = 20 ns) with pulse energy densities ranging from 0.3 to 1.0 J cm^{-2}. Laser annealing through a thin (~30 nm) SiO_2 encapsulant was also investigated. Both plan-view and cross-section electron microscopy techniques were used to study residual damage in ion-implanted and laser-annealed GaAs.

It was found that laser energy densities above about 0.36 J cm^{-2} were required to anneal the displacement damage completely. Typical cross-section [Fig. 2.50(a)] and plan-view [Fig. 2.50(b)]

SSDN 2514

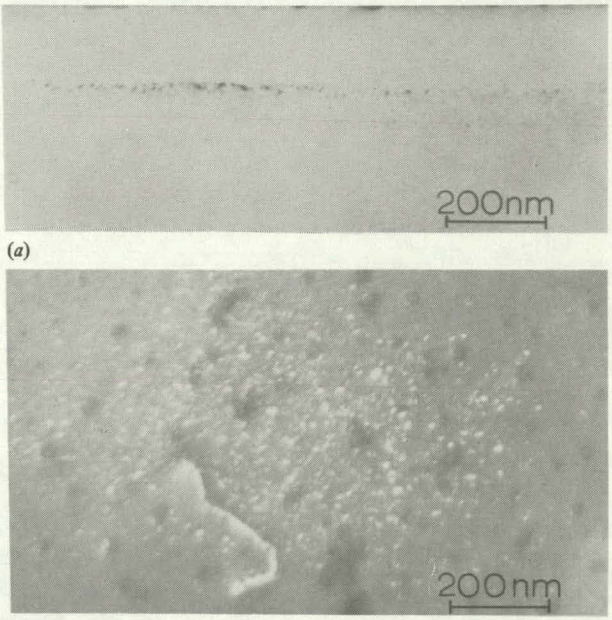

(*a*)

(*b*)

Fig. 2.50. Laser-annealed Se^+-implanted GaAs. Energy density is 0.36 J cm^{-2}. (a) Cross-section electron micrograph. (b) Plan-view electron micrograph showing loops L and dislocations D in the regrown layer.

micrographs are shown for Se^+-implanted GaAs specimens after laser annealing with a pulse of 0.36 J cm^{-2}. Figure 2.50(a) shows completely annealed regions where the melt front just exceeded the thickness of the damage layer and regions (indicated L) with some dislocation loops due to slight spatial inhomogeneity of the laser pulse. In the plan-view a region with dislocation loops D is surrounded by the defect-free regions. Laser-induced surface degradation of GaAs (laser annealed without encapsulation) was observed for all the dopants in the form of Ga precipitates on the surface. A typical example is shown in Fig. 2.51 for Zn^+-implanted specimens after laser

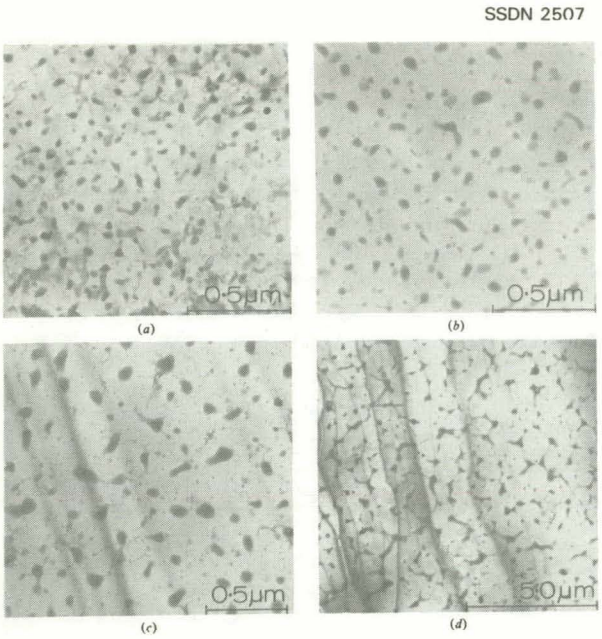

Fig. 2.51. Plan-view electron micrographs showing the presence of Ga-rich regions (darker regions) after laser annealing. (a) 0.25 J cm^{-2}. (b) 0.36 J cm^{-2}. (c) 0.49 J cm^{-2}. (d) 0.81 J cm^{-2}.

annealing with 0.25, 0.36, 0.49, and 0.81 J cm^{-2}. For the 0.81 J cm^{-2} specimen, Ga has started to form "cell-type" structures with a cell size of 1–2 μm. Precipitation, as well as surface damage, was more severe for laser pulses above about 0.82 J cm^{-2}. By using a 30-nm-thick SiO_2 encapsulant, it was possible to avoid the precipitation of Ga. However, the melting and volume changes under the SiO_2 layers resulted in the formation of surface ripples leading to uneven junction depths.

Electrical activation measurements on pulsed-ruby-laser-annealed, ion-implanted GaAs showed that there is an energy density range $0.5 \leqslant E_l \leqslant 0.8$ J cm^{-2} in which high activation of the implanted ions could be achieved. This gives a good correlation with the TEM observations that energy densities above 0.36 J cm^{-2} are required to remove the as-implanted damage and that energy densities above 0.82 J cm^{-2} produce severe degradation of the surface with resultant laser-induced damage. Although electrical activation in laser-annealed specimens (without encapsulant) was high, exceeding 60%, the mobility was rather low, 500–1000 cm^2/Vs. Laser annealing through thin encapsulants leads to electrical activation of about 30% with improved mobility. Therefore, for certain applications such as solar cells, where unevenness in the junction depth can be tolerated, laser processing through thin encapsulant layers seems at present to offer the best solution for processing GaAs.

---

1. Summary of paper: p. 421 in *Defects in Semiconductors,* ed. by J. Narayan and T. Y. Tan, North Holland, New York, 1981.

SEMICONDUCTOR PHYSICS AND PHOTOVOLTAIC CONVERSION

THE DEVELOPMENT OF HIGH-EFFICIENCY BACK SURFACE FIELD Si SOLAR CELLS BY LASER PROCESSING[1]

R. T. Young R. F. Wood
W. H. Christie[2]

Laser processing has been demonstrated to be a promising technique in the fabrication of high-efficiency Si solar cells. Conversion efficiencies of 14–15% AM1 have been reported for *p-n* junction cells formed either by ion implantation followed by laser annealing or by laser-induced dopant diffusion.[3,4] These efficiencies are comparable to or slightly higher than the efficiencies of cells fabricated by thermal diffusion to form the *p-n* junction and with no application of a back surface field (BSF). The special feature of these cells fabricated by laser techniques is that a high short-circuit current J_{sc} in the range 33–35.6 ma/cm^2 can be obtained without much attention to cell design. However, improvement in efficiency by the appli-

cation of a BSF has not been observed in these cells because of the limited minority carrier diffusion length (MCDL). Higher efficiency, laser-processed cells are possible only if the open-circuit voltage V_{oc} and fill factor (FF) can be improved.

In this work, we explored the feasibility of using laser-related techniques for the fabrication of high-efficiency BSF solar cells. During this study we found that the MCDL of the commercially available Cz Si is somewhat shorter than the cell thickness (250–300 μm). The gettering effect, which usually accompanies conventional diffusion processing, is absent from cells fabricated by laser processing. In order for the laser-processed cells to benefit from the high-low junction near the back surface, the enhancement of the MCDL in the base region is a crucial factor. It has been reported[5,6] recently that controlled mechanical damage created by high-power laser radiation on the back side of the sample can effectively improve the MCDL in Si. By using this gettering technique to enhance the MCDL, optimum laser annealing and ion-implantation conditions for formation of the emitter region and laser-induced dopant diffusion for creation of the BSF, Si solar cells with AM1 efficiencies as high as 16.6% have been obtained.

Generally, it is believed that the limitation of the MCDL in single-crystal Si is due to the presence of heavy metals in the as-grown material. Laser-induced damage gettering, using either a Nd:YAG or an Ar-ion laser, has been demonstrated by others to be an effective method for eliminating the detrimental effects of these heavy metals. This method relies first on forming defects on the back surface of the sample by intense laser radiation and then following with a heat treatment to generate dislocations. These dislocations act as effective gettering sites. In our study, uniform surface damage was produced by ruby-laser pulses of 2.0–2.5 J/cm^2 incident on the sample after transmission through a rough-ground glass diffuser plate, after which the samples were annealed in an oxidation furnace at 900–1000°C for 30–60 min. The effectiveness of laser gettering as a function of laser energy density is given in Table 2.7. The maximum gettering effect may not have been found in these experiments. However, the enhancement of the MCDL to 350–400 μm evidently is sufficient to make the application of a BSF improve the efficiencies of our cells.

Table 2.7. Improvement in the MCDL by laser-damage gettering as a function of laser energy density

Sample no.	Energy density (J/cm^2)	MCDL: before (μm)	MCDL: after (μm)
1	2.0	155	170
2	2.0	173	214
3	2.5	148	346
4	2.5	163	397

The p^+nn^+ BSF solar cells were fabricated by using laser-damage gettering to improve the MCDL, shallow boron implantation (5 keV, 6 $\times$ 10^{15} cm^{-2}) followed by laser annealing at 400°C to anneal the implantation damage, and laser-induced diffusion of Sb into the back surface region of the cells to form the BSF. The resulting sheet resistivities on the back surface were in the range 10–15 $\Omega/\square$. Measured performance of four selected p^+nn^+ BSF solar cells fabricated by this process are tabulated in Table 2.8; the improvement of V_{oc} by the incorporation of the BSF is evident. The illuminated I-V characteristics of sample number 9-3 are illustrated in Fig. 2.52.

Table 2.8. Measured performance of p^+nn^+ BSF Si solar cells

Sample no.	J_{sc} (mA/cm^2)	V_{oc} (mv)	FF	Efficiency (%)
9-1	34.7	585	0.79	16.0
9-2	34.8	592	0.79	16.5
9-3	34.3	605	0.80	16.6
9-4	34.1	605	0.80	16.0

We have demonstrated in this work that high-efficiency (>16%) p^+nn^+ cells can be obtained after a laser-gettering process to improve the MCDL in the starting material. Experimental evidence indicates that surface-recombination effects are still significant. Surface passivation will be required to improve further the efficiency of laser-processed cells.

1. Summary of paper to be published.
2. Analytical Chemistry Division, ORNL.
3. R. T. Young et al., *IEEE Trans. Electron Devices* **ED-27**, 807 (1980).

4. J. A. Muller et al., *IEEE Trans. Electron Devices* **ED-27,** 815 (1980).

5. G. H. Schwuttke and K. H. Yang, *Lifetime Control in Silicon Through Focused Laser Beam Damage,* Final Report, DARPA Order No. 3231, June 30, 1979.

6. P. M. Sandow, *Solid State Technol.* **23,** 74 (1980).

ORNL-PHOTO 5596-80

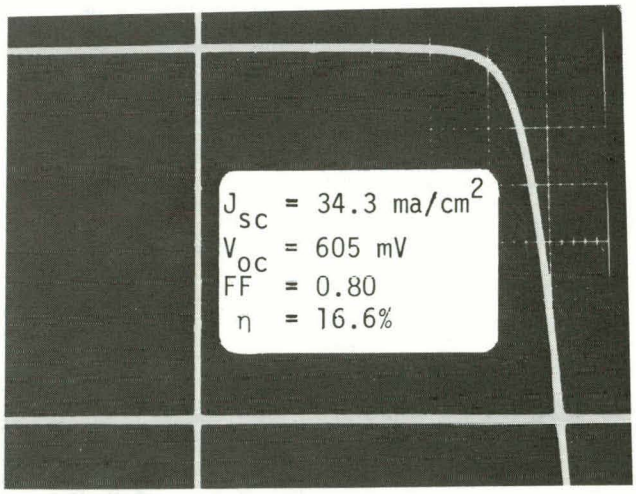

Fig. 2.52. Illuminated I-V characteristics of laser processed BSF Si solar cells.

SUBSTRATE HEATING AND EMITTER DOPANT EFFECTS IN LASER-ANNEALED SOLAR CELLS[1]

R. T. Young W. H. Christie[2]
R. F. Wood G. E. Jellison, Jr.

Several advantages of laser processing cannot be realized by conventional thermal annealing. For example, localization of the thermal effects of the laser radiation, precise control of the emitter dopant concentration over a wide range for a fixed junction depth, and complete electrical activation of dopants at concentrations well above the solid solubility limit, are important factors in solar cell study and design. Recently, model calculations[3] have indicated that V_{oc} becomes insensitive to surface recombination when the emitter dopant concentration N_s is increased to very high levels. Presently, there is a lack of experimental data because precipitates and/or dislocation networks develop in the heavily doped region during either thermal diffusion or ion implantation followed by thermal annealing. Solar cells made by ion implantation and PLA circumvent these problems and provide a unique opportunity to study heavy emitter doping effects. However, several reports[4] have indicated that point defects may remain in the laser-annealed layer and limit its quality for some applications. In this study we provide the first experimental evidence that the electrical properties of laser-regrown layers are improved when heating of the Si samples is used *during* PLA. This improvement is tentatively attributed to the reduction in point defects due to the slowing down of the regrowth velocity produced by the substrate heating.

The material used in the studies was (100)-oriented, 5 Ω-cm, n-type Czochralski Si. Boron was implanted at 5 keV in a dose range 2×10^{14} to 6×10^{15} cm^{-2}. Laser annealing was performed in air with one or two pulses from a ruby laser operating under multimode conditions with a pulse duration of ~20 ns. In order to concentrate attention entirely on the emitter region, no BSF was formed in the cells discussed here.

In the ideal case, the V_{oc} of a p^+n solar cell is given by

$$V_{oc} = \frac{kT}{q} \ln \frac{J_{sc}}{J_{eo} + J_{bo}} \quad ,$$

where J_{sc} is the short-circuit current density and J_{eo} and J_{bo} are the saturation current densities for the emitter and base regions, respectively. In cells with very nearly equal values of J_{bo}, differences in V_{oc} are primarily related to J_{eo}, which is governed by surface and bulk recombination in the emitter region. A series of cells fabricated from the same starting material by ion implantation and PLA should have nearly the same value of J_{bo} and surface-recombination velocity, because the base region is virtually undisturbed by the laser irradiation and the same surface treatment can be applied to all the cells. Therefore, the emitter bulk recombination even at very high doping levels can be monitored by measurements of V_{oc}.

Values of V_{oc} for p^+n cells fabricated from B-implanted (5 keV, 6×10^{15} cm^{-2}) Si, annealed at a pulse energy density E_l of 1.2 J/cm^2 and with T_s held at 25°C, 200°C, 400°C, and 600°C are shown in Fig. 2.53. The data show that V_{oc} increases substantially as T_s is increased from 25 to 400°C and then remains constant or drops slightly at 600°C. To our knowledge, the value of 585 mV for V_{oc} (measured at 21°C) as well as the cell efficiency of 15.3% obtained for T_s = 400°C is the highest reported for cells made from 5 Ω-cm

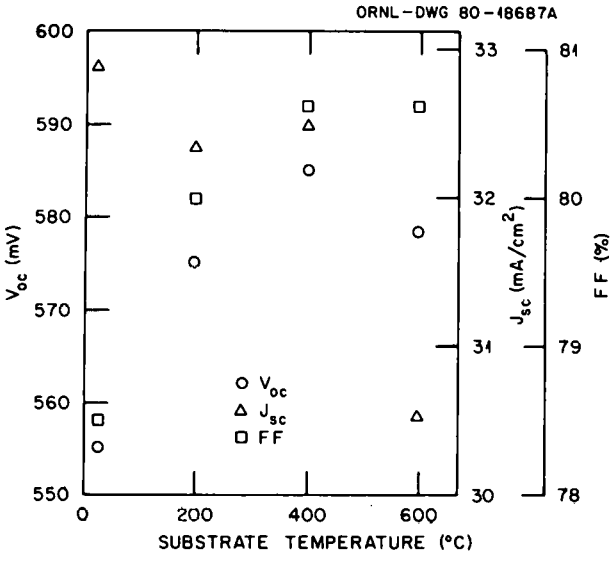

Fig. 2.53. Cell parameters as a function of substrate temperature.

Si *without a BSF*. To gain insight into the significance of substrate heating during PLA, dopant profiles were measured by secondary ion mass spectroscopy (SIMS). As expected, with E_l held constant, the dopant spread farther into the substrate when T_s was increased. The SIMS profiles were fit quite well with calculations of thermal and mass transport[5] during PLA. These calculations also provided information about the variation of melt depth d_m and regrowth velocity v with T_s, as shown in Table 2.9. Since the damaged layer from low-energy implantation of boron will not exceed 1500 Å, the melting depth of ~3000 Å achieved with T_s = 20°C and E_l = 1.2 J/cm^2 should be sufficient to give a good epitaxially regrown layer. The fact that V_{oc} reaches a maximum at 400°C suggests that the quality of the regrown layer is dependent on the regrowth velocity. Hence, it appears that the concentration of quenched-in point defects can be reduced by decreasing v, thus resulting in a smaller J_{eo} and a higher value of V_{oc}.

After demonstrating the importance of substrate heating, we studied the influence of N_s on cell performance. In Fig. 2.54, we show the results of measurements of cell parameters as a function of

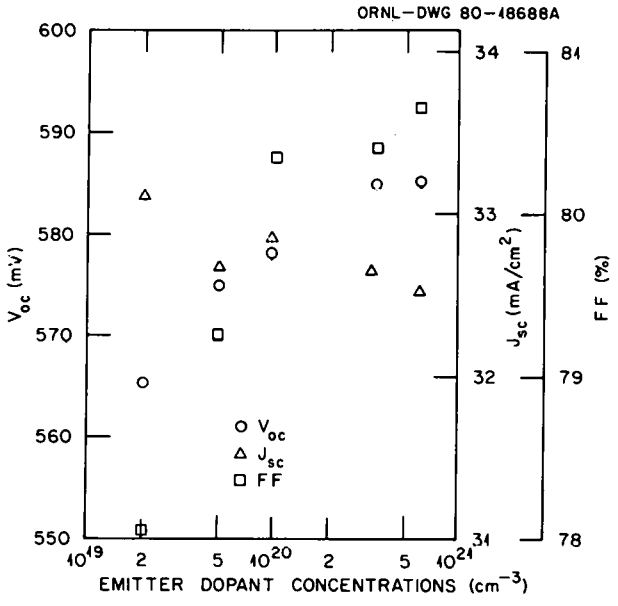

Fig. 2.54. Cell parameters as a function of emitter dopant concentration.

N_s in the range from 2 × 10^{19} to 6 × 10^{20} cm^{-3}. All the cells represented in Fig. 2.54 were made with T_s = 400°C. We note the following important results:

(1) Apparently due to decreasing sheet resistance, the FF improves with increasing N_s;

(2) J_{sc} is relatively unaffected by N_s, which is expected from the "transparent" nature of the emitter to minority carriers in shallow junction cells;

Table 2.9. Calculated melt depth and regrowth velocity as a function of substrate temperatures

T_s	20°C	200°C	400°C	600°C
Melt depth, μm	0.328	0.377	0.438	0.506
Regrowth velocity, m/sec	3.2	2.7	2.1	1.7

(3) V_{oc} increases with N_s up to approximately 3 $\times$ 10^{20} cm^{-3}, where it appears to saturate at a value of 585 mV (measured at 21°C).

This last result is in qualitative agreement with calculations of Shibib and Fossum,[3] which predicted that J_{eo} can be suppressed by increasing N_s. Large discrepancies between the experimental values of V_{oc} and the theoretical predictions of ref. 3 are observed for $N_s > 2 \times 10^{20}$ cm^{-3}, which may suggest that band-gap narrowing and recombination mechanisms are still not well understood at such high dopant concentrations (as assumed in ref. 3). In any case, the results from Fig. 2.54 clearly indicate that with fixed junction depth, the cell efficiency can be improved by increasing N_s.

1. Summary of paper: *Appl. Phys. Lett.* **39,** 313 (1981).

2. Analytical Chemistry Division, ORNL.

3. M. A. Shibib and J. G. Fossum, *J. Appl. Phys.* **52,** 1072 (1981).

4. J. L. Benton et al., *Appl. Phys. Lett.* **36,** 670 (1980).

5. R. F. Wood, J. R. Kirkpatrick, and G. E. Giles, *Phys. Rev. B* **23,** 5555 (1981); "Macroscopic Theory of Pulsed-Laser Annealing: II. Dopant Diffusion and Segregation," this report.

A COMPARISON BETWEEN PULSED- AND cw LASER ANNEALING FOR SOLAR CELL APPLICATIONS[1]

G. E. Jellison, Jr. R. F. Wood
R. T. Young A. Gat[2]

It is widely believed that pulsed-laser annealing (PLA) of ion-implanted samples involves the melting of the damaged layer, followed by epitaxial regrowth from the perfect single-crystal substrate. The resultant dopant profiles usually are broadened considerably from the preannealed condition; this broadening is explained readily by the melting model. Continuous-wave (cw) laser annealing has also been useful for the annealing of ion-implanted emitter regions. However, cw laser annealing apparently takes place via a solid-phase recrystallization process, which does not change the initial dopant profile appreciably. The purpose of this work was to compare the performance of solar cells made from ion-implanted Si laser annealed by the two types of lasers.

Solar cells were fabricated from *p*-type substrates (10 Ω-cm), ion-implanted with As at 100 keV, and cw laser annealed using an argon-ion laser. The laser power was 11 W, with a spot size of 100 μm, a scan rate of 25 cm/s, and a 50-μm lateral step after each scan. A backsurface field was fabricated by depositing B (10 nm) on the back of the cell and by PLA with a 1.8-J/cm^2 pulse. In addition to this procedure, some of the cw laser-annealed cells were subjected to a 700°C furnace anneal for 1 h. For comparison purposes, similar solar cells were fabricated using PLA techniques but with no gettering step. Three different implantation doses of As at 5 keV and one dose at 25 keV were used. Because of the lack of dopant redistribution during cw laser annealing, a higher energy As implant had to be employed for the cw laser-annealed samples than for the PLA samples to get similar junction depths (~200 nm). The resulting solar cell parameters are shown in Table 2.10. The results quoted for cells fabricated using PLA techniques were averaged over 2 to 4 cells, while the results quoted for the cw laser-annealed cells are for the best cells. Clearly, the PLA cells

Table 2.10. A comparison of solar cell parameters for cw laser annealing and PLA

Laser-annealing technique	As-implant energy (keV)	Dose ($\times 10^{15}$/cm^2)	Substrate temperature (°C)	*FF* (%)	V_{oc} (mV)	J_{sc} (mA/cm^2)	Efficiency (%)
Pulse	5	1	400	79	585	34.1	15.8
Pulse	5	2	400	78	587	34.2	15.7
Pulse	5	4	400	78	595	34 6	16.1
Pulse	25	2	400	77	550	34.7	14.7
CW	100	3	500	78	510	26.5	10.5
CW[a]	100	3	500	78	532	27.5	11.4

[a]These samples were subjected to a 700°C furnace anneal for 1 h.

performed better than the cw laser-annealed cells; both V_{oc} and J_{sc} are less in the cw laser-annealed samples, compared with the PLA samples, though a 700°C furnace anneal for 1 h increases both V_{oc} and J_{sc} somewhat. Note also that V_{oc} is decreased in the PLA cells if the As implantation energy is increased from 5 to 25 keV, though J_{sc} remains constant.

A further comparison can be made by examining the spectral response data for cells with no AR coating. The cw laser-annealed cells were found to have a lower quantum efficiency than the PLA cells at all wavelengths. A 700°C furnace anneal increases the quantum efficiency somewhat at all wavelengths, but this increase does not compare with the increase achieved using PLA. The poor blue response of the cw laser-annealed cells indicates very poor collection efficiency in the emitter region, while the poor red response is attributed to a low value of the MCDL in the base. Note that the cw laser-annealed cells were fabricated on different substrates than the PLA samples, and the MCDL should not be expected to be the same.

Continuous-wave laser annealing has been shown to be useful for many semiconductor device fabrication applications; however, the data presented here show that our best PLA solar cells are better than cells fabricated using the cw laser-annealing process. It was found from DLTS measurements that the cw laser-annealing process introduced a large number of recombination centers well into the bulk of the material and that the emitter region of cw laser-annealed cells was a very inefficient collector of minority carriers.

1. Summary of paper: p. 15 in *Space Photovoltaic Research and Technology,* NASA Conference Publication 2169, Washington, D.C., 1980.

2. Coherent Laser, Inc., Palo Alto, Calif.

TIME-RESOLVED OPTICAL TRANSMISSION AND REFLECTIVITY OF PULSED-RUBY LASER-IRRADIATED Si[1]

D. H. Lowndes

The purpose of these experiments was to probe the optical behavior of Si during and immediately after pulsed-laser irradiation to help resolve the controversy which has arisen regarding the physical phenomena involved. Despite impressive experimental and theoretical support for the thermal melting model of PLA, Compaan and co-workers[2] recently presented results which they claimed provided conclusive proof that this model could not be correct. In particular, they observed both the time-resolved reflectivity (at $\lambda = 0.633$ μm) and transmissivity (at $\lambda = 1.15$ μm) of ~400-μm-thick crystalline Si (c-Si) during PLA (at $\lambda = 0.485$ μm). They found that, although the transmission showed a sudden drop as the reflectivity rose and recovered when the reflectivity fell, the transmission minimum (duration ~50 ns) did not go to zero, as would be expected if the layer of molten Si (skin depth ~100 Å) implied by the melting model were present. They interpreted their results as arising from a laser-induced transition of Si to a new "fluid phase," arising from formation of a high-density, hot plasma.

In the experiments reported here, we measured both the time-resolved transmission (TRT) and time-resolved reflectivity (TRR) during pulsed-laser irradiation of Si and obtained results that contradict those of Lee et al.[2]

Our experiments were carried out using a pulsed ruby laser ($\lambda = 0.693$ μm) operated in the TEM_{00} mode with a pulse duration $\tau_l = 14 \pm 1$ ns. A 1-mW cw-He/Ne ($\lambda = 1.15$ μm) probe laser beam was used for the transmission measurements. Both a Si avalanche photodiode (APD) and a Ge PIN photodiode were used in the transmission experiments. However, the much higher response of the Si APD (~2 A/W vs ~0.2 A/W for the Ge PIN diode, at 1.15 μm) made it the preferred detector, since it was found necessary to use also a 1.15-μm bandpass filter (0.01-μm bandwidth and ~40% transmission) directly in front of the detector in order to prevent intense near band-gap radiation emitted by the Si sample from swamping the detector when it was close to the sample. A 3.4-mW cw-He/Ne laser ($\lambda = 0.633$ μm) and a Si APD were used for the reflectivity measurements.

The TRR signals were similar in shape to those reported earlier,[3,4] consisting of a flat-topped period of maximum reflectivity (duration τ_m) followed by a decaying reflectivity tail (duration τ_f). However, in the present experiments we found that the enhanced reflectivity was ≃2.06 times the initial reflectivity of c-Si (corresponding to reflectivities of 71% and 35%, respectively), in good agreement with the reported reflectivity for molten Si, while other experimenters[2,3] have found somewhat lower values in the enhanced reflectivity state. This difference between our experiments and those of others may be due to our use of a relatively large

probe beam (diameter < 1 mm) in contrast to the 30–100-μm beam diameters used by others.

Figure 2.55 shows typical results of a series of TRT measurements for ruby-laser pulses of energy E_l both below and above the threshold (E_l = 0.89

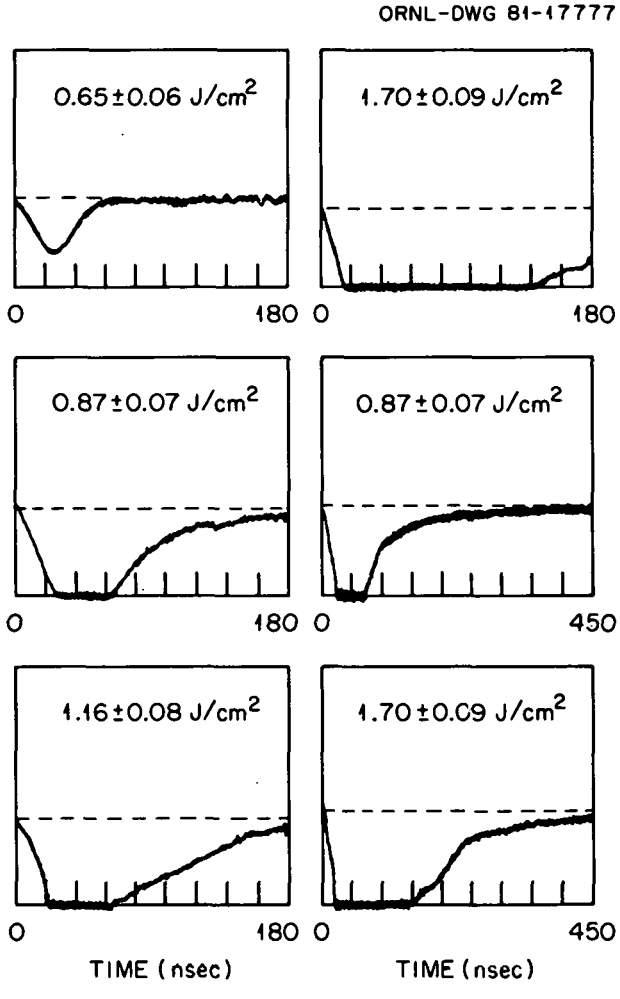

Fig. 2.55. TRT of c-Si for a series of laser pulses of energy density E_l and viewed on two different times scales (20 and 50 ns/div.). The upper left figure is for E_l *less* than the threshold for the fully enhanced reflectivity phase.

$\pm$ 0.06 J/cm^2) for the enhanced reflectivity signal. The probe beam transmission drops to zero and remains there for a period of time τ_m that increases with increasing E_l. As is shown in ref. 1, there is quantitative agreement between this and other corresponding features of the TRR and TRT signatures.

TRT measurements were also carried out *without* the cw probe beam and with the 1.15-μm bandpass filter removed and the Si sample mounted directly on the enclosure of the Si APD detector, about 9 mm from the detector chip. Figure 2.56 shows the time dependence of the intense

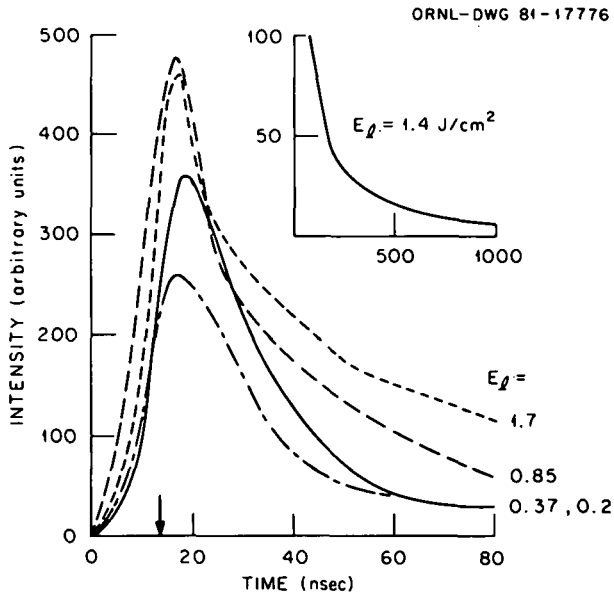

Fig. 2.56. Time-dependent intensity of NBG radiation emitted by laser-irradiated c-Si. The vertical arrow marks the time of the peak of the ruby laser pulse. Inset: Long time behavior of the slowly decaying tail.

near band-gap radiation that was detected in this case. The radiation can be separated into two components, a sharp initial peak and a long, slowly decaying tail. The initial peak occurs <4 ns after the peak in the ruby-laser pulse and appears to have a full width at half maximum comparable to the ruby pulse width. A semilog plot of the slowly decaying tail reveals that several decay processes may be involved, with time constants ranging from <100 to ~1000 ns. It should be noted that the 1-mW, 1.15-μm probe laser intensity corresponds to just seven of the arbitrary intensity units in Fig. 2.56 (i.e., it would be swamped completely by the near band-gap radiation signal) until nearly 1000 ns after the ruby-laser pulse, unless the bandpass filter is in place.

Thus, we find that the optical transmission of Si during pulsed-laser irradiation drops to zero and remains there during the time that the reflectivity

is at its maximum. The observed maximum value for the reflectivity also agrees with the known value for molten Si, and other corresponding features of the TRR and TRT "signatures" are in good agreement with each other. Thus, we conclude that the optical properties of Si during pulsed-laser irradiation are consistent with the presence of molten Si and do not require a transition to a long-lived (~100 ns) high-density plasma phase for their explanation.

1. Summary of paper to be published.
2. M. C. Lee et al., *Appl. Phys. Lett.* **38,** 499 (1981).
3. D. H. Auston et al., *AIP Conf. Proc.* **50,** 11 (1979).
4. D. H. Lowndes and R. F. Wood, *Appl. Phys. Lett.* **38,** 971 (1981).

OPTICAL ABSORPTION MEASUREMENTS OF PURE Si FROM 1.64 TO 4.73 eV

G. E. Jellison, Jr. F. A. Modine

The object of this work was to measure the optical absorption coefficient α of pure Si in the blue region of the solar spectrum using polarization modulation ellipsometry. The theory and operation of the polarization modulation ellipsometer (PME) are well documented in the literature.[1] By using the correct configuration of optical elements, one measures either N, S, or C, where $N = \cos 2\psi$, $S = \sin 2\psi \sin \Delta$, and $C = \sin 2\psi \cos \Delta$.

The quantities ψ and Δ are the customary ellipsometry parameters, which are given by $r_p/r_s = \tan \psi e^{i\Delta}$, where r_s and r_p are the perpendicular and parallel components, respectively, of the complex reflectance with respect to the plane of incidence. Because of the automated nature of the PME, the quantities ψ and Δ are determined as a continuous function of wavelength.

In order to transform the data for ψ and Δ into n and k (the real and imaginary parts of the refraction index), a model of the surface must be used. The simplest model, a one-boundary structure, can be solved analytically; however, since it is known that Si normally forms a surface oxide (~20 Å) which has quite different optical properties than bulk Si, this model is clearly inadequate. Therefore, a more complex two-boundary model must be employed. This model consists of a semi-infinite region of air (or vacuum), an oxide layer of thickness d_1 ($n_1 = 1.46$, $k_1 = 0$), and one conductive layer.

The ellipsometry parameters for a general two-boundary model can be expressed as

$$\psi = f(\phi, n_0, n_1, k_1, d_1, n_2, k_2) \qquad (1a)$$

and

$$\Delta = g(\phi, n_0, n_1, k_1, d_1, n_2, k_2) , \qquad (1b)$$

where f and g are complex functions of the given arguments. In general, we know that $n_0 = 1$; we assume that the oxide layer is SiO_2, so that $n_1 = 1.46$ and $k_1 = 0$. These values change very little over the wavelength range considered here.

The oxide thickness of the pure samples was measured using a Gaertner L117 nulling ellipsometer at $\lambda = 632.8$ nm and an angle of incidence of 70°; it was assumed from data in the literature that $n = 3.85$ and $k = 0.018$ for the pure Si at this wavelength. Equations (1a) and (1b) can then be solved using a two-dimensional analog of Newton's method. Extensive error analysis reveals that the error of α depends on the magnitude of α; for example, the error in α at $\alpha = 10^4$ cm^{-1} is 25%; at $\alpha = 10^5$ cm^{-1}, ~10%; and at $\alpha = 10^6$ cm^{-1}, ~1.5%.

The values of the optical constants (complex index of refraction $\hat{n} = n + ik$, or complex dielectric constant $\hat{\epsilon} = \hat{n}^2 = \epsilon_1 + i\epsilon_2$) for pure Si were calculated using a two-boundary model from ψ and Δ data taken for λ from 262–755 nm (1.64–4.73 eV). The absorption coefficient ($\alpha = 4\pi k/\lambda$, where λ is the photon wavelength), which is important for solar cell applications, can be accurately determined above ~2.5 eV using this technique. The resulting values of the absorption coefficient for pure Si are shown in Fig. 2.57 (solid line) along with data found in the literature. It is believed that our new data from ~2.5 to ~3.5 eV (350 to 500 nm), which corresponds to the blue end of the solar spectrum, is the most accurate optical data now available for Si.

1. S. N. Jasperson and S. E. Schnatterly, *Rev. Sci. Instrum.* **40,** 796 (1969).
2. H. A. Weakliem and D. Redfield, *J. Appl. Phys.* **50,** 1491 (1979).
3. W. C. Dash and R. Newman, *Phys. Rev.* **99,** 1151 (1955).
4. R. Braunstein, A. R. Moore, and F. Herman, *Phys. Rev.* **109,** 695 (1958).
5. R. Hulthen, *Physica Scripta* **12,** 342 (1975).
6. S. S. So and K. Vedam, *J. Opt. Soc. Am.* **62,** 16 (1972).
7. H. R. Philipp, *J. Appl. Phys.* **43,** 2835 (1972).

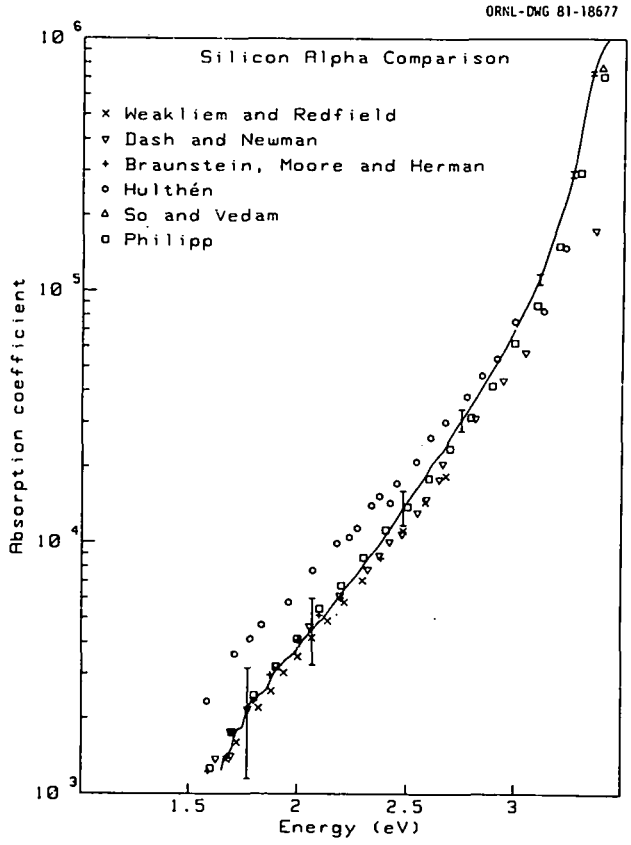

Fig. 2.57. Optical absorption coefficient for pure Si determined by polarization modulation ellipsometry shown by the solid line. Comparison data points are taken from (1) Weakliem and Redfield[2]; (2) Dash and Newman[3]; (3) Braunstein, Moore, and Herman[4]; (4) Hulthen[5]; (5) So and Vedam[6]; and (6) Philipp.[7]

OPTICAL PROPERTIES OF HEAVILY DOPED Si BETWEEN 1.5 AND 4.1 eV[1]

G. E. Jellison, Jr. C. W. White
F. A. Modine R. F. Wood
R. T. Young

The optical constants of heavily doped Si have been measured using polarization modulation ellipsometry. Samples were prepared by ion implantation followed by laser annealing with 10 pulses from a ruby laser at energy 1.3 J/cm^2. This form of sample preparation has several advantages: (1) the solubility limit can be exceeded to give higher doping densities than have been achieved previously, (2) the resulting near-surface region is free of electrically active extended (>10 Å) defects, (3) the surface is optically flat, and (4) the doping concentration profile is more nearly an abrupt junction than that obtained by diffusion.

The values of the optical absorption coefficient for As-doped Si are shown in Fig. 2.58 for several doping levels. As can be seen, there is a dramatic

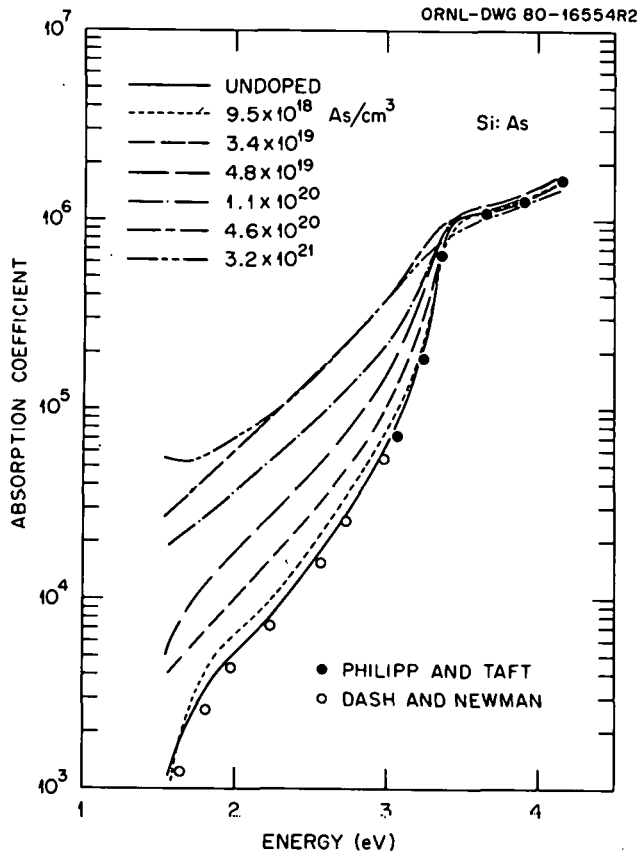

Fig. 2.58. Absorption coefficient vs photon energy for several As concentrations in Si. Data shown by the open circles and filled circles are representative data from refs. 2 and 3, respectively.

increase in the absorption coefficient for increased doping densities for all photon energies below the direct gap (at 3.4 eV) and above 1.5 eV. Similar experiments with B- and P-doped Si do not show this dramatic increase in absorption coefficient.

The correct interpretation of these results is not obvious and will probably require a significant theoretical effort to arrive at a completely satisfactory explanation. However, a few significant observations can be made, and a plausible interpretation can be proposed. Clearly, we can eliminate processes which depend upon the type of dopant (n or p), interband processes, and phonon perturbations, since there is no obvious correlation with the

mass of the dopants. Moreover, since As has a close lattice match (in terms of covalent radii) with Si, we do not expect large lattice strains to occur for As-doped Si, even at high doping levels. Therefore, we conclude that the large effects observed for As-doped samples are due to the presence of the *d* electrons in As. The As impurities will introduce either true localized levels or resonance states lying well below the top of the valence band $\Gamma_{25'}$ at the Brillouin-zone center. Orthogonality and screening effects due to the *d* electrons may influence the *energy levels* of higher lying states (in both the valence and conduction bands), but they will probably not alter greatly the joint density of states. It is much more likely that the presence of the *d* orbitals produces a rapid increase in many matrix elements of the dipole operator which vanish in the perfect crystal; the inclusion of *d* orbitals in the basis set introduces the possibility that strong *p-d* transitions can occur *on the same atom* where $\langle p|r|d\rangle$ is expected to be large. Thus, although the coefficient of the *d* orbitals may be rather small, the strength of the matrix elements and the fact that there are 10 *d* electrons will lead to a rapid increase in α as the concentration of As increases. In B- and P-doped Si the enhancement of α will not be nearly so great because the outer *s* and *p* orbitals of B and P do not differ significantly from their counterparts in the host Si lattice.

1. Summary of paper: *Phys. Rev. Lett.* **46,** 1414 (1981).

2. W. C. Dash and R. Newman, *Phys. Rev.* **99,** 1151 (1955).

3. H. R. Philipp and E. A. Taft, *Phys. Rev.* **120,** 37 (1960).

TRANSIENT CAPACITANCE STUDIES OF A LOW-LYING ELECTRON TRAP IN n-TYPE Si[1]

G. E. Jellison, Jr. J. W. Cleland
R. T. Young

A new electron trap has been observed by transient capacitance measurements in electron-irradiated n-type Si at $E_c - E_T = 0.105$ eV (E1). It was found that this trap is related to another trap at $E_c - E_T = 0.172$ eV (E2), in that one trap can be converted to the other by altering the voltage-pulsing scheme across the sample diode. However, it was also observed that not all the E2 traps can be converted to E1 traps (though all E1 traps can be converted to E2 traps); therefore, we must distinguish between the convertible E2's (E2c) and the nonconvertible E2's (E2n).

The experimentally observed height of the response from E1 is expressed as

$$h_{E1} = h^0_{E1}[1 - \exp(-t_p/\tau_p)]\exp(-t_w/\tau_w) , \quad (1)$$

where h^0_{E1} is the maximum response from the E1 trap, t_p and t_w represent the time between pulses and the pulse width, respectively, and τ_p and τ_w represent characteristic time constants. As can be seen from Eq. (1), the maximum response from the E1 trap occurs for $t_p \gg \tau_p$ and $t_w \ll \tau_w$. It is observed that $h_{E1} + h_{E2} =$ constant. The time constants τ_p and τ_w are associated with thermally activated processes and can be expressed as

$$\tau_p = \tau_p^\circ \exp(\Delta E_p/kT) \quad (2a)$$

and

$$\tau_w = \tau_w^\circ \exp(\Delta E_w/kT) , \quad (2b)$$

in which $\tau_p = 7.5 \times 10^{-13}$ s, $\tau_w = 7.3 \times 10^{-13}$ s, $\Delta E_p = 0.174$ eV, and $\Delta E_w = 0.145$ eV. Furthermore, it was determined that $\tau_p =$ the emission time of the E2 trap. Annealing experiments showed that the E2c and E1 traps annealed out at 350°C, while the E2n traps annealed out at 450°C.

A possible model explaining the experimental data involves an impurity-modified A center and is shown in Fig. 2.59. The activation energy, anneal-out temperature, and electron capture cross section ($\sigma_n > 10^{-14}$ cm^2) indicate that the E2n trap is just the well-known A center or oxygen-vacancy defect.[2] The E1 and E2c traps appear to be different configurations of the same trap. The observed dependence of the transient capacitance on the time between pulses indicates that, if the E2c trap is filled, it cannot be converted to an E1 trap but an unfilled E2c trap will convert to an E1. As t_p is increased, more E2c traps are emptied and, therefore, are converted to E1 traps. Since the captured electron of the A center is localized on the Si-Si bond (see Fig. 2.59), the E2n and E2c traps will have nearly the same activation energy and emission times because the unpaired electron will not significantly overlap the impurity of the E2c trap. On the other hand, the unpaired electron

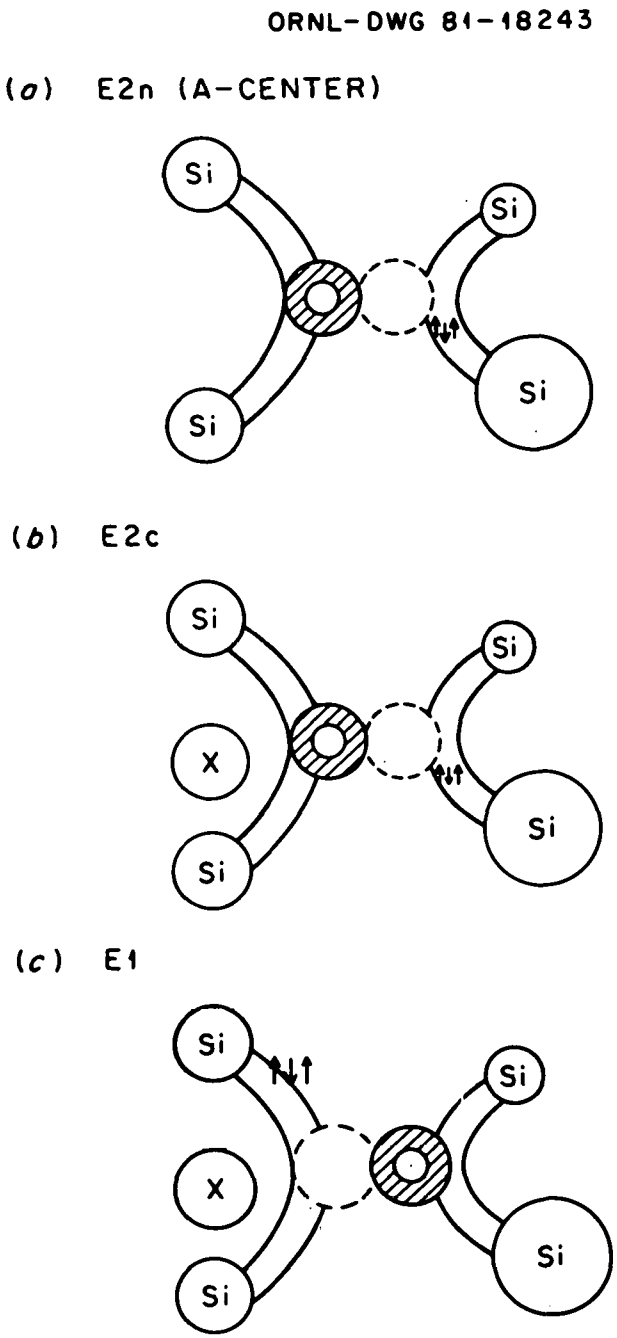

Fig. 2.59. Model for E2n, E2c, and E1 defects. (a) the A center, (b) the impurity-modified A center without vacancy-impurity interaction, and (c) the impurity-modified A center with vacancy-impurity interaction. The impurity atom is represented by the circled X, the oxygen atom by the crosshatched O, and the vacancy by the dashed circle. Note that the impurity position is not stipulated; it could be interstitial or substitutional.

in the E1 trap will overlap significantly the impurity (due to the proximity of the unpaired electron to the impurity atom), resulting in a different activation energy for the E1 trap than for the E2c or E2n trap. The pulse width indicates that there is a small probability for a filled E1 trap to convert to a filled E2c trap. This transformation is similar to stress-induced configurational changes seen in the A center[2] but has a smaller activation energy (0.145 eV for this case, compared with 0.38 eV for the A center[2]). The annealing experiments also support the conclusion that the E1 and E2c traps are different configurations of the same defect, while the E2n trap is a different defect.

1. Summary of paper to be published.
2. G. D. Watkins and J. W. Corbett, *Phys. Rev.* **121**, 1001 (1961); J. W. Corbett and G. D. Watkins, *Phys. Rev.* **121**, 1014 (1961).

ELECTRICAL AND STRUCTURAL PROPERTIES OF GRAIN BOUNDARIES IN POLYCRYSTALLINE Si

R. T. Young Y. K. Chang

Several individual high-angle (mismatch angle >15°) and low-angle (<1°) grain boundaries in 1 Ω-cm *n*-type polycrystalline Si have been investigated. The purpose of the investigation was to attempt to correlate the mismatch angle of a grain boundary with its barrier height and minority-carrier recombination properties. The mismatch angle was determined from Laue x-ray diffraction patterns. The grain boundary barrier height was determined from temperature-dependent resistivity measurements, and the carrier recombination was determined by precision line scans using the scanning laser spot technique. Our preliminary results show no simple correlations between mismatch angle and electrical properties (barrier height and/or recombination). Some high-angle grain boundaries exhibit neither a significant barrier height nor strong recombination in the untreated specimen. Minority-carrier recombination at grain boundaries often develops after boron diffusion at 950°C for 30 min. However, even after such treatment, it was not found that high-angle grain boundaries always exhibit higher recombination rates than do the low-angle grain boundaries. This indi-

cates that the dislocation configuration of a grain boundary and possibly the density of coincidence sites between the grains may affect the nature of the impurity segregation, which may have a large effect on the electrical properties of the grain boundaries.

LASER MODIFICATION OF GRAIN-BOUNDARY STRUCTURES

R. T. Young J. Narayan

Efficiencies of small-grained (1–50 μm) polycrystalline Si solar cells are low, primarily because of the detrimental effects of grain boundaries. Grain-boundary passivation and the modification of grain-boundary structures are thought to be promising methods for the improvement of cell efficiency.

In the work reported here, we used pulsed-laser-induced surface melting to change grain-boundary structures. We found that some electrically active grain boundaries can be converted to electrically inactive grain boundaries by laser irradiation. These findings may lead to the improvement of thin-film solar cells on low-cost substrates by laser-induced modification of grain-boundary structures before subsequent epitaxial film growth.

An example of the type of results that can be obtained is given in Fig. 2.60. Figures 2.60(a) and 2.60(b) show a comparison of SEM images in the

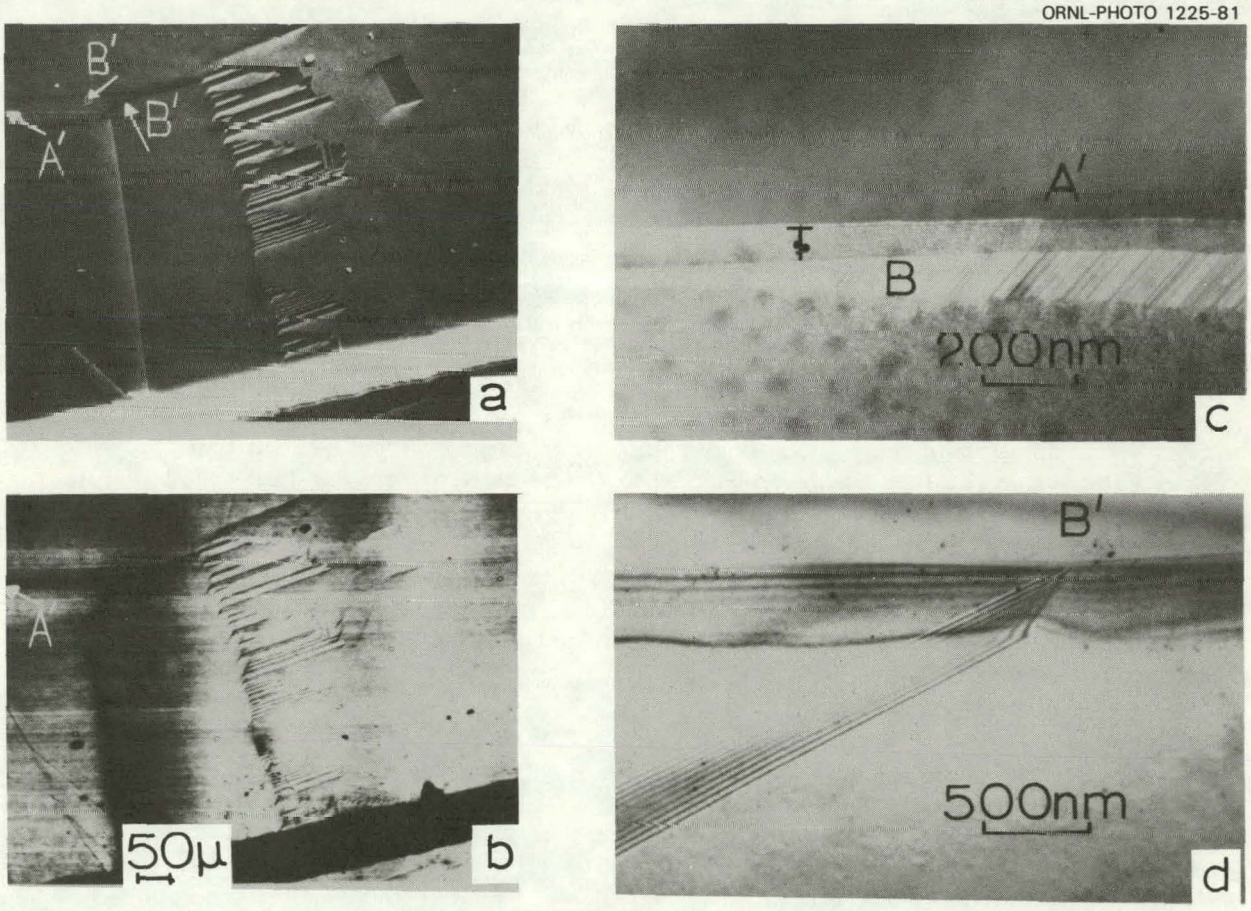

Fig. 2.60. Comparison of electrical and structural properties of coherent and incoherent grain boundaries. (a) Image of a portion of a laser-annealed polycrystalline solar cell taken with an electron microscope operating in the standard (secondary electron emission) operating mode. (b) Image of the same area on the sample taken with the microscope operating in the EBIC mode, showing A′ (electrically active) and B′ (electrically inactive) twin boundaries. (c) Area A′, the electrically active, incoherent twin boundary has transformed into an inactive, coherent twin boundary in the laser-melted region. (d) Area B′, a typical electrically inactive, coherent twin boundary.

secondary electron and EBIC modes of a selected area of a polycrystalline Si specimen after laser irradiation. These and other micrographs indicate that the linear boundaries exhibit a wide range of electrical activity, from completely inactive boundaries [for example B' in Fig. 2.60(a)], to boundaries which are electrically active only along certain sections, or to boundaries which are electrically active along their entire length (A'). The objectives of this work are to understand the differences between electrically inactive and electrically active boundaries by an investigation of the differences in the microstructures of the two linear boundaries and to study the modifications of the microstructures of these boundaries by laser irradiation. Figure 2.60(d) is a bright-field transmission electron micrograph of the electrically inactive boundary B'; the structure seen in the micrograph is typical of a *coherent* twin boundary. On the other hand, the electrically active boundary A' deviates from the ideal coherent twin morphology, as indicated by the presence of networks of partial twinning dislocations in the TEM micrographs. Figure 2.60(c) is a dark-field TEM micrograph (tilt 40°) of boundary A'. Two distinct regions are indicated in this micrograph. The bottom region B, which is seen to contain twinning dislocations, is responsible for the electrical activity of the boundary. The top region T shows the characteristics of a coherent twin and is presumably electrically inactive. The difference between the T and B regions was produced by laser melting, which evidently eliminates the twinning dislocations. However, the laser radiation did not alter the microstructure of the coherent twin boundary, as shown in Fig. 2.60(d). Coherent twin boundaries are believed to contain no "dangling" bonds and, hence, are electrically inactive.

Electrically active incoherent twin boundaries contain partial twinning dislocations, which are responsible for the electrical activity; apparently, these boundaries can be partially converted to coherent twins by laser radiation. Even though the depth of melting which can be obtained by laser annealing is not great (~0.5 μm), it may be enough to prevent the propagation of the electrically active grain boundaries into the epitaxial layer. Further study of the laser modification of other types of grain boundaries and the resulting changes in their electrical properties is under way.

EFFECTS OF HEAT TREATMENT ON GRAIN-BOUNDARY ELECTRICAL ACTIVITY

R. T. Young R. D. Westbrook

Recent investigations of grain boundaries by Redfield[1] indicated that grain boundaries are "very clean" in as-grown Si. He stated that he observed no potential barriers by simple two-point probe resistance measurements at grain boundaries in untreated n- or p-type Wacker Silso samples or in bicrystals grown at RCA and that he suspected that barriers are produced at grain boundaries by heating samples to temperatures of ~600–900°C, which causes diffusion of impurities (most likely oxygen) to the grain boundaries.

Investigations were initiated to study the above effects. Samples were cut from a large-grained polycrystalline Si ingot, which had been grown by a single pass Fz technique, with columnar grain structure so that identical grain boundaries could be found in samples from adjacent slices. p-n junctions were formed in these samples, either by glow-discharge implantation followed by laser annealing or by boron diffusion at 950°C for 30 min. The advantages of using glow-discharge implantation and laser annealing for junction formation in polycrystalline Si are that the substrate can be kept virtually at room temperature and enhanced dopant diffusion along grain boundaries can be eliminated. Careful studies of recombination effects at grain boundaries in these solar cells were made by scanning laser spot and EBIC techniques. Our preliminary results indicated that some grain boundaries, which were electrically inactive after glow-discharge implantation and laser annealing, were electrically activated as a result of thermal diffusion.

Further experiments to determine the cause of the electrical activation of these grain boundaries were carried out by high-vacuum annealing (8×10^{-8} torr, 950°C for 30 min) of samples both with and without implanted boron. The samples were then prepared for EBIC investigation. The results were that grain boundaries remain electrically *in*active after thermal treatment only for those samples *without* B sources at the surface during the heat treatment. This indicates that preferential diffusion along grain boundaries of the boron and/or certain contaminants introduced by the glow-discharge implantation may be one of the

:auses of electrical activation (see Fig. 2.61). On he other hand, Li diffusion (350°C for 3 h) did not activate these grain boundaries. The results we have obtained thus far are not sufficient to give a good overall picture of the effects involved. However, they reinforce our previous conclusions that ɔulsed-laser techniques do offer substantial advantages for the study and processing of polycrystalline Si.

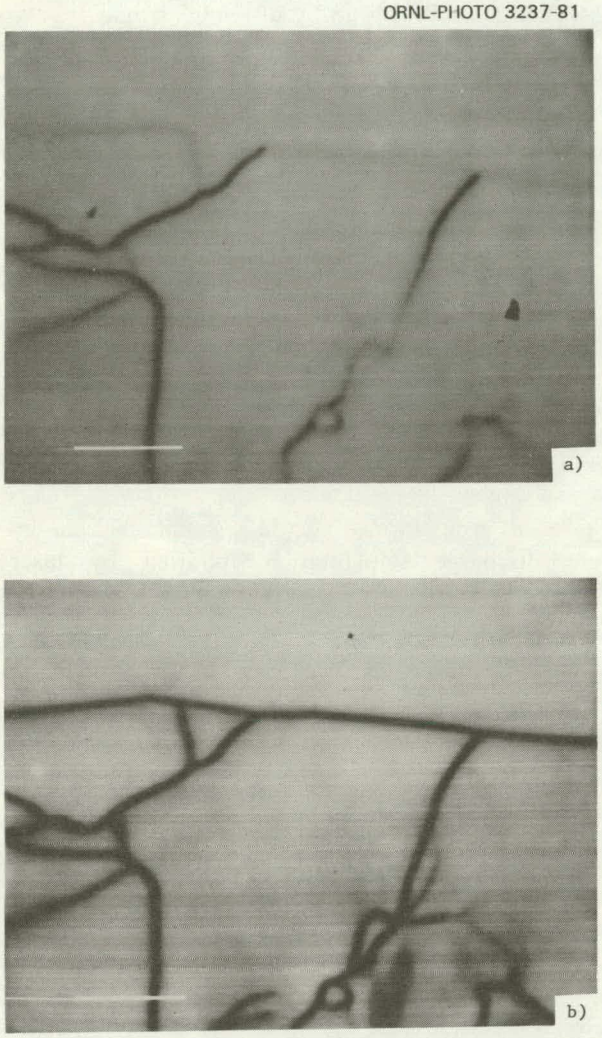

Fig. 2.61. EBIC maps of the electrical response of grain boundaries in a solar cell made by glow-discharge implantation and laser annealing: (a) before any heat treatment and (b) after heating at 950°C for 30 min in a high-vacuum ($\sim 8 \times 10^{-8}$ Torr) furnace. The dark lines indicate boundaries with high electrical activity, that is, minority-carrier recombination.

---

1. D. Redfield, *Bull. Am. Phys. Soc.* **26,** 444 (1981).

EFFECT OF Li DIFFUSION INTO POLYCRYSTALLINE Si SOLAR CELLS[1]

R. T. Young Y. K. Chang
G. E. Jellison, Jr. M. C. Lu[2]
G. A. van der Leeden

Recently, it has been reported that the presence of Li in polycrystalline Si can increase not only the majority carrier mobility[3] but also the minority carrier lifetime.[4] To what extent Li can both remove the potential barrier and reduce minority carrier recombination at an *individual* grain boundary has not been investigated. In this work, these questions are studied by temperature-dependent resistivity measurements and by the scanning laser spot (SLS) technique.

Polycrystalline-Si samples were cut from *n*-type, large-grain (mm size), single-pass Fz Si ingots with columnar grain structures. Identical grain boundaries can be found in samples cut from adjacent slices. Li was diffused from one side of the sample surface for 10 min to 1 h at 400°C. The potential barrier of a grain boundary before and after Li diffusion was determined by four-point probe temperature-dependent resistivity measurements in the temperature range 78–300 K on samples with a size of $\sim 1.0 \times 1.5 \times 10$ mm. The influence of Li on the reduction of minority-carrier recombination at a grain boundary was examined by precision SLS line scans on *p-n* junction cells made from this Si, before and after Li diffusion. Solar cells were fabricated. Only the areas in which the grain boundaries were distributed more uniformly were selected for this study. Cell parameters were measured both before and after Li diffusion.

Our experimental results indicate that Li can effectively remove potential barriers for almost every individual grain boundary but can only reduce the recombination at some grain boundaries, which agrees with our previous findings.[3] Since a grain boundary can involve very complicated defect configurations and possibly impurity segregation, the results presented in this paper may be applicable only to certain classes of grain boundaries. Even though Li may not be an effective passivation agent for certain grain boundaries as

far as the recombination mechanism is concerned, the incorporation of Li into the polycrystalline Si can lead to a better understanding of the physical and chemical properties of grain boundaries, which should be valuable in the search for a more effective way to passivate small-grain (~100 μm) polycrystalline Si.

---

1. Summary of paper: p. 1316 in *Proceedings of the Fifteenth IEEE Photovoltaic Specialists Conference—1981,* IEEE 81CH1644-4, New York, 1981.

2. Oak Ridge Associated Universities faculty participant from Walters State Community College, Morristown, Tenn.

3. R. T. Young et al., *Appl. Phys. Lett.* **38,** 628 (1981).

4. G. L. Miller and W. A. Orr, *Appl. Phys. Lett.* **37,** 1100 (1980).

EFFECT OF Li ON THE ELECTRICAL PROPERTIES OF GRAIN BOUNDARIES IN Si[1]

R. T. Young R. D. Westbrook
M. C. Lu[2] G. E. Jellison, Jr.

It is realized that improvements in cell efficiency of thin-film polycrystalline Si will result from a more detailed understanding of grain-boundary properties and their effects on cell performance. It has been demonstrated[3,4] theoretically and experimentally that grain boundaries may act as potential barriers to majority-carrier motion (and, conversely, as attractive potentials for minority carriers) and may contain high densities of minority-carrier traps. The discovery of a treatment for polycrystalline Si which removes or reduces the potential barriers and compensates the minority-carrier traps is considered a promising possibility for solving the grain-boundary problem. Seager, Ginley, and Zook[5] have indicated that treatment with atomic H can remove grain-boundary trapping states and reduce the minority-carrier recombination. However, it is not easy to introduce atomic H uniformly into the grain boundaries. We have obtained experimental evidence that grain boundaries can be passivated by the introduction of Li into polycrystalline Si.

Two types of polycrystalline Si were used in this study: large-grain *n*-type polycrystalline Si (MS-poly), with an average grain size of 1–2 mm, and small-grain *undoped* material (TI-poly), with an average grain size of ~25 μm, as determined by electron microscopy. Li was diffused from an oil suspension from one side of the sample surface fo 1 to 4 h between 300 and 400°C.

The electrical transport properties of Li-diffused polycrystalline Si were studied by van der Pauw measurements on TI-poly Si, in which the grain sizes are more uniformly distributed than they are in MS-poly Si. Figure 2.62 is a graph of the carrier mobility vs the measured carrier concentration of Li-diffused TI-poly Si. For comparison, a curve obtained from the same material doped by neutron transmutation is also included. There are two features of interest in Fig. 2.62: (1) the carrier mobility for both the NTD and Li-diffused samples increases with increasing carrier concentration and (2) the mobilities in the Li-diffused samples are consistently higher than those in the NTD samples. Our previous study of the carrier transport properties of NTD-doped TI-poly Si indicated that at a doping level of $>1 \times 10^{15}$ cm^{-3}, the concentration of free carriers begins to increase rapidly. At this and higher free carrier concentrations the calcu-

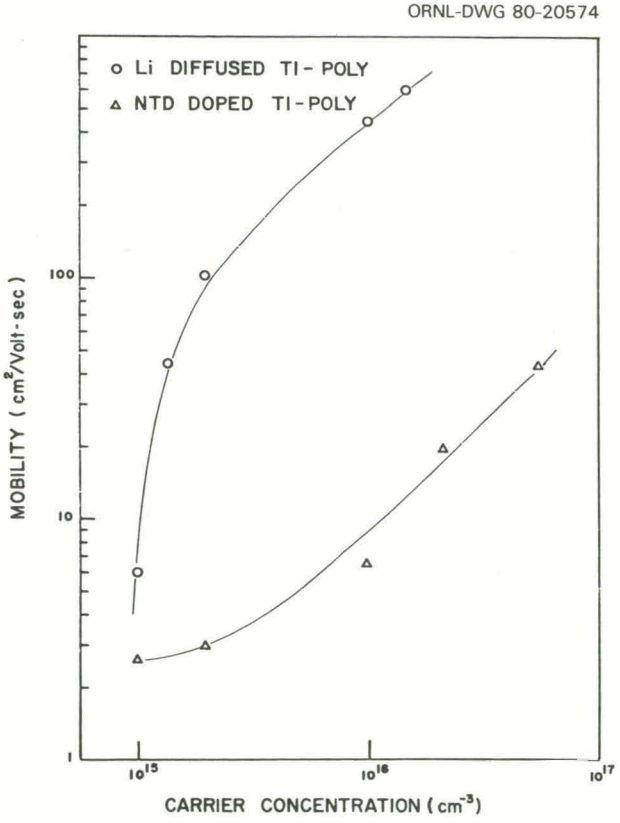

Fig. 2.62. Carrier mobility vs carrier concentration for Li-diffused and NTD polycrystalline Si.

lated barrier height V_B from Poisson's equation should be inversely proportional to the doping concentration N. If carrier transport across the boundaries is dominated by thermionic emission, the carrier mobility μ should be proportional to exp $(-eV_B/kT)$. The observed increase of μ with increasing N can then be explained, as previously reported by Seto.[3] Based on the Seto model, the observations of mobility at a fixed doping concentration should be a sensitive probe to monitor the changes in V_B. The fact that the carrier mobility of the Li-diffused samples is much higher than that of the NTD samples simply suggests that the potential barrier at the grain boundaries at a given dopant concentration can be effectively reduced by diffusion of Li into the polycrystalline Si.

To examine the effectiveness of Li in the reduction of minority-carrier recombination at the grain boundaries, a careful comparison of photoresponse maps generated by the SLS technique has been made on *p-n* junction solar cells before and after Li diffusion. A He-Ne laser, which gives radiation ($\lambda = 0.633$ μm) with an absorption depth of 2.8 μm in Si, was focused to a spot size $\sim$20 μm in diameter and was used as the light source in the measurements. The maps were obtained by rastering the laser beam over the sample with rotating galvanometer mirrors.

The effects of grain boundaries on the local photocurrent response produced by the He-Ne laser beam are shown in Fig. 2.63, which gives the comparison of the SLS map of the same area of a cell before and after Li diffusion. The two wide-band black images in the map, spaced 2 mm apart, are due to the light beam passing over the metal fingers on the top surface of the cell. The decrease of photocurrent, due to the minority-carrier recombination at the grain boundaries, is clearly shown in Fig. 2.63(a). Comparison of Figs. 2.63(a) and 2.63(b) shows that the recombination effects of some of the grain boundaries were significantly reduced after the introduction of Li into the cell.

In this study we demonstrated that Li may serve as a promising passivation agent for polycrystalline Si. However, caution needs to be taken in interpreting the effectiveness of the passivation. For example, one must separate the excess doping effect on the barrier height from the real passivation effect. Furthermore, the stability of Li in polycrystalline Si needs to be considered. Our preliminary

ORNL–DWG 80-17875

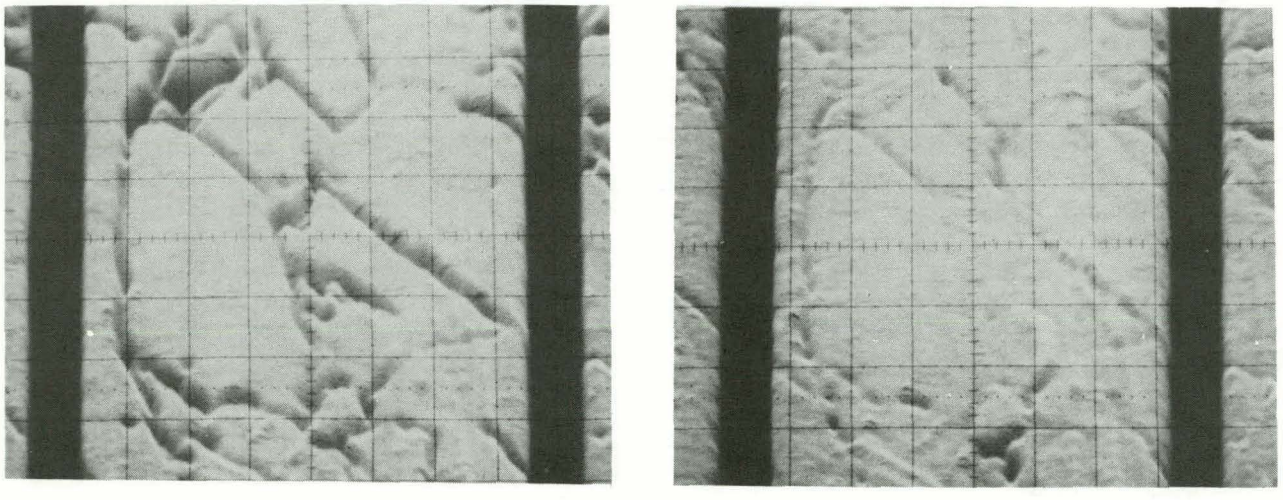

a b

Fig. 2.63. SLS maps showing the effect of Li passivation on grain boundaries: (a) before Li passivation, (b) after Li passivation.

results indicate that Li seems quite stable at room temperature for a period of two months. More quantitative information and long-term stability studies are needed to determine the actual potential of this process for improving polycrystalline Si solar cells.

1. Summary of paper: *Appl. Phys. Lett.* **38,** 628 (1981).

2. Oak Ridge Associated Universities faculty participant from Walters State Community College, Morristown, Tenn.

3. J. Y. W. Seto, *J. Appl. Phys.* **46,** 5247 (1975).

4. G. Baccarani, B. Ricco, and G. Spadini, *J. Appl. Phys.* **49,** 5565 (1978).

5. C. H. Seager, D. S. Ginley, and J. D. Zook, *Appl. Phys. Lett.* **36,** 831 (1980).

LASER-ANNEALED GASEOUS-DISCHARGE IMPLANTED Si[1]

R. D. Westbrook R. T. Young

It is known that shallow layers of dopant elements can be implanted in Si samples by bombarding a Si cathode with positive dopant ions in a simple, inexpensive gaseous-discharge chamber. As with any ion-implantation process, annealing is required to remove the damage created by ion bombardment. The purpose of this work is to study the effectiveness of pulsed-laser annealing techniques on gaseous-discharge implanted Si.

Most of the experiments were done on single-crystal Si with a resistivity range 5–10 ohm-cm. BF_3 and PF_5 were used as the dopant sources, and the gas flowed continuously through the discharge chamber during each run. Total charge transfer varied from ~0.1 to 2.0 C cm^{-2}, but calculation of the exact amount of dopant implanted is difficult because of the presence of several multiply ionized complexes.

It was found that the annealing energy density requirement using a 25-ns pulse from a ruby laser is similar to that needed for annealing damage from standard ion implantation (i.e., about 1.0–1.3 J cm^{-2}). Energy densities less than that resulted in incomplete activation of the dopant, lower mobilities, and poor characteristics for solar cells made from implanted samples.

The best cells were obtained with laser annealing performed at 400°C substrate temperature which gave open-circuit voltages around 560–570 mV. In all cases the short-circuit current density was about 21–22 mA cm^{-2}, with no AR coating, which is comparable to cells made by other methods. The short-circuit current density appeared to be relatively insensitive to the total implanted dopant concentration.

1. Summary of abstract: p. 1070 in *Extended Abstracts of the 158th Electrochemical Society Meeting–1980,* The Electrochemical Society, Pennington, N.J., 1980.

DEVELOPMENT OF Si CHEMICAL VAPOR DEPOSITION SYSTEMS WITH IN SITU LASER-IRRADIATION CAPABILITY

G. A. van der Leeden R. T. Young
L. S. Darken, Jr.

Chemical vapor deposition (CVD) has developed into one of the most important film-growth technologies of the semiconductor industry in the past decade. Apart from the practical applications, it constitutes an interesting field for fundamental material studies, especially in conjunction with recently developed laser-processing techniques. These techniques are expected not only to broaden the range of attainable film properties but also to add flexibility to semiconductor device design.

A versatile cold wall horizontal CVD Si system was designed, built, and put into operation during the last year. This system has the capability for growing amorphous, polycrystalline, and single-crystal films on substrates at well-controlled temperatures in the range 400–1100°C. Either dichlorosilane (SiH_2Cl_2) or silane (SiH_4) is used as the Si source gas; dilute hydrogen-diborane (B_2H_6) and hydrogen-phosphate (PH_3) mixtures are used as the dopant sources. Ultrahigh purity H is the carrier gas. A laser beam can be introduced into the reactor chamber by a 45° reflection mirror mounted directly above the sample position. With this arrangement, low-temperature film deposition with intermittent liquid-phase crystallization can be studied. Controllable dopant levels, via the conventional CVD process, are usually in the range

10^{16}–10^{19} cm^{-3}. With the aid of laser processing, good quality epitaxial films with dopant concentrations at least one order of magnitude higher than those obtained by conventional CVD have been grown.

Other studies, including the growth of good quality polycrystalline films on low-cost substrates and the control of interface diffusion are currently under investigation.

IN SITU LASER CRYSTALLIZATION OF THIN Si FILMS DEPOSITED BY LOW-TEMPERATURE CVD

G. A. van der Leeden R. T. Young
J. Narayan

The growth of high-quality thin epitaxial films on single-crystal substrates with a well-controlled dopant redistribution at the growth interface has been a subject of investigation for years. The device applications include bipolar technology, transistors, high-frequency microwave diodes, etc. The epitaxial process currently used in device fabrication is based primarily on CVD of SiH_2Cl_2 or SiH_4 at 1000–1100°C under atmospheric pressure. With this high-temperature process, dopant redistribution at the growth interface is virtually impossible to control. Furthermore, due to the relatively high deposition rates at these temperatures, it is very difficult to control the film thickness when a thin (0.2–0.3 μm) active layer is required for devices.

The objective of the present work is to explore the use of laser irradiation of Si in situ with the CVD process to grow high-quality epitaxial films at low temperatures (500–700°C) so that good control of the film thickness and interfacial dopant diffusion can be obtained. In preliminary experiments, Si films with a thickness of 0.3–1.0 μm were deposited on (100) and (111) Si substrates at 660°C using a silane source (0.35% in H_2) with a deposition rate of 150 Å/min. The as-deposited films had grain sizes of less than 1 μm. In situ laser recrystallization was performed with a pulsed ruby laser operating in the energy range of 0.5–0.7 J/cm^2 by irradiating the sample with a single 25-ns pulse after every ~500–1000-Å deposition without interrupting the deposition process. Single-crystal films were obtained in all cases. However, TEM investigations indicated that dislocations were present; their densities decreased from $\sim 10^6$/cm^2 in the vicinity of the substrate interface to $\sim 10^3$/cm^2 at the surface. We believe that these dislocations were formed during laser recrystallization by localized strain fields originating from contamination-induced microinclusions in the as-deposited film or from contaminants at the substrate surface itself. We found that they can be reduced greatly or removed completely when the completed epitaxial layer is irradiated with a final high-energy (2.0 J/cm^2) laser pulse. Methods for controlling the dislocation density and contamination are being investigated.

DOPANT ION REDISTRIBUTION DURING PLA OF ION-IMPLANTED GaAs[1]

R. F. Wood D. H. Lowndes
W. H. Christie[2]

In this summary we illustrate the results of recent studies of the redistribution of implanted dopants resulting from pulsed ruby laser annealing of GaAs and compare experimental dopant redistribution profiles and experimental durations of surface melting (the latter measured by TRR) with the predictions of the melting model[3] of PLA.

The unencapsulated GaAs samples implanted with 150-keV Zn and 35-keV Mg ions at doses of 5×10^{15} ions/cm^2 were irradiated at room temperature with single pulses (FWHM duration = 15–25 ns) from a ruby laser operating under multimode conditions, with the laser beam spatially homogenized using a bent diffusing light pipe. The results of electrical properties measurements on these and similar samples are described in an accompanying paper by Lowndes, Cleland, and Westbrook[4] in this report. SIMS measurements were obtained, in some cases with the samples overcoated with 30–50 nm of spectrographic grade carbon to eliminate spurious ion signals that would be generated by unfocused components of the primary ion beam. Uncertainties in the SIMS depth and concentration scales are each estimated to be ±10%. Dopant ion losses during PLA were estimated from the integrated numbers of secon-

dary ion counts. Essentially no losses were observed for the Mg-implanted samples, but the Zn-implanted samples showed losses monotonically increasing from ~2 to ~20%, for laser energy densities E_l in the range $0.5 \leq E_l \leq 1.0$ J/cm^2.

Several methods for calculating dopant diffusion during PLA have been described.[5] We have used these methods and the melt-front profiles to calculate the liquid-phase diffusion profiles of Mg and Zn in GaAs; the results for Mg are shown in Fig. 2.64 together with the SIMS data. Values of the

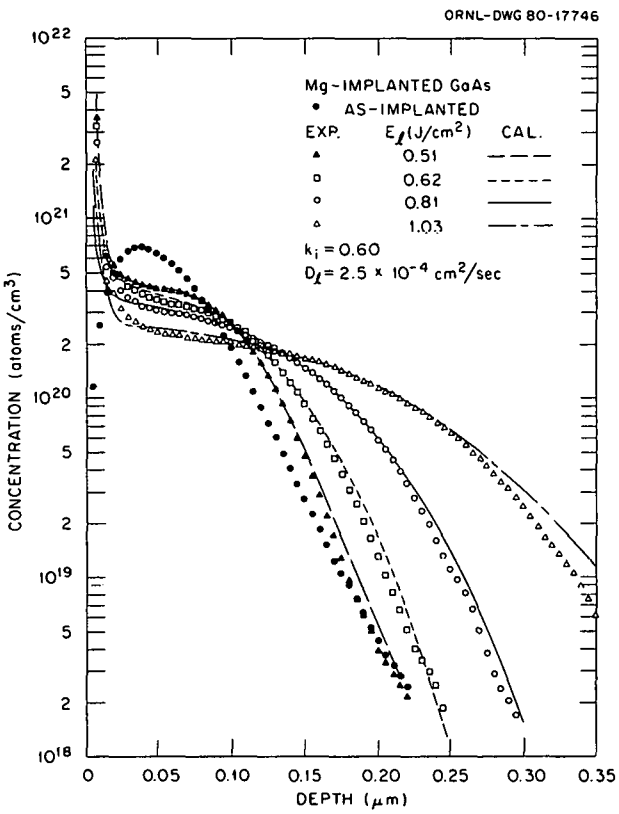

Fig. 2.64. Experimental and calculated profiles of Mg in GaAs.

diffusion coefficient D_l for dopants in liquid GaAs are not known, but we assumed that they would be of the same magnitude as D_l in Si. We first tried to fit the Mg data with $D_l = 5 \times 10^{-4}$ cm^2/s, but this gave results incompatible with the calculated melt-duration times. We eventually found that $D_l = 2.5 \times 10^{-4}$ cm^2/s gave good fits to the experimental curves, as indicated in Fig. 2.64. Since the Mg profiles show clear evidence of surface segregation, we also had to determine an appropriate value of the interface segregation coefficient k_i. The necessity to fit both the surface segregation "spike" and the profile far below the surface severely constrains k_i, and a few calculations were sufficient to determine that $k_i \simeq 0.6$. It should be emphasized that this value of k_i is not appropriate for crystallization under equilibrium conditions but is characteristic of nonequilibrium segregation during ultrarapid (~3 m/s) solidification.

The theoretical fits to the Zn data were somewhat less satisfactory than those to the Mg data. The SIMS measurements of the Zn profiles showed that there were substantial losses of Zn during laser annealing at the higher energy densities. Although the computer programs allow for dopant loss, such losses complicate the fitting procedure. Moreover, because of inherent difficulties with SIMS measurements in the close vicinity of the surface, the position of the surface in the experimental data is not known with great accuracy. In spite of this difficulty with the Zn data, the fit between experiments and calculations is quite satisfactory, for both Mg and Zn.

We conclude that by fitting a family of dopant redistribution profiles corresponding to various laser energy densities, both k_i and D_l may be simultaneously determined. In fact, the method used here appears to provide the only measurements available for diffusion coefficients of dopant ions in molten GaAs.

---

1. Summary of paper: p. 231 in *Laser and Electron Beam Solid Interactions and Materials Processing,* ed. by J. F. Gibbons, L. D. Hess, and T. W. Sigmon, North Holland, New York, 1981.
2. Analytical Chemistry Division, ORNL.
3. R. F. Wood and G. E. Giles, "Macroscopic Theory of Pulsed-Laser Annealing: I. Model for Thermal Transport and Melting," this report.
4. D. H. Lowndes, J. W. Cleland, and R. D. Westbrook, "Electrical Properties of Ion-Implanted, Pulsed-Laser Annealed GaAs," this report.
5. R. F. Wood, J. R. Kirkpatrick, and G. E. Giles, *Phys. Rev. B* **23,** 5555 (1981); "Macroscopic Theory of Pulsed-Laser Annealing: II. Dopant Diffusion and Segregation," this report.

ELECTRICAL PROPERTIES OF ION-IMPLANTED, PULSED-LASER ANNEALED GaAs[1]

D. H. Lowndes J. W. Cleland
R. D. Westbrook

During the past several years, PLA of ion-implanted Si has been shown to be well suited for formation of high-quality *p-n* junctions. In contrast, little application has been made of similar pulsed-laser techniques for the formation of *p-n* junctions in compound semiconductors. The purposes of the present study were (1) to determine whether there exists an energy density E_l "window" for PLA that results in high electrical activation of implanted ions, (2) to select ion-implanted species which provide the highest electrical activation and carrier mobility, (3) to determine spatial homogeneity requirements on the pulsed-laser beam to ensure uniform annealing and junction depth, and (4) to measure the electrical properties of *p-n* junctions formed by the ion implantation–PLA technique in GaAs.

Single-crystal (100) semiconducting GaAs wafers (doped $\sim 1 \times 10^{17}/cm^3$, opposite in carrier type to the implanted ions) were implanted with 80- and 150-keV Zn, 35-keV Mg, 85- and 160-keV Se, and 80-keV Si ions (all singly ionized) to doses of 1 and $5 \times 10^{15}/cm^2$. Samples were irradiated using single pulses from a ruby laser ($\lambda = 0.694$ μm, duration = 20–25 ns). The pulsed ruby laser beam was homogenized by passing it through a bent, diffusing fused-silica light pipe.

Figure 2.65 summarizes the results of Hall effect and sheet resistivity measurements that were carried out using the van der Pauw technique in order to evaluate the electrical properties of the shallow p^+ layers formed by ion implantation–PLA on *n*-GaAs substrates. The mean electrical activation [Fig. 2.65(a)] for $5 \times 10^{15}/cm^2$ Zn or Mg implants is 80 ± 5%, within a laser energy density window $0.4 \leq E_l < 0.8$ J/cm^2; there is also some evidence that the more shallow Zn implant produces still higher activation near 0.4 J/cm^2. These are the highest dopant ion activations reported to date for PLA of GaAs and are equal to the best results obtained via thermal annealing of GaAs. The Hall mobility [Fig. 2.65(b)] within the highly doped ion implanted–PLA near-surface region is a linearly increasing function of E_l up to $E_l = 0.8$ J/cm^2, above which the mobility decreases sharply, in conjunction with the onset of easily visible laser damage to the samples' surfaces. Thus, there is a

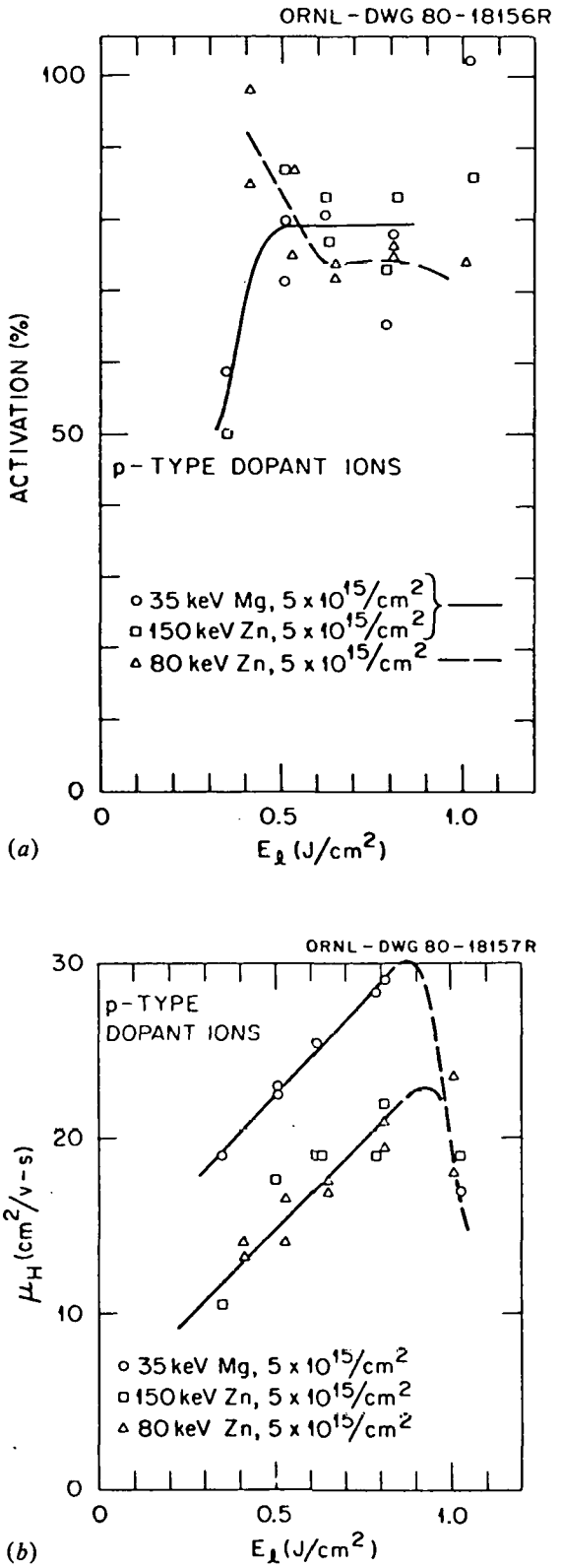

Fig. 2.65. (a) Percent electrical activation vs E_l for *p*-type implants and (b) Hall mobility vs E_l for *p*-type implants.

well-defined energy density window, $0.4 \leq E_I < 0.8$ J/cm^2, within which annealing of shallow ion implants in GaAs can occur. The upper bound is determined by the onset of catastrophic damage due to vaporization, while the lower bound is determined by the requirement of melting fully through the heavily damaged ion-implanted layer, so that epitaxial regrowth from the single-crystal substrate beneath can occur, in good agreement with the recrystallization threshold observed directly via TEM.

For the *n*-type implants Si and Se, the electrical activations obtained by PLA were lower, the best result being ≲40% activation for 1×10^{15} Si ions/cm^2, for $E_I \sim 0.45$ J/cm^2.

SIMS measurements also showed a well-behaved increasing penetration of the dopant profile with increasing E_I, suggesting that laser-beam spatial inhomogeneity is probably not a limiting factor in forming well-defined *p-n* junctions in GaAs. However, forward-diode characteristics clearly indicated a nonideal diode structure for the p^+-*n* junctions formed by ion implantation–PLA of *p*-type dopant ions (which produced the highest electrical activation).

A combination of capacitance-voltage measurements, model calculations, and SIMS and TEM defect studies was found to be consistent with a model in which defects formed during ion implantation diffuse well beyond the original implantation range during the laser annealing step, producing compensation of the substrate material and resulting in the presence of a semi-insulating layer where one would expect the junction to be. TEM and SIMS studies indicated that the most likely defects are arsenic vacancies, with compensation occurring in the Si-doped *n*-type substrate material through formation of either Si-As vacancy complexes or by Si atoms filling As-sublattice vacancies and acting as acceptors. The resulting diodes have a p^+-*i*-*n* structure rather than p^+-*n*.

Thus, even though implantation lattice damage can be almost entirely removed by PLA, the presence of a defect-induced semi-insulating layer in the junction region appears to be the limiting factor in obtaining useful *p-n* junctions in GaAs by the ion implantation–PLA technique.

1. Summary of paper: p. 45 in *Proceedings of the 15th IEEE Photovoltaic Specialists Conference*, IEEE 81CH1644-4, New York, 1981.

TIME-RESOLVED REFLECTIVITY DURING PULSED-LASER IRRADIATION OF GaAs[1]

D. H. Lowndes R. F. Wood

In this work we report the results of the first systematic TRR measurements on crystalline and ion-implanted GaAs, and their comparison with thermal-melting model calculations. GaAs samples were irradiated in air at room temperature, using single pulses (~12 ns duration) from a ruby laser operated in the TEM_{00} mode. A probe beam (≲1 mm diam) from a low-power (~5 mW) unpolarized cw He-Ne laser was incident at 45° on a polished (100) face of the sample. The reflected-probe beam was passed first through a bandpass filter centered at the He-Ne wavelength (633 nm) and then was detected by a high-speed ($\tau_r \sim 150$ ps), reverse-biased Si PIN diode connected directly to a Tektronix Model-7834 storage oscilloscope ($\tau_r \sim 2$ ns).

Figure 2.66 shows melt duration τ vs pulsed-laser energy density E_I for crystalline GaAs and for GaAs implanted with 160-keV Se ions at a dose of 5×10^{15} ions/cm^2. Also shown are the results of Auston et al.,[2] for a GaAs sample implanted with 50-keV Te ions to a dose of 1×10^{16} ions/cm^2. The results in Fig. 2.66 provide the first comparison of melt durations for laser-irradiated crystalline c- and amorphous a-GaAs.

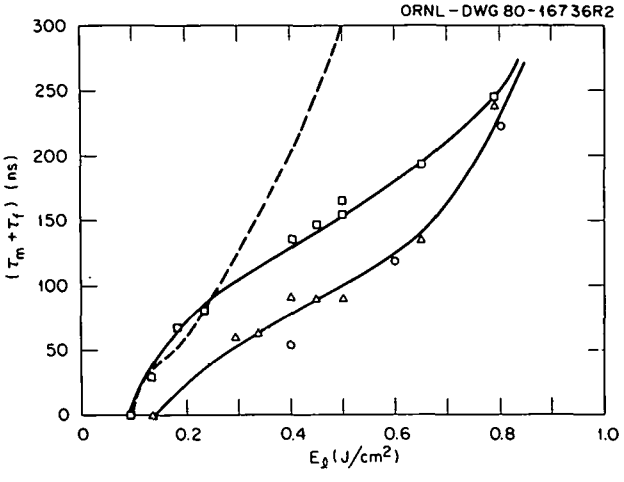

Fig. 2.66. Melt duration vs laser energy density for crystalline and ion-implanted GaAs samples: △, unimplanted c-GaAs; □, 160-keV Se, 5×10^{15}/cm^2; ---, 50-keV Te, 1×10^{16}/cm^2 (from ref. 2); ○, calculations (ref. 4). The solid lines are smooth curves passing through the experimental data points.

Near the threshold ($E_I \simeq 0.2$ J/cm^2) for attaining the maximum reflectivity, there is good agreement between the curves for the Se- and Te-implanted samples, and there are clear differences between them and the curve for the c-GaAs samples. These observations, together with the results of melting model calculations, suggest that the energy stored in the ion-implanted region prolongs the surface melting. Either the melting point or the latent heat of fusion, or both, may be lower for a-GaAs than for c-GaAs. This explanation is consistent with both the lower melt threshold and the longer melt durations that are observed for a-GaAs.

In the intermediate E_I range ($E_I \sim 0.5$ J/cm^2), τ for the Se- and Te-implanted samples differs by a factor of 2. However, model calculations, using reasonable combinations of the thermal and optical parameters of a-GaAs, were unable to reproduce this wide range of τ. To clarify this result, we conducted an additional set of experiments; using $E_I = 0.4$–0.5 J/cm^2, Se-implanted samples were subjected to repeated (up to 5) laser irradiations, and τ was measured each time. Although there was some variation in τ from pulse to pulse, the durations for a given sample never decreased to the substantially lower value for c-GaAs, even though TEM showed that these initially amorphous samples epitaxially recrystallized after a single irradiation at $E_I > 0.36$ J/cm^2. We, therefore, interpret the differences in τ for all three sets of samples for the higher E_I, as due primarily to chemical effects arising from substantial differences in the doping of the near-surface region. SIMS measurements showed that Se does segregate toward the sample surface as a result of PLA, with a mean Se concentration $\geq 2 \times 10^{20}$ atoms/cm^3 found in the first 0.1 μm below the surface following annealing at 0.5 J/cm^2.

Figure 2.66 also shows the results of calculations of the melt duration for c-GaAs.[3] The agreement between the calculated and measured melt durations is very good for c-GaAs. For $E_I > 0.8$ J/cm^2, the TRR for GaAs changes both qualitatively and quantitatively. These observations are in good agreement with model calculations which predict the onset of vaporization of c-GaAs at $E_I \gtrsim 0.8$ J/cm^2.[3] Dopant profiles, resulting from laser annealing of Mg and Zn implants in GaAs, were also calculated as functions of E_I, using calculated melt durations that differed only slightly from those for c-GaAs, and were found to be in good agreement with experimental SIMS profiles.[3] This result again supports the idea that the longer surface durations for the maximum reflectivity in Se- and Te-implanted GaAs are more characteristic of departures from stoichiometry and the formation of lower melting point liquids very near the surface than of stoichiometric GaAs. Inspection of the Ga-Se (Ga-Te) phase diagram shows a number of intermediate alloys and compounds with melting points around 1000°C (800°C), in addition to pure Ga (30°C). The model calculations also predict a threshold at $E_I \simeq 0.2$ J/cm^2 for melting to a depth of ~200 Å (equal to one optical skin depth at the He-Ne probe laser wavelength) in excellent agreement with the observed thresholds of ~0.22 (~0.18) J/cm^2 for c- (Se-implanted) GaAs.

---

1. Summary of paper: *Appl. Phys. Lett.* **38,** 971 (1981).

2. D. H. Auston et al., *Appl. Phys. Lett.* **34,** 777 (1979).

3. R. F. Wood, D. H. Lowndes, and W. H. Christie, p. 231 in *Laser and Electron Beam Solid Interactions,* ed. by J. F. Gibbons, L. D. Hess, and T. W. Sigmon, North Holland, New York, 1981.

PHOTOLUMINESCENCE OF PULSED-LASER-IRRADIATED *n*- AND *p*-GaAs[1]

D. H. Lowndes B. J. Feldman[2]

Recent studies of ion implantation followed by PLA in GaAs showed that nonideal electrical characteristics resulted for these p^+-n junctions.[3] It was postulated that this nonideality was the result of arsenic vaporization followed by formation of arsenic vacancy substrate-dopant ion complexes in the junction region. The purpose of the photoluminescence study reported here was to evaluate the effects of ion implantation and pulsed ruby laser irradiation, separately and in combination, on radiative recombination pathways in GaAs. The principal result of our study is that no photoluminescence is observed in GaAs subjected to high-dose ($\geq 10^{15}$ ions/cm^2) ion implantation, either with or without subsequent pulsed-laser annealing.

Both n-type (Si-doped ~6×10^{16}/cm^3) and p-type (Zn-doped ~1×10^{17}/cm^3) c-GaAs samples were used. Zn ions with 150-keV energy (projected range ~595 Å) were implanted to a dose of 5×10^{15}/cm^2 in some of the n-type samples, while

80-keV Si ions (projected range ~677 Å) were implanted at a dose of $1 \times 10^{15}/cm^2$ in some of the p-type wafers. All samples were irradiated at room temperature using single 20–25-ns pulses from the spatially homogenized beam of a ruby laser ($\lambda = 0.694$ μm). Photoluminescence spectra were obtained following PLA at both 77 and 300 K with samples mounted inside a variable temperature dewar. Photoexcitation was provided by a 100-mW, unfocused, 0.514- or 0.458-μm argon ion laser beam, with the photoluminescence dispersed by a grating monochromator and detected with a cooled-Ge photodiode.

Unirradiated control samples exhibited photoluminescence spectra centered near the GaAs band edge (1.3–1.5 eV range) for Zn-doped material or broadened and shifted toward the midgap region (0.7–1.3 eV) for Si-doped GaAs. However, irradiation of p- or n-type c-GaAs at $E_l = 0.6$ J/cm^2 resulted in a somewhat uniform reduction in photoluminescence intensity (in comparison with unirradiated samples), with the reduction more pronounced for p-type material and a shift of all spectra toward longer wavelengths. This pulsed-laser energy density lies in the center of the range of laser annealing energy density ($0.4 \leq E_l < 0.8$ J/cm^2), which we earlier found produced high activation of p-type ion implants in GaAs.[3] TRR measurements and model calculations show that $E_l = 0.6$ J/cm^2 should produce melting to a depth ~3300 Å in c-GaAs; by considering the much shorter absorption lengths (~550–1200 Å) for light at the photoexcitation wavelengths used, it was shown that the changes in photoluminescence spectra that were found are representative of bulk (not surface) processes of photoexcited electron-hole pairs that were produced entirely within material that was melted and recrystallized by the pulsed laser.

The complete lack of photoluminescence from high-dose ion-implanted samples, whether laser annealed or not, contrasts strongly with TEM cross-section micrographs and selected area diffraction patterns, which show unequivocally that pulsed ruby laser irradiation at $E_l \geq 0.4$ J/cm^2 is sufficient to produce complete epitaxial recrystallization of the ion-implanted samples used in this work. Thus, the present photoluminescence measurements allow us to infer that PLA (to within a photoluminescence detection sensitivity of $\sim 10^{-3}$) results only in nonradiative recombination centers in GaAs. These defects are probably the same, or closely related to, electrically active defects which strongly influence the electrical properties of ion-implanted laser-annealed GaAs.

1. Summary of paper to be published.
2. University of Missouri, St. Louis, Mo.
3. D. H. Lowndes, p. 45 in *Proceedings of the 15th IEEE Photovoltaic Specialists Conference,* IEEE 81CH1644-4, New York, 1981.

EFFECT OF SUBSTRATE RELIEF PATTERNS ON THE MORPHOLOGY OF Si CRYSTALLIZATION

L. S. Darken D. H. Lowndes
G. A. van der Leeden

The effect of a square-wave relief pattern in the substrate on the morphology of Si films grown on these substrates has been investigated for a variety of growth techniques to determine the suitability of these techniques for producing large-grain (>100 μm) Si films for solar cell fabrication. If nucleation can be induced at the relief groove corners, minimization of anisotropic surface energy may determine a unique crystallographic orientation for all nuclei, and a large-grained film should be obtained. The square-wave relief pattern was produced in thermally grown SiO_2 substrates by photolithographic and reactive ion etching techniques, similar to those reported by Geiss, Flanders, and Smith.[1] The acuity of the relief pattern is shown in Fig. 2.67. The periodicity and depth of the pattern shown are typical for the work performed.

Si hypereutectic (Si-rich) melts were formed by heating Si/Au couples evaporated on a patterned-SiO_2 substrate. These melts were slowly cooled (1°C/min) to allow Si to precipitate and grow as close to thermal equilibrium as possible. After complete cooling, the Au was removed by aqua regia, and the remaining Si was examined. Nucleation of the Si occurred at the melt/SiO_2 interface, preferentially in the groove corners, but the nuclei were not preferentially oriented crystallographically in the plane of the substrate.

Fine-grain (<0.1 μm) Si films 0.5 μm thick that had been deposited on a patterned substrate were recrystallized using a hydrogen torch. If the duration of melting was brief, the film did not coalesce

ORNL-DWG 81-20678

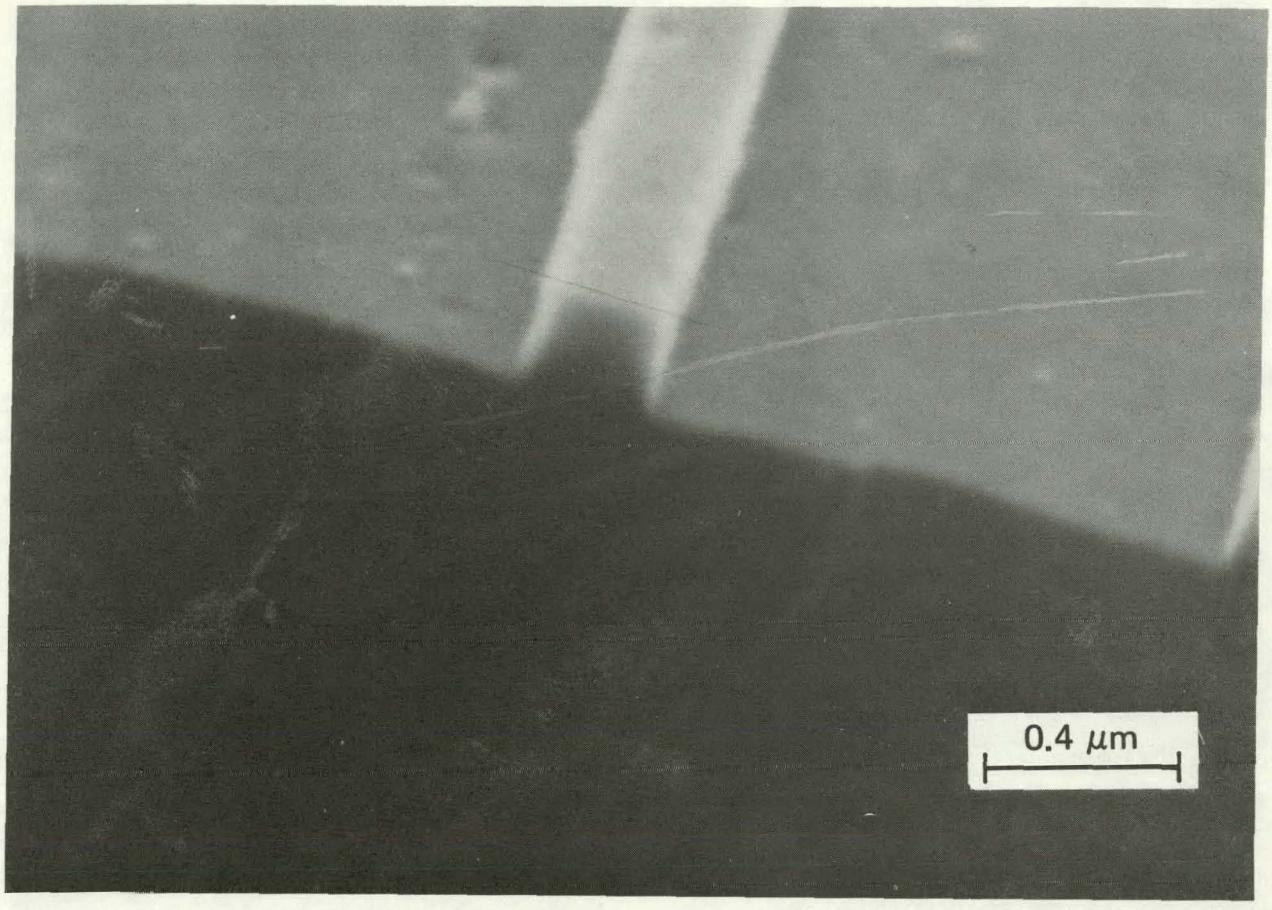

Fig. 2.67. SEM micrograph of substrate after reactive ion etching of square-wave pattern.

into droplets, but it recrystallized as a continuous film. Grain size increased to about 50 μm. Grain boundaries tended to follow the grating structure.

Fine-grain Si films on patterned SiO_2 substrates were pulsed-laser annealed with a ruby laser using a variety of parameter values, namely, energy density ranging from 0.1 to 1.3 J/cm^2, pulse repetition to 10 pulses, Si thickness 0.2–1.5 μm, oxide thicknesses 0.2–1.0 μm, pattern periodicity 1.5–8.9 μm, groove depth 0.1–0.5 μm, and with various degrees of substrate heating to 600°C. Reflectivity measurements were performed to determine the onset of melting. Higher energy densities and higher substrate temperatures promoted larger grain growth. Full exploitation of these trends was prevented by vaporization of the Si. Repetition of annealing pulses did not significantly promote grain growth at any energy density. The largest grains formed were on the order of 1 μm. A typical result is shown in Fig. 2.68. Here, larger grains grew on the higher plateau of the square-wave pattern. Crystallization apparently proceeded laterally from both sides, joining in a seam down the middle of the raised relief structure. We conclude that the techniques investigated do not appear to possess the potential for practical application to substrate fabrication.

---

1. M. W. Geiss, D. C. Flanders, and H. I. Smith, *Appl. Phys. Lett.* **35,** 71 (1979).

ORNL-DWG 81-20679

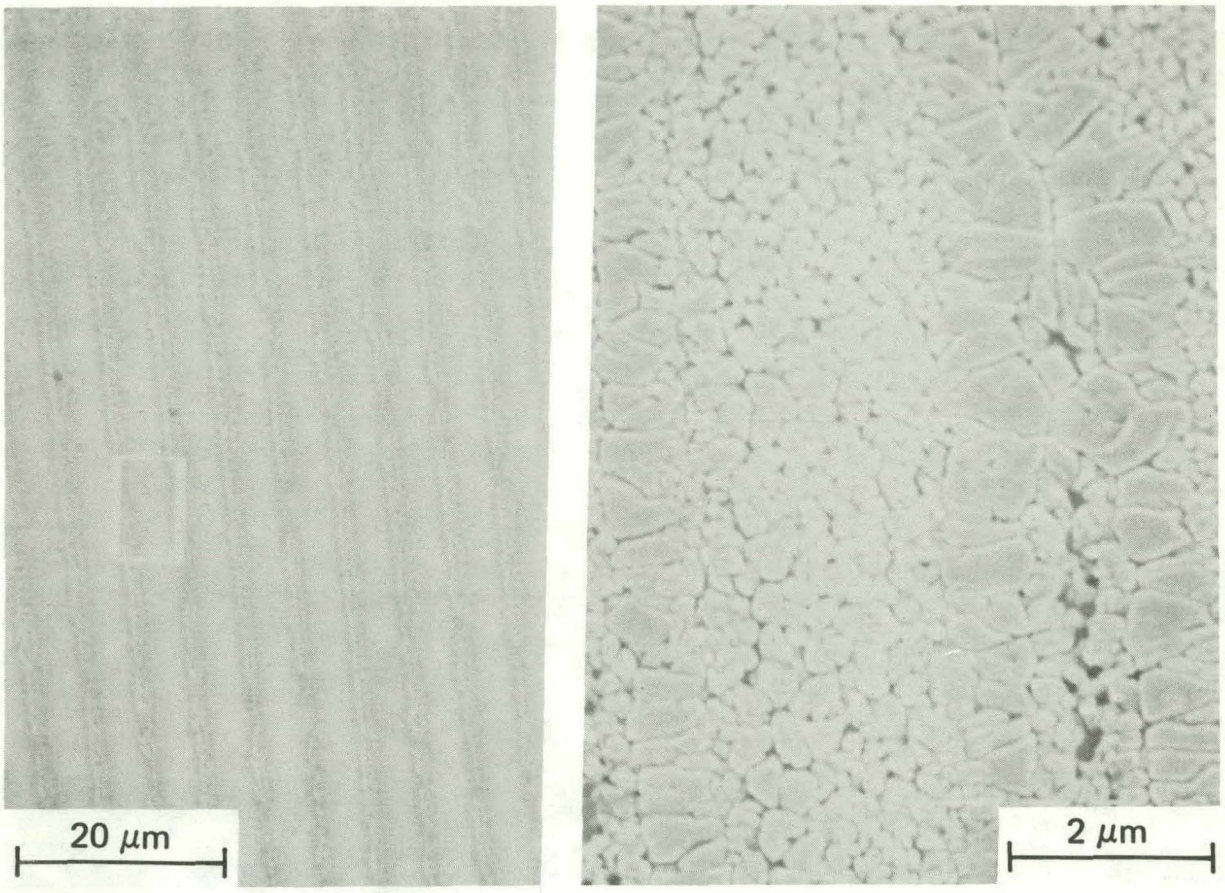

Fig. 2.68. SEM micrograph of a pulsed-laser-annealed Si film on a square-wave patterned oxide. The grain boundaries were revealed by Secco etching.

CRYSTALLOGRAPHIC ORIENTATION OF ELECTRODEPOSITED TIN BY SUBSTRATE RELIEF STRUCTURE

L. S. Darken D. H. Lowndes

Techniques for pattern definition of micron and submicron features in thermally grown SiO_2 have been developed for the integration and miniaturization of circuits on Si chips. This technology has been applied to the investigation of the effects of substrate-relief structure (usually a square-wave pattern) on the crystallographic orientation of deposited films.[1,2] The strategy is to fabricate features with corner radii smaller than the radius of the critical nuclei for crystallization, anticipating that the anisotropy of the surface energy will cause the individual nuclei to be oriented uniquely.[3] We report the orientation of electrodeposited tin islands by a square-wave relief pattern formed in the cathode of an electrolytic cell. A deposition is shown in Fig. 2.69.

Square-wave patterns in substrates were prepared by reactive ion etching SiO_2 through photolithographically produced Cr masks. The techniques employed were similar to those described by Geiss et al.[2] Typically, the square wave had a depth of 0.1 μm and a periodicity of 2.7 μm. The patterns were metallized for electrical continuity by evaporation of thin (100 Å) films of Cr, Si, or Au. Two evaporations with the substrate tilted in opposite directions were necessary to ensure coverage of the pattern.

In addition to the patterned cathode, the cell consisted of a platinum anode and an electrolyte containing stannous tin (4.75 g/L $SnCl_2 \cdot 2H_2O$, 5.6 g/L NaOH, 50 g/L NaCN). Potentials were

ORNL-DWG 81-20680

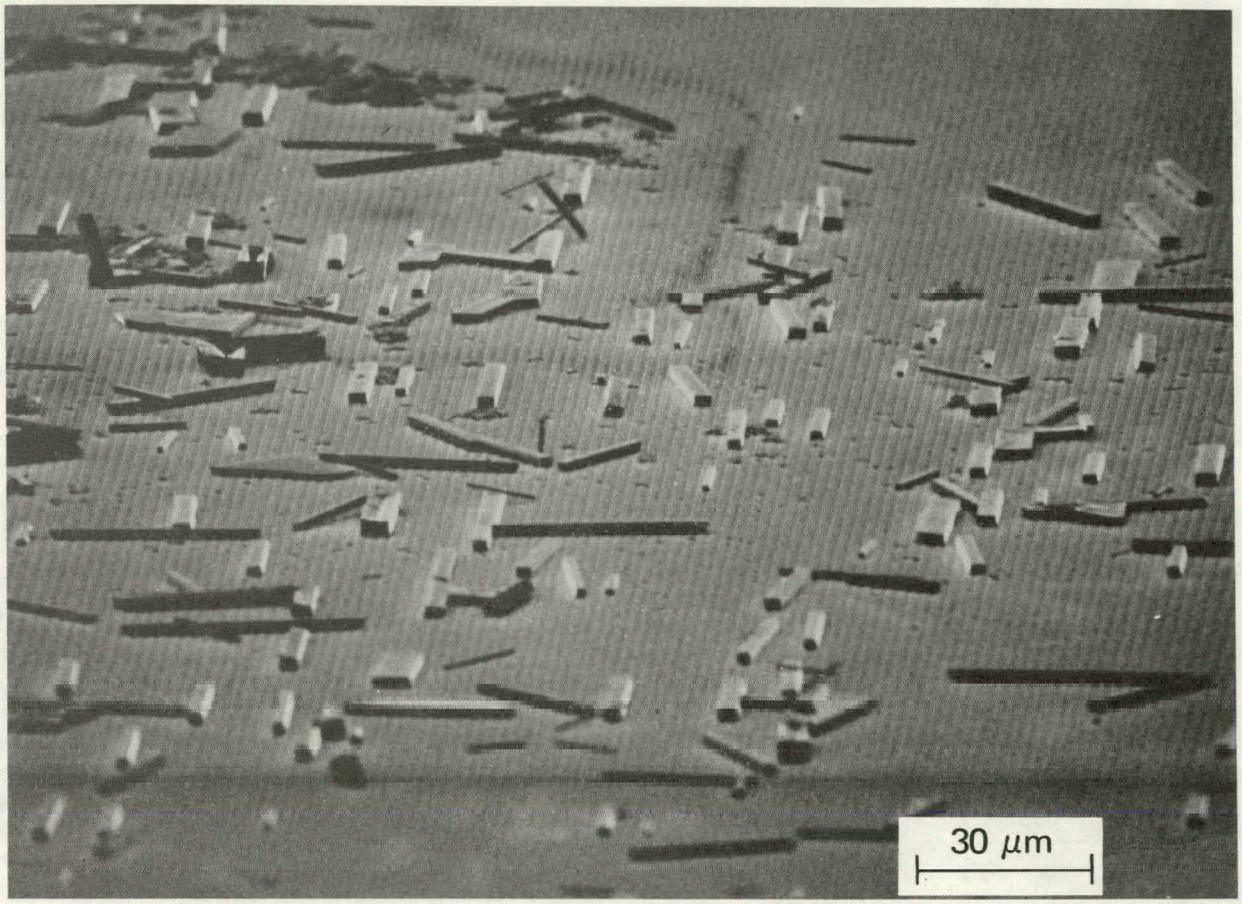

Fig. 2.69. SEM picture of electrodeposited tin on a patterned substrate.

measured with respect to a saturated calomel electrode (SCE). The system was purged by bubbling argon.

Highly oriented islands were formed at overvoltages η in the range 0.02 to 0.60 V. Islands had the form of elongated parallelepipeds with sides parallel to the {100}, {010}, and {001} crystallographic planes of tin. These islands grew with remarkable regularity as shown in Fig. 2.70. Orientation of the ⟨001⟩ crystallographic axis with the grating direction was observed on Cr-, Si-, and Au-coated substrates at both 23 and 70°C.

Tin was also deposited from a halogen electrolyte ($SnCl_2 \cdot 2H_2O$, 75 g/L; NaF, 25 g/L; KHF_2, 50 g/L; NaCl, 45 g/L) but the islands were square, and the tendency to orient, though present, was less pronounced. Similar results were obtained with a fluoborate bath [$Sn(BF_4)_2$, 200 g/L; HBF_4, 150 g/L]. The fluoborate bath had the undesirable feature of attacking the SiO_2 through any defects in the metallization.

Analysis of the x rays produced by fluorescing the deposits with the electron beam in an SEM revealed no second component in the tin deposits. Sensitivity was in the range 0.1–1% per element.

The crystallographic orientations of the islands were investigated with an x-ray diffractometer. In this technique, a large fraction of the substrate is irradiated; therefore, the orientations of many nuclei are averaged. The distribution of the ⟨100⟩ axis about the substrate normal was extremely narrow, ~0.2° FWHM. The distribution of the ⟨001⟩ axis about the grating direction was broader, ~5° FWHM.

ORNL-DWG 81-2068

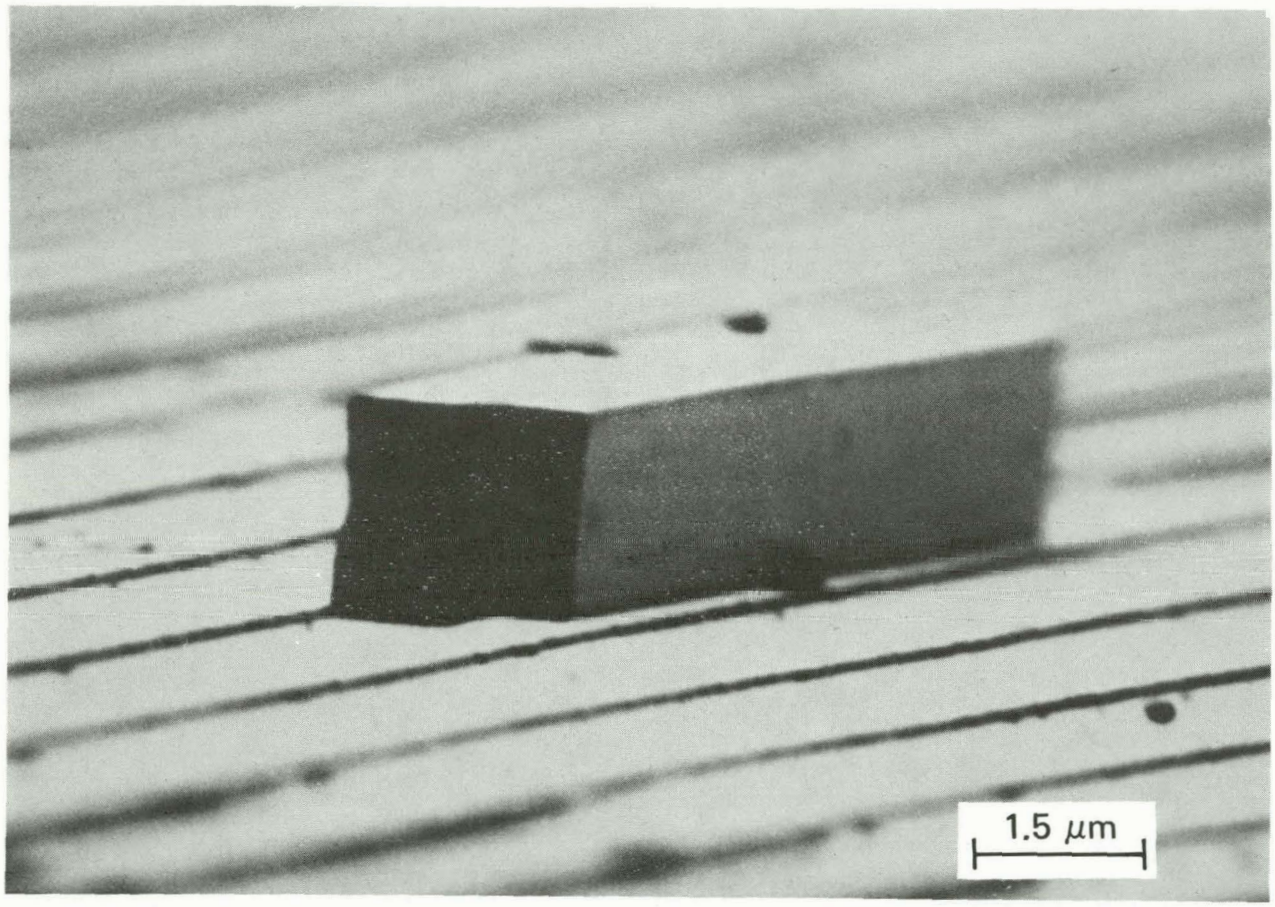

Fig. 2.70. SEM picture of individual tin island.

It is evident from the extreme elongation of the islands in Fig. 2.69 that their regular shape at this stage is not due to minimization of surface energy. Rather, these are growth forms bounded by the slowest growing crystal planes. To investigate nucleation, deposition was interrupted at an early stage, and the substrate was examined. Rectangular nuclei were found growing from the corners of the square-wave pattern.

In classical nucleation theory, the critical radius r^* is defined as the radius of the smallest stable nuclei. Ignoring anisotropy in surface energy, $r^* = -2\sigma/\Delta G_v$, where σ is the Gibbs free energy per unit interfacial area and ΔG_v is the bulk Gibbs free energy difference per unit volume between the condensed phase and the dissolved phase. A rough lower limit on r^* can be obtained by application of this equation to the case of the smallest negative potential for which orientation was observed (ΔG_v = 0.04 eV/atomic volume, $\sigma \approx 10^2$–10^3 erg/cm^2). For this range of σ, $r^* \approx 0.6$–6.0 nm. This is the same order of magnitude as the corner radius, which is expected to be about 5 nm.

In summary, the morphology, composition, and orientation of tin islands electrodeposited on a square-wave relief pattern have been investigated. From an electrolyte containing $SnCl_2$, NaOH, and NaCN, highly regular box-like islands were produced with ⟨100⟩ normal to the substrate and ⟨001⟩ parallel to the grating. No impurities or compositional irregularities were detected in the deposits.

1. H. I. Smith and D. C. Flanders, *Appl. Phys. Lett.* **32,** 349 (1978).

2. M. W. Geiss, D. C. Flanders, and H. I. Smith, *Appl. Phys. Lett.* **35,** 71 (1979); M. W. Geiss et al., *Appl. Phys. Lett.* **37,** 454 (1980).

3. D. C. Flanders, Ph.D Thesis, MIT, 1978; reprinted as MIT Laboratory Technical Report 533, 1978.

OPTICAL STUDIES OF LATTICE DAMAGE IN NEUTRON-TRANSMUTATION-DOPED Si[1]

N. Fukuoka[2] J. W. Cleland

A study with IR spectroscopy techniques was made of the near-edge absorption continuum and distinct absorption bands introduced by interstitial oxygen (O_i) in high purity Fz and Cz Si before and after reactor neutron irradiation.[3] The primary results of the present studies are that divacancy, near-edge absorption, and single-phonon bands were observed after irradiation of Fz or Cz Si, irrespective of O_i concentration, and the absorption coefficient of these IR-active defect centers increased with fluence. Higher order bands were formed in Fz or Cz Si after irradiation and annealing to 300°C, and the intensity of these bands decreased with increasing fluence. Formation of at least six distinct absorption bands in the 9.1–12.1 μm wavelength region in Cz Si, after irradiation and partial annealing, may have been associated with the formation of different oxygen-defect related centers. However, the complete removal of all of the absorption introduced, following annealing for 30 min at 750°C, even in very heavily irradiated samples, is taken as evidence that there was no special oxygen-lattice defect complex that remained in Cz Si under these irradiation and annealing conditions.

1. Summary of paper: *Proceedings of the Third International Conference on NTD Si* (in press).

2. Guest scientist from Osaka University, Osaka, Japan.

3. N. Fukuoka and J. W. Cleland, *Radiat. Eff.* **51**, 215 (1980).

HEAT TREATMENT EFFECTS IN NEUTRON-TRANSMUTATION-DOPED Si[1]

J. W. Cleland

It has been shown by electrical property measurements that a significant concentration (10^{14}–10^{15} cm^{-3}) of an impurity (presumably Li) that can be activated as a donor by short-term (30 min) heat treatment at ≥650°C is present in some commercially available Fz, Cz, or neutron-transmutation-doped (NTD) Si ingots. Most (90%) of these donors became inactive in Fz or Cz Si samples within a few days at ambient temperature, but many (40–70%) of them were still active in NTD Si samples after several months at ambient temperature. Virtually all these donors could be reactivated by a subsequent heat treatment at ≥650°C. These results are especially significant because (1) heat treatment for 1–3 h at 650°C is required to remove oxygen-related donors formed in Cz Si during cool-down after growth and (2) heat treatment for ≥20 h at 650°C or 30 min at 750°C is required to remove radiation damage and to obtain the anticipated carrier concentration in NTD Fz or Cz Si. The fact that the carrier concentration can be altered by 10^{14}–10^{15} cm^{-3} in Fz, Cz, or NTD Si by short-term heat treatment at ≥650°C should be considered in conventional device processing steps such as dopant diffusion for junction formation or heat treatment for removal of lattice defects produced by neutron irradiation or ion implantation.

1. Summary of paper to be published.

HEAT TREATMENT STUDIES OF OXYGEN-DEFECT-IMPURITY INTERACTIONS IN Si[1]

J. W. Cleland

It has been shown by electrical property measurements that extended (≥100 h) annealing at 450°C can introduce ≥10^{16} cm^{-3} O donors in Cz single-crystal Si samples that contain ~10^{18} cm^{-3} interstitial oxygen (O_i) initially. The maximum O donor concentration attained is (1) less if the Si contains C, (2) not altered by the presence of conventional *n*-type dopants (P, As, and Sb), and (3) larger if *p*-type dopants (B, Ga, and Al) are present. Short-term (30 min) heat treatment at ≥650°C is sufficient to remove most (≥90%) of the O donors in Cz single-crystal Si that does not contain Al. O-related donors are also formed by extended annealing at 450°C in Cz or cast polycrystalline Si; heat treatment at ≥650°C does not remove most of these donors. Intermediate-temperature (550–650°C) annealing can introduce a new type of O-related donor in Cz single-crystal or in polycrystalline Si that is stable against heat treatment to ≥900°C. No evidence of O donor formation has been observed in Fz single-crystal or in Fz polycrystalline Si of low initial O_i content as a consequence of similar annealings. Very extensive O-Al donor formation can occur in Al-doped Cz Si during conventional device processing heat treatments (30 min at ≥750°C); some of these donors are not removed by heat treatment for 30

min at 1300°C. If Li is present in Si, it can be activated as a donor by heat treatment at ≥550°C and can form a stable donor if associated with lattice defects.

1. Summary of paper to be published.

ELECTRICAL PROPERTY STUDIES OF O IN Cz-GROWN NEUTRON-TRANSMUTATION-DOPED Si[1]

J. W. Cleland N. Fukuoka[2]

The carrier concentration in Cz and NTD Cz Si samples was determined as a function of the initial dopant, oxygen, and P concentrations before and after isothermal or isochronal annealing. It was shown that low-temperature (350–500°C) heat treatment can introduce a significant O-donor concentration in Cz Si and in NTD Cz Si that contains radiation-induced lattice defects. Intermediate-temperature (550–750°C) heat treatment, which is intended to remove O donors or lattice defects, can introduce other O donors; annealing above 750°C is required to remove any of these species. Extended (20 h) high-temperature (1000–1200°C) annealing can remove O donors and lattice defects, but a significant concentration of O donors can still be introduced by subsequent low-temperature heat treatment. These results suggest that O-related donor formation in NTD Cz Si at temperatures below 750°C may serve to mask the annealing of lattice defects. It is concluded that annealing for 30 min at 750°C is sufficient to remove radiation damage in NTD Cz Si and to obtain the anticipated carrier concentration when the separate effects of any O-donor formation are included.

1. Summary of paper: *Proceedings of the Third International Conference on NTD Si* (in press).

2. Guest scientist from Osaka University, Osaka, Japan.

EXPERIMENTAL INVESTIGATION OF THE INFRARED ABSORPTION SATURATION IN *p*-TYPE Ge[1]

R. B. James[2] D. L. Smith[4]
E. Schweig[3] T. C. McGill[3]

The dominant absorption mechanism in *p*-Ge at room temperature for light having a wavelength of about 10 μm has been shown to be direct transitions between the heavy- and light-hole bands. The absorption due to the intervalence-band transitions is saturable, with the decrease in the absorption coefficient α with increasing intensity given approximately by an inhomogeneously broadened two-level model. It is found that

$$\alpha(I,\omega)=\frac{\alpha_0(\omega)}{1+I/I_s(\omega)}\ , \tag{1}$$

where $\alpha_0(\omega)$ is the absorption coefficient at low intensity and $I_s(\omega)$ is the saturation intensity. This intensity dependence of α has been found to be well satisfied experimentally for *p*-Ge, and values of the saturation intensity have been measured.

A theory describing the absorption saturation of *p*-Ge, which realistically accounts for the anisotropic and nonparabolic valence bands, has been presented; calculations based on the theory give results in close agreement with experimental results.[5,6] Theoretical results showed that for hole concentrations such that hole-impurity and hole-hole scattering rates were nonnegligible compared to hole-phonon scattering (i.e., $N_h \gtrsim 3 \times 10^{15}$ cm^{-3} at room temperature), the saturation intensity increases monotonically with increasing doping density.

We have performed transmission measurements on several samples of *p*-Ge with different hole densities to determine the dependence of the saturation intensity on the hole concentration. A transversely excited CO_2 laser operating at atmospheric pressure in the TEM_{00} mode was used as a source of saturation radiation. The measured values of I_s for *p*-Ge are shown in Fig. 2.71 for 10.6 and 9.6 μm radiation. Also shown are the calculated values for the dependence of the saturation intensity on the doping density. The calculated values of I_s vs N_h at 10.6 μm (solid line) are reproduced from ref. 5, and values of I_s at 9.6 μm (dotted line) are calculated in the same manner as discussed in that reference.

The experimental values of I_s indicate that the saturation intensity increases monotonically with increasing hole concentration for the Ge:Ga samples we studied. For the samples with larger hole concentrations, the scattering rates due to hole-impurity and hole-hole scattering are larger. The result of increasing the scattering rate is that higher intensities are required to reduce the free-hole population in the heavy-hole band in the resonant region, since the excited holes can relax at a faster rate. We also note that the experimental

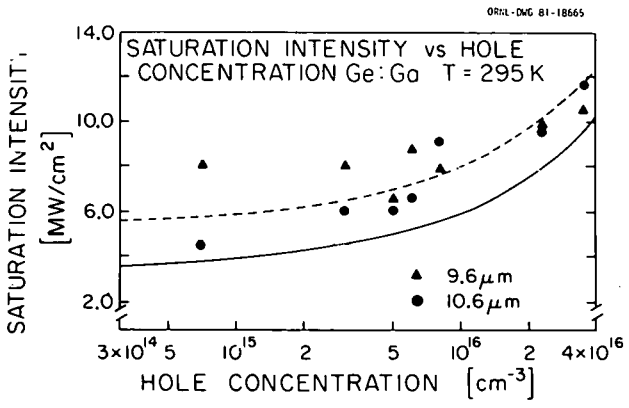

Fig. 2.71. Experimental and calculated values of the saturation intensity I_s vs the hole concentration for *p*-Ge.

values for I_s vs N_h are in fair agreement with theory, with the experimental values consistently larger than the calculated values by about 20%.

Similar absorption saturation has been observed in *p*-type Si. We find that the intensity dependence of the absorption coefficient can also be described by Eq. (1) and that the measured values of I_s range from about 40–70 MW/cm^2 for the samples we examined.

1. Summary of paper to be published.
2. Eugene P. Wigner Fellow.
3. California Institute of Technology, Pasadena, Calif.
4. Honeywell Systems and Research Center, Minneapolis, Minn.
5. R. B. James and D. L. Smith, *Phys. Rev. B* **21**, 2836 (1980).
6. R. B. James and D. L. Smith, *Solid State Commun.* **33**, 395 (1980).

SPECTRAL HOLE BURNING IN *p*-Ge AT 10.6 μm[1]

R. B. James[2]

Direct free-hole transitions between the heavy- and light-hole bands are primarily responsible for the absorption of 10.6 μm light in *p*-Ge. The absorption due to these intervalence-band transitions has been shown to saturate at high light intensities. This nonlinear behavior of the absorption coefficient results from a decrease in the population of free holes in the resonant region of the heavy-hole band by the high-intensity laser light. Experimental attempts have been made to understand the response of the hole distribution to a high-intensity pump laser of fixed wavelength by measuring the transmission of a weak tunable probe also resonant between the heavy- and light-hole bands.[3–5] Here the specific features of the absorption line shape of the probe beam give information on the distribution of hole states and fundamental relaxation constants.

We find that the absorption coefficient of the probe beam consists of two separate parts. One part is due to a decrease in the distribution of free holes in the resonant region of the heavy-hole band induced by the saturating beam, and the second part results from the response of the hole distribution to a forcing oscillation at the beat frequency Δ ($\Delta = \omega_+ - \omega_-$) for a pump laser with frequency ω_+ and a probe laser with frequency ω_-. The first part can be accurately accounted for in the hole-burning model, while the contribution from the second part depends on the presence of pulsations in the occupation probabilities for states in the resonant region of the heavy- and light-hole bands, which is not accounted for in the hole-burning model. The population pulsations act as a laser-induced grating which can scatter photons from the pump laser into the direction of the probe beam with the frequency of the probe, and vice versa. This contribution can have a significant influence on the light transmission as it is measured along the probe direction.

The two contributions to the probe absorption behave differently as ω_- is detuned from ω_+. The hole-burning contribution has a linewidth given by the homogeneous linewidth of the resonant transition, whereas the second part is more complex and depends on the dynamic model used to describe the pulsations of the distribution for the states in the resonant region. For cases in which the linewidths of each contribution are significantly different, one expects the existence of a double-dip saturation spectrum for the probe absorption coefficient as a function of the detuning Δ. We present a calculation of the composite line shape of a weak tunable probe beam in *p*-Ge in the presence of a high-intensity pump beam with a wavelength of 10.6 μm. Good agreement is found with the available experimental data, and values for the intensity dependence of the index of refraction are calculated.

1. Summary of paper to be published.
2. Eugene P. Wigner Fellow.
3. F. Keilmann, *IEEE J. Quantum Electron.* **12**, 592 (1976).

4. P. J. Bishop, A. F. Gibson, and M. F. Kimmitt, *J. Phys. D* **9**, L101 (1976).
5. F. Keilmann, *Appl. Phys.* **14**, 29 (1977).

AVALANCHE FORMATION IN *n*-TYPE Ge BY IMPACT IONIZATION PROCESS: HOT-ELECTRON EFFECTS[1]

R. B. James[2]

The results of a quantitative investigation of the formation of a laser-induced plasma in Ge by the absorption of 10-μm light are presented. For this spectral region, the material is relatively transparent at low intensity and is often used as a window material for CO_2 lasers. Recently, amplified reflection at 10.6 μm has been observed via degenerate four-wave mixing in an optically induced free-carrier plasma in Ge.[3] Values for the onset of the formation of the plasma are calculated for a unidirectional beam and are in good agreement with the observed threshold values.

It is observed experimentally that *n*-type Ge exhibits an increase in the absorption coefficient with increasing intensity. This laser-induced "opacity" has a decay time of about 100 μs, which is on the order of the electron-hole recombination time in Ge. Physically, the high-intensity light increases the average energy of the conduction electrons via indirect transitions within the conduction band. When an electron (or hole) has an energy relative to its band minimum in excess of the band-gap energy, the hot electron is able to lose its energy by creating an electron-hole pair. As the free-carrier density increases, the absorption due to these free carriers also increases. In the calculations, rate equations were solved to determine the hot-electron distribution as a function of the laser intensity and of the various scattering mechanisms.

The rate for the inelastic scattering of electrons by the production of electron-hole pairs was computed by first-order perturbation theory. Because there are three occupied final states, the cross section near threshold is a strongly rising function of the hot-electron energy. The densities of states of Ge involved in the impact ionization rates are calculated using nonlocal pseudopotential theory.[4]

We find that, for sufficiently high intensities, a significant fraction of the total electron density is excited to states with energy greater than the bandgap E_g by successive one-photon intraband transitions. For example, the calculated electron density with energy greater than E_g is 0.017%, 0.070%, and 2.4% of the total electron density for light with a wavelength of 10.6 μm, room temperature conditions, and intensities of 20, 50, and 100 MW/cm^2, respectively.

Using the values for the electron scattering rates by impact ionization and the calculated values for the occupation probabilities for states with energy greater than E_g, we find

$$\frac{dN_e}{dt} = \sum_{\substack{i \\ E>E_g}} N_i w(E_i) \equiv cN_e \ , \qquad (1)$$

which defines an exponential growth rate constant c. In the numerical calculations, energy intervals of 1 meV were used in the sum over i in Eq. (1). Here N_e is the total electron density, $w(E)$ is the impact ionization rate for energy E, and N_i is the electron density in the ith energy interval. In Fig. 2.72, the calculated values for the exponential

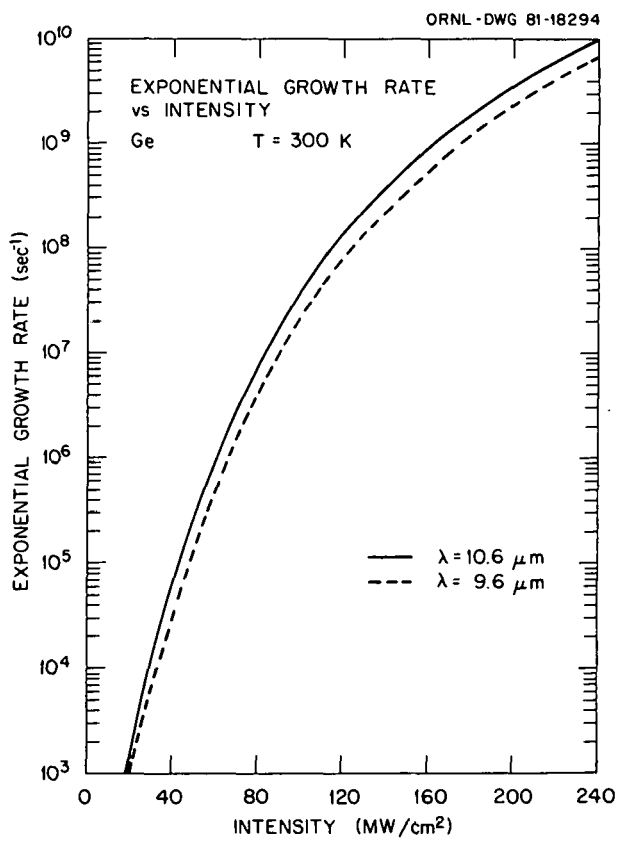

Fig. 2.72. Values for the exponential growth rate of the free-electron density vs intensity for Ge at $T = 300$ K. The solid curve is for light with a wavelength of 10.6 μm, and the dashed curve is for light with a wavelength of 9.6 μm.

buildup rate are shown for intensities in the range 0–240 MW/cm^2. The calculations were performed for room-temperature conditions with the solid line showing the results at 10.6 μm and the dashed line showing the results at 9.6 μm. The free-carrier density and the absorption coefficient have also been calculated as a function of the laser intensity.

Experimentally, the free-carrier density has been measured as a function of the peak-input intensity for *p*-type, optical grade (lightly doped *n*-type), and intrinsic Ge at room temperature for light with a wavelength of 10.6 μm. The laser pulses were approximately Gaussian in time with a FWHM of about 2 ns.[3] The transmission data show the formation of a plasma for a peak intensity of ~250–300 MW/cm^2, which is in good agreement with our calculations. The measurements show that above this peak input intensity, the excess carrier density increases with intensity to about 5.5 power, which is in approximate agreement with our results.

---

1. Summary of paper to be published.
2. Eugene P. Wigner Fellow.
3. D. E. Watkins, C. R. Phipps, Jr., and S. J. Thomas, *Opt. Lett.* **6**, 76 (1981).
4. J. R. Chelikowsky and M. L. Cohen, *Phys. Rev. B* **14**, 556 (1976).

3. Defects in Solids

It has long been recognized by scientists working to develop new materials that defects can alter or even dominate the properties of a material. Radiation damage is the major limitation to the choice and lifetime of materials in nuclear power applications; defects and defect interactions are the dominant limitations in solar cells and semiconductor devices; and defects play a critical role in initiating or controlling a wide range of mechanical, electrical, and chemical properties of metals and insulators. This section deals primarily with fundamental studies of defects, but reference to work reported in other sections, particularly Sect. 2, shows that characterization of defect structures is an essential element for understanding interactions in a wide range of materials systems.

The unique capabilities of the low-temperature irradiation facility continue to provide information on nuclear radiation effects in materials of interest to both fission and fusion technologies. Such studies ranged from the cyclic irradiation and annealing behavior of Cu to be used in fusion-reactor magnets to evaluation of the mechanical strengths of polyimides and epoxies irradiated at low temperatures. Results from the Gases in Metals Program initiated last year highlight the importance of defect interactions in understanding the behavior and release of ion-implanted gases.

The scope of the electron microscopy and x-ray diffraction research on crystal defects and defect structures has been increasingly directed toward a broader range of research within the laser annealing, ion implantation, ion-solid interactions, photovoltaic, fast-ion conductivity, and high-temperature materials programs. These techniques have contributed significantly to understanding the fundamental nature of laser-solid interactions in semiconductors, of rapid solidification and recrystallization, of ion-beam and laser-induced materials interactions, and of defect interactions in ion-implanted solids.

In situ studies of crack propagation under tensile deformation in an electron microscope have identified the role of defects in fracture phenomena. Direct observations of crack-tip blunting by edge dislocations, of the formation of plastic zones ahead of crack tips, and of dislocation motion near crack tips during stress cycling have resulted in a firm theoretical understanding which links the microscopic dislocation theory of fracture and macroscopic fracture mechanics.

One of the greatest needs in the various energy technologies is for insulating materials which can withstand high temperatures and hostile environments. In many applications it is necessary to alter the mechanical, optical, or electrical properties of conventional insulators to meet these needs. The work reported here shows that the introduction of impurities during fabrication, by thermochemical reduction, and even by ion implantation (see Sect. 2), can lead to impurity-defect interactions which significantly change the properties of the material.

RADIATION EFFECTS

THE CYCLIC IRRADIATION (4.0 K) AND ANNEALING (307 K) OF Cu FOR FUSION-REACTOR MAGNETS

R. R. Coltman, Jr. C. E. Klabunde

The stabilizer (normal metal) of a composite superconductor safely carries the current during a localized momentary normalization of the superconducting matrix. The amount of normal metal needed for safe operation depends upon its resistivity. As a result, the design of large composite superconducting magnets for fusion reactors will depend sensitively upon increases in the resistivity of the stabilizer produced by irradiation during its lifetime. To minimize these increases and, hence, the cost of magnets and their radiation shielding, consideration is given to periodic warming of the magnets to remove annealable portions of the radiation-produced resistivity. For large power reactors such warming cycles are costly, and the frequency of these operations becomes a "trade-off" parameter with various capital cost parameters.

Presently, Cu stands as the choice candidate for the stabilizer, although some consideration is given to Al. While there have been many radiation experiments on Cu, none have been made under the combination of conditions present in fusion-reactor magnets. These include magnetic fields up to 10 T, the use of commercial-grade Cu containing various amounts of cold work, irradiation near 4 K by a broad spectrum of fast neutrons, and the cyclic anncaling just mentioned. Although there is presently no irradiation facility which can precisely simulate the range of conditions in a fusion-reactor magnet, some such as the ORNL low-temperature irradiation facility (LTIF) can provide conditions which make it possible to observe trends of behavior needed by magnet designers.

In response to these needs, resistivity changes were studied in eight specimens of Cu throughout five cycles of an alternate irradiation (4.0 K) and annealing (14 h at 307 K) program carried out in the LTIF. At each step, measurements were made at zero and six transverse magnetic field strength values up to 3.8 T. Six specimens were prepared from a commercial OFHC-type Cu now in use for large magnets. The states of preparation were high-temperature internal oxidation and low-temperature recrystallization treatments from each of which one fully annealed and two states of cold-worked specimens were made. This assembly produced zero-field resistance ratio values which encompass those now found in large magnets. In addition, one fully annealed and one cold-worked specimen of ASR research-grade Cu were studied for comparison.

The operational mode chosen for the LTIF gave a mix of neutron-flux components, consisting of a fast spectrum (slightly harder than fission) which produced 55% of the damage and thermal neutrons which produced 45% of the damage by means of low-energy recoils resulting from an (n,γ) reaction. For comparison, it is calculated that the neutron spectrum present at a fusion-reactor magnet typically will be softer than a fission-reactor spectrum.[1] Since the LTIF (n,γ)-damage component is equivalent to that produced by collision with neutrons having a soft spectrum, the LTIF neutron conditions may bear some equivalence to a magnet spectrum. Calculations of the details will be made. The irradiation dose given in the first cycle was based upon an average consensus among designers of a 25%-allowable increase in the initial field-on resistivity. The allowed increase was applied to one representative sample, while increases in the other samples were greater or smaller depending upon their initial condition. The irradiation increments for succeeding cycles were terminated when the resistivity of the chosen sample again reached the allowed value.

The experiment yielded a large multidimensional body of data which is now being analyzed. The following are some early results and trends. They should be considered from the design view of the three most desirable field-on properties of a stabilizer (i.e., a minimum initial resistivity, a minimum incremental damage resistivity increase, and the minimum damage resistivity retained after an annealing cycle).

1. In the commercial Cu the incremental damage resistivity increases were greater (~9% at 0 T and 10–18% at 3.8 T) in the cold-worked samples compared to the annealed samples. Increments measured at 3.8 T were overall about 18% less than at 0 T.
2. During the first annealing cycle, the cold-worked specimens showed smaller percent retention than the annealed specimens (i.e., 6 and 16%, respectively, at 0 T.) At 3.8 T the values decreased slightly by 1 to 2%. During subse-

quent cycles all samples showed progressively less retention with the annealed samples approaching but not exceeding that of the cold-worked samples.

3. Using an extrapolation of the field-on data to 10 T, it was found that during a cyclic program having a fixed field-on resistivity value after each irradiation increment, the approach to a prescribed accumulated fluence required fewer annealing cycles for the lightly cold-worked samples than either the heavily cold-worked or fully annealed samples.

The results given above show, from the design viewpoint, that a given material can exhibit both beneficial and adverse effects from neutron irradiation which must be carefully sorted out in a data analysis involving several samples with different initial conditions.

---

1. R. T. Santoro, V. C. Baker, and J. M. Barnes, *Nucl. Technol.* **37**, 274 (1978).

MECHANICAL STRENGTH OF LOW-TEMPERATURE-IRRADIATED POLYIMIDES: A FIVEFOLD TO TENFOLD IMPROVEMENT IN DOSE RESISTANCE OVER EPOXIES[1]

R. R. Coltman, Jr. C. E. Klabunde

A program is under way at ORNL to study the irradiation behavior of organic insulating materials that may be used in the construction of large superconducting coils which provide magnetic containment for the plasma in a fusion reactor. Recent calculations by Engholm[2] show that without additional shielding even the first test reactors such as the Fusion Engineering Device (FED) may produce lifetime doses at magnet insulator locations that exceed the radiation tolerance of glass-fabric-filled (gff) epoxies in present use. Only recently have gff-polyimide materials, which have a strength in the unirradiated condition comparable to gff epoxies and sufficient to meet design needs, become available. For these reasons a study of the mechanical properties of pure and gff polyimides was made on specimens irradiated at 4.9 K to various gamma-ray doses up to 100 MGy (10^{10} rads).

Tests were made after irradiation at 4.9 K *and* warm-up to room temperature. This is a meaningful procedure, since it is expected that over their lifetime fusion-reactor magnets occasionally will be warmed to 300 K. Knowledge of the strength of insulators under cyclic conditions is just as essential as that under static cold conditions.

Gff materials were especially prepared by cooperating manufacturers, while the unfilled polyimide, Vespel, is available commercially. The following list gives the material designation as used in this report and a brief description of each. The epoxies are discussed in ref. 3.

1. Vespel—(SP-1) unfilled polyimide; E. I. du Pont de Nemours & Company.
2. Spaulrad (formerly called Spauldite)—SPAULDITE® SPAULRAD™; Spaulding Fibre Company; a high-pressure laminate composed of aromatic polyimide resin reinforced with continuous filament E glass-woven fabric 70–71% by weight.
3. Norplex (formerly called Kerimid)—Norplex NP 520; Norplex Division, UOP, Inc.; a balanced resin of bismaleimide and aromatic diamines reinforced with E glass-woven fabric 40–60% by weight.

Flexure tests were made at 300 and 77 K, while compression tests were made only at 77 K. Compression tests of Spaulrad were only in the direction parallel to the glass fiber laminations, while tests of Norplex were parallel and perpendicular to the laminations. Flexure tests at 77 K on Spaulrad and Norplex were made in three-point bending, while all others were made in four-point bending with 25 mm between supports for both cases.

All doses in this report are given only in terms of energy deposition by gamma rays, which is common to all the materials. It is important to note that while we calculate the additional dose received by each material from ^{10}B fission in the glass,[3] there are insufficient data to determine if energy deposition is a valid criterion for predicting property changes which are produced by radiations having different damage-production mechanisms such as gamma rays and ^{10}B fission fragments. The calculations gave the following results.

Material	Dose Ratio (^{10}B fission/gamma ray)
Vespel	0
Spaulrad	1.33
Norplex	0.95

Values for the highest dose to the samples were:

Gamma-ray dose: 100 MGy (10^{10} rads)
Thermal-neutron fluence: 3.1×10^{21} n/m^2

Fast-neutron fluence: 8.7×10^{20} n/m^2 > 0.1 MeV
Irradiation time: 189 h

Values for smaller doses are reduced proportionately.

The results of all fracture strength tests of the polyimides studied in this experiment are shown in Fig. 3.1. For comparison the results for similarly prepared epoxy materials irradiated under the same conditions are shown in Fig. 3.2. Some distinguishing features were noted for the flexure-strength results:

1. At 100 MGy Vespel loses only 8%, Norplex 30%, and Spaulrad 38% of initial strength at 77 K, but the latter remains about 25–40% stronger than Norplex throughout the entire dose range, possibly because of the greater glass content in Spaulrad.
2. At a dose of 24 MGy, the better gff polyimide (Spaulrad) is about five times stronger than the best gff epoxy (G-11 CR) for tests at 77 K. At this dose the epoxy probably has insufficient strength for practical use, while, in contrast, the polyimide remains usable to a dose four times as large.

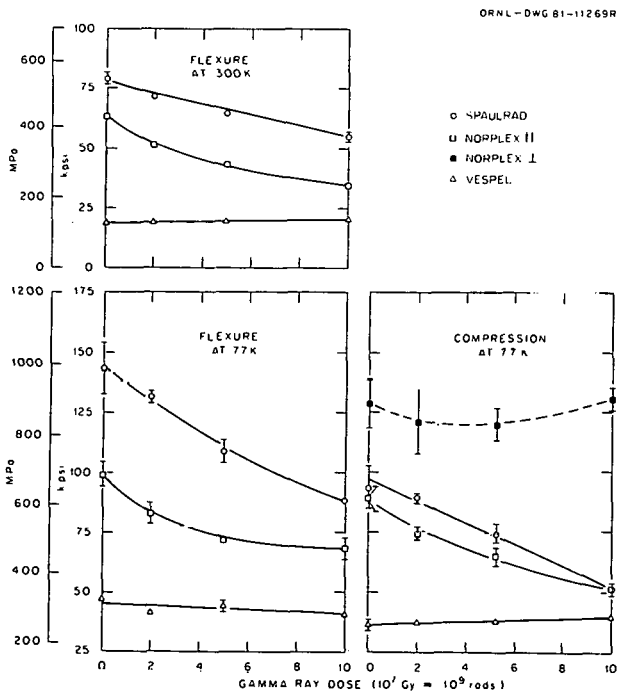

Fig. 3.1. Results of fracture strength tests on pure and gff polyimides after irradiation at 4.9 K followed by warmup to 307 K. Each data point shows the average value of three tests, and error bars indicate average deviation. Points without error bars indicate that data scatter was too small to show. See text for accompanying ^{10}B fission dose.

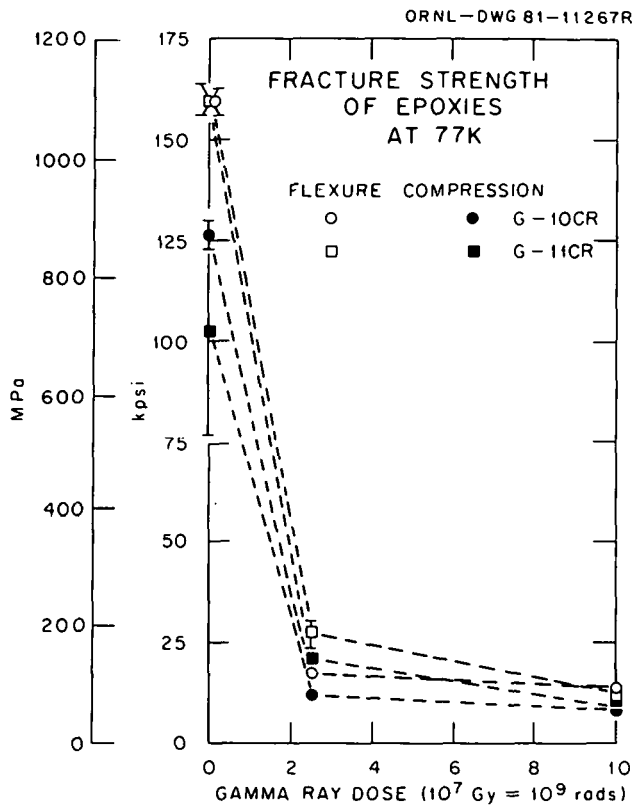

Fig. 3.2. The effect of irradiation on gff epoxies obtained as in Fig. 3.1. The dashed lines serve only as a guide for connecting related data points and are not intended to give intermediate strength values.

In the case of compression tests, all of which were made at 77 K, Norplex material was available to prepare specimens that could be loaded perpendicular (Norplex ⊥) as well as parallel (Norplex ||) to the glass fabric laminations, while Spaulrad was tested only with loading parallel to the laminations. The results shown in Fig. 3.1 have some notable features:

1. Spaulrad shows a nearly linear decrease in strength with dose compared to the slight concave-up response of Norplex ||. Although the responses follow different paths, the two materials reach nearly the same strength at 100 MGy, down about 45% from initial unirradiated values.

2. In the case of Norplex ⊥ no loss in strength was observed for 100 MGy. Since present reactor designs show some material stressed perpendicular to the laminations, further study to doses greater than 100 MGy to determine the radiation tolerance for this orientation could give useful results.

From the results given above, two main conclusions emerge:

1. The gff-polyimide data in Fig. 3.1 indicate the loss in strength with dose reaches an average of ~35% at 100 MGy. In comparison, Fig. 3.2 shows no data for the gff epoxies in the fluence range where the loss of strength is most responsive. To make an approximate comparison between the two materials, we assumed no loss in epoxy strength up to 2 MGy (see results for G-10)[4] and a linear decrease thereafter to the values indicated at 24 MGy. We then compared radiation doses for 30% and 40% losses in both flexure and compressive strength at 77 K. Overall, the span of comparative results shows that polyimides are 5–10 times more radiation resistant than comparably prepared epoxies.
2. In this experiment ^{10}B fission-fragment damage accompanied that produced by gamma rays. In terms of energy deposition these two types of radiation were determined to be about equal in the gff materials. In his neutronics calculations for the FED, Engholm[2] found a corresponding situation at magnet locations where energy deposition by fast neutrons is about equal to that by gamma rays. At this time, however, there are not enough data to determine if energy deposition is a valid criterion for predicting property changes produced by radiations whose damage-producing mechanisms differ greatly. For these two situations, however, ^{10}B fission-fragment and fast-neutron damage are far more comparable with each other than either is with gamma-ray damage. From this viewpoint we estimate, by comparing the present results with Engholm's calculations, that the use of gff polyimide materials as magnet insulators in the FED would make present designs for shields and magnet coils feasible.

1. Summary of paper: *Journal of Nuclear Materials* (in press).

2. B. A. Engholm, *Proceedings of the Fourth ANS Topical Meeting on the Technology of Controlled Nuclear Fusion* (in press).

3. R. R. Coltman, Jr., et al., *Radiation Effects on Organic Insulators for Superconducting Magnets, Ann. Prog. Rep., Sept. 30, 1979,* ORNL/TM-7077; p. 1696 in *Proceedings of the Symposium on Engineering Problems of Fusion Research,* IEEE 79CH1441-5NPS, New York, 1979.

4. R. H. Kernohan, R. R. Coltman, Jr., and C. J. Long, *Radiation Effects on Organic Insulators for Superconducting Magnets, Ann. Prog. Rep., Sept. 30, 1978,* ORNL/TM-6708.

FISSION-NEUTRON DAMAGE RATES IN SEVERAL METALS AT 4.7 K

C. E. Klabunde R. R. Coltman, Jr.

We have extended the data base[1] of resistivity-damage production rates in metals under pure fission-spectrum neutron irradiation[2] at 4.7 K. Among the eight metals added here are three fcc (Pd, Ag, and Pt); two bcc (Ta and W), all heavier elements than those previously reported; and three hcp (Mg, Ti, and Zr). The same facilities and techniques as described earlier[1,2] were used.

The measured initial damage rates, corrected for all known extraneous effects (thermal-neutron damage, electrical size-effect, and other non-specific, initial transient effects) are listed in Table 3.1, column 1. These rates carry uncertainties of about 5% except in two cases where the uncertainties are somewhat larger. (1) W: The sample was of such low purity (99.95%) that it could not be annealed without becoming too brittle to be bent into the required shape; therefore, it was studied in the as-rolled, highly cold-worked state. Such a state is known to enhance the damage rate of Cu by as much as 35%.[3] In W we suppose the effect might be 20–50%. (2) Mg: In agreement with O'Neal and Chaplin,[4] we found that some recovery occurs at the irradiation temperature. It appears to cause so much nonlinearity in the damage rate that there is about ±15% uncertainty in the choice of a rate which includes all stable defects as well as those belonging to the recovering species.

These damage-rate data can help test present and future theoretical models of damage production. The modified Kinchin-Pease relation is presently used,[5] generally with an empirical "efficiency factor" ξ in lieu of any explicit theoretical accounting of the instability of a portion of the supposedly stable displacements created in a cascade. It is

$$\frac{d\rho}{d\Phi} = \frac{0.8\,\xi\,\rho_F\,\langle\sigma T\rangle}{2\,T_d}\,, \qquad (1)$$

Table 3.1. Damage rates and efficiencies

	Damage rate $\left.\frac{d\rho}{d\Phi}\right\|_0$ (10^{-31} Ω m³/n)	Damage energy cross-section $\langle\sigma T\rangle$ (keV-b)	Frenkel defect resistivity ρ_F (10^{-6} Ω m)	Displacement threshold T_d (eV)	Empirical damage efficiency ξ
Pd	1.90	73[b]	9	41	0.30
Ag	0.666	72[b]	2.1	39	0.43
Pt	1.59	51[b]	10	44	0.34
Ta	2.52	54.7	17	85	0.58
W	4.2[a]	52.2	14	100	1.45
Mg	7.0[a]	92.7	4.5	16	0.67
Ti	22.4	97.6	45	30	0.38
Zr	24.0	74.8	50	40	0.62

[a] Large uncertainty; see text.
[b] Estimated.

where the irradiation-induced resistivity ρ and the neutron fluence Φ are related to the specific resistivity of Frenkel defects ρ_F, the spectrum-averaged product of cross section and damage energy $\langle\sigma T\rangle$, and the threshold energy for displacements T_d.

These parameters are listed in columns 2 4 of Table 3.1. Values of $\langle\sigma T\rangle$ were calculated by the code RECOIL,[6] except in the cases of the three precious metals not available in the data base of RECOIL, which were estimated by a calculation involving interpolation from other RECOIL-available elements. The experimental parameters, ρ_F and T_d, are as compiled or estimated by Lucasson[7] or are estimated in similar fashion. Damage efficiencies implied by Eq. (1) are shown in the last column of Table 3.1.

These efficiencies generally fit the trends of crystal structure which have been noted in several overviews of fast-neutron damage, namely, that ξ is about 0.3 for fcc and 0.5 for bcc, while hcp has not been studied enough yet to establish a clear trend. Apparent anomalies in these (Ti, low; Ag, high; W, very high) suggest problems with the other parameters, especially ρ_F and T_d. Adjustment for the impurity of our W sample, as mentioned above, could reduce its very high efficiency to about 1.0, where it would be in agreement with results of field-ion microscopy work.[8]

Further interrelations between these data and our similar data on six other metals,[1] as well as data from other types of irradiations, are to be pursued in some detail in a conference report.[9]

1. R. R. Coltman, Jr., C. E. Klabunde, and J. M. Williams, *Journal of Nuclear Materials* (in press).
2. C. E. Klabunde, J. M. Williams, and R. R. Coltman, Jr., *Journal of Nuclear Materials* (in press).
3. R. R. Coltman, Jr., T. H. Blewitt, and C. E. Klabunde, *Solid State Div. Ann. Prog. Rep., Aug. 31, 1959*, ORNL-2829, p. 74.
4. T. N. O'Neal and R. L. Chaplin, *Phys. Rev. B* **5**, 3810 (1972).
5. M. A. Kirk and L. R. Greenwood, *J. Nucl. Mater.* **80**, 159 (1979).
6. T. A. Gabriel, J. D. Ambrgy, and N. M. Greene, *Radiation Damage Calculations: Primary Recoil Spectra, Displacement Rates, and Gas-Production Rates*, ORNL/TM-5160 (1976).
7. P. Lucasson, p. 42 in *Fundamental Aspects of Radiation Damage in Metals*, Vol. 1, ed. by M. T. Robinson and F. W. Young, Jr., ERDA CONF-751006-P1, Oak Ridge, Tenn., 1976.
8. M. I. Current and D. N. Seidman, *Nucl. Instrum. Methods* **170**, 377 (1980).
9. Proceedings of the International Conference on Neutron Irradiation Effects, *Journal of Nuclear Materials* (to be published).

LOW-TEMPERATURE RELEASE OF ION-IMPLANTED He FROM Ni[1]

D. B. Poker J. M. Williams

Helium is introduced into the structural alloys of fission and fusion reactors by (n,α) reactions and will be injected into the first wall of the latter from the plasma. The He diffuses and precipitates at extended defects, producing profound effects on the

mechanical integrity of materials. Low-temperature studies are essential to an understanding of the processes by which He migrates to these defects because the diffusion is expected to consist partly of motion as freely moving interstitials with small activation energies (0.1–0.4 eV).[2,3] In this work, the thermal desorption of He from Ni below room temperature and after ion implantation at 18 K is used to investigate this diffusion.

Polycrystalline-Ni samples were implanted at 18 K with 35-keV He to doses in the range 5×10^{14} to 4.4×10^{16} cm^{-2}. Implantation was made with the ion beam at a 45° angle to the surface normal to reduce the mean depth of penetration, increasing the amount of He which migrates to the surface without being trapped at defects. One implantation was made at 150 keV to a dose of 1.4×10^{16} cm^{-2} with the sample normal to the beam for comparison. The annealing program consisted of 4-min isochrones at 5 K intervals up to 90 K, followed by a linear heating rate of 5 K/min up to 300 K. Partial pressure of He released from the sample was measured with a quadrupole mass spectrometer.

Figure 3.3 shows He release rates vs temperature at a dose of 1.4×10^{16} cm^{-2} for a 35-keV 45° and a 150-keV 90° implantation. For the 35-keV 45° implant, there was a sharply peaked release centered at approximately 50 K, designated Stage I, followed by a more diffuse release extending from 90 K to 300 K, designated Stage II. No Stage-I release was detected for the 150-keV 90° implant, while the Stage-II release had almost exactly the same form though it was a factor of 10 smaller than that of the 35-keV 45° implant.

The fractions released in each of the stages are plotted vs dose in Fig. 3.4. The total release below room temperature (~5%) was independent of dose, except for the highest dose, for which about 29% was released. Most of this increase occurred in Stage I where the release increased from 1.5 to 22%, rather than in Stage II where the release increased from 4 to 7%.

For the Stage-I release, the activation energy was determined by the change-of-slope method to be 0.11 ± 0.02 eV over the entire range of doses.

The calculated He-implantation profile was peaked at 0.07 μm and for the lowest dose corresponded to an average He concentration of about 0.03 at. % to a depth of 0.14 μm. Some tens of atomic displacements were produced per

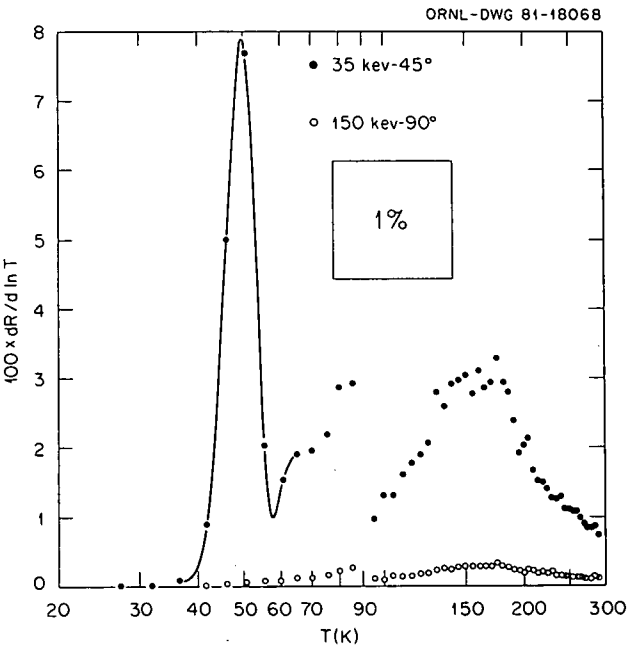

Fig. 3.3. Release rate of implanted He from Ni as a function of temperature. A cubic spline fit has been drawn through the 35-keV 45° Stage-I release as a guide to the eye. The discontinuity at 90 K is a result of the change in effective heating rate in the transition from an isochronal annealing program to a linear ramp. The area under each curve represents the accumulated release. An area representing a 1% release is contained within the square box for comparison.

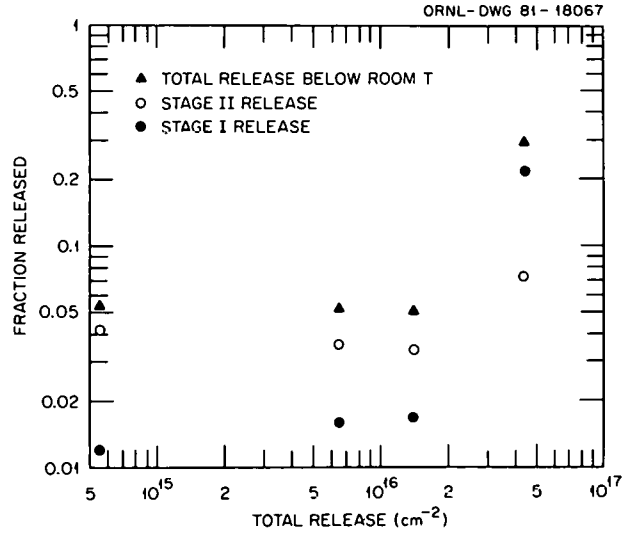

Fig. 3.4. Fractional release of He from Ni in each stage below room temperature vs total release through melting for the 35-keV implants.

He-atom implant. Since the vacancy and self-interstitial concentrations should have reached saturation at approximately 0.2 at. % as a result of spontaneous recombination,[4] these concentrations were presumed to be nearly uniform over the implantation depth and relatively dose independent.

Two interpretations of the Stage-I release are apparent. The first presumes that a large fraction of the He comes to rest interstitially and first diffuses when the temperature is raised to 50 K. The release is the fraction of He that avoids capture by vacancies as it diffuses. The results of Fig. 3.4 imply that the trapping of He continues until approximately 10 He atoms per vacancy have been captured, corresponding to a dose of 1.4×10^{16} cm^{-2}. Above this dose the vacancies become saturated, so that they can capture no more He, resulting in the much larger fraction being released for the dose of 4.4×10^{16} cm^{-2}. The saturation number (10 He atoms/vacancy) is not inconsistent with predictions of Wilson et al.[5]

The second model is suggested by the proximity to temperature of the Stage-I-release peak to the well-known Stage-ID-E annealing peaks of radiation damage in Ni, which are associated with the migration of Ni self-interstitials. Some calculations have suggested that it may be energetically favorable for a migrating self-interstitial to recombine with a vacancy at which He has been trapped, freeing the He to migrate.[2] This model would imply that the migration energy for interstitial He in Ni is less than 0.1 eV.

While our data are not sufficient for a choice between the two models, either would imply that the migration energy of interstitial He in Ni is $\leq$ 0.1 eV.

1. Summary of paper to be published.
2. D. J. Reed, *Radiat. Eff.* **31**, 129 (1977).
3. C. F. Melius, C. L. Bisson, and W. D. Wilson, *Phys. Rev. B* **18**, 1647 (1978).
4. M. Nakagawa et al., *Phys. Rev. B* **16**, 5285 (1977).
5. W. D. Wilson, M. I. Baskes, and C. L. Bisson, *Phys. Rev. B* **13**, 2470 (1976).

He RELEASE FROM NEUTRON-IRRADIATED Ni

D. B. Poker J. M. Williams

Measurement of the diffusivity of He in Ni was attempted by the thermal degassing of neutron-irradiated samples in which He was produced by the (n,α) reaction. Open-ended cylinders of commercial "A" Ni so irradiated were heated in a vacuum furnace, and the emitted He was detected using a quadrupole mass spectrometer. A result reported earlier,[1] that all of the He was released at temperatures above 900°C, has since been shown to be erroneous. Chemical analysis of this Ni indicated a significant concentration of ^{10}B which enhanced the production of He by a factor of approximately 1000 because of the large cross section of ^{10}B for the (n,α) reaction. Measurements of He release on melting these samples confirmed the higher production of helium. The total release before melting was determined to be approximately 2%, most of which could be accounted for by the Ni surface evaporation alone.

In an effort to determine the total release of He from Ni at room temperature, cylindrical capsules of MARZ-grade Ni were evacuated, sealed, and neutron irradiated at ~100°C so that He doses of approximately 1 ppba (B content of this Ni was negligible) could be produced. After irradiation, the capsules were placed in a vacuum system and punctured, releasing that He which had diffused to the inside of the capsule. The release corresponded to approximately 0.04% of the total amount of He in the sample, indicating that a small amount of the He was being released at room temperature. The capsules were then heated to melting. A negligible amount of He (~2%) was released prior to melting, and the remainder of the He was released as a burst on melting. These experiments suggest that He may be mobile in Ni at room temperature or below; however, the large preponderance of He introduced by nuclear transmutation is immobile (trapped) in Ni at temperatures up to its melting point.

1. D. B. Poker and J. M. Williams, *Solid State Div. Prog. Rep., Feb. 29, 1980,* ORNL-5640, p. 131.

ABSENCE OF ANELASTIC RELAXATION OF TRITIUM IN NIOBIUM BELOW 77 K[1]

D. B. Poker

The mechanical properties of metals are sensitive to the interactions between hydrogen and defects in the metal. Oxygen has been shown to be an effective trap for hydrogen, reducing the effects of precipitation and embrittlement at low temperatures. The properties of hydrogen and deuterium trapped

at interstitial oxygen have been studied[2] using ultrasonic anelastic relaxation. Defect symmetries and relaxation times and strengths were measured at low temperatures and indicated the existence of relaxation frequencies of about 10 MHz at temperatures as low as 2.4 K. Large nonclassical effects were observed in the relaxation strengths as a function of temperature and in the isotope shift of relaxation frequency. It was concluded that the relaxation proceeded via transitions between delocalized tunnel-split eigenstates of the hydrogen.[2]

In an effort to obtain more information on the quantum mechanical nature of the system, measurements were extended to include the isotope tritium. Attenuation of 10–250 MHz longitudinal ultrasonic waves in the [100] and [110] directions was measured from 2–300 K on Nb single crystals containing approximately 3000 ppma each of oxygen and tritium. To ensure that the sample had been properly tritiated, measurements were made of relaxations near 150 K, which had previously been identified as due to oxygen-tritium complexes. No evidence of relaxations similar to those produced by hydrogen and deuterium at low temperatures was seen below 60 K.

Implications of this result are twofold, depending upon the assumption of the classical or quantum mechanical nature of the system. If the oxygen-hydrogen system is represented by classical behavior, then the predicted isotope shift would have located the relaxation within the temperature range of measurements. The experimental uncertainty would place an upper limit on the tritium relaxation strength of only 4% of the corresponding value for hydrogen and only 1% of the value for deuterium. If the oxygen-hydrogen system represents quantum mechanical behavior, then the predicted isotope shift would locate the relaxation above room temperature for these measurement frequencies.

The upper limit on the relaxation strength imposed by a classical model is a serious difficulty, whereas the experimental results are consistent with the predictions of a quantum mechanical model.

1. Summary of paper to be published.

2. D. B. Poker et al., *Z. Phys. Chem. N.F.* **116,** 39 (1979).

THERMAL ANNEALING OF DISLOCATION LOOPS IN Cu

B. C. Larson J. F. Barhorst
T. S. Noggle

The thermally induced evolution of vacancy and interstitial loops during elevated temperature irradiation represents an important aspect of the defect clustering process in metals. The annealing characteristics of vacancy loops in metals are of particular interest in this regard because of their role in void formation, which occurs after prolonged irradiation at high temperatures. The small size of vacancy loops and the tedious measurements required to differentiate between vacancy and interstitial loops have limited electron microscopy work in this area. In this study, we have made use of x-ray diffuse scattering measurements to investigate vacancy and interstitial loop annealing from 40 to 300°C in Ni-ion-irradiated Cu. The irradiation was carried out at 4 K using a primary beam of 17.4-MeV Ni ions, which was selectively degraded in energy by absorber foils[1] such that a uniformly damaged layer (110 eV/A) 2.4 μm thick was produced.

The x-ray diffuse scattering arising from a concentration C_i of dislocation loops of radius R_i and scattering cross section $d\sigma/d\Omega$ is given by

$$I(\mathbf{K}) = \frac{I_0}{\mu} \sum_i C_i \frac{d\sigma_i}{d\Omega}(\mathbf{K}) \Delta\Omega \ , \qquad (1)$$

where $\mathbf{K}$ is the scattering vector, $\Delta\Omega$ is the solid angle subtended by the detector, I_0 is the incident beam power, and μ is the absorption factor for the geometry used. The scattering cross section can be written as

$$\frac{d\sigma_i}{d\Omega}(\mathbf{K}) = (r_e F)^2 |A_i(\mathbf{K})|^2 \ , \qquad (2)$$

where r_e is the classical electron radius, F is the atomic scattering factor, and $A(\mathbf{K})$ represents the diffuse scattering amplitude. Since $A(\mathbf{K})$ can be calculated[2] numerically for this case, Eqs. (1) and (2) provide a direct means of analyzing diffuse scattering measurements in terms of vacancy and interstitial loops.

Figure 3.5 shows the measured diffuse scattering from the irradiated Cu after warming to 40°C and

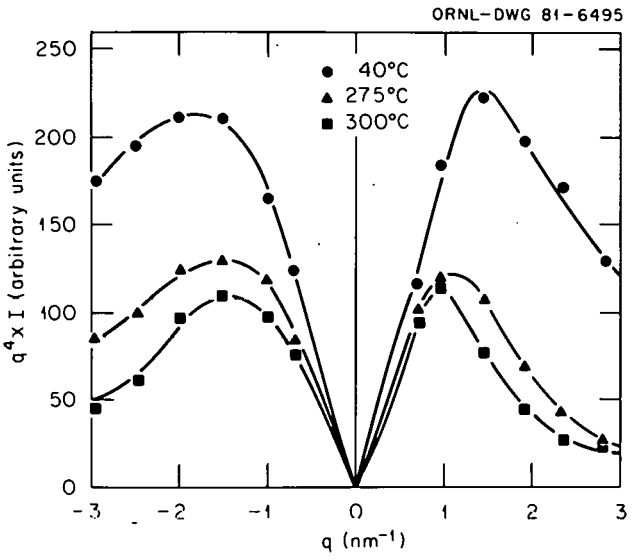

Fig. 3.5. X-ray diffuse scattering measurements on ion-irradiated Cu near the (222) reflection.

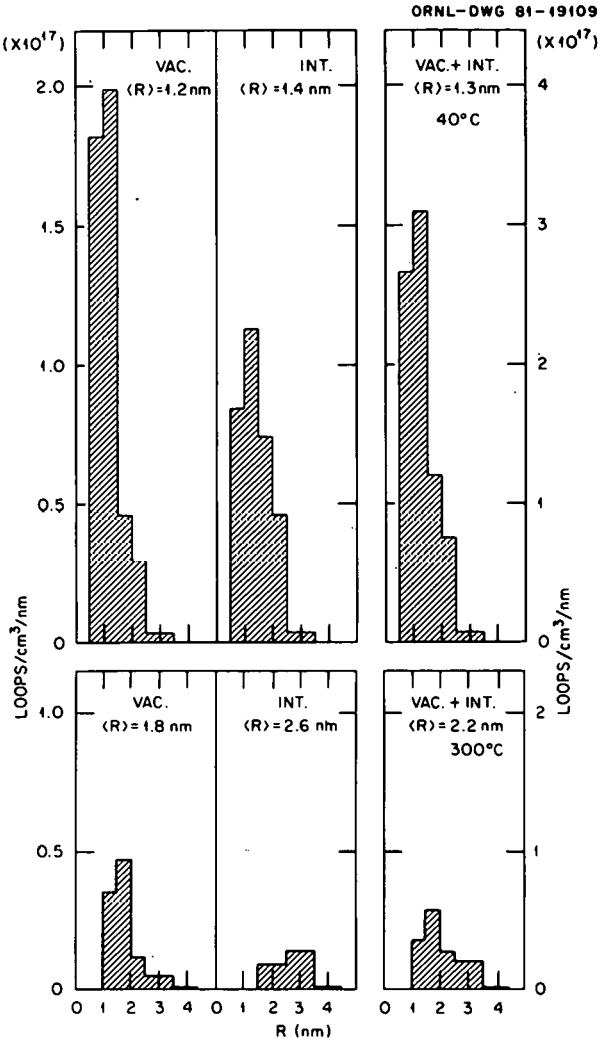

Fig. 3.6. Vacancy and interstitial loop size distributions for 40 and 300°C anneals of ion-irradiated Cu.

after anneals to 275 and 300°C. These data were collected along the [111] direction near the (222) reflection and have been scaled by q^4 (where q is the distance to the reciprocal lattice point) to emphasize the scattering in the so-called "asymptotic" scattering region. Calculations have shown this region to be sensitive to the vacancy-interstitial nature of dislocation loops as well as their number and sizes; therefore, these measurements allow the investigation of the annealing characteristics of each type of loop separately. This aspect is demonstrated directly in Fig. 3.6, where size distributions determined from the solid line fits to the data in Fig. 3.5 are shown for the 40 and 300°C anneals. Loops of radii 1.0, 1.5, 2.0, 3.0, and 4.0 nm were used in the fitting procedure, and the concentrations have been distributed over 1 nm in Fig. 3.6 to produce a continuous size distribution with the area equal to the total loop concentration.

At 40°C the size distributions of the vacancy and the interstitial loops are rather similar, with average sizes of 1.2 and 1.4 nm, respectively. After a 30-min anneal at 300°C, ~55% of the total defects have been lost (~40% by 275°C) through vacancy-interstitial annihilation; and, in addition, significant size distribution changes can be seen. Throughout the annealing program, the numbers of vacancies and interstitials condensed into loops were found to be equal to within ±7%. The vacancy loop size distribution coarsened somewhat as a result of the loss of the smaller loops, while the interstitial loop distribution indicates not only preferential loss of the small loops but also increasing numbers of larger loops.

These results can be interpreted as preferential shrinkage of the smaller vacancy loops, due to dislocation line tension effects, with the free vacancies annihilating at interstitial loops. The increase in numbers of larger interstitial loops is interpreted in terms of interstitial loop glide and climb, resulting in loop coalescence, thereby removing small loops while producing larger loops. The lack of evidence for increasing numbers of larger

vacancy loops indicates that vacancy loop motion is not as prominent as that for the interstitials.

1. T. S. Noggle et al., p. 225 in *Proceedings, Fourth Conference on Scientific and Industrial Applications of Small Accelerators*, ed. by J. L. Duggan and I. L. Morgan, IEEE 76CH1175-9, NTS, Piscataway, New Jersey, 1976.

2. B. C. Larson and W. Schmatz, *Phys. Status Solidi B* **99**, 267 (1980).

X-RAY DIFFUSE SCATTERING OF DEFECTS IN IRRADIATED Si[1]

B. C. Larson J. F. Barhorst

A considerable gap has existed in our knowledge of defect clusters in irradiated Si between the small (<6-atom) clusters identified using magnetic resonance[2] and optical techniques and the larger (>50-atom) clusters reported[3] in TEM investigations. X-ray diffuse scattering measurements offer the possibility of bridging this gap, as, in principle, lattice defects from single interstitials up to defect clusters containing >1000 atoms can be studied. In this investigation Huang scattering and asymptotic x-ray diffuse scattering near Bragg reflections were used to investigate defect clustering in neutron-irradiated (10^{20} n/cm^2) Si. The results of this study are presented in the form of size distributions of vacancy and interstitial loops, and they show large numbers of both vacancy- and interstitial-type defect clusters present in size ranges below TEM resolution.

The cross section for x-ray diffuse scattering from defect clusters is given by

$$I(K) = \frac{I_0}{\mu} \sum_i C_i \frac{d\sigma_i}{d\Omega}(\mathbf{K})\Delta\Omega \ , \qquad (1)$$

where I_0 is the incident beam power, μ is the absorption factor for the scattering geometry, **K** is the scattering vector, $d\sigma_i(\mathbf{K})/d\Omega$ is the scattering cross section, C_i is the volume concentration of clusters with radius R_i, and $\Delta\Omega$ is the solid angle subtended by the detector. Loop concentrations are determined by fitting Eq. (1) to the measured diffuse scattering profiles with C_i as parameters. The symmetry of the Huang scattering, close to the reciprocal lattice vector, provides information on defect symmetries.

Figure 3.7 shows x-ray diffuse scattering measurements made near the (111) reciprocal lattice point of 10^{20}-n/cm^2 irradiated Si. These data were

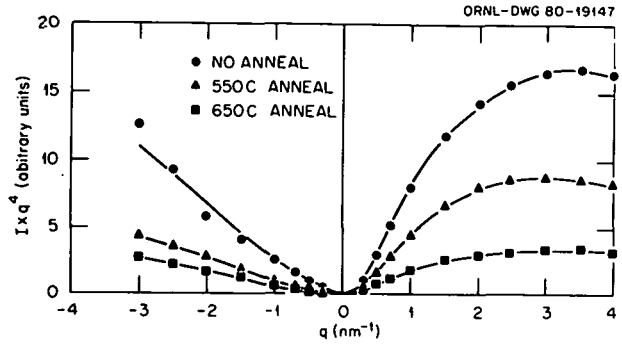

Fig. 3.7. X-ray diffuse scattering measurements made on neutron-irradiated Si in the as-irradiated state and after 30-min anneals at 550 and 650°C.

collected at 10 K using a position-sensitive detector, and they represent the net scattering after removing thermal diffuse and Compton scattering. The data have been scaled by q^4, where q is the distance (along the Ewald sphere) of the measuring point from the (111) reciprocal lattice point. Measurements are shown for the as-irradiated (~50°C) state and after 30-min anneals to 550 and 650°C. The solid lines represent the results of fitting Eq. (1) to the measured points using vacancy and interstitial loops of 0.375-, 0.75-, 1.0-, 1.5-, and 2.0-nm radius. The scattering cross sections used in the fitting were calculated for edge loops on {111} planes, using numerically calculated displacement fields and taking the elastic anisotropy of Si into account. Figure 3.8 shows a semilog plot of the size distributions corresponding to the no-anneal data in Fig. 3.7. Separate size distributions are shown for vacancy and interstitial loops. The average size of the loops is quite small, although some interstitial loops are indicated for larger sizes. Also shown is a comparison of the combined loop size distribution found here with the results of an electron microscopy study[3] made on Si irradiated with 5×10^{19} n/cm^2 (scaled linearly to 10^{20} n/cm^2). The agreement between the electron microscopy and the x-ray results is quite good at the larger sizes where electron microscopy can be sure to resolve all loops; however, at the small sizes where the resolution of the electron microscope becomes questionable, the x-ray results reveal the presence of large numbers of defect clusters. These small loops tend to bridge the gap that has existed between the large loops observed in TEM and the small atomistic-like clusters observed

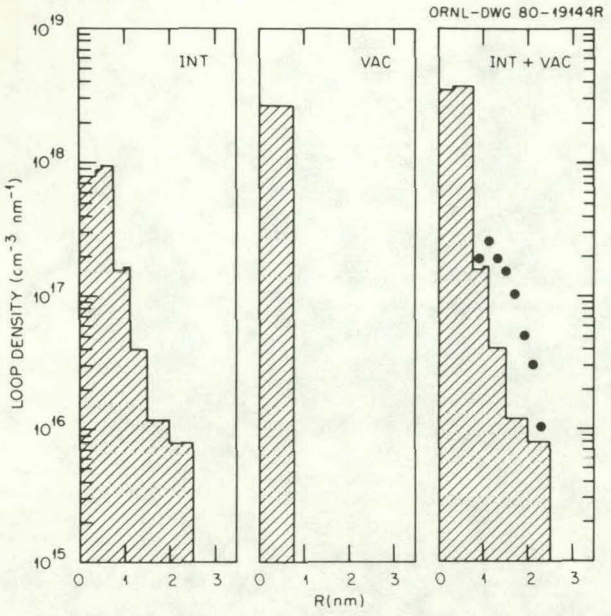

Fig. 3.8. Size distributions of vacancy and interstitial dislocation loops in neutron-irradiated Si.

in other studies discussed above. The results of the 550 and 650°C anneals were found to be largely a reduction in dislocation loop densities (by factors of 2.2 and 5, respectively) with little or no size distribution changes.

1. Summary of paper: p. 151 in *Defects in Semiconductors,* ed. by J. Narayan and T. Y. Tan, North Holland, New York, 1981.

2. J. W. Corbett et al., p. 1 in *Radiation Effects in Semiconductors 1976,* ed. by N. B. Urli and J. W. Corbett, Institute of Physics, Bristol, England, 1977.

3. J. M. Pankratz, J. A. Sprague, and M. L. Rudee, *J. Appl. Phys.* **39,** 101 (1968).

RADIATION DAMAGE AND ITS ANNEALING IN SEMICONDUCTORS[1]

J. Narayan J. Fletcher

Residual damage in the form of point defect clusters and amorphous regions has been investigated in ion- and neutron-irradiated Si specimens. Annealing of this damage during conventional heating, flame annealing, and pulsed-laser irradiation has been studied by plan-view and cross-section electron microscopy techniques. The displacement damage in neutron-irradiated Si was observed in the form of interstitial and vacancy loops. On subsequent thermal annealing, relatively small changes were observed up to 600°C, but most of the damage annealed out by 750°C. The results on B^+-implanted specimens show that most of the intrinsic damage anneals out by 750°C, and the dislocation loops observed above 750°C are presumably due to clustering of self-interstitials generated as a result of dopant substitution and a "kick-out mechanism." Annealing studies in As^+-implanted Si suggest that divacancy migration in the temperature range 200–400°C repairs the disorder associated with tetrahedra in the outer regions of the cascades. In the temperature range ~500°C, core regions of the cascades anneal out by solid phase epitaxial regrowth. At still higher temperatures dislocation loop annealing occurs similar to that observed in neutron- and B^+-implanted Si. A complete annealing of displacement damage was accomplished by an oxy-acetylene flame at 1150 ± 20°C. The results on laser annealing of displacement damage were consistent with the melting model.

1. Summary of paper: p. 191 in *Defects in Semiconductors,* ed. by J. Narayan and T. Y. Tan, North Holland, New York, 1981.

FRACTURE

DIRECT OBSERVATIONS OF CRACK TIP BLUNTING BY EDGE DISLOCATIONS IN ALUMINUM[1]

J. A. Horton S.-J. Chang[2]
S. M. Ohr

Recent TEM fracture experiments in various metals and alloys have shown that the in situ deformation technique is a useful tool for studying crack tip dislocation behavior of propagating cracks. In the present study, direct observations have been made in aluminum of dislocations of primarily edge character emitted at a crack tip undergoing Mode I fracture. The observations have shown, for the first time, that crack tips can be blunted by emitting dislocations on planes inclined to the crack plane.

Figure 3.9 shows a pileup of dislocations of edge character which were emitted at a crack tip. The Burgers vector, tensile axis, and pileup direction

SSDN 265

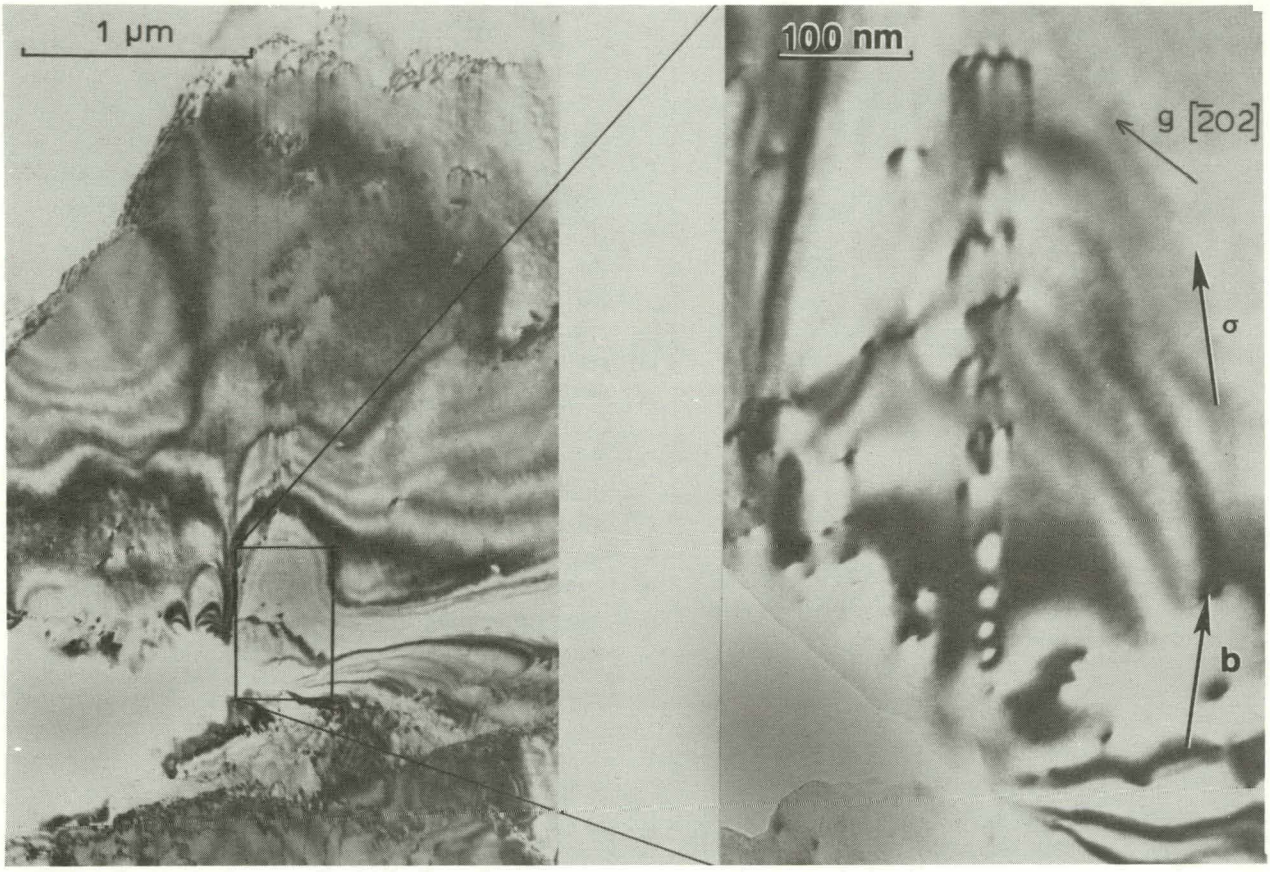

Fig. 3.9. Electron micrographs showing edge dislocations produced during Mode I fracture. The tensile axis and Burgers vector are parallel to the direction of dislocation pileup and are nearly perpendicular to the crack propagation direction. The electron beam direction, *B*, is near [101], the foil normal is near [233], and the Burgers vector of the dislocations is $\mathbf{a}/2[0\bar{1}1]$.

are all nearly perpendicular to the direction of crack propagation. The appearance of the dislocation pileup is similar to previous observations of screw dislocation pileups produced by Mode III shear cracks in stainless steel, nickel, and copper. Screw dislocation pileups were also observed in aluminum; but due to a higher stacking fault energy, more cross slip tended to occur and the plastic zone was broader. A dislocation-free zone is present in Fig. 3.9 between the crack tip and the first dislocation, since this distance is about four times the distance between the first and second dislocations. The dislocations are also in the form of an inverse pileup.

In general, under a constant applied load, cracks propagated in discrete jumps and then between jumps were blunted by emitting dislocations at angles between 45 and 90° to the direction of crack propagation. Such a sequence is shown in Fig. 3.10. During this sequence the specimen was held under constant load conditions. Between the second, third, and fourth micrographs, no forward crack propagation occurred while dislocations continued to be emitted. Between the fourth and fifth micrographs, slight forward crack propagation occurred and dislocations were emitted at the new crack tip on new slip planes parallel and adjacent to the previous set. These results have shown that crack tip blunting dislocations do exist as predicted.

We have treated the problem of edge dislocation pileup by a singular integral equation, which

SSDN 2582

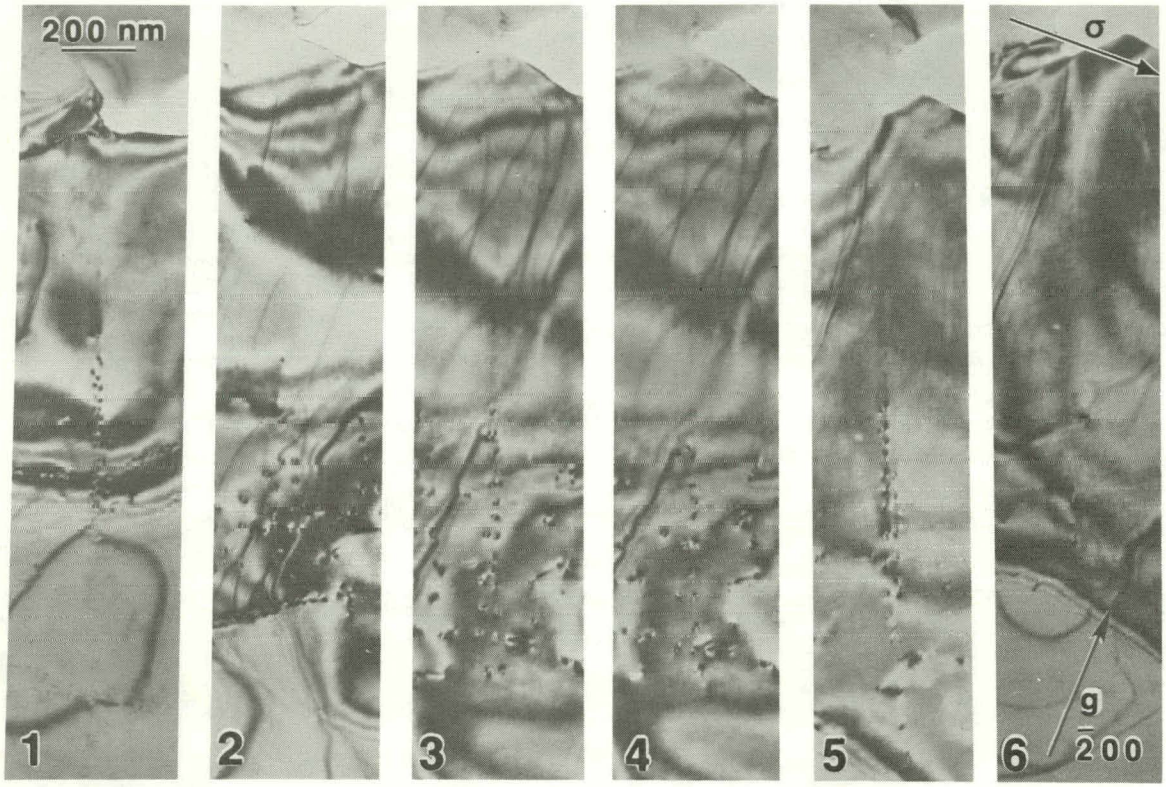

Fig. 3.10. A sequence of electron micrographs showing crack tip blunting by edge dislocations. Between 2, 3, and 4 crack blunting has occurred. Between 4 and 5 the crack has propagated slightly, and the dislocations are now on a new set of slip planes parallel and adjacent to the previous set. *B* is near [011].

describes the distribution of dislocations on an inclined plane in equilibrium with the crack. The integral equation is formulated by a superposition of the forces on each dislocation due to the presence of other dislocations as well as the crack. The force on the dislocation is calculated by making use of the elasticity solution of a single edge dislocation near a finite crack. The integral equation is then solved numerically. The results show that the stress field is relaxed within the dislocation-free zone in the direction of the pileup, whereas the stress is greater in the direction opposite to the pileup. These results are being applied to interpret the observed behavior of dislocations near the crack tip.

1. Summary of paper to be published.
2. Computer Sciences Division, UCC-ND.

DISLOCATION MOTION NEAR CRACK TIPS DURING STRESS CYCLING[1]

J. A. Horton T. C. Estes
S. M. Ohr

Direct observations by TEM have been made of the behavior of dislocations in the plastic zone ahead of a crack tip during in situ cyclic deformation of aluminum. In this experiment, a thin foil specimen was deformed in tension in an electron microscope until a crack and a plastic zone were created. The stress was then cycled, and the response of the dislocations in the plastic zone was studied.

It was found that during stress cycling dislocations were observed to originate and travel away from a crack tip during loading and then, upon unloading, to travel back to the crack tip and to disappear. Upon reloading, new dislocations were

generated at the crack tip on the same slip plane. This required at least a 20% reduction in stress for the dislocations to reverse directions. This is the first direct evidence indicating that a dislocation can return to and partly heal a crack. This phenomenon was observed only for crack tip blunting dislocations.

A series of micrographs taken during an unloading cycle are shown in Fig. 3.11. A dislocation, marked by an arrow in each micrograph, is shown to be approaching the crack tip in a, b, and c. In d, the dislocation is about to disappear into the crack tip, and in e, it has completely vanished. The entire sequence shown in Fig. 3.11 occurred in about one second; in this time the dislocation traveled about 140 nm. The micrographs were made from a video recording which was recorded at a rate of 30 frames per second. In order to understand the observed dislocation behavior near the crack tip, the distribution of dislocations in the plastic zone during cyclic loading is being analyzed in terms of the dislocation pileup model of fatigue crack growth.

1. Summary of paper to be published.

ELECTRON MICROSCOPE STUDY OF CRACK TIP—CAVITY INTERACTIONS[1]

J. A. Horton S. M. Ohr
W. A. Jesser[2]

One of the major fracture modes which occur in structural materials is microvoid coalescence or dimple rupture. This fracture mode occurs by a process of void nucleation and void growth ahead of the crack tip, which results from plastic deformation processes. In order to study crack tip interactions with cavities, specimens with preexisting cavities were tensile tested at room temperature in the Philips EM400T electron microscope. Type

SSDN 2689

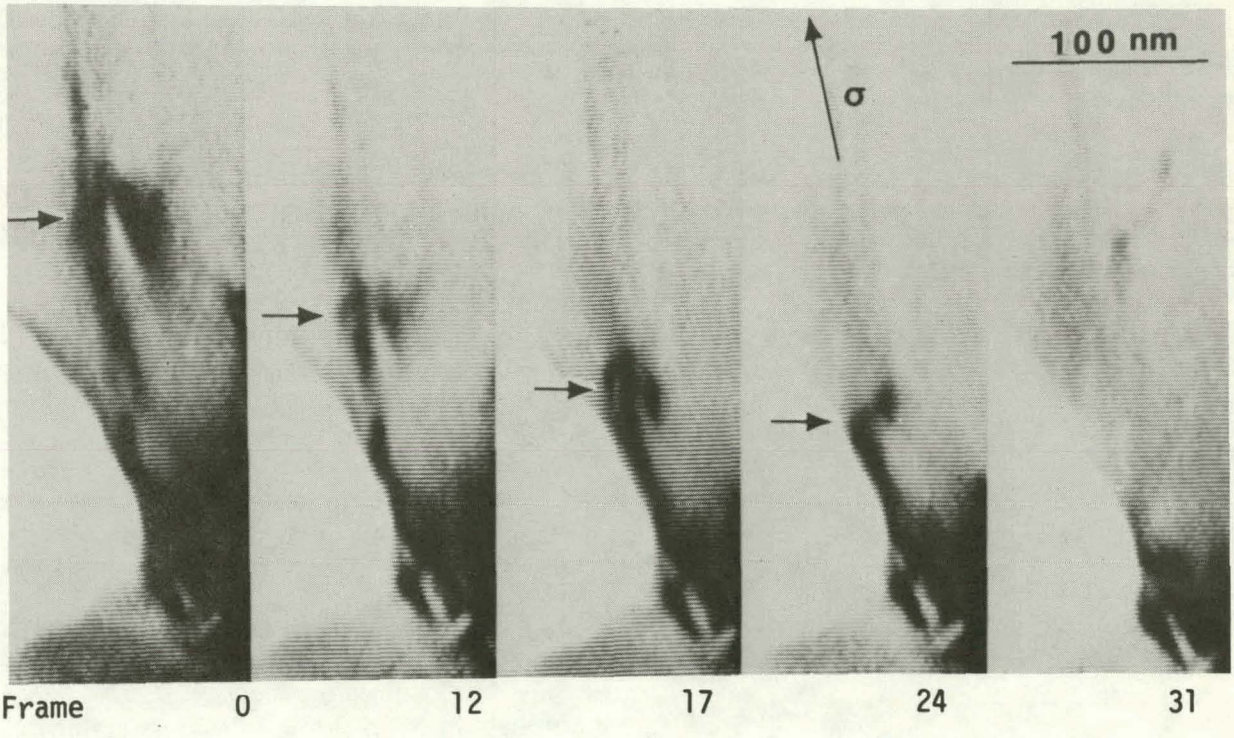

Fig. 3.11. A series of micrographs depicting a dislocation returning to and disappearing at a crack tip during an unloading cycle. This sequence occurred within a period of one second.

316 stainless steel tensile specimens were irradiated with either 5-MeV iron ions or 80-keV helium ions, which produced cavities up to 60 and 12 nm in diameter, respectively.

The irradiated stainless steel fractured in a manner similar to unirradiated stainless steel in that screw dislocations were generated by a Mode III shear crack and moved along a distinct set of slip planes without any dislocation cross slipping. As shown in Fig. 3.12, dislocations at distances up to 6 μm from the crack tip cut, sheared, and, thereby, elongated cavities which intersected the slip planes. Figure 3.12(a) shows elongated cavities with the dislocations out of contrast. Figure 3.12(b) shows the crack-tip-generated dislocations in contrast, which resulted in the cavity elongation. No apparent volume change in the cavities occurred. Near the crack tip, more generalized plastic deformation processes produced local strains up to 400% over a limited region, which was sometimes within only 12 nm of the crack flank. This resulted in an apparent volume enlargement of the cavities. The cavities did not continue to enlarge until they intersected, but instead an intercavity fracture occurred in a brittle fashion as evidenced by the lack of ligament formation. The normally quoted vacancy formation energies and the number of vacancies produced per unit strain of plastic deformation did not account for the observed cavity volume enlargement. These results indicate that on a local scale the dislocation processes near a crack tip are substantially modified from those in bulk material.

---

1. Summary of paper: *Journal of Nuclear Materials* (in press).
2. University of Virginia, Charlottesville, Va.

IN SITU FRACTURE EXPERIMENTS IN bcc METALS[1]

S. Kobayashi[2] S. M. Ohr

Plastic deformation ahead of a crack tip has been the subject of numerous theoretical and experimental investigations in the past, because the stress distribution and the displacement near the crack are strongly affected by the extent of the deformation. The fracture toughness of a material also depends critically on the amount of plastic deformation preceding catastrophic crack propaga-

SSDN 2691

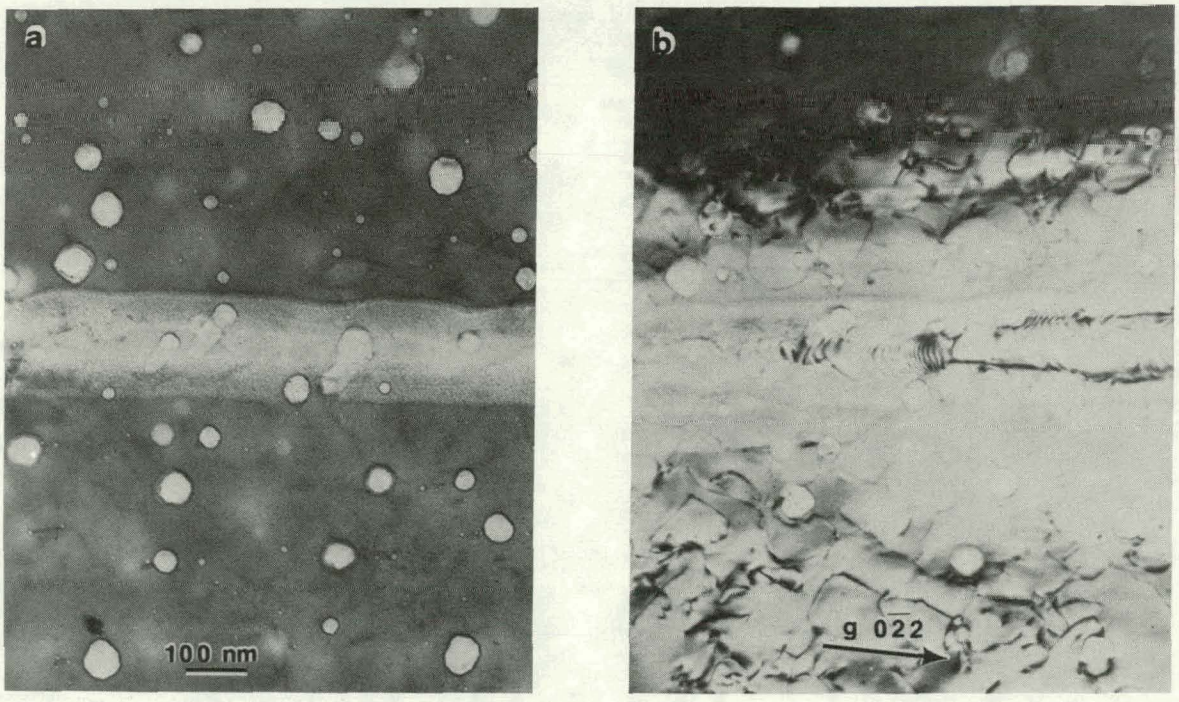

Fig. 3.12. (a) TEM micrograph of cavities near a crack tip elongated by crack tip dislocations in ion-irradiated Type 316 stainless steel. (b) Same area with dislocations in contrast and electron beam direction near [011].

tion. The elasticity solutions for the stress and strain ahead of the crack are valid only when the yielded region is small compared with the size of the crack. It is, therefore, of great interest to seek experimental information concerning the extent and the mechanism of plastic deformation around propagating cracks to establish a model of crack-tip plasticity and its relationship to fracture criteria. Recently, Ohr and Narayan[3] studied the fracture of stainless steel single crystals using an in situ electron microscope technique and found that the extent of crack tip plasticity was determined by the critical crack opening displacement required to propagate the crack. In the present study, the in situ fracture experiment was extended to the bcc metals, molybdenum and tungsten.

Figure 3.13 shows plastic zones observed in a thin foil of a tungsten single crystal. Two small cracks were nucleated simultaneously at the edge of the electropolishing hole, and their plastic zones intersect each other. Although the cracks are still very small, their plastic zones have extended far into the specimen. The area between the crack tip and the plastic zone is free of dislocations, and this dislocation-free zone is nearly as long as the plastic zone itself. Under constant applied stress, it was possible to observe a number of dislocations being emitted from the crack tip. These dislocations moved through the dislocation-free zone and joined other dislocations in the plastic zone. The dislocations in the plastic zone had the Burgers vector $\mathbf{a}/2[111]$ and were on a $(1\bar{1}0)$ slip plane.

According to the BCS theory of fracture,[4] the dislocation density in the plastic zone is highest at the crack tip; hence, the dislocation-free zone of the type observed in the present study is not expected. To examine the implication of the present observation, calculations were made to determine the stable positions of the dislocations ahead of an elastic crack as a function of the number of dislocations in the plastic zone. An equilibrium equation was set up for an individual dislocation by balancing the crack stress, the stress due to other dislocations, and the friction stress. The equilibrium equation was solved numerically by applying the Newton-Raphson method[5] and by treating each dislocation discretely. The results of the calculations are shown in Fig. 3.14, which shows that the dislocation-free zone is expected when the number of dislocations in the plastic zone is less than that required to relax completely the stress concentration established at the crack tip.

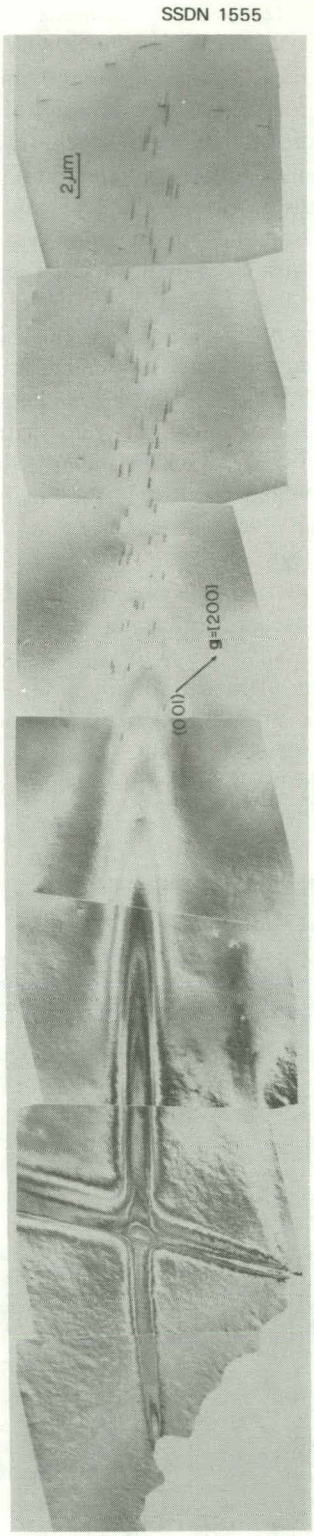

Fig. 3.13. Electron micrograph showing plastic zones in tungsten single crystals observed during an in situ fracture experiment. The area between the crack tip and the plastic zone is free of dislocations.

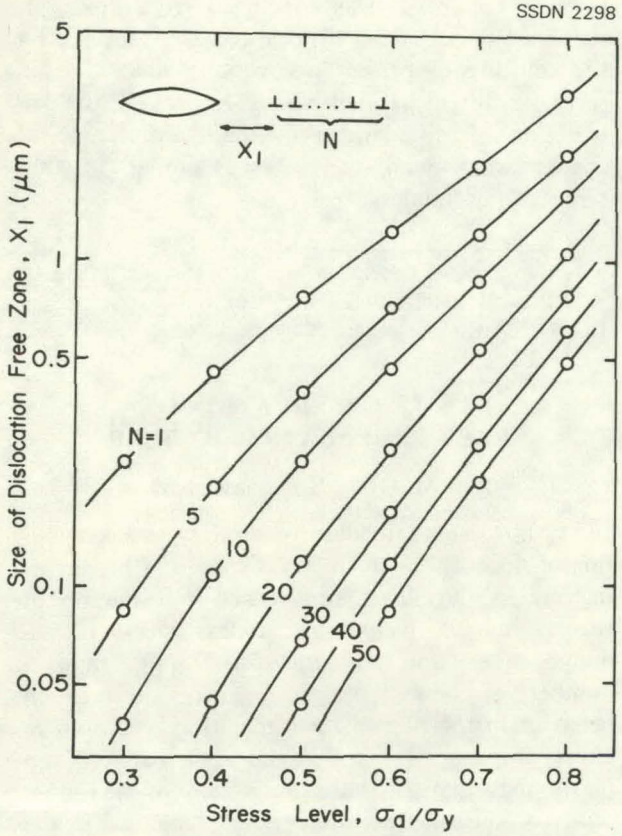

Fig. 3.14. The calculated size of the dislocation-free zone as a function of the ratio of the applied stress σ_a to the friction stress σ_f. The size of the dislocation-free zone increases with the applied stress and decreases with the number of dislocations N in the plastic zone.

The size of the dislocation-free zone increases with the applied stress and decreases with the number of dislocations in the plastic zone. The presence of the dislocation-free zone, therefore, can be attributed to the difficulty associated with the generation of dislocations at the crack tip.

1. Summary of paper: *Philos. Mag.* **A42,** 763 (1980).
2. Present address: Toyota Central Research and Development Laboratories, Nagoya, Japan.
3. S. M. Ohr and J. Narayan, *Philos. Mag.* **A41,** 81 (1980).
4. B. A. Bilby, A. H. Cottrell, and K. H. Swinden, *Proc. Royal Soc. London* **A272,** 304 (1963).
5. F. B. Hildebrand, *Introduction to Numerical Analysis,* McGraw-Hill, New York, 1974.

IN SITU OBSERVATIONS OF THE FORMATION OF PLASTIC ZONE AHEAD OF A CRACK TIP IN COPPER[1]

S. Kobayashi[2] S. M. Ohr

In situ electron microscopy has been shown to be a useful technique to study the structure of the plastic zone ahead of a crack. In thin foils of stainless steel, the plastic zone consisted of an inverse pileup of screw dislocations, which have split into partial dislocations with stacking faults between them. Similar structures were also observed in bcc metals, but the dislocations were not split and frequently cross slipped out of the original slip plane. Since it was found that the detailed structure of the plastic zone ahead of a crack depended on the stacking fault energy of the materials, we have extended the studies to copper, a metal of medium stacking fault energy.

From polycrystalline copper sheets of commercial purity, tensile specimens were punched out and then annealed at 900°C for 3 h. The specimens were electropolished at 20°C to perforation in an electrolyte of 24% ethyl alcohol, 5% isopropyl alcohol, 24% phosphoric acid, and 47% water.

When the tensile stress was applied gradually to the specimen, dislocations started to move, and the number of dislocations in motion increased as the stress was increased. Following the initial slip activities, cracks were initiated at the edge of the hole and propagated rapidly into the specimen. During this propagation, many dislocations were generated at the crack tip and moved into the specimen, forming a plastic zone.

Figure 3.15 shows a crack and a plastic zone that is in the form of a thin ribbon of dark contrast. The dislocations in the plastic zone are split into partial dislocations, and the fringes due to stacking faults can be seen between the partials. From the trace analysis, the slip plane was identified as (111). It can be seen that part of the plastic zone immediately ahead of the crack is free of dislocations. Beyond this dislocation-free zone, the dislocations are in the form of an inverse pileup (i.e., the dislocation density is higher near the crack tip and gradually decreases toward the end of the plastic zone). In order to study the structure of the plastic zone in more detail, contrast analyses were carried out by imaging the area using various dif-

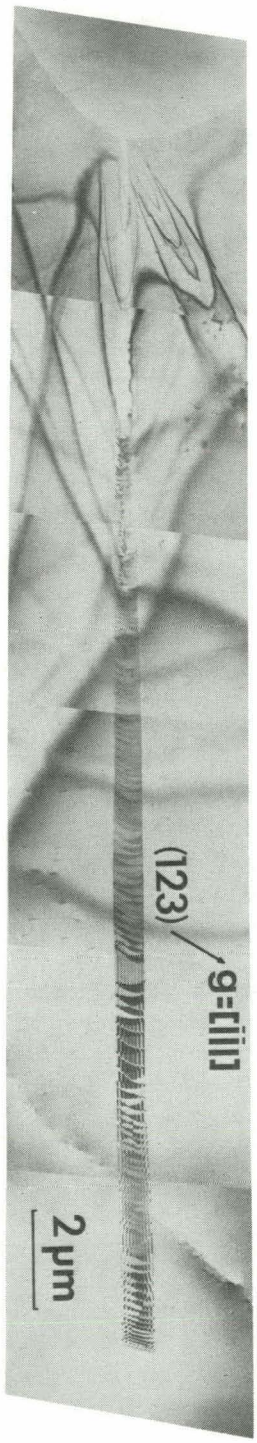

Fig. 3.15. Electron micrograph showing a shear crack of Mode III type and its plastic zone in copper. The dislocations in the plastic zone are in the form of a linear array and are split into partial dislocations. A dislocation-free zone is present between the crack tip and the plastic zone.

fraction vectors. It was concluded from the analyses that these partial dislocations were formed by the splitting of perfect dislocations which lay on several different parallel planes. In general, the distribution of dislocations in the plastic zone of copper was found to be very similar to that reported for stainless steel.

---

1. Summary of paper: *Scripta Met.* **15,** 343 (1981).
2. Present address: Toyota Central Research and Development Laboratories, Nagoya, Japan.

IN SITU OBSERVATION OF CRACK PROPAGATION BY TEM[1]

S. M. Ohr S. Kobayashi[2]

TEM was used to observe directly the distribution of dislocations in the plastic zone of propagating cracks during in situ tensile deformation of various metals including stainless steel, nickel, molybdenum, and niobium. The results show a number of new findings regarding dislocation behavior in the plastic zone and its relationship to crack propagation. The plastic zone results from plastic deformation on the slip system of maximum resolved shear stress that is coplanar with the crack. Dislocations in the plastic zone are in the form of an inverse pileup, and the number of dislocations in the plastic zone corresponds to the displacement at the crack tip. It is also noted that a zone devoid of dislocations is present in all the metals studied near the crack tip. The presence of a highly stressed elastic zone free of dislocations between the crack tip and the plastic zone has been discussed,[3] but the present observation provides the first experimental evidence for such a zone.

These observations have shown that the phenomenon of crack propagation is closely related to the extent to which a material can deform plastically. Dislocations, generated at the crack tip to relieve the stress concentration, contribute in turn to the crack opening displacement. The availability of various slip systems, as well as the stacking fault energy, determines the geometry of the plastic zone. Grain boundaries can act as barriers to dislocation motion and, hence, control crack propagation. These results have demonstrated that in situ TEM is very useful in studying the physical phenomena occurring at the crack tip. Further application of the technique is expected to contribute greatly to a better understanding of fracture processes in various structural materials.

1. Summary of paper: *J. Met.* **32,** 35 (1980).
2. Present address: Toyota Central Research and Development Laboratories, Nagoya, Japan.
3. R. Thomson, *J. Mater. Sci.* **13,** 128 (1978).

SPECIALIZED DEFORMATION STAGES FOR THE PHILIPS EM400T

J. A. Horton R. L. Wallace[1]

In order to perform the electron microscope experiments described in other contributions of this section, several specialized deformation stages were designed and constructed for the Philips EM400T transmission electron microscope. These stages were designed to deform a rectangular sheet specimen in pure tension. The specimens were spark machined before being electropolished until perforation. Upon tensile testing in the microscope, cracks initiated at the edge of the electropolishing hole and propagated toward the thicker areas of the specimen.

The stage shown in Fig. 3.16 is a constant-load, hydraulically operated stage which can perform stress cycling. In this stage, force on a hydraulic fluid-filled bellows is transferred to the bellows mounted on the stage, which provides the tensile stress. The load on the specimen is indicated by the fluid pressure. A low-viscosity fluid was used to allow rapid stress cycling. Another tensile stage was designed and constructed to perform tensile experiments by controlling the crosshead displacement with a mechanically driven screw. This stiff stage is necessary for specimens of low ductility.

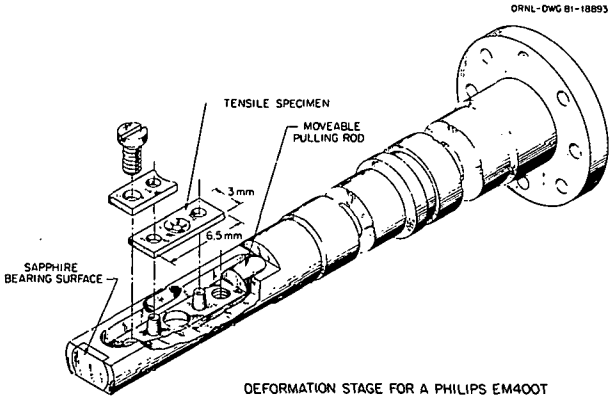

Fig. 3.16. Sketch of a deformation stage for the Philips EM400T electron microscope designed and constructed at ORNL.

Both stages allow single axis eucentric tilting over a $\pm 45°$ range in the electron microscope. The stability of the hydraulic stage is such that the maximum magnification of the microscope can be utilized during the deformation.

A low-temperature deformation stage is currently being built. This stage uses the nitrogen gas flow from a liquid nitrogen reservoir mounted on the stage to cool the specimen to $-150°C$. Temperature measurement and control are provided by two thermocouples.

1. Plant and Equipment Division, ORNL.

DISLOCATION-FREE ZONE MODEL OF FRACTURE[1]

S.-J. Chang[2] S. M. Ohr

Recent observations by electron microscopy[3] have shown that a dislocation-free zone (DFZ) is present between the crack tip and the linear pileup of dislocations in the plastic zone. The presence of the DFZ implies that the crack tip can remain atomically sharp, and Griffith's fracture criteria can be valid even in the presence of a considerable amount of plastic deformation at the crack tip. In order to understand the physical origin of the DFZ, we have studied the distribution of dislocations in equilibrium with the crack and the applied stress. A singular integral equation is formulated, and the distribution function of the dislocations is obtained from the equation in terms of elliptic integrals. The condition of compatibility and the elastic stress intensity factor at the crack tip are also derived.

Figure 3.17 shows a plot of the stress intensity factor K as a function of the applied stress T. The size of the DFZ (e/c) and the size of the plastic zone (a/c) relative to the crack size (c) are used as two parameters. It can be seen for moderate values of K and T that the stress intensity factor K is primarily a function of the size of the DFZ (e/c) and that the size of the plastic zone (a/c) is determined primarily by the applied stress T. This is a remarkable result which can be used to determine experimentally the value of K by measuring the size of the DFZ. Similar studies have been made of the dependence of the crack opening displacement (COD) on the applied stress, the plastic zone size, and the length of the DFZ.

Based on the mechanism of dislocation generation at the crack tip proposed by Rice and

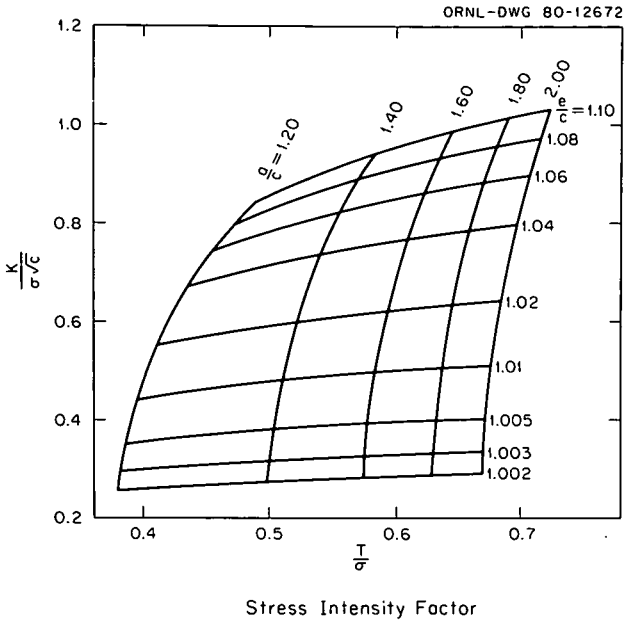

Fig. 3.17. Stress intensity factor K vs applied stress T for various sizes of the DFZ (e/c) and the plastic zone (a/c), where c is the crack length. It shows that K is primarily a function of the size of the DFZ.

Thomson,[4] it is shown that the formation of the DFZ is anticipated when the stress intensity factor K is less than a critical stress intensity factor K_g defined for a spontaneous generation of dislocations. The magnitude of K_g, relative to the critical stress intensity factor for brittle fracture K_c, determines the brittle-ductile nature of a material.

1. Summary of paper: *Journal of Applied Physics* (in press).
2. Computer Sciences Division, UCC-ND.
3. S. M. Ohr and S. Kobayashi, *J. Met.* **32,** 35 (1980).
4. J. R. Rice and R. Thomson, *Philos. Mag.* **29,** 73 (1974).

A MODEL OF SHEAR CRACKS WITH DISLOCATION-FREE ZONES[1]

S.-J. Chang[2] S. M. Ohr

TEM observations of the distribution of dislocations in the plastic zone of cracks have shown that, in many instances, there is a zone near the crack tip which is free of dislocations. In order to treat this problem, an integral equation was formulated in terms of a distribution of dislocations. The distribution function was obtained in a closed form in terms of elliptic integrals of the first and third kinds. The relationship between the sizes of the crack and the DFZ was obtained as a function of applied stress, similar to the condition derived in the BCS theory of fracture. Because of the presence of the DFZ, the stress diverges at the crack tip, leading to a finite elastic stress intensity factor. A simple analytical expression for the stress intensity factor was obtained.

1. Summary of paper: p. 23 in *Dislocation Modelling of Physical Systems,* ed. by M. F. Ashby, R. Bullough, C. S. Hartley, and J. P. Hirth, Pergamon, New York, 1981.
2. Computer Sciences Division, UCC-ND.

FRACTURE MECHANICS OF ELASTIC-PLASTIC CRACKS[1]

S. M. Ohr S.-J. Chang[2]

Direct observations by TEM of the plastic zone of propagating cracks in various metals have shown that the area immediately ahead of the crack tip is devoid of dislocations. Under a constant applied stress, the dislocations are generated at the crack tip, move through the DFZ, and join other dislocations in the plastic zone. The length of the DFZ is shorter, and the thickness of the specimen in the DFZ is thinner in ductile materials than in brittle materials. In ductile materials, the cracks propagate into the DFZ, which is thinned appreciably by plastic deformation, by rupturing thin ligaments in a zigzag manner. In brittle materials, the fracture of the DFZ occurs by cleavage which, in some instances, is accompanied by the emission of dislocations.

Figure 3.18 shows schematically the crack tip geometry observed in these fracture experiments. The crack tip is located at c, and the DFZ is present between the crack tip and the beginning of the plastic zone e. The plastic zone, represented by an inverse pileup of dislocations, extends to a. The crack tip displacement δ_p is the portion of the COD which is contributed by the dislocations in the plastic zone. Thus, $\delta_p = bN$, where b is the Burgers vector and N is the number of dislocations in the plastic zone. The final step of the fracture process is accomplished by an elastic fracture of the thin ligament within the DFZ.

The stress intensity factor of this elastic-plastic crack has been calculated from the DFZ theory of fracture[3] as a function of the applied stress and the number of dislocations in the plastic zone. The

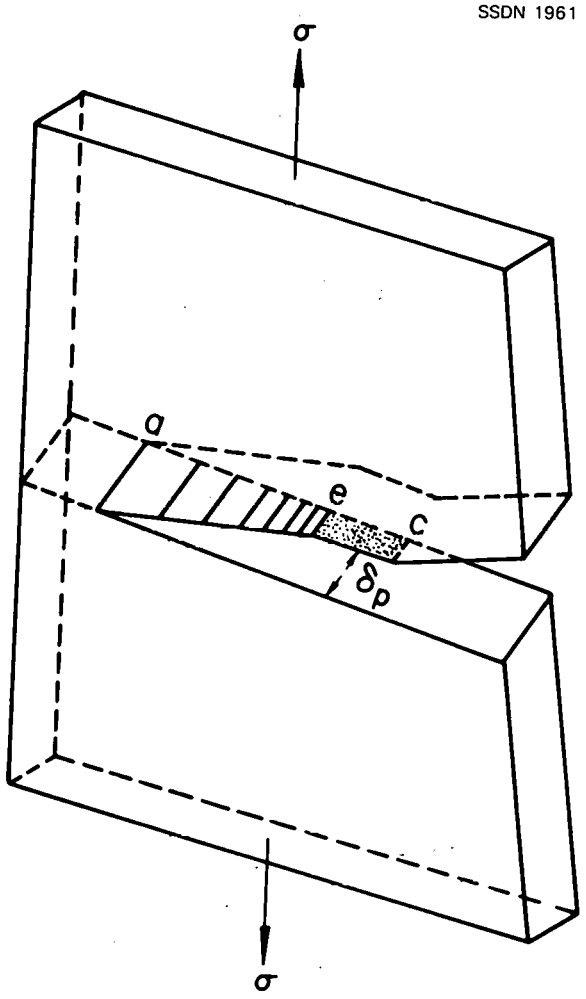

Fig. 3.18. Schematic drawing of crack-tip geometry observed during in situ TEM fracture experiments of thin sheet specimens. It shows that cracks propagate by a combination of elastic and plastic fracture processes.

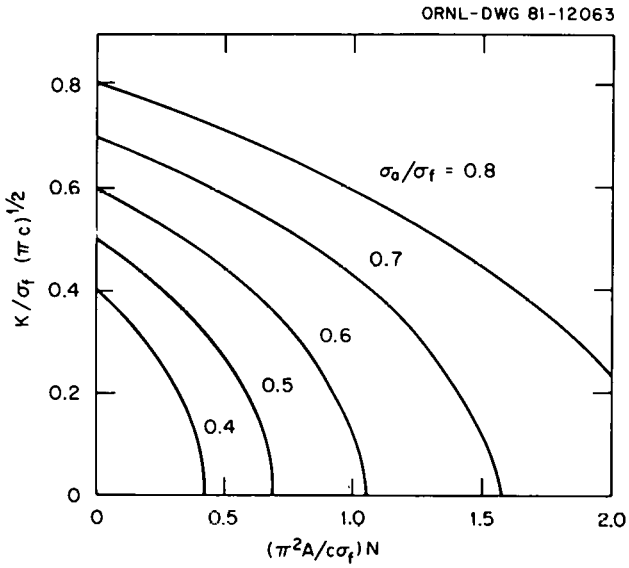

Fig. 3.19. Dependence of stress intensity factor K on the number of dislocations in the plastic zone N for a series of values of applied stress σ_a.

result is shown in Fig. 3.19. As the number of dislocations N in the plastic zone increases, the stress intensity factor K decreases from the elastic value at first slowly and then rapidly to zero. The crack with zero stress intensity factor is a crack which is completely relaxed by plastic deformation and, hence, may be called a plastic crack. Between the elastic and plastic cracks, a wide range of elastic-plastic cracks having the crack-tip stress singularity, as well as the plastic zone, is possible. These elastic-plastic cracks are expected if there is a critical stress intensity factor K_g associated with the generation of dislocations at the crack tip. The expression for K_g is obtained from the crack tip dislocation nucleation model of Rice and Thomson.[4] In most materials, the magnitude of K_g is less than the critical stress intensity factor K_c for brittle fracture.

To test the validity of the DFZ theory of fracture, we have compared the predictions of the theory with the geometry of the plastic zone observed directly in the electron microscope in a number of metals and alloys. The values of the crack tip stress intensity factor K are determined from the experimentally measured lengths of the crack, the DFZ, and the plastic zone. For the friction stress σ_f, the measured values of yield stress of these metals are used. In Table 3.2, we have tabulated the measured values of K, along with σ_f, for the seven metals that were studied. These values are then compared with the theoretical values of K_g for dislocation generation and of K_c for brittle fracture. It can be seen that for all of the ductile fcc metals and niobium, the measured values of K are in very good agreement with the theoretical values of K_g. In semibrittle molybdenum and tungsten, the measured values of K are greater than K_g but are less than K_c. This may be taken as evidence that in many structural materials of interest, the physical parameter, which is important in determining the critical stages of crack propagation, is the stress intensity factor required

Table 3.2. Comparison of measured stress intensity factor K with theory

Material	σ_f (10^7 Pa)	K (10^5 N/m$^{3/2}$)	Theory K_g (10^5 N/m$^{3/2}$)	Theory K_c (10^5 N/m$^{3/2}$)
S. steel	4.3	1.6	1.8	7.6
Copper	1.5	0.9	0.9	5.2
Nickel	3.4	1.8	1.7	7.2
Aluminum	2.3	0.8	0.6	2.9
Niobium	2.5	1.7	1.6	7.9
Molybdenum	24.3	10.8	5.0	13.0
Tungsten	16.0	12.3	6.5	16.5

for the generation of dislocations at the crack tip rather than the surface energy of the materials.

1. Summary of paper to be published.
2. Computer Sciences Division, UCC-ND.
3. S.-J. Chang and S. M. Ohr, *Journal of Applied Physics* (in press).
4. J. R. Rice and R. Thomson, *Philos. Mag.* **29,** 73 (1974).

CONDITION OF FINITE STRESS FOR THE STRIP-YIELDING MODEL WITH DISLOCATION-FREE ZONE[1]

S.-J. Chang[2] S. M. Ohr
J. A. Horton

Recently, we have developed a DFZ theory of fracture by considering a linear array of dislocations in equilibrium with a sharp elastic crack of Mode III type.[3] In this theory, the elastic stress intensity factor K is given by

$$\frac{K}{\sigma_f\sqrt{\pi c}} = \frac{2}{\pi}\frac{\sqrt{\alpha^2-k^2}}{\alpha}F\left(\frac{\pi}{2},\ k^2\right) , \qquad (1)$$

where σ_f is the friction stress, c is the crack length, and F is the complete elliptic integral of the first kind. The parameters α^2 and k^2 are related to the sizes of the DFZ (e/c) and the plastic zone (a/c). The condition for finite stress at both ends of the plastic zone requires that the applied stress T is related to the crack tip geometry by

$$\frac{\pi}{2}\frac{T}{\sigma_f} = \frac{\sqrt{\alpha^2-k^2}\sqrt{1-\alpha^2}}{\alpha}\Pi\left(\frac{\pi}{2},\ \alpha^2,\ k^2\right) , \qquad (2)$$

where Π is the complete elliptic integral of the third kind. These two relations link the microscopic crack tip parameters with the macroscopic fracture mechanics parameters.

In the present work, the DFZ theory is shown to be an extension of the BCS theory[4] by demonstrating that the results of the BCS theory can be obtained as a special limiting case of the present theory. As a first step, it is shown that the elliptic integral of the third kind appearing in Eq. (2) is expressed in terms of Heuman's lambda function. It is then shown that as the size of the DFZ is made to approach zero, Eq. (2) is reduced to the BCS condition in the form of the inverse cosine function

$$\frac{\pi}{2}\frac{T}{\sigma_f} = \cos^{-1}(c/a) . \qquad (3)$$

The case of an elastic crack can also be obtained from the present theory by considering the limit of a vanishingly small plastic zone. By combining Eqs. (1) and (2) and by forcing e to approach a, we have obtained the well-known relationship

$$T = \frac{K}{\sqrt{\pi c}} , \qquad (4)$$

between the applied stress T and the stress intensity factor K of an elastic crack. We have also considered the case of a plastic zone, which is very much longer than the length of the DFZ. It is found that in the limit the applied stress T approaches the friction stress σ_f. These results demonstrate the validity of the DFZ theory and, hence, support the contention that the theory is a generalization of the BCS theory.

1. Summary of paper: *International Journal of Fracture* (in press).
2. Computer Sciences Division, UCC-ND.
3. S.-J. Chang and S. M. Ohr, *Journal of Applied Physics* (in press).
4. B. A. Bilby, A. H. Cottrell, and K. H. Swinden, *Proc. Royal Soc. London* **A272,** 304 (1963).

DEFECTS AND IMPURITIES IN INSULATING CRYSTALS

SUBSTITUTIONAL H^- ION VIBRATIONS IN THE ALKALINE-EARTH OXIDES REDUCED AT HIGH TEMPERATURES[1]

R. R. Gonzalez[2] Y. Chen
Mark Mostoller

The infrared spectra of MgO, CaO, and SrO crystals containing high concentrations of hydrogen were studied. The crystals were heated at high temperatures (2000–2400 K) and high pressures (4–7 atm) in magnesium or calcium vapor in a closed tantalum vessel and then were rapidly cooled. This treatment produces oxygen vacancies. When hydrogen impurities are present in the crystals, they can be trapped at oxygen-vacancy sites and form H^- ions. We investigated the infrared spectra of such crystals and found evidence that structure appearing in the low-frequency region arises from vibrations of H^- ions substituting for O^{2-} ions in the crystals. These experiments are of particular interest because the conditions that prevail in the operation of some energy-efficient devices, such as the Stirling engine, are the same as those which produce H^- ions, namely, high temperatures and high pressures of a reducing gas.

In MgO, sharp lines at 1027, 1034, and 1056 cm^{-1} emerged after the high-temperature reduction (see Fig. 3.20). The intensity of these lines depends strongly on both the initial hydrogen content and the temperature for the reduction. The relative intensities of the lines, however, were roughly constant from sample to sample. We attribute these lines to fundamental vibrations of substitutional H^- ions. A low-intensity signal at 2106 cm^{-1} can also be observed in Fig. 3.20. This line is attributed to the first harmonic vibration for the 1056-cm^{-1} absorption. The evidence is (1) an intensity correlation with the 1056-cm^{-1} line, (2) a doubling of the frequency, and (3) a larger thermal shift than that of the fundamental H^- vibration. Similar lines were observed in similarly treated CaO and SrO crystals.

Table 3.3 summarizes our data on absorption lines attributed to substitutional H^- ion vibrations

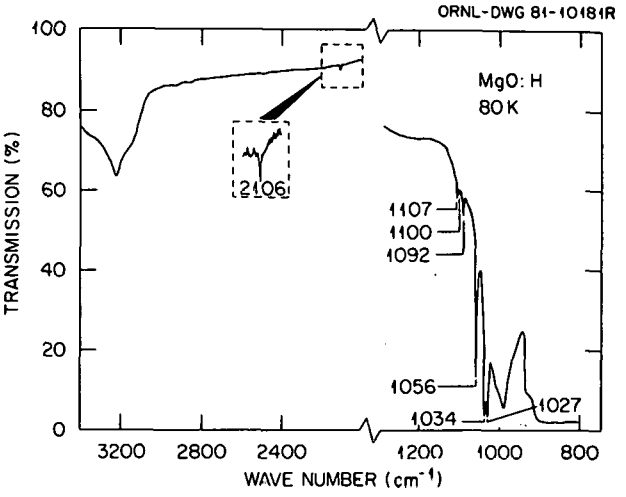

Fig. 3.20. Infrared spectrum of an MgO crystal with relatively high hydrogen content after reduction at 2400 K in Mg vapor. The sample thickness was 0.6 mm. In the inset, the band of 2106 cm^{-1} is magnified 5× in the vertical direction.

Table 3.3. Substitutional H^- ion vibrational frequencies in MgO, CaO, and SrO, in cm^{-1}

The numbers in parentheses are estimated relative intensities within each series of lines

	H^- lines		Other lines	
	80 K	295 K	80 K	295 K
MgO	1056 (1.0)	1053 (1.0)	1092 (1.0)	
	1034 (0.9)	1032 (0.9)	1100 (0.3)	
	1027 (0.9)	1024 (0.9)	1107 (0.8)	1104
	2106 (<0.1)	2098 (<0.1)		
CaO	885 (1.0)	880 (1.0)		
	916 (0.3)	911 (0.3)		
SrO	815 (1.0)	809 (1.0)		
	822 (0.3)			
	832 (0.3)	827 (0.3)		

in MgO, CaO, and SrO. Figure 3.21 is a log-log plot of local mode frequency vs lattice constant, which to a good approximation is a straight line, as it is in the alkali halides,[3] with about the same slope as the corresponding plot for NaCl, KCl, and RbCl. In each of the three oxides, the fundamental H^- ion vibrations produce two or more sharp, closely spaced lines, whose intensities in a given crystal are comparable but not necessarily equal or

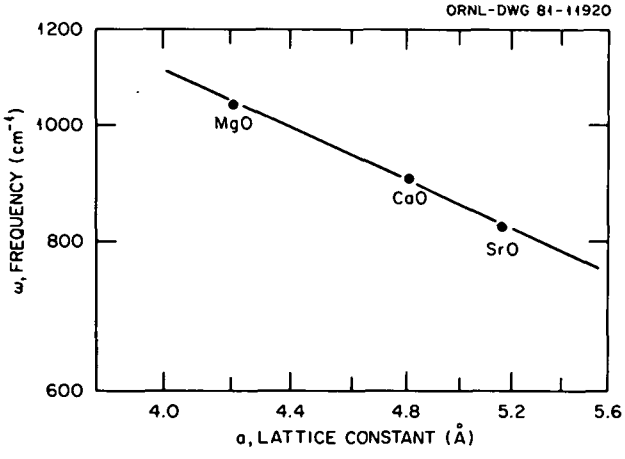

Fig. 3.21. Plot of H^- ion frequency vs lattice constant in the alkaline-earth oxides.

rationally related. This may indicate a lowering of the point-group symmetry around the H^- ion from O_h to a less symmetric configuration, which may be due to local charge compensation. The observation of the first harmonic in MgO is further evidence of reduced symmetry around the H^- ion in that crystal, since the first harmonic is not an optically allowed transition in O_h symmetry. It is also possible, particularly in MgO where two sets of three lines are observed at 80 K, that H^- ions are present in local environments of slightly different symmetries. Satellite lines arising from this effect have been observed in the alkali halides[4] and the alkaline-earth fluorides.[5]

1. Summary of paper to be published.
2. Guest scientist from Universidad Complutense, Madrid, Spain.
3. D. Kuhner and M. Wagner, *Z. Physik* **207**, 111 (1967).
4. T. Timusk and M. V. Klein, *Phys. Rev.* **141**, 664 (1966).
5. R. J. Elliott et al., *Proc. Roy. Soc. London* **A289**, 1 (1965).

LUMINESCENCE IN THERMOCHEMICALLY REDUCED MgO: THE ROLE OF HYDROGEN[1]

B. T. Jeffries[2] Y. Chen
R. R. Gonzalez[3] G. P. Summers[2]

One of the characteristics of thermochemically reduced MgO crystals is the long-lived green luminescence (or phosphorescence) observed following optical excitation of *F* centers (oxygen vacancy with two electrons) near room temperature. The nature of the emission has long been the subject of debate.[4] We present the first unambiguous interpretation of the origin of the long-lived luminescence, which reopens the debate on recent models that have been proposed.[5]

The main optical absorption transition of the *F* center in MgO and CaO takes an electron from the $^1A_{1g}$ ground state to a $^1T_{1u}$ excited state. During the subsequent relaxation of the center in CaO, the electron falls nonradiatively into a $^3T_{1u}^{\dagger}$ excited state from which it then decays radiatively to the ground state with a transition energy of 2.0 eV and an intrinsic lifetime of 3.3 ms. Above 100 K the electron is able to escape into the conduction band by thermal excitation from the $^3T_{1u}^{\dagger}$ excited state. It can then become captured by a metastable trap, which gives rise to the long-lived phosphorescence. The kinetics of this process is well understood in CaO, but until now no evidence was available concerning the nature of the traps involved in either CaO or MgO.

The results presented below show that these traps are mostly isolated H^- ions which substitute for O^{2-} ions. Hydrogen is a common impurity in the alkaline-earth oxides, and local modes at 1053, 1032, and 1024 cm^{-1} have been identified as due to H^- ions in MgO.[6] Results are presented on three representative samples, labeled MgO I, MgO II, and MgO III (see Table 3.4). The concentrations of *F* centers and H^- ions were estimated from the absorption coefficients at 4.95 eV and 1053 cm^{-1}, respectively. Samples held at 260 K were illuminated until the emission reached a maximum intensity, and then the excitation was removed. The results are shown in Fig. 3.22, in which the intensities at $t = 0$ have been normalized. It is clear that as the concentration of H^- ions increases, the phosphorescence at 2.3 eV becomes increasingly long lived. In fact, for MgO I, which has the highest H^- concentration, the phosphorescence was still visible to the eye after 15 min. None of the curves can be fitted with a single

Table 3.4. Characteristics of thermochemically reduced MgO samples
α_F and n_F are absorption coefficients and concentrations of F centers, respectively, α_H and n_H refer to the same parameters for H^- ions, and τ is the phosphorescence lifetime

Sample	α_F (cm^{-1})	n_F (cm^{-3})	α_H (cm^{-1})	n_H (cm^{-3})	τ (s)
MgO I	330	(1.6×10^{18})	11	(3.3×10^{18})	330
MgO II	820	(4.1×10^{18})	0.5	(1.5×10^{17})	27
MgO III	110	(5.5×10^{17})	0.2	(6×10^{16})	3

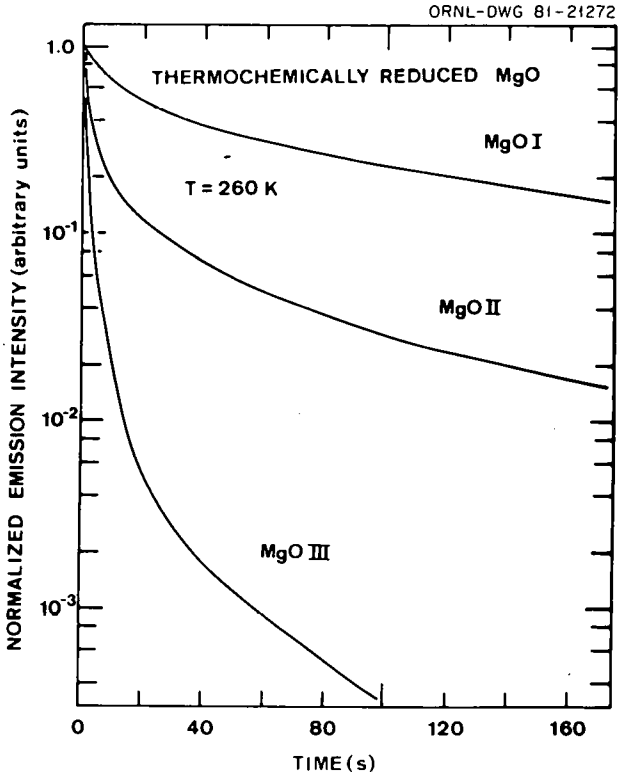

Fig. 3.22. Luminescence decay at 260 K of the 2.3-eV band in thermochemically reduced MgO. The concentration of H^- ions decreases from MgO I to MgO III (see Table 3.4).

simple function, although in each case after an initial relatively rapid decay, the curves correspond to a second-order process. However, if one takes the period over which the intensity falls to 1/10 the initial value as a reasonable measure of the phosphorescence lifetime, then the characteristic times τ for samples I, II, and III are 330, 27, and 3, respectively. The luminescence is not due to H^- ions alone, since a crystal which contained H^- ions but no detectable F centers showed no 2.3-eV emission. F centers are required. In addition, contrary to general belief, the extent of phosphorescence does not increase with the concentration of F centers as any process involving interacting pairs of F centers would require. Specifically, sample II contained about three times the F-center concentration contained in sample I, but it has a characteristic time an order of magnitude smaller.

H^- ions enter the lattice substitutionally for O^{2-} ions and, therefore, represent a region of net positive charge in the lattice. Our measurements indicate that these electron traps cause the long-lived phosphorescence observed near room temperature. We also observed a 2.3-eV luminescence when an electron is released from the H^{2-} trap with a thermal activation energy of 0.7 eV. Although this energy may appear to be small for thermal release of the electron from H^{2-} ions, the polarization energy associated with the surrounding O^{2-} ions is quite large and tends to reduce substantially the binding energy for electrons in oxygen vacancy defects.

---

1. Summary of paper to be published.
2. Oklahoma State University, Stillwater, Okla.
3. Guest scientist from Universidad Complutense, Madrid, Spain.
4. A. E. Hughes and B. Henderson, in *Point Defects in Solids,* ed. by J. H. Crawford, Jr., and L. Slifkin, Plenum Press, New York, 1971.
5. P. Edel et al., *J. Phys. C* **12,** 5245 (1979).
6. R. Gonzalez, Y. Chen, and M. Mostoller, *Physical Review B* (in press).

DISTRIBUTION OF Fe^{3+} IN Fe-DOPED MgO SINGLE CRYSTALS[1]

R. A. Weeks J. F. Gastineau[2]
E. Sonder

It has become apparent[3] that Fe^{3+} has an anomalously high mobility in MgO, and thus the high-temperature equilibrium distribution of substitutional Fe^{3+}, aggregates of Fe^{3+} ions, and cation vacancies are not retained upon rapid cooling to room temperature. We have measured the intensities of electron-paramagnetic-resonance (EPR) spectra due to a number of Fe^{3+} species in Fe-doped MgO samples as a function of thermal treatments. These treatments have included quenching from temperatures between 800 and 1600°C at different rates and isochronal and isothermal anneals. The following conclusions were reached: (1) Fe^{3+} dissolved in MgO is sufficiently mobile that, even with the fastest possible quench rates (>5000 K/sec) for which samples usually are destroyed, high-temperature equilibrium cannot be retained. For the fastest quench rate (in water), the concentration of isolated Fe^{3+} detected in octahedral Mg sites is approximately 1.5 times larger than for the slowest quench rate (in air). (2) Aggregation begins at temperatures as low as 350°C. (3) Ferromagnetic precipitates of $MgFe_2O_4$ do not form for temperatures less than 450°C, even if anneals are carried out for more than 1000 h. However, the concentration of isolated Fe^{3+} in Mg sites decreases by more than a factor of 2 for isochronal anneals between 400 and 550°C.

The two spectral components, shown in Fig. 3.23, appear after isochronal anneals at 650 and 750°C and then disappear after anneals at temperatures ~800°C. The temperature dependence of their intensity indicates that both are due to ferrimagnetic particles, which we suggest are aggregates of Fe^{3+}.

The mobility of the Fe^{3+} is much higher than that predicted by extrapolation of the high-temperature (>1000 K) diffusivity. We tentatively attribute this higher mobility to a high mobility of cation vacancies and of Fe^{3+}-Mg vacancy dimers.

1. Summary of paper: *Phys. Status Solidi* **61**, 265 (1980).

2. Great Lakes College Association Science Semester student from Lawrence College, Appleton, Wis.

3. E. Sonder, J. Gastineau, and R. A. Weeks, *Solid State Div. Prog. Rep., Feb. 29, 1980,* ORNL-5640, p. 142.

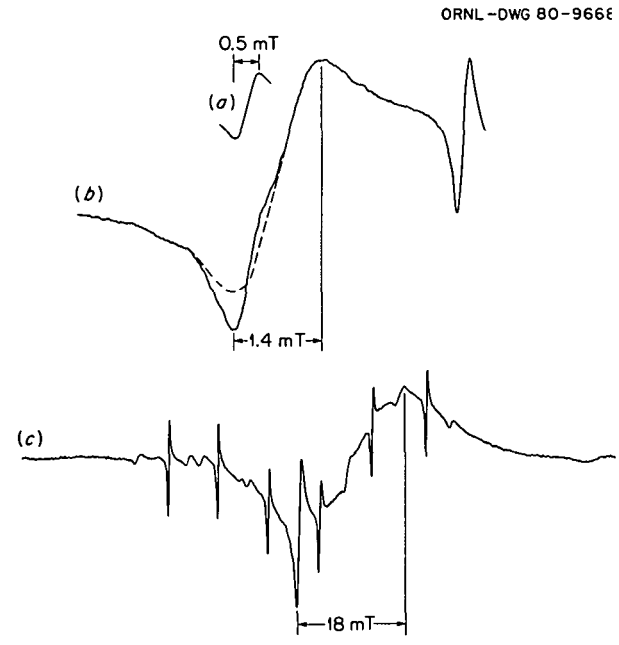

Fig. 3.23. EPR spectra of MgO:Fe after annealing to permit aggregation of Fe oxide. The solid line in curve (b) represents experimental data obtained after annealing at 650°C, and the dashed line is a correction for asymmetry; curve (a) shows the difference between these two curves. Curve (c) shows the experimental data obtained after annealing at 750°C.

NEUTRON IRRADIATIONS IN OXIDIZED Li-DOPED MgO CRYSTALS[1]

Y. Chen J. L. Boldu[3]
E. Montesa[2] M. M. Abraham

The effect of neutron irradiations in Li-doped MgO crystals was investigated using optical absorption and EPR measurements. Unlike electron irradiations, neutron irradiations do not produce stable [Li]° defects (axial configuration: O^{2-}-Li^{+}-O^{-}) in as-grown MgO crystals doped with Li. In crystals containing stable [Li]° defects produced by oxidation at high temperatures, the ionizing property of the electrons increased the concentration of the defects. Neutron irradiations, however, resulted in the loss of [Li]° defects, attended by the formation of stable V°, V^{-}, V_{OH}, and V_F defects with configurations [O^{-}-(Mg vacancy)-O^{-}], [O^{2-}-(Mg vacancy)-O^{-}], [OH^{-}-(Mg vacancy)-O^{-}], and [F^{-}-(Mg vacancy)-O^{-}], respectively. The loss of [Li]° defects is attributed to the recombination of holes from these defects with electrons at multivacancy defects created by neutrons.

1. Summary of paper: *Phys. Rev. B* **24**, 5 (1981).
2. Philippine Atomic Energy Commission, Quezon City, Philippines.
3. Instituto de Fisica, U.N.A.M., Mexico, D.F.

PENETRATION OF SURFACE DAMAGE RESULTING FROM ABRASION AND HEATING OF MgO CRYSTALS[1]

E. Sonder J. V. Spadaro[2]
R. A. Weeks

Chemical polishing and dislocation etch pit observations have been applied to the study of the depth of penetration of dislocations produced by abrading (100) surfaces of MgO. From the results it has been concluded that such dislocations penetrate from 100–700 μm, depending on the source of the material. Heating of the abraded samples up to 1300°C for short times has little influence on the depth of penetration.

1. Summary of paper: *J. Am. Ceram. Soc.* **64**, C65 (1981).
2. Oak Ridge Associated Universities undergraduate research trainee from Stockton College, Union, N.J.

MAGNETO-OPTICAL PROPERTIES OF METALLIC COLLOIDS IN INSULATORS[1]

F. A. Modine V. M. Orera[2]

Colloidal particles of metal are formed in insulating materials when a metallic impurity or constituent precipitates as the result of thermal treatment, photothermal treatment, or redox reaction. Metallic colloids are a stable end product of radiation damage, and they have been produced by ion implantation. Colloids are of interest in connection with nuclear waste storage and with solar absorbers.

The absorption and scattering of light by colloids often give a characteristic color to a transparent insulator, and the associated optical spectra have been extensively studied. In order to probe colloid properties more deeply, a magneto-optical study was made of two colloids, sodium and calcium precipitates in NaCl and CaF_2, respectively. These colloids were chosen because the known optical properties of Na and Ca, together with their approximately free-electron conductivity, allowed a theoretical interpretation of experimental data.

The optical spectrum produced by a colloid is described by an absorption coefficient α that can be computed as a series from either scattering or composite media theory. For small particles, the first term of the series is a good approximation.

$$\alpha \sim \frac{18\pi n_0^3 F}{\lambda} \frac{\epsilon_2}{(\epsilon_1 + 2n_0)^2 + \epsilon_2^2} , \qquad (1)$$

where F is the volume fraction of the metal, n_0 is the refractive index of the host, and ϵ_1 and ϵ_2 are the real and imaginary dielectric functions of the particles. At the wavelength where $\epsilon_1 = -2n_0^2$, Eq. (1) predicts a plasma-type resonance in the absorption.

Magnetic circular dichroism (MCD) is simply the magnetically induced difference between the absorption of left- and right-circularly polarized light. The theory of the MCD follows, if the effect of the magnetic field on the dielectric function can be established. The field enters the intraband terms as the cyclotron frequency ω_c, and it enters the interband terms as a frequency shift $\Delta\omega$ in interband transitions. When these effects are included, the dielectric function is of the form:

$$\epsilon_1^{\pm} = 1 - \frac{\omega_p^2(\omega \mp \omega_c)}{\omega[(\omega \mp \omega_c)^2 + \omega_0^2]} + \beta_1^{\pm}(\omega \mp \Delta\omega) , \quad (2a)$$

$$\epsilon_2^{\pm} = \frac{\omega_p^2\omega_0}{\omega[(\omega \mp \omega_c)^2 + \omega_0^2]} + \beta_2^{\pm}(\omega \mp \Delta\omega) , \quad (2b)$$

where $\omega_p = 4\pi Ne^2/m^*$ and $\omega_c = |e|H/m^*c$, respectively, denote the plasma and cyclotron frequencies, and $\omega_0 = 1/\tau$ is a relaxation frequency. The upper and lower signs, respectively, refer to left- and right-circular polarization, and β_1 and β_2 denote interband contributions. Because a detailed knowledge of the band structure is required, the interband terms are difficult to evaluate. Moreover, the usual Landau description is not valid, because the particles are smaller than Landau orbits. Thus, the induced changes in the interband energies were simply assumed to have a linear-field dependence: $\Delta E = h\Delta\omega = g_{\text{eff}}\mu_B H$, where g_{eff} is an effective g factor.

An approximate description of the MCD was obtained by ignoring interband contributions:

$$\Delta\alpha = \alpha^+ - \alpha^- \sim -\omega_c \frac{\partial\alpha(\omega)}{\partial\omega} \qquad (3)$$

Equation (3) predicts the shape of the MCD and implies that the effect of the magnetic field is to shift the position of the band by $+\omega_c/2$ or $-\omega_c/2$ in energy when it is observed with left- or right-circularly polarized light, respectively.

A detailed analysis required that particle size effects be recognized and that adjustments of the dielectric functions of the bulk metals be made. The shorter relaxation time τ in a small particle was assumed to be: $\omega_0 = 1/\tau \sim \omega_{0b} + V_f/r$, where ω_{0b} is the relaxation frequency for the bulk metal and V_f is the Fermi velocity. A distribution of particle sizes was also assumed. A suitable size distribution function was not found for Na colloids, but for Ca colloids the distribution used by Orera and Alcala[3] to study particle ripening gave a good description of the optical band. This distribution function is

$$F(\rho) = 3\rho^5 \times \exp[3/2(2\rho-3)]/[(3/2-\rho)^{11/3}(\rho+3)^{7/3}] \ , \quad \rho < 3/2 \ ;$$
$$F(\rho) = 0 \ , \quad \rho \geq 3/2 \ ; \qquad (4)$$

where $\rho = r/r_c$ and r_c is the critical radius for ripening. Finally, Orera and Alcala have deduced that Ca colloids are under a hydrostatic pressure of 7.8 kbar and that there is a 10% reduction in the plasma frequency as a consequence.[3]

Figure 3.24 shows measured optical spectra for Na colloids. Recourse to Eq. (3) gave a good fit to the MCD. The intensity of the MCD is predicted by assuming a cyclotron mass equal to Smith's value for the optical mass.[4] Figure 3.25 shows spectra of calcium colloids together with theoretical curves that were computed from Ca dielectric functions obtained by adjusting Hunderi's data[5] to account for pressure and retaining terms through quadrupole in the Mie series. The fit to the MCD of Ca colloids required a magnetic contribution to the interband portion of the dielectric function. The fit was obtained by using $m^* = 2.4$ (in units of free electron mass) and $g_{\text{eff}} = 2m/m^*$. The increase over Hunderi's value of $m^* = 2.0$ for the bulk metal is consistent with the assumption that the plasma frequency is 10% less in the particle than in the bulk metal. The effective g factor is consistent with the expectation that a g value should scale inversely with the effective mass from the free electron g factor.

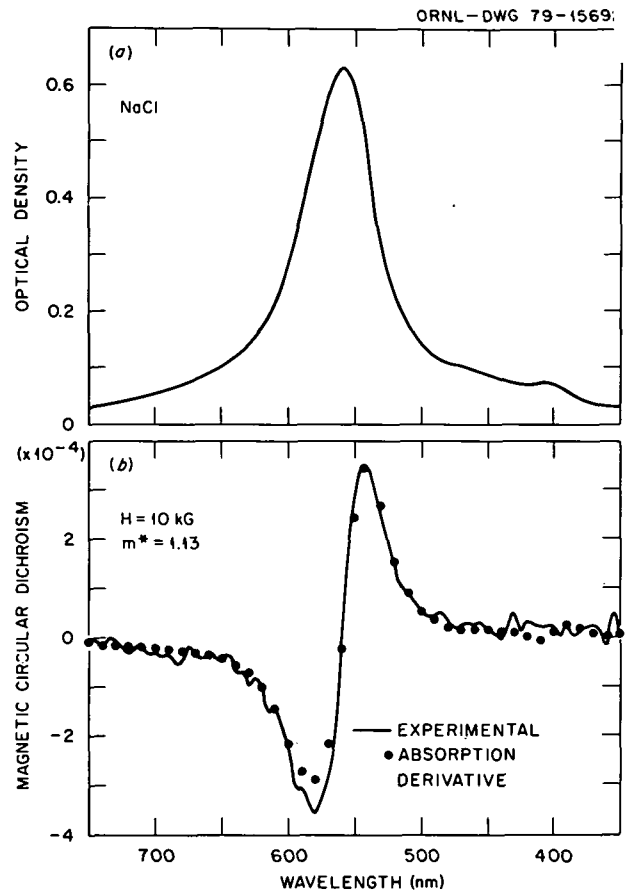

Fig. 3.24. The optical absorption and MCD spectra of Na precipitates in NaCl. The solid points represent the dichroism that is predicted from the derivative of the absorption spectrum. Units are base-10 absorbance.

For both colloids reasonable agreement between theory and experiment was obtained for parameters fixed by other measurements, a priori expectations, or reasonable assumptions. The magneto-optical spectra of both colloids are due mostly to intraband effects. Since neither the measurement temperature nor the particle sizes would allow observation of cyclotron resonance, it is remarkable that rough values for cyclotron resonance frequencies can be inferred. The results support Orera and Alcala's conclusion that Ca precipitates in CaF_2 are under pressure.

1. Summary of paper: *Phys. Rev. B* **24,** 1159 (1981).
2. Guest scientist from University of Zaragoza, Zaragoza, Spain.
3. V. M. Orera and R. Alcala, *Phys. Status Solidi A* **44,** 717 (1977).

4. N. V. Smith, *Phys. Rev.* **183,** 634 (1969).
5. O. Hunderi, *J. Phys. F* **6,** 1223 (1976).

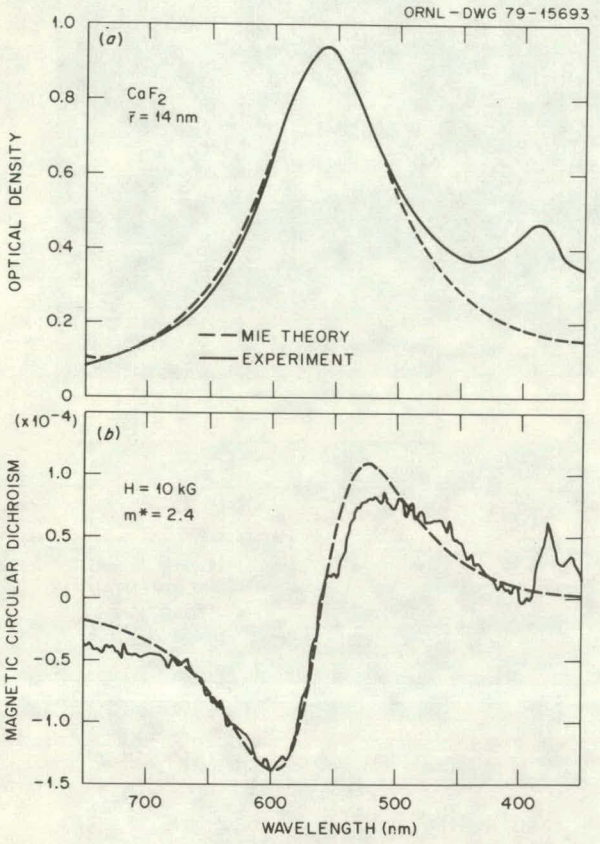

Fig. 3.25. The optical absorption and MCD spectra of Ca precipitates in CaF_2. The dashed curves are the predictions of Mie theory. The smaller band near 380 nm is attributed to a defect.

Ni COLLOIDS IN REDUCED Ni-DOPED MgO[1]

J. Narayan Y. Chen
R. M. Moon

Colloidal particles with dimensions of 1–200 nm in alkali halides are known to produce interesting modifications of physical properties of these materials.[2] Improved mechanical properties (yield stress and ductility), selective absorption of solar energy, cathodochromic, photochromic, and data storage applications represent a few examples of modifications of physical properties produced by colloids in alkali halides. In this work, we report a method to produce Ni precipitates in the bulk of MgO. The precipitates were characterized using analytical techniques of TEM, neutron-magnetic scattering, and optical spectroscopy. Ni-doped MgO crystals were prepared by an arc-fusion technique. As-grown crystals exhibited a light green color associated with Ni^{2+} ions in substitutional sites. Clustering of Ni into precipitates (formation of colloids) was achieved by heating the Ni-doped crystals at 2100 K in a strong reducing atmosphere and subsequently cooling these crystals rapidly.

Figure 3.26(a) shows a bright-field micrograph obtained with the use of the [200] diffraction vector. The average size (first moment) of the precipitates was determined to be 50 nm with number density 1.0×10^{19} m^{-3}. Figure 3.26(b) is a micro-diffraction pattern from a precipitate located near the edge of the specimen. The micro-diffraction pattern in Fig. 3.26(c), which was from a precipitate inside the matrix, contains precipitate reflections of Fig. 3.26(b) in addition to the matrix reflections corresponding to the [001] orientations. From the symmetry and the lattice spacings corresponding to the various diffraction spots in Figs. 3.26(b) and 3.26(c), it was possible to index the precipitate pattern as a (112) pattern of fcc Ni with a lattice constant (a_0) of 0.352 nm. The following precipitate p and matrix m orientation relationship was deduced: $[11\bar{1}]_p \,||\, [100]_m$ and $[1\bar{1}0]_p \,||\, [010]_m$. A convergent-beam-diffraction (CBD) pattern, after tilting the specimen 19.5° around the [010] axis of the matrix, is shown in Fig. 3.26(d). The CBD patterns provide information on the three-dimensional symmetry of materials and are very useful for unequivocal determination of symmetry and space groups. The indexed CBD pattern showing $(\bar{5}\bar{3}9)$, $(\bar{3}\bar{5}9)$, and $(\bar{7}71)$ higher order Laue zone (HOLZ) lines in Fig. 3.26(d) are similar to the (111) pattern of fcc Ni. Moiré patterns result from the interference between {111} precipitate and {200} matrix planes shown in Fig. 3.26(a). From a moiré spacing of 7.0 nm and with a value of 0.210 nm for the matrix d_{200} (lattice spacing), the d_{111} for the precipitate was calculated to be 0.204 nm, which was in good agreement with the value obtained from the diffraction patterns.

Figure 3.27 shows the results of a polarized-neutron experiment in which the intensity in a (111) precipitate peak was measured when the incident neutrons were polarized first in a direction parallel (flipper off) and then in a direction antiparallel (flipper on) to the sample magnetism.

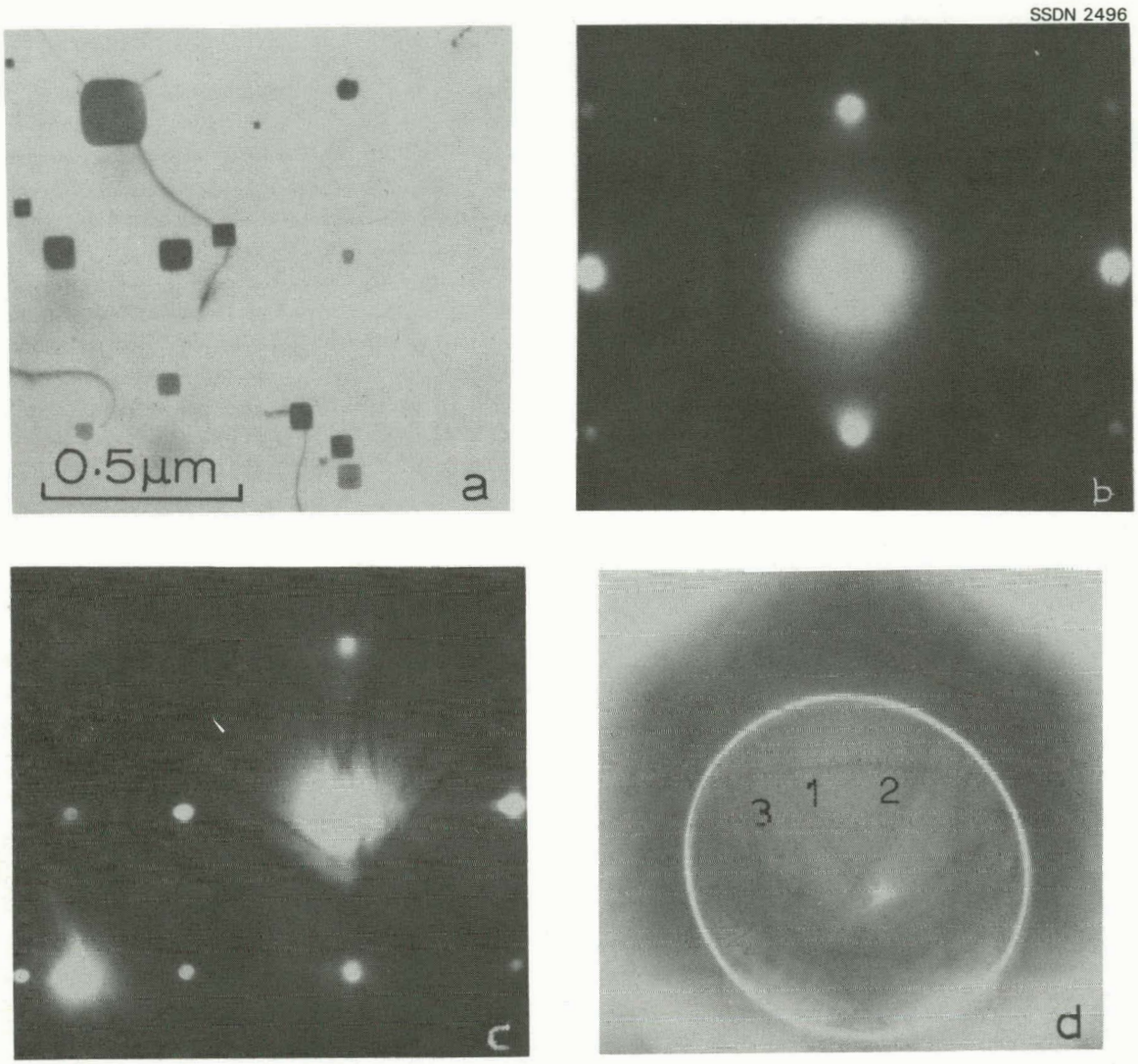

Fig. 3.26. Electron micrographs for the analysis of colloids. (a) Bright-field electron micrograph showing the size distribution and moiré fringes associated with the precipitates; (b) (112) fcc microdiffraction pattern from a precipitate near the edge; (c) (112) precipitate and (100) matrix diffraction patterns superimposed; and (d) (111) fcc Ni CBD pattern where 1, 2, and 3 represent $(\bar{5}\bar{3}9)$, $(\bar{3}\bar{5}9)$, and $(\bar{7}71)$ HOLZ lines, respectively.

From the ratio of these intensities, known as flipping ratio, the ratio of magnetic-to-nuclear scattering amplitudes for the (111) precipitate reflection was found to be about 17% below the value for pure Ni, indicating the probable presence of some impurities in these precipitates. From the d_{hkl} values for (111), (200), and (220) precipitate reflections, the lattice constant of the precipitate was determined to be 0.352 nm, in good agreement with the microscope results.

The optical absorption measurements before and after the reducing treatment showed that the metallic colloids modify the absorption spectra of oxides in such a way that these materials are ideally suited for efficient solar-energy absorption. An ideal solar absorber is characterized by a high absorption coefficient α for $\lambda \lesssim 2.0\ \mu$m and by low values of α and emissivity for $\lambda \gtrsim 2.0\ \mu$m to retain the absorbed energy. The optical spectra of these materials were found to be unchanged after a long

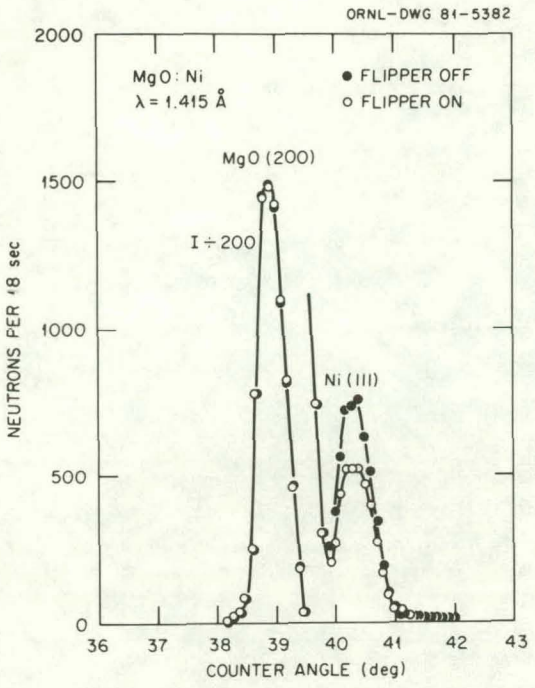

Fig. 3.27. Neutron scattering intensity as a function of scattering angle in a $\theta - 2\theta$ scan along the matrix [200] direction. Peaks correspond to (200) MgO matrix and (111) Ni precipitates with flipper on (O) and off (●), respectively. Note that the MgO peak has been scaled down by a factor of 200.

(100 h) annealing at 1073 K, thus making them suitable for high-temperature, solar-absorber applications. Such materials are not presently available.

1. Summary of paper: *Phys. Rev. Lett.* **46,** 1491 (1981).

2. A. E. Hughes and S. J. Jain, *Adv. Phys.* **28,** 719 (1979).

CHARGE TRAPPING AND RELEASE IN ELECTRON- AND GAMMA-IRRADIATED LEAD SILICATE GLASSES[1]

C. M. Hong[2] R. A. Weeks
D. E. Day[2] D. L. Kinser[3]

Many multicomponent glasses exhibit spontaneous dielectric breakdown when irradiated with a beam of electrons or gamma rays. The most spectacular occurrence of this phenomenon has been observed in lead silicate glass used as shielding windows in hot cells. This effect has also been observed in borosilicate glass,[4–6] a glass which has been used for encapsulation of radioactive waste.

Radiation-induced dielectric breakdown does not correlate directly with either bulk dc conductivity or dielectric strength.[7] The determining factor has been tentatively attributed[7] to glass microstructure (i.e., phase separation). However, other factors must also influence the tendency for radiation-induced breakdown, since some phase-separated glasses do not exhibit these phenomena. In this work the thermally stimulated depolarization currents (TSDC) of irradiated lead silicate glasses were compared with the TSDC of these glasses polarized with electric fields. From such a comparison, a relationship between the polarization mechanism and charge-trapping sites and a correlation between TSDC and radiation-induced breakdown were found.

The measurements were made on glasses whose lead content varied between 30 and 55 mol % PbO. The range of temperature over which the measurements were made was $290 \leqslant T \leqslant 1450$ K. The thermal release of trapped charge and polarization in irradiated glasses was the same as that observed in samples polarized by electric fields. The tendency for dielectric breakdown was found to be determined by the recombination time of electrons displaced by radiation with the sites from which they were displaced. This time decreased with increasing PbO content.

The radiation-induced breakdown tendency of these lead silicate glasses is attributed to their microstructure, which both provides charge-trapping sites and controls the relaxation time of the thermal release of the trapped charge. The higher breakdown tendency for glasses having a microstructure consisting of isolated droplets in a low-conductivity matrix phase (30 mol % PbO)[7] results from the combination of (1) a somewhat higher concentration of charge-trapping sites at the immiscible phase boundaries; (2) a relaxation time for charge release at room temperature, which essentially eliminates any dissipation of the internal field created by the trapped charge; and (3) a nonuniform distribution of trapped charge, which created higher localized fields than would occur in a more homogeneous material containing the same amount of trapped charge. The lack of breakdown in structurally homogeneous glasses, such as fused silica, can be explained by a more uniform distribution of trapping sites and their higher dielectric breakdown strength. Also, compositional changes, such as the addition of alkali oxides, which increase the bulk dc conductivity, can also be

expected to reduce the tendency for breakdown. The resulting reduction in the relaxation time for charge release at room temperature prevents the internal field from exceeding the dielectric breakdown strength.

1. Summary of paper to be published.
2. University of Missouri, Rolla, Mo.
3. Oak Ridge Associated Universities faculty participant from Vanderbilt University, Nashville, Tenn.
4. B. Gross, *Phys. Rev.* **107,** 368 (1957).
5. B. Gross, *Phys. Rev.* **110,** 337 (1958).
6. P. V. Murphy and S. C. Ribeiro, *J. Appl. Phys.* **34,** 2061 (1963).
7. R. A. Weeks, D. L. Kinser, and J. M. Lee, p. 266 in *Proceedings of the Fourth International Conference on Physics of Non-Crystalline Solids,* ed. by G. H. Frischat, Trans Tech Publications, Aedermansdorf, Switzerland, 1977.

HIGH-TEMPERATURE ELECTRON-MAGNETIC-RESONANCE SPECTROSCOPY

R. A. Weeks A. Chatelain[1]

Electron-magnetic-resonance spectroscopy of materials at high temperatures (>800 K) can be used for studies of phase changes (e.g., ferromagnetic-paramagnetic), of the nature of charge compensation of aliovalent impurities in ionic crystals, and of changes in crystal-field potentials near melting temperatures. We report here preliminary measurements on the Curie temperature and temperature dependence of the magneto-crystalline anisotropy energy of small (~150 Å), spherical iron particles.

Measurements were made at ~9.5 GHz in a system in which sample temperatures up to 1100 K could be attained, while the microwave cavity remained at room temperature. Two types of samples were measured; one was a natural silica glass (mineral name "fulgurite") containing spherical particles of metallic iron,[2] and the second was silica glass fused in the laboratory which also contained spherical metallic particles of iron.[3] Based on the temperature dependence of the intensity of magnetization in the temperature range 100–500 K, we concluded that the iron particles had diameters ranging between 100 and 250 Å.

The results of measurements of the temperature dependence of the intensity of magnetization and the magneto-crystalline anisotropy energy of the iron particles in these two materials are shown in Fig. 3.28. In the case of the natural silica glass

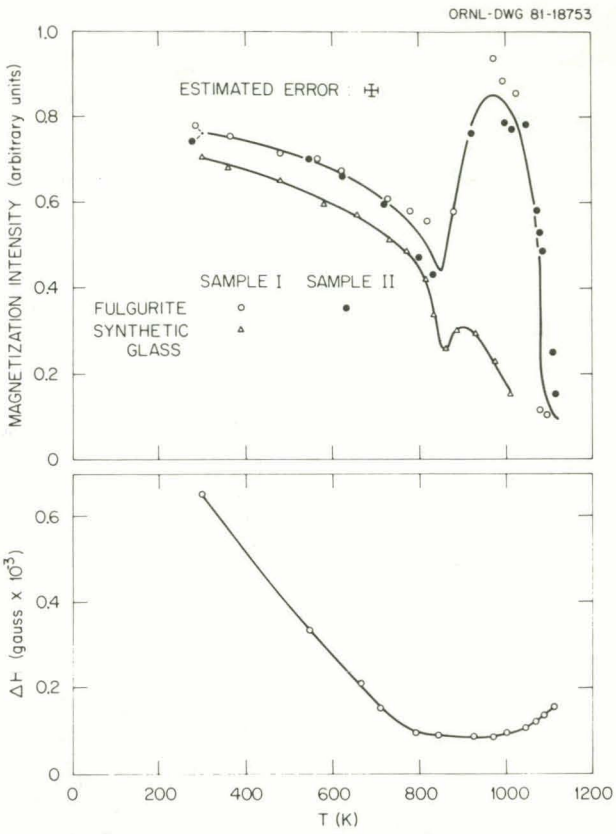

Fig. 3.28. Temperature dependence of magnetization intensity and magneto-crystalline anisotropy energy of small spherical iron particles precipitated in silicon glass. (a) The ordinate is the intensity of the ferromagnetic resonance of the iron particle, which is proportional to the intensity of magnetization. (b) The ordinate is the width ΔH of the ferromagnetic resonance measured between the extremal inflection points of the first derivative of the resonance; the first-order magneto-crystalline anisotropy energy K_1 is proportional to ΔH.

sample, a striking feature of the temperature dependence of the intensity of magnetization is a significant change in the relationship near 858 K followed by a sharp increase in intensities at higher temperatures. There is a sharp decrease in the region of 1043 K which continues up to 1100 K. On the other hand, the magneto-crystalline anisotropy energy [Fig. 3.28(b)] decreases monotonically from room temperature up to ~800 K. Above this temperature its effect on the spectrum is negligible. In the case of the other samples, the spectrum of the iron particles has the same general features except that the increase in magnetization intensity at $T > 858$ K is much less pronounced.

The Curie temperature T_c of Fe_3O_4 and of Fe metal are 858 K and 1043 K, respectively. Thus, the sharp decrease in magnetization intensity at these two temperatures, which is observed in Fig. 3.28(a), are attributed to Fe_3O_4 and to metallic Fe. If Fe_3O_4 and Fe were present in the samples as separate particles randomly dispersed in the glass matrix, the observed magnetization intensity would be expected to decrease at the T_c of Fe_3O_4 and then decrease again at the T_c of Fe. The large increase in the intensity of magnetization at $T >$ 858 K indicates that there is an interaction between the magnetization of Fe_3O_4 and Fe. Since the total intensity of magnetization increases above T_c of Fe_3O_4, the magnetic field of Fe_3O_4 must oppose the field of Fe. We suggest that this type of interaction could arise if Fe_3O_4 and Fe were in intimate contact. Since the low-temperature spectrum is that which is characteristic of spherical Fe particles, we suggest that Fe particles have a Fe_3O_4 shell.

On the basis of this suggestion, the difference between the spectrum of the natural glass and the laboratory-prepared samples is due to a difference in the thickness of the Fe_3O_4 shell. This explanation of the difference is consistent with the thermal treatments which the samples have received. The natural glass was cooled from its fusion temperature[2] in a normal atmosphere, while the laboratory sample was never exposed to a normal atmosphere at high temperatures after the iron particles were formed.

1. Ecole Polytechnique Institut, Lausanne, Switzerland.

2. R. A. Weeks et al., *J. Non-Cryst. Solids* **38,** 129 (1980).

3. David L. Griscom, *IEEE Transactions on Magnetics* (to be published).

MODIFICATIONS OF PHYSICAL PROPERTIES OF HIGH-TEMPERATURE CERAMICS

J. Narayan Y. Chen
B. R. Appleton

Because of their high melting point and stability at elevated temperatures, ceramic materials lend themselves to many high-temperature applications. However, many of these material applications are limited by poor fracture toughness, lack of ductility, and limited electrical and thermal conductivity. We have used high-temperature reducing treatments, which produce metallic colloids or high concentrations of H^- ions in the bulk, and laser-induced diffusion of metallic impurities to modify the physical properties of these materials. Although we expect that many physical properties can be modified in a useful way, we have concentrated primarily on mechanical and optical properties of these materials.

Mechanical Properties

Metallic particles in oxides can provide sources of dislocations and, hence, can improve the ductility. Figure 3.29 shows dislocations associated with the precipitates after deforming the specimens to a 3.0% plastic strain. The number density of dislocations around the precipitates was estimated to be at least two orders of magnitude higher compared with that in the regions away from the precipitates. Table 3.5 shows a 50% increase in room-

SSDN 2680

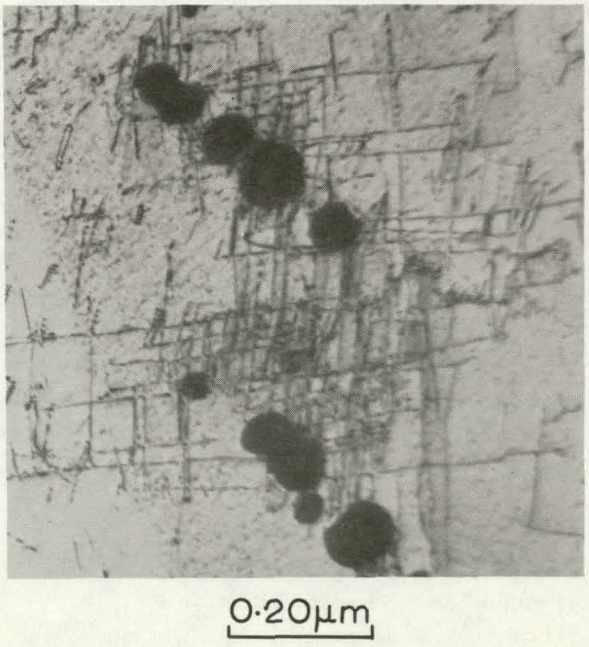

Fig. 3.29. Bright-field electron micrograph showing Ni precipitates and dislocations associated with them after 3.0% plastic deformation. The precipitates transformed from coherent to incoherent upon deformation.

Table 3.5. Mechanical properties of doped oxides

	MgO:Pure	MgO:Ni, Ni-Substitutional	MgO:Ni, Ni-Precipitates	MgO:H
Yield stress	180 kg cm^{-2}	530	690	190
Ductility[a]	8.0%	8.0	13.0	13.0

[a]Total percentage elongation until fracture.

temperature ductility in MgO containing Ni precipitates. The precipitates can anchor the dislocations and may increase the yield stress of these materials (see the comparison in Table 3.5 between virgin crystals and crystals containing Ni precipitates). In situ (TEM) deformation studies on the MgO:Ni system showed an increased plastic deformation associated with cracks due to the presence of the precipitates. Thus, the Ni precipitation served to retard or in some cases completely stop the propagation of the crack.

Another approach taken to improve the mechanical properties of oxides involved the introduction of OH^- and H^-. This led to marked enhancement in ductility of these materials (see Table 3.5). Such enhancements may result from an increase in the velocity $\bar{v}$ of mobile dislocations. Although the causes of velocity enhancement are not known with certainty, it is speculated that the electronic properties of the core structure of dislocations are modified by the introduction of H^- and OH^-, which leads to increased velocity of dislocations.

Laser-induced diffusion to modify the physical properties of ceramics involves the deposition of a thin layer of metal such as Pt or Al on Al_2O_3 followed by pulsed-laser irradiation. This leads to melting of the metal as well as thin oxide layers and to doping of the thin oxide layers with the desired impurities. Ion-scattering analysis showed that the Pt was incorporated into the surface of Al_2O_3 following pulsed-laser annealing. Electron microscopy and x-ray dispersive analysis indicated the presence of Pt inside the matrix.

Optical Properties

Metallic colloids can modify the absorption spectra of oxides in such a way that the materials are ideally suited for efficient solar absorption. Efficient solar absorbers are characterized by an absorption edge near a wavelength λ of 2.0 μm in the solar spectrum. We found that the oxides containing metallic colloids exhibit high absorption for $\lambda < 2.0$ μm (thus absorbing most of the solar radiation) and low absorption for $\lambda > 2.0$ μm (thus inhibiting the reirradiation of absorbed energy). These materials were much more stable at high temperatures (~1100 K) for extended periods of time compared with presently available cermets (oxide-metal mixed composites), which are stable only up to 600 K.

In addition to the modifications of mechanical and optical properties, the oxides containing colloids should exhibit unique electrical properties. Thermionic emission associated with metallic precipitates is known to enhance electronic conduction in alkali halides. The enhancement was found to be proportional to the total surface area associated with these precipitates. We propose to investigate the electrical transport properties of oxides with different size distributions of precipitates and to evaluate the phenomenon of thermionic emission in these materials. Materials containing fine dispersions of magnetic precipitates often exhibit unique magnetic properties. This area needs to be explored further to obtain novel magnetic alloys contained in high-temperature matrices.

4. Transport Properties of Solids

Within the Division studies of transport properties are emphasized in programs examining fast-ion conduction processes, superconductivity, and the physical properties of ceramic materials in harsh environments. Because research is often a cooperative effort among various groups and is capable of classification under several broad categories, information pertinent to transport is also given in other sections of this report, particularly in those treating theory, crystal growth and characterization, and defects in solids.

During the reporting period, work at ORNL and elsewhere established that H_2O can diffuse into the conducting planes of β-alumina and cause a marked decrease in conductivity. Because H_2O diffuses much more rapidly in Liβ- than in Naβ-alumina, the former material was chosen for extensive studies of hydration processes. The H_2O molecules were determined from neutron diffraction studies to occupy randomly one of three equivalent positions about the anti-Beevers Ross site; infrared absorption and Raman scattering techniques were employed to establish that hydrogen bonding occurs between the water molecules and oxygen ions in the spinel blocks and that dissociation of some H_2O takes place to produce hydroxyl ions and complex hydronium ion derivatives. The mechanism for H_2O diffusion has been determined, as have the kinetic and thermodynamic properties of the system. Also reported here is significant progress in understanding conduction processes in the β''-aluminas.

The properties of flux-line lattices (FLL) in superconducting materials continue to be a subject of great interest and emphasis. The neutron diffraction results reported for the FLL in single-crystal V_3Si are the first obtained for a high-T_c A15 material, and they demonstrate that flux-line interactions in the low-field region can be described properly by the simplest theoretical model of an extreme Type II superconductor. While possible explanations for an observed correlation between the FLL morphology and the crystal symmetry are offered, a fundamental understanding of this behavior is yet to be obtained. Both theoretical and experimental studies of FLL pinning have continued during the reporting period, and those results are reported here. Also described in this report are efforts to produce stoichiometric A15 compounds using the combined techniques of ion implantation and laser annealing, an apparatus for magnetization studies, and the magnetic and/or superconducting properties of several different materials.

Processes involved in the dielectric breakdown of insulating ceramics are extremely complex, especially at high temperatures. Nevertheless, an increased understanding of some of the more fundamental causes has been gained during this reporting period. The first quantitative description of the high-temperature electrical breakdown of MgO, a common insulating refractory material, has been obtained, and the role of impurities in the breakdown process has been further elucidated. In Ni-doped MgO, it now appears that thermoelectric breakdown at high temperatures is related to the space charge induced by injection of electrons and holes in the near surface of the sample by the attached electrodes. Also, an

understanding of the similarities in conductivities at high temperatures, as well as the dissimilarities at low temperatures, between single-crystal and polycrystalline MgO appears to be achievable. Reported also are results which are interpreted to show that cation vacancies act as carriers of current in $MgAl_2O_4$ spinel. Recently, research on ceramic materials has been extended to include the transition metal carbides and nitrides. The last two papers in this section are reports of initial research efforts dealing with this important class of materials.

FAST-ION CONDUCTORS

STRUCTURE AND SPECTRA OF H_2O IN β-ALUMINA[1]

J. B. Bates G. M. Brown[2]
N. J. Dudney J. C. Wang
R. Frech[3]

The reaction of H_2O with sodium β-alumina is a potentially serious problem in the application of this material as the solid electrolyte in the sodium-sulfur battery. Work at ORNL and elsewhere has established that H_2O can diffuse into the conduction planes of β-alumina, causing a marked decrease in conductivity. There is also evidence to suggest that the reaction with H_2O can lead to mechanical failure due to anisotropic expansion. The structure and vibrational spectra of hydrated Liβ-alumina are described here. The thermodynamics and kinetics of the hydration reaction and the mechanism of H_2O diffusion in Liβ-alumina are discussed elsewhere in this report.[4] Most of the results are reported for Liβ-alumina rather than Naβ-alumina because high equilibrium concentrations of H_2O can be obtained much more rapidly in the Li compound.

The structure of H_2O in Liβ-alumina was determined from a neutron diffraction study of a single crystal treated in 0.8 atm of H_2O vapor at 235°C. The space group of the crystal was confirmed to be $P6_3/mmc$, as expected. The H_2O content of the hydrated crystal determined from refinement of the diffraction data, 1.55 H_2O molecules/unit cell (Table 4.1), is close to the theoretical saturation limit of 1.8/unit cell. Based on the composition of the starting material, the formula unit of the hydrate is $1.55H_2O \cdot 1.19Li_2O \cdot 11Al_2O_3$. Compared to the anhydrous material, the c-lattice parameter of the hydrate is about 0.7% larger, while the a parameter remains about the same.

The H_2O molecule was located in the structure (Fig. 4.1) from Fourier difference maps and least-squares refinement of the diffraction data. The H_2O molecule occupies one of three equivalent positions about the anti-Beevers Ross (aBR) site. The dotted outline in Fig. 4.1 represents the molecule at these positions. The oxygen atom of H_2O is located on a 6-h-m site; the protons are located on 12-j-m sites above and below the conduction plane and are hydrogen bonded to the O(4) oxygen ions in the adjacent spinel layers located directly above and below the aBR site. Thus, the molecular plane of H_2O is perpendicular to the conduction plane, and the molecular twofold rotation axis lies along the line connecting the aBR and BR sites. The HOH bond angle of 114° (Table 4.1) is large compared to the mean value for H_2O in other hydrates (~109°) and is appreciably larger than the gas-phase value of 105°. Possibly because of interference due to scattering from the water molecules, we were not able to locate the Li^+ ions with confidence. The Li^+ location at the BR site shown in Fig. 4.1 is purely schematic.

Table 4.1. Structural parameters of hydrated Liβ-alumina

Composition:		1.55 (±0.05) H_2O/unit cell
Cell parameters: a_0	=	5.5914(8) Å
c_0	=	22.714(3) Å
Space group:		$P6_3/mmc$
< HOH	=	114°
< (0(4)--H-O)	=	159.3°
|O-H|	=	0.992 Å
|0(4)---0(W)|	=	2.623 Å
|0(4)---H|	=	1.671 Å

Infrared absorption and Raman scattering measurements of hydrated single crystals containing H_2O, D_2O, or HDO were made at 300 K and below. Examples of the absorption spectra using unpolarized light and with E in the conduction plane ($E \perp c$) are shown in Fig. 4.2. Assignments of the observed peaks to various proton-containing

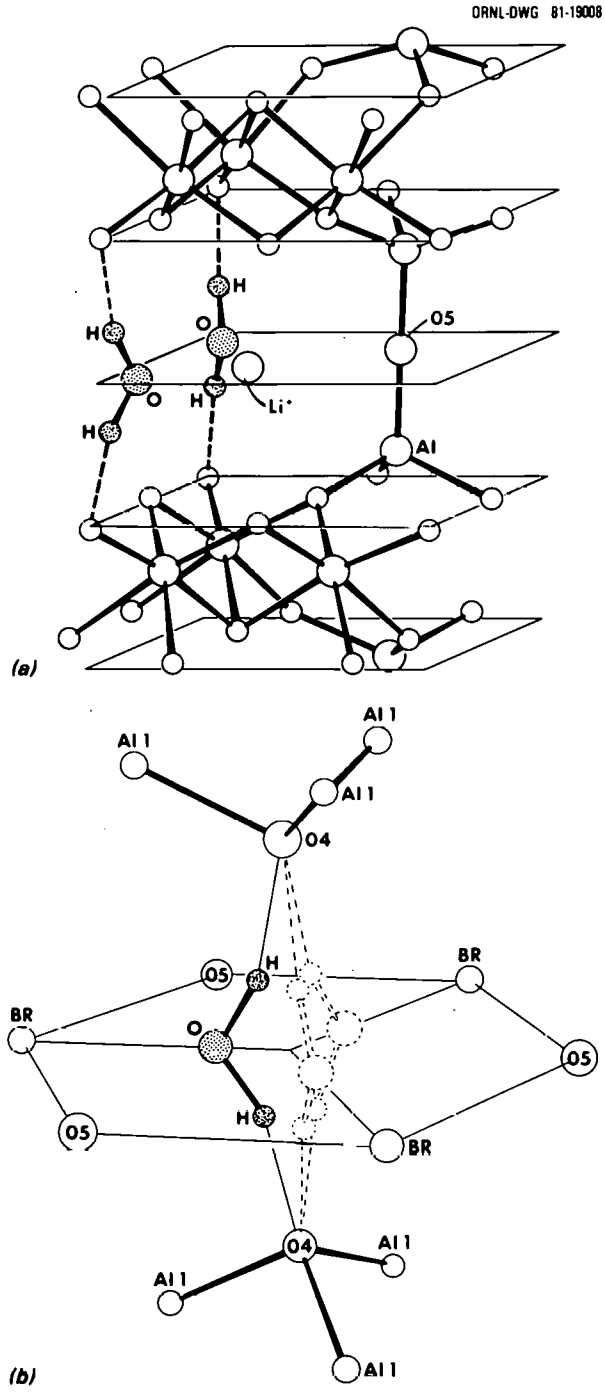

Fig. 4.1. (a) Unit cell of hydrated Liβ-alumina (the Li^+ ion location is schematic). (b) H_2O molecule near the aBR site. Dotted outlines indicate equivalent positions occupied by H_2O.

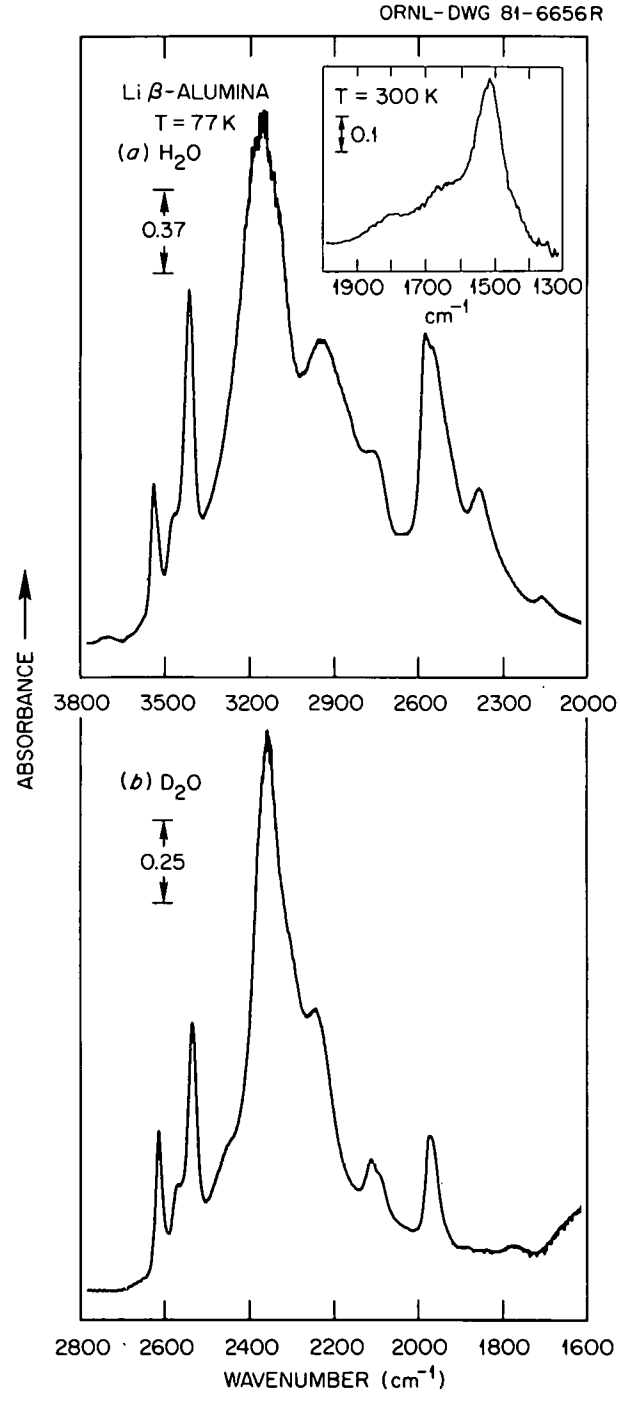

Fig. 4.2. Absorption spectra of hydrated Liβ-alumina for light polarized in the conduction plane. The inset in (a) is the region near the bending mode of H_2O (ν_2) to which we assign the peak near 1500 cm^{-1}.

species are based on isotope frequency shifts and on the change in intensity with the H_2O vapor pressure.[4]

The major peak in Fig. 4.2(a) is assigned to the symmetric-stretching mode ν_1 of H_2O [D_2O in Fig. 4.2(b)]. The antisymmetric-stretching mode ν_3 is observed when the incident light is polarized parallel to the c-axis ($E \| c$).[5] Curve resolution of the polarized spectra gives the peak positions for ν_3 and ν_1 at 3170 and 3150 cm^{-1}, respectively. In the gas phase, these modes occur at 3756 cm^{-1} and 3657 cm^{-1}. The 500–600 cm^{-1} shift to lower frequencies in the solid is attributed to hydrogen bonding. As observed in other hydrates, hydrogen bonding causes a large reduction in the difference of the ν_3 and ν_1 frequencies from the gas phase value of $\sim$100 cm^{-1}. Additional absorption bands in the vicinity of the major ν_1 and ν_3 peaks are attributed to H_2O molecules oriented as in Fig. 4.1 but with a different local environment of Li^+ ions. The absorption band near 2940 cm^{-1} in Fig. 4.2 (2235 cm^{-1} for D_2O) is assigned to the accidentally degenerate ν_1 and ν_3 modes of molecules which lie in the conduction plane (i.e., parallel to the conduction plane). These molecules were undetected in the neutron diffraction analysis because they account for less than 10% of the total number of H_2O species in the lattice. The sharp peaks above 3400 cm^{-1} are due to OH^- ions produced by dissociation of H_2O in the lattice. The corresponding peaks of the OD^- ions appear above 2500 cm^{-1}. As a consequence of the dissociation of water, additional complex ions are formed. The broad peaks near 2760 and 2380 cm^{-1} are assigned to the stretching modes of nonequivalent H_3O^+ species, and a pair of bands near 2565 cm^{-1} is assigned to the terminal OH stretching modes of $H_5O_2^+$ ions. While the frequencies of these features assigned to the H_3O^+ and $H_5O_2^+$ species are consistent with those reported for other systems, our assignments rely on the intensity changes observed as a function of H_2O vapor pressure.[4]

The absorption coefficients for the ν_1 and ν_3 modes of H_2O in Liβ-alumina were calculated from the values reported for liquid H_2O. The calculations included the contribution of the local fields in the lattice, which have an appreciable effect on the absorption coefficients of water and other species and are primarily responsible for the large dichroic ratios observed.[5] The calculated absorption coefficient for ν_1, ϵ = 60–80 L/mole-cm, agrees reasonably well with the value estimated from weight-loss and infrared measurements, $\epsilon \simeq 85$ L/mole-cm. The absorption coefficients for the OH^- ions were also estimated from the value reported for OH^- in TiO_2. In these calculations it was necessary to consider the orientation and position of the ions. The OH^- peak at 3425 cm^{-1} is observed for $E \perp c$ but not for $E \| c$. This means that the O-H bond lies in the conduction plane, and we believe that the ion is formed by attachment of a proton to the O(5) ion. The OH^- peak at 3514 cm^{-1} is observed for both polarization directions. This peak is attributed to interstitial OH^- ions in which the O-H bond tilts out of the conduction plane. Because the magnitudes of the local fields are sensitive to location, the absorption coefficient for this ion depends both on the position and on the angular deviation of the bond from the plane. From the observed dichroic ratio and the local field correction, we find the deviation is between 40 and 50°.

1. Summary of paper to be published.
2. Chemistry Division, ORNL.
3. Oak Ridge Associated Universities faculty participant from University of Oklahoma, Norman, Okla.
4. N. J. Dudney, J. B. Bates, and J. C. Wang, "Hydration of Liβ-Alumina," "Mechanism for Diffusion of H_2O in Liβ-Alumina," and "Rate of Hydration of Liβ-Alumina," this report.
5. J. B. Bates, J. C. Wang, and N. J. Dudney, "Local Field Effects and Polarized Infrared Absorption from H_2O Molecules in β-Alumina," this report.

HYDRATION OF Liβ-ALUMINA[1]

N. J. Dudney J. B. Bates
J. C. Wang

Liβ-alumina readily hydrates when exposed to H_2O vapor. The H_2O molecules diffuse into the conduction planes[2] causing a significant decrease in the ionic conductivity.

We have investigated the thermodynamics of the hydration reaction by measuring the amount of water adsorbed by single-crystal samples equilibrated under different temperature and H_2O vapor pressure conditions. The results are shown in Fig. 4.3. The sample was equilibrated at the indicated temperature in a flowing H_2O/N_2 gas mixture. Equilibration required approximately 24 h. Following treatment, the infrared absorbance of the hydrated sample was measured at room temperature with the incident beam normal to the conduction planes. Typical absorbance spectra are shown

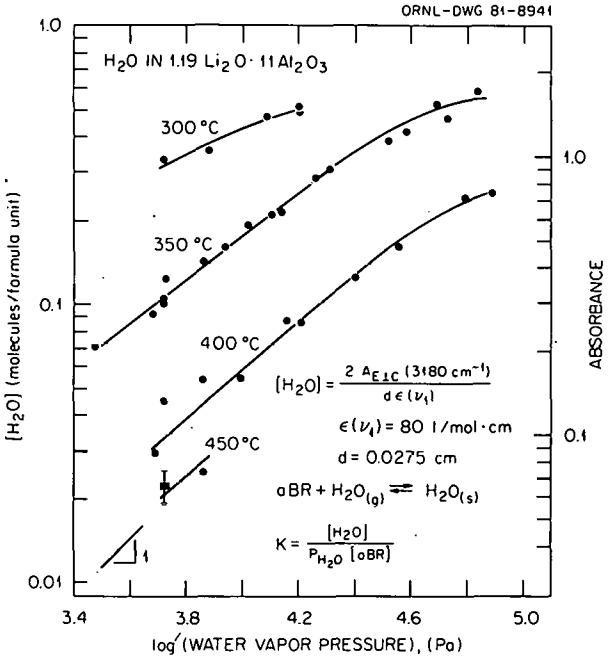

Fig. 4.3. Concentration of H_2O in Liβ-alumina as a function of the treatment temperature and H_2O vapor pressure.

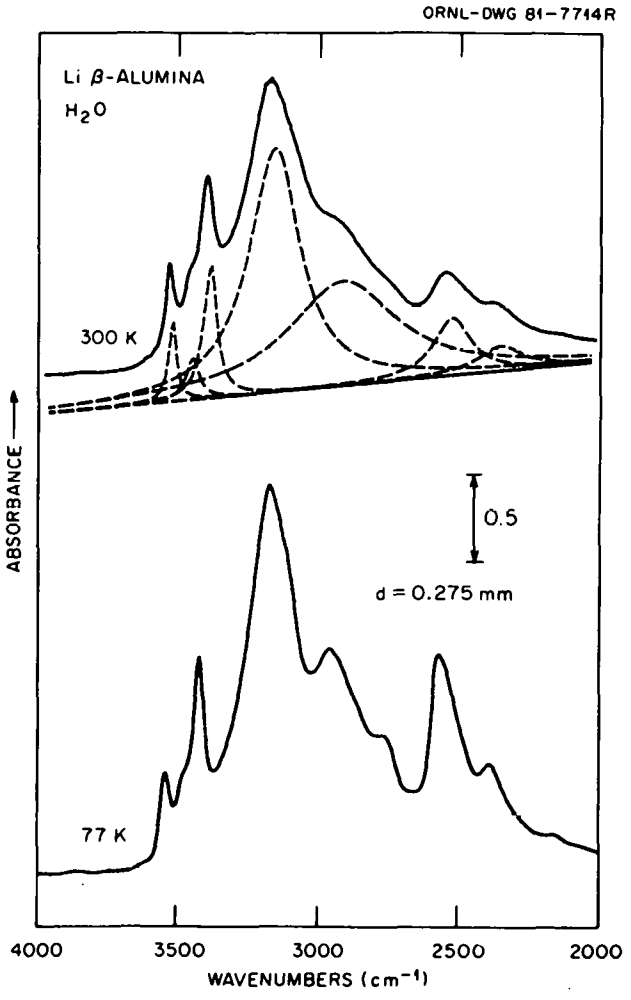

Fig 4.4. Infrared absorbance spectra of hydrated Liβ-alumina measured at 300 and 77 K. The dashed curves in the upper trace are Lorentzian components fitted to the observed band contours. Such curve fits were used to determine the concentrations of each protonated species as a function of the treatment conditions.

in Fig. 4.4. The largest infrared peak at 3180 cm^{-1} is attributed to the ν_1 vibrational mode of H_2O. Under conditions where Beer's law is applicable, the absorbance divided by sample thickness is proportional to the H_2O concentration. The H_2O concentration (left-hand scale in Fig. 4.3) was calculated from the measured absorbance (right-hand scale) using the equation given in Fig. 4.3. The molar absorption coefficient ϵ was obtained from the value for ν_1 of liquid H_2O corrected for the orientation of the molecules and the local field contribution in β-alumina.[3] The calculated concentrations are in good agreement with gravimetric determinations of the H_2O concentration. As demonstrated in Fig. 4.3, the absorbance varies continuously and reversibly as a function of the H_2O vapor pressure and temperature. There is no evidence for the formation of specific hydration compounds within the observed composition range. The hydration reaction can, therefore, be described as an intercalation process. The observed dependence of the H_2O concentration on the H_2O vapor pressure is consistent with the chemical reaction shown in Fig. 4.3, where H_2O from the gas phase enters an unoccupied interstitial site (aBR) in the conduction plane. Far from saturation, the H_2O concentration is proportional to the H_2O vapor pressure. The pressure dependence decreases as the saturation limit is approached and the concentration of available sites decreases. We believe that the structure becomes saturated when the number of molecules equals the number of available aBR sites. For our β-alumina crystals, the saturation limit is $1.81H_2O \cdot 1.19Li_2O \cdot 11Al_2O_3$.

There are a number of other infrared absorbance peaks besides the large one attributed to the ν_1 mode of H_2O. These peaks have been assigned to specific protonated species on the basis of the spectroscopic results, described elsewhere in this

report,[2] and also on the basis of the observed change in intensity as a function of the H_2O vapor pressure. The sharp peaks at high energy are due to the OH^- ions formed when water dissociates: $H_2O = OH^- + OH^+$. Association of the H^+ with an oxygen ion in or near the conduction plane will form an additional OH^- species. As expected, the equilibrium concentration of OH^- species was found to be approximately proportional to the square root of the H_2O vapor pressure. The H^+ may also associate with one or more H_2O molecules to form H_3O^+ or $H_5O_2^+$ species. The lower energy peaks which grow very rapidly with increases in the H_2O vapor pressure are attributed to these species.

Most of our infrared measurements were made after cooling the sample to room temperature. From measurements of the water diffusivity, we know that the total proton concentration in the sample remains constant during cooling.[4] The relative concentration of the different protonated species, however, changes significantly. Several sets of infrared spectra measured as a function of the sample temperature showed that equilibrium between the H_2O and OH^- species is maintained even at room temperature. The dissociation reaction is exothermic with an enthalpy of $\sim$10 kJ/mol.

Taking the association of OH^- ions during cooling into account, the room-temperature data in Fig. 4.3 were evaluated to determine the values of the enthalpy and entropy for the hydration reaction. The fitted values are $\Delta H = -85$ kJ/mol and $\Delta S = -140$ J/mol·K. The data fall within expermental error of the fitted curves, except for the largest H_2O concentrations where deviations from the ideal dilute solution approximations are expected to occur. Our estimates for the binding energy of H_2O to a Li^+ ion and for the entropy change when a H_2O molecule is put into a solid are in reasonable agreement with the experimental thermodynamic parameters.

Similar measurements have been made for single crystals of Naβ-alumina. Naβ-alumina requires a much longer equilibration time than does Liβ-alumina, and it absorbs only 1% as much H_2O under identical conditions. Due to these factors, fewer measurements have been made for hydrated Naβ-alumina samples. The currently available data, however, fall within experimental uncertainty of curves calculated using the same hydration reaction, saturation concentration, and hydration entropy as for Liβ-alumina. The observed hydration enthalpy is -66 kJ/mol, which again is approximately equal to the estimated binding energy of H_2O with a Na^+ ion.

---

1. Summary of paper to be published.
2. J. B. Bates, et al., "Structure and Spectra of H_2O in β-Alumina," this report.
3. J. B. Bates, J. C. Wang, and N. J. Dudney, "Local Field Effects and Polarized Infrared Absorption from H_2O Molecules in β-Alumina," this report.
4. N. J. Dudney, J. B. Bates, and J. C. Wang, "Rate of Hydration of Liβ-Alumina," this report.

MECHANISM FOR DIFFUSION OF H_2O IN Liβ-ALUMINA[1]

N. J. Dudney J. B. Bates
J. C. Wang

Measurements of the hydration kinetics have demonstrated that H_2O is very mobile in Liβ-alumina.[2] It is not clear, however, what diffusion path a large H_2O molecule might follow through the conduction plane. The molecule could remain intact and move through the plane by displacing the intervening Li^+ ions. Alternatively, the molecule might temporarily dissociate allowing oxygen transport to occur by an interstitialcy jump mechanism. As a test of these possible mechanisms, we measured the oxygen isotope distribution obtained when a Liβ-alumina crystal was hydrated in $H_2{}^{18}O$ vapor. An interstitialcy type of mechanism would require exchange of the ^{18}O from the H_2O with the ^{16}O ions in the crystal lattice.

Infrared absorption techniques were used to measure the H_2O concentration and the oxygen isotope distribution in hydrated Liβ-alumina. Single-crystal samples were prepared as thin disks. The faces of the disks were parallel to the conduction planes, so that during hydration the water diffused into the sample in a radial direction. The infrared absorbance was measured through different annular sections of the sample by using a set of concentric masks in front of the sample. Two identical anhydrous samples were treated for 16 h at 350°C in a flowing N_2/H_2O gas mixture (P_{H_2O} = 7.4 kPa). One sample was hydrated in $H_2{}^{16}O$ vapor and the other in $H_2{}^{18}O$. After 16 h the H_2O concentration of the disks was almost homogeneous.

In Fig. 4.5 we compare part of the infrared absorbance spectra of the two hydrated samples.

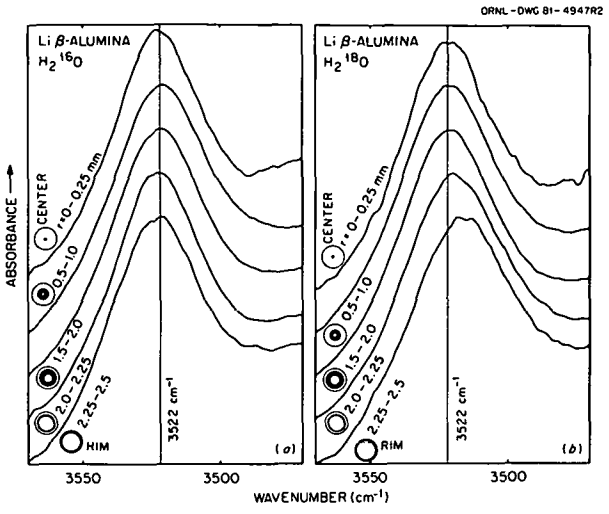

Fig. 4.5. Infrared absorption spectra of the OH^- band for different annular sections of each sample. (a) Sample treated in $H_2{}^{16}O$. (b) Sample treated in $H_2{}^{18}O$. Absorbance was measured at room temperature.

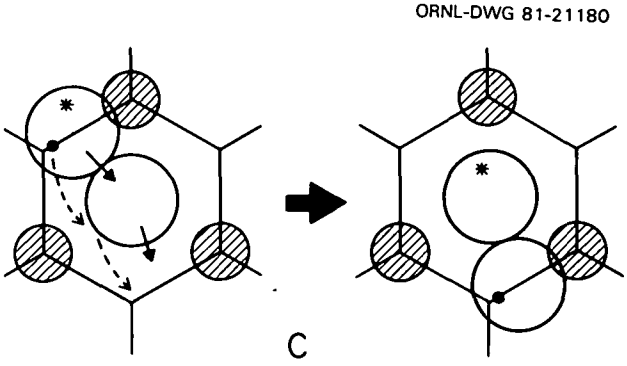

Fig. 4.6. Diffusion mechanism for H_2O in the conduction plane of Liβ-alumina. The shaded circles are Li^+ ions. The H_2O molecule dissociates, and the oxygen ion (large circle) moves by an interstitialcy mechanism. The protons move independently (small black dots and dashed arrows), and the H_2O molecule is reformed at a new position.

The shaded area of the circles and the values of R beside each spectrum indicate the cross-sectional area through which the absorbance was measured. The infrared peak shown in Fig. 4.5 is attributed to a small concentration of OH^-, which is one of the protonated species found in hydrated Liβ-alumina in addition to H_2O.[3,4] There is a distinct shift in the frequency of the peak between the rim and the center of the sample treated in $H_2{}^{18}O$. From a comparison of the spectra in Fig. 4.5(a) and Fig. 4.5(b), it is clear that the $^{18}OH^-$ was located near the rim of the sample, but only $^{16}OH^-$ was found near the center. We believe that the radial $H_2{}^{18}O$ distribution must be identical to that observed for the $^{18}OH^-$ due to the rapid proton exchange that occurs to maintain equilibrium between these two species. The relatively small isotope shift expected for the ν_1 mode of H_2O, however, was not detectable in the broad (FWHM = 250 cm^{-1}) infrared peak. The observed radial oxygen-18 gradient could only result from frequent dissociation of the H_2O molecule and exchange of oxygen ions with the lattice, as would occur for an interstitialcy type of diffusion mechanism.

We proposed that the interstitialcy motion described by Fig. 4.6 is the most likely diffusion mechanism. This proposal was supported by a comparison of the observed and calculated oxygen-18 profiles. The oxygen-18 distribution that would result from the interstitialcy mechanism was calculated using a finite difference technique. The calculated distribution agrees well with the $^{18}OH^-$ distribution determined from analysis of the infrared curves in Fig. 4.5.

1. Summary of paper to be published.
2. N. J. Dudney, J. B. Bates, and J. C. Wang, "Rate of Hydration of Liβ-Alumina," this report.
3. N. J. Dudney, J. B. Bates, and J. C. Wang, "Hydration of Liβ-Alumina," this report.
4. J. B. Bates et al., "Structure and Spectra of H_2O in β-Alumina," this report.

RATE OF HYDRATION OF Liβ-ALUMINA[1]

N. J. Dudney J. B. Bates
J. C. Wang

The concentration of H_2O in Liβ-alumina equilibrates very rapidly with the ambient H_2O vapor. The rate of change is controlled by diffusion within the conduction plane for a wide variety of temperature (200 to 450°C) and H_2O vapor pressure (2 to 80 kPa) conditions.

The hydration kinetics have been observed using infrared techniques. Single-crystal Liβ-alumina samples were prepared as thin disks 5 mm in diameter and less than 1 mm thick. The faces of the disks, formed by cleaving the crystal, were parallel to the conduction plane. Transmission infrared measurements were made with the incident beam normal to the face of the disks. Because the H_2O

diffuses within the conduction planes, different concentric masks could be placed in front of the sample to observe concentration gradients along the diffusion direction. When the hydration reaction was interrupted at a nonequilibrium concentration, we observed a gradient in the H_2O concentration from the rim to the center of the Liβ-alumina disk.

In Fig. 4.7 we have plotted data taken during the hydration of a Liβ-alumina sample at 350°C. At each time point the infrared absorbance (A) was measured through different concentric areas of the sample. Initially, the sample was anhydrous.

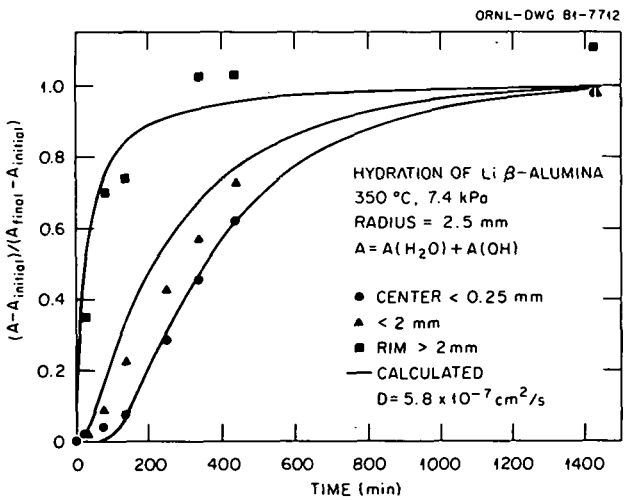

Fig. 4.7. Relative infrared absorbance as a function of the hydration time for a circular disk of Liβ-alumina.

The final concentration was about $0.12H_2O$ per formula unit, which is less than 10% of the saturation limit for Liβ-alumina.[2] The total concentration of the diffusing species is approximately proportional to the sum of the absorbances due to the H_2O, A(H_2O), and an OH^- species A(OH). These infrared features are at 3180 and 3525 cm^{-1}, respectively (Fig. 4.4).

The curves through the data were calculated for a concentration distribution obeying Fick's second law assuming that the rim of the disk is in equilibrium with the gas phase and that the chemical diffusion coefficient is independent of the H_2O concentration. A diffusion coefficient equal to 5.8×10^{-7} cm^2/s gives a good fit to the data for the area at the center of the sample. This diffusivity is comparable to values reported for the self-diffusion coefficient of Li^+ in Liβ-alumina at 350°C.[3] A detailed discussion of a possible diffusion mechanism for H_2O is given elsewhere in this report.[4] The agreement between the calculated and observed absorbances is poorer for the region near the rim of the sample; nevertheless, we can conclude that diffusion controls the rate of hydration and that the diffusion coefficient is approximately constant for small H_2O concentrations.

Radial gradients in the H_2O concentration have also been observed for single crystals of Naβ-alumina. Therefore, as for Liβ-alumina, the rate of hydration of Naβ-alumina appears to be controlled by diffusion through the conduction planes. The time required for Naβ-alumina to reach equilibrium is, however, roughly 20 times longer than that for Liβ-alumina.

---

1. Summary of paper: *Solid State Ionics* (in press).
2. N. J. Dudney, J. B. Bates, and J. C. Wang, "Hydration of Liβ-Alumina," this report.
3. J. T. Kummer, p. 141 in *Progress in Solid State Chemistry*, vol. 7, Pergamon Press, New York, 1971.
4. N. J. Dudney, J. B. Bates, and J. C. Wang, "Mechanism for Diffusion of H_2O in Liβ-Alumina," this report.

LOCAL FIELD EFFECTS AND POLARIZED INFRARED ABSORPTION FROM H_2O MOLECULES IN β-ALUMINA

J. B. Bates J. C. Wang
N. J. Dudney

Infrared spectroscopy is the principal analytical tool used in our investigation of the reaction of H_2O with the β- and β''-aluminas.[1] During the course of these studies, we observed a large difference in the absorption intensities of the stretching modes of H_2O for two polarization directions of the incident light with respect to the crystallographic c-axis, $\mathbf{E} \perp c$ and $\mathbf{E} \parallel c$. This difference is attributed primarily to a large local field anisotropy in the conduction plane of β-alumina.

In an isolated H_2O molecule, the symmetric ν_1 and antisymmetric ν_3 stretching modes give rise to transition dipole moments (denoted by $\mathbf{P}_1$ and $\mathbf{P}_3$), which lie in the molecular plane and are parallel and perpendicular, respectively, to the twofold rotation axis. In a dilute gas of noninteracting molecules, the ratio R of the intensity of light absorbed at the resonance frequency of ν_3 to that absorbed at the resonance frequency of ν_1 is given

by $R = |\mathbf{P}_3|/|\mathbf{P}_1|$ with $|\mathbf{P}_i| \sim |<1|q_i|0>|^2 \times (d\mathbf{P}_i/dq_i)^2$, where q_i is the normal coordinate. The absorption coefficients for the vibrational modes of H_2O in the gas phase or in liquid H_2O are not well determined because of the overlap of ν_1 and ν_3 and because of the contribution to the absorption near ν_1 from $2\nu_2$ (overtone of the bending mode). Published data for liquid H_2O typically give values of R from 1.3 to 1.5. It can be shown to a good approximation that $R = \tan^{-1}(\phi/2)$, where ϕ is the HOH angle. For $\phi = 105°$ (gas-phase angle), this gives $R = 1.3$.

As described elsewhere in this report,[1] the H_2O molecule in Liβ-alumina is located near the anti-Beevers Ross (aBR) site in the conduction plane and is oriented such that the molecular plane is perpendicular to the conduction plane. Because of this symmetric location, we expect $\mathbf{P}_3$ to be parallel to the crystallographic c axis and $\mathbf{P}_1$ to be perpendicular to the c axis and to lie in the conduction plane.

An example of the polarized absorption in the ν_1-ν_3 region of H_2O in Naβ-alumina is shown in Fig. 4.8. These spectra are less complex than those of hydrated Liβ-alumina,[1] which contain absorption peaks due to protonic species other than H_2O. The location and orientation of H_2O molecules in Naβ-alumina have not been determined by neutron diffraction (the H_2O concentration is too small to make such a determination practicable), but from our polarized absorption measurements and from considerations of hydrogen bonding and packing, we can assume that the orientation is the same as in Liβ-alumina. The absorption curves were fit to a function consisting of two Lorentzian peaks and a linear background. The two peaks resolved in the $\mathbf{E} \| c$ spectrum are assigned to the ν_3 mode of two nonequivalent H_2O molecules, while those of the $\mathbf{E} \perp c$ spectrum are assigned to the ν_1 mode of the same molecules. Differences in the coordination of Na^+ ions about the H_2O molecules could account for the nonequivalence. The ratios of fitted peak heights and, for comparative purposes, the ratio measured for hydrated Liβ-alumina are listed in Table 4.2.

In order to compare the absorption intensities of ν_1 and ν_3, the absorption from ν_1 ($\mathbf{E} \perp c$) must be corrected for the random occupation of H_2O molecules at three equivalent sites,[1] which are related by a threefold rotation about an axis parallel to c. The absorption intensity for ($\mathbf{E} \perp c$) is proportional to $\overline{\cos^2\theta}$, where θ is the angle between $\mathbf{E}$ and $\mathbf{P}$. The average of $\cos^2\theta$ taken over the three equivalent H_2O sites is given by

$$\overline{\cos^2\theta} = \frac{1}{3}\sum_{i=1}^{3}\cos^2\left[\theta + (i-1)\frac{2\pi}{3}\right] = \frac{1}{2} .$$

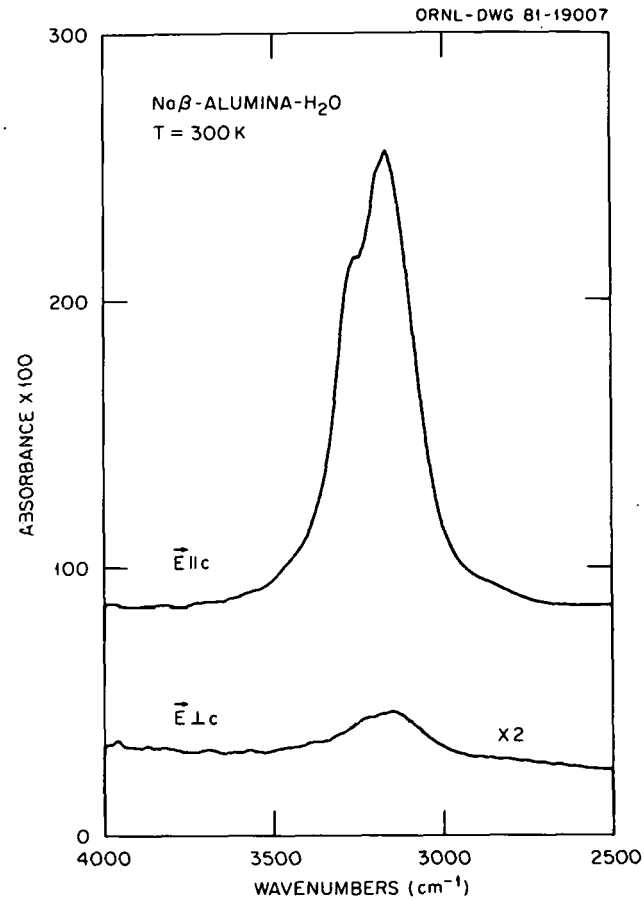

Fig. 4.8. Polarized absorption spectra of H_2O in Naβ-alumina measured at 300 K.

Table 4.2. Observed and calculated absorbance ratios for the ν_3 and ν_1 modes of H_2O in β-aluminas

R(obs)[a]		R(calc)[b]	
Naβ	Liβ	mO	OP
9.0			
	4.3	5.5	11.4
11.0			

[a] Ratio of fitted peak heights.
[b] mO = mid-oxygen; OP = observed position of H_2O in Liβ-alumina.

Since this effect of disorder does not apply for $\mathbf{E} \| c$, the absorption from ν_1 must be multiplied by a factor of 2 in order to be compared with that from ν_3, and the ratios in Table 4.2 include this factor. It is seen in Table 4.2 that the observed ratios are from two to four times larger than the value for H_2O in a gas of noninteracting molecules. Furthermore, R is about twice as large for H_2O in Naβ-alumina as in Liβ-alumina.

In general, the absorption coefficient for an oscillator in a dielectric medium is proportional to $\mathbf{P} \cdot \mathbf{E}_{loc}$, where $\mathbf{P}$ is the induced moment and $\mathbf{E}_{loc}$ is the local electric field at $\mathbf{P}$. The complete expression for the absorption of infrared radiation by H_2O molecules in β-alumina must also contain terms to account for the response of the ions in the host lattice to the transition dipole moment on the molecules. We represent the transition moment of either ν_1 or ν_3 by $\mathbf{P}_w$, where $\mathbf{P}_w = \mathbf{P}_w' + i\mathbf{P}_w''$. The real part $\mathbf{P}_w'$ vanishes at the resonance frequency. The imaginary part $\mathbf{P}_w''$, which is out of phase with the incident radiation and gives rise to absorption, induces a dipole moment at the surrounding ions in the lattice. This moment at the ith ion is given by $\mathbf{P}_i'' = \alpha_i \mathbf{e}_i$, where α_i is the electronic polarizability of the ith ion. The field $\mathbf{e}_i$ which is produced by $\mathbf{P}_w''$ is given by

$$\mathbf{e}_i = \left(\frac{3\epsilon + 2}{3}\right)\left(\frac{3\hat{r}_i(\mathbf{P}_w'' \cdot \mathbf{r}_i) - \mathbf{P}_w''}{|\mathbf{r}_i|^3}\right),$$

where $\mathbf{r}_i$ is a position vector from H_2O to ion i, $\hat{r}_i = \mathbf{r}_i / |\mathbf{r}_i|$, and ϵ is the dielectric constant. If $\mathbf{E}_{i,loc}$ is the local field at ion i, the total absorption from this contribution is proportional to $\Sigma_i \mathbf{P}_i'' \cdot \mathbf{E}_{i,loc}$, where the sum includes all ions contained in a spherical region of radius a about the H_2O molecule. Outside of the region, the medium is treated as an isotropic continuum so that $E_{loc} = [(\epsilon + 2)/3]E$, where E is the applied field. The dipole moment induced by $\mathbf{P}_w''$ in the outer region is given by $\mathbf{P}_o'' = [4(\epsilon - 1)/3\epsilon a]\mathbf{P}_w''$. The total absorption is, therefore, derived from three sources: (1) the transition moment at the H_2O molecule $\mathbf{P}_w''$, (2) the moment induced by $\mathbf{P}_w''$ at each ion within the spherical cavity of radius a about the H_2O molecule, and (3) the dipole moment induced by $\mathbf{P}_w''$ in the region exterior to the cavity.

The results of the local-field calculation expressed as the ratio of the absorbances R_{calc} are given in Table 4.2. The calculated ratio is largely determined by the term $\mathbf{P}_w'' \cdot \mathbf{E}_{loc,w}$, where $\mathbf{E}_{loc,w}$ is the local field at the protons of H_2O. As seen in Table 4.2, R_{calc} is sensitive to the location chosen for the molecule: $R_{calc} \sim 6$ at the mid-oxygen site and increases to ~ 11 at the location of water in Liβ-alumina determined from the neutron diffraction study. Perhaps the difference in R observed for H_2O in Liβ-alumina and Naβ-alumina can be attributed to a small difference in location. Although we have not obtained quantitative agreement between the observed and calculated ratios, the calculated results can qualitatively explain the large difference in absorption intensities for ν_3 and ν_1 of H_2O in β-alumina.

1. J. B. Bates et al., "Structure and Spectra of H_2O in β-Alumina," this report.

STUDY OF β- and β"-ALUMINAS BY MEANS OF POTENTIAL ENERGY CALCULATIONS[1]

J. C. Wang N. J. Dudney
J. B. Bates H. Engstrom[2]

The solid electrolytes β- and β"-alumina provide a family of materials with interesting and unusual properties. These materials have unusually high ionic conductivities and low activation energies for a number of monovalent and divalent cations. When cations such as K^+ and Na^+ are mixed, the conductivity goes through a minimum as the concentration ratio is changed. The conductivity of β"-aluminas also shows a non-Arrhenian behavior; that is, the absolute value of the slope of $\log(\sigma T)$ vs $1/T$ decreases gradually with increasing temperature. While interesting experimental data like these are being reported in the literature at a rapid pace, there is a real need to correlate and understand the various results through microscopic model calculations.

In general, for each ionic arrangement (configuration), the monopole field $\mathbf{F}_i$ and dipole field $\mathbf{G}_i$ at ion i produced by all other ions and induced dipoles, respectively, are calculated first. The total field (or local field) at ion i is then given by

$$\mathbf{E}_i = \mathbf{F}_i + \mathbf{G}_i \quad . \tag{1}$$

Because the induced dipoles interact with one another, the fields $\mathbf{G}_i$ must be calculated self-consistently by either solving a system of linear equations or by making approximations. The total

potential energy of the ionic configuration can be calculated from

$$V = \frac{1}{2}\sum_i \sum_{j\neq i} \frac{q_i q_j}{r_{ij}} + \frac{1}{2}\sum_i \sum_{j\neq i} A_{ij} e^{-\rho_{ij} r_{ij}} - \frac{1}{2}\sum_i \alpha_i \mathbf{E}_i \cdot \mathbf{F}_i \ , \qquad (2)$$

where q_i and α_i are the charge and ionic polarizability, respectively, of ion i; r_{ij} is the distance between ions i and j; and A_{ij} and ρ_{ij} are the short-range repulsive potential parameters. Physical quantities such as activation energy, defect vibrational frequency, and equilibrium ionic configuration can be obtained by calculating the change in potential energy as the configuration of mobile ions is varied.

The properties which have been investigated include the conduction mechanism,[3] mixed-ion effects,[4] and charge compensation mechanisms[5] in β-aluminas, and the non-Arrhenian behavior of β"-aluminas.[6] The results of the last two studies are described elsewhere in this report.[5,6] In general, the agreement with experimental results is reasonably good.

It is concluded that potential energy calculations can provide useful information for understanding the properties of β- and β"-aluminas. Some of the general results can either be applied to explain experimental data directly and/or can be used as a basis for more advanced theoretical models.

1. Summary of paper: *Solid State Ionics* (in press).
2. Present address: Sperry Univac, Santa Clara, Calif.
3. J. C. Wang, M. Gaffari, and Sang-il Choi, *J. Chem. Phys.* **63,** 772 (1975).
4. J. C. Wang et al., p. 379 in *Fast Ion Transport in Solids, Electrodes and Electrolytes,* ed. by P. Vashishta, J. N. Mundy, and G. K. Shenoy, North Holland, New York, 1979.
5. J. C. Wang, *J. Chem. Phys.* **73,** 5786 (1980); also, "On the Charge Compensation Mechanism in β-Alumina," this report.
6. J. C. Wang et al., "On the Non-Arrhenian Behavior of β"-Alumina," this report.

COMPOSITION, ION-ION CORRELATIONS, AND CONDUCTIVITY OF β"-ALUMINA[1]

J. B. Bates
H. Engstrom[2]
J. C. Wang
B. C. Larson
N. J. Dudney
W. E. Brundage

Recent diffuse x-ray scattering measurements[3] have shown that the mobile ions in Naβ"- and Kβ"-aluminas tend to order on a two-dimensional superlattice. The extent of short-range ordering or correlation length L decreases continuously with increasing temperatures above 25°C, but the onset of a rapid change in L with T occurs near 200°C. In the $\log(\sigma T)$ vs $1/T$ graphs of these β"-aluminas, a noticeable decrease in the slope begins near 200°C, which implies a decrease in the activation energy at high temperatures. These results suggest that conduction at low temperatures and the curvature in the $\log(\sigma T)$ vs $1/T$ plots of the β"-aluminas are strongly influenced by the extent of the mobile cation ordering on the superlattice. Based on the results of earlier theoretical work,[4] we expect these properties to be sensitive to the concentration of conducting ions. In this report we summarize the results of a current investigation of the effect of composition on conductivity and cation ordering in β"-alumina single crystals.

Large single crystals of Naβ"-alumina, stabilized with either Mg or Zn, were grown in platinum crucibles by a flux evaporation technique at temperatures from 1600–1725°C. Based on optical methods of analysis, the Mg-stabilized crystals (Naβ"Mg) grown at 1650 and 1700°C had the same composition, $Na_{1.67}Mg_{0.67}Al_{10.33}O_{17}$. Conductivity and composition measurements indicate that some Zn^{2+} ions are incorporated into the conduction layers during crystal growth of Zn-stabilized β"-alumina. Treatment of as-grown crystals in molten $NaNO_3$ replaced these Zn^{2+} ions with Na^+ ions. Based on the analysis for Na and Zn, crystals grown at 1700°C have the composition $Na_{1.57}Zn_{0.57}Al_{10.43}O_{17}$ after treatment in $NaNO_3$.

The impedance of the β"-alumina crystals was measured in vacuum from 25 to 500°C using a two-probe ac technique. The results of these measurements are illustrated in Fig. 4.9. The data for

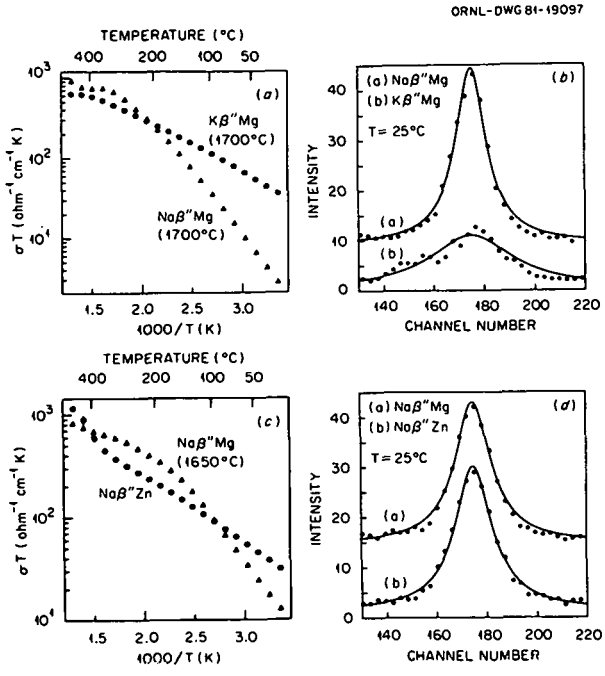

Fig. 4.9. Conductivity and x-ray diffuse scattering results for β''-aluminas.

Naβ"Zn were obtained after treatment in $NaNO_3$. The activation energies E_a, taken as the absolute value of the slope of the low-temperature region of the $\log(\sigma T)$ vs $1/T$ curves, and values of σ at 25 and 300°C are given in Table 4.3. Diffuse x-ray scattering measurements[5] were made on single crystals of the Naβ"- and Kβ"-aluminas prepared from the same parent material used in the conductivity study. The results of the x-ray measurements are shown in Fig. 4.9. To simplify the illustrations, each data point represents the average of three points collected in the experiment. The solid curves are the results of fitting each full data set to a function consisting of a Lorentzian peak and a background parameter. The correlation length was calculated from the diffuse scattering linewidth. Values of L for each of the four β"-aluminas studied are listed in Table 4.3.

Table 4.3 Conductivities measured at 25 and 300°C, C_a and L for Mg- and Zn-stabilized β''-aluminas

Material	Conductivity (Ω^{-1} cm^{-1}) 25°C	300°C	E_a (eV)	L (Å)
Naβ"Mg, 1700°C	0.01	1.00	0.33	67
Naβ"Mg, 1650°C	0.04	1.06	0.26	57
Kβ"Mg, 1700°C	0.12	0.79	0.15	30
Naβ"Zn, 1700°C	0.10	0.43	0.14	55

Based on the crystal composition, the fraction of vacant Na sites (ρ_v) in our Mg-stabilized Naβ"-alumina (Naβ"Mg) is 0.17, and in the Zn-stabilized material $\rho_v = 0.22$. Mutual coulombic interaction among the vacancies in these compounds causes them to order on a superlattice. From the earlier x-ray work,[3] the cell constant of the superlattice is $\sqrt{3}a_0$. An ideal $\sqrt{3}a_0$ cell can be constructed when $\rho_v = 0.167$. This value is close to $\rho_v = 0.17$ observed in Naβ"Mg and perhaps explains why this compound has a large L at room temperature (Table 4.3). It is reasonable to expect that the ordered distribution of vacancies on a superlattice will cause the activation energy for vacancy diffusion to be higher than that for a random distribution. Since L decreases with increasing temperatures, we can expect the activation energy to decrease as well. This picture is consistent with the conductivity and x-ray data for Naβ"Mg; (i.e., the decrease in L on replacement of Na^+ by K^+ is accompanied by a decrease in E_a). However, it is not clear why replacing Na^+ with K^+ causes the extent of ordering of the superlattice to decrease by more than a factor of 2 (Table 4.3).

The results obtained for Naβ"Mg (1650°C) and Naβ"Zn suggest that factors other than vacancy concentration can affect the ordering within the conduction layers and the activation energy. Although the Naβ"Mg grown at 1650°C has the same composition as the material grown at 1700°C (within experimental error), it has smaller values of L and E_a (Table 4.3). This difference might be caused by differences in the distribution of Mg^{2+} ions on Al(2) sites.[6] The degree of ordering of cations on a superlattice in Naβ"Zn is evidently comparable to that of Naβ"Mg grown at 1650°C, as evidenced by similar values of L. Yet E_a for Naβ"Zn is almost two times smaller than that of the Mg-stabilized compound, and the room-temperature conductivity is more than twice as large. A possible explanation for this result is that, because of the higher vacancy concentration in Naβ"Zn than in Naβ"Mg, there is a larger number of vacancies which do not occupy order positions. These "free" vacancies will have a higher mobility than those on ordered sites, and increasing their

number will lead to a net decrease in E_a and an increase in conductivity at low temperatures.

1. Summary of paper: *Solid State Ionics* (in press).
2. Present address: Sperry Univac, Santa Clara, Calif.
3. J. P. Boilot et al., *Phys. Rev. B* **22,** 5912 (1980).
4. Hiroshi Sato and Ryoichi Kikuchi, *J. Chem. Phys.* **55,** 677 (1971).
5. B. C. Larson et al., "Effect of Hydration on Conduction Ion Correlations in Naβ"-Alumina," this report.
6. J. C. Wang et al., "Study of β- and β"-Aluminas by Means of Potential Energy Calculations," this report.

EFFECT OF HYDRATION ON CONDUCTION ION CORRELATIONS IN Naβ"-ALUMINA[1]

B. C. Larson N. J. Dudney
J. B. Bates J. F. Barhorst

X-ray diffuse scattering studies have shown that Na ion vacancies in Naβ"-aluminas have a tendency to form superlattice structures in the conducting planes. The diffraction widths of the resulting superlattice streaks have been used[2] as a measure of the lateral size (correlation lengths) of coherently ordered regions, and there is convincing evidence that the activation energies of the Na ions are strongly influenced by the extent of this ordering.[3] During the course of an investigation of the relationship between ion correlations, crystal composition, and ionic conductivity in Naβ"-aluminas, it was found that the presence of H_2O in the conducting planes has a strong influence on conduction ion correlations, and we report here the results of a systematic study of the effect of intercalated water on Na ion correlations in Mg- and Zn-stabilized Naβ"-alumina.

Water was introduced into flux grown (1700°C) Mg- and Zn-stabilized Naβ"-alumina by treating the crystals for extended times at temperatures from 70-150°C and water vapor pressures up to 80 kPa. Additional samples were selected from crystals that were hydrated under ambient atmospheric conditions. The extent of hydration was monitored by means of infrared absorption measurements using the H_2O band at 3400 cm^{-1}. X-ray measurements of the superlattice diffraction widths and relative peak heights were carried out near the l = 28.5 position of the (4/3, 1/3, l) superlattice streak using a rotating anode x-ray generator, a flat graphite monochromator, and a linear position-sensitive detector. The Scherrer expression, $L = 0.94\lambda/\delta \sin(\phi)$, relating diffraction linewidths to particle sizes was used to determine the correlation lengths L. In this expression, λ is the x-ray wavelength, δ is the full width at half maximum of the measured peak, and ϕ is the scattering angle.

The results of these measurements are shown as a function of the H_2O content in Table 4.4 and in graphical form in Fig. 4.10. An absorption coefficient of α = 38 cm^{-1} (base-10) corresponds to ~0.2 H_2O molecules per planar unit cell. These peak height and peak width data were obtained by fitting Lorentzian lineshapes to the measured diffraction profiles, as the measured profiles were found to differ significantly from Gaussian shapes, suggesting a short-range-order superlattice structure rather than discrete domains.[3] It can be seen that under dry (α = 0) conditions, the correlation lengths for Mg-stabilized materials are intrinsically ~20% larger than for Zn-stabilized materials; however, the effect of H_2O on the peak widths is seen to be more than twice this amount, and the effect of H_2O on the peak heights is even larger. This result underscores the need to remove all H_2O from samples to be used in superlattice structure studies.

Table 4.4. Lineshape and correlation length parameters for hydrated Naβ"-alumina

α (cm^{-1})	Peak height	δ (°)	L (Å)	Stabilized material
0.0	287	1.65	56	Zn
3.8	251	1.63	56	
10.1	191	1.85	49	
18.2	149	2.27	41	
24.0	112	2.33	39	
38.4[a]	65	4.16	22	
0.0	350	1.39	66	Mg
2.7	306	1.40	66	
8.7[a]	195	1.76	52	
18.4[a]	114	2.00	46	
35.0[a]	38	2.90	32	

[a] Hydrated under ambient conditions

Although it is not possible to draw definitive conclusions on the mechanism of the superlattice disruption from these measurements, these results do suggest that a (statistically) homogeneous distribution of H_2O molecules (presumably at vacant Na sites) is responsible for the reduction in the

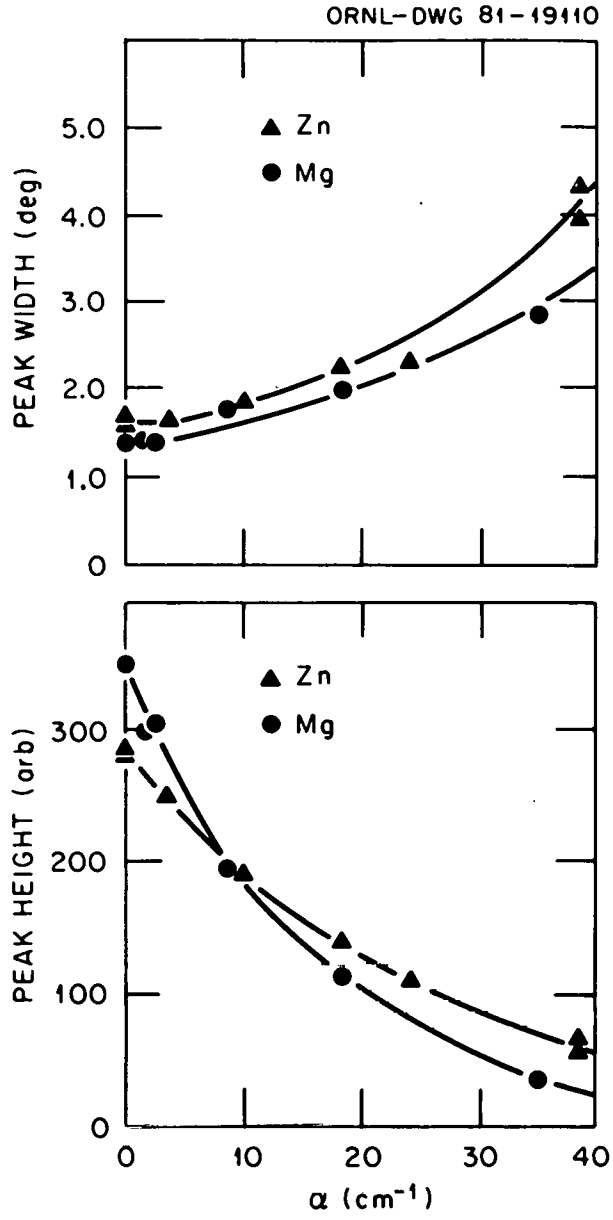

Fig. 4.10. Effect of H_2O on peak heights and peak widths in Zn- and Mg-stabilized Naβ''-alumina.

correlation lengths. A heterogeneous distribution of H_2O molecules, completely destroying the superlattice in some regions and leaving others undisturbed, would lead to decreasing peak heights but would not cause peak broadening.

ON THE NON-ARRHENIAN BEHAVIOR OF β''-ALUMINAS[1]

J. C. Wang H. Engstrom[2]
J. B. Bates D. F. Pickett, Jr.[3]

The ionic conductivity of β''-aluminas shows an unusual non-Arrhenian behavior; that is, the absolute value of the slope of $\log(\sigma T)$ vs $1/T$ is high at low temperatures and decreases gradually with increasing temperatures.[4,5] If the true" activation energy $E(T)$ is defined as the potential barrier height in the thermally activated form of conductivity

$$\sigma T = \sigma_0 e^{-E(T)/kT} \tag{1}$$

and the "apparent" activation energy $E_a(T)$ is defined from the slope of $\log(\sigma T)$ vs $1/T$ as

$$E_a(T) \equiv -\frac{d \ln(\sigma T)}{d(1/kT)}, \tag{2}$$

then $E(T)$ and $E_a(T)$ are not identical for β''-aluminas. They are related by

$$E_a(T) = E(T) - T\frac{dE(T)}{dT}. \tag{3}$$

By choosing reasonable values for the attempt frequencies, $E(T)$ and $E_a(T)$ for several β''-alumina samples were obtained by fitting the experimental $\log(\sigma T)$ vs $1/T$ curves discussed elsewhere in this report.[5] As can be seen from Fig. 4.11, $E(T)$ and $E_a(T)$ are quite different. This is an important property of β''-aluminas which is due to the temperature dependence of the potential barrier height $E(T)$. The problem of understanding the non-Arrhenian behavior now becomes one of understanding the form of $E(T)$. From Fig. 4.11 we can see that it decrease rapidly with temperatures from 300 to 500 K. Above 500 K, it approaches a constant value.

To understand this behavior, we first consider an ideal case of a single vacancy in the conduction layer. Potential energy calculations using coulomb, short-range repulsive, and polarization energy terms showed[6] that because of the correlated motion of the Na^+ ions nearby, the potential barrier height for the vacancy to hop is about 0.02 eV. This number is much smaller than the values of $E(T)$ shown in Fig. 4.11, suggesting that a single vacancy is nearly free. In actual crystals, the number of vacancies is about 1/6 that of the avail-

1. Summary of paper: *Solid State Ionics* (in press).
2. D. B. McWhan et al., *Phys. Rev. B* **17**, 4043 (1978).
3. J. B. Bates et al., "Composition, Ion-Ion Correlations, and Conductivity of β''-Alumina," this report.

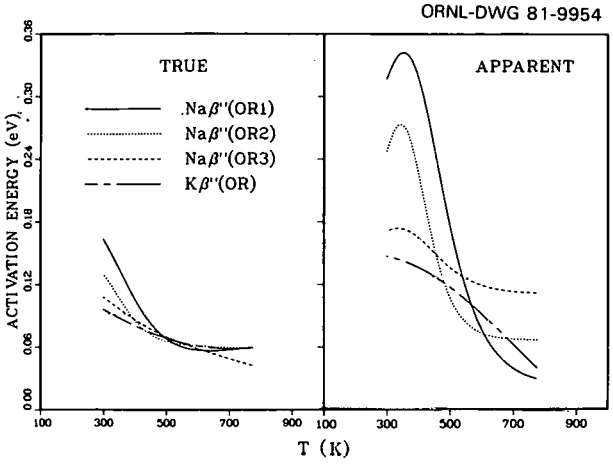

Fig. 4.11. $E(T)$ and $E_a(T)$ obtained by fitting the conductivity data reported in ref. 5. The attempt frequencies for Naβ''- and Kβ''-aluminas are taken to be 50 and 40 cm^{-1}, respectively. The stabilizing impurities and crystal growth temperatures for the Naβ''-alumina samples are OR1(Mg,1700°C), OR2(Mg,1650°C), and OR3(Zn,1700°C).

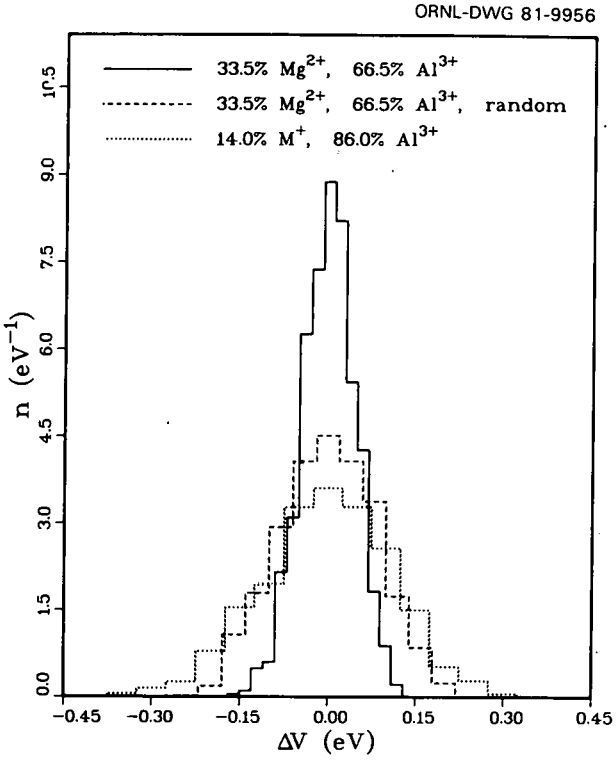

Fig. 4.12. Distributions of the potential energy differences between neighboring Na^+ sites produced by the stabilizing impurities on Al(2) sites in the spinel block. The areas of all the histograms are normalized to one.

able Na^+ sites. Because of coulomb interaction among the vacancies, they tend to order on a 2-d superlattice. The extent of ordering increases with decreasing temperature but approaches a limiting value at zero T because of the structure of the crystal. At low temperatures, the main contribution to $E(T)$ comes from the energy needed to excite a vacancy out of the superlattice site. This contribution, taken to be 1/2 of the formation energy of a Frenkel pair, was calculated to be 0.15 eV. As can be seen from Fig. 4.11, this is in reasonable agreement with the low-temperature values of $E(T)$.

At high temperatures, when the ordering of vacancies is destroyed by thermal agitation, it can be expected that $E(T)$ approaches a small constant value. This value may be controlled by the electrostatic potential fluctuation in the conduction layer produced by the stabilizing ions in the spinel block. To estimate this fluctuation, we filled randomly the Al(2) sites with 33.5% Mg^{2+} ions and 66.5% Al^{3+} ions with the restriction that no two Mg^{2+} ions can occupy neighboring Al(2) sites in a spinel block. This corresponds to the Mg^{2+} content observed in single crystals of Naβ''-alumina.[5] The coulomb potential differences between all neighboring Na^+ sites ΔV's were calculated. The distribution of ΔV's is shown by the solid histogram in Fig. 4.12. The sample standard deviation (half-width) was calculated to be 0.05 eV. It is interesting to note that this is quite close to the high-temperature limits of $E(T)$ for Naβ''- and Kβ''-aluminas shown in Fig. 4.11. Notice that the width of the distribution depends on the arrangement of the impurities among the available Al(2) sites in the spinel block and on the valence of impurities. This result may explain why the conductivity of β''-aluminas depends on sample preparation conditions.

---

1. Summary of paper to be published.
2. Present address: Sperry Univac, Santa Clara, Calif.
3. Hughes Aircraft Company, Los Angeles, Calif.
4. J. L. Briant and G. C. Farrington, *J. Solid State Chem.* **33**, 385 (1980).
5. J. B. Bates et al., "Composition, Ion-Ion Correlations, and Conductivity of β''-Alumina," this report.
6. J. B. Bates et al., p. 261 in *Fast Ion Transport in Solids, Electrodes and Electrolytes*, ed. by P. Vashishta, J. N. Mundy, and G. K. Shenoy, North Holland, New York, 1979.

AUTOMATED MULTIFREQUENCY MEASUREMENTS OF THE COMPLEX IMPEDANCE OF FAST-ION CONDUCTORS[1]

H. Engstrom[2] J. C. Wang

The dc conductivity is an important property of solid electrolytes. Direct measurements of this quantity for materials such as the β-aluminas pose serious experimental difficulties and limitations associated with the necessity of using molten salt or liquid alkali metal electrodes. Most measurements of the dc conductivity are, therefore, made indirectly using blocking electrodes and ac techniques.

A variety of ac methods has been applied to the β-aluminas. The most common method employs an ac bridge, but pulse, microwave, and phase-synchronous detection techniques have also been applied. These techniques present their own sets of experimental difficulties, such as the effects of stray lead capacitance and inductance, and require more complicated procedures for data analysis. In addition, we have recently observed non-Debye electric susceptibility in Naβ-alumina.[3] To account for this behavior properly, it is necessary to make complex impedance measurements over a wide range of frequencies.

In this work we describe an automated system which permits a rapid, convenient, and accurate determination of the complex impedance of the sample. The heart of the system is a network analyzer combined with a frequency synthesizer. Together, these two devices constitute a highly accurate, digital, superheterodyne lock-in detector, which is capable of measuring the amplitude and phase of a signal over a frequency range 50 Hz–13 MHz and has a dynamic range of 100 dBm. During an experiment, the network analyzer and synthesizer operate under the control of a programmable calculator, which also controls the sample temperature, frequency of measurement, and a number of input/output devices.

Samples of single-crystal β-alumina are cut as slabs with the approximate dimensions of 5 mm $\times$ 3 mm $\times$ 0.5 mm. The conduction plane of the crystal is parallel to the large sample face. Electrical contacts are made by sputtering platinum to a depth of $\sim$3 μm on the two smallest faces of the sample. The sample is held between two platinum contacts in a ceramic sample holder which is placed inside a quartz tube located in the core of a tube furnace. Electrical leads from the Pt contacts terminate in a load circuit at the end of the sample holder. The load circuit must be carefully selected so that the measured signal strength will fall within the specifications of the network analyzer. To minimize interference with the signal from the sample, active oscilloscope probes are used to connect the load circuit with the network analyzer.

Measurements of the sample impedance are made automatically with the apparatus described above at equally spaced $1/T$ intervals from a selected upper temperature (usually 500°C) to room temperature. The phase and amplitude of the output signal from the sample at each temperature are measured from 100 Hz to 10 MHz. These data are stored on magnetic tape for later analysis.

The commonly applied methods of characterizing fast-ion conductors, that is, phase-synchronous detection, ac bridge, and pulse, can all yield the same information about the sample. However, all of the β-aluminas that we have studied exhibit a non-Debye susceptibility, and for this reason the pulse method is the least reliable and most difficult to interpret. The bridge technique, in principle, yields the best accuracy but is difficult to automate and, therefore, is quite slow. We have found that automated, phase-synchronous network analysis offers the best combination of speed, accuracy, versatility, and ease of use. Furthermore, except for the sample holder itself, all of the component parts of the apparatus are readily available from commercial sources.

---

1. Summary of paper: *Solid State Ionics* **1**, 441 (1980).
2. Present address: Sperry Univac, Santa Clara, Calif.
3. H. Engstrom, J. B. Bates, and J. C. Wang, *Solid State Commun.* **35**, 543 (1980).

SUPERCONDUCTIVITY

MICROSCOPIC MAGNETIC FIELD PROFILE OF THE FLUX-LINE LATTICE IN V_3Si

D. K. Christen S. T. Sekula
H. R. Kerchner Y. K. Chang

Small-angle neutron diffraction was used to deduce the microscopic magnetic-field profile of the flux-line lattice (FLL) in the superconducting

mixed state of a single crystal of V_3Si.[1] In principle, this information is obtained from the form factor, found by measuring the integrated intensity I_{hk} in the peaks of the various order hk Bragg reflections of the quasi-two-dimensional FLL. The form factor is obtained from the equation

$$I_{hk} = S_0 \frac{(\gamma/4)^2 \lambda_n^2 V 2\pi}{(\mathbf{K}_{hk}) A_c^2} |F_{hk}|^2 \ . \qquad (1)$$

Here, S_0 is the incident neutron flux, $\gamma = 1.91$ is the neutron moment expressed in nuclear magnetons, $\lambda_n = 0.26$ nm is the neutron wavelength, and V is the illuminated sample volume. The scattering vector $\mathbf{K}_{hk}$ is related to the Bragg angle $2\theta_{hk}$ by $\mathbf{K}_{hk} = 2\theta_{hk} 2\pi/\lambda_n$, and the FLL unit cell area A_c determines the bulk flux density $B = \phi_0/A_c$, where ϕ_0 is the flux quantum.

The scattering form factor F_{hk} is related to the microscopic FLL field profile $h(r)$ through the Fourier transforms,

$$F_{hk} = \phi_0^{-1} \int h(\mathbf{r}) \exp(i\mathbf{K}_{hk} \cdot \mathbf{r}) \ d^2r \qquad (2)$$

and

$$h(\mathbf{r}) = \phi_0/A_c \sum_{hk} F_{hk} \exp(-i\mathbf{K}_{hk} \cdot \mathbf{r}) \ . \qquad (3)$$

The FLL is somewhat unique in relation to other magnetic systems in the sense that the scattering vector, for a given order reflection hk, can be varied continuously by changing the magnitude of the applied magnetic field within the mixed state. This property provides valuable information regarding the microscopic behavior of the FLL. If curves of $F(\mathbf{K}_{hk})$ vs $\mathbf{K}_{hk}$ lie on a universal curve for all hk, then the FLL microscopic field $h(\mathbf{r})$ is given by

$$h(\mathbf{r}) = \sum_l h_0(\mathbf{r} - \mathbf{R}_l) \ , \qquad (4)$$

where $h_0(\mathbf{r} - \mathbf{R}_l)$ is the single, isolated FL field for an FL centered on the FLL site l. That is, the total field is simply the linear superposition of the isolated FL fields, and

$$h_0(\mathbf{r}) = \phi_0/(2\pi)^2 \int F(\mathbf{K}) \exp(-\mathbf{K} \cdot \mathbf{r}) \ d^2\mathbf{K} \ . \qquad (5)$$

It is now well known that pure niobium does not satisfy this simple criterion, even at the lowest flux densities.[2] On the other hand, some nondilute alloys of Nb do indicate superposition.[2]

Figure 4.13 shows the present results for V_3Si, the first obtained for a high-T_c A15 material. The closed circles are data obtained from Eq. (1) for the lowest-order (10) reflection as a function of the scattering vector $\mathbf{K}$. The two open circles represent form factors found from higher order (20) reflections. These data correspond to a flux density range 10–400 mT.

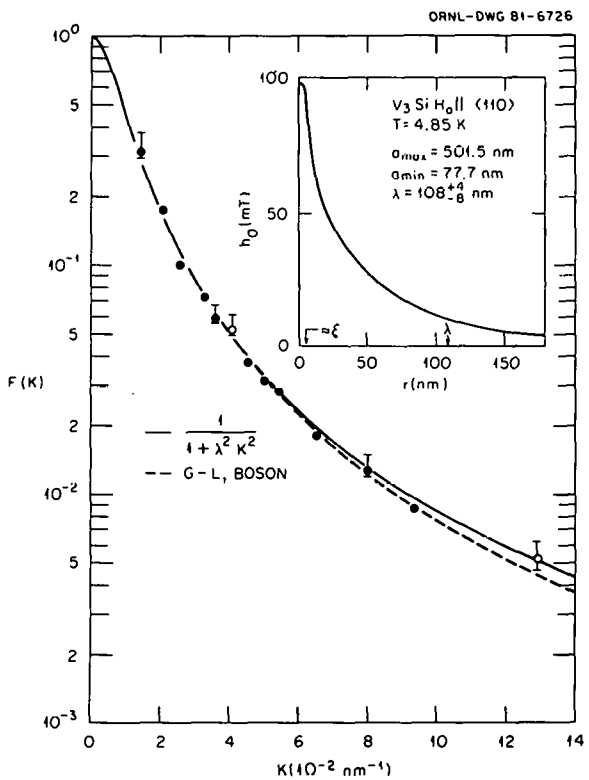

Fig. 4.13. The form factor of the FLL microscopic field at $T = 4.85$ K. The solid curve is the London model form factor for $l = 1.08.0$ nm, while the dashed curve is derived from either the Ginzburg-Landau or the boson theories. The inset shows the single FL field profile. The quantities a_{max} and a_{min} are the largest and the smallest inter-FL spacing, respectively, experimentally used, and ξ is the coherence length deduced from the measured l and for $\kappa \simeq 21$.

From Fig. 4.13, it is seen that, within experimental error, linear superposition of the vortex fields holds. Moreover, the K dependence of $F(K)$ is nearly Lorentzian, indicting the FL interaction is London-like over the range of inter-FL spacings experimentally employed and for a superconducting penetration depth $\lambda = 108.0$ nm. A London model is the simplest description of an extreme Type II

superconductor. A more detailed analysis is provided by the Ginzburg-Landau theory[3] and the boson theory,[4] the results of which both fall near the dashed line over this K range.

In view of this agreement, it would appear that FL interactions in the low-field region of V_3Si are described relatively simply, without need of the complicated nonlocal corrections required in the case of Nb. However, at present it is not clear how these observations are reconciled with the more complicated anisotropies in the FLL morphology.[1,5]

1. D. K. Christen et al., *Physica B&C* **107,** 301 (1981).
2. J. Schelten, H. Ullmaier, and G. Lippmann, *Z. Physik* **253,** 219 (1972).
3. E. H. Brandt, *Phys. Status Solidi B* **51,** 345 (1972).
4. M. Tachiki and H. Umezawa, *Phys. Rev. B.* **15,** 3332 (1977).
5. D. K. Christen et al., "Anisotropy of the Flux-Line-Lattice Morphology in V_3Si," this report.

ANISOTROPY OF THE FLUX-LINE-LATTICE MORPHOLOGY IN V_3Si

D. K. Christen S. T. Sekula
H. R. Kerchner Y. K. Chang

Using the high-resolution, double-crystal, small-angle neutron diffractometer at HB-3A at the HFIR, we have obtained the first direct observations of a well-defined two-dimensional FLL in the superconducting mixed state of a single-crystal sample of the A15 compound V_3Si.[1] Subsequently, systematic investigations were conducted to correlate several structural properties of the FLL with the real crystal symmetries parallel to the applied magnetic field. In the following, we present data that reveal the existence of strong anisotropic correlations at the microscopic level of the FLL morphology.

In these studies, the FLL were grown by applying the magnetic field at a temperature above T_c = 16.8 K and reducing the temperature of the sample to a controlled value 4.85 K. In this way the macroscopic flux density B could never exceed the applied field. In fact, independent bulk magnetization measurements confirmed that in the range of applied fields used for these studies (10–400 mT), the sample traps nearly all the applied field.

Using a scattering geometry where the applied field is vertical and orthogonal to the incident horizontal neutron beam, the symmetry, mosaic distribution, and orientation of the FLL within the sample could be deduced from the scattered intensity as a function of a sample rotation about a vertical axis (rocking curves). The FLL interplanar spacing was derived from the scattering angle 2θ.

For two different field intensities, H = 60.0 mT and H = 200.0 mT, and for four different orientations of the V_3Si crystal, some representative results are shown in Fig. 4.14. A calculation of the bulk flux density $B = n\phi_0/A_c$ obtained from the measured FLL unit cell area A_c indicates that n must be unity, so that each flux line possesses exactly one flux quantum $\phi_0 = 2.07 \times 10^{-15}$ Tm^2.

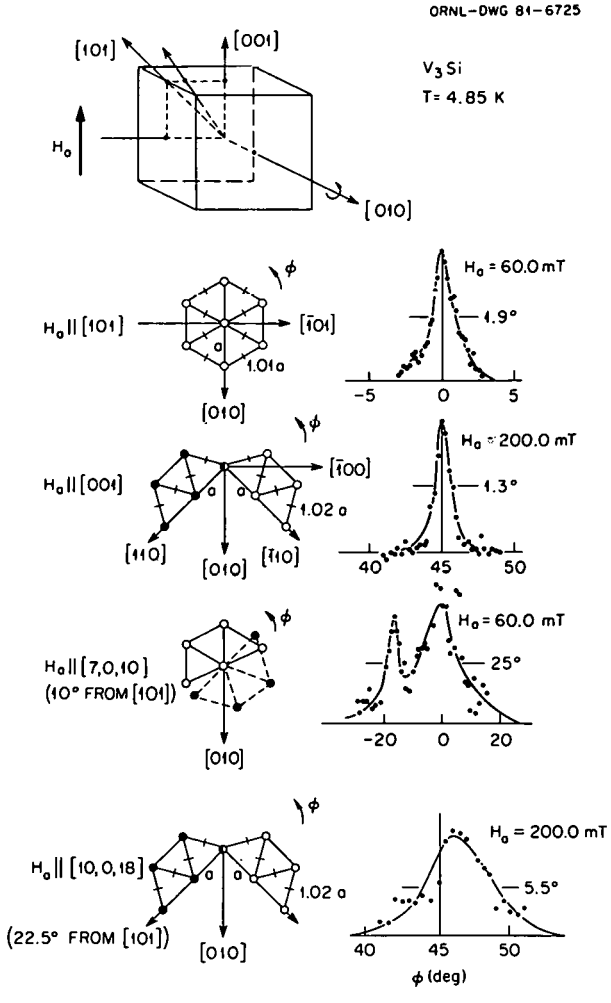

Fig. 4.14. The FLL morphology for the applied magnetic field parallel to four different V_3Si crystal directions in the (010) plane.

The uppermost lattice in Fig. 4.14 represents the observed FLL morphology for the field parallel to the [101] twofold axis. The width of a representative rocking curve illustrates that the mosaic distribution is small, so that the FLL is a well-defined "single crystal." Note that for this orientation the FLL near-neighbor direction is a [101] and that the FLL deviates only slightly from hexagonal symmetry. The half-unit cell is an isosceles triangle with the legs about 1 or 2% longer than the base.

The dramatic anisotropy in the FLL is seen when the field is applied parallel to a fourfold symmetric [001] axis. Again the FLL is well defined but is comprised of distinct domains of isosceles triangular lattice of identical symmetry but oriented 90° apart. In this case the near-neighbor directions lie along ⟨110⟩ axes.

At the off-symmetry direction [7, 0, 10] (10 degrees from a [101]), the FLL undergoes a splitting from the single-domain case, as it apparently evolves toward the highly resolved two-domain situation. The rocking curves are broad and smeared, indicating that the anisotropic forces are much weaker. Finally, by the time one is at a field orientation midway between the twofold and fourfold axes, the two domains characteristic of the [001] are nearly fully developed, although we observed one of the domains to occupy a larger fraction of the sample; and as revealed by the rocking curve width, the FLL is less perfect than for the high-symmetry directions.

Several theories have been formulated to describe the FLL morphology, and they entail mapping the anisotropies in the microscopic electronic system into inter-FL forces in an equilibrium lattice. This mechanism can be applied separately to a uniaxially symmetric or a cubic system. The uniaxial case may apply to the tetragonal domains of martensitically transformed V_3Si. Tachiki and Umezawa[2] have calculated the FLL symmetry in the tetragonally distorted material. Since the present crystal has a resistivity ratio $R(300)/R(20) \sim 31$, we expect that it should transform. However, it is not possible to reconcile the observed FLL symmetry with that in ref. 2, which would predict an isosceles triangular FLL half cell having a leg-to-base ratio about 1.5 instead of the observed 1.02.

For the case of a cubic crystal, much work has been done for application to low-κ materials such as niobium. Accounting for the effects of nonlocal electrodynamics, Fischer and Teichler[3] have obtained an asymptotic interaction energy between two flux lines that depends on an anisotropic coherent length, $F_{12} \sim \exp[-r_{12}/\xi(\hat{r})]$, while in the local limit Roger and co-workers[4] generalized a London-like interaction to include anisotropic effects via an orientation-dependent penetration depth $F_{12} \sim \exp[-r_{12}/\lambda(\hat{r})]$. The applicability of either of these regimes is not obvious, and at present it is difficult to estimate the orientation dependence of these parameters based on known electronic properties.

Finally, we mention a possible mechanism which is heuristic but consistent with the observations. This entails supposing an interaction whereby flux lines should align along the boundary wall between martensitically transformed domains. These walls are believed to be twin boundaries lying in (110) planes. The model would assume that once the flux lines are locked into their near-neighbor orientation, the remaining FLL symmetry properties are determined in the usual way by the nearly isotropic equilibrium energetics.

Although it is clear that strong anisotropic correlations exist between the FLL and the real crystal, fundamental questions regarding the role of anisotropy in the superconducting properties of high-T_c A15 materials have remained largely unanswered. At the theoretical level, this is due to a lack of details in the microscopic electronic and elastic anisotropies and to the difficulty involved in relating that information to calculations of relevant superconducting observables (e.g., critical fields, transition temperatures, and flux-pinning effects). Recently, advances in high-magnetic-field technology and materials preparation have enabled the experimental determination of upper-critical-field anisotropies in V_3Si and Nb_3Sn,[5] and these were found to be relatively small $[H_{c2}(\langle 110\rangle)/H_{c2}(\langle 100\rangle) \sim 1.04]$. Since the mixed-state energy in the high-field regime is directly related to H_{c2}, these results have been interpreted to preclude anistropy effects as a major contributing factor to flux pinning by grain boundaries in these materials. However, the detailed mechanism by which grain boundaries pin flux presently is unresolved. In view of this, we propose that the energy required for reorientation of an FLL from one grain to another may provide an alternate mechanism for a barrier to flux motion.

Extension of this work, designed to separate out effects on the FLL due to martensitically transforming and nontransforming crystals, is in progress.

1. D. K. Christen et al., *Physica B&C* **107,** 301 (1981).
2. M. Tachiki and H. Umezawa, *Phys. Rev. B* **15,** 3332 (1977).
3. K. Fischer and H. Teichler, *Phys. Lett.* **58A,** 402 (1976).
4. M. Roger, R. Kahn, and J. M. Delrieu, *Phys. Lett.* **50A,** 291 (1974).
5. S. Foner and E. J. McNiff, Jr., *Solid State Commun.* **39,** 959 (1981).

THEORY OF THE STATISTICAL SUMMATION OF FLUX-LINE-PINNING FORCES IN TYPE II SUPERCONDUCTORS—BEYOND THE DILUTE LIMIT

H. R. Kerchner

The microscopic theory of the critical state of Type II superconductors presently is inadequate because it fails to take into account the finite density of flux-line-pinning defects in real materials. As a result, there exists a wide gap between the predictions of the dilute-limit theory and experimental observations. The most glaring discrepancy is between the dilute-limit-theory prediction that many weakly interacting defects should not contribute to the critical-current density and the fact that all Type II superconductors show evidence of nonzero critical currents. Just as important is the absence of any conceptual basis for understanding quantitatively the behavior of materials containing a high density of crystalline defects. This class of materials includes all technologically important Type II superconductors. It is of interest, therefore, to begin developing a "many-body" type of theory to take into account the finite density of flux-line (FL) pins.

The statistical-summation theory is the prescription for evaluating the configurational average of flux-line-pinning forces due to a random array of crystalline defects. For a perfectly rigid lattice of FL, the forces will have random directions and will nearly cancel. However, the FLL will be distorted by the pinning forces. A significant critical-current density (arising from a nonzero sum of the pinning forces) is due to correlations between defect positions and FL positions. For a random array of defects, these correlations must be associated with elastic instabilities induced in the FLL by the defect-FL interactions. Then, the mathematical problem to be addressed is the stability of solutions of the force-balance equation which describes distortions of the FLL from perfect periodicity. This problem has several similarities to the theory of disordered alloys; therefore, some of the techniques that are useful there have been adapted to the present problem.

The matrix of derivatives of the displacement of the FLL at one point $\mathbf{r}$ with respect to an arbitrary force at $\mathbf{r}'$ is the elastic Green's function $\mathbf{G}(\mathbf{r}, \mathbf{r}')$. Elastic instabilities arise at points $\mathbf{r}$ where

$$J(\mathbf{r}) = \det\{\mathbf{1} - \int d^3\mathbf{r}'[\mathbf{G}(\mathbf{r}, \mathbf{r}')\cdot\nabla]\mathbf{f}(\mathbf{r}')\} < 0 \ , \quad (1)$$

where $\mathbf{f}(\mathbf{r})$ is the pinning force exerted on the FL element at $\mathbf{r}$. Moreover, $J(\mathbf{r})$ is the Jacobian determinant of the coordinate transformation from the periodic to the distorted FLL. The configurational average $\langle J(\mathbf{r})\rangle$ is a relative density of defects on the distorted FLL; it contains the information required to evaluate the critical-current density.

The configurational average of the elastic Green's function has been evaluated in the coherent potential approximation (CPA),[1] and with an additional approximation in the same spirit, $\langle J(\mathbf{r})\rangle$ has been obtained for a model array of strong, point-like pinning defects.[2] In the CPA the effect of the pinning interactions is described by a simple mean field. This mean field is the derivative of the volume pinning-force density (the sum of the pinning forces in a unit volume) with respect to the average FLL displacement, a measurable quantity. It is a positive (i.e., it stabilizes the FLL), monotonically increasing function of the defect density. Just as the CPA only includes scattering from a single site in the theory of electronic states of an alloy,[1] so here it can only give instabilities associated with individual defects. If the pinning interaction of a given defect is weaker than a threshold value, that defect cannot induce an instability in the FLL and cannot contribute directly to the critical-current density.

It is clear from preliminary calculations made in the initial stage of this investigation that a set of many defects can induce an instability cooperatively when none of them interacts sufficiently strongly to do so individually.[3] Evidently, the correct theory requires taking into account the analog to cluster scattering. One can expect, however, that calculations based on small clusters of defects will be inadequate. The appropriate cluster should contain many defects. It has been found that for weak pinning interactions, short-range components of the Green's function may be

eglected, and $\mathbf{G}(\mathbf{r}, \mathbf{r}')$ may be averaged over $\mathbf{r}$ and $'$ within the regions occupied by two sets of defects s and s', respectively. Then $\mathbf{G}(\mathbf{r}, \mathbf{r}')$ may be replaced by the simpler quantity

$$\mathbf{G}_{s,s'} = V_s^{-1} V_{s'}^{-1} \int_{V_s} d^3\mathbf{r} \int_{V_{s'}} d^3\mathbf{r}' \mathbf{G}(\mathbf{r}, \mathbf{r}') \ , \qquad (2)$$

where V_s is the volume of the region occupied by the set s of defects. Furthermore, if the number N_s of defects in s is large and if correlations between the FLL and subsets of s may be neglected, the total pinning force due to the defects in s is $N_s^{1/2}\mathbf{f}(\mathbf{r}_s)$, $\mathbf{f}(\mathbf{r}_s)$ is the force for a typical defect in the set, and $\mathbf{r}_s$ is the average of the defects' positions. If bundles of FL interacting with sets s and s' of defects are taken to be the sites of a lattice, then $\langle \mathbf{G}_{s,s'} \rangle$ may be evaluated in the CPA. The volume pinning-force density calculated in this approximation depends on the division of defects into sets. Since the critical state is the metastable state carrying the largest current density, this choice of how to divide the defects into sets is made to maximize the current density.

Since the questions that presently arise in the theory of the critical state are order-of-magnitude questions, the calculations that have been performed rely on making a number of rather crude (~20%) approximations to obtain analytic results. The kind of agreement one obtains with experiment is shown in Fig. 4.15, where the normalized critical pinning-force density F_c is plotted vs the normalized flux density B/B_{c2} for a vanadium sample containing carbide precipitates.[4] Here B_{c2} is the flux density at the upper critical field, H_c is the thermodynamic critical field, ξ is the Ginzburg-Landau coherence length, n is the number density, and α is the volume of the precipitates. The value of $n\alpha^2$ required to obtain a reasonable fit to the F_c data is within the experimental uncertainty of the value obtained by transmission electron microscopy. Although the theoretical B dependence of F_c matches the experimental curves only roughly, the magnitude of F_c and the trends with changing temperature are predicted accurately by the theory.

The theory of the critical state has been modified to take into account effects associated with the finite density of FL pins. The mean-field description via the CPA leads to quantitative but not qualitative changes in the critical-current density because this description permits only instabilities that are induced by individual defect-FL interactions. When the individual interactions are too weak to induce instabilities, the theory must be generalized to include instabilities induced by sets of many defects. This last step removes the threshold effect and leads to calculations that are in reasonable quantitative agreement with experiment.

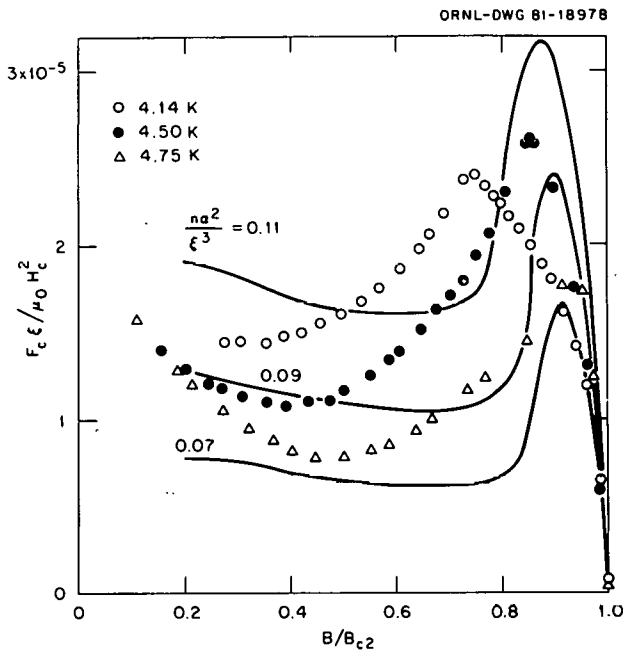

Fig. 4.15. Flux-density dependence of the critical pinning-force density for a vanadium sample containing carbide precipitates. Theoretical curves corresponding to three values of the temperature-dependent parameter $n\alpha^2/\xi^3$ are compared with experimental data for three temperatures.

1. The CPA and its limitations are reviewed in R. J. Elliot, J. A. Krumhansl, and P. L. Leath, *Rev. Mod. Phys.* **46,** 465 (1974).

2. H. R. Kerchner, *Journal of Low Temperature Physics* (in press).

3. H. R. Kerchner, *Solid State Div. Prog. Rep., Feb. 29, 1980,* ORNL-5640, p. 173.

4. A. J. Marker III et al., *J. Low Temp. Phys.* **31,** 175 (1978).

EXPERIMENTAL CHARACTERIZATION OF THE ELASTIC INSTABILITY OF THE FLUX-LINE LATTICE IN THE CRITICAL STATE OF A TYPE II SUPERCONDUCTOR

H. R. Kerchner S. T. Sekula

The measurement of thermally activated creep of magnetic flux in the critical state has long held the promise of yielding information about microscopic flux-line-pinning interactions. Unfortunately, it has not been clear precisely how one should interpret those measurements. A new phenomenological argument has been developed and has been applied to the interpretation of some new data. A single-crystal Nb–5 at. % Zr rod was cold swaged for a factor-of-4 reduction in the cross-sectional area. The experimental evidence indicates that the critical-current density in this sample is due primarily to individual interactions between flux lines and dislocation tangles.

Near the ideal critical state, regions of FLL that are near elastically unstable configurations may be thermally activated over the small energy barrier to the instability and then move irreversibly to a new, lower energy configuration. The rate of flux motion obeys an Arrhenius expression with an energy barrier U that is proportional to the amount by which the current density J is reduced from its ideal (zero-temperature) critical value J_c.[1] The energy barrier may be written

$$U = \left(f \Big/ \frac{dJ}{d\bar{u}} \right) (J_c - J) \ , \qquad (1)$$

where f is the elementary pinning force at the instability and $dJ/d\bar{u}$ is the derivative of J with respect to the reversible average displacement $\bar{u}$ of the FLL. The quantities $f/(dJ/d\bar{u})$, $(dJ/d\bar{u})$, and J_c can be deduced from the ac response experiments performed by placing the cylindrical sample in a large longitudinal dc magnetic field and a small parallel ac field and measuring the ac voltage induced in a pickup coil wound around the sample.[2,3] Moreover, by comparing the order of magnitude of the configurationally averaged elastic Green's function $G'(0) = \langle \mathbf{G}(\mathbf{r}, \mathbf{r}) \rangle$, which is independent of $\mathbf{r}$,[4] with the ratio of f to the FLL spacing a_0, one can deduce whether the defect responsible for the instability is point-like or an extended defect.

Experimental values of the elementary pinnin force f, divided by one-sixth of the FLL spacin a_0, are compared with the reciprocal of the elastic Green's function in Fig. 4.16. The fact that the quantities are of the same order of magnitude indicates that the single-particle pinning dominates and the conventional, dilute-limit theory should be

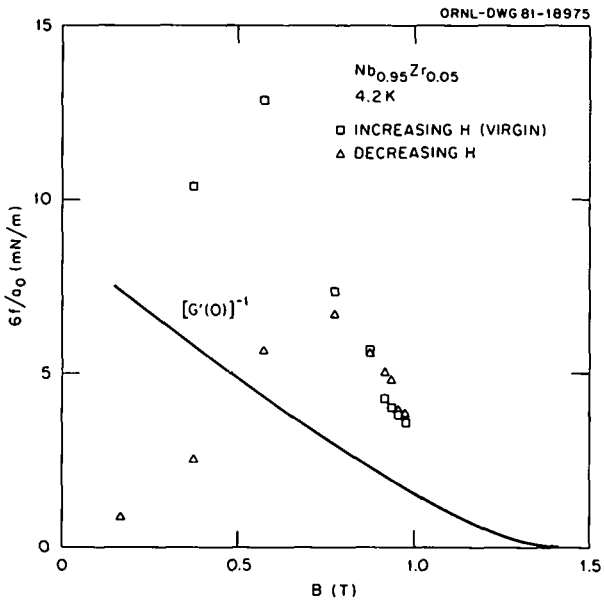

Fig. 4.16. The elementary pinning force f, divided by one-sixth of the FLL spacing a_0, is compared with the reciprocal of the theoretical elastic Green's function $G'(0)$.

applicable. This sample shows a strong history effect at low field; the critical-current density is much smaller after the field is lowered from above the upper critical field than after the field is first raised from zero (the virgin state). The sharp drop in $6f/a_0$ below $[G'(0)]^{-1}$ for the decreasing field history indicates that the FLL deforms more easily than the theory indicates and more easily than in increasing field. This result is exactly opposite to what is generally believed to be the cause of the field history effect. A more careful investigation of this phenomenon is indicated.

The elementary pinning force has been deduced from ac-response measurements on a moderately cold-worked, superconducting sample. The magnitude of this force is consistent with the interaction between the FLL and a dislocation tangle involving about 1-μm length of dislocation. Comparison with the theoretical elastic response of the FLL indi-

cates that the conventional, dilute-limit, statistical-summation theory should apply to this sample.

1. P. W. Anderson and Y. B. Kim, *Rev. Mod. Phys.* **36,** 39 (1964).
2. H. R. Kerchner, *J. Low Temp. Phys.* **34,** 33 (1978).
3. A. M. Campbell, *Philos. Mag. B* **37,** 149 (1978).
4. H. R. Kerchner, "Theory of the Statistical Summation of Flux-Line-Pinning Forces in Type II Superconductors—Beyond the Dilute Limit," this report.

LOW-TEMPERATURE-IRRADIATION STUDY OF FLUX PINNING IN TYPE II SUPERCONDUCTORS

H. R. Kerchner R. R. Coltman, Jr.
C. E. Klabunde

Wire samples of Nb and Nb–20 at. % Ta have been irradiated at liquid helium temperature in two different modes. In one mode, 75% of the damage was produced by thermal neutrons, while in the other mode, 85% of the damage was produced by fast neutrons. The critical current of these samples has been measured as a function of the neutron fluence. The theory of pinning by weakly interacting defects predicts that the critical-current density J_c will be proportional to the square of the defect density n, while it will be proportional to n if the pins are strong enough to contribute individually to J_c.[1] A low-temperature irradiation allows us to control defect density. Niobium was previously irradiated at low temperatures by electrons (producing weak pins only),[2] by fast neutrons (producing weak pins and possibly some strong pins),[3,4] and by high-energy neutrons (producing mainly strong pins).[5] All those results are consistent with a linear relation between J_c and n. Because of the important fundamental significance of this result, however, it was worthwhile to confirm it by repeating and extending the measurements.

Figure 4.17 shows the increase in the critical current I_c as a function of thermal-neutron fluence for two Nb samples that differ in their dislocation density and for a NbTa sample. The increase in I_c is nearly linear in fluence, but in each case the total increase is only a fraction of the initial I_c, even though the initial values of I_c differed by nearly two orders of magnitude. Clearly, at least for the larger-I_c Nb sample, the radiation-induced defects are somehow assisting the dislocations to pin flux lines. Comparison of the increase in I_c for

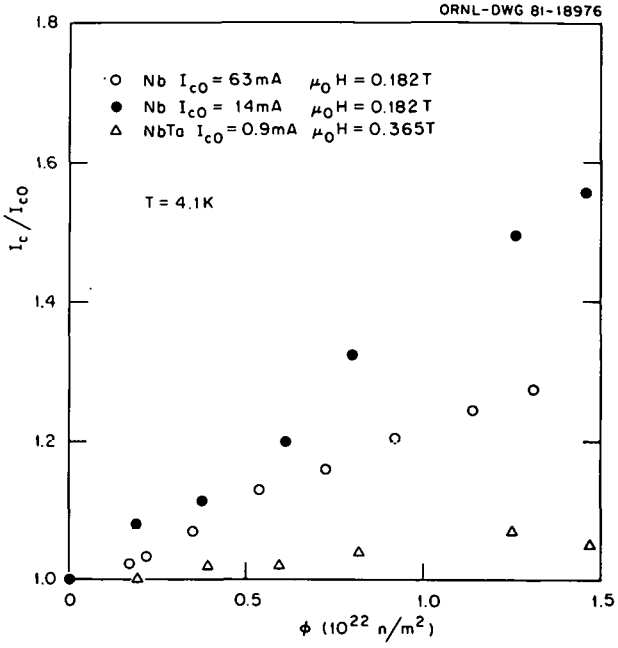

Fig. 4.17. The relative increase in I_c over the preirradiation value I_{co} with thermal-neutron irradiation at 4.1 K. Data for two samples of Nb and one sample of Nb–20 at. % Ta are shown.

the two Nb samples shows that the radiation-induced defects contribute more to I_c when more dislocations are present.

Figure 4.18 shows the increase in I_c in the low-I_c Nb sample and the NbTa sample with fast-neutron fluence. The NbTa sample shows two different types of behavior at different fields. The 365-mT data are representative of most of the data, while at 400 mT there is a narrow peak in I_c. This peak appears only after irradiation and rises rapidly out of the background with increasing damage. In Nb and at the peak in NbTa, I_c rises nonlinearly with fluence, approximately confirming the n^2 theoretical dependence. At other fields in NbTa, I_c rises linearly with fluence.

Although the data have not yet been analyzed in detail, one conclusion may be drawn immediately. The increase in the critical current with irradiation is not simply proportional to the number of radiation-induced defects in the sample. For the fast-neutron damage in Nb and NbTa at 400 mT, where the pinning interactions are strongest, I_c is approximately proportional to n^2. The data suggest that when the pinning interactions are weak, they contribute to I_c through some interaction with

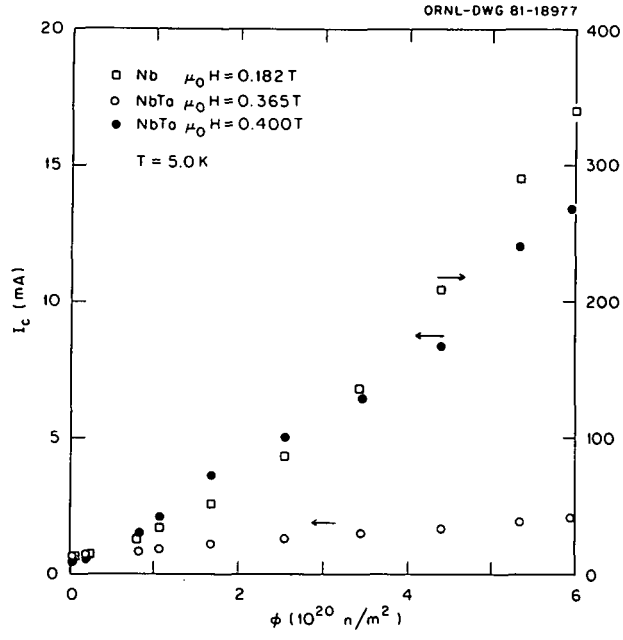

Fig. 4.18. I_c vs fast-neutron fluence ($E > 1$ MeV) for a Nb sample and a Nb–20 at. % Ta sample.

defects (dislocations and grain boundaries) already present in the samples before the irradiation. A careful analysis of the data and detailed comparison with previous work and with theories of the critical state are now under way.

1. H. R. Kerchner, "Theory of the Statistical Summation of Flux-Line-Pinning Forces in Type II Superconductors—Beyond the Dilute Limit," this report.
2. H. Ullmaier et al., *Phys. Status Solidi* **41,** 671 (1970).
3. H. Berndt, N. Kartascheff, and H. Wenzl, *Z. Angew. Phys.* **24,** 305 (1968).
4. B. S. Brown, p. 200 in *Proceedings of the International Discussion Meeting on Flux Pinning in Superconductors,* ed. by P. Haasen and H. C. Freyhardt, Akademie der Wissenschaften, Gottingen, 1975.
5. H. R. Kerchner et al., *J. Nucl. Mater.* **72,** 233 (1978).

ION-IMPLANTATION–LASER-ANNEALING STUDIES

J. R. Thompson[1] J. M. Williams
S. T. Sekula C. W. White

Superconductivity in Ion-Implanted NbGe and MoGe

An effort to produce the stoichiometric A15 form of NbGe, using ion-implantation and/or laser-annealing techniques, was continued. Polycrystalline, but single-phase, (A15) slabs of $Nb_{1-x}Ge_x$, $x = 0.18$, were implanted with 200-keV Ge ions at nominally room temperature. Implanted fluences corresponded to $\bar{x} = 0.22$, 0.25, and 0.28 in a thin layer below the surface. These samples were then installed in an apparatus for low-temperature laser annealing and T_c measurements. Ruby laser pulses ($\lambda = 694$ nm, $\tau \sim 15$ ns) were applied in fluences of 0.2–1.7 $\times$ 10^4 Jm^{-2}. Annealing of the implanted layers took place on "substrates" of A15-phase NbGe maintained at low temperatures, a circumstance which might promote a more orderly regrowth of the crystal and a corresponding high superconducting T_c in the implanted layer. However, no increase in T_c above 6.5 K, that of the underlying material, was observed. Four contact ac measurements of the sample resistance were used.

One possible cause of this negative result is the formation of equilibrium mixed-phase Nb_5Ge_3 with the stable A15 material, rather than the metastable, stoichiometric A15 Nb_3Ge. An alternate mechanism is the retention of excessive disorder in the implanted and annealed layer.

In a preliminary experiment, a foil of Mo was implanted with Ge ions under the conditions described above, producing a layer with $x \sim 12$ at. % Ge. No superconductive transition above 2.1 K was observed for this material. The $Mo_{1-x}Ge_x$ system is reported, however, to have metastable crystalline and amorphous phases for larger Ge concentrations with $T_c \lesssim 9$ K. Further investigations of this and similar systems using ion-implantation methods are appropriate.

Low-Temperature Laser Irradiation of Nb Films

A study to correlate superconductive transition temperatures T_c and electrical resistivity in Nb thin films has been undertaken. Films, previously evaporated to 100-nm thickness on sapphire substrates, were mounted in a cryostat for low-temperature laser irradiation and in situ electrical measurements. Two sets of films were investigated, "as-prepared" and "outgassed" by heating to 1800°C in a vacuum of 10^{-6}–10^{-5} Pa. In both sets $T_c = 7.2 \pm 0.1$ K before laser irradiation.

Light pulses from a ruby laser ($\lambda = 694$ nm, $\tau = 15$ ns) were applied at fluences to 1×10^4 Jm^{-2}. This led to a depression of T_c and to increases in the normal-state film resistance R_n. For the as-prepared film, the effects were quite large: after 1×10^{-4} Jm^{-2}, T_c was reduced to ~2 K and was accompanied by a fourfold increase in R_n. For the outgassed film, the T_c depression was much smaller, with $T_c = 6.75$ K after 10 pulses of 0.75×10^4 Jm^{-2}. The electrical resistivity of the film, after irradiation, followed Matthiessen's rule within experimental uncertainty $\rho = \rho_0 + \rho_{Nb}(T)$.

The differences in behavior of the two sets of films suggest that volatile impurities strongly affect the damage produced. Also, the original depression of T_c from the value 9.2 K for bulk Nb to 7.2 K in the unirradiated films is indicative of other impurities or defects in the virgin films and shows that films of higher purity are required.

1. Adjunct research and development participant from The University of Tennessee, Knoxville, Tenn.

APPARATUS FOR MAGNETIZATION STUDIES UP TO 10 TESLA

S. T. Sekula J. R. Thompson[1]

A vibrating sample magnetometer (VSM) has been constructed for magnetization studies in applied fields up to 10 T. The apparatus has been utilized over the temperature range 4.5–280 K and employs a hybrid superconducting magnet (NbTi and Nb_3Sn). Low remanent fields, necessary for many investigations, result from the use of multifilamentary wire in the magnet; for example, a residual field of ~3 mT was observed at the magnet center after cycling to fields of 3 to 7 T. Thermometry (in zero field) is accomplished with a very small Si diode sensor in close thermal contact with the material under investigation, while temperature regulation is achieved using a more distant field-insensitive carbon-glass sensor. Magnetization samples are mounted in a capsule on the lower end of the drive rod, which is mechanically vibrated by a transducer at the head of the cryostat. The amplitude of vibration is electronically regulated.

The usable sensitivity to a magnetic moment m in applied field B_0 is $m/B_0 \simeq 5 \times 10^{-6}$ J/T^2. It is limited by background signals and noise arising primarily from interactions between the magnetic field and the metal He dewar and also from construction materials in the drive rod, etc. Nonetheless, the sensitivity is more than adequate for many types of investigations. For example, the apparatus has been used for characterization of samples of $NbSe_2$ and the A15 compounds V_3Si and V_3Ge. Also, in collaboration with the neutron scattering group, the magnetic susceptibility of single crystals of Nd and SmS is being investigated. Finally, this apparatus was employed in a study of MgO:Ni materials.[2]

1. Adjunct research and development participant from The University of Tennessee, Knoxville, Tenn.

2. J. R. Thompson, S. T. Sekula, and Y. Chen, "Magnetic Properties of Ni in MgO," this report.

MAGNETIC PROPERTIES OF Ni IN MgO

J. R. Thompson[1] S. T. Sekula
Y. Chen

Magnetic properties of two forms of Ni in single-crystal MgO have been studied.[2] When in solution at densities of 10^{25}–10^{26} m^{-3}, the Ni ions exhibited classical paramagnetic behavior. Taking the spin $S = 1$ as appropriate for Ni^{2+}, a "g" factor of 2.28 was obtained from the saturation magnetization, a value slightly larger (3%) than that observed elsewhere in ESR studies on more dilute materials ($g = 2.215$). No evidence of ferromagnetic inclusions was observed, indicating a thorough dispersal of Ni in the MgO matrix.

The "as-prepared" materials were subsequently processed for an extended time (~24 h) at 1800°C in a reducing atmosphere of Mg vapor and then were quenched. This heat treatment produced small Ni-containing precipitates. These precipitates were ferromagnetic in character, displaying a remanent moment and magnetic hysteresis. The (extrapolated) zero-temperature, saturated mag-

netic moment per Ni atom ranged from 0.25 to 0.48 μ_B in various samples. The moments were roughly proportional to the observed magnetic T_c. The T_c values, defined as the temperature at which the magnetization in a small field vanished, ranged from 275 to 595 K. Thus, both the moment/atom and T_c were below those observed in bulk fcc Ni, 0.616 μ_B and 627 K, respectively. A lesser reduction in moment/atom was also observed in the precipitated materials by polarized neutron scattering.[3] These properties indicate a reduced magnetic exchange in the Ni-containing precipitates, perhaps due to incorporation of impurities, although one cannot rule out the possibility of surface effects in the small precipitates. Further investigation would be required to characterize more fully the materials.

The low-temperature experiments (4.5–280 K) were carried out in a vibrating sample magnetometer[4] with a superconducting solenoid providing magnetic fields to 10 T. The determinations of T_c were made in a low-field, high-temperature vibrating sample magnetometer.

1. Adjunct research and development participant from The University of Tennessee, Knoxville, Tenn.
2. J. R. Thompson, S. T. Sekula, and Y. Chen, *Physica B&C* **107**, 87 (1981).
3. R. M. Moon, private communication.
4. S. T. Sekula and J. R. Thompson, "Apparatus for Magnetization Studies up to 10 Tesla," this report.

SUPERCONDUCTING TRANSITION TEMPERATURES OF $(V_{1-x}Ti_x)_3Ge$

Y. K. Chang H. R. Kerchner
H. E. Harmon

Materials with high superconducting transition temperatures T_c continue to be of interest due to their potential for application in energy-related systems. In particular, the A15 compounds A_3B have attracted a great deal of attention as a result of the discovery of the highest known T_c in this family of materials. It is well known that T_c is closely related to the electron density of states and the phonon distribution. The high density of states at the Fermi surface, arising from the A-atom chains, is believed to be responsible for the high values of T_c that are frequently found for the A15 compounds. Recently,[1] a band structure calculation for binary compounds which was extended by the rigid-band method to pseudobinary compounds has predicted a peak value of T_c for the A15 phase $(V_{1-x}Ti_x)_3Ge$ with $x = 0.13$. Such a compound was prepared by casting an appropriate mixture in an arc melter and then remelting the material several times in an induction-heated silver boat. Specimens with a 1-mm^2 cross section and 7 mm in length were cut with a wire saw and then chemically etched to minimize the cutting-induced damage. The value of T_c was determined using a four-probe method in a low-temperature cryostat with controlled, continuous helium flow. A T_c of about 6.1 K was obtained. This value is slightly lower than that of V_3Ge and is much lower than the predicted value of 15 K. Specimens with x values deviating from the predicted value of $x = 0.13$ will be prepared for use in future determinations of T_c.

1. B. M. Klein, D. A. Papaconstantopolous, and L. L. Boyer, p. 455 in *Superconductivity in d- and f-Band Metals*, ed. by H. Suhl and M. B. Maple, Academic Press, New York, 1980.

EXPERIMENTAL SEARCH FOR VERY LOW TEMPERATURE SUPERCONDUCTIVITY IN SEMICONDUCTING $KTaO_3$ [1]

J. R. Thompson[2] L. A. Boatner
J. O. Thomson[3]

A series of experiments has been conducted in an effort to detect the presence of superconductivity in semiconducting $KTaO_3$ single crystals. Semiconducting $KTaO_3$ has a number of properties in common with semiconducting $SrTiO_3$, which is a widely studied material that has been found to be superconducting below ~0.3 K. For $SrTiO_3$, the T_c first increases and then decreases rapidly as a function of carrier concentration. Both $KTaO_3$ and $SrTiO_3$ are perovskite structure oxides, and both have high dielectric constants at low temperatures ("incipient ferroelectrics"). The similar properties of these materials suggest that semiconducting potassium tantalate might also exhibit superconductivity. Superconductivity was not observed for $KTaO_3$, however, down to 0.01 K.

Single-crystal samples of $KTaO_3$ were rendered semiconducting by a substitution of Ca^{2+} for K^+ ions during the crystal growth process. The (measured) carrier concentrations lay in the range 0.4–7.0 $\times$ 10^{25} m^{-3}. The search for a superconducting transition extended over the temperature range 0.01–4.2 K, and the applied magnetic fields

ere on the order of 10^{-4}–10^{-5} T. For $T < 1.5$ K, ıe search was carried out in a ^{3}He-^{4}He dilution refrigerator equipped for measurements of dc magnetization with a SQUID-based system and for ac susceptibility studies. The system sensitivity was verified by observation of the paramagnetic signal from Dy_2O_3-doped $KTaO_3$ and was adequate to detect the diamagnetism due to flux exclusion from <1% of the volume of the sample.

The failure to observe superconductivity in $KTaO_3$, as opposed to the case of $SrTiO_3$, may ultimately aid in understanding the mechanism of superconductivity in the latter material. One difference between $KTaO_3$ and $SrTiO_3$ is that the effective electronic mass is larger for $SrTiO_3$. This leads to a higher density of states and higher transition temperatures. A second difference is that $SrTiO_3$ undergoes a transition to a tetragonal symmetry phase at 105 K, while $KTaO_3$ remains cubic to the lowest temperatures. This suggests that possibly there is a substantial difference in the strength of the electron-electron interaction in the two materials. The absence of superconductivity in $KTaO_3$ for $T > 0.01$ K may also help to differentiate between the many mechanisms assumed in various calculations of transition temperatures in degenerate semiconductors.

1. Summary of paper to be published.
2. Adjunct research and development participant from The University of Tennessee, Knoxville, Tenn.
3. The University of Tennessee, Knoxville, Tenn.

PHYSICAL PROPERTIES OF INSULATING MATERIALS

THERMOELECTRIC BREAKDOWN OF MgO CRYSTALS AT HIGH TEMPERATURES

K. L. Tsang[1] Y. Chen

All materials conduct electricity to a greater or lesser extent, and all suffer some form of breakdown in a sufficiently strong electric field. In the case of insulators, it is commonly referred to as dielectric (or perhaps more aptly, thermoelectric) breakdown. Although it has been a subject of experimental and theoretical investigations for many years, there does not exist an unambiguous model of breakdown,[2] even though models for ecific materials occasionally arise.[3]

There has been a dearth of research on electrical breakdown in refractory materials, and most of the previous work has been confined to near room temperature. In this study, MgO crystals were chosen as a prototype refractory material for an investigation of breakdown, because of the simple crystal structure and the availability of high-quality crystals. Previous studies have indicated that breakdown in MgO is impurity related and that it occurs in tens to hundreds of hours at ~1500 K with moderate fields.[4,5] To understand the role that impurities play in thermoelectric breakdown, efforts were concentrated on Ni-doped MgO. The goal is to obtain a reasonable model for the phenomenon at high temperatures.

Field Reversal

A constant electric field of 1500 V cm^{-1} was applied across Ni-doped MgO samples at 1473 K, and the current was measured as a function of time (Fig. 4.19). Initially, the current decreased from 0.20–0.12 mA in 40 min (top inset) and then increased approximately at an exponential rate until an arbitrarily chosen value of 18 mA was reached after 18 h. Upon field reversal, the current in the opposite direction instantaneously (<1 s) reached a maximum, which was also ~18 mA. It then decreased to a minimum value of 0.7 mA in 25 min, followed by an exponential increase which was faster than in the first cycle. Only 9 h were required to reach 18 mA in the second cycle. Several more field reversals were performed subsequently. The current behavior was similar to that

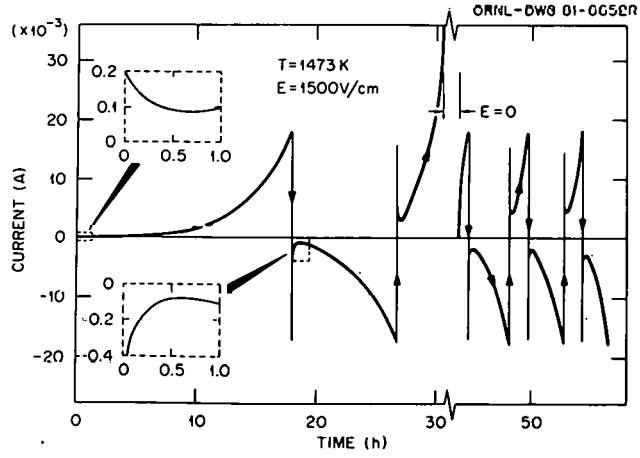

Fig. 4.19. Current vs time at 1473 K with E = 1500 V cm^{-1} for several polarity reversals.

of the first reversal, but the times to reach 18 mA diminished with each reversal. Ultimately, only 2 h were required for each cycle, and no further decrease in time dependence was observed. Figure 4.20 shows a plot of the time required to reach 18 mA as a function of the sequential field reversals. The trend of the diminishing times required is evident. The time-dependent current after a reversal can be described as the sum of two exponential terms $I(t) = I_{01}e^{-c_1 t} = I_{02}e^{c_2 t}$ for $t > 0$, where I_{01}, I_{02}, c_1, and c_2 are positive constants, and c_2 is of the form $\exp(Q/kT + \beta E)$.

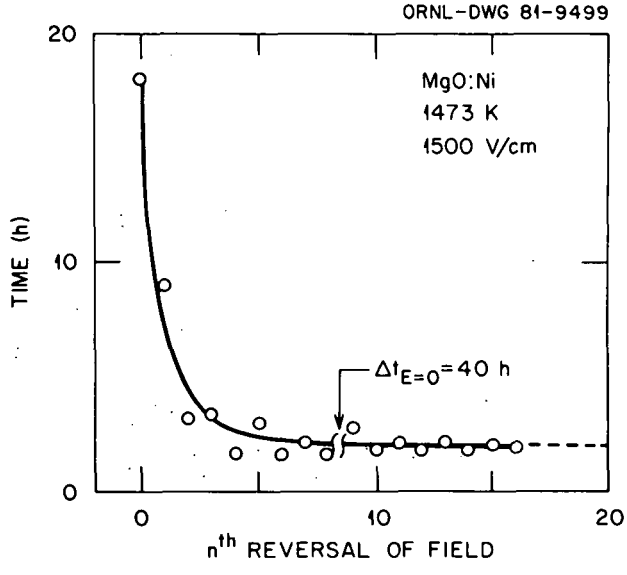

Fig. 4.20. Time necessary for the current to reach 18 mA vs the *n*th field reversal.

Instantaneous Current After Time Interval with $E = 0$

An instantaneous current (<1 s), similar to that shown in Fig. 4.19, can be obtained in either direction upon restoration of the field following a time interval without field, denoted as $\Delta t(E = 0)$. An illustration is shown in Fig. 4.21. An electric field was applied initially at $t = 0$ and removed at $t = 10$ (in arbitrary units) when the current reached I_{i0}. When the same field was reapplied at $t = 11$, an instantaneous current I_i was obtained. The subsequent current increase was slowed before increasing exponentially. If the field was removed at $t = 12$ and a field reversal was applied at $t = 13$, an

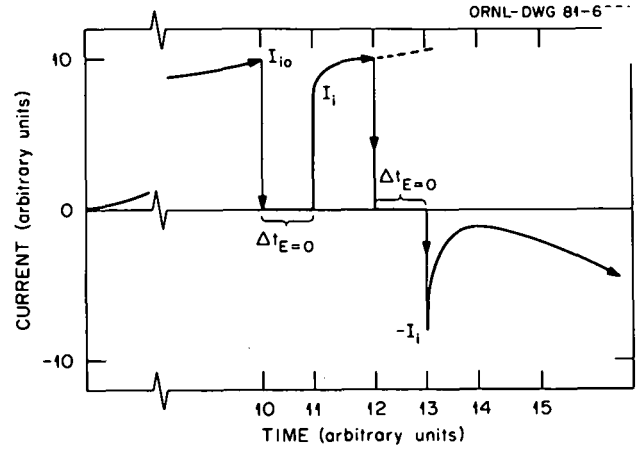

Fig. 4.21. Current behavior after a time increment without electric field ($\Delta t_{E=0}$).

instantaneous current in the opposite direction $-I_i$ was obtained, followed by a current behavior similar to that shown in Fig. 4.19.

The magnitude of I_i in either direction is a function of the time interval with the field removed, as shown in the top portion of Fig. 4.22. The current decreases rapidly in the first minute, but it eventually reaches a value which is nearly constant.

Short-Circuit Current

A method which provides information on the distribution of electric charges inside the sample and, therefore, on the mechanism of thermoelectric breakdown is to measure the short-circuit current I_{sc}, which is the current that flows from one sample surface to the other via an external conductor when the electric field is removed. The I_{sc} was measured as a function of time after the field was removed at $t = 0$, chosen to be when $I_i = +18$ mA. The result is shown in the bottom of Fig. 4.22. The I_{sc} was found to flow in the *opposite* direction. It decreased rapidly in the first minute and then became nearly constant. While the shape of the I_{sc} curve is similar and symmetric to the I_i curve, the former was about three orders of magnitude smaller.

The direction of the I_{sc} suggests that electrons flow from the cathode end of the sample to the other sample surface via the external conductor. The relatively small I_{sc} and the time-dependent shape of the I_{sc} and I_i curves indicate that annihilation of charges occurs mostly within the crystal.

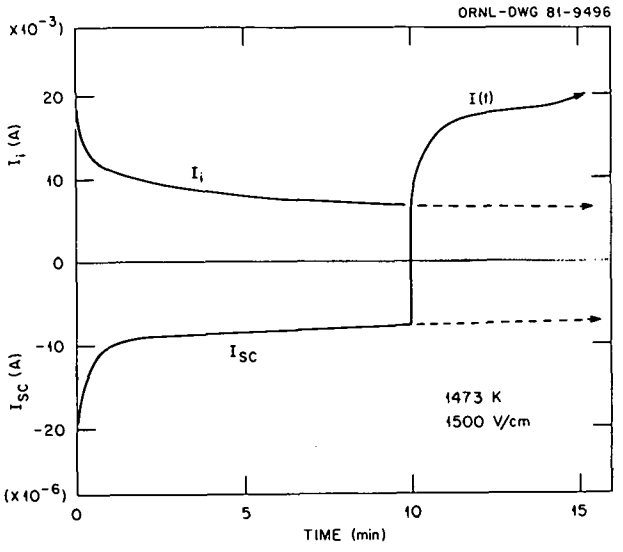

Fig. 4.22. Top curve: I_i vs time increment without electric field. Bottom curve: I_{sc} as a function of time.

The initial surge of I_i shown in Figs. 4.19 and 4.21 implies that most of the stored charges are localized in the sample surface regions at the electrodes. We tentatively conclude that the thermoelectric breakdown at high temperatures is due to a space charge incurred by injection of electrons and holes into the crystal.

1. Graduate laboratory participant from the University of Alabama, Birmingham, Ala.

2. J. J. O'Dwyer, *The Theory of Electrical Conduction and Breakdown in Solid Dielectrics*, Oxford University Press, England, 1973.

3. A. E. Hughes and S. C. Jain, *Adv. Phys.* **28,** 717 (1979).

4. R. A. Weeks, E. Sonder, and J. Narayan, to be published.

5. F. A. Modine et al., *Bull. Am. Phys. Soc.* **24,** 413 (1979).

ELECTRICAL CONDUCTIVITY OF POLYCRYSTALLINE MgO

E. Sonder R. A. Weeks

Extensive studies of the electrical properties of many MgO single crystals[1] have revealed variations of conductivity that could not be attributed to observable aliovalent impurities, and it was proposed that dislocations and small-angle boundaries may influence the conductivity. Moreover, it has been shown that the destructive changes brought about by moderate electric fields during long anneals are related to the dislocation and grain boundary structure.[2] Thus, it appeared useful to compare the electrical conductivity of polycrystalline MgO with that of single crystals over a wide range of temperatures. Polycrystalline material was obtained from Eastman Kodak. The material was commercially manufactured under the name "IRTRAN 5" for infrared windows. Analysis of the impurity content by atomic absorption and spark-source mass spectroscopy revealed that the samples contained large amounts of Li(400μg/g) and moderate amounts of Al(35μg/g), B(15μg/g), Cu(15μg/g), Fe(45μg/g), Ni(35μg/g), Si(70μg/g), and W(35μg/g).

When dc conductivity measurements were attempted with a battery supply and electrometer, as employed for studies of single crystals,[1] polarization currents were observed that were orders of magnitude greater than those found in single crystals. These currents were so large, in fact, that dc measurements of conductivity were impractical. Consequently, a ratio arm bridge (GenRad Model 1620A) was employed to make ac conductivity and capacitance measurements as a function of frequency over the range 20 Hz–100 kHz. A guarded sample configuration was used to prevent errors due to surface and gas-phase conduction. The capacitance of the electrode-sample configuration was relatively temperature independent and changed only a small amount with frequency. The values measured, approximately 2 *pF,* can be accounted for by simply considering the sample to be in parallel with a small capacitor.

The resistance of the polycrystalline MgO sample was strongly dependent on sample treatment and temperature. Measurements made in the first temperature cycle, as the temperature was progressively increased from 500 to 1200°C, yielded conductivities almost two orders of magnitude greater than that of single crystals of MgO. However, after the sample had been heated to 1200°C, the conductivity decreased, but after a long period at this temperature, it stabilized at values that were comparable to the conductivities of MgO single crystals.

Figure 4.23 illustrates the frequency dependence of the conductance for a number of selected measurements. The log of the measurement frequency is plotted vertically, and the log of the conductance

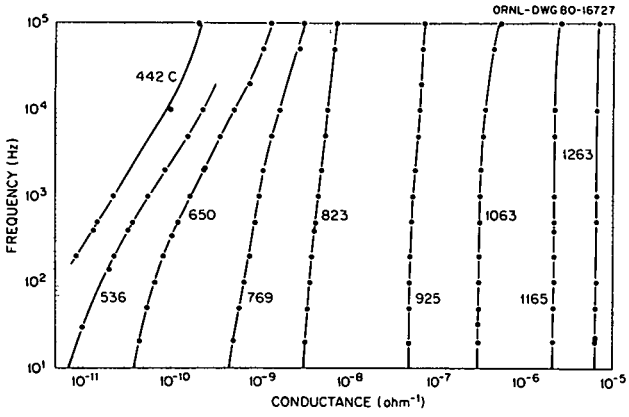

Fig. 4.23. Conductance of a polycrystalline MgO sample as a function of frequency and temperature. The curve labels give the temperature in degrees Celsius.

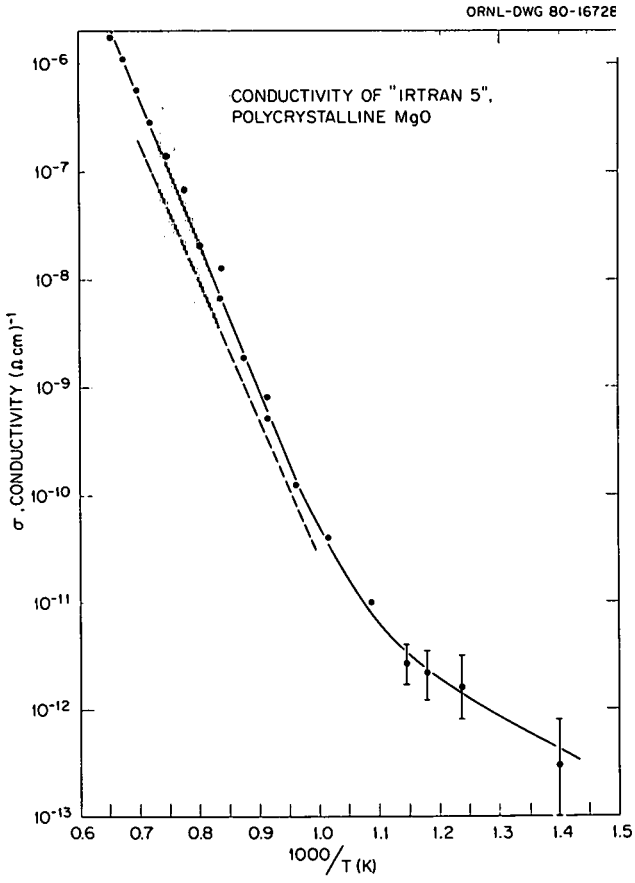

Fig. 4.24. Temperature dependence of the conductivity of polycrystalline MgO. The dashed line reflects data obtained for a nominally pure, single crystal; the crosshatching indicates the variations observed by different people for single-crystal conductivity.

is the abscissa. The high conductance values which were obtained at the higher temperatures exhibit a very small variation with frequency, particularly for frequencies below 10 kHz. However, for data obtained below approximately 1000°C, frequency-dependent conductance becomes more prevalent as the measuring temperature decreases.

Since the capacitance for this sample was independent of frequency and temperature, the ordinate scale of Fig. 4.23 is proportional to the imaginary component of the admittance $2\pi fC$, where f is the frequency and C is the capacitance. Thus, Fig. 4.23 can be considered an admittance plot according to the formalism that has been developed by a number of investigators[3] for fitting complex impedance data to equivalent circuits. Within such a formalism a simple parallel circuit consisting of capacitance and resistance would produce vertical straight lines such as those observed at high temperatures. If an additional capacitance was present in series with the resistor, a linear plot of the data of Fig. 4.23 would exhibit a half circle at low conductance values, ending in a vertical line at some higher limiting value of conductance. Clearly, such a slope is not observed for IRTRAN 5 polycrystalline MgO; and the frequency dependence at the lower temperatures cannot be attributed to capacitive surface contacts or to a single series capacitance that might be due to the grain boundaries present.

Figure 4.24 is a plot of the conductivity of IRTRAN 5 polycrystalline MgO vs reciprocal temperature. The data points were obtained from extrapolating to 10 Hz the curves of Fig. 4.23. The error bars shown with the lower temperature data points indicate measurement uncertainties, which were due to difficulty in balancing the bridge when the resistances exceeded 10^{11} ohms. The dashed line represents conductivity values for a single-crystal sample of Norton MgO (nominally pure), and the crosshatching indicates the range of values that have been observed for a variety of single-crystal samples.[1] It is clear that above 700°C the conductivity of the IRTRAN 5 material is only slightly greater than that of single-crystal MgO. However, at lower temperatures the conductivity rises significantly above the extrapolation of the high-temperature single-crystal data, indicating that another mechanism of conduction is becoming active. It is probable that this mechanism involves

the grain boundaries. However, it should be borne in mind, particularly in view of the large concentrations of impurities in the polycrystalline samples, that the effects observed here, which do not occur in single crystals (i.e., the enormous polarizations, the large changes that take place after initially heating the sample, and the low-temperature conductivity), may be due in part to impurities. Increases in conductivity and slow changes due to heat treatment have been observed in MgO single crystals doped with Li_2O.[4] Also, large changes in the conductivity of single crystals of undoped MgO upon initial heat treatments have recently been attributed to diffusion and removal of carbon from near-surface regions of the crystals during heating.[5] It is possible that similar effects occur in the polycrystalline samples.

1. E. Sonder et al., *J. Appl. Phys.* **49,** 5971 (1978).
2. J. Narayan, R. A. Weeks, and E. Sonder, *J. Appl. Phys.* **49,** 5977 (1978).
3. See, for example, J. E. Bauerle, *J. Phys. Chem. Solids* **30,** 2657 (1969).
4. N. J. Dudney, E. Sonder, and R. A. Weeks, *Solid State Div. Prog. Rep., Feb. 29, 1980,* ORNL-5640, p. 149.
5. H. Kathrein, U. Knipping, and F. Freund, *Mater. Res. Bull.* **15,** 1393 (1980).

IDENTITY OF CURRENT CARRIERS IN SPINEL

E. Sonder

Oxides of the light elements Mg, Al, and Si are the predominant constituents of high-temperature, electrically insulating ceramics. Thus it is surprising that little data exist in the literature on electrical behavior of one of the simpler compounds of two of these oxides, $MgAl_2O_4$. We have reported[1] the temperature dependence of the conductivity of $MgAl_2O_4$ spinel and have proposed that the results are consistent with purely ionic conduction. The present measurements of the transference number were designed to test this hypothesis.

If an oxygen concentration cell is set up in which a spinel sample acts as an electrolyte between gases of differing oxygen partial pressures, a potential is created across the sample due to different equilibrium levels of O^{2-} at the respective surfaces in equilibrium with the two gases. The voltage developed across such a cell, in the absence of any electronic conductivity, is

$$V_0 = \frac{RT}{4F} \ln(p_1/p_2) \quad ,$$

where R is the gas constant, T is the absolute temperature, F is the Faraday constant, and p_1 and p_2 are the respective oxygen pressures. However, if electronic conduction is present, the cell will act as a partial short circuit so that the measured voltage V is less than V_0. The ionic transference number, $t_i = V/V_0$, is a measure of the ratio of ionic to total conductivity.

Using mixtures of O_2 with Ar or CO with CO_2, we have measured the voltage produced across pure and lightly iron-doped, single-crystal spinel samples. Transference numbers obtained from these measurements are given as a function of oxygen partial pressure in Fig. 4.25(a). Measurements of the conductance vs oxygen partial pressure are given in Fig. 4.25(b).

The data of Fig. 4.25(a) indicate that for two different temperatures and for both nominally pure and iron-doped spinel (1000 ppm Fe), the transference number is 1.0, within experimental error, for oxygen partial pressures between $1–10^{-12}$ atm. Therefore, we conclude that conduction in both undoped and lightly iron-doped spinel is wholly ionic.

The conductance measurements shown in Fig. 4.25(b) indicate that the number of current carriers is independent of the oxygen partial pressure. If, for example, electronic holes h were produced by a reaction such as

$$2Fe^{2+} + \frac{1}{2} O_2(gas) \rightarrow 2Fe^{3+} + O^{2-} + V \quad ,$$

followed by

$$Fe^{3+} \rightarrow Fe^{2+} + h^+ \quad ,$$

then the concentration h^+ would be a function of the oxygen partial pressure. In a similar fashion, if the cation vacancies V compensating for the inclusion of excess O^{2-} in the lattice were the current carriers, their concentration would be sensitive to oxygen pressure. Thus, observed lack of sensitivity of the conductivity to oxygen pressure rules out reactions such as those indicated above as the

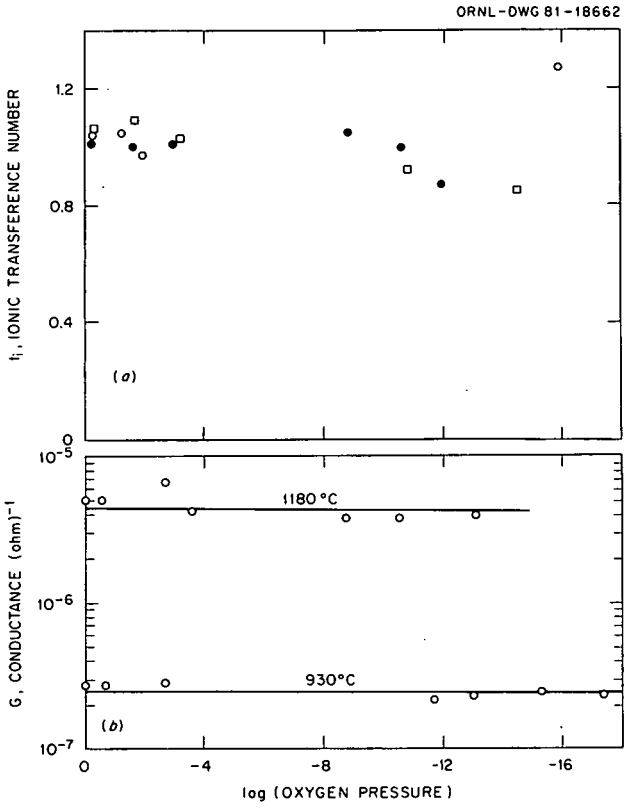

Fig 4.25. Transference number and conductance of $MgAl_2O_4$ spinel as a function of oxygen partial pressure. (a) Transference numbers are given for two samples and two temperatures: o nominally pure spinel, 800°C; • nominally pure spinel, 1180°C; and □ Fe-doped spinel (1000 ppm), 1050°C. (b) Conductance is given for nominally pure spinel at the two temperatures indicated.

source of the predominant current carriers. It is well known that spinel can be prepared with an excess of Al^{3+} but that excess Mg^{2+} produces a two-phase system. Thus, it is probable that in "stoichiometric" spinel, such as that used in the present experiments, there exists a small excess of Al_2O_3, accompanied by cation vacancies. The latter act as current carriers; their concentration would not depend on ambient oxygen pressure, in agreement with the observation depicted in Fig. 4.25(b).

1. R. A. Weeks and E. Sonder, *J. Am. Ceram. Soc.* **63**, 93 (1980).

OPTICAL ELLIPSOMETRY STUDIES OF TRANSITION METAL CARBIDES

F. A. Modine G. R. Gruzalski

A systematic investigation of the optical properties of the transition metal carbides has been undertaken. The investigation is based upon ellipsometry measurements, which are supplemented by optical reflectance studies. The optical properties of only a few of the transition metal carbides have been studied previously, principally in connection with electronic-band-structure calculations, and only the optical properties of TiC have been investigated in detail by more than one research group.[1-3] Moreover, the various results for TiC are in poor agreement. Because ellipsometry is inherently superior to the reflectance techniques used exclusively by the previous investigators of carbides, more dependable results can be expected from the current investigation. The studies emphasize the relatively low-energy region of the optical spectrum (i.e., the near-infrared to near-ultraviolet), which is most readily accessible to ellipsometry and least accessible to complementary techniques utilizing synchrotron radiation. In this spectral region, optical properties supply information on both chemical bonding and electron transport. Furthermore, because the density of states of these materials is low near the Fermi energy, optical properties are quite sensitive to the observed wide variations in stoichiometry.

An automated scanning ellipsometer of the polarization modulation type has been constructed to perform these studies. Typically, the ellipsometer permits a 500-nm spectral scan to be made in as little as 100 s, while random noise is maintained at an insignificant level. The apparatus has a low-temperature (10–300 K) measurement capability. Computer codes have been developed to reduce the ellipsometry data to optical constants (e.g., dielectric functions, refractive index, absorption coefficient, optical conductivity, and reflectance). Moreover, techniques for accurate calibration and for reduction of small systematic errors have been established, and the apparatus has been tested on materials having known optical properties.

Initial efforts have focused primarily on TiC and VC because these crystals are most readily avail-

able, though still difficult to obtain. Studies of TiC have given results similar to, but nevertheless significantly different from, those of other investigators. The previous optical properties data for TiC stem solely from reflectance measurements, and Fig. 4.26, which shows various reflectance spectra, reveals the differences. The reflectance spectra differ more than can be attributed to stoichiometry; in fact, the differences are greater than those found by a single investigator measuring crystals of different stoichiometry. How much these reflectance variations can be attributed to measurement technique and surface preparation is yet to be established. Optical constants computed from such different reflectance spectra are necessarily different, but they can also differ because the reflectance must be extrapolated to both zero and infinite energy to obtain phase information from a Kramers-Kronig analysis. Such extrapolations are unnecessary in ellipsometry analysis because phase information is obtained directly. Reflectance data are very useful as a verification of ellipsometry results, and the reflectance computed from ellipsometry measurements on TiC and other carbides has been found to be in excellent agreement with our directly measured spectra.

Figure 4.27 shows representative ellipsometry results for a single crystal of $VC_{0.88}$, which is the ordered structure of V_8C_7. The crystal had been

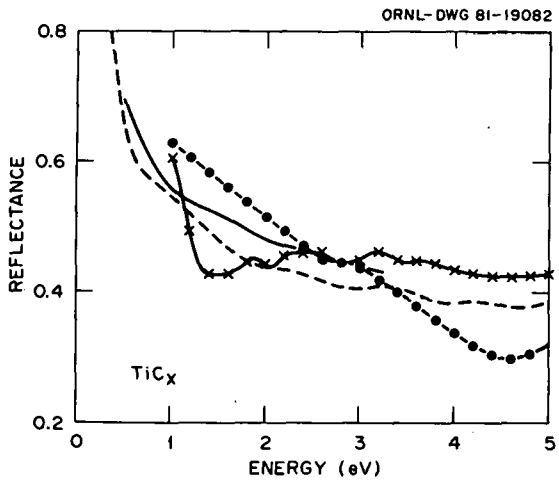

Fig. 4.26. The optical reflectance of TiC_x as measured by various investigators. The solid curve is from the present work (X = 0.92). The dashed curve is from ref. 1 (X = 0.90, measured at 4.2 K). The curve labeled by crosses is from ref. 2 (X = 0.999, a hot-pressed sample). The curve labeled by circles is from ref. 3 (X = 0.794).

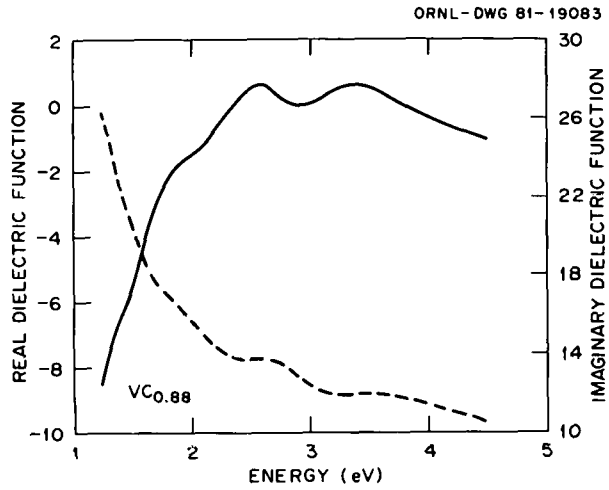

Fig. 4.27. The optical dielectric function of a single crystal of VC. The dashed curve is the imaginary part.

mechanically and electrolytically polished.[4] Rutherford backscattering disclosed very little surface damage and revealed that any surface oxide could amount to no more than a monolayer. The divergence of the dielectric functions at low energy is typical of metallic materials and is due to interband transitions. The electrical conductivity of VC is much higher than that of group IV carbides, such as TiC, and the more metallic character of VC is apparent in the optical spectra. For example, the real dielectric function is positive throughout the visible spectrum for TiC, whereas it is negative, or depending upon stoichiometry, nearly so for VC; the sensitivity of the optical functions to Fermi-level changes induced by deviations in stoichiometry was readily observed.

The structure at higher energy in the VC spectra is due to interband transitions between the hybridized vanadium d and carbon p bands that span the Fermi surface in the cubic transition metal carbides. The portions of Brillouin zone contributing to the structure have not been established. The $VC_{0.88}$ exhibits more pronounced structure than does $VC_{0.84}$, probably because the vacancies on the carbon lattice are highly ordered, rather than because of the higher stoichiometry. Much less structure is observed for disordered TiC of higher stoichiometry. Fermi-level differences can change interband structures, but the changes are expected to be most pronounced at low energies where they are masked by intraband transitions. If the intraband contributions can be subtracted, they may be observable.

Further work on optical properties of the transition metal carbides will focus on: (1) obtaining reliable optical properties data, (2) separating intra- and interband effects, (3) interpreting Fermi-level changes due to variations in stoichiometry, (4) carbon lattice ordering, (5) parameters associated with electron transport, and (6) interpreting optical properties in terms of band structure.

1. D. W. Lynch et al., *Phys. Rev. B* **22,** 3391 (1980).
2. J. F. Alward et al., *Phys. Rev. B* **12,** 1105 (1975).
3. R. G. Lye and E. M. Logothetis, *Phys. Rev.* **147,** 622 (1966).
4. G. R. Gruzalski, "Electrolytic Polishing of Vanadium Monocarbides," this report.

OPTICAL REFLECTANCE OF TANTALUM CARBIDE

F. A. Modine R. W. Major[1]
G. R. Gruzalski

Among the cubic transition metal carbides, TaC_x displays the most apparent sensitivity of optical properties to stoichiometry. The color of the compound changes from gold to silver as carbon content is reduced, presumably as the consequence of an increasing Fermi level. In order to investigate the electrical properties and electronic structure of TaC_x and their dependence on stoichiometry, optical studies of the material have been undertaken. The optical reflectance of TaC_x has been measured, and the measurements have been extended to the infrared in an attempt to resolve interband effects.

Figure 4.28 shows the optical reflectance of TaC_x for the spectral range 0.05–5.8 eV. The inset shows the low-energy reflectance plotted so that it can be interpreted in terms of the Drude theory and the Hagen-Rubens approximation.[2] The solid line of the inset represents a fit of the Drude theory to the data shown as points. The dashed line is fit to the slope of the curve at zero energy. In the Hagen-Rubens approximation the slope is equal to the dc electrical resistivity. The result implies a resistivity equal to 70 $\mu\Omega\cdot$cm, which compares to a directly measured value of 34 $\mu\Omega\cdot$cm.[3] The difference is significant and may be attributed either to differences in surface and bulk conduction or to interband contributions to the reflectance. The latter is suggested by the fit to Drude theory which implies a plasma energy equal to about 40 eV, which is much too high.

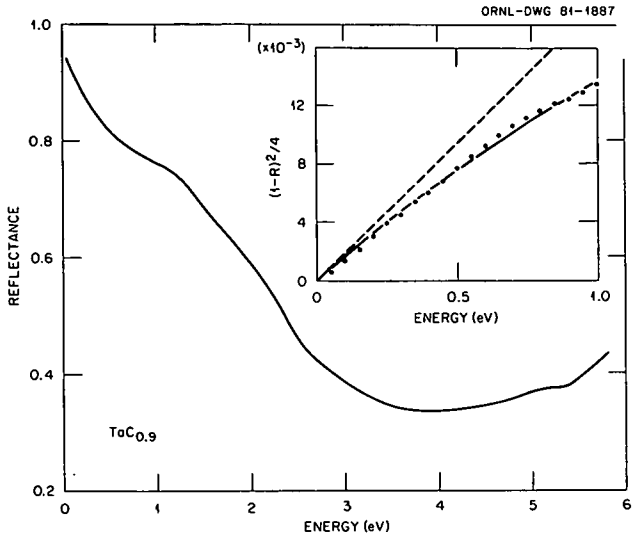

Fig. 4.28. The reflectance spectrum of TaC. The inset depicts a fit of the low-energy reflectance to Drude theory and the Hagan-Rubens approximation.

Further work is planned in which other samples will be measured, and more powerful methods for separating intra- and interband effects will be applied to calculated dielectric functions.

1. Summer faculty research participant from University of Richmond, Richmond, Va.
2. M. Born and E. Wolf, *Principals of Optics,* Macmillan, New York, 1964.
3. G. R. Gruzalski, T. M. Haywood, and F. A. Modine, "Electrical Properties of Transition Metal Carbides," this report.

5. Neutron Scattering

The objective of the Neutron Scattering Program continues to be the study of the structure and dynamics of condensed matter on a microscopic level. Much of the information obtained through neutron scattering is unique, in that it cannot be obtained through other experimental techniques, and it is important, in that it provides fundamental details of structures and of atomic interactions. Such information is essential for increasing our knowledge of the solid state and in providing insight to, and guidance for, the solution of our long-range energy-related materials problems.

There has been a growing involvement with outside users of ORNL neutron scattering facilities, a trend which will surely continue in the future. A highlight of this reporting period was the completion of the 30-m SANS instrument, funded by the NSF and DOE as part of the National Center for Small-Angle Scattering Research, which has been established at ORNL under a joint interagency agreement between these two organizations. Since its dedication in January 1981, this instrument has been in steady demand by outside users. A total of 78 proposals has been received, 44 of them in the field of polymer science. Our informal program for the use of the remainder of the neutron facilities continued in successful operation with about 36 outside participants during this period. This program will be placed on a more formal basis with increased visibility beginning in January 1982. A conceptual design for the wide-angle neutron diffractometer to be constructed as part of the United States–Japan Cooperative Program on Neutron Scattering has been completed. Our close and productive collaboration with the Ames Laboratory staff has continued.

The small-angle scattering program in this Division has been strengthened by the transfer of the small-angle x-ray laboratory from the Metals and Ceramics Division. A major new facility developed in this laboratory is a dynamic deformation device for studying transient structural effects in polymers while under deformation. The locally originated SANS program has featured a number of polymer studies and a continuation of the work on oil shale and coal solutions.

In lattice dynamics, the study of the fascinating behavior of α-U has continued with observations of the pressure and temperature dependences of two sets of charge density waves, one commensurate and one incommensurate. New information on the lattice dynamics of superconductors has been obtained through studies of the A15 compound Nb_3Sb, of the layered superconductor $PdTe_2$, and of Nb alloys. Strong coupling between valence fluctuations and phonons was observed in TmSe and in the high-pressure phase of SmS. Studies of the dynamics of water biological systems (brine shrimp) have been initiated. Phonon dispersion curves for $SbCl_5$ intercalated in graphite have been measured for two stages of intercalation.

In the area of magnetic properties a wide variety of phenomena have been investigated. Unusual phase transitions have been studied in MnP, where Lifshitz behavior was confirmed, and in Gd, where a second-order spin reorientation transition occurs. A variety of structures and phase transitions have been observed

in the system $Ho_{1-x}Er_xRh_4B_4$ and in the related material HoB_4. Spin density measurements have been performed on Ni, which have been focused on the temperature dependence of the asymmetry, and on the itinerant ferromagnet $TiBe_{1.8}Cu_{0.2}$. The distribution of atomic moments in ferromagnetic alloys has been measured in Co-V and in compositionally modulated Ni-Cu. The polarization analysis technique has been used to reveal new information on the complex magnetic behavior of the Cu-Mn spin-glass system. In a preliminary experiment, with eventual application to the study of true two-dimensional magnetic systems, diffraction patterns of very thin samples of manganese stearate have been observed and analyzed. The temperature dependence of the magnetic excitations in EuO and Gd has been studied, and in both cases, magnon-like excitations were observed above T_c.

Two major improvements to our experimental facilities are nearing completion. New computer systems for the four triple-axis instruments will result in better and more flexible control of experiments and in greatly expanded capability for data analysis. A new monochromator system for the correlation chopper should result in higher intensity and better energy resolution. This monochromator system features ultrasonically pulsed, perfect Si crystals.

SMALL-ANGLE SCATTERING

ONE YEAR'S EXPERIENCE WITH THE ORNL–NSF–DOE NATIONAL FACILITY FOR SMALL-ANGLE NEUTRON SCATTERING[1]

W. C. Koehler R. W. Hendricks[2]
H. R. Child J. S. Lin
G. D. Wignall

In SANS experiments it is the fluctuation in scattering-length density that is important. Moreover, the "contrast" can be varied by substituting isotopes, such as D for H, and this has made possible tremendous progress in understanding the properties of macromolecules in the bulk and in solution. Important investigations on polymers have been carried out over the past decade or so at C.E.N., Saclay; KFA, Jülich; and ILL, Grenoble; and experiments on suitably labeled systems are now being done on the 30-m SANS instrument at ORNL. Of the 78 proposals received for this instrument, 44 are in the area of polymer science. We give here a few selected results.

SANS experiments on amorphous polymers have confirmed the general predictions of Flory's random coil model that the overall molecular size as measured by the radius of gyration in the bulk state is the same as in an ideal solution.[3] These experiments are currently being extended to higher values of K to test how far the local configuration in the melt is described by this model. Projects are in progress on a range of polymers, including polyisobutylene (P. J. Flory, Stanford University) and polymethyl methacrylate (J. O'Reilly, Eastman Kodak Company). The first results on the latter polymer (Fig. 5.1) indicate that the scattering at intermediate K values $0.1 < K < 0.6$ Å^{-1} is markedly dependent on the chain tacticity and that

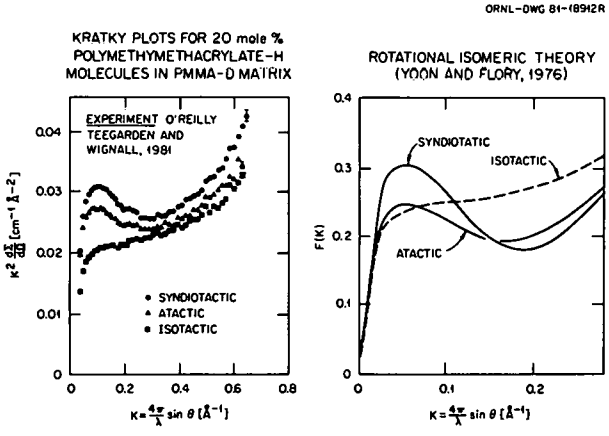

Fig. 5.1. Experimental Kratky plots for 20 mole % polymethyl methacrylate H in PMMA-D matrix compared to the qualitative predictions of the rotational isomeric theory for different polymer tacticities.

the qualitative shape of the scattering curve as a function of tacticity is consistent with the random coil model using rotational isomeric statistics. The model calculations will now be refined by Flory's

roup using the appropriate tacticity parameters or the three polymer samples measured to check the degree of quantitative agreement between theory and experiment.

Until recently, SANS experiments on polymers have been conventionally performed with small relative concentrations (<5%) of labeled polymer, but recent measurements on the 30-m SANS instrument and elsewhere have confirmed that the same information may be obtained with concentrations of labeled molecules up to 50%.[4] This development means that experiments can be performed with much greater statistical accuracy, and it has been particularly useful in the intermediate K-range measurements described above, where the scattered intensities are relatively low.

Several projects aimed at developing a fuller understanding of polymer-polymer interactions in multicomponent polymer blends (alloys) are in progress. SANS studies have shown that polystyrene-polyphenylene oxide, marketed commercially as Noryl, forms a truly compatible blend with a statistical distribution of the two components.[5] Extensive studies are in progress on both compatible and incompatible (phase-segregated) blends by Stein's group (University of Massachusetts). Experiments aimed at providing information on the domain organization, chain configuration within the domain, and nature and extent of the interface regions in phase-separated diblock copolymers (C. V. Berney and R. Cohen, MIT) are also in progress.

Several projects are in progress or are scheduled to investigate the response of individual molecules to a macroscopic deformation of a sample. The first results have been collected on extrudates of oriented polystyrene samples prepared by a new technique developed by R. S. Porter and R. S. Stein (University of Massachusetts) to produce polymers of ultrahigh orientation and chain extension. The results show that the radii of gyration transform in the same manner as the external dimensions (affine deformation). This result is in marked contrast to studies made on drawn polystyrene in which the chain deformation has been shown to be strongly nonaffine.[6] Further projects will extend these studies to semicrystalline polymers.

Proposals in the chemistry and materials area are the next most numerous, 30 of 78. Two groups are currently investigating micellar systems. These are significant in many practical areas, namely, enhanced oil recovery, detergent action, and catalysis, as well as in fundamental surface and solution chemistry. Studies are also under way on the unfolding of model protein systems.

For spherical micelles, in the range of concentration where interparticle interaction occurs, the intensity is proportional to a product of two terms $I(K) \sim P(K)S(K)$. The first term is the single particle form factor, and it is a monotonically decreasing function of K. The second term is the interparticle form factor, and in the range of K covered by the SANS experiments, it is monotonically increasing. The net effect is an "interaction" peak in the small-angle scattering spectrum. In most cases this peak is well within the Guinier region so that the particle dimensions can be extracted from the K region beyond the peak.

S. Chen and D. Bendedouch (MIT) have studied the inter- and intraparticle structure factors of protein bovine serum albumin (BSA) and micelles formed by the ionic detergents sodium dodecyl sulfate (SDS) and lithium dodecyl sulfate (LiDS) in aqueous solutions of various ionic strengths at temperatures ranging from 20–65°C. At low ionic strengths and moderate concentrations, a dominant electrostatic interaction causes a dramatic sharpening of the interparticle structure factor in such a way that a prominent interaction peak in the SANS pattern is observed. As the ionic strength is increased (by adding salt), the structure factor is gradually washed out, with the result that the pattern is reduced to a normal intraparticle form factor for spheres. This latter effect is shown in Fig. 5.2 for LiDS at 50°C, with and without additions of LiCl. The ultimate aims of this series of experiments are to extract the interparticle structure factor from the data and to study it as a function of concentration, ionic strength, and temperature. The experimental results are to be compared with the recent theoretical results of liquid structure factors for charged hard spheres in the presence of neutralizing counter ions.

C. K. Johnson, R. Triolo, L. J. Magid, and P. C. Ho (ORNL) have investigated aqueous solutions of the surfactants sodium p (1-pentylheptyl) benzene sulfonate ($6\phi C_{12}SNa$) and sodium p (1-heptylnonyl) benzene sulfonate ($8\phi C_{16}SNa$). A prominent feature in the scattering curves is the existence of an interaction peak at the higher surfactant concentrations due to intermicellar interactions. The R_g values, determined from the K region beyond the peak, range from 11.3 Å for the

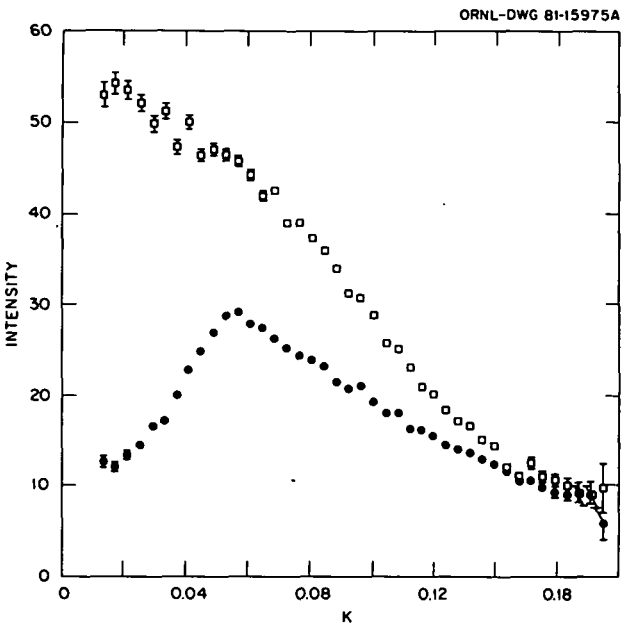

Fig. 5.2. $I(K)$ for LiDS at 50°C with LiCl (upper curve) and without salt (lower curve).

most dilute to 14.9 Å for the most concentrated solutions. The main effect of the addition of salt in this system is to increase $I(O)$. Calculations of $S(K)$ are being made using the mean spherical approximation.

In the metal physics area, two related experiments on the formation of grain boundary cavities have been performed (J. Weertman, Northwestern University, and M. Yoo and J. C. Ogle, ORNL). The mechanism of phase transitions (decomposition) is being studied in binary Fe-Cr alloys (L. Schwartz, Northwestern University) and in ternary Fe-Cr-Co alloys (S. Spooner, Georgia Institute of Technology).

In general, last year's experience with the ORNL–NSF–DOE SANS facility has been satisfactory for the staff and for the user community. There remain a few instrumental problems to be solved and sources of background to be tracked down and eliminated, but generally even the weakest scatterers studied (J. Weertman's Cu samples) have given useful data. For many specimens the turnaround time is as low as ten minutes, but a more usual measuring period is a few hours.

1. Summary of paper to be published.
2. Present address: Technology for Energy Corporation, Knoxville, Tenn.

3. J. S. Higgins and R. S. Stein, *J. Appl. Crystallog.* **11,** 346 (1978).
4. G. D. Wignall et al., *Polymer* **22,** 886 (1981).
5. G. D. Wignall, H. R. Child, and F. Li-Aravena, *Polymer* **21,** 131 (1980).
6. C. Picot et al., *Macromolecules* **10,** 436 (1977).

CHARACTERIZATION OF OIL-BEARING DIATOMITES BY SMALL-ANGLE SCATTERING[1]

G. D. Wignall H. R. Child
R. L. Schmidt[2] W. C. Koehler
J. S. Lin

Little information is currently available on the size distributions of pores in oil-bearing shales, diatomites, and chalks, and these important untapped petroleum reserves have only recently become the subject of systematic scientific study. Shale oil recovery techniques center on a variety of methods for increasing the porosity and permeability of the material, and a detailed knowledge of the pore size distribution is, therefore, fundamental to controlling the permeability of oil in these systems. SANS and SAXS techniques are ideally suited to the characterization of pores in the size range 20–2000 Å, though preliminary work on shale systems[3] demonstrated that other scattering heterogeneities present (minerals, iron pyrites, etc.) could also make a significant contribution to the small-angle scattering patterns and that these heterogeneities would affect the SANS and SAXS patterns differently. Recent work has, therefore, centered on separating the contribution of pores and other potential scattering heterogeneities in a series of biogenically precipitated silicas (diatomites), which are known to contain the minimum heterogeneity levels of all important oil-bearing formations. Combined SANS and SAXS experiments have been made on the same diatomite sample using methods developed by Vonk and co-workers,[4] which have been shown to reproduce accurately the known pore size distributions of standard precalibrated samples.[5] Figure 5.3 shows the pore size distributions determined independently from SAXS and SANS measurements on the same sample of a potentially rich (9.4 wt % organic carbon) diatomaceous formation, after removal of the oil by physicochemical extraction and oxidation techniques. The close agreement between the two distributions indicates that the contribution of other scattering heterogeneities is

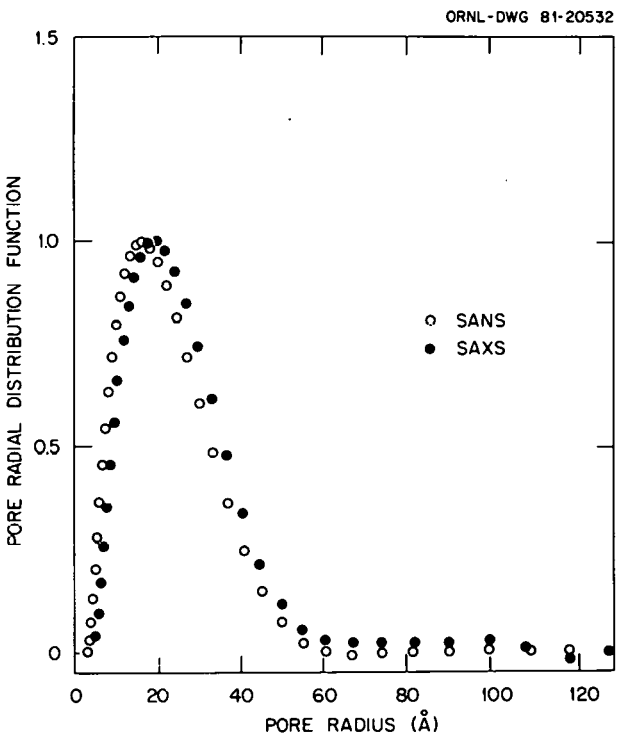

Fig. 5.3. Radial distribution functions of pores in diatomite sample 4 (well depth, 1897 m) determined by SANS and SAXS.

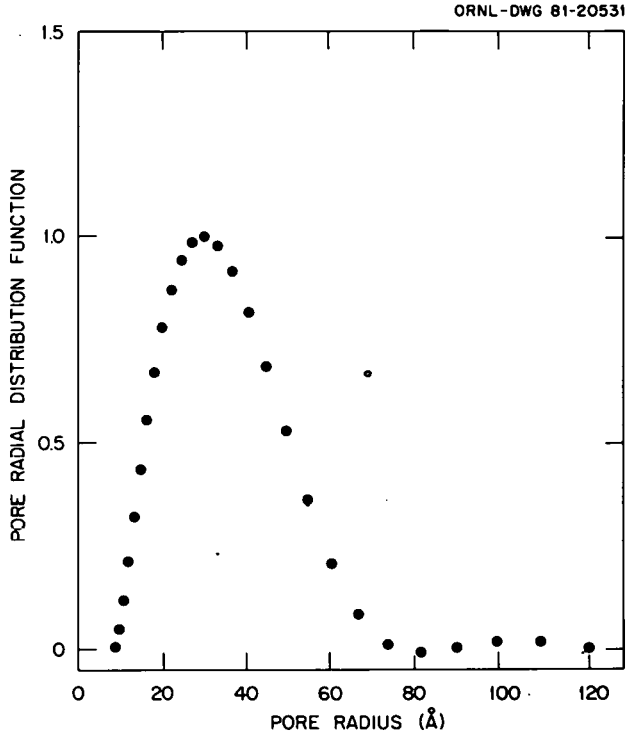

Fig. 5.4. Radial distribution of oil-bearing pores in diatomite sample 1 (well depth, 1772 m) determined from SANS difference experiments.

small. The peak pore radius determined by these techniques (16–19 Å) compares favorably with values of 21 Å measured by gas adsorption and 25 Å measured by transmission electron microscopy (TEM) on similar diatomites.[6] The latter value was obtained by averaging the results of five independent observers whose individual results revealed wide differences in the number of peaks in the distribution (1–3) and divergencies up to 20 Å in the peak positions. Thus, small-angle scattering techniques seem to be superior to TEM methods with regard to reproducibility and lack of subjective bias.

To obtain information on the oil-bearing pores, difference experiments were performed between samples treated to remove the oil and the original untreated materials. The physicochemical methods used are believed to remove the oil without changing the matrix or pore distribution. In view of the extremely strong scattering cross sections of this type of sample, the differences are easily measured in short run times (<1 h) for both SANS and SAXS, and Fig. 5.4 shows the pore size distribution of oil-bearing pores for a diatomite containing 11.6 vol % of oil. The peak in the oil-filled pore size distribution occurs at $r = 30$ Å compared to a value of $r = 22$ Å for the total pore distribution, indicating that the oil has been preferentially removed from the larger pores by the physicochemical methods involved. The distribution has a long tail out to $r \simeq 800$ Å, and after weighting for the pore volume, it may be estimated that over 80% of the oil removal occurs from pores with radii in the range $180 < r < 800$ Å. In this range the pore size distributions were found to be less reliable due to oscillations introduced by the mathematical constraints applied to the data, and alternative methods for examining the larger pores were explored. This indicates another potential advantage of small-angle techniques, that is, the ability to focus on a particular part of the pore size distribution by an appropriate choice of the range of scattering vector K measured. In general, the intensity observed at smaller K is sensitive to the larger scattering fluctuations in the system, and hence SANS measurements in the limit $K \rightarrow 0$ can give information on the technologically important larger oil-bearing pores. Furthermore, the strong-

est scattering signals occur in this limit and thus facilitate accurate characterization of these pores. Methods originated by Debye and co-workers[7,8] have been shown to be applicable in this limit,[3] and for the difference intensity data used to derive the oil-bearing pore distribution (Fig. 5.4), the Debye plots are linear in the range $0.2 \times 10^{-4} \leq K^2 \leq 2 \times 10^{-4}$ Å^{-2} with a measured correlation length, $a = 378 \pm 20$ Å, equivalent to an average particle diameter of 640 ± 30 Å for the larger pores.

Finally, the difference techniques developed in this work should be applicable even to systems where other scattering heterogeneities make an appreciable contribution to the measured intensity, as long as the matrix is unaffected by the physicochemical methods employed.

1. Summary of paper to be published.
2. Chevron Oilfield Research Company, La Habra, Calif.
3. G. D. Wignall et al., *Solid State Div. Prog. Rep., Feb. 29, 1980,* ORNL-5640, p. 184.
4. C. G. Vonk, *J. Appl. Crystallogr.* **9,** 433 (1976).
5. R. Triolo and H. R. Child, "Small-Angle Scattering from Ludox Particles," this report.
6. D. C. Hurd et al., *Am. J. Sci.* **281,** 833 (1981).
7. P. Debye and A.M.J. Bueche, *J. Appl. Phys.* **20,** 518 (1949).
8. P. Debye, H. R. Anderson, Jr., and H. Brumberger, *J. Appl. Phys.* **28,** 679 (1957).

SANS FROM COAL EXTRACT SOLUTIONS

R. R. Triolo[1] H. R. Child

Recently, Maxwell, Child, and Narten[2] reported SANS measurements on several samples of extracts of Illinois No. 6 coal. The different samples were prepared with different techniques, and the only conclusion possible at that time was that SANS seemed to be a promising method for measuring weight-average molecular weights of coal extracts.

Here, we will present some SANS data obtained on similar Illinois No. 6 coal extracts as a function of time and of concentration. The purpose of this study was to assess the stability of the extracts with time and to determine whether a "molecular weight" which is independent of concentration can be determined. If the apparent molecular weight, which is related to the extrapolated zero-angle scattering, is not independent of concentration, then the scattering unit should clearly not be identified as a molecule but rather as a particle with a concentration-dependent size.

The samples for this study were obtained by extraction of Illinois No. 6 vitrinite with perdeuterated pyridine with a thermal gradient of 100°C. After extraction, the sample was centrifuged at 20,000 rpm for 30 min and then was filtered through a 0.2-μ Teflon Millipore filter. The filtrate was collected in a quartz cylindrical spectrophotometric cell. Further dilutions were made in situ by withdrawing a predetermined amount of solution and replacing it with pure perdeuterated pyridine. All manipulations were done under inert atmosphere N_2. Another sample of the same extract was sealed in another similar cell, and the scattering was measured at the beginning of the experiment (time 0) and after 18, 75, 180, and 400 h. An apparent difference, noticeable in two runs, is due to the fact that the runs after 180 and 400 h were done with different slits; but when normalized to the same exposed area, the results of all the runs agreed within the experimental errors. We can conclude, therefore, that samples prepared in this way maintain their scattering properties for periods of time which are long compared to the length of the experiment.

The results for a study of the same solution as a function of concentration are shown in Fig. 5.5. After correcting for the solvent scattering, the data were fitted by least squares to the Debye scattering law[3]

$$I(K) = \frac{I_0}{(1 + K^2 a^2)^2} + C \quad , \tag{1}$$

with the three parameters I_0, a, and C. The values obtained are shown in Fig. 5.6 for all the solutions except the most dilute, which did not seem to give reasonable values because the scattering was too small. As shown in Fig. 5.6, Eq. (1) gives an excellent fit to the observations.

The linear increase of the constant C is consistent with the incoherent scattering from H in the coal particles. The decrease in the correlation length a indicates that the scattering particles are decreasing in size as the concentration increases. Particles of constant size should show a linear relationship between I_0 and the concentration; hence, the I_0 behavior also indicates that the particles are decreasing in size as the concentration is increased.

Our present conclusion is that the particle sizes obtained in these experiments are not fundamental

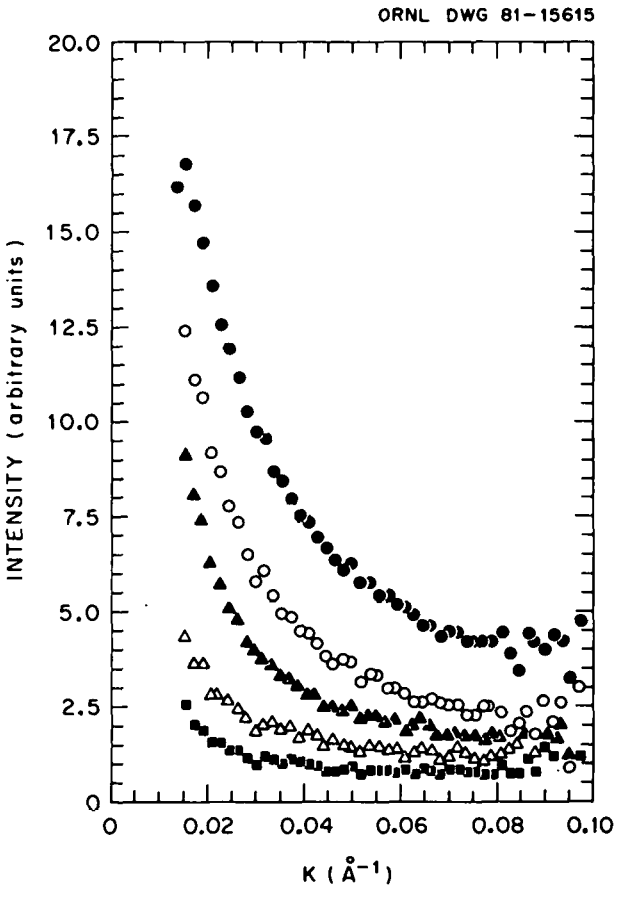

Fig. 5.5. SANS intensity vs $K = 4\pi \sin\theta/\lambda$ for an extract of Illinois No. 6 coal solution in perdeuterated pyridine as a function of concentration. Solid lines are calculated from Eq. (1) with parameters shown in Fig. 5.6.

properties of the coal samples but depend on the mechanical and chemical processing and on the particle concentration. Further analyses of these data will be performed when the chemical analyses of the coal samples are completed.

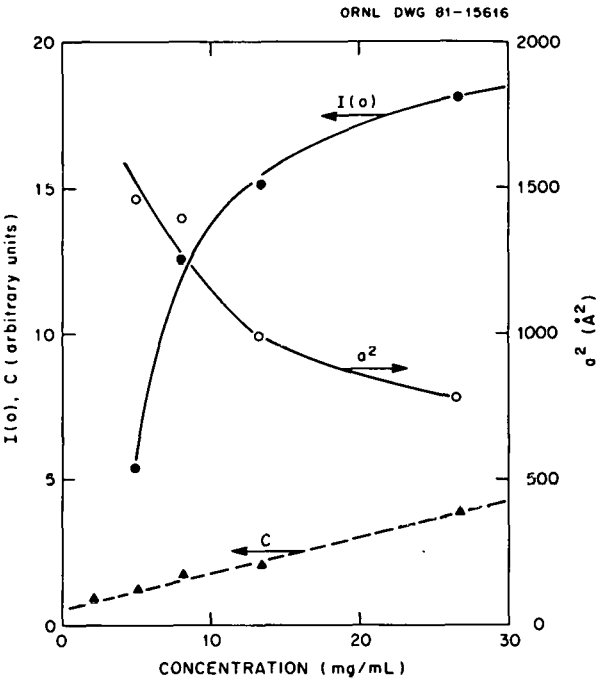

Fig. 5.6. Parameters I_0, a, and C of Eq. (1) vs concentration for the coal solutions shown in Fig. 5.5. Errors of the points are estimated to be ±5 to 10%.

SMALL-ANGLE SCATTERING FROM LUDOX PARTICLES

R. Triolo[1] H. R. Child

An important step in the process of analyzing small-angle diffraction curves of polydisperse systems is the inversion of experimental data to obtain size distribution functions. Several methods are currently available, each presenting some positive and negative aspects. The ideal situation would be one in which synthetic size distributions obtained by mixing components of different sizes could be analyzed by the different methods. Such analyses could then be compared to evaluate the methods.

Unfortunately, in nature no system is strictly monodisperse and very often polymodal and polydisperse distributions are encountered. Systems of this type are common in enhanced oil-recovery technology as well as in coal-extract technology. We present here some preliminary data on polydisperse, colloidal silica suspensions (Ludox) as well as bimodal polydisperse suspensions obtained by mixing different samples of Ludox.

Six grades of Ludox colloidal silica are commercially available: AM, AS, HS, SM, LS, and TM.

1. Chemistry Division, ORNL.

2. B. E. Maxwell, H. R. Child, and A. H. Narten, *Solid State Div. Prog. Rep., Feb. 29, 1980,* ORNL-5640, p. 186.

3. P. Debye and A. M. Bucche, *J. Appl. Phys.* **20,** 518 (1949); P. Debye, H. R. Anderson, Jr., and H. Brumberger, *J. Appl. Phys.* **28,** 679 (1957).

The stabilization of the suspension is due to a slight negative charge on the surface of the particle. The AS grade uses ammonium ions as counter ions; the other five grades use sodium ions as counter ions. In addition, the type AM also has some Al atoms replacing Si atoms on the surface.

We decided to study three types that have the same chemical composition but differ in the size of the particles. Typical properties of the samples used (before dilution) are presented in Table 5.1.

Table 5.1. Properties of initial Ludox colloidal silica solutions

Type	SM	HS	TM
Concn %, v/v	30	40	30
Concn SiO_2, wt %	30	40	50
Particle radius, Å	38	77	118
Viscosity at 25°C, cP	6.5	26	40
Density at 25°C, g/ml	1.22	1.31	1.39

We have studied these three types and some of their mixtures with both SAXS and SANS. The machines used were the 10-m SAXS instrument and the 30-m SANS instrument at ORNL. All the dilutions of the samples have been done volumetrically with D_2O to achieve maximum contrast for the SANS experiments. The same solutions were also used for the SAXS studies. Experimental results have been obtained in the concentration range 40–0.05% (v/v) for x rays and 40–0.5% when neutrons were used.[2] In addition, we also studied some mixtures, SM-TM and HS-TM, at the highest concentration.

Interesting effects from the interacting spherical particles are reflected in the scattered intensity for the more concentrated solutions, and these effects will be studied in more detail in the future. Our primary interest at present, however, is the use of the dilute solutions to try out the methods of extracting particle distributions available to us.

For the data obtained for Ludox solutions as a function of concentration, the measured values of the radii of gyration[3] at small K are consistent with the size of the particles as specified by the manufacturer (DuPont), so long as the dilution is small. More concentrated solutions show interaction effects as mentioned above; therefore, in this region of concentration the particles are no longer ideal polydisperse systems; and hence, the methods of extracting particle-size distributions are not applicable.

We are presently analyzing dilute solution data with all the methods currently available to us for extracting size distributions; these include Schmidt's method,[4] Glatter's method,[5] and Vonk's method.[6] As an example, in Fig. 5.7 (left) we show typical experimental (•) and calculated (o) points using the size distribution function shown on the right of Fig. 5.7, which was obtained from the observed data by weighted and constrained least-squares fit by a version of Vonk's program. The data are for a sample of Ludox HS diluted 1:50 with D_2O. The experimental curve is actually a combination of three different data sets obtained with the detector set at different distances to measure different K ranges.

Vonk's method appears to be the most satisfactory at present for reproducing the size distributions observed for these Ludox solutions by electron microscopy. When the concentration of the solution gets so large that interference effects appear, none of the methods we have tried appear to be applicable.

1. Chemistry Division, ORNL.
2. Concentrations are specified in terms of the ratio (100)(vol SiO_2)/(vol H_2O).
3. A. Guinier and G. Fournet, *Small-Angle Scattering of X-Rays*, John Wiley and Sons, New York, 1955.
4. J. H. Letcher and P. W. Schmidt, *J. Appl. Phys.* **37**, 649 (1966); O. L. Brill and P. W. Schmidt, *J. Appl. Phys.* **39**, 2274 (1968).
5. O. Glatter, *Acta Phys. Austriaca* **47**, 83 (1976).
6. G. G. Vonk, *J. Appl. Crystallogr.* **9**, 433 (1976).

SANS STUDY OF CHEMICAL AND MAGNETIC INHOMOGENEITIES IN Fe-BASED METALLIC GLASSES[1]

G. E. Fish[2] H. R. Child

Important questions remain about how the observed bulk properties of ferromagnetic metallic glasses arise from the microscopic structure. Consequently, a series of such splat-cooled metallic samples has been examined by SANS. For these studies, SANS has two unique characteristics: (1) the high penetration of neutrons, as opposed to x rays, provides a better sampling of the bulk material, and (2) the magnetic interaction of the

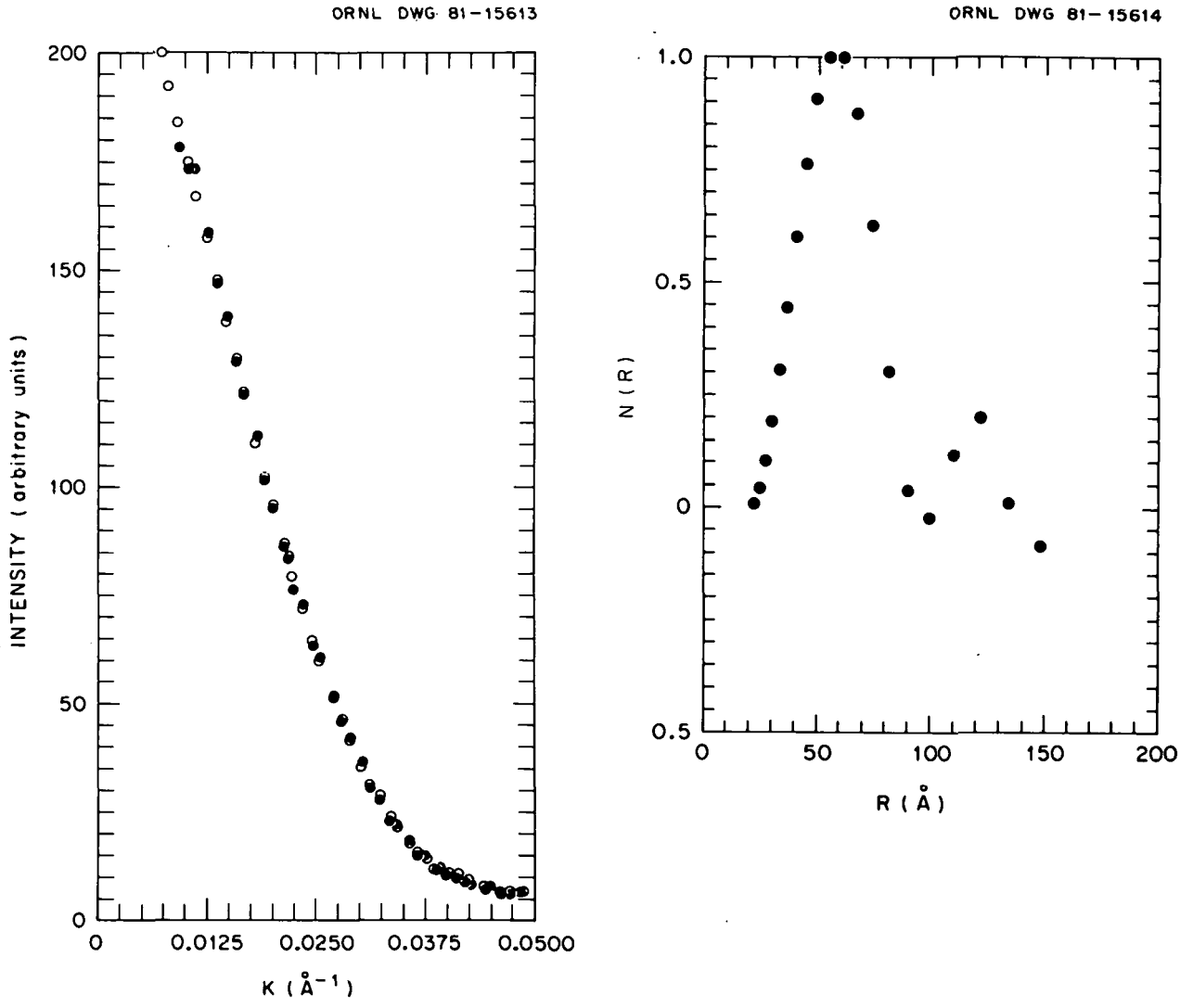

Fig. 5.7. Left: SANS intensity for a 1:50 dilution by volume of Ludox HS in D_2O (● experimental, ○ fitted points). Right: Normalized distribution of number of particles of radius R vs R obtained by least-squares fitting the data on the left, using Vonk's method.[6]

neutron with the sample provides a probe of the magnetic inhomogeneities. The samples were $Fe_{1-x}B_xSi_y$, enriched in ^{11}B, in the form of splat-cooled ribbons wrapped on a frame until a sufficient thickness was obtained. SANS measurements were made at the ORR facility with and without a magnetic field applied to the samples.

The data showed a large intensity peak concentrated at small K and a weak intensity extending out to $K = 0.03$ Å^{-1}. The strong, small K peak could be described by the Guinier approximation with a radius of gyration ~420 Å. This peak was essentially eliminated by the application of a 1k (~500 G) magnetic field. Based on the field dependence, we attribute this peak primarily to magnetic-domain-wall scattering, a subject which is by no means well understood. There was a direct correlation between the zero-field intensity for different samples and domain-wall density as seen in electron microscopy studies.

The larger K intensity was quite low and was comparable to the high background at the ORR instrument. We saw no evidence for a Porod limit (K^{-4}) in this scattering but, due to the low intensity, could not completely rule it out. This result, if confirmed by more accurate data, could indicate the absence of sharp interfaces on the regions causing this scattering. This region of the data was not greatly affected by the field and yielded an Rg ≃ 80 Å. Further experiments are planned to investigate this portion of the data more fully at the HFIR SANS facility.

1. Summary of paper: *J. Appl. Phys.* **52,** 1880 (1981).
2. Allied Chemical Corporation, Morristown, N.J.

MAGNETIC SANS FROM MAGNETIC CORRELATIONS IN $Fe_{0.7}Al_{0.3}$[1]

H. R. Child

Ordered $Fe_{0.7}Al_{0.3}$ becomes ferromagnetic below 400 K, paramagnetic on cooling below 170 K, and mictomagnetic below 92 K. A previous neutron scattering study of this material[2] showed magnetic-diffuse scattering over this entire temperature range with little or no change except for a gradual increase at lower temperatures. It was proposed that this system represents a case where the moment of an Fe atom is strongly dependent on the number of Fe nearest neighbors. Statistical fluctuation in the concentration of Al is presumed to be responsible for the development of clustering. The present paper presents an extension of the previous neutron results to smaller $K = 4\pi\sin\theta/\lambda$ to establish sizes of the clusters and to see if any behavior would occur at small K indicative of spin-glass behavior.

Figure 5.8 shows the most important results and shows the temperature dependence of the scattered neutron intensity at three small K values. The peak or hump at about 500 K is thought to correspond to the ferromagnetic Curie temperature of the clusters themselves, and the temperature at which the peak occurs is apparently independent of K. The second peak at ~200 K is not as easily explained but is tentatively assigned to the so-called spin-glass freezing temperature at which the clusters become frozen in place due to interactions between them. The temperature corresponding to this peak increases for smaller K, and this behavior has been associated with magnetic spin-glass materials.[3]

The K dependence of the scattering can be well represented by the square of a Lorentzian function plus a constant, and the parameters of such a functional form have been obtained by least-squares fits to the data. The correlation range obtained in this way varies from ~60 Å at 160 K to ~150 Å at 9 K and room temperature. These numbers represent very large clusters containing thousands of atoms with a very large cluster moment, although each atom's moment is small. These clusters are present at all temperatures and near T_c merge into the ordinary critical fluctuations one would expect. Scattering from magnetic domains must also be present, but their large size would probably confine their effects to smaller K than we can observe here.

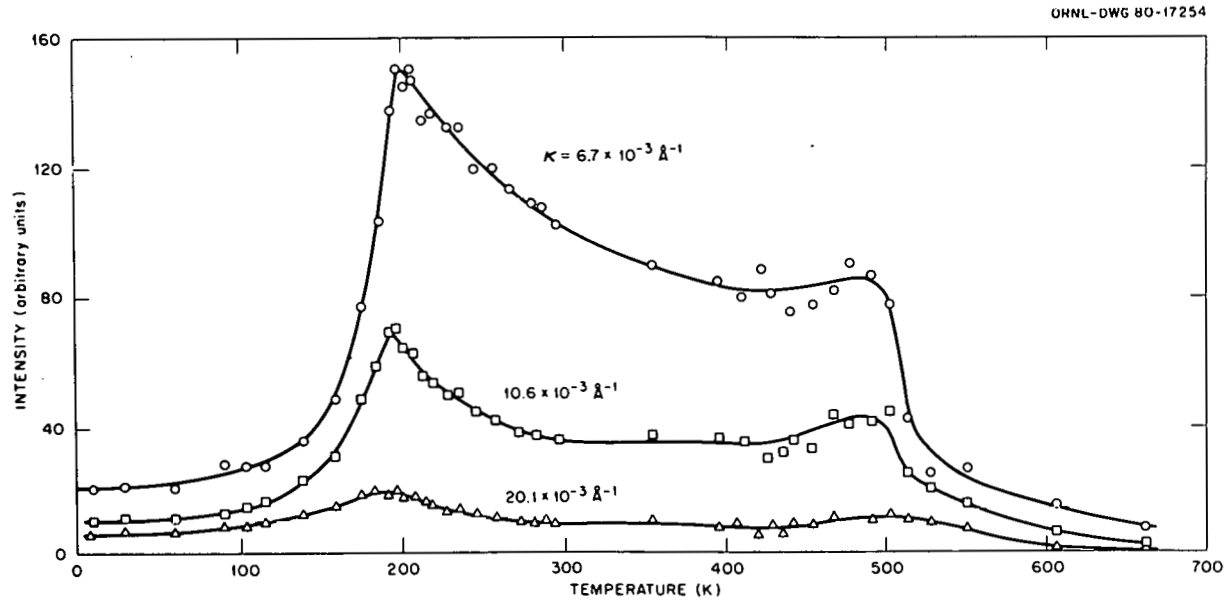

Fig. 5.8. Temperature dependence of the intensity from $Fe_{0.7}Al_{0.3}$ at three different values of $K = 4\pi\sin\theta/\lambda$.

To investigate the possible effect of domains, a magnetic field was applied to the sample with a rather dramatic and unexpected result; the scattering essentially disappeared completely. This is not just the disappearance of magnetic scattering due to the turning of the magnetic moments into the direction of the scattering vector, because these measurements were made with an area detector which could record data for K parallel and perpendicular to the magnetic field simultaneously, and the scattering disappeared in both directions. The only reasonable explanation is that the magnetic field is sweeping out the clusters (the disorder) in the system and putting the magnetic scattering into the Bragg peaks by transforming the sample into a normal ferromagnet. Since these measurements were designed to observe only the diffuse or disorder scattering, the normal ferromagnetic scattering was not visible, and the disorder scattering seemed to disappear.

---

1. Summary of paper: *J. Appl. Phys.* **52,** 1732 (1981).

2. J. W. Cable, L. David, and R. Parra, *Phys. Rev. B* **16,** 1132 (1977).

3. A. P. Murani and A. Heidemann, *Phys. Rev. Lett.* **41,** 1402 (1978); A. P. Murani, *J. Magn. Magn. Mater.* **5,** 94 (1977).

MEASUREMENTS OF SINGLE-CHAIN FORM FACTORS BY SMALL-ANGLE NEUTRON SCATTERING FROM POLYSTYRENE BLENDS CONTAINING HIGH CONCENTRATIONS OF LABELED MOLECULES[1]

G. D. Wignall, J. S. Lin
R. W. Hendricks[2], M. P. Wai[3]
W. C. Koehler, E. L. Thomas[3]
R. S. Stein[3]

SANS measurements on samples composed of a host polymer matrix in which a proportion of isotopically labeled molecules is dispersed have been used in a wide variety of studies of amorphous and crystalline polymers.[4,5] These measurements have conventionally been performed with small relative concentrations of labeled molecules and have involved an extrapolation to zero concentration to eliminate interchain interference effects. The intensity of the scattering signal is limited by the small number of labeled chains, and this has restricted the SANS measurements to strongly scattering systems to achieve a reasonable signal-to-noise ratio.

Recent developments in scattering theory[6,7] have indicated that it is possible to extract both the single-chain and interchain (interference) functions by performing measurements at high relative concentrations of labeled polymers. In this work we show, with well-defined polystyrenes, that the single-chain form factor of the polymer in bulk may be obtained from a single concentration measurement for any concentration of labeled molecules, provided that the molecular weights of the parent and labeled molecules are the same and that the molecular weight distributions are narrow. With these conditions, scattering theory shows that the small-angle intensity is

$$I(K) = X_1 X_2 (a_1 - a_2)^2 N P(K) \ , \qquad (1)$$

where X_i is the mole fraction of polymer component i, a_i is the total scattering amplitude of monomer i, N is the total number of polymer molecules, and $P(K)$ is the single-chain form factor. This shows that the form of the scattering curve in this case is governed only by the single-chain form factor $P(K)$. The mole fraction of each component will modulate the scattered intensity with the maximum coherent scattering of the blend occurring at a 50:50 mixture of the two components. The analogy between this result and the Laue monatomic scattering from binary alloys is apparent.

For the SANS studies, blends of atactic hydrogenated polystyrene (PSH M_W = 77,400) and deuteropolystyrene (PSD M_W = 75,000) containing 5, 10, 20, 30, 40, and 50 mole % PSD in PSH were prepared in addition to pure PSH and PSD blanks. The experiments were performed on the 30-m SANS facility (HFIR), and the area detector (64 × 64 cm^2 with 1-cm^2 element size), which is mounted on rails inside a 20-m vacuum flight path, was positioned at a distance of 10 m from the sample. The labeled samples were typically measured for ~1 h, and after correcting for instrumental backgrounds, incoherent scattering, and sample transmission, the scattered intensities were normalized to a constant sample thickness. Samples of both pure PSD and PSH were also measured to check that no voids or scattering heterogeneities were present and to provide a basis for subtracting incoherent scattering, arising principally from ^{1}H nuclei. Values of the (weight-averaged) molecular radius of gyration R_g^w were

obtained from conventional Zimm plots of the scattered intensity from the labeled molecules. Figure 5.9 shows the plot of $R_g^w/M_w^{1/2}$ concentration of the labeled chain. The average value of 0.266 Å $g^{-1/2}$ is in excellent agreement with previous measurements made at low concentrations[6] and with the value for polystyrene in an ideal solvent.[7] No concentration dependence was observed.

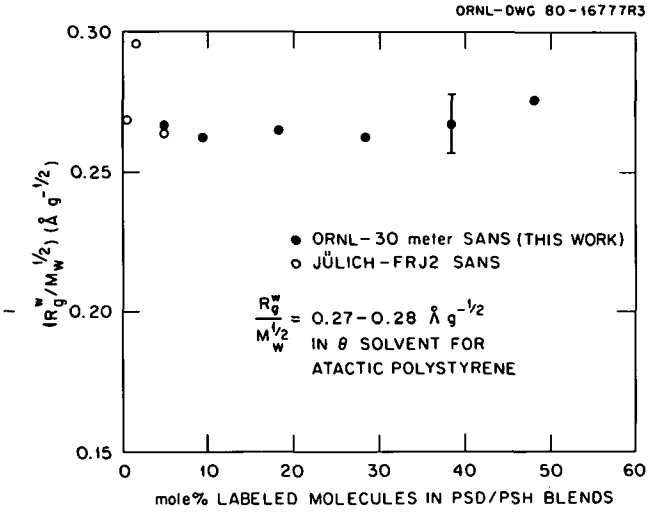

Fig. 5.9. Variation of $R_g^w/M_w^{1/2}$ with mole % labeled molcules in PSD/PSH blends.

Figure 5.10 shows the normalized forward scattering (extrapolated to $2\theta = 0$) vs concentration of the labeled chains. A straight line could be drawn through all the points, indicating that the intensity of the scattering is simply dependent on the mole fraction of the labeled chain [see Eq. (1)].

These results indicate that provided the molecular weights of the parent and labeled molecules are the same and their distributions are narrow, the single-chain form factor of the polymer in bulk may be obtained from a scattering measurement at a single concentration for any concentration of labeled molecules. The theory given above has, therefore, been confirmed for well-defined polystyrenes over the range of concentration 5–50 mole % deuterated polystyrene. For the special case of matched parent and labeled molecules, the radius of gyration is independent of the concentration of labeled molecules, and there is no need to restrict

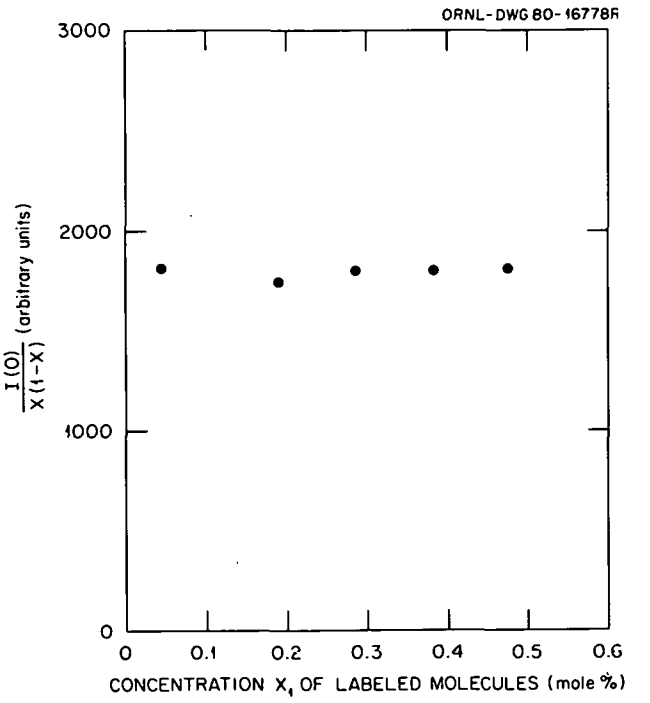

Fig. 5.10. Variation of $I(0)/X_1(1 - X_1)$ with mole % labeled molecules in PSD/PSH blends.

SANS measurements to dilute concentrations of labeled molecules or to extrapolate to zero concentration, thus permitting a significant gain of scattering intensity for weak scattering systems. While the maximum coherent scattering occurs at a 50:50 mixture of the two components, it may be advisable to work at a somewhat lower ratio of PSH in PSD to maximize the ratio of coherent to incoherent scattering.

1. Summary of paper: *Polymer* **22,** 887 (1981).
2. Present address: Technology for Energy Corporation, Knoxville, Tenn.
3. University of Massachusetts, Amherst, Mass.
4. R. W. Richards and A. Maconnachie, *Polymer* **19,** 739 (1978).
5. J. S. Higgins and R. S. Stein, *J. Appl. Crystallogr.* **11,** 346 (1978).
6. G. D. Wignall, D.G.H. Ballard, and J. Schelten, *Eur. Polym. J.* **10,** 861 (1974).
7. J. Brandrup and E. H. Immergut, p. IV-40 in *Polymer Handbook,* Interscience, New York, 1965.

STRUCTURAL CHARACTERIZATION OF SEMICRYSTALLINE POLYMER BLENDS BY SMALL-ANGLE NEUTRON SCATTERING[1]

G. D. Wignall H. R. Child
R. J. Samuels[2]

Polymer blends ranging from completely compatible mixtures to phase-separated systems are gaining in commercial importance, though little information is available on how the configuration of individual molecules within the blend is perturbed from the configuration in the homopolymer. Furthermore, in cases where incompatibility of the components leads to phase separation, knowledge of the structural nature of the phase-separated domains is necessary if the observed properties are to be interpretable. Semicrystalline polymer blends are particularly difficult to characterize since the components may form lamella structures consisting of alternating regions of crystalline and amorphous materials in addition to phase separating into domains. Information on domain sizes and molecular characteristics is also difficult to obtain in polyolefin blends by conventional techniques, and it is the object of this work to demonstrate the application of SANS to the solution of this problem.

The SANS technique has been used increasingly for the study of chain configuration in bulk amorphous and crystalline homopolymers, and many examples of the exploitation of this method are given in two recent review articles.[3,4] Jahshan and Summerfield[5] have shown that for an incompressible blend of two polymer species, designated P and S, where a fraction X of the P species has been labeled by substituting deuterium atoms for hydrogen, the coherent differential scattering cross section per unit solid angle per unit sample volume is given by

$$\frac{d\Sigma}{d\Omega}(K,X) = X(1-X)(a_H - a_D)^2 N_p S_S(K) + [a_H(1-X) + a_D X - a_S']^2 \frac{S_T(K)}{V} , \qquad (1)$$

where a_H and a_D are the coherent neutron scattering amplitudes for the normal (hydrogenated) and deuterated monomer (repeat) units of the P species, a_S' is the neutron scattering amplitude of the monomer unit of the S species, V is the total sample volume, and N_p is the number of chains per unit volume of the P species. $S_S(K)$ is the single-chain form factor which describes the configuration of an individual chain within a domain, and $S_T(K)$ is the matrix form factor which describes the phase-separated domain structure. It was the object of this study to obtain both $S_S(K)$ and $S_T(K)$ from SANS measurements on labeled polymer blends. Measurements were made on 50:50 wt % blends of polyethylene (P species) and polypropylene (S species) in which a fraction of the normal polyethylene (PEH) has been replaced by deuteropolyethylene (PED). $S_T(K)$ was obtained from measurements of the scattering cross section $d\Sigma/d\Omega$ (K) of a blend where all the P species had been deuterated ($X = 1$), and thus the first term in Eq. (1) is zero. $S_S(K)$ was obtained from the scattering of a partially labeled ($X = 0.09$) blend after subtracting a term proportional to $S_T(K)$, which had already been determined.

For a sample in which all the P species have been labeled ($X = 1$), the scattering cross section is proportional to $S_T(K)$ and arises from the fluctuations in scattering length density in the system, which can be described by the theory first introduced by Debye and co-workers.[6,7] The latter characterizes the fluctuations by an exponential correlation function, and for a fully labeled blend ($X = 1$) the differential scattering cross section is given by

$$\frac{d\Sigma}{d\Omega}(K)_{x=1} = \frac{2F\langle\eta^2\rangle a^3 [a_D - a_S']^2}{V[1 + K^2a^2]^2} , \qquad (2)$$

where $\langle\eta^2\rangle$ is the mean square fluctuation in scattering length intensity, F is a proportionality factor with the dimensions of length, and a is a correlation length from which the mean chord intercept lengths of each phase can be calculated. The single-chain form factor may be obtained from the scattering of a partially labeled blend ($0 < X < 1$) after subtracting the scattering from the phase structure $S_T(K)$ measured on a blend with a fully labeled P phase. The remaining scattering is given by the first term in Eq. (1), which in the Guinier region ($R_g^2K^2 < 1$) may be expanded to give

$$\left[\frac{d\Sigma}{d\Omega}(K)\right]^{-1} = \frac{1}{k_N M_W}\left[1 + \frac{R_g^2K^2}{3}\right] , \qquad (3)$$

where K_N is a neutron calibration constant, R_g is the radius of gyration, and M_W is the molecular

weight of the labeled chain. Thus R_g and M_W may be obtained from the slope and intercept of plots of $d\Sigma/d\Omega\ (K)^{-1}$ vs K^2 for a partially labeled blend.

The experiments were performed on the SANS instrument in operation at the ORR.[8] The SANS results from a 50% PED:50% PPH blend ($X = 1$) are shown in the form of a Debye plot in Fig. 5.11 for a sample slow cooled from the melt. The

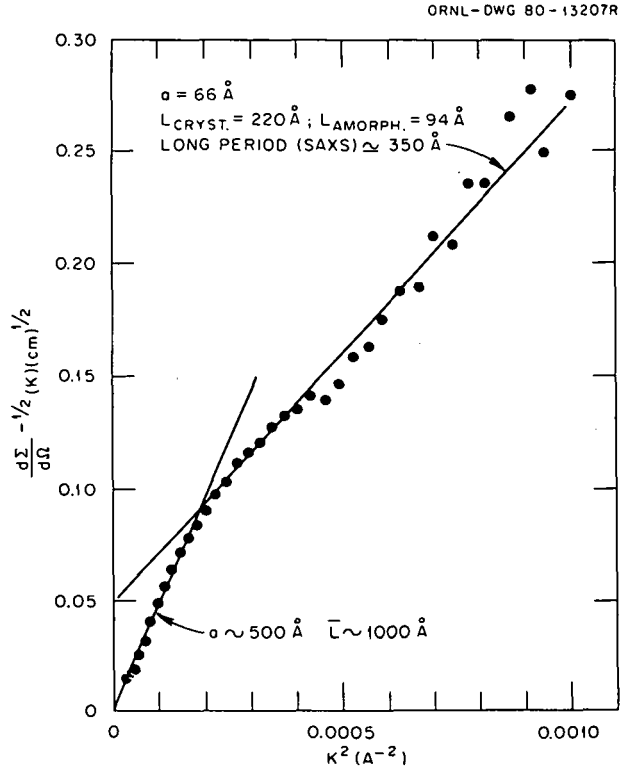

Fig. 5.11. Debye plot for 50:50 blend of PPH and PED slow cooled from melt at 5°C/min.

Debye theory given in Eq. (2) predicts that these plots will be linear in the low K region, and since this is generally true for the blends, an exponential correlation function appears to be a reasonable approximation for these systems. The correlation length a can then be calculated from the ratio of slope to intercept of this line and is in the range $a = 600 \pm 100$ Å. This indicates that the mean chord intercepts of the polyethylene and polypropylene phases, L_1 and L_2, exceed 1000 Å.

The single-chain form factor was obtained from the measured coherent scattering from a partially labeled sample ($X = 0.09$) and was analyzed according to Eq. (3) to calculate the radius of gyration and molecular weight of an individually labeled molecule as shown in Fig. 5.12 for a melt-quenched sample. The extrapolated forward scattering may be used to calculate the molecular weight of the labeled PED molecules and gives a value $M_W = 148{,}000$ in excellent agreement with a value of $M_W = 149{,}000$ obtained by chromatographic methods prior to blending the samples. It also confirms that the PED molecules are statistically distributed in the polyethylene domains. The radius of gyration of the PED molecule measured in the blend, $R_g = 139$ Å, is close to values measured in the homopolymer, $R_g \simeq 165$ Å, as expected when the domain size is large.

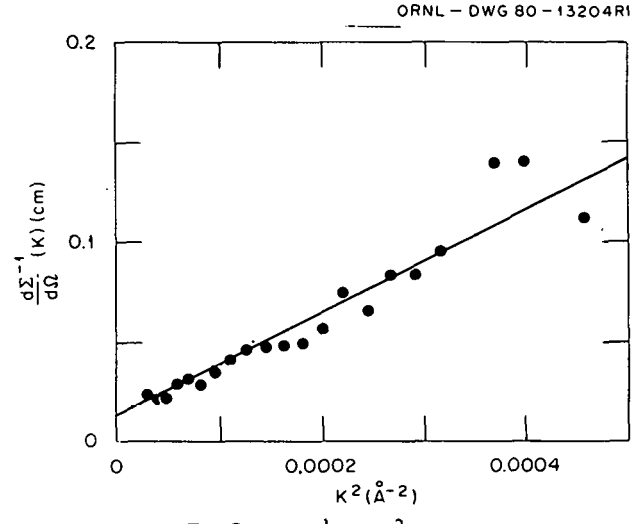

Fig. 5.12. $[d\Sigma/d\Omega\ (K)]^{-1}$ vs K^2 for 5 wt % labeled PED molecules in 50:50 blend of PPH and PEH (melt quenched).

In the higher K region ($K^2 > 0.0002$ Å^{-2}) of Fig. 5.11, the data deviate from the simple Debye theory and may be approximated by straight lines with correlation lengths (50–70 Å) much lower than those observed at lower K. This scattering might be expected to originate from the internal scattering heterogeneities within the domains arising from the alternation of crystalline and amorphous lamellae within each semicrystalline component phase. If we use the measured SANS correlation lengths and sample crystallinity to calculate the lengths of the crystalline and amorphous

regions, we obtain values of L_{cryst} = 220 Å and $L_{amorphous}$ = 94 Å using a crystal volume fraction ϕ = 0.7, typically measured on this type of blend by calorimetric or wide-angle x-ray diffraction methods. Thus the long period calculated from the Debye plot (L = 314 Å) compares with a value of L = 350 measured by SAXS. The periodicity of the amorphous and crystalline regions is, therefore, of the correct order to produce an approximately linear Debye plot with the measured correlation length a = 66 Å in the region $0.0002 \leqslant K^2 \leqslant 0.001$ Å^{-2}.

In summary, the results of the present study of model blends demonstrate that isotopic labeling can produce strong SANS contrast in mixed polyolefin systems, where the application of microscopy is limited by lack of electron density contrast between the components. By appropriate labeling of the components, the SANS method can be used to determine both the domain dimensions and the size of individual molecules within the domains. SANS studies can also be used to study the blend structure in the melt and could yield important new information about the effect of different crystallization/processing routes on the domain character of the blend.

1. Summary of paper to be published.
2. Georgia Institute of Technology, Atlanta, Ga.
3. R. W. Richards and A. Maconnachie, *Polymer* **19,** 739 (1978).
4. J. S. Higgins and R. S. Stein, *J. Appl. Crystallogr.* **11,** 346 (1978).
5. S. N. Jahshan and G. C. Summerfield, *J. Polymer Sci.* **18,** 1859 (1980).
6. P. Debye and A. M. Bueche, *J. Appl. Phys.* **20,** 518 (1949).
7. P. Debye, H. R. Anderson, Jr., and H. Brumberger, *J. Appl. Phys.* **28,** 679 (1957).
8. H. R. Child and S. Spooner, *J. Appl. Crystallogr.* **13,** 259 (1980).

HIGH-RESOLUTION SANS STUDY OF POLYMER BLENDS

D. K. Christen H. R. Child
G. D. Wignall R. J. Samuels[1]

In recent years, SANS techniques have provided important new information on the structure and compatibility of homopolymers and blends.[2,3] Samples analyzed by this technique are made up of a host polymer matrix in which a fraction of isotopically labeled (deuterated) polymer molecules is substituted for normal (hydrogenous) molecules in the blend components. The difference in coherent scattering length between deuterium (b_D = 0.66 × 10^{-12} cm) and hydrogen (b_H = −0.37 × 10^{-12} cm) results in a marked contrast between the normal and deuterated molecules. In this way, SANS can be used to study systems where the lack of electron-density contrast limits the application of electron microscopy or optical techniques (e.g., polyolefin blends). Previous SANS studies[4] on these systems have provided information on both the domain structure and molecular configuration within the blend, though the resolution limit of the ORR HB6 SANS instrument precluded the observation of large structures (up to 10,000 Å), which were thought to be present in those systems. These studies have been corroborated and extended by using the high-resolution, double-crystal HFIR HB3A instrument. In previous work, mean chord intercepts of both phases were found to be ~1000 Å (100 nm). The existence of larger structures could not be quantitatively assessed due to a lack of resolution for scattering vectors $K < 7 \times 10^{-2}$ nm^{-1}. The double-crystal instrument has provided better than an order-of-magnitude extension in the small-K data and in so doing revealed strong forward scattering due to significantly larger structures.

These results are shown in Fig. 5.13, plotted in terms of the vertically integrated differential cross-section/unit volume $\int d\Sigma/d\Omega \, d\theta_v$ and horizontal scattering vector K_h. The reason for this particular parametric representation involves instrumental properties of the double-crystal device, which possesses extremely high-K resolution in the horizontal direction but virtually relaxed vertical collimation. The system response is shown schematically in the inset of Fig. 5.13.

The previous SANS studies[4] have shown that for $K < 0.015$ Å^{-1} the differential scattering cross section of a fully labeled 50:50 blend of deuterated polyethylene (PED) and normal polypropylene (PPH) may be reasonably approximated by

$$\frac{d\Sigma}{d\Omega} = \frac{d\Sigma}{d\Omega}(O)\frac{1}{(1+a^2K^2)^2} \quad , \tag{1}$$

where a is a correlation length directly related to the mean chord length and $d\Sigma(O)/d\Omega$, the for-

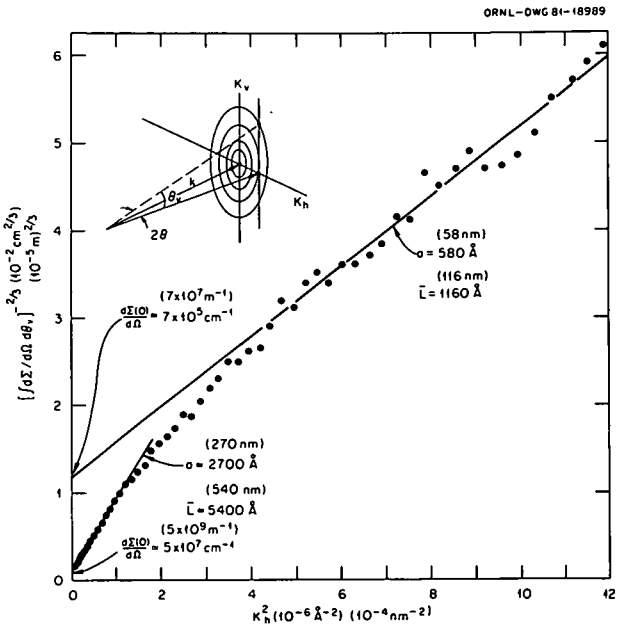

Fig. 5.13. $[\int d\Sigma/d\Omega\, d\theta_v]^{-2/3}$ vs K_h^2 for a 50:50 blend of PED in PPH. The inset illustrates the instrumental response with the thin vertical slice being the resolution element.

ward scattering cross section, involves constants of the material.[4] From this, it is easily found that

$$\int d\Sigma/d\Omega\, d\theta_v = \frac{\pi}{2ka} \frac{d\Sigma(O)/d\Omega}{(1 + a^2K_h^2)^{2/3}} ,$$

where $k = 2\pi/\lambda$ is the incident neutron wave number. If Eq. (1) is valid, then a plot of $[\int d\Sigma/d\Omega\, d\theta_v]^{-2/3}$ vs K_h^2 should yield a straight line, with a ratio slope/intercept $= a^2$.

From Fig. 5.13, this relationship is seen to exist down to $K \simeq 0.002$ Å^{-1}, below which excess scattering due to larger structures comes into play. For $K > 0.002$ Å^{-1}, one finds $a \simeq 580$ Å corresponding to a mean chord length $L = 1160$ Å, which merges very well with the low-K results of the earlier study ($a = 600 \pm 100$ Å). Extrapolation of this region to $K_h = 0$ yields a large $d\Sigma(O)/d\Omega \simeq 7 \times 10^7$ m^{-1}, also in good agreement with the previous results. Analysis at the lowest K, within the context of Fig. 5.13, would imply structures with $a \sim 2700$ Å, $L \sim 5400$ Å, and a distribution of domain sizes between these two values.

In summary, the double-crystal instrument, though ideally suited for systems possessing translation invariance in one dimension (e.g., flux-line lattices or filamentary structures), has found utility in the quantitative assessment of domain-structure sizes in polymer blends. In general, its applicability to analysis of other large structures in polymers should be good provided the scattering is isotropic.

1. Georgia Institute of Technology, Atlanta, Ga.
2. R. W. Richards and A. Maconnachie, *Polymer* **19,** 739 (1978).
3. J. S. Higgins and R. S. Stein, *J. Appl. Crystallogr.* **11,** 346 (1978).
4. G. D. Wignall, H. R. Child, and R. J. Samuels, "Structural Characterization of Semicrystalline Polymer Blends by Small-Angle Neutron Scattering," this report.

WIDE-ANGLE NEUTRON SCATTERING STUDIES OF MIXED CRYSTALS OF POLYETHYLENE AND DEUTEROPOLYETHYLENE[1]

G. D. Wignall C. Edwards[2]
L. Mandelkern[2] M. Glotin[2]

The arrangement of molecular chains within the lamellae of semicrystalline polymers has long been disputed, and this topic has attracted renewed attention in the light of current experimental and theoretical developments.[3] It is generally agreed that the melt consists of interpenetrating random coils and that on crystallization molecular chains traverse one or more lamellae many times, with some type of return on "folding" at the interlamella, amorphous boundaries. The question is whether the molecule returns with either predominantly adjacent or with random reentry to the crystallite of origin. Recent discussion has centered on the interpretation of SANS and IR data from mixed crystals of polyethylene (PEH) and deuterated polyethylene (PED), crystallized both from the melt and from dilute solution. Generally, the SANS experiments reveal that the radius of gyration R_g of molecules remains unchanged upon crystallization from the melt[4,5] and, hence, has an $M^{1/2}$ dependence in both the molten and crystalline states. These results, along with the general shape of the scattering curve, have been interpreted as favoring predominantly random reentry.[4-7]

Infrared studies on mixed crystals of PEH and PED, however, have been interpreted in terms of predominantly adjacent reentry in (100) planes for melt crystallized materials.[8] More recently, attention has been focused on scattering measure-

ments at higher values of the scattering vector $K = 4\pi\sin\theta/\lambda$, where λ is the incident wavelength and 2θ is the angle of scattering; Stamm[9] has calculated the scattering functions of small numbers (2–10) of adjacent crystalline stems in the wide-angle neutron scattering range ($K > 0.5$ Å^{-1}). These calculations show that the adjacent sequences should give rise to measurable modulation of the diffuse scattering pattern and that these modulations are centered at the position of the previously forbidden Bragg reflections. We have, therefore, made a careful search to see if such features are present in the wide-angle neutron scattering patterns of mixed crystal samples, and on the basis of these experiments, we are able to rule out regular folding in (100) or (010) planes. The results are particularly relevant to the discussion of folding in the melt-crystallized polyethylene because they disagree with the interpretation of the IR results.

Figure 5.14 shows the wide-angle neutron scattering pattern of a 75% PED:25% PEH mixed crystal sample measured on the HB2 spectrometer with $\lambda = 1.28$ Å together with the predicted modulation of the pattern centered at $2\theta \simeq 15°$ for five adjacent stems folded in the (100) direction. No extra intensity above background which might be indicative of predominantly adjacent reentry within subunits was observed. In the case of (010) folding, the scattering curve should exhibit an even stronger modulation (by a factor of ~4) at $2\theta \simeq 10°$, which is also not observed. Thus, the magnitude of the predicted modulations compared with the statistical accuracy of the measurement rules out regular (100) or (010) folding with five or more adjacent stems for more than a fraction (~0.2) of the melt-crystallized materials.

There are several possible reasons for the apparent contradiction between the IR results on the one hand and the SANS and the present wide-angle neutron scattering data on the other. At the outset of the neutron scattering studies, it was recognized that the technique was extremely sensitive to small compositional heterogeneities,[10] and for this reason studies with polyethylene have generally been made on samples rapidly quenched from the melt directly into liquid media cooled below room temperature. To date, no successful SANS study free of the effects of composition heterogeneities has been made on polyethylene samples slowly cooled from the melt. The IR studies, on the other hand, have been made on

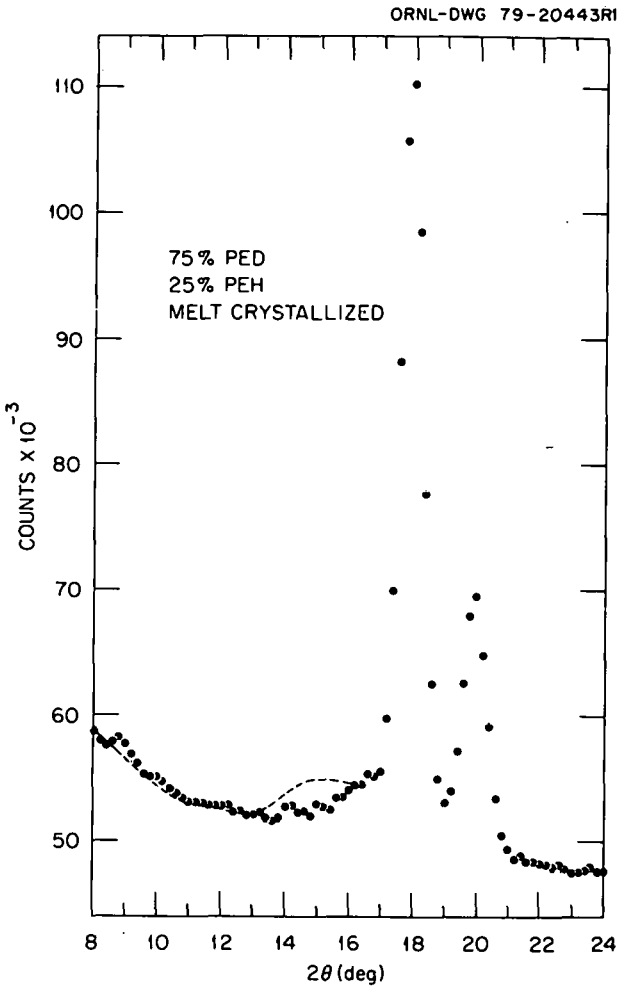

Fig. 5.14. Wide-angle neutron scattering for melt-crystallized specimen (25% PEH:75% PED). The broken line represents the calculated scattering for subunits of five adjacent stems in the (100) plane.

polyethylene samples crystallized relatively slowly from the melt, with cooling rates of 0.5–2°C/min. In two independent studies of polyethylene,[4,11] samples crystallized at 115°C or by cooling from the melt at 0.6°C/min were found to show strong macroscopic segregation of PEH and PED as demonstrated by calorimetry and wide-angle diffractometry. If it is still maintained that adjacent reentry folding along (100) planes makes a significant contribution to crystallite structure, then combined IR neutron scattering studies on the same sample would be appropriate.

1. Summary of paper: *Journal of Applied Physics* (in press).

2. Florida State University, Tallahassee, Fla.
3. "Symposium on Organization of Molecules in the Condensed State," *Discuss. Faraday Soc.* **68,** 1–127 (1980).
4. J. Schelten et al., *Polymer* **17,** 751 (1976).
5. D.G.H. Ballard et al., *Polymer* **19,** 379 (1978).
6. P. J. Flory and D. Y. Yoon, *Nature* **272,** 226 (1978).
7. D. Y. Yoon and P. J. Flory, *Polymer* **28,** 509 (1977).
8. M. Tasumi and S. J. Krimm, *Polymer Sci.* **6,** 995 (1968); M. Bank and S. Krimm, *Polymer Sci.* **7,** 1785 (1969).
9. M. Stamm, private communication.
10. J. Schelten et al., *Polymer* **18,** 1111 (1977).
11. M. Stamm et al., *Discuss. Faraday Soc.* **68,** 263 (1980).

THE NATIONAL CENTER FOR SMALL-ANGLE SCATTERING RESEARCH[1]

H. R. Child
W. C. Koehler
L. B. Maddox[2]
S. P. King
J. S. Lin
G. D. Wignall

Since the end of the last report period, February 29, 1980, the National Center for Small-Angle Scattering Research (NCSASR) has undergone a number of significant changes. Construction of the 30-m SANS facility and machine testing were completed, and the first user of the instrument was scheduled on October 20–21, 1980. From that date to the present, users have been generally scheduled for five days per week with two days dedicated to machine physics. The instrument was formally dedicated in January 1981.

The machine-physics periods permitted the staff to make any necessary repairs. In addition, this time was used to install a four-disk system to contain data and operating programs. The ModComp II memory is no longer used to accumulate neutron counts; instead, they are read into a CAMAC-controlled histogramming memory module, thus freeing 4-K words of computer core for other tasks. A completely new and more flexible data analysis package was written and installed.[3] A hard-copy unit that makes copies of data directly from the screen of the Tektronix terminal was purchased.

The mechanical components of the device for in situ small-angle x-ray and neutron scattering (SAXS and SANS) studies of polymer deformation have been built. The new x-ray chamber, the hydraulic loading system, and CAMAC-modular programmable function generator are operable. A number of problems that developed in the operation of the fast Mostek memory system have now been overcome, and the software modifications to the ModComp II operating system have been written. Preliminary studies have been carried out using the ModComp II memory with satisfactory results. It is expected that the system will be operated with the 250-K word memory in the near future.

From January 1, 1978, to September 15, 1981, a total of 138 proposals has been received. In the early years, of course, the proposals were for the 10-m SAXS apparatus. In the last year, however, since the SANS facility became operational, the majority of proposals was for the neutron facility. A breakdown of the SANS proposals and of the total proposals according to scientific disciplines is given in Table 5.2.

Table 5.2. Summary of proposals received by NCSASR (January 1, 1978–September 15, 1981)

	SANS	Total
Biology	4	13
Chemistry and Materials	30	50
Polymer Science	44	75
Total	78	138

One of the more recent experiments was carried out by G. Zaccäi, ILL, Grenoble, at our request. He studied samples of ATPase in an H_2O buffer and in a D_2O buffer. These were samples similar to ones he had previously investigated on the D11 instrument at the ILL. Briefly, he concluded that for the Q range ($0 < Q < 0.3$ Å^{-1}, $R_g \simeq 30$ Å) the ORNL-NSF SANS facility has a better signal-to-background ratio and better stability than the D11 instrument for equivalent samples and experiment times. This result means that a wide range of biological investigations can easily be performed on the 30-m SANS instrument. For investigations of higher R_g values, the current signal-to-noise ratio is greater at Grenoble by a factor of 3 ($R_g \sim$ 100–200 Å) or 10 ($R_g \sim$ 500 Å), but even for these systems useful data are currently being obtained in experimental times from 15 min to 6 h.

In the near future we expect to install straight-beam guide sections in the presample flight path,

ch as those already used at the ILL. These will effectively transport the source closer to the specimen with a corresponding increase in intensity. Furthermore, in the intermediate future (1983), we plan to replace the 12 graphite reflectors with crystals whose mosaic spread is closer to the instrumental design specifications, which will provide a further overall flux increase.

Contracts for the execution of proprietary research have been arranged with the DuPont Company and with Firestone Tire and Rubber Company, and negotiations are under way with several other industrial organizations. The first proprietary experiment was performed in August 1981.

1. This Center is operated under an agreement between the U.S. Department of Energy and the National Science Foundation (Interagency Agreement DOE No. 40-637-77, NSF No. DMR-7724458).

2. Computer Sciences Division, UCC-ND.

3. H. R. Child and L. B. Maddox, "New System Software for the HFIR 30-m SANS Instrument," this report.

RECENT DEVELOPMENT OF A DYNAMIC DEVICE FOR PLASTIC DEFORMATION RESEARCH

J. S. Lin R. W. Hendricks[1]
S. Suehiro[2]

Polymeric materials are becoming more and more important in their technological applications. An understanding of the relationship of the mechanical properties and the structure at the level of lamellae is crucial for the development of commercially useful materials. SAXS and SANS have in recent years proven to be powerful tools for providing information about the microstructure of semicrystalline polymers.

A dynamic device that is being developed at the small-angle x-ray laboratory is intended for studies that fall into three broad classes: (1) dynamic microstructural relaxation in semicrystalline polymers and elastomers; (2) dynamic microstructural orientation under periodic loads in semicrystalline polymers and in elastomers; and (3) crystallization of polymers, in general, and segregation phenomena of amorphous polymers, in particular. The device is essentially designed for two types of experiments, namely, (1) transient deformation/relaxation or deformation/crystallization experiments in which the sample will be deformed very rapidly to a large extension ratio, and then the relaxation, reorientation, or phase transformation of the lamellae will be followed by SAXS and (2) oscillatory experiments in which the specimen will be prestretched to a given elongation ratio and an oscillatory load will be applied at both variable frequency and variable strain amplitude. Both types of experiments will be performed at constant, but adjustable, temperatures.

To meet the design criteria for such plastic deformation research, a fast-data-acquisition system with a large memory capacity for data storage, along with a two-dimensional position-sensitive detector system for simultaneous data acquisition in 64 × 64 data arrays, is required. The design, construction, and development of such a sophisticated system were initiated by R. W. Hendricks and S. Suehiro and were continued by them until Suehiro returned to Japan in May 1980 and Hendricks left ORNL in March 1981. Since then, the development of the dynamic device, particularly the fast-data-acquisition system, has been continued with the assistance of R. Willems, Instrumentation and Controls Division, ORNL. A thorough test has been performed of all associated CAMAC modules, such as the data bus display, position-sensitive detector interface, time-correlator, mapper, programmable function generator, and Mostek input/output interface. The Mostek memory system with a memory capacity of 256-K size has also been successfully tested with a diagnostic program. The Mostek system is currently capable of storing time-slicing experimental data in up to 64 arrays, each 64 × 64.

The calibration of the Terratek hydraulic loading with a loading capacity of 1000 lb and an actuator stroke of 2 in. has been carried out. Load cells of 1000, 200, and 25 lb have each been tested; under normal conditions, the 200-lb load cell will be used.

The temperature system was originally designed to be controlled via the host computer through CAMAC modules. Two heating elements and associated thermocouples have been acquired. The calibration of the sensor thermocouple and the measuring thermocouple has been completed; however, the total temperature control system, including the development of control algorithm, remains to be completed.

The software package for data analysis includes the background correction, sensitivity correction, in-phase and out-of-phase analysis, and Fourier expansion and transformation. Progress on further software development is being made with help from S. Suehiro and a group of researchers under R. S. Stein, University of Massachusetts.

1. Present address: Technology for Energy Corporation, Knoxville, Tenn.
2. Consultant from Kyoto University, Kyoto, Japan.

NEW SYSTEM SOFTWARE FOR THE HFIR 30-m SANS INSTRUMENT

H. R. Child L. B. Maddox[1]

The software which has been used for the NCSASR SANS 30-m instrument at the HFIR thus far has been a modified version of that developed for the SAXS camera at ORNL. The data analyses necessary for the two types of data are slightly different; therefore, it was recognized from the beginning that new versions of the software would be desirable. Furthermore, the addition of two more disk drives, making a total of four, for the ModComp computer would allow more convenient data storage and data plotting capabilities than had been available for the SAXS machine. For these reasons a new set of software programs has been written and installed on the HFIR and the ORR instruments and will shortly be installed on the SAXS instrument.

One major effort in the utilization of the four-disk system was involved with using one entire disk for storage of the raw two-dimensional data runs. Previously, a region of the program disk was used for this purpose, limiting the number of data sets which could be accommodated to about 100 and requiring frequent shifting of these data to archive disks. By using an entire disk, more than three times the number of runs can be stored, and when the disk is full, a copy of it automatically becomes the archive. This scheme essentially eliminates the shifting of data. It also has the advantage that the program disk is entirely separate so that modification of programs can be made and installed with no changes in the data runs available. The necessary software changes for these improvements were not difficult and were made quickly.

The second improvement was the hardware installation as well as necessary software modifications for an external memory in the CAMAC crat within which the data runs can be accumulatec This addition results in freeing 4 K of computer memory for other tasks. The external memory has 16 K of 24-bit words, providing sufficient space for four 64 × 64 data arrays or one 128 × 128 data array. The main computer can read the external memory at any time via the CAMAC data way even while data are being accumulated from the microprocessor via the external port.

The new software, while maintaining the previous capabilities, has resulted in several significant improvements. The data-taking process is considerably simplified by a new method of handling the descriptive header identifying each data set. The data analyses process is improved in accuracy by a new method of subtracting background, which is especially important for low scattering samples, and by providing the correct statistical error on the $I(K)$ vs K curves. Several types of linear least-squares fits to find radii of gyration, Porod constants, and extrapolated $I(K)$ at $K = 0$ parameters are available with the more sophisticated plotting programs. Also, plots with more than one $I(K)$ vs K data set on the same plot can be obtained for easy intercomparison, because all such data are normalized for monitor counts, thickness of sample, and transmission. There are also easier methods of data base management possible with the new software system such as the ability conveniently to correct values in the header record which may have been incorrectly entered when the run was made, to off-load data sets to a user's private disk, and to transfer data to the central computers.

1. Computer Sciences Division, UCC-ND.

LATTICE DYNAMICS

PRESSURE AND TEMPERATURE DEPENDENCE OF THE CHARGE DENSITY WAVES IN ALPHA-URANIUM

H. G. Smith R. M. Nicklow
N. Wakabayashi[1] G. H. Lander[2]
E. S. Fisher[2]

The pressure and temperature dependence of the incommensurate $(0.5,q_y,q_z)$ and commensurate $(0.5\text{-}\delta,0,0)$ charge density waves (ICDW and CCDW) in α-U have been investigated by both elastic and inelastic neutron scattering techniques

The initial zero-pressure elastic scattering measurements confirmed the preliminary low-temperature measurements of the ICDW of Marmeggi and Delapalme,[3] ILL, Grenoble. However, a detailed comparison of the CCDW and the ICDW (see Fig. 5.15) revealed a broadened peak for the former compared with the latter (which was of the order of the instrumental resolution), suggesting a coherency region of the CCDW of only about 50 unit cells in the c direction. Both CDW's are

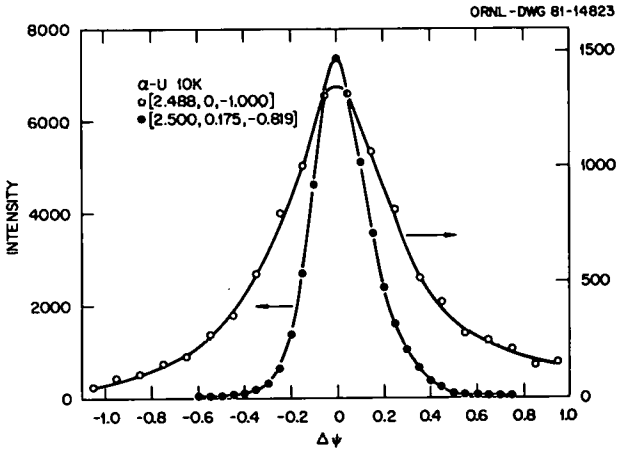

Fig. 5.15. Rocking curves of the ICDW and CCDW in U at 10 K.

related to soft phonons; however, the relation between them is not understood and will require further studies, particularly inelastic scattering studies. The CCDW involves a phonon with a predominatcly x displacement of optic character and a small y displacement with acoustic character, but no z displacement because of the crystal symmetry. However, the ICDW involves an off-symmetry axis phonon which allows a z displacement as well. The lattice dynamical model, which fits the room-temperature dispersion curves, predicts an instability in the $(0.5,y,z)$ direction and a z displacement of optic character comparable in magnitude to the y displacement.

It is tempting to suggest that the CCDW is actually associated with discommensurations between the domains of the ICDW. The weak scattering ($I_{\mathrm{CCDW}} \approx 1/40\ I_{\mathrm{ICDW}}$) of the CCDW is consistent with this idea of a smaller volume if its x displacement is of the order of the x displacement of the ICDW. It may be even larger.

The two-charge density waves exhibit quite different behavior as a function of pressure. The intensity of the CCDW decreased dramatically as pressure was applied (at 10 K) and was very weak and more diffuse after application of 2–3 kbar of pressure (see Fig. 5.16). This behavior is not consistent with the elastic constant measurements

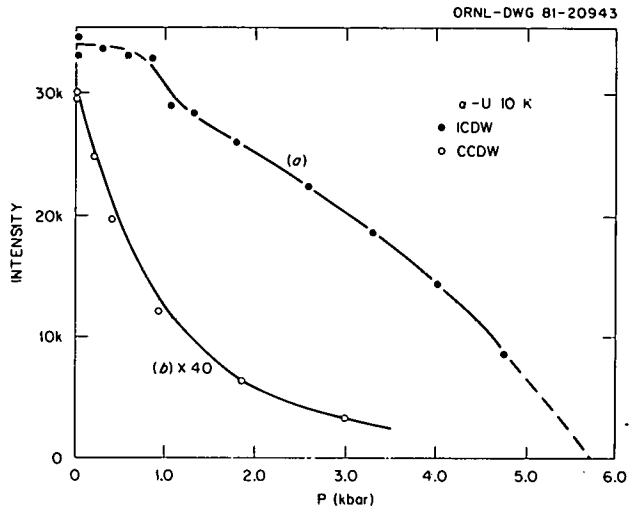

Fig. 5.16. Pressure dependence of ICDW (curve a) and CCDW (curve b) in U at 10 K.

vs temperature and pressure reported by Fisher and Dever[4] nor with the variation of its superconducting transition temperature with pressure as reported by Smith and Fisher.[5] However, the pressure dependence of the ICDW is consistent with Fisher's observed shift of the elastic constant anomalies vs pressure and is not incompatible with Smith's observation of a linear increase of the superconducting transition temperature as pressure is increased until a pressure of 6 kbar is reached. Smith observed a further increase of T_c at about 8 kbar until a pressure of 12 kbar was obtained, whereupon T_c decreased with increasing pressure. These latter observations suggest additional changes in the modulated structures of U at lower temperatures and higher pressures than have been used before in the neutron scattering studies. It is unlikely that the necessary experimental conditions are attainable with our present equipment for subsequent neutron experiments, but this possibility will bc examined.

1. Present address: Keio University, Yokohama, Japan.

2. Argonne National Laboratory, Argonne, Ill.

3. J. C. Marmeggi and A. Delapalme, *Physica* **102B**, 309 (1980).
4. E. S. Fisher and D. Dever, *Solid State Commun.* **8**, 649 (1970).
5. T. F. Smith and E. S. Fisher, *J. Low Temp. Phys.* **12**, 631 (1973).

LATTICE DYNAMICS OF THE A15 COMPOUND Nb_3Sb

L. Pintschovius[1] W. Reichardt[3]
H. G. Smith G. W. Webb[4]
N. Wakabayashi[2] Z. Fisk[4]

A knowledge of the lattice dynamics and the detailed phonon behavior of the A15 compounds is considered essential for obtaining a better understanding of the electron-phonon interactions in these materials. Inelastic neutron scattering techniques are extremely valuable in this regard; and coupled with complementary techniques such as ultrasonics, Raman scattering, and superconducting tunneling measurements, they have shed much light on the role of phonons in many superconducting metals, alloys, and compounds.[5] Several of the highest T_c A15 compounds, which are of current interest, are Nb_3Sn, V_3Si, Nb_3Ge, and Nb_3Al. Unfortunately, large single crystals are necessary to determine completely the phonon dispersion curves in the search for phonon anomalies and direct measurements of the phonon linewidths. Of the above-mentioned A15 compounds, large crystals (>1 cm^3) could be grown only for V_3Si and V_3Ge, but the neutron scattering properties are so poor that only measurements of the lowest phonon branches could be made. Even in this case, however, much valuable information concerning phonon softening and lattice instabilities has been obtained. A similar situation exists[5] for Nb_3Sn, where only small crystals have been grown, but the limited amount of phonon data obtained by inelastic neutron scattering has also contributed substantially to furthering the state of knowledge of the lattice instabilities in this compound.

It is often very informative to compare the phonon dispersion curves of a moderate- or high-T_c material with a low-T_c or nonsuperconducting material to determine which regions, if any, of the dispersion curves are anomalous. This has proved very useful in the past for many different types of superconductors. A large crystal (>1 cm^3) of Nb_3Sb ($T_c \approx 0.2$ K) has been grown by Webb and Fisk and made available to us for lattice dynamic studies by coherent inelastic neutron scattering. Nb and Sb have excellent neutron scattering properties, which make a fairly complete lattice dynamics study feasible. The phonon studies were made at room temperature on the HB-1A, HB-2, and HB-3 triple-axis spectrometers at the HFIR. The determination of a rather complete set of dispersion curves in the [001] and [111] directions and a partial determination in the [110] direction along with a Born-von Kármán force constant analysis are the subjects of this report.

Although the A15 structure is cubic, the lattice dynamics is rather complex because there are two A_3B units in the primitive cell thereby giving $3n = 24$ branches in the Brillouin zone. However, in the [001] and [111] directions some branches are twofold degenerate, which reduces the number of branches to be determined to 17 and 16, respectively. It is extremely difficult, if not impossible, to identify all the branches without a group theoretical study *and* a knowledge of the polarization vectors of the modes. For the latter, it is necessary to have a lattice dynamics model to calculate the expected intensities of the phonon groups based on the polarization vectors.

A rather complete group theoretical analysis for all the symmetry points and directions for the A15 structure has been published by Achar and Barsch,[6] and these results have proved useful in the initial stages of this work. The calculated results reported herein for Nb_3Sb are based on a KfK, Karlsruhe, program which utilizes a Born-von Kármán force constant model fit to the experimental data. The model was first based on the acoustic branches and a few optical frequencies only, which yielded approximate values of the dominant force constants. This model was a great help in predicting yet unobserved phonon groups. In later refinements, more and more data were included, and finally we were able to reproduce not only the experimental frequencies but also the observed intensities quite accurately. (See Fig. 5.17.) This allowed us to assign with confidence all the modes at the Γ, X, and R points and most of the modes in the Δ and Λ directions. Only for some q values, where there is a great deal of mixing of the polarization vectors of certain branches and the instrumental resolution is too poor to resolve the different contributions to the observed intensity, could there be some error in the proper assignment of the observed phonon groups.

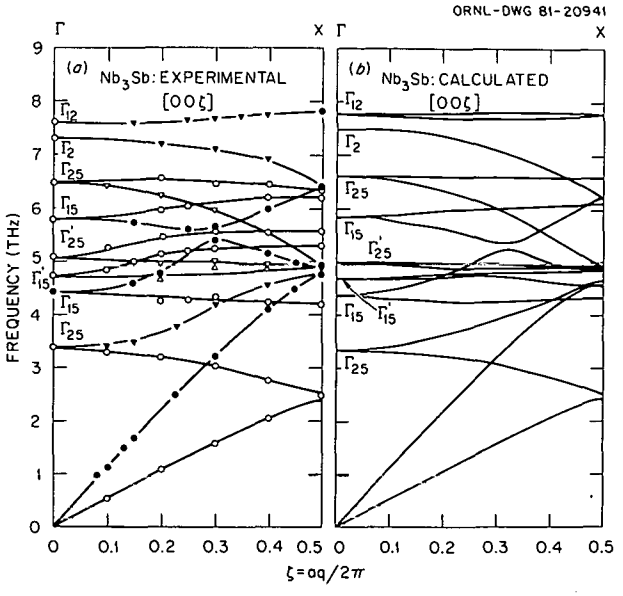

Fig. 5.17. (a) Measured phonon dispersion curves for Nb_3Sb in the [001] direction. (b) Calculated phonon dispersion curves based on Born-von Kármán model.

Our model included axially symmetric forces up to the seventh nearest neighbors. We note, however, that all interactions beyond those between third nearest neighbors yielded only minor improvements in the quality of fit. As was to be expected, the longitudinal force constant for the nearest-neighbors Nb-Nb (intrachain) interaction turned out to be the largest of all (i.e., 6.7×10^4 dyne/cm). However, the Nb-Sb interaction ($f_L = 4.5 \times 10^4$ dyne/cm) and the Nb-Nb interchain coupling ($f_L = 1.8 \times 10^4$ dyne/cm) are also rather strong.

Nb_3Sb is a very low T_c superconductor, and any anomalous features in the phonon dispersion curves due to electron-phonon interactions are thought to be small. There is no evidence from other experiments, such as temperature-dependent resistivity studies, to suggest any kind of phase transition, real or incipient. It is of interest to compare the limited phonon dispersion curves of Nb_3Sn obtained previously[5] by coherent inelastic neutron scattering with the results of this study. Since the atomic masses involved are almost identical, the observed differences can be attributed more directly to the differences in the electronic properties. The electron-phonon coupling constant λ is much larger in Nb_3Sn ($\lambda = 1.4$) than in Nb_3Sb ($\lambda = 0.4$), reflecting the large difference in their superconducting temperatures. There is an overall softening of the acoustic modes in Nb_3Sn all the way out to the Brillouin zone boundary.[6] The further softening of these modes as the temperature is reduced reflects the instability of the A15 lattice in this compound. (Nb_3Sn undergoes a martensitic transformation in the vicinity of 45 K.) The dispersion curves of Nb_3Sb are not expected to show appreciable change at low temperatures. Klein et al.[7] have observed two modes in Nb_3Sb by Raman scattering techniques. These modes show a frequency increase of about 3% on cooling to 90 K. The frequencies and the assignment of these modes (Γ_{12}, Γ_{25}) given by Klein et al. agree with the neutron scattering results.

1. Guest scientist from Kernforschungszentrum, Karlsruhe, Federal Republic of Germany.
2. Present address: Keio University, Yokohama, Japan.
3. Kernforschungszentrum, Karlsruhe, Federal Republic of Germany.
4. University of California at San Diego, La Jolla, Calif.
5. J. D. Axe and G. Shirane, *Phys. Rev. B* **8**, 1965 (1973).
6. B.N.N. Achar and G. R. Barsch, *Phys. Status Solidi (B)* **76**, 677 (1976).
7. M. V. Klein, private communication.

PHONON DISPERSION CURVES IN $PdTe_2$: A LAYERED SUPERCONDUCTOR

H. G. Smith
N. Wakabayashi[1]
T. Finlayson[2]
T. F. Smith[2]

The physical properties of layered compounds continue to be of high interest, as can be seen by the number of publications and special meetings devoted to this subject. The materials of greatest interest are those with strong intralayer interactions and weak interlayer interactions. This is particularly true for the metals, semimetals, and semiconductors, although the area of superionic conductors is also of interest. To understand these materials better, it is desirable to know their lattice dynamical properties as well as their electronic properties, since they are intimately related.

Inelastic neutron scattering has already proved useful, if not essential, in revealing many of the vibrational characteristics of such materials as pyrolytic graphite, MoS_2, $TiSe_2$, and $TaSe_2$.

Because of the size and/or quality of available crystals, it has not been possible to make a complete lattice dynamical study of these and similar compounds. However, a very large single crystal of $PdTe_2$ has recently become available for neutron scattering studies, and preliminary phonon measurements indicate that all the branches in the symmetry directions of the crystal should be observable.

$PdTe_2$ is a superconductor with a $T_c \sim 1.7$ K. It is isomorphous with $NiTe_2$, which is not superconducting but is magnetic, and dilution of $PdTe_2$ with Ni reduces its superconducting temperature markedly. Other physical properties of $PdTe_2$ have been determined. Extensive de Haas-van Alphen measurements have been made, and recently most of the experimental band structure has been obtained from angle-resolved photoemission spectroscopy.[3] Both of these studies have been compared to several band structure calculations and have revealed some discrepancies in the ordering of some of the calculated bands. A complete determination of the experimental phonon dispersion curves and a successful theoretical interpretation should be valuable in assessing the degree of the two dimensionality of the crystal and should also aid in the evaluation of the corrections of the various band structure calculations.

$PdTe_2$ belongs to the space group D_{3d}-P_{3m1} and has one formula unit per unit cell. This requires nine branches in the phonon dispersion curves. However, because of the crystal symmetry, there is a simplification in the c direction, and one should observe only six branches—three doubly degenerate branches polarized in the x-y plane (one acoustic branch and two optic branches) and three singlet branches polarized along the z direction (again, one acoustic and two optic branches).

The crystal was cleaved diagonally from a large cylindrical specimen about 4 cm long and 1 cm in diameter. The crystal cleaves very easily parallel to the c face, and the resulting surface is a highly reflecting silver surface. The lattice constants are a = 4.0365 Å and c = 5.1262 Å. This gives an abnormally low value for the c/a ratio of 1.270 compared to the ideal 1.63 ratio for close-packed structures which some of the layer compounds exhibit (e.g., the c/a ratio of $SnSe_2$ is 1.61). However, $TiSe_2$ and $TiTe_2$ have c/a ratios larger than the ideal—1.69 and 1.73, respectively.

The crystal was mounted with the (120) axis vertical, permitting phonon measurements in the ($h0l$) plane. The modes in the c direction are shown in Fig. 5.18. The highest branch at 5.4 THz is the doubly degenerate E_g optic mode involving symmetric motions of only the Te atoms, and they are constrained to the x-y plane. The next lowest branch at 5.15 THz is the totally symmetric A_{1g} optic mode which involves displacements only of the Te atoms, and these are constrained to the z direction. The mode at 4 THz is the nonsymmetric A_{2u} mode involving Pd motion out of phase with the Te atoms and along the z direction. The lowest optic mode at 2.25 THz is the Eu optic mode involving Pd motion out of phase with the Te atoms (x-y plane).

The so-called rigid layer modes correspond to the LA and TA modes at point A in the Brillouin zone. These modes have relatively high frequencies compared to several transition metal selenides which have much lighter masses. This may be a

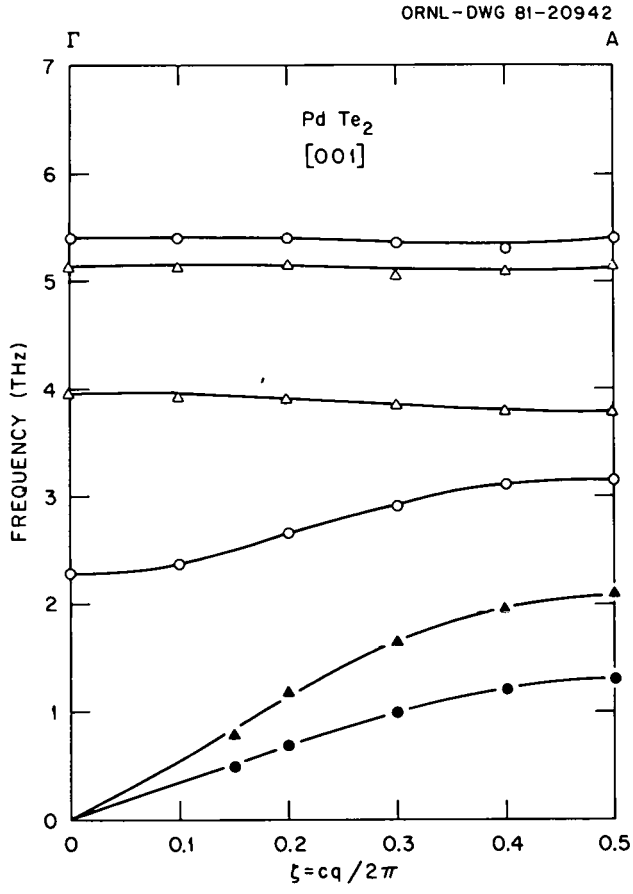

Fig. 5.18. Phonon dispersion curves for $PdTe_2$ in the [001] direction.

flection of the greater polarizability of Te vs Se id, therefore, leads to larger van der Waals forces between the layers.

In the Σ direction those branches with x-z polarizations have been measured. These branches, however, cannot cross, and in regions where they try to do so, their identification is not certain. Model calculations will be necessary to sort them out, and this will be attempted shortly.

1. Present address: Keio University, Yokohama, Japan.
2. Monash University, Clayton, Australia.
3. P. J. Orders, *Angle-Resolved Ultraviolet Photoelectron Spectroscopy of Some Transition Metal Ditellurides*, Thesis, La Trobe University, Bundoora, Victoria, Australia, 1980.

MEASUREMENTS OF PHONON DISPERSION CURVES, SPECIFIC HEATS, AND SUPERCONDUCTIVITY IN 4d NIOBIUM ALLOYS[1]

R. L. Cappelletti[2] W. A. Kamitakahara[4]
N. Wakabayashi[3] J. G. Traylor[5]
A. J. Bevolo[6]

Alloys consisting of Zr, Nb, and Mo show interesting physical phenomena; the superconducting T_c increases by the addition of Zr to Nb, which has T_c = 9.2 K. The maximum in T_c has been reported to occur for the Nb-Zr alloy containing approximately 20% of Zr (T_c = 11 K). The Zr-rich Nb-Zr alloys have been studied in connection with the ω phase, which is generally interpreted as a manifestation of the electronically driven phase transition in this alloy system. The addition of Mo to Nb, on the other hand, lowers T_c drastically. The anomalies in the phonon dispersion curves in Nb become weaker, resulting in higher phonon frequencies as Mo is added, and they are eventually replaced by a different set of anomalies found in Mo. These anomalies are believed to be closely related to the number of conduction electrons per atom, the *e/a* ratio.

In the present study inelastic neutron scattering measurements of phonon dispersion curves at room temperature have been carried out for three alloys: $Zr_{0.12}Nb_{0.88}$, $Zr_{0.05}Nb_{0.95}$, and $Zr_{0.033}Nb_{0.879}Mo_{0.088}$. The specific heats and room temperature elastic constants were also measured to determine the electronic density of states parameter γ and to provide information on the phonon energies at very small q. The phenomenological charge fluctuation model (CFM) was used to fit the phonon dispersion curves and to generate the phonon density of states for each sample. Moments of this distribution along with T_c and γ are used to determine $\langle I^2 \rangle$, the average electron-phonon interaction, for comparison with Butler's rigid-muffin-tin calculations.[7] Although detailed numerical agreement is not expected and does not occur, nevertheless, the general trend around Nb is reproduced. The Zr-Nb-Mo alloy is found to behave in detail like a Nb-Mo alloy of the same electron/atom ratio both in its dispersion curves and in other properties, indicating the importance of this parameter.

1. Summary of paper: *Physical Review B* (in press).
2. Ohio University, Athens, Ohio.
3. Present address: Keio University, Yokohama, Japan.
4. Present address: Ames Laboratory, Ames, Iowa.
5. Present address: Buena Vista College, Storm Lake, Iowa.
6. Ames Laboratory, Ames, Iowa.
7. W. H. Butler, *Phys. Rev. B* **15**, 5267 (1977).

PHONON ANOMALIES AND SUPERCONDUCTIVITY IN THE hcp METALS Tc, Re, AND Ru[1]

H. G. Smith N. Wakabayashi[2]

The phonon dispersion curves have been measured for the hcp metals Tc, Re, and Ru in the [100] direction at room temperature. A pronounced phonon anomaly has been observed for the LO mode in Tc and Re which is absent in Ru. A low-temperature study of Tc revealed a strong temperature dependence of the anomaly. It is suggested that the magnitude of the phonon anomaly is correlated with the strength of the electron-phonon interaction in these metals.

1. Abstract of paper: *Solid State Commun.* **39**, 371 (1981).
2. Present address: Keio University, Yokohama, Japan.

LATTICE DYNAMICS OF Ti, Co, Tc, AND SOME OTHER hcp METALS[1]

N. Wakabayashi[2] R. Scherm[3]
H. G. Smith

New phonon dispersion curves as determined by inelastic neutron scattering experiments are presented for the hcp metals Ti, Co, and Tc, along with their theoretical analyses in terms of the phenomenological charge fluctuation model.[4] The model was also used to reanalyze the phonon data for some other hcp metals Sc, Y, Zr, and Hf. For all the metals other than Sc and Y, it was found that the data could be successfully analyzed only with a *dipolar* charge fluctuation (DCF) model, in contrast to Nb which required only monopolar terms. For Sc and Y, the dispersion curves were satisfactorily analyzed in terms of a third-neighbor Born–von Kármán model without any charge fluctuation terms.

The softening of the longitudinal [001] mode near Γ observed in some of the metals appears to be closely related to an incipient instability in the electronic system toward the formation of a dipolar charge density wave. The temperature dependence of the large anomaly in Tc could be reproduced by extremely small changes in one of the parameters of the DCF model.

1. Summary of paper to be published.
2. Present address: Keio University, Yokohama, Japan.
3. Physikalisch Technische Bundesanstalt, Braunschweig, Federal Republic of Germany.
4. N. Wakabayashi, *Solid State Commun.* **23**, 737 (1977); *Comments Solid State Phys.* **10**, 11 (1981).

LATTICE DYNAMICS OF THE INTERMEDIATE VALENCE COMPOUNDS TmSe AND SmS

H. A. Mook F. Holtzberg[1]
R. M. Nicklow D. B. McWhan[2]

Intermediate valence effects have been the subject of considerable experimental and theoretical interest in the last few years.[3] A number of unusual physical properties result from mixed-valent effects, and several mixed-valent materials have been studied with neutron scattering so that a better understanding of the nature of the intermediate-valence ground state can be obtained. We have found that the lattice dynamics strongly affected by valence fluctuations in tl alloy system $Sm_{0.75}Y_{0.25}S$ and that the phonons in the LA mode in the (111) direction are coupled particularly strongly to valence fluctuations. Good agreement has been obtained between our results and a number of lattice dynamical calculations that correctly take into account the mixed-valent effects.[4] Recently additional neutron inelastic scattering measurements have been made on stoichiometric TmSe, which has a mixed-valent ground state. Phonon softening was again observed, particularly for the longitudinal modes in the [111] direction. It appears that valence fluctuations couple strongly to the phonons in TmSe.

Recently, we have been able to extend our phonon measurements to SmS under pressure. SmS at standard pressure is not mixed valent, and we would expect that the phonon dispersion curves would be typical of a standard rock salt material. At about 6.5 kbar, SmS undergoes a first-order transition to a metallic phase that has a mixed-valent ground state. We were successful in compressing a single crystal of SmS isotopically enriched in ^{154}Sm in a clamped pressure cell through the 6.5-kbar transition so that phonons could be measured in the mixed-valent state. Figure 5.19 shows the phonon dispersion curves for

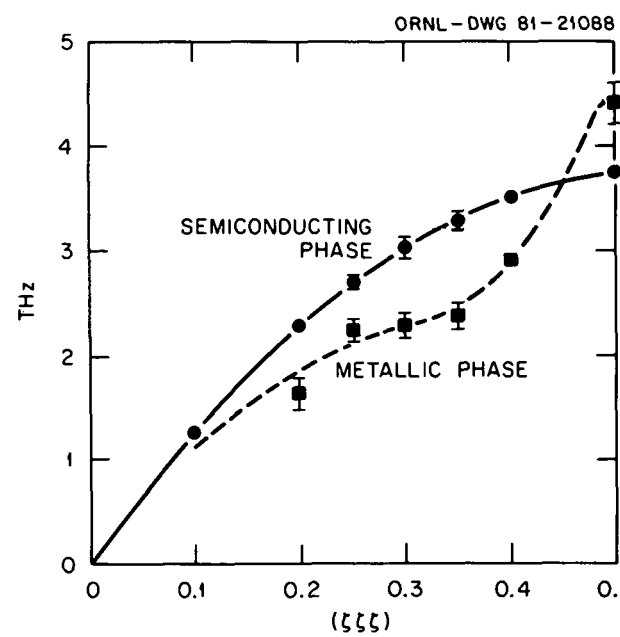

Fig. 5.19. Longitudinal acoustic [111] phonon dispersion curve for SmS at standard pressure and at 7 kbar.

SmS in the semiconducting state at standard pressures and in the metallic-mixed-valent state at high pressures. We see that there is a dramatic softening of the [111] LA phonon branch about halfway to the zone boundary. One can determine from symmetry considerations that the LA [111] phonon at the zone boundary does not couple to valence fluctuations, and we see that the phonon energy at the zone boundary increases with pressure as would be expected. The strong phonon softening for the [111] LA mode shows that there is a strong coupling between the valence fluctuations and the phonons in intermediate-valent SmS. Thus, any theory of the mixed-valent state for this material must correctly take into account the coupling between phonons and valence fluctuations.

1. IBM Thomas J. Watson Research Center, Yorktown Heights, N.Y.

2. Bell Laboratories, Murray Hill, N.J.

3. *Valence Fluctuations in Solids,* ed. by L. M. Falicov, W. Hanke, and M. B. Maple, North Holland, New York, 1981.

4. H. A. Mook and F. Holtzberg, p. 113 in *Valence Fluctuations in Solids,* ed. by L. M. Falicov, W. Hanke, and M. B. Maple, North Holland, New York, 1981.

LATTICE DYNAMICS OF $LaSn_3$[1]

C. Stassis[2] C.-K. Loong[2]
J. Zarestky[2] O. D. McMasters[2]
R. M. Nicklow

The room-temperature dispersion curves of $LaSn_3$ have been measured using inelastic neutron scattering techniques along with a selection of phonon frequencies at 750 K and 1200 K. No pronounced anomalies were observed, even though $LaSn_3$ has a high superconducting transition temperature (T_c = 6.42 K). This observation is consistent with other evidence[3] that the 5d conduction electrons contribute very little to the superconducting nature of $LaSn_3$, implying that this compound can be treated as a simple metal.

There does exist, however, a subtle feature of the $LaSn_3$ dispersion curves which can be seen in comparison with $CeSn_3$.[4] With nearly equal masses and similar outer electronic configurations, the dispersion curves for $CeSn_3$ and $LaSn_3$ should be identical, but near the lower Γ_{15} point, the $LaSn_3$ frequencies are much lower than the $CeSn_3$ frequencies (Fig. 5.20). We speculate that the difference may be due to the electron-phonon interaction in superconducting $LaSn_3$.

The behavior of the frequencies near the lower Γ_{15} point motivated the high-temperature measurement on $LaSn_3$. Except for these phonons, the frequencies showed the normal temperature dependence. However, at and near the lower Γ_{15} point, the phonons showed soft mode behavior quite similar to the behavior of the upper optic mode at Γ in Zr (ref. 5) and Tc.[6] In fact, the electronic density of states for both $LaSn_3$ (ref. 7) and Zr (ref. 8) have a peak just below E_F arising from doubly degenerate bands. Therefore, the soft mode behavior of the lower Γ_{15} mode could be explained by the lattice distortions from this mode splitting the degeneracy and lowering the electronic energy. These qualitative arguments are supported by

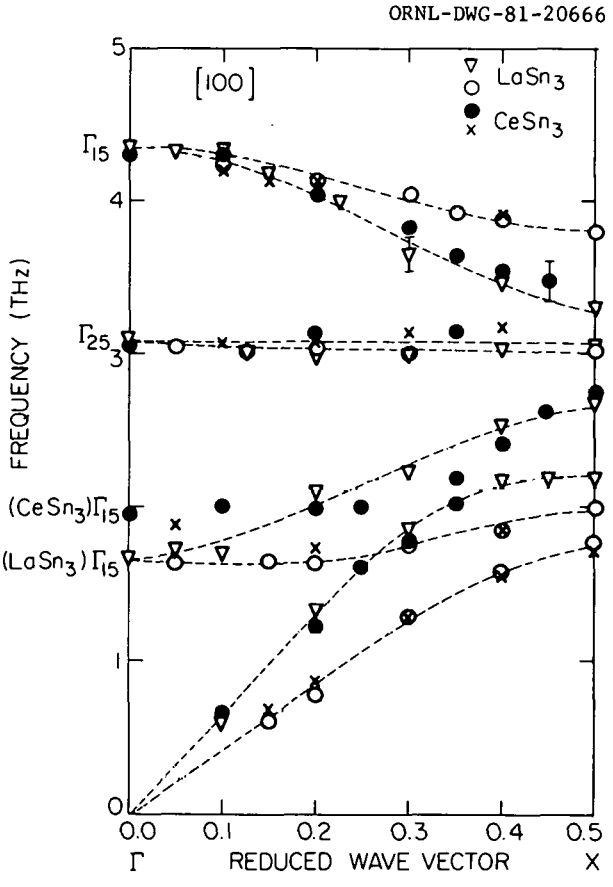

Fig. 5.20. Comparison of the room-temperature phonon dispersion curves along the [100] direction of $LaSn_3$ and $CeSn_3$.

frozen phonon calculations[8] for Zr and by recent theoretical models of the softening in superconducting hcp metals.[9]

The phonon frequencies were used in a conventional Born–von Kármán three nearest-neighbor model to obtain the atomic force constants which were then used to calculate the phonon density of states $g(\nu)$, the Debye temperature $\theta_D(T)$, and the lattice contribution to the specific heat.

1. Summary of paper: *Phys. Rev. B.* **23,** 2227 (1981).
2. Ames Laboratory and Iowa State University, Ames, Iowa.
3. A. M. Toxen, R. J. Gambino, and L. B. Welsh, *Phys. Rev. B* **8,** 90 (1973).
4. C. Stassis et al., *Solid State Commun.* **36,** 679 (1980).
5. C. Stassis et al., *Phys. Rev. B* **18,** 2637 (1978).
6. H. G. Smith and N. Wakabayashi, *Solid State Commun.* **39,** 371 (1981).
7. J. A. Begum and B. N. Harmon, private communication.
8. C. Stassis et al., *Phys. Rev. B* **19,** 181 (1979).
9. S. H. Liu, C. Stassis, and K. M. Ho, *Physical Review B* (in press).

NEUTRON SCATTERING STUDIES OF THE INTERCALATE $SbCl_5$ IN GRAPHITE

H. G. Smith P. C. Eklund[1]
R. M. Nicklow V. Yeh[1]

Many of the physical and electronic properties of graphite are related to its predominately two-dimensional nature resulting from the strong intralayer bonding and very weak interlayer bonding. This latter property permits the intercalation into graphite of a wide variety of atoms, such as the rare gases, alkali metals, $SbCl_5$, and SbF_5. It is probable that the molecules intercalate as several molecular species (e.g., $SbCl_6^-$, $SbCl_3$, and perhaps $SbCl_5$ to a limited extent). The degree of intercalation is very dependent upon the conditions of preparation and on the atomic or molecular species incorporated into the graphite lattice. Some are donor systems (i.e., electrons donated to the lattice, as exemplified by the alkali metals), and others are acceptor systems (electrons received from the lattice, as exemplified by the species $SbCl_6^-$). The amount of intercalation is described in terms of stages. Stage 1 implies every other layer is an intercalate layer, and Stage n implies there are n graphite layers between intercalate layers. A structural model for $SbCl_5$:graphite based on the results of an x-ray study[2] is shown in Fig. 5.21.

The system $SbCl_5$:graphite was considered very suitable for neutron scattering studies. Large samples can readily be made, they are stable in air, and Sb and Cl have very favorable neutron scattering properties. A sample consisting of about eight

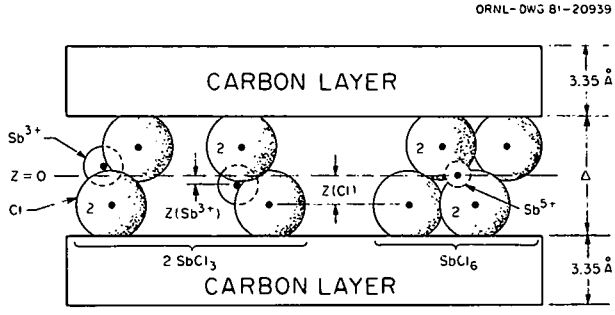

Fig. 5.21. Geometry of the centrosymmetric intercalate sandwich of $SbCl_5$:graphite.

platelets [10 × 10 × 1.5 cm] of Stage 2 material was investigated on the HB-3 spectrometer (HFIR) at room temperature. Preliminary phonon measurements were limited mostly to determining the longitudinal acoustical optic branches in the c direction, although a few trial measurements were made in searching for other modes. The results are shown in Fig. 5.22(a). Similar measurements for the Stage 4 material are shown in Fig. 5.22(b). The highest branch in each case is very tentatively assigned to the center-of-mass mode, where the intercalate sandwich vibrates against the carbon layers. The gaps between branches at the zone center and zone edge are a measure of the zone-folding interactions in the two materials. Clearly, additional measurements are desirable and necessary to elucidate the lattice dynamics of this interesting material, particularly with regard to the molecular species incorporated in the crystals. Low-temperature phonon studies are also contemplated so that a search for possible ordering of the intercalates within the planes can be made.

The elastic neutron scattering measurements have revealed an interesting anomaly associated with the (00l) reflections. For example, the even reflections $l = 2n$ (except for $l = 10$) all give the

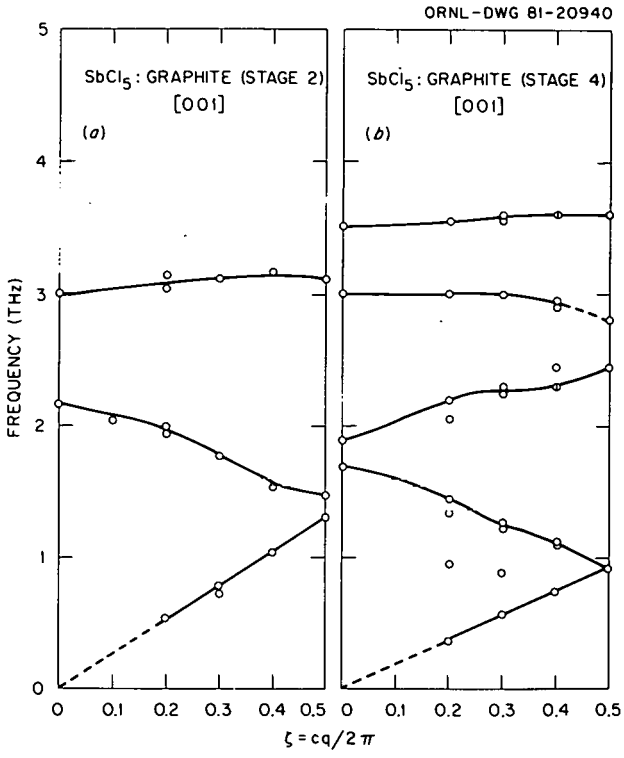

Fig. 5.22. (a) C-axis dispersion of the LA and LO phonons in State 2 $SbCl_5$:graphite. The lines are guides for the eye. **(b) C-axis dispersion of LA and LO phonons in State 4 $SbCl_5$:graphite.** The lines are guides for the eye.

same value of the *c*-lattice constant, as expected, whereas odd reflections (plus 0,0,10) give experimental peak positions that are slightly displaced from the calculated positions based on the lattice constant determined from the even reflections. This unusual, but interesting, behavior is possibly associated with some sort of correlated disorder in the intercalate layers.

A by-product of this investigation is the observation of the relatively large intensity of the (001) reflection which occurs for both materials. This suggests that both materials show promise as long-wavelength neutron monochromators (~10–20 Å) since, in principle, large samples can be made from pyrolytic graphite, and they are relatively stable in air.

1. University of Kentucky, Lexington, Ky.
2. M. L. Saylors et al., p. 117 in *Extended Abstracts of the 15th Biennial Carbon Conference,* American Carbon Society, Philadelphia, Pa., 1981.

NEUTRON SCATTERING STUDY OF WATER DYNAMICS IN BIOLOGICAL AND MODEL SYSTEMS[1]

E. C. Trantham[2] J. C. Clegg[4]
H. E. Rorschach[3] C. F. Hazlewood[5]
R. M. Nicklow

The role of water in biochemical and biological processes is one of the most important unsolved problems in biology. Nuclear magnetic resonance (NMR) spin-echo techniques have been used extensively to study water properties in biological cells by measurements of orientational relaxation times and translational diffusion coefficients. Present pulse technology requires a measuring time of a few milliseconds, which for water gives a diffusion distance >1 μ. This introduces difficulties in the interpretation of the results for a heterogeneous system such as the biological cell where the scale size is also of the order of a micron. The measured diffusion coefficient is then an average over the cellular environment, and it has not been possible to obtain a clear picture of the microscopic disposition of water within a cell.

The method of quasi-elastic neutron scattering (QNS) offers the possibility both to reduce the "measuring distance" to a few angstroms and to obtain details about the diffusion dynamics not available from NMR data. Our initial QNS study has been carried out on three systems: a model system of a 20% gel of polysaccharide agarose, a biological system of the cyst of brine shrimp (*Artemia*), and pure water. Agarose gel is a polymer $(C_{12}H_{17}O_9)_n$ of known structure. It contains 4 OH groups and 13 covalently bonded protons in each repeat unit. It was selected for a pilot study to determine if the spectrometer resolution was sufficient to separate the quasi-elastic line due to the diffusing water protons from the elastic line of the polymer nondiffusing protons. The brine shrimp cysts have a diameter of ~0.2 mm and consist of an inner mass of about 4000 cells surrounded by a complex noncellular shell. Their biochemical and physical properties have been studied, and the diffusion coefficient of water for various degrees of hydration has been measured by NMR methods. The degree of hydration can be varied over a wide range (0.02–1.5 g H_2O/g dry cyst), while still retaining viability for the extended periods needed for the neutron spectrometer scans.

The neutron measurements were obtained on the HB-2 triple-axis spectrometer at the HFIR.

Pyrolytic graphite monochromator and analyzer crystals, a neutron beam energy of 4 meV, and a Be filter were employed, giving an energy resolution of 0.10 meV. The samples were contained in aluminum sample holders sealed with an indium gasket.

Data were obtained for various values of Q between 0.7 and 1.9 $Å^{-1}$, where Q is the magnitude of the neutron scattering vector. The quasi-elastic peaks measured for each Q were analyzed by a least-squares fit with a five-parameter function, which included a linear background and the convolution of the spectrometer resolution function with an elastic line and with a Lorentzian quasi-elastic line. The width Γ of the Lorentzian line and the intensities of the two components were determined at each value of Q from the fitting parameters. The contribution from the agarose protons was determined by scattering from a D_2O gel. For the brine shrimp, the contribution from the protons of the "dry" cyst was determined from an extrapolation of line intensity vs hydration to zero water content.

Figure 5.23 shows the line width Γ as a function of Q^2 for pure water (solid curve) and for the 20% agarose and the 1.2-H_2O/g dry solid cysts. The data points are not shown for water. Their error bars are similar to those for the agarose and brine shrimp results.

The line width $\Gamma(Q^2)$ for water and the agarose gel could be fitted by a jump diffusion model with Γ given by

$$\Gamma = Q^2 \frac{D}{1 + Q^2 D \tau_0} .$$

For water, a fit of $\Gamma(Q^2)$ gives $D = 2.4 \times 10^{-5}$ cm^2/s and $\tau_0 \simeq 10^{-12}$ s. For agarose, the initial slope of $\Gamma(Q^2)$ is nearly the same as for pure water, although data at smaller Q are needed to be certain of this. There are deviations from the water curve at large Q, indicating an increased value of τ_0.

The brine shrimp data show substantial deviations from pure water. The line width is relatively independent of Q and is much narrower than that of pure water. This behavior is consistent with the NMR data on translational diffusion, which shows that the diffusion coefficient is greatly reduced from the pure-water value. The constancy of the line width with Q is also consistent with a rotational diffusion model, but we have not yet developed a model which is consistent with all the features of the spectra.

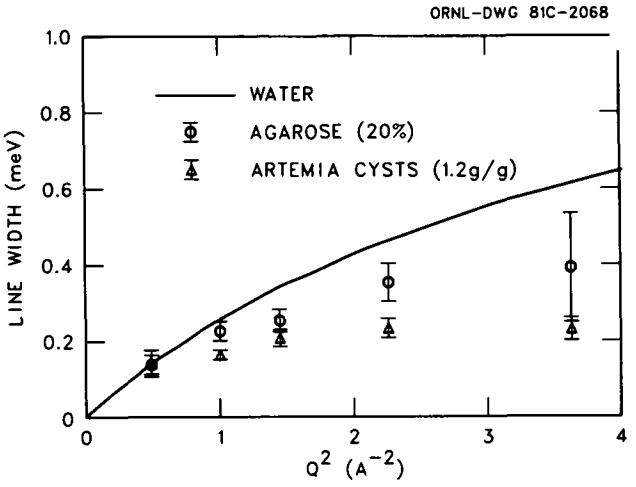

Fig. 5.23. The line width Γ for quasi-elastic neutron scattering from water, agarose gel, and artemia cysts.

1. Summary of paper to be published.
2. Oak Ridge Associated Universities thesis participant from Rice University, Houston, Tex.
3. Oak Ridge Associated Universities faculty participant from Rice University, Houston, Tex.
4. University of Miami, Coral Gables, Fla.
5. Baylor College of Medicine, Houston, Tex.

USE OF ULTRASONIC WAVES TO PRODUCE HIGH-INTENSITY PULSED NEUTRON BEAMS FOR TIME-OF-FLIGHT SPECTROSCOPY

H. A. Mook

High-quality large crystals of Si are now readily available for use in the semiconductor industry. These crystals reflect few neutrons since their mosaic spread is so small (a few seconds of arc). If high-power ultrasonic waves are introduced into the Si, the effective mosaic spread can be made as large as a few tenths of a degree, making the crystal useful as a neutron monochromator. If high-frequency ultrasonic waves are used, the neutron beam may be pulsed by rapidly switching the ultrasonic signal. An assembly of Si crystals has been built for use as a pulsed monochromator for the time-of-flight spectrometer at the HB-4 beam port at the HFIR. The separate crystals are placed

so that time focusing is utilized. The crystal assembly gives short neutron pulses of a few microseconds so that good energy resolution is obtained. The use of a series of focused crystals and the use of the cross-correlation technique of taking time-of-fight neutron data give a high neutron intensity. The spectrometer is expected to be particularly useful where high-energy resolution is needed.

DATA ACQUISITION SYSTEM FOR HFIR NEUTRON SPECTROMETERS

R. M. Nicklow S. P. King
E. Madden[1] D. E. Smith[1]

A new data acquisition system for the four triple-axis neutron spectrometers (HB-1, HB-1A, HB-2, and HB-3) at the HFIR has been designed, and it was installed during the fall of 1981.

The major components of the system consist of four PDP11/23 "satellite" computers, one for each of these spectrometers, and a fifth "host" computer, which is a PDP11/34. Each satellite computer has 128-K words of memory, two 2.5-M word disks, a Decwriter II, a Tektronix 4006 graphics terminal, and CAMAC interfacing to the experiment. The host computer has a 128-K word memory, four 2.5-M word disks, a high speed Decwriter III, a DEC VT100 graphics terminal, a Tektronix 4014 graphics terminal, and a Versatec 1200 plotter/line printer.

The system software for each satellite and the host is DEC RSX11-M, allowing for multiuser, multitask real-time data acquisition, data analysis and display, and some program development plus DECNET software to provide communication between each satellite computer and the host computer. Each satellite computer is a completely self-contained data acquisition system providing experimental control and some data analysis and display capabilities. To carry out extensive program development or complex data reduction, plotting, and analysis, the data and program files can be transferred to the host computer via the DECNET. For very extensive data analysis problems, a dedicated hardwired link to the ORNL PDP-10 computer is provided.

The custom operating programs are designed to provide the maximum flexibility of experimental control consistent with great simplicity of interactive communication between the experimenter and the system. For example, most of the spectrometer control and associated computational tasks can be initiated by typing simple two- or three-letter commands which are acronyms of the task description that the command initiates.

1. Instrumentation and Controls Division, ORNL.

MAGNETIC PROPERTIES

NEUTRON SCATTERING EVIDENCE ON LIFSHITZ BEHAVIOR IN MnP[1]

R. M. Moon J. W. Cable
Y. Shapira[2]

Many theoretical studies of the Lifshitz point (LP) have been published in recent years,[3] but there has been a notable absence of positive experimental evidence on the existence of this effect. In a magnetic system, this multicritical point has the following three essential characteristics: (1) The LP is a meeting point of three phases: a paramagnetic phase, a ferromagnetic phase, and a helicoidal phase with a variable wave vector, which is a function of thermodynamic parameters. (2) The transitions from the paramagnetic phase to both ordered phases should be of second order. (3) The wave vector **q** in the helicoidal phase should approach zero continuously as the LP is approached.

Based on a study of the phase diagram and on susceptibility measurements, it was recently concluded that the ferro-fan-para triple point of MnP is an LP.[4] However, neither the phase diagram nor the susceptibility gives direct evidence of the variation of **q** in the fan phase. The purposes of the present work are to measure the variation of **q** in the fan phase and to check whether indeed $\mathbf{q} \rightarrow 0$ as the LP is approached. We also attempted to determine the critical exponent β_k, which governs the variations of **q** along the fan-para phase boundary.

MnP has an orthorhombic cell and is ferromagnetic below 291 K, with a magnetic phase change at 50 K.[5] Neutron diffraction studies[6,7] have shown the low-temperature (zero-field) structure to be a spiral with the wave vector along **a** ($a > b > c$). Application of a magnetic field along **b** produces a fan phase, as shown by magnetization[8] and neutron diffraction studies.[9] The Mn moments are

ferromagnetically coupled in planes perpendicular to **a**, but the direction of these moments wobbles about the **b** direction in a periodic fashion with a wave vector

$$\mathbf{q} = 2\pi \frac{\delta}{a} \hat{a} \quad . \tag{1}$$

We have measured the position and intensity of the resulting magnetic satellites at the (2 ± δ 0 0) positions as functions of applied field and temperature (89–117 K).

Our results are summarized in Fig. 5.24, which shows the satellite peak intensity and δ as functions of field and temperature. The intensity curves may be used to construct the phase diagram. At a fixed temperature and low applied field, the system is ferromagnetic and the satellite intensity is zero.

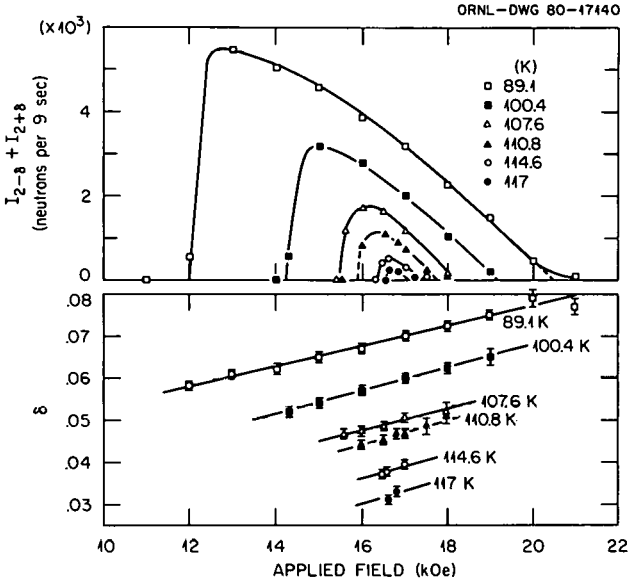

Fig. 5.24. Satellite peak intensity and wave vectors as functions of applied field and temperature.

The abrupt increase marks the ferro-fan phase boundary at H_1. In the fan phase the intensity rises rapidly with increasing field and then gradually falls to zero at the fan-para boundary. There is some ambiguity in the location of this boundary, as indicated by the 89.1-K data, because the intensity gradually tails off in the paramagnetic phase, indicating critical behavior. We have used an intuitive extrapolation, as indicated in Fig. 5.24, to locate this phase boundary at H_2. Our results for $H_1(T)$ are in excellent agreement with magnetostriction results on the same sample, but $H_2(T)$ as determined from Fig. 5.24 is consistently higher by roughly 600 Oe than the corresponding magnetostriction result. We believe that our extrapolation of the neutron intensities may lead to H_2 values which are slightly high, but there may be also a real difference attributable to the completely different experimental techniques.

The theory of the LP predicts a characteristic variation of **q** along the para-helicoidal segment of the λ line. In the theoretical papers[3] the phase diagram is in the P-T plane, where P is a general thermodynamic parameter. Very close to the LP and along the para-helicoidal boundary, **q** is predicted to vary as $(P - P_L)^{\beta_k}$, where P_L is the value of P at the LP. In mean-field theory $\beta_k = 0.5$, and to a better approximation $\beta_k = 0.54$.[3] To translate this theoretical prediction to the present case where the phase diagram is in the T-H plane, it is necessary to introduce scaling axes as discussed in ref. 4. Using their procedure, we expect that near the LP on the fan-para boundary

$$\delta = K(T_L - T)^{\beta_k}, \tag{2}$$

where T_L is the temperature at the LP.

Using the data of Fig. 5.24, we have determined $\delta(T)$ along the fan-para boundary and have made a least-squares fit of Eq. (2) with K, T_L, and β_k as adjustable parameters. The results are displayed in Fig. 5.25 with $\beta_k = 0.44 \pm 0.05$ and $T_L = 121.7 \pm 1.3$ K. Recalling the difficulty in exactly determining the fan-para boundary, we have also used the phase diagram of ref. 4 and our measurements of δ to establish $\delta(T)$ along the λ line. This results in a curve very similar to Fig. 5.25 with $\beta_k = 0.49 \pm 0.03$ and $T_L = 122.6 \pm 0.9$ K. It is not clear that the theoretical power law should extend over our temperature range, so that our value of β_k may only be approximate. Nevertheless, it appears that the temperature dependence of **q** is in approximate agreement with the theoretical prediction for LP behavior.

---

1. Summary of paper: *J. Appl. Phys.* **52,** 2025 (1981).
2. Francis Bitter National Magnet Laboratory, Massachusetts Institute of Technology, Cambridge, Mass.
3. For a review, see R. M. Hornreich, *J. Magn. Magn. Mater.* **15–18,** 387 (1980).

4. C. C. Becerra et al., *Phys. Rev. Lett.* **44,** 1692 (1980).
5. E. E. Huber and D. H. Ridgley, *Phys. Rev. A* **135,** 1033 (1964).
6. G. P. Felcher, *J. Appl. Phys.* **37,** 1056 (1966).
7. J. B. Forsyth, S. J. Pickart, and P. J. Brown, *Proc. Phys. Soc.* **88,** 333 (1966).
8. T. Komatsubara, T. Suzuki, and E. Hirahara, *J. Phys. Soc. Japan* **28,** 317 (1970).
9. Y. Ishikawa, T. Komatsubara, and E. Hirahara, *Phys. Rev. Lett.* **23,** 532 (1969).

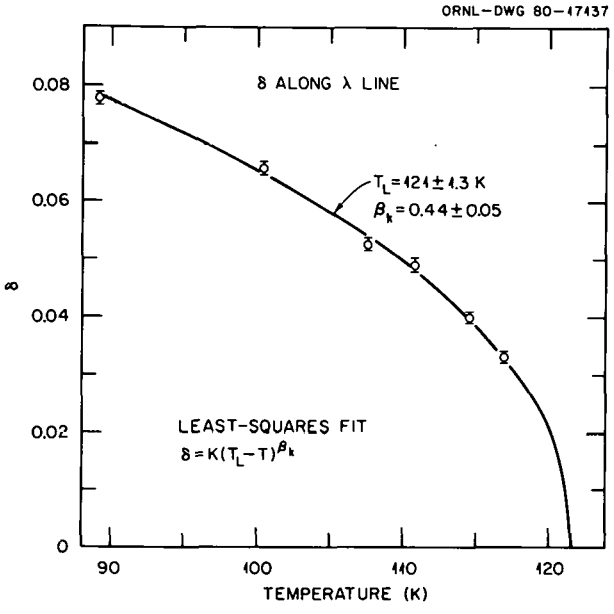

Fig. 5.25. Temperature dependence of δ along the fan-para phase boundary. The solid line is a least-squares fit of the theoretical relation to the experimental data.

A NEUTRON STUDY OF THE SPIN-REORIENTATION TRANSITION IN Gd[1]

J. W. Cable W. C. Koehler

The easy axis of magnetization in Gd is parallel to the hexagonal c axis between the Curie temperature (T_c = 293 K) and the spin-reorientation temperature ($T_r \simeq$ 235 K). The easy axis moves away from the c axis below T_r and lies on the surface of a c-axis cone of semiapex angle θ. The temperature dependence of θ has been determined both from torque magnetometer[2,3] and neutron diffraction[4] measurements, and although there are differences in detail, the results are in general agreement. θ lies in the 30–40° region at low temperatures; this increases up to about 70–90° in the 150–200 K region and then decreases precipitously to 0° at T_r. There is a small a-axis resistivity anomaly associated with T_r, and recent measurements by Sousa et al.[5] show that $d\rho/dt$ follows a $(T_r - T)^{-1/2}$ dependence below T_r. They assume that this resistivity anomaly is predominantly due to orientation fluctuations. If that is the case, then the observed $d\rho/dt$ behavior implies that sin θ should vary as $(T_r - T)^{1/4}$. One of the characteristic features of a second-order, spin-reorientation transition is that the Landau theory should be valid over a wide temperature range around T_r.[6] The order parameter sin θ should, therefore, follow a $(T_r - T)^{1/2}$ dependence, in contrast to the conclusions from the resistivity data.

In an attempt to resolve this apparent discrepancy, we have remeasured $\theta(T)$ with particular emphasis on the region near T_r. Intensity data were collected for the (002) and (100) Bragg reflections from a ^{160}Gd single crystal as a function of temperature in the region 9–310 K. The intensities for $T \geqslant 298$ K were assumed to be purely nuclear so that approximate magnetic intensities could be obtained from temperature differences. Here, peak height intensities were used rather than integrated intensities to minimize the effects of the quasi-elastic paramagnetic scattering near T_c. The temperature dependences of the raw magnetic-to-nuclear intensity ratios are shown in Fig. 5.26. The unusual temperature dependences shown here reflect the spontaneous spin-reorientation effects of Gd. These intensity ratios were corrected for thermal motion using a Debye temperature of 195 K to obtain squared structure factor ratios. In a ferromagnet, these ratios are

$$\frac{F_M^2}{F_N^2} = \frac{p^2 q^2}{b^2} \quad , \tag{1}$$

where p and b are the magnetic and nuclear amplitudes while $q^2(002) = \sin^2\theta$ and $q^2(100) = 1 - \frac{1}{2}\sin^2\theta$. The nuclear amplitude of ^{160}Gd is $b = 0.915 \times 10^{-12}$ cm, while the magnetic amplitude is a function of scattering vector and temperature. This dependence is given by

$$p(K,T) = 0.27\mu f(K)\frac{\sigma(T)}{\sigma(0)} \quad , \tag{2}$$

where $\mu = 7\ \mu_B$, $\sigma(T)/\sigma\ (0)$ is the relative magnetization, and $f(K)$ is well established by the

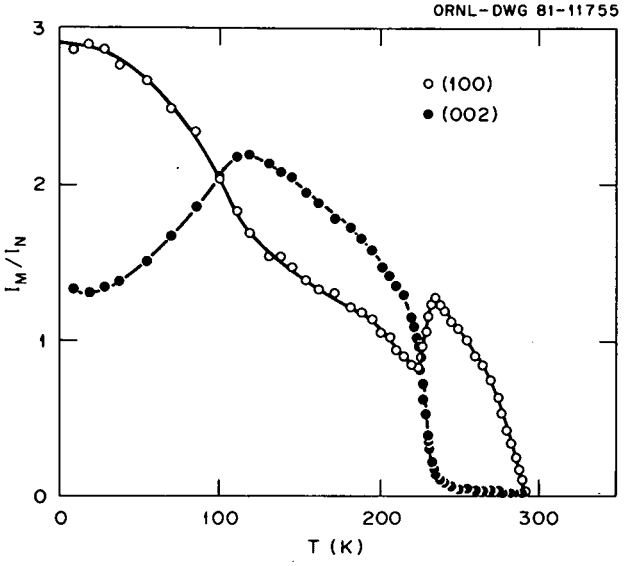

Fig. 5.26. Temperature dependence of the magnetic-to-nuclear intensity ratios for the (100) and (002) reflections of Gd.

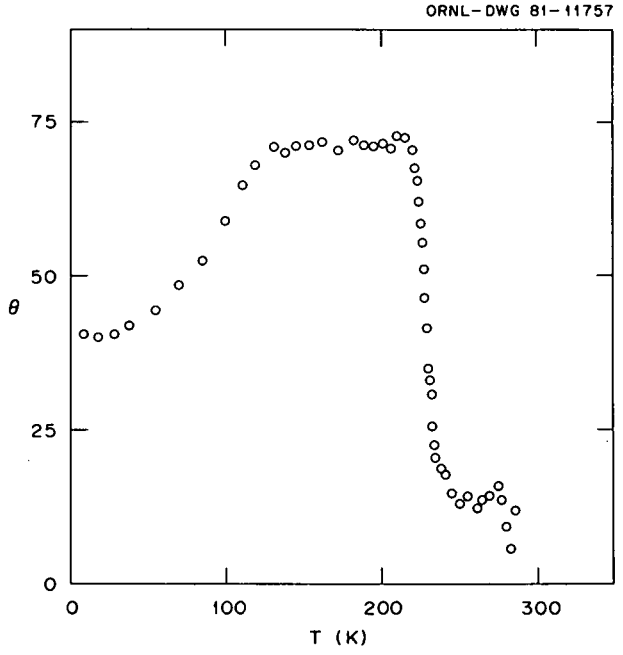

Fig. 5.27. Temperature dependence of the cone angle θ in Gd. For $T > 235$ K, the observed θ actually corresponds to fluctuations about zero θ.

form factor measurements of Moon et al.[7] The neutron results for $\sigma(T)/\sigma(0)$, which are obtained by an appropriate combination of the (002) and (100) data, agree with the magnetization data of Nigh, Legvold, and Spedding[8] over the entire ferromagnetic region, with discrepancies of only a few percent in those temperature regions where the intensity ratios are changing most rapidly.

The neutron results for $\sigma(T)/\sigma(0)$ were used in Eqs. (1) and (2) to determine the temperature dependence of θ shown in Fig. 5.27. This curve is similar to those previously determined[2-4] for Gd but contains more detail, especially in the phase transition region near T_r. A surprising result is that θ does not go to zero at T_r but, instead, remains finite out to about 285 K. This can also be seen in Fig. 5.26 where the (002) intensity ratio remains finite above T_r. Temperature difference curves in this temperature region show that the intensity appears at the Bragg position with no apparent broadening. Another characteristic feature of a second-order, spin-reorientation transition is that the spin-orientation fluctuations have correlation lengths that are typically 10^3 times larger than those associated with the moment fluctuations at T_c. We, therefore, attribute the magnetic intensity remaining at (002) above T_r to long-wavelength spin-orientation fluctuations. If such fluctuations have an amplitude of $\pm\delta\theta$ from an average $\bar{\theta}$, then instead of $q^2 = \sin^2\theta$ for (002) we should use $q^2(002) = \sin^2\bar{\theta}\cos^2\delta\theta + \cos^2\bar{\theta}\sin^2\delta\theta$. Above T_r, where θ is presumably zero, the (002) intensity is then proportional to $\sin^2\delta\theta$, and the finite values shown in Fig. 5.27 for $T > T_r$ actually correspond to $\delta\theta$ fluctuations about $\bar{\theta} = 0$. The correlation length of these fluctuations is necessarily large enough that only Bragg scattering is observed (~500 Å). These fluctuations should also occur below T_r, and this complicates the determination of the temperature dependence of the order parameter, which in the presence of fluctuations becomes $\sin\bar{\theta}$. Fortunately, $\delta\theta$ is small, and to first order we can neglect the fluctuations and use $q^2(002) = \sin^2\theta$ as the square of the order parameter for this transition. The temperature dependence of this parameter just below T_r shows that the order parameter follows a $(T_r - T)^{1/2}$ dependence as expected within the framework of the Landau theory. Since this is inconsistent with the spin-orientation fluctuation interpretation of the $d\rho/dT$ behavior, we conclude that the resistivity anomaly at T_r is not associated with spin-orientation fluctuations. Instead, this anomaly is probably associated with magnetoelastic

fects which produce an anomaly in the elastic nstant C_{33} just below T_r.[9] This constant describes the velocity of propagation of longitudinal acoustic phonons along the c axis, and the observed softening just below T_r should increase the a-axis resistivity through the electron-phonon interaction.

1. Summary of paper: *Journal of Applied Physics* (in press).
2. C. D. Graham, *J. Phys. Soc. Japan* **17,** 1310 (1962).
3. W. D. Corner, W. C. Roe, and K.N.R. Taylor, *Proc. Phys. Soc. London* **80,** 927 (1962).
4. J. W. Cable and E. O. Wollan, *Phys. Rev.* **165,** 733 (1968).
5. J. B. Sousa et al., *J. Magn. Magn. Mater.* **15–18,** 892 (1980).
6. K. P. Belov et al., *Sov. Phys. Usp.* **19,** 574 (1976).
7. R. M. Moon et al., *Phys. Rev. B* **5,** 997 (1972).
8. H. E. Nigh, S. Legvold, and F. H. Spedding, *Phys. Rev.* **132,** 1092 (1963).
9. M. Long, A. R. Wazzan, and R. Stern, *Phys. Rev.* **178,** 775 (1969).

SUPERCONDUCTIVITY AND MAGNETISM IN $Ho_{1-x}Er_xRh_4B_4$[1]

H. A. Mook, D. G. Hinks[2], W. C. Koehler, M. B. Maple[3], S. K. Sinha[2], Z. Fisk[3], G. W. Crabtree[2], D. C. Johnston[3], L. D. Woolf[3]

Since the discovery of reentrant superconductivity in $ErRh_4B_4$,[4] there has been considerable interest in the nature of the magnetic transitions in these types of materials. The $Ho_{1-x}Er_xRh_4B_4$ alloy system is an ideal system to study the interaction between magnetism and superconductivity since a wide variety of phenomena occurs throughout the alloy system. We have made neutron diffraction measurements on several alloys in this system to determine the type of magnetic ordering and its temperature dependence. $HoRh_4B_4$ is not a superconductor but orders ferromagnetically at 6.80 K with the moment directed along the c axis. A mean-field model gives an excellent description of the temperature dependence of the magnetization. This is unusual and is found in no other metallic system.

As Er is introduced into $HoRh_4B_4$, the magnetic ordering temperature drops, but the materials become superconducting at higher temperatures. $Ho_{0.6}Er_{0.4}Rh_4B_4$ is superconducting at about 7 K and magnetic at 3.60 K. We have found ferromagnetic c-axis ordering in this material also, with a moment consistent with only the Ho ordering. The magnetic transition now becomes first-order, superconductivity is destroyed, and long-range ferromagnetism is created in a sharp transition at 3.60 K.

Magnetic ordering in $ErRh_4B_4$ is in the basal plane so that Er and Ho have orthogonal competing magnetic anisotropies in the alloy system, and alloys near 75% Er have compositions in the vicinity of a multicritical point. Alloys in this region have complex ordering in which two transitions are found. $Ho_{0.3}Er_{0.7}Rh_4B_4$ has a magnetic transition with c-axis ordering at 1.1 K and an additional transition with basal plane ordering at 0.87 K. Superconductivity is destroyed in a first-order transition at 1.1 K where Ho aligns ferromagnetically along the c axis.

A single crystal of $ErRh_4B_4$ has become available, and more detailed data have been obtained for this material. Basal-plane ferromagnetic ordering that coexists with superconductivity is found below about 1.2 K, but in addition, satellites are found near the magnetic reflections, showing that a sinusoidally modulated state also exists. The magnetization as determined from the (101) reflection is shown in Fig. 5.28. As the material is cooled, ferromagnetism and superconductivity coexist with a modulated phase until 0.7 K, when both superconductivity and the modulated phase disappear in a first-order transition, leaving a simple ferromagnetic structure. Large hysteresis is found upon warming, and superconductivity is regained at 0.74 K. There is considerable interest in the nature of the coexisting state, and further SANS measurements are planned.

1. Summary of paper to be published.
2. Argonne National Laboratory, Argonne, Ill.
3. University of California at San Diego, La Jolla, Calif.
4. W. A. Fertig et al., *Phys. Rev. Lett.* **38,** 987 (1977).

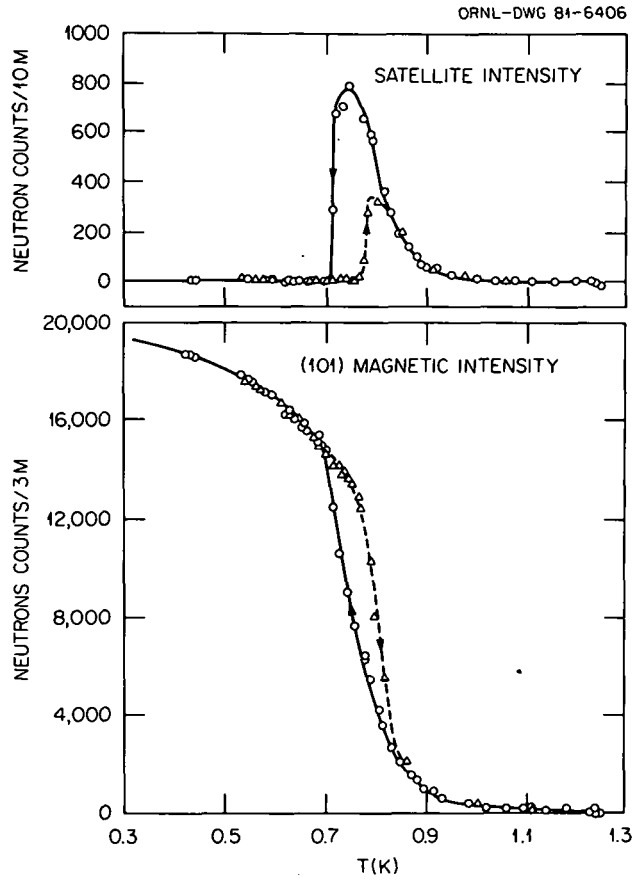

Fig. 5.28. Magnetic intensity vs temperature for the (101) reflection and for a satellite reflection in $ErRh_4B_4$.

MAGNETIC STRUCTURES OF HoB_4

W. C. Koehler Z. Fisk[1]
H. A. Mook M. B. Maple[1]

In a previous report,[2] we presented a brief summary of the magnetic properties of HoB_4 as determined from neutron diffraction from polycrystalline specimens. Since then, we have investigated a number of single-crystal specimens. Our earlier conclusions about the complexity of the magnetic structures have been confirmed.

Magnetic susceptibility, specific heat, and resistivity measurements by Fisk et al.[3] have revealed two ordering transitions in HoB_4 at temperatures near 7.1 and 5.7 K. Moreover, the macroscopic measurements indicate that the higher temperature transition is of second order and the lower one is of first order. The present neutron scattering data on single crystals confirm these results.

The data in both temperature ranges have thus far resisted a complete interpretation, and there are some inconsistencies in the data obtained with different specimens. However, a number of conclusions can be reached.

In the higher temperature phase the principal ordered mode is an incommensurate-ordered structure characterized by two wave vectors, $k_1 = (0, 0, 0.425)$ and $k_2 = (\delta, \delta, 0)$, and equivalent [110] directions. The magnitude of δ varies with temperature, but it is 0.021 reciprocal lattice vector units at 5.7 K. Polarization analysis experiments have established that the moments in a given domain are parallel to a [110] direct-lattice direction, thus normal to the c axis of the tetragonal unit cell.

Below 5.7 K, at which temperature a first-order transition occurs, the magnetic structure changes to a commensurate antiferromagnetic structure of the type previously reported for ErB_4 by Schafer, Will, and Buschow.[4] An analysis of the powder data at 4.2 K yields values of the components of the moment parallel and perpendicular to the c axis of $\mu_\parallel = 6.7\ \mu_B$ and $\mu_\perp = 4.0\ \mu_B$.

1. University of California at San Diego, La Jolla, Calif.
2. W. C. Koehler et al., *Solid State Div. Prog. Rep., Feb. 29, 1980,* ORNL-5640, p. 202.
3. Z. Fisk, M. B. Maple, D. C. Johnston, and L. D. Woolf, private communication.
4. W. Schafer, G. Will, and H.H.J. Buschow, *J. Chem. Phys.* **64,** 1994 (1976).

TEMPERATURE DEPENDENCE OF THE SPIN DENSITY ASYMMETRY IN Ni[1]

J. W. Cable

Magnetic form factor measurements[2] on ferromagnetic Ni show an unpaired spin density that is highly asymmetrical and arises mostly from unpaired d electrons with t_{2g} symmetry (81% t_{2g} at 295 K). This symmetry character depends quite strongly on the details of the electronic band structure and thus provides an important check on the validity of such calculations. Alternatively, the observed symmetry may be used as input data for adjusting the interaction matrix elements in these calculations. This latter approach is used, for example, by Cooke and Davis[3] in their highly successful calculations of the dynamical susceptibili-

ties of Fe and Ni. Clearly, this symmetry character and its dependence on temperature are important to an understanding of the spin dynamics of these materials at elevated temperatures. Previous measurements showed no temperature dependence of the symmetry properties for Fe,[4] Co,[5] and a series of Co-Fe and Co-Ni alloys.[6] In this paper we report the first observation of a thermal effect on this symmetry character for a transition metal.

The magnetic form factor of Ni can be written as[1]

$$f(K)=\frac{2}{g}(1+\alpha)f_{3d}(K)-\frac{2}{g}\alpha[f_{NL}(K)] + \frac{g-2}{g}f_{\text{orb}}(K) \ , \quad (1)$$

where $2/g$ is the fractional spin moment; α is the fraction of the spin moment with nonlocal character; and f_{3d}, f_{NL}, and f_{orb} are appropriate form factors for the local spin, nonlocal spin, and orbital components, respectively, of the moment. The form factor for d electrons in a cubic field is given by[7]

$$f_{3d}(K)=\langle j_0\rangle+\left(\frac{5}{2}\gamma-1\right)A_{hkl}\langle j_4\rangle \ , \quad (2)$$

where $\langle j_0\rangle$ and $\langle j_4\rangle$ describe the spherical and aspherical parts of the spin density, A_{hkl} depends on direction in the crystal, and γ is the fraction of the spin density with e_g symmetry. Mook[1] found that this form factor reproduces his room temperature Ni data with $g = 2.20$ taken from magnetomechanical data and with $f_{NL}(K)$ contributing only at $K = 0$. The best fit was obtained with Hartree-Fock Ni^{2+} functions for $\langle j_0\rangle$, $\langle j_4\rangle$, and $f_{\text{orb}}(K)$ and with $\alpha = \gamma = 0.19$.

We assume this formalism to determine the temperature dependence of the asymmetry parameter γ. In so doing, we use the (333)(511) pair of reflections that occurs at the same scattering angle and therefore has the same $\langle j_0\rangle$, $\langle j_4\rangle$, $f_{NL}(K)$, and $f_{\text{orb}}(K)$. The difference between the form factors for these reflections thus contains only an aspherical term,

$$\Delta f \equiv f_{333}-f_{511} = \frac{2}{g}(1+\alpha)\left(\frac{5}{2}\gamma-1\right)\langle j_4\rangle(A_{333}-A_{511}) \ , \quad (3)$$

from which γ can be determined if α and $\langle j_4\rangle$ are known. The simplest approach is to assume the same α and $\langle j_4\rangle$ values used by Mook for his room temperature data. Because form factor measurements for a variety of ferromagnetic alloys show that the nonlocal moment is proportional to the average moment, it is reasonable to assume that α is indeed a constant and is independent of temperature. We must, however, recognize the possibility that $\langle j_4\rangle$ is temperature dependent. The wave functions and, therefore, the form factors are expected to be slightly different for spin-up and spin-down electrons. As a result, the spin density contains a contribution from the paired electrons in addition to the usual unpaired electron term. In an itinerant system, where the number of unpaired electrons may vary with temperature, this could result in temperature-dependent $\langle j_0\rangle$ and $\langle j_4\rangle$ functions. However, the magnitude to be expected for such an effect is not known. Fortunately, there is an experimental cross-check on the constancy of these parameters. Since the A_{hkl} for this pair of reflections is nearly equal in magnitude and opposite in sign ($A_{333} = -0.667$, $A_{511} = 0.650$), the aspherical term contributes less than 1% to the sum of their form factors and can be neglected. We can then define an average form factor at this K, given by

$$\langle f\rangle \equiv \frac{1}{2}(f_{333}+f_{511}) = \frac{2}{g}(1+\alpha)\langle j_0\rangle+\frac{g-2}{g}f_{\text{orb}}(K) \ , \quad (4)$$

where $f_{NL}(K)$ has been dropped because it contributes only at small K. We note that the $\langle j_0\rangle$ term is the major part of $\langle f\rangle$, so that any temperature dependence in either α or $\langle j_0\rangle$ should be observed in $\langle f\rangle$. In fact, we find that $\langle f\rangle$ is constant within 5% limits and conclude that α and $\langle j_0\rangle$ are temperature independent. In that case $\langle j_4\rangle$ should also be temperature independent, and Eq. (3) can be used to obtain $\gamma(T)$ from $\Delta f(T)$.

Polarized-neutron flipping-ratio measurements were made on an isotopic single crystal of ^{60}Ni in the temperature range from 4 to 634 K. Form factors were obtained by using the magnetization data of Crangle and Goodman,[8] and $b(^{60}Ni) = 0.291 \times 10^{-12}$ cm. The latter was determined by comparison of the room temperature p/b values with

those of Mook[2] assuming $b_{Ni} = 1.03 \times 10^{-12}$ cm for natural Ni.

The temperature dependence of $\langle f \rangle$ and Δf is shown in Fig. 5.29. The average form factor remains essentially constant with a value of 0.070, compared with a calculated value of 0.068 for the Hartree-Fock Ni^{2+} ion. By contrast, the form factor difference decreases continuously with increasing temperature. The corresponding e_g population, shown in Fig. 5.30, increases from 19% at 4.2 K up to about 26% at 634 K. The temperature dependence of γ shows that the t_{2g} magnetization falls off more rapidly with temperature than does the e_g magnetization. The origin of this difference in thermal behavior for the two subbands is not presently understood. The only intrinsic temperature dependence in the electronic band structure is in the Fermi distribution function. However, calculations by Cooke[7] indicate that this thermal effect, although significant, is insufficient to account for the observations. We suggest that the increasing e_g population is caused by a different temperature dependence of the spin-splitting for the two subbands. Specifically, we expect the t_{2g} splitting to decrease more rapidly with temperature than does the e_g.

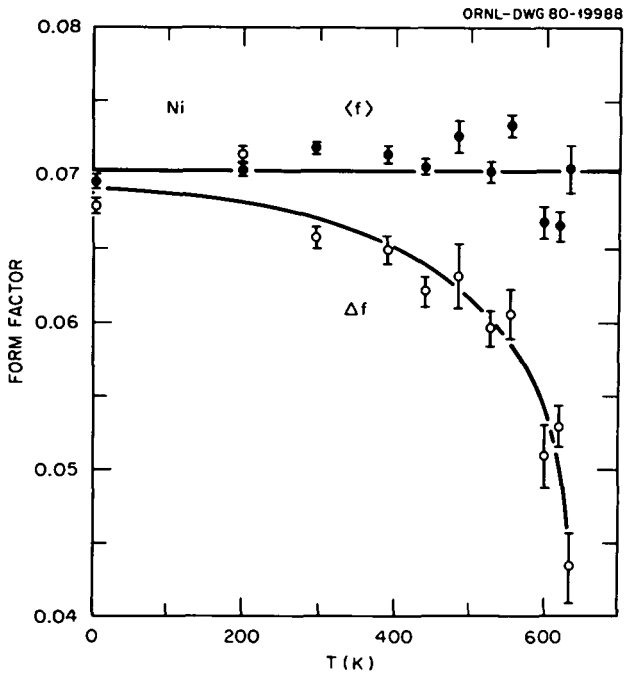

Fig. 5.29. Temperature dependence of the average $\langle f \rangle$ and the difference Δf form factors for the (333)(511) pair of Bragg reflections of Ni. Equations (3) and (4) define Δf and $\langle f \rangle$, respectively. The solid curves serve only as a visual aid and have no theoretical significance.

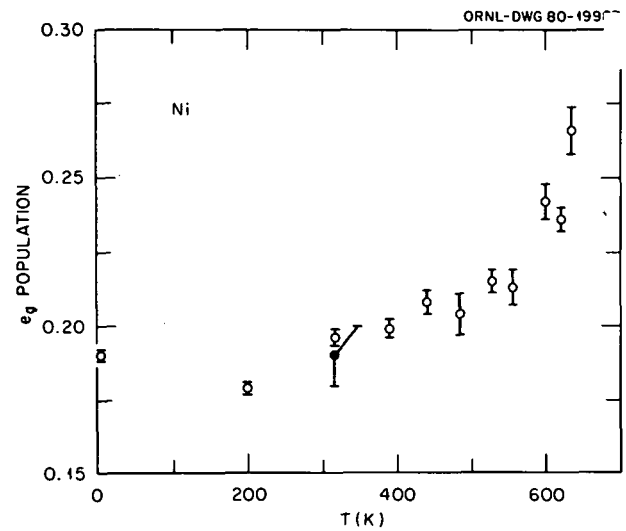

Fig. 5.30. Temperature dependence of γ, the e_g population, in Ni as determined from Eq. (3). The filled data point is from Mook.[2]

1. Summary of paper: *Phys. Rev. B* **23,** 6168 (1981).
2. H. A. Mook, *Phys. Rev.* **148,** 495 (1966).
3. J. F. Cooke and H. L. Davis, *AIP Conf. Proc.* **10,** 1218 (1973).
4. R. C. Maglic, *AIP Conf. Proc.* **5,** 1420 (1972).
5. F. Menzinger and A. Paoletti, *Nuovo Cimento* **10B,** 565 (1972).
6. G. Kadar and F. Menzinger, *Solid State Commun.* **12,** 909 (1973).
7. J. F. Cooke, private communication.
8. J. Crangle and G. M. Goodman, *Proc. Roy. Soc. London A* **321,** 477 (1971).

MAGNETIZATION DENSITY IN FERROMAGNETIC $TiBe_{1.8}Cu_{0.2}$[1]

G. P. Felcher[2] J. W. Cable
J. L. Smith[3]

The compound $TiBe_2$ has recently received a considerable amount of attention as one of the few cases in which the onset of magnetic ordering comes about as a result of the unique properties of the band structure of the material.[4,5] Pure $TiBe_2$ is reported[5] to be antiferromagnetic; however, the

>artial substitution of beryllium with copper .esults[6] in ferromagnetism for $TiBe_{2-x}Cu_x$ with $x \geq 0.14$. The Curie temperature increases rapidly with x, and the magnetizations give linear Arrott plots which are indicative of a Stoner-like, or itinerant, character of the ordering. The magnetization shows no tendency toward saturation at 1.6 K and 5.4 T, where the magnetization achieved is a mere fraction of that appropriate to the free titanium ion. The purpose of the present experiment is to determine by polarized-neutron diffraction the magnetic density distribution in this weak itinerant ferromagnet.

Flipping-ratio measurements were made on a polycrystalline sample of $TiBe_{1.8}Cu_{0.2}$ maintained at 4.2 K in a field of 1.0 T applied normal to the scattering plane. In these conditions the magnetization equals 0.112 ± 0.004 μ_B per Ti atom. All the Bragg reflections up to and including the (444) reflection were measured. Extinction and double Bragg scattering effects were neglected because of the small crystallite size.

After the polarized-neutron measurements, the sample was crushed into a fine powder, and the crystal structure was examined by unpolarized neutron diffraction. This latter test confirmed the finding of earlier x-ray work,[6] namely, that $TiBe_{1.8}Cu_{0.2}$ crystallizes in the cubic Laves phase C-15 with a cell parameter of 6.5 Å and with the Cu atoms going entirely in substitution on the Be sites.

The magnetic structure factors obtained from the flipping-ratio measurements were Fourier transformed to obtain the magnetic density. The [110] cut, which contains the direct bonds between Ti atoms, is presented in Fig. 5.31. The contour levels have an uncertainty due both to the error of the original data points and to the truncation of the Fourier series after the (444) term; however, we estimate the uncertainty to be less than half of the step between the contour levels.

The magnetization of $TiBe_{1.8}Cu_{0.2}$ is concentrated around the Ti positions. The distribution is tetrahedral, reflecting the point symmetry of such positions in the crystal structure, and elongated along the Ti-Ti bond.

This picture is in rather sharp contrast to that of the isostructural $ZrZn_2$, which is also a weak ferromagnet. In the latter compound, a polarized-neutron experiment showed[7] the presence of a very diffuse magnetization weakly concentrated around ıe Zr sites. The trend is not entirely unexpected, ɔecause the radial extent of the 4-d wave functions

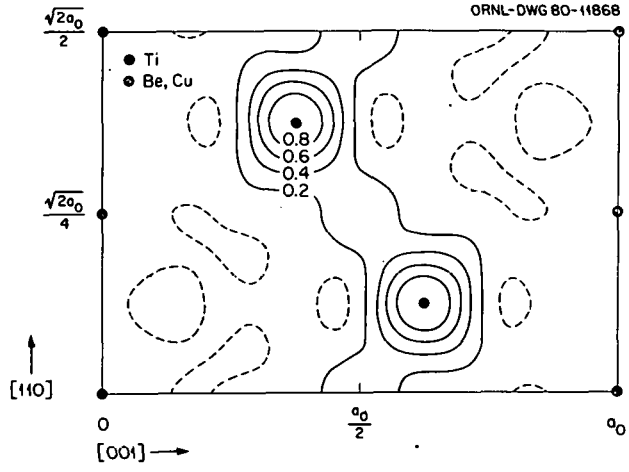

Fig. 5.31. (110) section of the magnetic moment density in $TiBe_{1.8}Cu_{0.2}$. The contours are in units of 0.04 $\mu_B/Å^3$. The dashed lines are zero contours and enclose low negative density regions.

of Zr is certainly larger than the corresponding 3-d wave functions of titanium.

The form factor of Ti as measured in the present compound and, for comparison, the Hartree-Fock form factor[8] of Ti^{2+} (spin only) are plotted in Fig. 5.32. The present form factor is considerably more

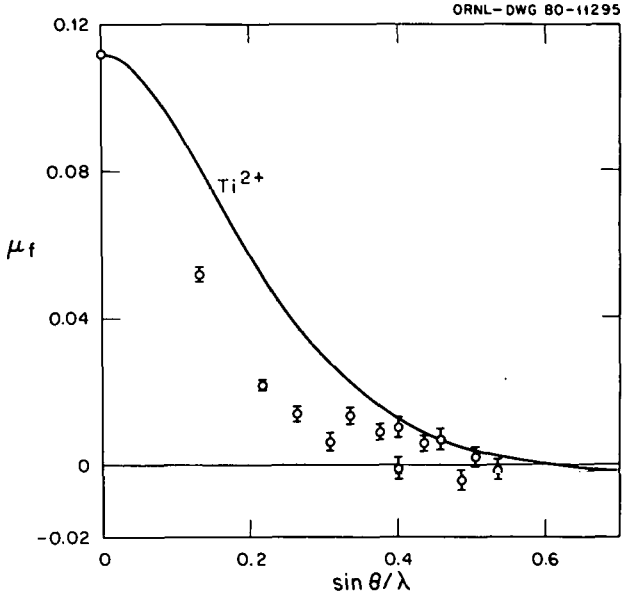

Fig. 5.32. The moment-form factor product for $TiBe_{1.8}Cu_{0.2}$. The solid curve is the spin-only Hartree-Fock form factor of Ti^{2+} multiplied by the magnetization at 4.2 K and 1.0 T.

contracted than the ionic one, which is to be expected in a metal for an element at the beginning of the 3-d series. No band calculations have been performed yet on the spatial extent of the d-electrons in any Ti compound.

In conclusion, the present experiment confirms conclusively that in this material Ti is ferromagnetically active. It also presents a rather detailed description of the magnetic distribution which is concentrated around the Ti atoms but with a nontrivial radius of 0.6 Å. The considerations made here apply to the average Ti site; whether this average is attained by summing over widely different states depending upon the microscopic concentration of copper around the Ti or if it is a description of the state of each Ti still has to be tested.

1. Summary of paper: *Phys. Rev. Lett.* **45,** 751 (1980).
2. Guest scientist from Argonne National Laboratory, Argonne, Ill.
3. Los Alamos National Laboratory, Los Alamos, N.M.
4. C. P. Enz and B. T. Matthias, *Science* **201,** 828 (1978).
5. B. T. Matthias et al., *Phys. Lett.* **69A,** 221 (1978); *J. de Phys.* **39,** L441 (1978).
6. A. L. Giorgi et al., *Solid State Commun.* **32,** 455 (1979).
7. S. J. Pickart et al., *Phys. Rev. Lett.* **12,** 444 (1964).
8. R. W. Watson and A. J. Freeman, *Acta Crystallogr.* **14,** 27 (1961).

NEUTRON DIFFRACTION ANALYSIS OF A COMPOSITIONALLY MODULATED ALLOY OF NICKEL-COPPER[1]

G. P. Felcher[2] Z. Q. Zheng[3]
J. W. Cable J. B. Ketterson[3]
J. E. Hilliard[3]

The new techniques of controlled vapor deposition have made possible the preparation of materials with distinct and novel physical characteristics.[4] These materials are the compositionally modulated alloys (CMA), where the two components are deposited alternately on a convenient substrate forming a periodically stratified layer structure. By a proper choice of the substrate and of the conditions of deposition, each component can be made to grow along some particular crystallographic orientation; hence, the material is, at least along the direction of deposition, a single crystal whose basic properties can be examined by diffraction techniques.

We have studied a CMA alloy $Ni_{0.4}Cu_{0.6}$ to determine its microscopic magnetic behavior using polarized neutrons. Nickel-copper is very appropriate for this purpose, since the magnetic and crystallographic properties of the bulk alloy have been studied extensively. Thus, it is well known that the average magnetization of disordered Ni-Cu alloys and the temperature at which they order magnetically decrease linearly with increasing copper concentration to a critical concentration near 60% copper. It has been found that annealing causes a clustering of the two components with an enhanced magnetization. It is to be expected that a CMA would also exhibit an enhanced magnetization over a similar disordered alloy, and such a result has been found in recent ferromagnetic resonance measurements.[5]

Our alloy of composition $Ni_{0.4}Cu_{0.6}$ was deposited on a substrate of sapphire. It was confirmed that the CMA had grown with excellent expitaxiality along the [111] direction of the fcc structure common to both components. First-order satellites were detected around the (111) Bragg reflection, at the positions expected for a repeat period of 22 Å, and with an intensity lower by two to three orders of magnitude than that of the main (111) peak. No higher order satellites were detected with our diffractometer.

The polarized-neutron diffraction work was performed with the sample located in the bore of a split-coil superconducting magnet producing an external magnetic field parallel to the layers and normal to the scattering plane defined by the incoming and scattered beam. The measurements were taken at different temperatures in magnetic fields of 1.0 and 0.06 T, the latter being the minimum field required to saturate the sample. The measurements were carried out on the two most prominent peaks of the structure, namely, the (111) fundamental reflection and the (000^+) satellite. The observed magnetic-to-nuclear-amplitude ratios for these reflections are given by

$$A_M/A_N(111) = \frac{0.27\,\bar{c}\,\bar{\mu}_{Ni} f_{Ni}(K)}{\bar{b}} \qquad (1)$$

and

$$A_M\frac{(000^+)}{A_N} = \frac{0.27(\Delta c_1 \bar{\mu}_{Ni} + \bar{c}\,\Delta\mu_1) f_{Ni}(K)}{\Delta c_1 \Delta b}\,, \qquad (2)$$

here μ_{Ni} is the average Ni moment, Δc_1 and $\Delta\mu_1$ are the amplitudes of the concentration and the Ni moment modulation, $f_{Ni}(K)$ is the magnetic form factor, $\bar{b} = \bar{c}\, b_{Ni} + (1-\bar{c})b_{Cu}$, and $\Delta b = b_{Ni} - b_{Cu}$ with $b_{Ni} = 1.03$ and $b_{Cu} = 0.76 \times 10^{-12}$ cm. For the (000^+) reflection note that $f_{Ni}(K) = 1$ and $\Delta b = 0.27$ so that the observed ratio becomes

$$A_M/A_N(000^+) = \bar{\mu}_{Ni} + \frac{c}{\Delta c_1}\Delta\mu \ . \qquad (3)$$

Therefore, the average Ni moment is obtained directly from the amplitude ratios of the (111) fundamental, while the moment fluctuation about that average is given by the amplitude ratio of the (000^+) satellite. Here, $\Delta c_1 = 0.26$ is obtained from the 111^+ and 111^- satellite intensities. If the Ni atoms were randomly distributed in each atomic layer, then with $c = 0.4$ and $\Delta c_1 = 0.26$ the Ni-rich layers would contain up to 66% Ni and the Cu-rich layers would contain only 14% Ni. From the magnetization-vs-concentration behavior of the bulk alloys, we estimate that the Ni moment should then vary from about 0.35 μ_B in the Ni-rich regions to zero in the Cu-rich regions with an average value of about 0.15 μ_B.

The observed moment behavior is shown in Figs. 5.33 and 5.34. Figure 5.33 shows the temperature dependence of the average Ni moment in two external fields. The data show $\mu_{Ni} \simeq 0.3\ \mu_B$/Ni at low temperatures; this moment decreases with increasing temperature in the usual manner with a Curie temperature near 250 K as indicated best by the low-field data. There is a strong field dependence of the magnetization near T_c. The amplitude ratio data for the (000^+) satellite are shown in Fig. 5.34. Surprisingly, the magnitudes and the temperature and field dependences are essentially the same as for the average Ni moment in Fig. 5.33. This shows clearly that moment fluctuations are negligible and thus that the Ni moment is the same in each layer regardless of the Ni concentration in that layer. This cannot happen for a situation in which the Cu and Ni atoms are randomly distributed in the layers; however, any clustering effect in the layer increases the magnetization of Ni and reduces its dependence on the concentration in the layer. Such an effect is further reinforced if the clustering in a layer is correlated with the clustering in adjacent layers.

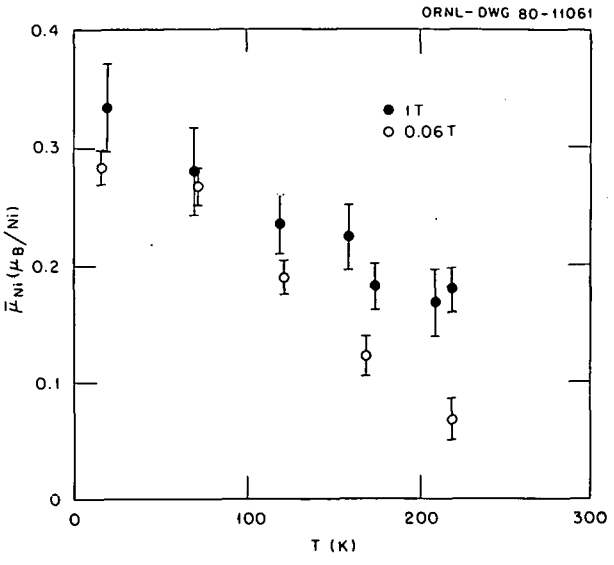

Fig. 5.33. Temperature dependence of the average Ni moment in externally applied fields of 1 and 0.06 T.

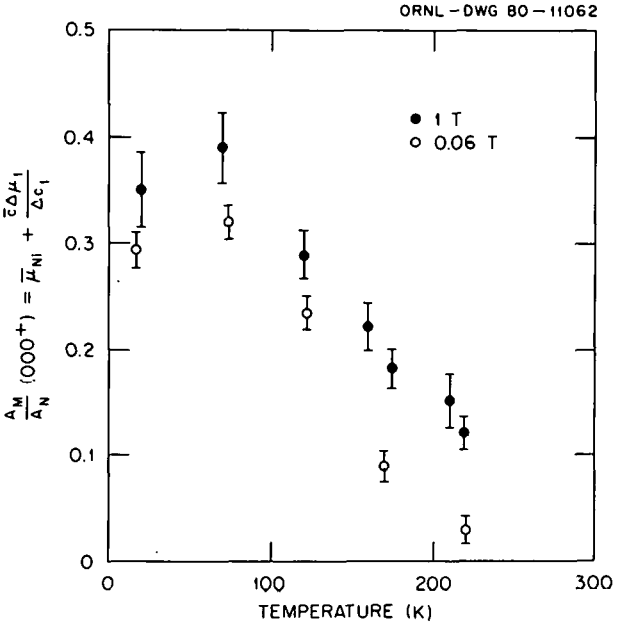

Fig. 5.34. Temperature dependence of the magnetic-to-nuclear-amplitude ratio of the (000^+) satellite. The ratio is given by $\bar{\mu}_{Ni} + \bar{c}\Delta\mu_1/\Delta c_1$ and is shown in units of μ_B per Ni atom.

On the basis of the knowledge accumulated on the disordered alloys of Ni-Cu, both by magnetization measurements and by diffuse neutron scattering, we can construct a crude model that substantiates our claim. In a layer with an average Ni

concentration, we arrange the Ni atoms in clusters, with a size defined so that the Ni atoms in the interior of the cluster have the full Ni moment of 0.6 μ_B, while those on the perimeter of the cluster have zero moment. The size of this intralayer cluster is adjusted to give 0.3 μ_B per Ni, and it comes to about 37 Ni atoms. For the other layers, enriched or depleted in Ni, we accordingly enlarge (or reduce) the size of the cluster. We then obtain clusters ranging from about 50 Ni atoms in the Ni-rich regions to about 20 atoms in the Cu-rich regions. In each of these intralayer clusters the average moment per Ni is quite close to 0.3 μ_B; the variation of the size of the cluster produces a fluctuation of only 0.05 μ_B/Ni in much closer agreement with our findings.

1. Summary of paper: *J. Magn. Magn. Mater.* **21,** L198 (1980).

2. Guest scientist from Argonne National Laboratory, Argonne, Ill.

3. Northwestern University, Evanston, Ill.

4. W.M.C. Yang, T. Tsakalakos, and J. E. Hilliard, *J. Appl. Phys.* **48,** 876 (1977).

5. B. J. Thaler, J. B. Ketterson, and J. E. Hilliard, *Phys. Rev. Lett.* **41,** 336 (1978).

MAGNETIC MOMENT DISTRIBUTION IN Co-V ALLOYS[1]

J. W. Cable

Magnetization measurements[2] on Co-rich Co-V alloys show that both the average moment and the Curie temperature decrease linearly with V concentration out to about 12 at. % V. Both properties decrease more rapidly at higher concentrations, and ferromagnetism no longer occurs above the critical concentration of 23 at. % V. In the linear region, $d\mu/dc = -6\ \mu_B$ per V atom, and neutron-diffuse scattering data[3] show that most of this moment decrease occurs at the Co sites due to the presence of V atoms in neighboring shells. The previous neutron measurements[3] were confined to the 5 at. % impurity level, where only hcp and hcp-fcc mixed-phase samples are available. Here, we extend the measurements to higher concentrations and to the fcc region in an attempt to determine the local environment effects on the magnetic moment distribution in these alloys.

Polycrystalline Co-V alloys containing 10, 15, and 20 at. % V were prepared by arc melting, drop casting, and quenching from 1385 K. The two more dilute alloys are disordered fcc, with some hcp phase contamination for the 10% alloy, while the 20% alloy is atomically ordered in the Cu_3Au structure. Polarized-neutron-diffuse scattering measurements were made at 4.2K in a saturating field of 2 T. For the two disordered alloys, these yield the K-dependent moment disturbance functions $M(K)$ presented in Fig. 5.35. These functions were fitted to the expression

$$M(K)/f_{Co}(K) = \Delta\mu + \sum_{R\neq 0} z(R_i)\phi(R_i)\frac{\sin KR_i}{KR_i}, \quad (1)$$

where $\Delta\mu = \mu_V - \mu_{Co}$, $\phi(R_i)$ is the moment disturbance at any site caused by a V atom at distance R_i, and $z(R_i)$ is the number of atoms at distance R_i. Here, the Co form factor was approximated by $f_{Co}(K) = e^{-0.049K^2}$, and an exponential decay of the moment disturbance with the form

$$\phi(R_i) = \frac{R_1}{R_i}\phi(R_i)e^{-\kappa(R_i-R_1)} \quad (2)$$

was assumed. The fitting parameters are then $\Delta\mu$, $\phi(R_1)$, and κ, the inverse correlation length. The best fits are represented by the solid curves in Fig. 5.35 with the parameters given in Table 5.3. The parameters are similar for both compositions and show that the moment difference term $\Delta\mu$ is only a

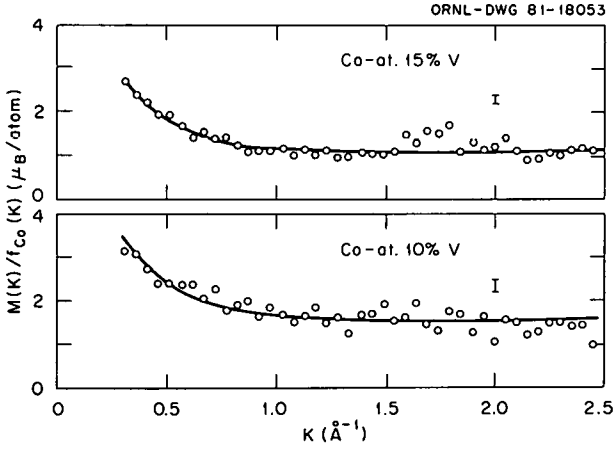

Fig. 5.35. The K-dependent moment disturbances for disordered Co-V alloys. Solid curves are fitted to Eqs. (1) and (2) with the parameters in Table 5.3.

Table 5.3. Moment disturbance parameters for Co-V alloys[a]

at. % V	$\Delta\mu$	$\phi(R_1)$	$\kappa(A^{-1})$	$M(0)$	$\langle\mu_V\rangle$	$\langle\mu_{Co}\rangle$
10	-1.64	-0.062	0.26	-6.1	-0.26 ± 0.08	1.38 ± 0.01
15	-1.16	-0.055	0.20	-7.0	-0.11 ± 0.03	1.05 ± 0.01

[a] All parameters are in μ_B/atom except for κ.

small part of the total moment disturbance $M(0)$ caused by a V atom. This disturbance has a maximum value of only -0.06 μ_B on a nearest-neighbor atom but extends over several shells of atoms so that the net effect is quite large. The average V and Co moments were obtained by combining $\Delta\mu$ with the magnetizations, and these are given in the last two columns of Table 5.3. The average V moments are quite small and antiparallel to the Co moments, while the average Co moments are large but decrease very rapidly with increasing V content.

The above analysis cannot be applied to the 20 at. % V alloy, which exhibits long-range atomic order (LRO). In the usual treatment of LRO in an A_3B structure, the normal lattice and superlattice structure factors are $F_{NL} = f_\beta + 3f_\alpha$ and $F_{SL} = f_\beta - f_\alpha$, where f_α and f_β are the amplitudes on the $\alpha(\beta)$ sites preferred by the A(B) atoms. For nuclear scattering, these reduce to $F_{NL} = 4\bar{b}$ and $F_{SL} = \Delta bS$, where S is the LRO parameter. For magnetic scattering, the magnetic amplitudes depend on local environment, and this site dependence must be explicitly included in the structure factors. These are

$$F_{NL} = 3r_\alpha p^\alpha_{Co} + w_\beta p^\beta_{Co} + r_\beta p^\beta_V + 3w_\alpha p^\alpha_V \qquad (3)$$

and

$$F_{SL} = w_\beta p^\beta_{Co} - r_\alpha p^\alpha_{Co} - r_\alpha p^\beta_V - w_\alpha p^\alpha_V \ , \qquad (4)$$

where r and w are the fraction of "rightly" and "wrongly" occupied subscripted sites and p is the magnetic amplitude of the subscripted atom on the superscripted site. The site occupations can be determined from the nuclear LRO parameter for which we obtain $S = 0.84 \pm 0.04$ from the (100) to (200) intensity ratio. This corresponds to the maximum possible order at this concentration for which $r_\alpha = 1$, $w_\alpha = 0$, $r_\beta = 0.8$, $w_\beta = 0.2$, and $S(\max) = 0.8$. Flipping-ratio measurements were made for the first three reflections to obtain the magnetic structure factors. The results, which have been corrected for instrumental imperfection and sample depolarization, are given in Table 5.4.

Table 5.4. Magnetic structure factors of LRO Co–20 at. %

hkl	R	F_M/F_N	F_N	F_M
100	1.084 ± 0.050	0.020	0.230	0.0046(28)
110	1.065 ± 0.025	0.016	0.230	0.0036(14)
220	2.46 ± 0.10	0.221	0.768	0.170(7)

Here, $R = (F_N + F_M)^2/(F_N - F_M)^2$, and we have used $b_{Co} = 0.250$, $b_V = -0.038$, and $S = 0.8$ to obtain F_N. With the Co form factor and Eqs. (3) and (4), these F_M values yield $\langle\mu^\alpha_{Co}\rangle = 0.28 \pm 0.01$ μ_B and $\langle\mu^\beta_{Co}\rangle + 4\langle\mu^\beta_V\rangle = 1.32 \pm 0.06$ μ_B. Because the molecular field at a V site is smaller here than for the more dilute disordered alloys, we expect that $\langle\mu^\beta_V\rangle \sim 0$ so that $\langle\mu^\beta_{Co}\rangle \sim 1.3$ μ_B. These results clearly demonstrate the dramatic effects of local environment on the Co moment. Those Co atoms on β sites have 12 Co nearest neighbors and large moments, while those on α sites have an average of 8.8 Co nearest neighbors and small moments. Co atoms on β sites have the same nearest-neighbor chemical environment as pure fcc Co, but their moments are only 1.3 μ_B compared with 1.76 μ_B for fcc Co. This reduction probably arises mostly from magnetic environment effects since the 12 nearest-neighbor α site Co atoms have small moments. More distant neighbor effects will also contribute to this reduction. As a consequence of this strong dependence of the Co moment on local environment, it is quite likely that there are large fluctuations in μ^α_{Co} because of the distribution of environments for the α sites. Fluctuations in μ^β_{Co} should be smaller because environment fluctuations occur only beyond the first-neighbor shell. Even so, there are moment fluctuations associated with the β sites because they are populated by both Co and V atoms. Both of these effects contribute to the observed

magnetic-diffuse scattering. Although the site occupation probabilities are different because of the LRO, these are the same moment fluctuation effects as in the disordered alloys, and the magnetic-diffuse cross sections are similar in shape. However, the K dependence is sharper for the ordered alloy ($\kappa = 0.14$), indicating longer-range moment disturbances. This type of behavior, in which the range of disturbance increases with increasing solute content, has been observed for several Ni-based alloy systems and is taken as evidence for a magnetic environment effect. The present results indicate that the magnetic moment on a Co atom also depends on both its chemical and magnetic environment.

---

1. Summary of paper: *Journal of Applied Physics* (in press).

2. Y. Aoki and M. Yamamoto, *Phys. Status Solidi A* **22,** K131 (1974); **26,** K137 (1974); and **33,** 625 (1976).

3. J. W. Cable and T. J. Hicks, *Phys. Rev. B* **2,** 176 (1970).

NEUTRON SCATTERING EXPERIMENTS ON THE MAGNETISM IN Cu-Mn SINGLE CRYSTALS[1]

S. A. Werner[2] J. W. Cable

The curious magnetic properties of Cu-Mn alloys in the α-solid solution range have attracted considerable attention for a very long time. In spite of the fact that a large number of neutron scattering experiments have been carried out on these alloys, a full understanding of the static and dynamic magnetic structure of these materials has not yet evolved. Fundamentally, we are faced with the problem of understanding the origin of the cusp in the low-field magnetic susceptibility occurring at some temperature, which is dependent upon Mn concentration, in the absence of the development of long-range antiferromagnetic order at low temperatures. Since there is no abrupt change in the entropy at the temperature at which the susceptibility cusp occurs (now commonly called the freezing temperature T_f), the low-temperature magnetic structure of these alloys is thought to resemble the static (metastable) structure of a glass. The spin-glass or mictomagnetic behavior now appears to be a general characteristic of many, more or less disordered, alloys [such as Au(Fe), Ag(Mn), and $(La_{1-x}Gd_x)Al_2$] irrespective of the concentration of magnetic atoms.

It is clear that the macroscopic magnetic properties of these alloys depend intimately upon the spatial distribution of atoms in the crystals, that is, on the short-range atomic order. This fact is particularly apparent from the drastic changes in the magnetic susceptibility upon heat treatment. For example, in $Cu_{75}Mn_{25}$ the height of the cusp in the low-field susceptibility is a factor of 4 larger in an annealed sample than in a quenched sample.[3] It is known from neutron scattering experiments that the short-range atomic order increases with annealing. This suggests that short-range atomic order, or inhomogeneity, may be a prerequisite to spin-glass behavior.

The microscopic connection between the short-range atomic order and the Mn spin-spin correlations can be observed using elastic neutron scattering in which the nuclear and magnetic scattering cross sections are separated by polarization analysis. Experiments of this type have previously been carried out on quenched, polycrystalline Cu-Mn samples,[4,5] yielding conflicting results. Ahmed and Hicks[4] concluded that the nearest-neighbor Mn-Mn interaction is ferromagnetic, while the more recent results of Davis, Burke, and Rainford[5] have been analyzed to yield antiferromagnetic coupling at nearest-neighbor distances.

In order to clarify this situation, we have carried out polarization analysis experiments on a series of annealed Cu-Mn single-crystal samples grown by the Bridgman technique. The Cu-Mn crystals were placed at the sample position of the triple-axis spectrometer in a horizontal field of 20 mT directed along the scattering vector. The scattered neutrons were then analyzed with a Co(Fe) crystal. The polarization state of the incident beam was controlled by an rf flipper coil, thus permitting a measurement of the spin-flip and the non-spin-flip cross sections separately.[6] In this geometry, all of the magnetic scattering is spin-flip scattering, while the coherent nuclear scattering is non-spin-flip scattering.

The Cu-Mn crystals were oriented with the [001] fcc axis normal to the scattering plane. Peaks in the nuclear-diffuse scattering occur at the [½,1,0]-type positions while the magnetic-diffuse scattering peaks at the [½ ± δ,1,0]-type positions. The intensity of both the nuclear- and magnetic-diffuse scattering decreased rapidly with decreasing Mn concentration, as shown by the results of scans

along the [l,1,0] line displayed in Fig. 5.36. As a function of increasing temperature, the peaks in the magnetic-diffuse scattering decrease in intensity and broaden continuously.

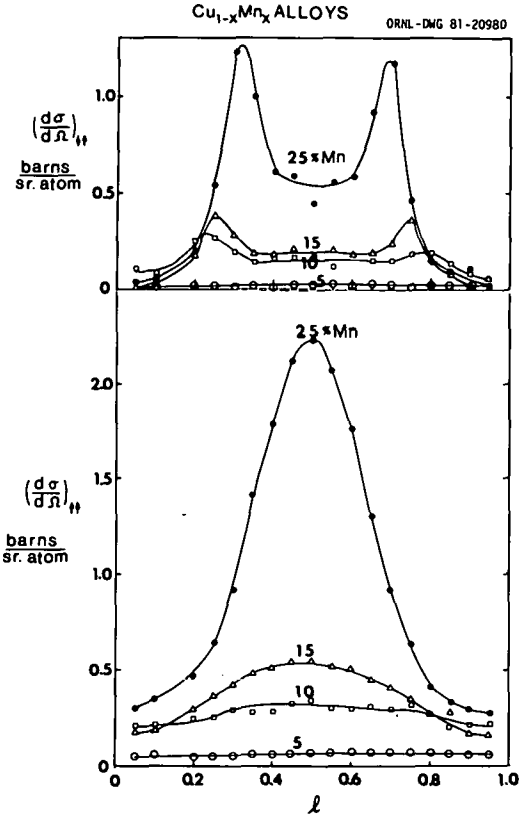

Fig. 5.36. Lower half: The non-spin-flip scattering cross section (nuclear-diffuse scattering) measured along the line [l,1,0]. Upper half: The spin-flip scattering cross section (magnetic-diffuse scattering) measured along the line [l,1,0]. These data were taken at 8 K.

In order to determine more precisely the positions in reciprocal space where the magnetic-diffuse scattering peaks, we have also carried out unpolarized neutron scattering experiments to take advantage of the increased intensity available. Knowing from the polarization analysis experiments that the nuclear scattering is essentially constant over the temperature range 8–295 K and that the magnetic scattering decreases to near zero at a temperature just above room temperature, a subtraction of the unpolarized scattering cross section at 295 K from the cross section at 8 K yields the magnetic-scattering cross section at low temperatures. The results of this procedure are shown in Fig. 5.37. The splitting of the magnetic-diffuse peaks is observed to decrease as the Mn concentration decreases.

It is clear that the magnetic-diffuse scattering is symmetry related to the short-range order nuclear scattering. We interpret the scattering along the line [l,1,0] to be due to one of three possible orientations of short-range ordered clusters. That is, the magnetic-diffuse peaks at [½ ± δ,1,0] along this line arise from scattering from the same regions of the macroscopic crystal as those that give rise to the diffuse nuclear scattering at [½,1,0]. Similar symmetry-related magnetic and nuclear scattering is observed along the two other equivalent directions, namely, [1,k,0] and [1,0,h].

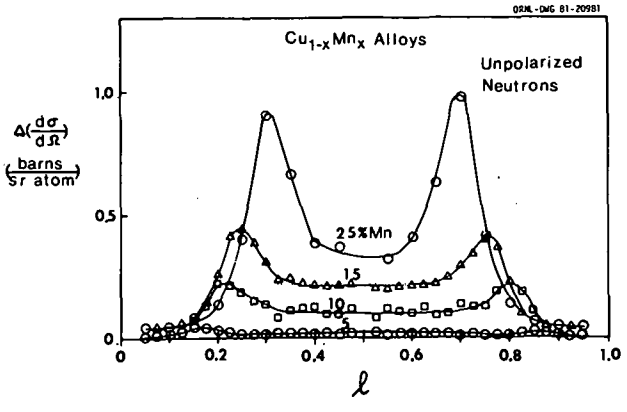

Fig. 5.37. Magnetic-diffuse scattering along [l,1,0] line in reciprocal space as measured with unpolarized neutrons at 8 K.

In view of the fact that the small-angle neutron scattering from Cu-Mn alloys clearly shows the freezing of spin fluctuations,[7] it may appear surprising that this magnetic-diffuse scattering displays no hint of a freezing transition at low temperatures. However, we believe that these data are precisely the information needed to justify the qualitative model which has emerged over many years and has guided our thinking about magnetism in these spin-glass alloys. This model involves the formation of magnetic clusters at some temperature well above T_f and an increase in their concentration and average moment as the temperature is lowered toward T_f. The fluctuations within and among these clusters slow down as T approaches T_f. Whether or not critical slowing

down should be expected is not clear. We would like to suggest that the model magnetic clusters are the short-range order domains and that the data of Figs. 5.36 and 5.37 represent the Fourier decomposition of the magnetism within these regions. With these data as the basis, we are currently working on various models to obtain a physical picture of the magnetic structure of these clusters in real space.

1. Summary of paper: *J. Appl. Phys.* **52,** 1757 (1981).
2. Consultant from University of Missouri, Columbia.
3. R. W. Tustian, *Solid State Commun.* **19,** 1075 (1976).
4. N. Ahmed and T. J. Hicks, *J. Phys. F* **5,** 2168 (1975).
5. J. R. Davis, S. K. Burke, and B. D. Rainford, *J. Magn. Magn. Mater.* **15–18,** 151 (1980).
6. R. M. Moon, T. Riste, and W. C. Koehler, *Phys. Rev.* **181,** 920 (1969).
7. A. P. Murani, *Phys. Rev. Lett.* **41,** 1406 (1978).

NEUTRON DIFFRACTION FROM SMALL NUMBERS OF LANGMUIR-BLODGETT MONOLAYERS OF MANGANESE STEARATE[1]

R. M. Nicklow M. Pomerantz[2]
A. Segmüller[2]

The goal of this study is to determine the magnetic structure of the ordered state of magnetic multilayers by neutron diffraction. Many quasi-two-dimensional magnetic crystals have been investigated. In almost every case, if magnetic ordering occurred, it was three-dimensional, implying that the interaction between the magnetic layers was ultimately significant. One wonders if the layers can be spread sufficiently far apart, reducing the coupling such that individual planes only will have magnetic order. There are mean-field theoretical arguments denying this possibility. The reasoning is that, as an individual layer approaches T_{2-d}, an ordering temperature, its susceptibility diverges. Then any interplanar field, however small, will produce ordering between the planes which sets in slightly below T_{2-d}.

We have begun to investigate this question using magnetic monolayers of manganese stearate [$Mn(C_{18}H_{35}O_2)_2$, abbr. $MnSt_2$]. It has been shown[3] that with the Langmuir-Blodgett technique this compound can be deposited on polished Si wafer substrates as individual monolayers or as precisely repeating multilayers with spacing between Mn layers of about 50 Å. A monolayer of the material seems to order magnetically[4] below about 2 K to a weak ferromagnetic state. Since the interplanar spacing is more than twice that of any other reported quasi-2-d magnet and could easily be made larger, this seems to be an appropriate material to study weak interlayer interactions.

Such experiments require very low temperatures and have not yet been completed. Our initial measurements were carried out at room temperature to determine whether it is possible to observe successfully neutron diffraction from a few monolayers with an area of a few cm^2. The mass of the sample is $\sim 10^{-6}$ g, which is probably the smallest ever to give observable neutron diffraction.

The neutron measurements were carried out on the triple-axis neutron spectrometer located at the HB-2 beam hole of HFIR. The (002) planes of a pyrolytic graphite crystal, having a mosaic spread of approximately 0.4°, were used as the monochromator. Because of the large cell spacing ($\sim$50 Å) of the sample, a relatively long neutron wavelength of 4.15 Å was used to resolve the Bragg reflections better. This wavelength also permitted the use of a Be filter to suppress higher-order wavelength contamination (λ/n, n = 2, 3, 4, etc.) from the monochromator which would have given diffraction peaks from the Si substrate in the same angular range as the peaks from the $MnSt_2$ films. The collimation of the incident beam was 20 ft (FWHM). No collimation was used after the sample.

The results for standard diffraction measurements on three samples with different numbers of layers are shown in Fig. 5.38. The solid lines are theoretical calculations. It is interesting to note that, because of the small number of layers, the diffraction pattern contains considerable structure and intensity in addition to the familiar Bragg peaks. However, much of the predicted structure is smeared by the instrumental resolution. Nevertheless, good overall agreement between the measured and calculated patterns for both deuterated (shown) and protonated (not shown) samples is obtained. The calculated patterns were in fact "fitted" to the measurements to give structural information about the $MnSt_2$ layers, which is complementary to that obtained by previous x-ray measurements.[3]

1. Summary of paper: *Phys. Rev. B* **23,** 1081 (2981).
2. IBM T. J. Watson Research Center, Yorktown Heights, N.Y.

3. M. Pomerantz, F. Segmüller, and F. Dacol, *Phys. Rev. Lett.* **40,** 246 (1978).
4. M. Pomerantz, *Solid State Commun.* **27,** 1413 (1978).

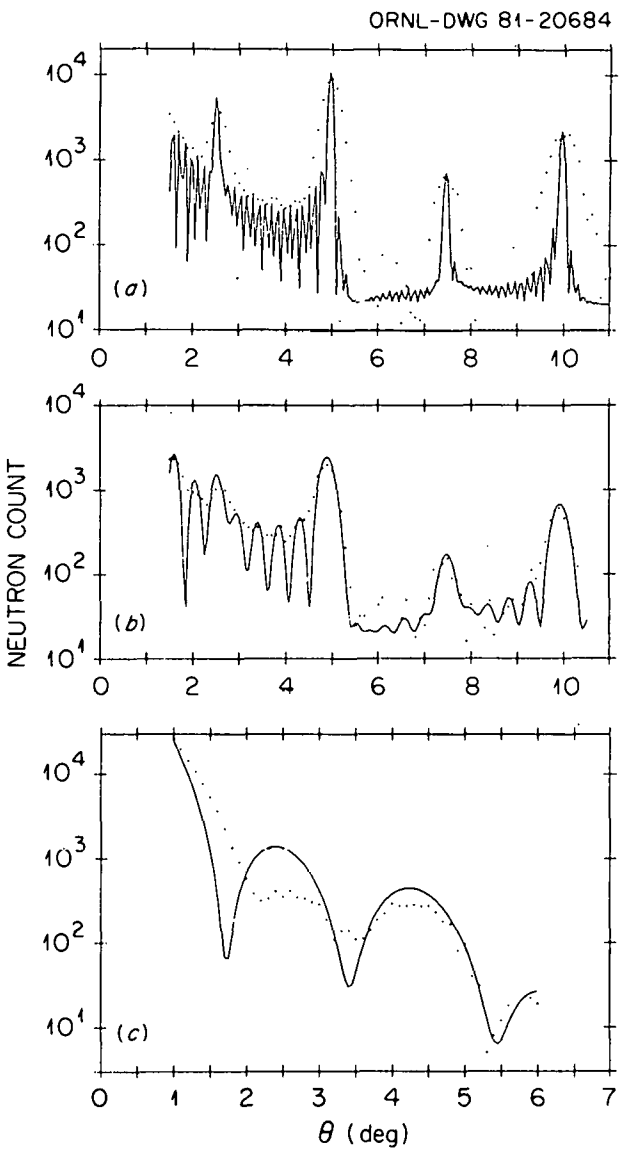

Fig. 5.38. Neutron diffraction from $MnSt_2$ films: (a) 43-layer film, (b) 11-layer film, and (c) 3-layer film. The dots are experimental points, and the lines are calculated patterns. Note the logarithmic intensity scale.

THE MAGNETIC FORM FACTOR OF METALLIC IRON AND NICKEL AS SEEN BY INELASTIC NEUTRON SCATTERING FROM PHONONS[1]

O. Steinsvoll[2] W. C. Koehler
R. M. Moon C. G. Windsor[3]

The magnetic form factors of the 3d metals have been studied by means of coherent elastic scattering of polarized neutrons in a number of investigations. However, with this technique one has access only to discrete values of momentum transfer equal to the reciprocal lattice vectors. We have utilized the coherent inelastic scattering of polarized neutrons by phonons to study the neutron magnetic scattering amplitudes of metallic Fe and Ni for momentum transfers which are different from the reciprocal lattice vectors. For a ferromagnetic sample the magnetic electrons are expected to follow the nuclei in their thermal oscillations. Thus, in addition to the usual coherent nuclear scattering by phonons, there is also coherent magnetic scattering (magnetovibrational scattering) with the same dependence on energy and momentum transfer as for the nuclear scattering. As in the elastic case, the use of polarized neutrons leads to constructive (or destructive) interference effects between the nuclear and magnetic scattering, depending upon the neutron polarization direction relative to the direction of atomic moments. The sensitivity of the experiment is thereby increased. The inelastic vibrational scattering has been separated from other inelastic and polarization-dependent scattering phenomena by energy analysis using a triple-axis, polarized-neutron spectrometer with a non-polarizing crystal as the analyzer.

Part of the motivation for these experiments originated with Marshall and Lovesey,[4] who have pointed out that "the form factor for inelastic scattering in a metal need not be a smooth interpolation of the factor measured at reciprocal lattice points in Bragg scattering experiments." This was based on a simplified treatment of magnetic scattering by itinerant electrons and involves the difference between Wannier functions and localized atomic functions.

Our results for longitudinal phonons in Fe along the three principal symmetry axes are shown in Fig. 5.39. The closed circles are taken from the Bragg scattering data of Shull and Yamada,[5] and the smooth curve is based on a fitted atomic model in order to interpolate between the reciprocal lattice points. It is evident that our phonon data, given by the open circles, consistently lie below the elastic curve in the [100] and [110] directions. In

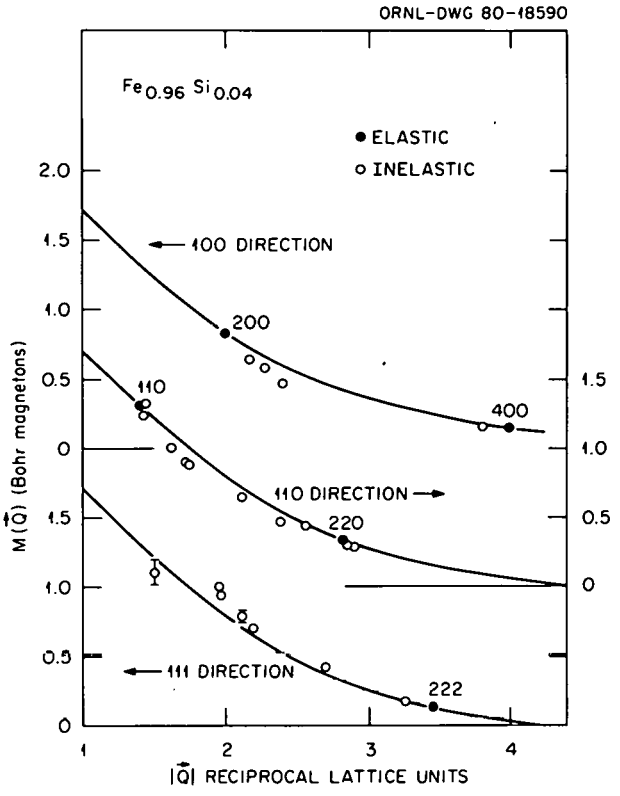

Fig. 5.39. The Fourier transforms of the magnetization density $M(\mathbf{Q})$ as measured by inelastic scattering along different crystallographic directions in Fe. The smooth curves are interpolations of the experimental elastic form factors for these directions, as explained in the text. For data points without error bars, the uncertainties are equal to or smaller than the size of the points.

the [111] direction, however, our results are higher than the elastic curve. At values of momentum transfer approaching the reciprocal lattice vectors, the deviation from the elastic curve is within the experimental error.

The Ni results, obtained mostly in the [100] direction, are shown in Fig. 5.40 in comparison

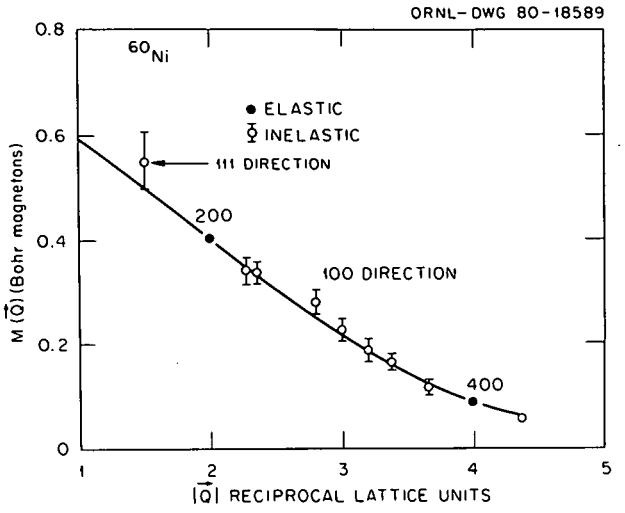

Fig. 5.40. The Fourier transform of the magnetization density $M(\mathbf{Q})$ as measured by inelastic scattering along the 100 direction for Ni. The smooth curve is an interpolation of the experimental elastic form factor for this direction.

with the elastic data of Mook.[6] A ^{60}Ni crystal was used for most of these measurements to avoid the high incoherent scattering from natural Ni. It was not possible to make measurements inside the 200 position with the ^{60}Ni crystal; therefore, the innermost point was obtained with a natural Ni crystal. Note that this point is along [111] rather than [100]. It is shown in Fig. 5.40 because the elastic [111] and [100] curves are almost equal at such a low-Q value. In contrast to the Fe case, the phonon data for Ni are in satisfactory agreement with the elastic results. The weighted mean of the fractional deviations between the inelastic data along the [100] and the elastic curve is 0.01 ± 0.02.

Using a tight-binding formalism, we have obtained an expression for the form factor at general Q values. This contains an oscillating term which vanishes at reciprocal lattice positions and causes a deviation from a smooth interpolation between the Bragg positions. However, this calculation predicts a negative deviation along all three symmetry directions in Fe and an even larger negative deviation for the [100] direction in Ni. The orthogonalized wave functions of this treatment are very similar to the Wannier functions of the Marshall and Lovesey treatment. In both cases the departure from the elastic form factor comes from the spreading of atomic wave functions onto near-neighbor sites. In the tight-binding formalism the

magnitude of this spreading is determined, through the orthogonality condition, by the near-neighbor overlap integral.

We believe that any static band theory lacks an essential element of the physics involved in our experiment, namely, the relative motion of neighboring atoms during a selected phonon vibration. It seems probable that the 3d electron distribution is dynamically distorted during a phonon vibration. The extent and nature of this distortion would depend on the phonon wave vector and the phonon polarization vector. Viewed from a vibrating nucleus, the surrounding electron distribution would have a time-dependent, real-space density function, oscillating in phase with the nuclear motion. It may be that the charge density distortion is relatively small, but there is a dynamic repopulation of symmetry orbitals resulting in a time-dependent spin density. If there is any truth to the notion of dynamic distortion of the electron cloud, one would expect that the ratio of the 3d radii to the near-neighbor distance would be an important factor in determining the magnitude of the effect. On this basis we would expect a smaller effect in Ni than in Fe, as observed. We would also expect the magnitude of the departure from the elastic form factor to depend on the amplitude of the phonon vibration and, hence, on the temperature. Therefore, experiments on the temperature dependence of this effect would be of some interest.

1. Summary of paper: *Physical Review B* (in press).
2. Institutt for Energiteknikke, Kjeller, Norway.
3. Atomic Energy Research Establishment, Harwell, England.
4. W. Marshall and S. W. Lovesey, p. 124 in *Theory of Thermal Neutron Scattering*, Oxford University Press, England, 1971.
5. C. G. Shull and Y. Yamada, *J. Phys. Soc. Japan* **17**, 1 (1962).
6. H. A. Mook, *Phys. Rev.* **148**, 495 (1966).

NEUTRON SCATTERING STUDY OF THE SPIN DYNAMICS OF EuO[1]

H. A. Mook

Europium oxide is a simple Heisenberg ferromagnet, and thus the material serves as an ideal testing ground for theoretical efforts to understand magnetic behavior. Extensive neutron scattering measurements have been made on powders of EuO by Passell, Dietrich, and Als-Nielson.[2] However, it is difficult to study excitations with wave vectors near the zone boundary with powders, and we have used high-quality single crystals of EuO to extend the earlier measurements. The temperature dependence of the magnetic excitations has an interesting behavior as the momentum transfer reaches values near the zone boundary. At temperatures near and above the Curie temperature T_c, the magnetic excitations can be well described by a Lorentzian peak centered at zero energy for small momentum transfers. As the momentum transfer is increased to values near halfway to the zone boundary, the peaks become non-Lorentzian, and near the zone boundary rather well-defined peaks are observed.

Figure 5.41 shows the magnetic excitations for the [111] zone boundary for four temperatures. At T_c-10 a broad, but well-defined, spin-wave peak is found. At T_c the peak broadens further and shifts downward in energy. Similar peaks are found at 1.27 T_c and at 2 T_c. Calculations by Hubbard[3] for a near-neighbor ferromagnet have been made for

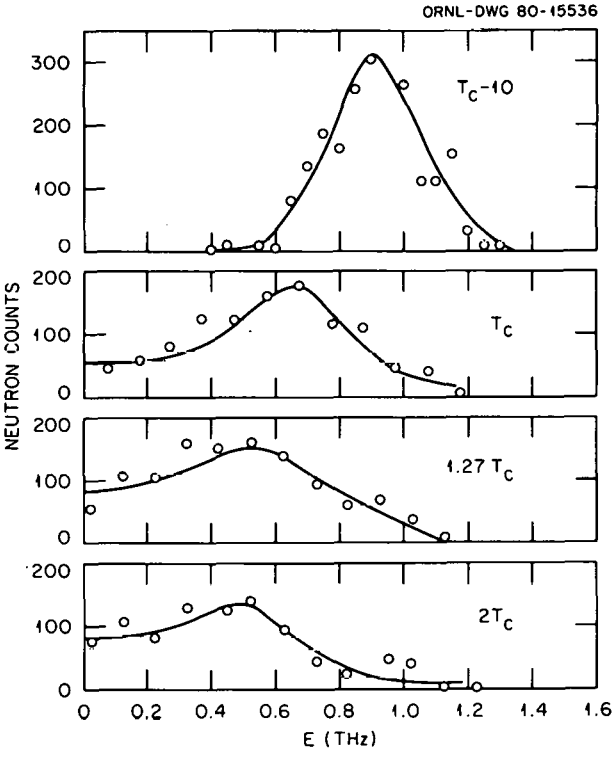

Fig. 5.41. Magnetic excitations in EuO for the [111] zone boundary measured at four temperatures.

magnetic excitations at these temperatures and momentum transfers. The agreement is quite good, although the calculations show somewhat broader peaks than have been observed. Well-defined spin waves have been found in Ni and Fe at much smaller momentum transfers than for EuO. This suggests that the spin correlation length above T_c is much longer for Fe and Ni than for EuO.

1. Summary of paper: *Phys. Rev. Lett.* **46,** 511 (1981).

2. L. Passell, O. W. Dietrich, and J. Als-Nielson, *Phys. Rev. B* **14,** 4897 (1976); **14,** 4908 (1976); and **14,** 4923 (1976).

3. J. Hubbard, *J. Phys. C* **4,** 53 (1971).

TEMPERATURE DEPENDENCE OF THE MAGNETIC EXCITATIONS IN Gd[1]

J. W. Cable N. Wakabayashi[2]
R. M. Nicklow

Metallic Gd is an isotropic Heisenberg ferromagnet with a Curie temperature of 293 K. The Gd atoms behave electronically as tripositive ions with half-filled f shells; therefore, there is a spin-only moment and very little anisotropy. This makes Gd an ideal candidate for neutron inelastic scattering studies of spin dynamics since the spin coupling is dominated by the exchange interactions. In earlier papers[3,4] we reported the spin-wave dispersion for Gd in the temperature range 78–232 K. We have now extended these measurements to temperatures above T_c to determine if spin waves persist in the paramagnetic region for this Heisenberg system similar to those observed[5,6] in the itinerant systems Fe and Ni.

The sample was the same single crystal of ^{160}Gd that was used in the previous studies.[3,4] Neutron measurements were made with a triple-axis spectrometer in the constant-Q mode of operation. Energy scans were made by varying the incident energy with fixed final energies of either 1.0 or 3.6 THz depending on the resolution requirements. Higher-order wavelength contaminants were essentially removed from the scattered beam by the use of either Be or pyrolytic graphite filters. Measurements were made out to the Brillouin zone boundaries in the [001] and [100] directions in the temperature range 9–593 K. Some of the raw data are shown in Figs. 5.42 and 5.43, which illustrate typical temperature dependences of the spin-wave spectra at small and large q .

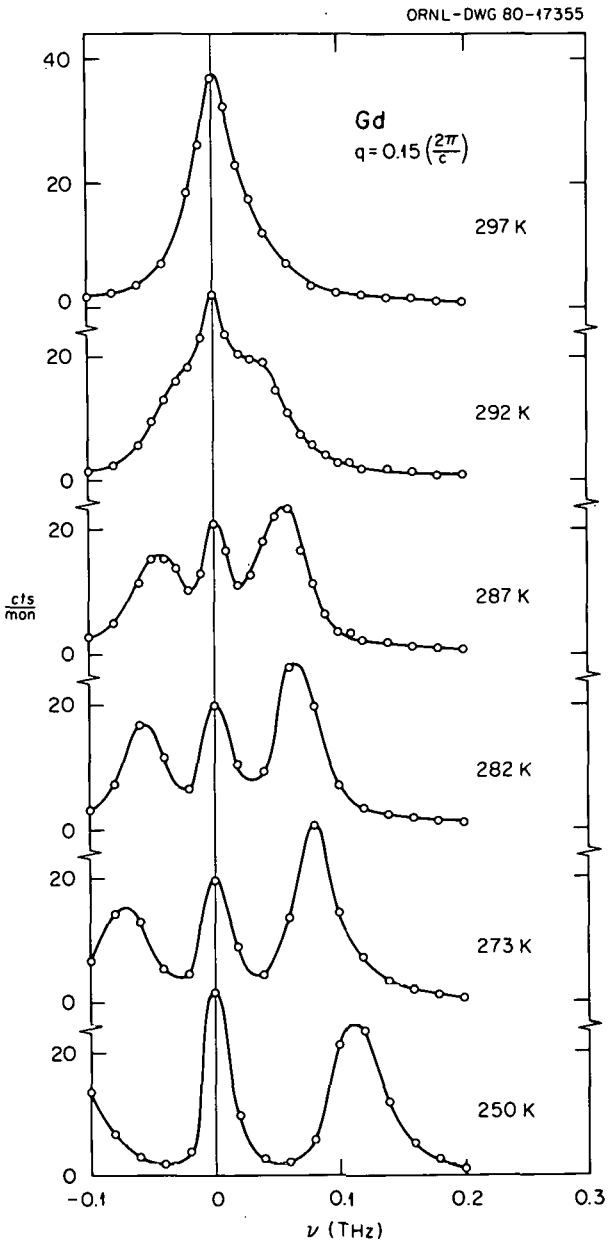

Fig. 5.42. Temperature dependence of the magnetic excitation spectrum of Gd at q = 0.15 in the [001] direction (q is given in units of $2\pi/c$).

Figure 5.42 shows high-resolution data at temperatures near T_c for a wave vector of 0.15 $2\pi/c$ along the [001] direction. The central peak consists of a temperature-independent component, which is probably the incoherent scattering from the furnace, plus a component that increases with decreasing temperature and may be domain-wall scattering. The peaks symmetrically displaced about the central peak correspond to spin wave

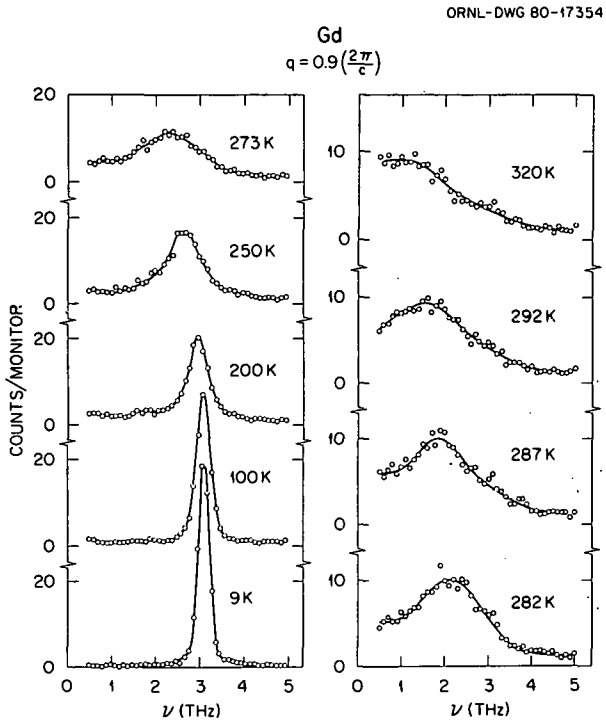

Fig. 5.43. Temperature dependence of the magnetic excitation spectra of Gd at $q = 0.9$ along [111] (q is given in units of $2\pi/c$).

propagating along the c-axis direction. These move continuously inward with increasing temperature and collapse into a single peak centered at $\omega = 0$ at T_c. This is the expected behavior at small q, where the spin-wave energies should follow the magnetization and vanish at T_c.

Typical large-q behavior is illustrated in Fig. 5.43. These are medium-resolution data for a wave vector of 0.9 $2\pi/c$ along [001]. These spectra show a pronounced broadening of the spin-wave linewidths near T_c and an energy renormalization less rapid than that observed at small q. The peaks do not collapse into a single peak at T_c; instead, a distinct shoulder remains in the excitation spectrum above T_c. Other data, not included in Fig. 5.43, show that this shoulder persists up to about 350 K. Because of the strong damping, it is not clear that these excitations above T_c should be characterized either as propagating or as overdamped spin waves. Their shapes suggest that there are characteristic frequencies associated with the spin correlations, and this feature remains up to about 1.2 T_c.

The temperature dependence of the magnetic excitations in Gd is qualitatively similar to that reported for Fe and Ni in that the small wave vector behavior follows the predictions of hydrodynamic theory, while strong departures from that behavior are observed at larger wave vectors. However, the spin-wave peaks above T_c in Fe and Ni are more pronounced and persist to higher temperatures (1.4 T_c in Fe, 2.0 T_c in Ni) than in Gd. The presence of spin waves in the paramagnetic region is presumably associated with short-range ordered regions which exist over large enough correlation lengths and times to support short-wavelength, high-frequency spin waves. It would then seem that short-range order is much more pronounced in Fe and Ni than in Gd.

1. Summary of paper: *J. Appl. Phys.* **52,** 2231 (1981).
2. Present address: Keio University, Yokohama, Japan.
3. W. C. Koehler et al., *Phys. Rev. Lett.* **24,** 16 (1970).
4. W. C. Koehler et al., *J. Phys. C Paris* **32,** C1-296 (1971).
5. H. A. Mook, J. W. Lynn, and R. M. Nicklow, *Phys. Rev. Lett.* **30,** 556 (1973).
6. J. W. Lynn, *Phys. Rev. B* **11,** 2624 (1975).

SPIN-WAVE DISPERSION RELATIONS IN DISORDERED Fe-V ALLOYS[1]

Y. Nakai[2] N. Kunitomi[2]
N. Schibuya[3] N. Wakabayashi[4]
J. F. Cooke

The spin-wave dispersion relations of ferromagnetic metals and alloys with parallel moments are expressed in most cases by the power law,

$$E = D_q^2(1 - \beta q^2) \ , \qquad (1)$$

for small values of q, where E, q, and D are the spin-wave energy, spin-wave momentum, and stiffness constant, respectively. However, if the orientation of the magnetic moment of the impurity atoms with respect to the host moment is taken into consideration, deviations from the power law are predicted theoretically. Several theories show the existence of extra spin-wave modes in a Heisenberg ferromagnet containing an isolated impurity, which has its magnetic moment antiparallel to those of

host atoms. Fe-V alloy systems are considered to be one of the most appropriate for studying the deviation from the power law, because V atoms have moments of about 1 μ_B aligned antiparallel to the host moment of 2.2 μ_B and because single-crystal specimens can be easily grown.

The exchange stiffness constants of several Fe-V alloys were previously determined indirectly by means of the small-angle scattering of neutrons[5] without energy analysis and by the analysis of the temperature dependence of the bulk magnetization.[6] A direct determination of the stiffness constant can, however, be made by the inelastic neutron scattering experiment on a single crystal using a triple-axis spectrometer. The purpose of the present study was to observe possible anomalies in the dispersion relation as well as to determine the stiffness constants D and β for these alloys. Four specimens containing 7.6, 13.5, 16.0, and 18.7 at. % V were studied. Neutron scattering experiments for the 16.0 at. % V specimen were performed with the TUNS triple-axis spectrometer at the JRR-2 at the Japan Atomic Energy Research Institute, and the HB-2 and the HB-3 triple-axis spectrometers at the HFIR were used for the measurements on the other specimens.

The spin-wave dispersion relation for each specimen at room temperature was determined, as shown in Fig. 5.44, after the resolution function corrections were made. The smallest momentum transfer observable in the present experiment is restricted by the interference due to high-intensity phonon peaks. Broken curves in Fig. 5.44 show the dispersion curves evaluated by using the stiffness constants deduced from the results of Lowde et al.[5] Plots of $E(q)/q^2$ vs q^2 made for each sample show no significant deviation from a straight line in the energy range between 5 and 80 meV, indicating that there is no resonance-like anomaly of the spin waves in these alloys. The stiffness constant D and the parameter β, determined from these plots, yield the dispersion curves, shown in Fig. 5.44 by solid curves. It is concluded, therefore, that Eq. (1) adequately describes the spin-wave spectrum of the Fe-V alloys in a wide range of the excitation energy, as it does for other metals and alloys. These results may be interpreted on the basis of two different pictures, the Heisenberg model and the band model.

First, we consider the analysis based on the Heisenberg model for the virtual metal corresponding to the alloy $Fe_{1-x}V_x$. Within the molecular

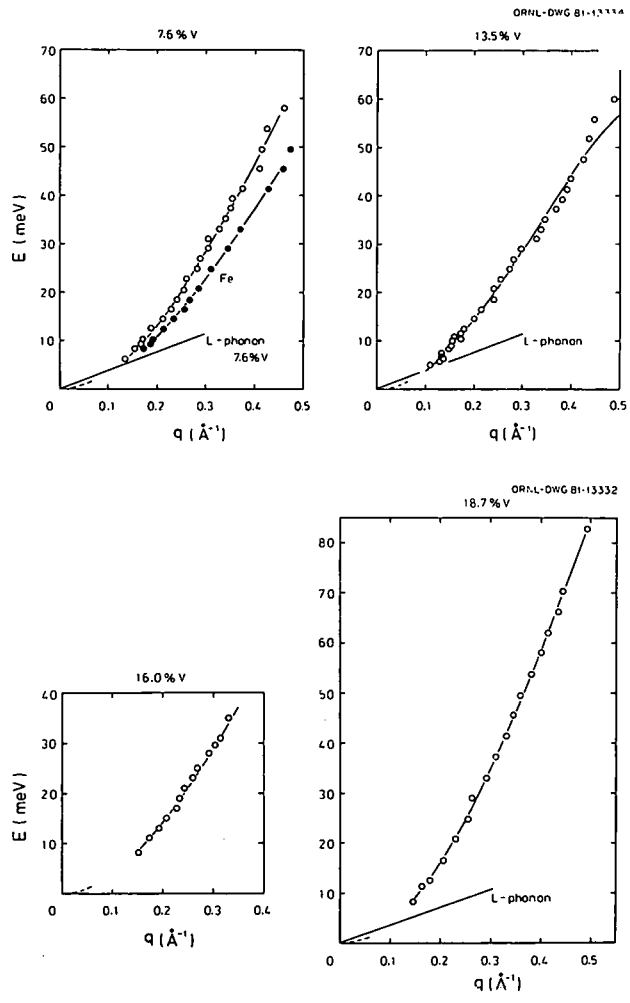

Fig. 5.44. Spin-wave dispersion curves for Fe-V alloys containing (a) 7.6 at. % V and pure Fe, (b) 13.5 at. % V, (c) 16.0 at. % V, and (d) 18.7 at. % V. Solid curves show the calculated dispersion relation given by Eq. (1) with the stiffness constant and the parameter β determined by the present experiment. Broken lines near the origin represent the dispersion relation given by D deduced from the work of ref. 5.

field approximation, the stiffness constant D for the alloy can be written in the form

$$D = (z/3)R_n^2 \bar{J}\bar{S} \quad , \tag{2}$$

where R_n and z are the nearest-neighbor distance and the coordination number, respectively. The virtual spin $\bar{S}$ can be determined from bulk magnetization data, and the value of the effective exchange constant $\bar{J}$ is fixed by host exchange constants and the derivative of the Curie temperature with

--spect to concentration. Values of D determined this way are found to be in reasonable agreement with experiment for concentrations of $V <$ 10% but give the wrong behavior above this range.

Although the data on the dynamical properties presented in this report can be interpreted within the Heisenberg model, a more fundamental interpretation based on band theory seems more desirable but requires extremely time-consuming computer calculations associated with rigorous theoretical formulations. Along these lines, Cooke, Lynn, and Davis[7] have been quite successful in calculating the spin-wave energies in various d-band metals including bcc Fe. Their calculations involve KKR bands and two exchange parameters which are associated with the terms in the spin-dependent part of the Hamiltonian corresponding to the e_g and t_{2g} symmetries. These parameters are adjusted to reproduce the experimentally determined magnitude and symmetry character of the moment. Using this more rigorous approch, the change in the spin-wave energy due to the addition of V atoms was estimated within the rigid-band approximation. The exchange parameters were assumed to be the same as those determined for Fe. The Fermi energy was adjusted so that the calculated moment agrees with the observed value for the average moment. For the alloy with the average magnetic moment of 1.95 μ_B, which corresponds to concentrations of V of about 10%, the calculated spin-wave dispersion curve was then found to be in reasonable agreement with the experiment for small values of the wave vector ($q < 0.5$ Å^{-1}). For larger wave vectors, the calculated curve actually falls below that for pure Fe, and the agreement is lost. This may be interpreted as an indication of the inadequacy of the rigid-band model. Extension of the theory beyond this rigid-band approach is very difficult and, at present, not tractable. It is, therefore, quite important to acquire more experimental data which could not only help improve our understanding of these types of alloys but also aid in the future development of the theory. We are currently studying the spin waves in the Ni-Pt alloy system.

---

1. Summary of paper: *Physical Review B* (in press).
2. Osaka University, Osaka, Japan.
3. Tokyo University of Agriculture and Technology, Tokyo, Japan.
4. Present address; Keio University, Yokohama, Japan.
5. R. D. Lowde et al., *Phys. Rev. Lett.* **14,** 698 (1965).
6. A. T. Aldred, *Int. J. Magn.* **2,** 223 (1972).
7. J. F. Cooke, J. W. Lynn, and H. L. Davis, *Phys. Rev. B* **21,** 4118 (1980).

6. Crystal Growth and Characterization

The development of advanced energy systems and continued improvement in the efficiencies of current systems can only be achieved by solving a variety of materials and materials-related problems. The Crystal Growth and Characterization Program has multiple purposes: (1) identifying materials problems that relate to DOE research objectives; (2) preparing and characterizing high-quality research specimens for use in research programs in the Solid State Division, in other ORNL divisions, and in other laboratories; and (3) performing collaborative work with various groups engaged in energy-related research.

The program investigating the suitability of the lanthanide orthophosphates for the primary containment of nuclear waste was expanded during the period covered by this report. Single crystals of the lanthanide orthophosphates with both the monazite and zircon structures were grown and characterized, and it was demonstrated that the lanthanide orthophosphates have the potential of serving as a primary containment matrix for defense, nuclear power reactor, and actinide wastes. Also, the preparation and characterization of ferroelectric materials were continued, as were the growth and characterization of superconducting materials with the A15 structure and the growth of large, optical-quality single crystals of Naβ"-alumina; refractory metals and alloys were prepared for investigations of fluxoid pinning in superconductors, phonon spectra, fracture, H absorption, and many other phenomena.

Although the Research Materials Information Center was eliminated, some of the publishing activity was continued temporarily; two additional volumes of the *Solid State Physics Literature Guides* are scheduled for publication by Plenum Press.

CRYSTAL GROWTH AND CHARACTERIZATION PROGRAM

L. A. Boatner, M. M. Abraham, W. E. Brundage, G. R. Gruzalski, Y. K. Chang, H. E. Harmon, J. O. Ramey, B. C. Sales, M. Petek

A continuing policy of the program to loan samples to cooperating research groups for supplementary physical property measurements is maintained in order to realize the maximum utilization of these often unique specimens. Measurements made on these samples usually complement the research efforts of Solid State Division members, and the investigations carried out by workers in foreign research institutions serve as a means of enhancing exchanges of technical information. Representative examples of some of the research specimens and their utilization are provided in Table 6.1.

NUCLEAR WASTE FORMS

LANTHANIDE ORTHOPHOSPHATES AS A MATRIX FOR SOLIDIFIED RADIOACTIVE DEFENSE, REACTOR, AND ACTINIDE WASTES[1]

L. A. Boatner, M. M. Abraham, M. Petek, J. O. Ramey, B. C. Sales

The problem of selecting a suitable primary immobilization medium for nuclear wastes is complicated by the long half-lives of many of the iso-

Table 6.1. Loan of samples for research outside the Research Materials Program

Material	Type of study	To whom sent	Organization
$LuPO_4$, YPO_4	Optical absorption	N. Edelstein	LBL
$KTaO_3$, KTN	Raman scattering	L. Chase	Indiana University
$K_{1-x}Li_xTaO_3$	Raman scattering	L. Chase	Indiana University
$KTa_{1-x}Nb_xO_3$	Electro-optics	E. Krätzig	University of Osnabrück, Germany
$KTa_{1-x}Nb_xO_3$	Neutron scattering	J. Axe	BNL
$KTa_{1-x}Nb_xO_3$	Electro-optics	R. Orlowski	Philips Research Labs, Hamburg, Germany
$K_{1-x}Li_xTaO_3$	Thermal conductivity	A. de Goër	Centre d'Etudes Nucléaires, Grenoble, France
$LuPO_4$	Crystallography	D. Mullica	Baylor University
$LaPO_4$	Thermal conductivity	R. Pohl	Cornell University
$CaTiO_3$	Dissolution and stability	M. Bancroft	University of Western Ontario, Canada
$LaPO_4$, $LuPO_4$	Raman scattering	G. Begun	ORNL
$LaPO_4$, $LuPO_4$	Mössbauer	P. Huray	University of Tennessee
$KTaO_3$:Ca	Superconductivity	J. Thompson	University of Tennessee
MgO	Studies of adsorptive and catalytic properties	J. Cunningham	University College, Dublin, Ireland
MgO	Light scattering	W. Unruh	University of Kansas
MgO:Ni	Light scattering	W. Unruh	University of Kansas
MgO:Co	Light scattering	W. Unruh	University of Kansas
MgO:V	Light scattering	W. Unruh	University of Kansas
$TiC_{0.92}$	Optical properties	F. Modine	ORNL
$TiC_{0.87}$	Optical properties	F. Modine	ORNL
$TiC_{0.92}$	Electrical conductivity	H. Engstrom	ORNL
$TaC_{0.9}$	Optical properties	F. Modine	ORNL
$VC_{0.88}$	Optical properties	F. Modine	ORNL
$VC_{0.88}$	Ion channeling	C. White	ORNL
$VC_{0.88}$	Ion implantation	J. Williams	ORNL
$VC_{0.84}$	Optical properties	F. Modine	ORNL
$(VTi_3)C_{0.88}$	Optical properties	F. Modine	ORNL
$(V_3Ti)C_{0.88}$	Neutron diffraction	H. Smith	ORNL
ZrC	Optical properties	F. Modine	ORNL
Ni	Grain boundary cavitation	J. Schneibel	ORNL
Ni	He diffusion	J. Williams	ORNL
Ni	Diffusion	D. Poker	ORNL
V_3Si	Superconductivity	D. Christen	ORNL
V_3Si	Neutron and x-ray scattering	J. Staudenmann	Ames Laboratory
V_3Si	Superconductivity	S. Sekula	ORNL
Nb_3 18 at. % Ge	Superconductivity	S. Sekula	ORNL
Nb_3Ge	Neutron and x-ray scattering	J. Staudenmann	Ames Laboratory
V_3Ge	Neutron and x-ray scattering	J. Staudenmann	Ames Laboratory
V_3Ge	Ion channeling	B. Stritzker	ORNL
Nb	Current resistance	H. Kerchner	ORNL
Nb	Positron annihilation	G. Stocks	ORNL

Table 6.1 (continued)

Material	Type of study	To whom sent	Organization
NbMo	Positron annihilation	G. Stocks	ORNL
Ti_3Au	Neutron and x-ray scattering	J. Staudenmann	Ames Laboratory
Ti_3Pt	Neutron and x-ray scattering	J. Staudenmann	Ames Laboratory
NbTa	Current resistance	H. Kerchner	ORNL
Ni-29,30,50 at. % Pt	Neutron scattering	N. Wakabayashi	ORNL
β-brass	Neutron scattering	N. Wakabayashi	ORNL
Cu-Au-Ln	Neutron scattering	N. Wakabayashi	ORNL
Naβ"-alumina (Mg)	Fast-ion conductivity	J. Bates	ORNL
Naβ"-alumina (Zn)	Fast-ion conductivity	J. Bates	ORNL
Al_2O_3	Light scattering	W. Unruh	University of Kansas

topes present in these materials. In order to realize a reasonable level of confidence in the potential long-term stability of a given waste form, it is necessary to devise various means of simulating, during a practical time span, the long-term effects of diverse conditions that the waste form might experience. Because the half-lives of some of the α-active actinides are as long as $\sim 10^6$ years, the reliability of simulations of this type is frequently subject to question. This situation has fostered an approach for selecting potential waste forms that consists of examining naturally occurring mineral systems whose stability under various environmental conditions has been established by geological investigations. This type of approach was responsible for the decision to investigate the lanthanide orthophosphates.

The mineral monazite is a mixed lanthanide orthophosphate that occurs as beach sands, alluvial deposits, microcrystalline inclusions in granite rock, and large (~ 25 kg) crystals. The geological age of various monazites has been found to range from 5×10^8 to 2×10^9 years, and the geological history of some alluvial monazites indicates that they have survived more than one cycle of rock-forming and metamorphic processes. Accordingly, there is a considerable body of evidence indicating that monazite is an extremely stable mineral. Additionally, monazite ores are a source of both uranium and thorium, so that their ability to incorporate large quantities of at least two actinide elements is already established. Since many monazites contain significant amounts of thorium, they have naturally been subjected to α-particle radiation damage over long periods of time. It was found, however, that these minerals maintained their structure even in the presence of relatively high fluxes of α particles and did not undergo extensive metamictization. Finally, the mobility of uranium and thorium in monazite has been shown to be low in comparison with that of other minerals such as uraninite, orthite, pyrochlore, and zircon. All these factors are consistent with the concept that synthetic analogs of monazite (i.e., lanthanide orthophosphate compounds $LnPO_4$) may represent a potentially ideal primary containment medium for the immobilization of α-active actinide wastes.

An experimental program with both fundamental and applied aspects was undertaken to evaluate the applicability of lanthanide orthophosphates to the problem of isolating nuclear wastes. The goals of the fundamental portion of these studies include the achievement of an understanding on a microscopic level of the solid state chemical and physical properties of mixed lanthanide-actinide systems. To this end, investigations of the valence states, site symmetries, etc., of actinide and other impurities in the lanthanide orthophosphates are being carried out. The more applied segment of this effort is directed toward studies of processing techniques having potential for practical production of waste forms via remote operations.

The properties of lanthanide orthophosphates loaded with simulated Savannah River defense wastes (SRW) and simulated reprocessed light water reactor wastes have been investigated. Pure $LaPO_4$ was selected as the host matrix for the incorporation of composite SRW without aluminum removal and a reprocessed reactor fuel waste, as represented by the PW-4b composition. In both cases the solidified waste forms were prepared from nitric acid solutions of the simulated calcined waste oxides and La_2O_3. The formation and precipitation of the composite phosphates were accomplished by adding $(NH_4)_2HPO_4$ or by combining the $(NH_4)_2HPO_4$ addition with a precipitation from molten urea.

For the case of simulated SRW, the effects of waste loading on compaction and sintering properties of the composite material and on the formation of crystalline phases other than the monoclinic monazite phase were investigated. Waste loadings from 10 to 50 wt % relative to La_2O_3 were used. For loadings up to 20 wt % no additional phases were detected in x-ray powder diffractometer measurements. At higher loadings, however, an extra phase identified as an orthorhombic form of $AlPO_4$ was detected. The relative fraction of this phase increased proportionally with increased waste loading. A similar series of measurements is in progress using a mixture of lanthanides as they are obtained commercially from Molycorp, Inc.

Dilatometry measurements on cold-pressed powders of SRW-$LaPO_4$ composite powders showed that sintering occurs in the range 700–1000°C. Accordingly, the sintering temperatures for these composites can be held below ~1050°C. Cold-pressed, sintered pellets of SRW-loaded $LaPO_4$ were hard, uniform, and yellow-green in color. SRW-$LaPO_4$ pellets produced by cold pressing and sintering had densities of 3.2 to 3.9 g/cm^3 depending on the waste loading, and hot-pressed pellets with a density of 3.5 g/cm^3 were produced using material with a 15 wt % loading.

In the case of $LaPO_4$-(PW-4b) composites the effect of varying the amount of urea used in the precipitation on the particulate size and the associated compaction properties was studied. The quantity of urea was varied between 0 and 200 moles of urea per mole of La. Waste form pellets with 92 ±2% of the theoretical density of pure $LaPO_4$ were formed by cold pressing and sintering (T_{max} = 1200°C) $LaPO_4$ powder loaded with 10 wt % PW-4b. Hot pressing at 4000 psi and 1050°C resulted in the formation of pellets with a density of 96% of the theoretical value of $LaPO_4$. No additional phases were detected in the (PW-4b)-loaded orthophosphate material. Representative examples of compacted bodies of both SRW- and (PW-4b)-loaded $LaPO_4$ are shown in Fig. 6.1.

ORNL-PHOTO 4346-81

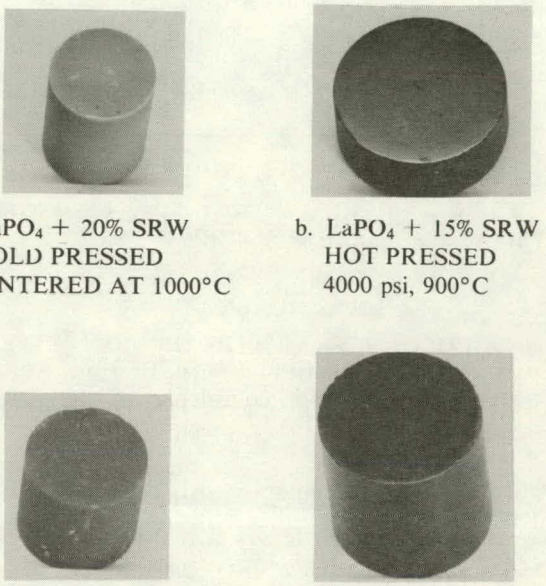

a. $LaPO_4$ + 20% SRW COLD PRESSED SINTERED AT 1000°C

b. $LaPO_4$ + 15% SRW HOT PRESSED 4000 psi, 900°C

c. $LaPO_4$ + 10% PW-4b COLD PRESSED SINTERED AT 1200°C

d. $LaPO_4$ + 10% PW-4b HOT PRESSED 4000 psi, 1050°C

Fig. 6.1. Compacted $LaPO_4$ waste forms.

The sintering properties of (PW-4b)-loaded $LaPO_4$ were investigated using continuous reading dilatometry, and a typical sintering curve is shown in Fig. 6.2. It can be seen that sintering occurred between 800 and 1200°C and that the sintering process still appeared to be in progress when the cooling cycle was initiated.

Leaching data for Cs, Sr, and U are being obtained, and these results will be compared to the results obtained for other types of radioactive waste forms.

1. Summary of paper to be published.

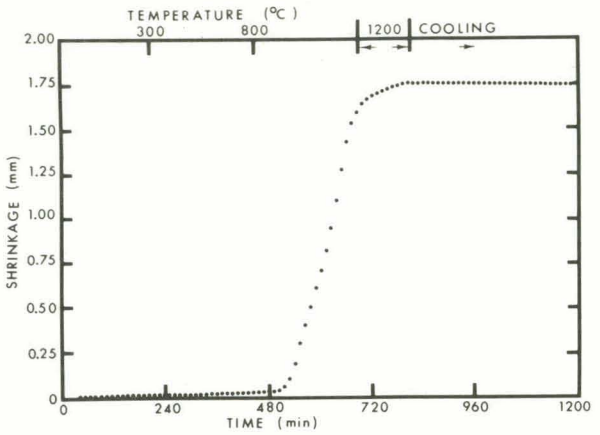

Fig. 6.2. The effect of temperature on sintering of $LaPO_4$ loaded with 10 wt % of PW-4b waste.

GEOLOGIC STABILITY OF MONAZITE AND ITS BEARING ON THE IMMOBILIZATION OF ACTINIDE WASTES[1]

R. J. Floran[2] L. A. Boatner
M. M. Abraham M. Rappaz[3]

An approach that is now a commonly used aid in evaluating crystalline substances that are potential high-level waste forms is to examine the long-term stability of natural analogs of these materials in geological/geochemical environments. In view of the increased attention recently accorded monazite, the geologic evidence for its stability during weathering (i.e., at ambient T and P), under hydrothermal conditions (at elevated T and P), and with regard to radiation damage (metamictization) has been examined. Monazite [$(Ce,La)PO_4$], the major member of the monazite group of minerals, is widely distributed and occurs in a variety of igneous, metamorphic, and sedimentary terrains. It occurs as an accessory phase in granitic and gneissic rocks, as large crystals in pegmatites, in vein deposits of hydrothermal origin, and as a heavy detrital mineral in sedimentary deposits and unconsolidated beach sands. The tendency of monazite to be concentrated along with other relatively insoluble heavy minerals in placer deposits is a reflection of its chemical and physical inertness. The stability of the monazite structure is demonstrated by the extreme rarity of reported partially metamict occurrences, not only of monazite but also of the isostructural mineral huttonite. Totally metamict or fully amorphous examples of these minera have never been reported. A puzzling observatio worth noting is an apparent discrepancy in susceptibility to metamictization by minerals with very similar crystal structures. This is well illustrated by comparing the monoclinic/tetragonal polymorphs of $ThSiO_4$ (huttonite/thorite) with their rare-earth orthophosphate counterparts (monazite/xenotime). Thorite, like zircon ($ZrSiO_4$), is often found in either a partially or fully metamict state. In contrast, xenotime (YPO_4) is rarely, if ever, metamict despite the fact that it is isostructural with both thorite and zircon. The reason for this differential response toward metamictization is not known. Based on the available geologic data, it appears that additional critical information needs to be gathered and evaluated. Research needs include a better understanding of the following: the leaching mechanism(s) in monazite and how these mechanisms could affect the mobility of rare-earth elements as well as U-Th-Pb systematics, the relative stabilities of the monazite group of minerals as a function of kinetic and thermodynamic parameters (e.g., pH and Eh), and the physical and chemical conditions under which monazite can (?) become metamict and the potential role that alteration may play in metamictization. Detailed investigations of a large suite of monazites are needed as well as a careful reexamination of the partially metamict monazites reported in the literature. A comparative study of monazite and related minerals that examines the critical role of crystal structure in the metamictization process might shed considerable light on this problem.

---

1. Summary of paper: p. 507 in *Scientific Basis for Nuclear Waste Management,* Vol. 3, ed. by J. G. Moore, Plenum Press, New York, 1981.

2. Union Oil Company, Brea, Calif.

3. Swiss National Fund for Scientific Research Fellow from Ecole Polytechnique Fedérale de Lausanne, Switzerland.

RAMAN SPECTRA OF THE RARE-EARTH ORTHOPHOSPHATES[1]

G. M. Begun[2] L. A. Boatner
G. W. Beall[3] W. T. Gregor[4]

Single crystals of all the lanthanide orthophosphates (except $PmPO_4$) doped with small amounts of Gd^{3+} were prepared for the initial purpose

erforming a series of electron paramagnetic resonance (EPR) experiments. The availability of these samples, however, made it possible to carry out a study of the Raman spectra for essentially the entire series of rare-earth orthophosphates. This study was directed toward two main objectives. First, baseline spectra were to be obtained that could be used as a basis of comparison with subsequent lanthanide orthophosphate crystals that would be doped with α-active actinides and, consequently, would be subjected to heavy-particle radiation damage. Second, a classification and correlation of the Raman spectra of the entire group of rare-earth orthophosphates were desired. Yttrium orthophosphate was included in the investigation because its properties are known to correlate well with those of the orthophosphates of the second half of the rare-earth series (i.e., $TbPO_4$ through $LuPO_4$) and also because YPO_4 is the analog of the natural mineral xenotime. Raman spectra of the Group I (La, Ce, Pr, Nd, Sm, Eu, and Gd) orthophosphates are shown in Fig. 6.3. The Raman spectra of the zircon-structure orthophosphates were also obtained. All these data were interpreted in a systematic manner based on the known structures of the compounds, and assignments and correlations were made for many of the observed bands.

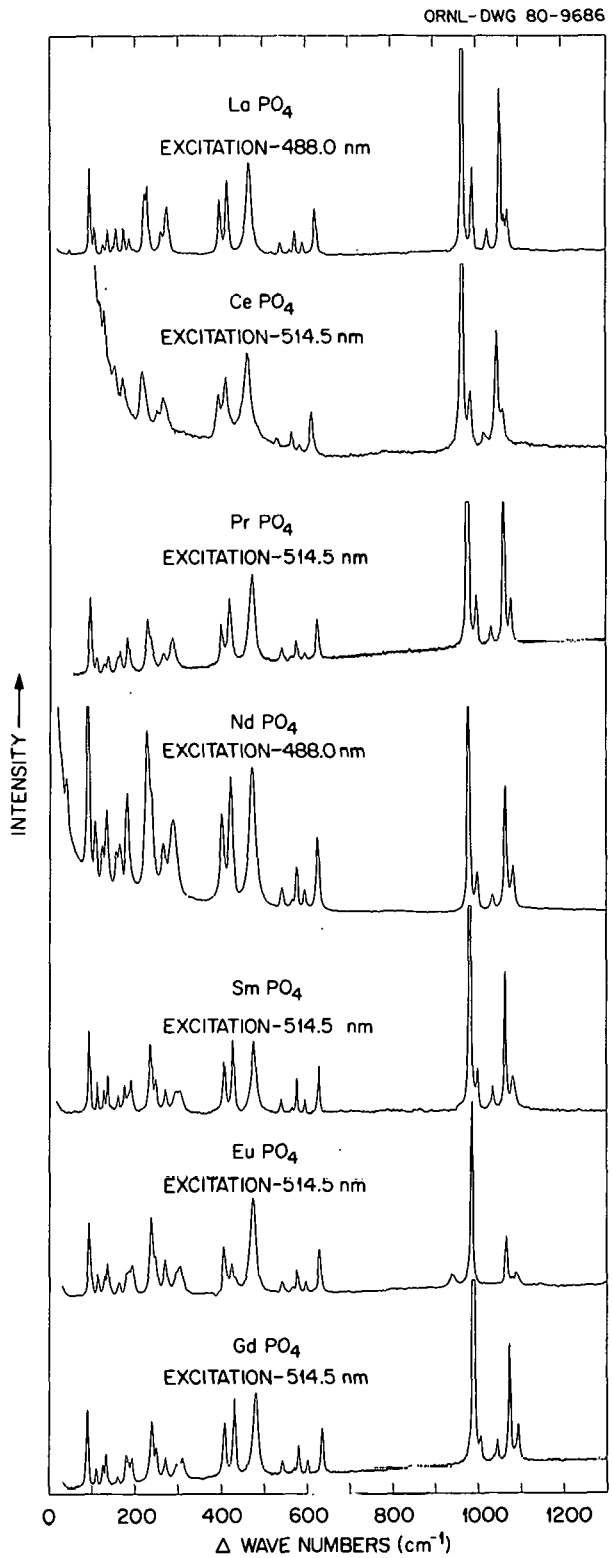

Fig. 6.3. Raman spectra of the Group I (La, Ce, Pr, Nd, Sm, Eu, and Gd) orthophosphates.

1. Summary of paper: *J. Raman Spectrosc.* **11**, 273 (1981).
2. Chemistry Division, ORNL.
3. The Radian Corporation, Austin, Tex.
4. The University of Tennessee, Knoxville, Tenn.

VALENCE STATES OF ACTINIDES IN SYNTHETIC MONAZITES[1]

K. L. Kelly[2] J. P. Young[3]
G. W. Beall[2] L. A. Boatner

A series of investigations has been initiated to determine the chemical properties of various actinides doped into the lanthanide orthophosphates. These investigations have included an identification of actinide valence states and studies of changes in the host crystal produced by radiation damage and subsequent annealing. An examination of undoped single crystals of $LaPO_4$ showed that this material was transparent over the entire spectral region of interest; and, accordingly, $LaPO_4$

was selected as a host for the incorporation of actinide impurities. Single crystals of $LaPO_4$ containing either ^{238}U, ^{242}Pu, ^{237}Np, ^{241}Am, or ^{246}Cm were prepared from starting mixtures which contained 10.0 wt % UO_2, PuO_2, or NpO_2, 0.5 wt % Am_2O_3, or 0.7 wt % Cm_2O_3 relative to La_2O_3. The actual concentrations of the actinides in the doped crystals were determined by means of analytical techniques. In order to obtain optical absorption spectra, the actinide-doped orthophosphate crystals were placed in a quartz capillary that was then mounted in a microscope spectrophotometer.

Crystals of $LaPO_4$ doped with ^{238}U were characterized by a bright green color, and the optical absorption spectrum shows that uranium is primarily in the tetravalent state. Several small peaks were observed at 630, 790, and 900 nm, which indicates that a small amount (~5%) of U^{3+} is also probably present.

Plutonium-doped single crystals of $LaPO_4$:5.0 wt % Pu exhibited a dark purple coloration. The optical absorption spectrum indicates that plutonium, like uranium, is incorporated in $LaPO_4$ in the tetravalent state. There is no indication of the presence of Pu^{3+} in the $La(Pu)PO_4$ spectrum.

The absorption spectra of $LaPO_4$ crystals doped with 0.2 wt % ^{241}Am show that americium is incorporated in the trivalent state (see Fig. 6.4). The americium-doped $LaPO_4$ crystals were characterized by an amber color when removed from the Pt crystal growth crucible. $La(^{241}Am)PO_4$ crystals were annealed at ~500°C for 16 h; and they became colorless, indicating that the amber color was due to radiation damage and was not associated with optical absorption arising from americium ions. The amber color returned to the crystals within a short time following their removal from the annealing furnace.

Single crystals of $LaPO_4$ doped with ~0.2 wt % ^{246}Cm are also characterized by an amber color. The optical spectra obtained for the $La(^{246}Cm)PO_4$ specimens did not exhibit any absorption peaks that could definitely be assigned to curium. Curium is expected to be in the 3+ valence state, and the absence of any observable Cm(III) absorption peaks can be explained by the poor spectral sensitivity of this ion coupled with its low concentration in the crystal.

The absorption spectrum of $La(Np)PO_4$ (~2.0 wt % Np) was also studied. These crystals are characterized by a bright green color. A comparison of the $La(Np)PO_4$ spectrum with that of

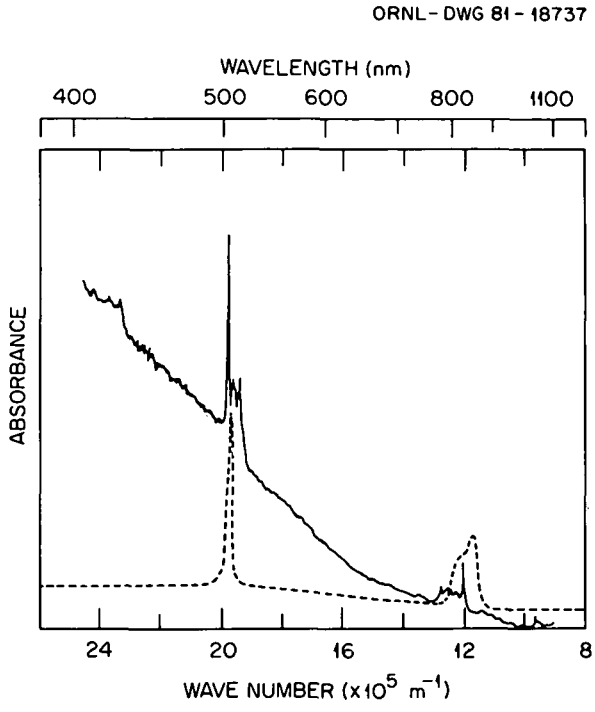

Fig. 6.4. The optical absorption spectrum of La(Am 0.2 wt %)PO_4 (solid curve). For purposes of comparison, the dashed curve shows the absorption spectrum of Am^{3+} in fayolite.

Np(IV) in an aqueous solution of $HClO_4$ shows that tetravalent neptunium is present in the orthophosphate single crystal. No changes in the crystal color as a function of time were observed in the case of ^{237}Np-doped $LaPO_4$.

In summary, the valence states of the actinides doped into single crystals of $LaPO_4$ were found to be U(IV), U(III), Pu(IV), Np(IV), Am(III), and most probably Cm(III). Since it is known that trivalent and tetravalent ions are generally less mobile in geologic media than pentavalent or hexavalent ions, the present determination that the actinides are in these "less mobile" valence states in $LaPO_4$ can be a significant factor in reinforcing the viability of employing analogs of monazite as a primary containment form for high-level transuranic wastes.

1. Summary of paper: p. 189 in *Scientific Basis for Nuclear Waste Management*, vol. 3, ed. by J. G. Moore, Plenum Press, New York, 1981.
2. The Radian Corporation, Austin, Tex.
3. Analytical Chemistry Division, ORNL.

EPR SPECTROSCOPIC CHARACTERIZATION OF Gd^{3+} IN THE MONAZITE-TYPE RARE-EARTH ORTHOPHOSPHATES: $LaPO_4$, $CePO_4$, $PrPO_4$, $NdPO_4$, $SmPO_4$, AND $EuPO_4$[1]

M. Rappaz[2] J. O. Ramey
M. M. Abraham L. A. Boatner

Materials for the primary containment of long-lived radioactive wastes must satisfy a number of stringent criteria. These criteria include high retention of actinide and other radioactive ions at the elevated temperatures associated with useful concentrations of nuclear waste, long-term chemical and physical stability under the conditions that can exist in a geological repository, and resistance to α-particle and recoil radiation damage. The various possible scenarios inherent to storage in a deep geological formation include exposure of the waste form to hydrothermal conditions. Recent findings[3,4] have indicated that borosilicate glasses which have been seriously considered as primary radioactive waste forms are, in fact, both chemically and physically unstable under hydrothermal conditions, and these results have prompted a reconsideration of alternative crystalline materials for the containment of nuclear wastes.

The mineral monazite, a mixed lanthanide orthophosphate $LnPO_4$, may represent an ideal host for geologic disposal of actinides, rare earths, and possibly other elements formed during nuclear reactor operation. Synthetic monazite-type orthophosphates of all the elements of the first half of the lanthanide series (except Pm) have been prepared; single crystals were grown using a flux technique, and powders were precipitated in molten urea. The EPR spectra of intentionally added Gd impurities show that the Gd^{3+} ions occupy predominantly substitutional rare-earth sites in both the flux-grown single crystals and the precipitated powders. Though these sites have a very low (triclinic C_1) symmetry, the spectra were successfully interpreted using an orthorhombic spin-Hamiltonian. It has been found that, while the main spin-Hamiltonian parameter b_2^0 is almost constant through the series from $LaPO_4$ to $EuPO_4$ ($b_2^0 \simeq +830 \times 10^{-4}$ cm^{-1}), the parameter b_2^2 decreases monotonically from $+373 \times 10^{-4}$ cm^{-1} to $+283 \times 10^{-4}$ cm^{-1}, respectively. A complete analysis (i.e., angular variations of the EPR lines and position of the principal electric-field axes relative to the crystallographic axes) of the EPR single-crystal spectra was done for the two diamagnetic hosts $LaPO_4$ and $EuPO_4$, where the observed EPR lines were the sharpest. The angular variation of the Gd^{3+} EPR spectrum in $EuPO_4$ is illustrated in Fig. 6.5. It was shown that the two magnetically inequivalent EPR spectra (i.e., 14 lines) observed for the monazite-type single crystals are equivalent when the magnetic field is applied parallel or perpendicular to the b-axis of the monoclinic structure (i.e., for these directions, only seven doubly degenerate lines are observed). These results are in perfect agreement with the description of the monazite structure whose unit cell contains four "different" rare-earth sites that transform with the symmetry operations of the C_{2h} group. The present investigations constitute an indispensable basis for subsequent studies of actinide-doped monazite orthophosphates or of α-induced radiation damages in these hosts.

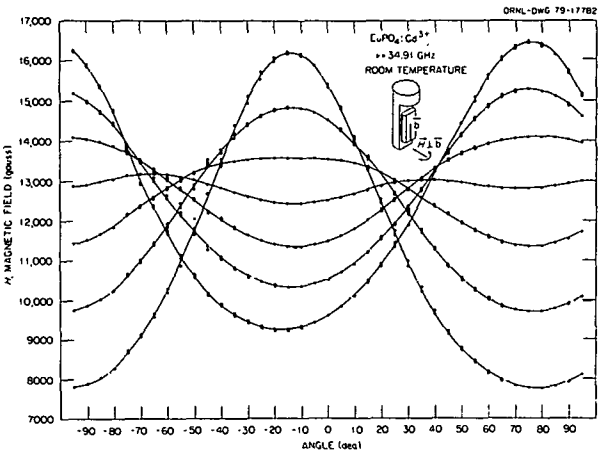

Fig. 6.5. Angular dependence of the EPR lines of Gd^{3+} in a $EuPO_4$ single crystal when the applied magnetic field H is rotated in a plane perpendicular to the b-axis of the crystal [i.e., the (010) plane]. Each curve is doubly degenerate. The resolution of the superimposed lines, which occurs for certain angles due to a small misalignment of the crystal, is more evident for the $\pm 7/2 \Leftrightarrow \pm 5/2$ transitions.

1. Summary of paper: *Phys. Rev. B* **23**, 1012 (1981).
2. Swiss National Fund for Scientific Research Fellow from Ecole Polytechnique Fedérale de Lausanne, Switzerland.
3. G. J. McCarthy et al., *Nature* **273**, 316 (1978).
4. R. C. Ewing, *Science* **192**, 1336 (1976).

EPR INVESTIGATIONS OF RARE-EARTH IMPURITIES IN THE LANTHANIDE ORTHOPHOSPHATES[1]

M. M. Abraham L. A. Boatner
M. Rappaz[2]

The function of a crystalline substance in the role of a primary waste form is to incorporate or stabilize radioactive (and other) impurities in its crystal structure. The properties of such an impurity-host ensemble can be determined, to a substantial degree, by the application of EPR spectroscopy. Prior to the investigations of radioactive actinide-doped samples, a systematic EPR study of their isoelectronic rare-earth analogs has been performed. Isotopically enriched impurities were employed, and EPR spectra of the Kramers' ions, Ce^{3+}, Nd^{3+}, Dy^{3+}, Er^{3+}, and Yb^{3+}, were observed in the tetragonal hosts $LuPO_4$, YPO_4, and $ScPO_4$. Unambiguous identifications of the various elements were facilitated by the use of the enriched isotopes and their corresponding hyperfine structures.

An example of an EPR spectrum in which the spectral complexity has been reduced by employing an enriched isotope is illustrated in Fig. 6.6. Here, a single crystal of YPO_4 (xenotime) has been deliberately doped with the enriched isotope ^{145}Nd. The characteristic eight-line hyperfine pattern, coupled with the measured spectroscopic parameters, can be used to identify the responsible ion as $^{145}Nd^{3+}$. The spectrum of Nd^{3+} is of particular interest since its electronic properties (it is characterized by a $4f^3$ electronic configuration) are analogous to those of trivalent uranium, which has a $5f^3$ configuration. By investigating the spectroscopic properties of Nd^{3+}, it is possible to identify and investigate impurities of ^{238}U and to avoid the necessity of employing the radioactive uranium isotopes ^{233}U or ^{235}U. It should be noted that EPR transitions due to Gd^{3+} and Er^{3+} (naturally abundant) are also present in the spectrum shown in Fig. 6.6. These EPR results, combined with studies of other impurity ions, show that it is possible to incorporate 2+, 3+, 4+, and 5+ ions in the lanthanide orthophosphates. The ability to deter-

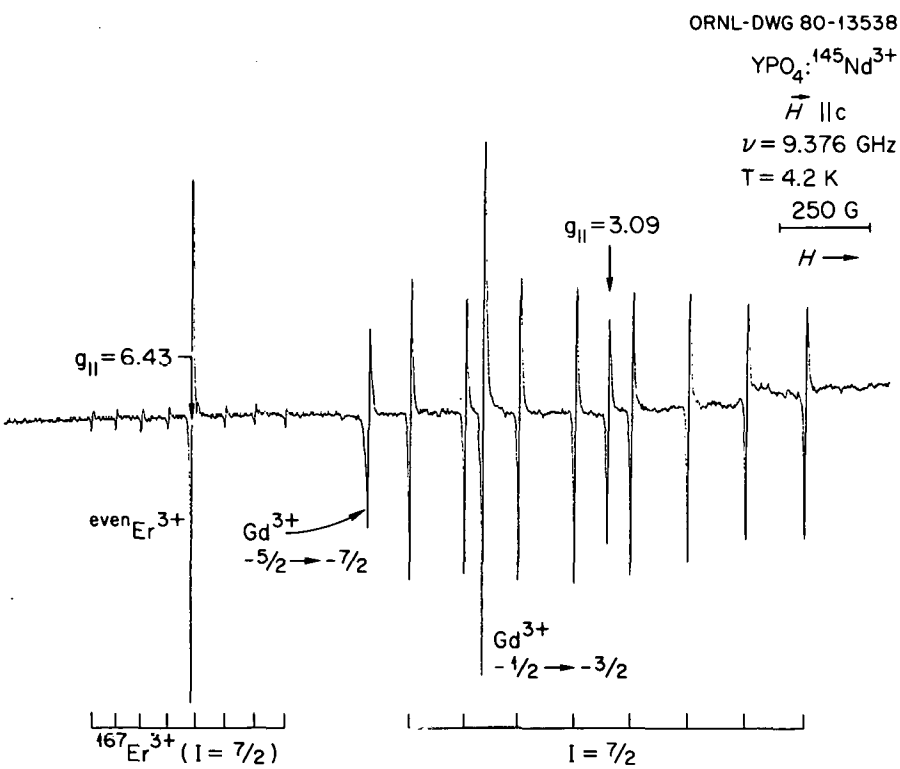

Fig. 6.6. The EPR spectrum of $^{145}Nd^{3+}$ in YPO_4. Positions of the eight ^{145}Nd ($I = 7/2$) hyperfine lines are indicated. The spectrum of naturally abundant Er^{3+} is also in evidence along with two Gd^{3+} fine-structure lines.

nine the valence states of various impurities and to obtain information regarding the location of ions in the host orthophosphate lattice represents an important capability in the evaluation of these materials as radioactive waste forms.

1. Summary of paper: p. 475 in *Nuclear and Electron Resonance Spectroscopies Applied to Materials Science*, vol. 3, ed. by E. N. Kaufmann and G. K. Shenoy, North Holland, New York, 1981.

2. Swiss National Fund for Scientific Research Fellow from Ecole Polytechnique Fedérale de Lausanne, Switzerland.

OPTICAL SPECTRA AND ZEEMAN EFFECT FOR Er^{3+} IN $LuPO_4$ AND $HfSiO_4$[1]

T. Hayhurst[2] N. Edelstein[2]
G. Shalimoff[2] L. A. Boatner
M. M. Abraham

Synthetic analogs of the mineral monazite [(La, Ce, Nd, Y, ...)PO_4] have chemical and physical properties that make them attractive candidates as host materials for long-term storage of actinide wastes. Accordingly, the characterization of possible sites where actinide (and other) impurity ions can be incorporated in these materials and a determination of the oxidation states of these ions are pertinent to understanding the interrelationship between the chemical and physical properties of the lanthanide orthophosphate impurity systems and the parameters appropriate to an acceptable stable waste form. Optical absorption and Zeeman effect studies were carried out in the range 0.4–3.0 nm for Er^{3+} as a dilute impurity in $LuPO_4$. Energy levels were assigned to states derived from the constraint of an f^{11} configuration restricted to D_{2d} point symmetry and were fit to a semiempirical Hamiltonian by a least-squares minimization. Parameters describing the electrostatic, spin-orbit, and crystal-field interactions were adjusted. Results of this analysis, along with the previously reported EPR measurements, were used to assign the optical spectra of Er^{3+} in $HfSiO_4$. Although hafnium silicate is isostructural with $LuPO_4$, it appears that the trivalent Er ion could substitute in more than one site in the silicate host crystal. By a close comparison with the Er^{3+}:$LuPO_4$ system, the spectra associated with only the D_{2d} site were assigned, and good agreement was obtained between the experimental and calculated energy levels. The crystal-field parameters obtained in this work provide a basis for future work on tetrapositive actinide ions (e.g., Np^{4+}) in this type of host crystal.

1. Summary of paper: *J. Chem. Phys.* **74,** 5449 (1981).

2. Lawrence Berkeley Laboratory, Berkeley, Calif.

A NOVEL MEASUREMENT OF HYPERFINE INTERACTIONS IN SOLIDS: $^{207}Pb^{3+}$ IN YPO_4 AND $LuPO_4$[1]

M. M. Abraham L. A. Boatner
M. Rappaz[2]

In order to characterize the rare-earth and related orthophosphates systematically in the laboratory, numerous synthetic single crystals of these materials have been grown by means of a lead-based flux technique. Ensuing EPR investigations indicated that Pb^{3+} impurities were present in single crystals of $LuPO_4$ and YPO_4 produced by this method. A positive identification of Pb^{3+} was made from the observation of the spectrum of the 20.8% naturally abundant isotope ^{207}Pb, which has a characteristically large hyperfine interaction. The hyperfine constants, which proved to be larger than any reported previously for ^{207}Pb, were fortuitously in a range that made the application of a new measurement technique possible.

The electronic configuration of Pb^{3+} is [Xe] $4f^{14}$ $5d^{10}$ $6s^1$, and the associated ground state is $^2S_{1/2}$. In the absence of a nuclear spin, the EPR spectrum for such a state will consist of a single line whose g value is close to the free electron value of $g = 2.00232$. This line was observed in both the $LuPO_4$ and YPO_4 single crystals and is due to the ~80% naturally abundant even-even Pb^{3+} nuclei. The g value of this line was slightly anisotropic as a result of the tetragonal symmetry characteristic of these particular orthophosphate hosts. The isotope ^{207}Pb has a nuclear spin $I = 1/2$, but since the hyperfine constant is larger than the frequencies commonly employed in EPR measurements, the usual spectrum consisting of two allowed $\Delta M_S = \pm 1$, $\Delta m_I = 0$ transitions was not observed. EPR spectrometers were available in the X-band (~10 GHz), K-band (~25 GHz), and K_A-band (~35 GHz) regions. The transitions observed in these three microwave regions are indicated in Fig. 6.7

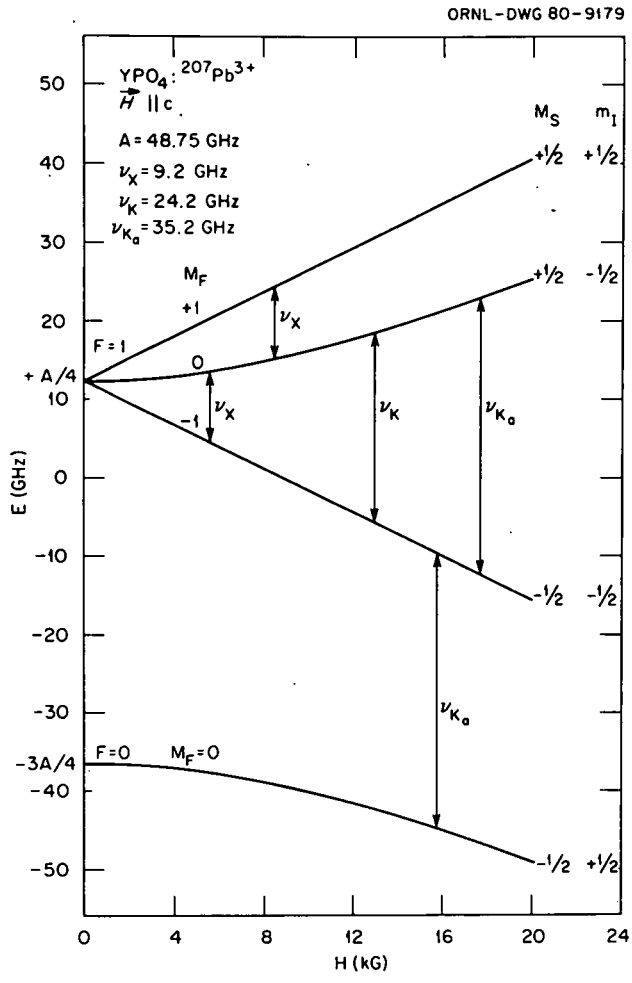

Fig. 6.7. Breit-Rabi diagram for $^{207}Pb^{3+}$ in a YPO_4 single crystal. The indicated transitions were observed in three different microwave frequency ranges [X, K, and K_A bands]. The two K_A-band transitions are shown in Fig. 6.8 as a function of the microwave frequency.

for representative frequencies within the available ranges. The particular value of the $^{207}Pb^{3+}$ hyperfine constant in YPO_4 and $LuPO_4$, relative to the K_A-band frequency range, presented a unique opportunity for a determination of the hyperfine spin-Hamiltonian parameters. The microwave frequency ν could be adjusted so that both the allowed and forbidden transitions shown in Fig. 6.7 occurred at exactly the same magnetic field position. The uniqueness of this procedure lay in the fact that a measurement of the laboratory magnetic field was precluded and the hyperfine values could be determined to the same accuracy as the microwave frequency. Figure 6.8 shows the allowed

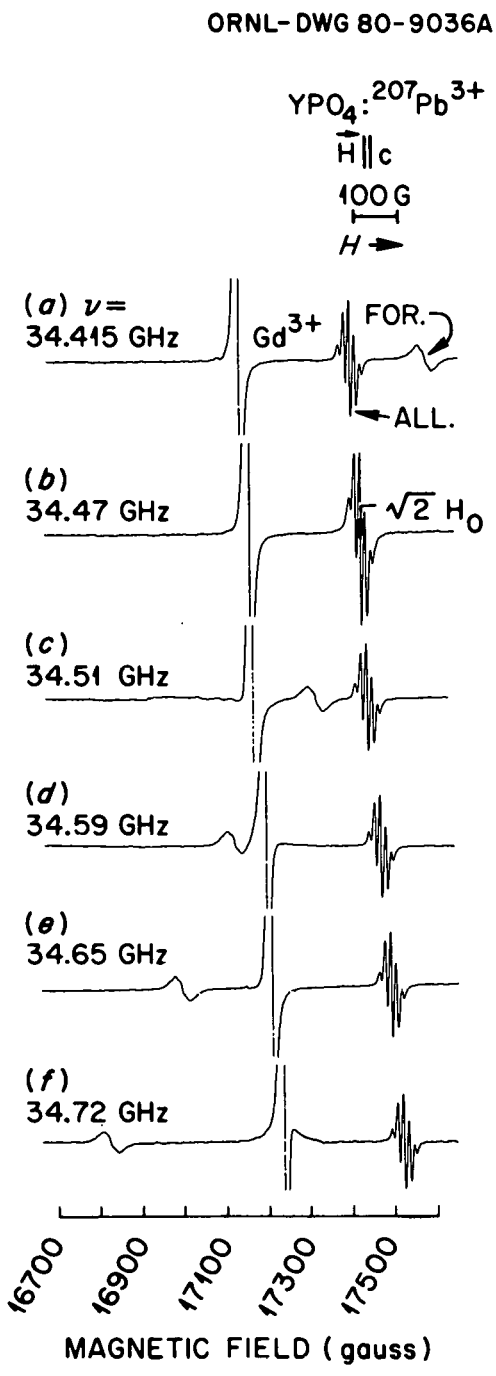

Fig. 6.8. Microwave frequency dependence of $^{207}Pb^{3+}$ (I = 1/2) EPR transitions in YPO_4. The allowed transition corresponds to $\Delta M_S = \pm 1$, $\Delta m_I = 0$; and the forbidden transition corresponds to $\Delta M_S = 0$, $\Delta m_I = \pm 1$. The coincidence of the two lines occurs at $\nu = 34.47$ GHz and provides a direct measurement of A. The extreme position of the M_S: $+7/2 \Leftrightarrow +5/2$ transition shown for Gd^{3+} was established at each frequency and provided an accurate method for orienting the crystal.

and forbidden transitions for several frequencies, at and near coincidence, in the YPO_4 host. If the approximation $A_\parallel = A_\perp$ is made, then the "isotropic" value of A is $A_{iso} = \sqrt{2}\,\nu$. The allowed hyperfine transition in Fig. 6.8 shows a resolution into superhyperfine satellites which arise from the interaction with neighboring nuclei. The forbidden hyperfine line shown in Fig. 6.8, however, does not exhibit a well-resolved superhyperfine structure.

The hyperfine interaction determined here for $^{207}Pb^{3+}$ in both YPO_4 and $LuPO_4$ is the largest ever found for Pb^{3+} in solids and indicates that these particular orthophosphates have a strong ionic character. By comparison with the free atom value, however, it is evident that the wave function is still distorted to a large extent. Trivalent lead is apparently stabilized in the substitutional rare-earth site by the solid state chemical restraints of the host lattice. This situation is similar to the stabilization of divalent rare-earth ions in the divalent alkaline-earth halides. In this case, however, no irradiation or electrochemical reduction was necessary.

1. Summary of paper: *Phys. Rev. Lett.* **45**, 839 (1980).

2. Swiss National Fund for Scientific Research Fellow from Ecole Polytechnique Fedérale de Lausanne, Switzerland.

EPR INVESTIGATIONS OF Fe^{3+} IN SINGLE CRYSTALS AND POWDERS OF THE ZIRCON-STRUCTURE ORTHOPHOSPHATES $LuPO_4$, YPO_4, AND $ScPO_4$[1]

M. Rappaz[2] L. A. Boatner
J. O. Ramey M. M. Abraham

In an actual nuclear waste form, the actinides and rare earths may not be separated from a number of other elements that are present in the waste material. Accordingly, the properties of mixed systems in which these other elements are combined with the lanthanide orthophosphates are of considerable practical importance; therefore, investigations oriented toward impurity elements other than those of the 4f and 5f transition series were undertaken. Iron was investigated since this element is found in relatively high concentrations in some high-level waste compositions (e.g., 58 mol % Fe is contained in the PW-7a composition and up to 30 mol % Fe is found in the PW-8a composition). Additionally, the $^6S_{5/2}$ ground state resulting from the $3d^5$ configuration of Fe^{3+} is characterized by magnetic properties that are similar in many ways to those associated with the $^8S_{7/2}$ ground state of Gd^{3+}, which was previously studied.

The EPR spectra of Fe^{3+} in both powders and single crystals of the zircon-type orthophosphates $ScPO_4$, YPO_4, and $LuPO_4$ were examined. Iron-doped single crystals of these orthophosphates were grown by means of a flux technique. Corresponding powders were prepared independently by a urea precipitation technique, and EPR measurements demonstrate that the Fe^{3+} impurity is situated in the same substitutional site in both the single crystals and the powders for all three hosts (see Fig. 6.9). The sign of the crystal-field parameter b_2^0 was shown to be positive (opposite to that found for Gd^{3+} in these hosts). Of the three hosts, the crystal-field splittings were found to be largest for scandium and smallest for yttrium. Accordingly, iron can be incorporated into a substitutional crystallographic site in material prepared by either a high-temperature process or by a low-temperature precipitation and calcination ($\sim$800°C). These findings have implications for the use of lanthanide and related orthophosphates as a host material for the isolation of nuclear wastes.

1. Summary of paper to be published.

2. Swiss National Fund for Scientific Research Fellow from Ecole Polytechnique Fedérale de Lausanne, Switzerland.

EPR INVESTIGATIONS OF ^{243}Cm AND ^{244}Cm IN $LuPO_4$ SINGLE CRYSTALS[1]

M. M. Abraham L. A. Boatner

The natural mineral monazite is characterized by an established long-term stability under a variety of geological conditions; additionally, monazites contain appreciable amounts of uranium and thorium. Accordingly, the lanthanide orthophosphates that are synthetic analogs of monazite are of interest as hosts for the immobilizaton of α-active actinide wastes.

EPR spectroscopy has been used in characterizing orthophosphate-impurity systems, because the number of observed EPR transitions and their position as a function of the strength and relative

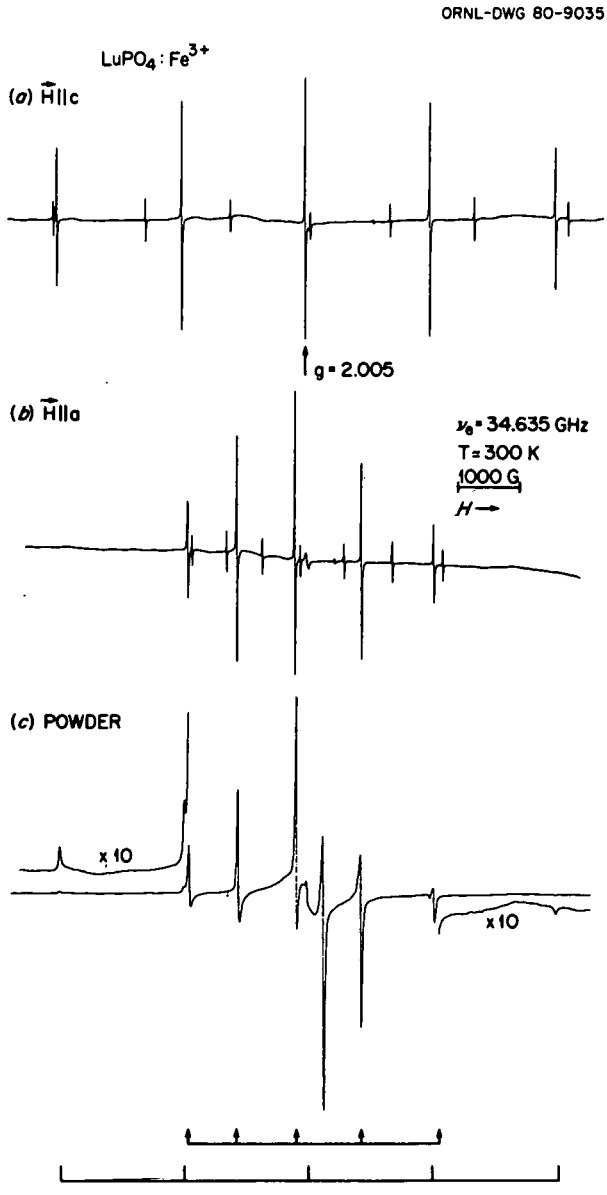

Fig. 6.9. EPR spectrum, at K_A band and room temperature, of Fe^{3+} in $LuPO_4$: (a,b) single crystal with H parallel and perpendicular, respectively, to the c-axis and (c) powder. The Fe^{3+} transitions are labeled at the bottom. The divergence of the central line that occurs for θ = arc cos $\pm \sqrt{5}/3$, as well as extra lines due to Gd^{3+}[6] and Pb^{3+}, is not labeled.

orientation of the magnetic field can be used to determine the valence state of the paramagnetic impurity and the site occupied by the impurity and can also provide information regarding the local crystal structure. Previous EPR studies of Gd^{3+} ($4f^7$) in the orthophosphate hosts have established that, while the impurity ion is located in the substitutional rare-earth site, the crystal-field interaction, which splits the S = 7/2 ground state, is positive for the monoclinic hosts and negative for the tetragonal hosts. The actinide analog of Gd^{3+} (i.e., Cm^{3+}, $5f^7$) was incorporated into the tetragonal host $LuPO_4$, and the EPR spectra of both ^{243}Cm and ^{244}Cm were observed. The I = 5/2 nuclear spin of the ^{243}Cm isotope allows a positive identification to be made, and Fig. 6.10 shows the spectrum observed at T = 4.2 K with the magnetic field applied parallel to the crystal tetragonal c axis. The g value in this parallel orientation is 7.98(1), while the corresponding value in the perpendicular orientation is 4.096(4). These values

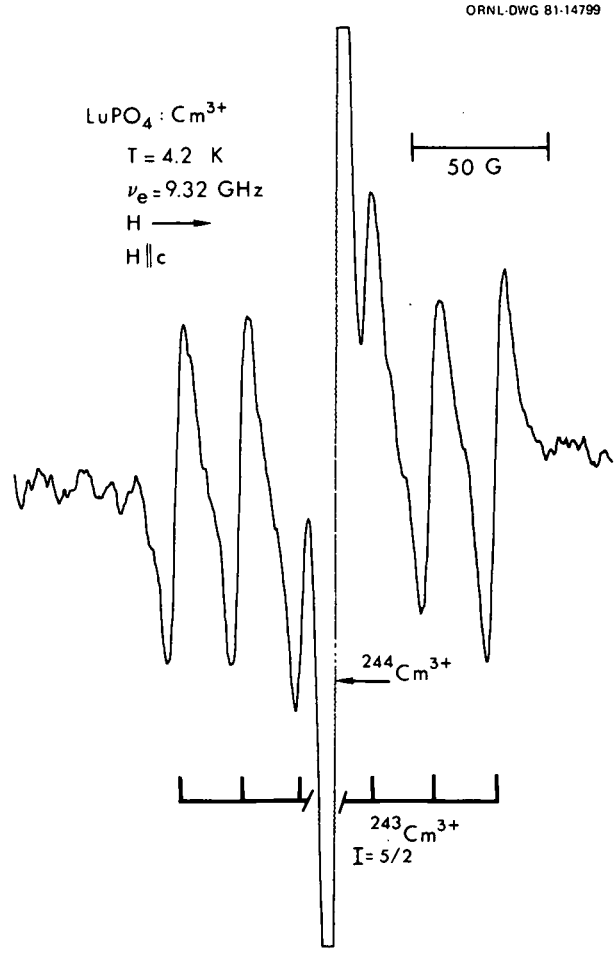

Fig. 6.10. The EPR spectrum of trivalent ^{244}Cm in a single crystal of $LuPO_4$. The six hyperfine lines associated with the I = 5/2 nuclear spin of ^{243}Cm are identified by the bar graph at the bottom of the figure.

innot be fit to a doublet wave function $\alpha \mid \pm /2\rangle + \beta \mid \mp 1/2\rangle$ to give a consistent Landé g factor but can be fit to the doublet wave function $\alpha \mid \pm 5/2\rangle + \beta \mid \mp 3/2\rangle$ yielding a Landé g factor of 1.92. Further verification of this doublet identification comes from the observation that lowering the temperature to $=1.5$ K reduces the intensity of the EPR signals, clearly indicating that this is an excited doublet. Therefore, the sign of the crystal-field interaction for the $5f^7$ ion in the tetragonal $LuPO_4$ host is negative and is the same as that found previously for the $4f^7$ ion.

Additional investigations of Np and other actinide impurities are in progress.

1. Summary of paper to be published.

RUTHERFORD BACKSCATTERING INVESTIGATION OF THE CORROSION OF BOROSILICATE GLASS[1]

B. C. Sales H. Naramoto[2]
L. A. Boatner C. W. White

Borosilicate glass is one of the candidate primary containment materials currently being evaluated for use in the long-term storage of nuclear wastes. The French have adopted borosilicate glass as their official nuclear waste form, and it may be chosen as the first-generation waste form for radioactive U.S. defense wastes. One of the major concerns regarding the use of glass, however, is its ability to retain hazardous radioactive nuclei when exposed to groundwater at temperatures above ambient. The removal of radioactive nuclei from glass in an aqueous environment is referred to as leaching or corrosion. Predictions of the long-term leaching characteristics of glass must necessarily be based on the extrapolation of data from experiments with durations much shorter than the half-lives of the more dangerous radioactive nuclei. Obviously, the ability to extrapolate reliably the results from these studies depends on how well one understands the mechanisms of glass corrosion. Although there is a good qualitative understanding of the leaching of simple borosilicate glasses, more quantitative data and theories are needed. In particular, it is not sufficient for a theory to account for the concentration of ions found in the leachant solution during an experiment. The chemical structure of the leached glass surface must also be considered, since this layer greatly affects subsequent leaching characteristics of the glass.

The technique of depth profile analysis by means of Rutherford backscattering (RBS) has been used to study changes due to leaching in the chemical composition of the 1–2 micron surface layer of borosilicate glass. Several prototype borosilicate glasses were prepared by melting appropriate amounts of the constituent oxides in a platinum crucible at 1160°C. The molten glass was poured into a mold of spectroscopically pure carbon, annealed at 550°C for 2 h, and then slowly cooled to room temperature. Samples measuring $0.5 \times 1.0 \times 0.2$ cm^3 were cut from the resulting glass billets. One surface of each sample was polished to a 1.0-μ finish with Al_2O_3 powder. The samples were then leached in distilled water at 90°C in a Teflon container for times ranging from 0.5–48 h.

A beam of 2 MeV $^4He^+$ ions was scattered from both leached and unleached borosilicate glass surfaces. Analysis of the energies of the $^4He^+$ ions scattered by the nuclei of the elements in the glass allows one to determine quantitatively the concentration of each element as a function of depth in a 1–2 micron surface layer. The depth resolution is about 150 Å. The sensitivity of RBS to a particular element is proportional to its atomic number squared. Hence, in a simple borosilicate glass composed mainly of the elements Si, Na, B, and O, one can detect much less than 1 at. % of the heavier nuclear waste elements such as Sr, Cs, U, and the other actinides. The large atomic numbers of the waste elements also simplify the depth-vs-concentration calculations.

Some typical results are shown in Fig. 6.11. A prototype borosilicate glass, with the composition developed at the Savannah River facility, was prepared and doped with 5 wt % $^{238}UO_2$. Four glass samples cut from this billet were leached in distilled water at 90°C for 0, 0.5, 3, and 24 h. After leaching, the polished surface of each sample was coated with a 100-Å film of Al to prevent charging. The backscattering spectra which consist of the total backscattering yield in counts vs energy are shown in Fig. 6.11 for the leached and unleached glass samples. The RBS spectra of the unleached glass indicate that the ^{238}U concentration is uniform to a depth of 1–2 μ. The magnitude of the ^{238}U concentration calculated from the spectra is consistent with the amount of $^{238}UO_2$ added to the glass. After leaching the glass for 0.5 h, there is a threefold increase in the

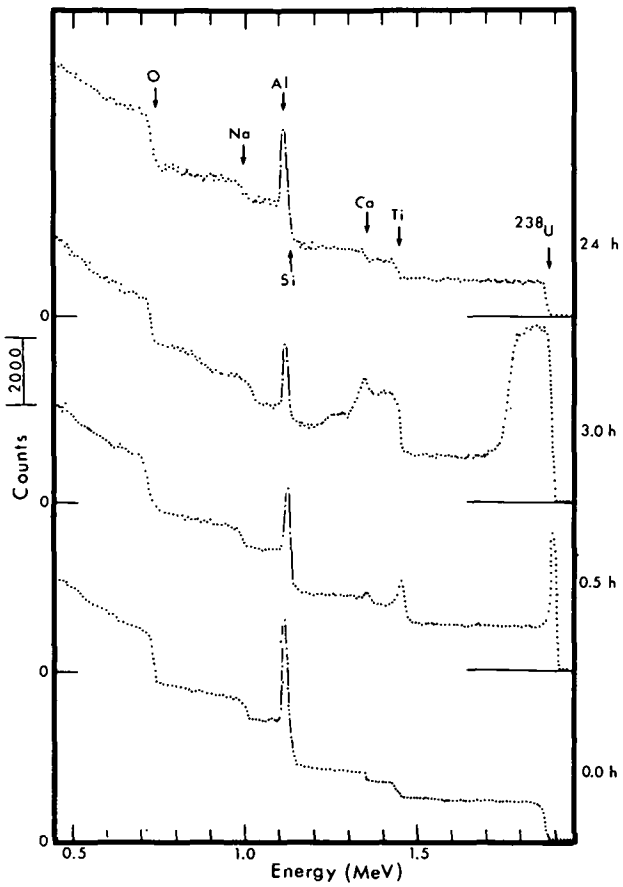

Fig. 6.11. Energy spectra of 2 MeV $^4He^+$ ions backscattered from leached and unleached borosilicate glass doped with 5 wt % UO_2. The glass was leached in distilled water at 90°C for 0, 0.5, 3, and 24 h.

U concentration within 150 Å of the surface. The near-surface concentrations of Ti and Ca also increased. After leaching for 3 h, the U concentration increases even further and extends to a depth of about 1 μm. A similar increase is observed for Ti and Ca, but there is a depletion of both Na and Si from a 1-μm-thick surface region.

After leaching for 24 h, however, the composition of the leached surface layer is virtually identical to the unleached surface. This is probably due to the large increase in the pH of the water, which attained a value of 10.1 after 24 h. For a pH $\gtrsim$ 9, the entire glass network begins to dissolve, and apparently the rate of dissolution is faster than the rate of formation of the surface layer. Experiments are under way to test this hypothesis. Experiments on Sr-, Cs-, Gd-, Nd-, and Fe-doped glasses are also in progress.

1. Summary of paper to be published.
2. Guest scientist from Japan Atomic Energy Research Institute, Tokai-mura, Japan.

FERROELECTRIC MATERIALS

RAMAN SCATTERING STUDIES OF THE IMPURITY-INDUCED FERROELECTRIC PHASE TRANSITION IN $KTaO_3$:Nb[1,2]

R. L. Prater[3] L. L. Chase[3]
L. A. Boatner

Potassium tantalate is a cubic perovskite-structure material that exhibits the characteristics of a ferroelectric whose transition temperature is near absolute zero. In the purest $KTaO_3$ samples investigated thus far, an actual transition to a ferroelectric phase has not been observed at temperatures as low as 1.6 K. Potassium tantalate and strontium titanate are currently the only two known substances which exhibit this type of behavior, and term "incipient ferroelectric" has been applied to these special materials. For both $KTaO_3$ and $SrTiO_3$, deviations of the behavior of the dielectric constant from a Curie law dependence have been attributed to the presence of a paraelectric phase that is "quantum stabilized" (i.e., the zero-point motion of the lattice is comparable to or larger than the energy corresponding to a distortion of the lattice into a ferroelectric structure).

Raman scattering and optical depolarization measurements have been employed in investigations of the ferroelectric phase transition in $KTa_{1-x}Nb_xO_3$ in the limit $x \leq 0.05$. The critical niobium concentration for which $T_c \approx 0$ K was found to be $x_c = 0.008$, in agreement with previous acoustic resonance results. Electric-field-induced Raman scattering and disorder-induced Raman scattering were used to study the zone center TO frequency as a function of x and temperature. At a given temperature, the TO frequency decreases with increasing x and no new low frequency vibrational features due to the Nb are observed. The Raman spectra as a function of temperature are indicative of a soft-mode-dominated displacive transition to a rhombohedral ferroelec-

ric phase. The soft mode frequencies in both phases, however, remain finite ($\sim 10\ cm^{-1}$) in the immediate vicinity of T_c. Disorder-induced scattering features in the paraelectric phase in all of the samples (including pure $KTaO_3$) are attributed to first-order scattering from the coupled TO and TA branches. The TA peak has previously been associated with a resonance mode of lithium impurities. The observed TA scattering was modeled using parameters obtained previously from neutron scattering investigations, and good agreement was found for the frequency of this feature as a function of the soft mode energy. The presence of Nb has no effect on the intensity of any of the disorder-induced features, and the exact source of the disorder is presently undetermined.

1. Research sponsored in part by NSF grant DMR 78-09426.

2. Summary of paper: *Phys. Rev. B* **23**, 221 (1981).

3. Indiana University, Bloomington, Ind.

PHOTOREFRACTIVE EFFECTS IN THE CUBIC PHASE OF POTASSIUM TANTALATE-NIOBATE[1]

R. Orlowski[2] L. A. Boatner
E. Krätzig[3]

Light-induced changes in the index of refraction (i.e., photorefractive effects) arise as a result of optically generated space-charge fields. When an electro-optic crystal is exposed to a light interference pattern, electrons in the regions of high light intensity are excited and displaced. The internal electric fields generated by this charge transport modulate the refractive index by means of the electro-optic effect. Uniform illumination of the specimen produces a corresponding uniform redistribution of the charge and returns the crystal to its original state.

The Curie point of single crystals of potassium tantalate-niobate (i.e., $KTa_{1-x}Nb_xO_3$ or KTN) can be varied by controlling the niobium/tantalum ratio; and, accordingly, the electro-optic properties of these substances can be effectively "tailored" by means of a variation of this type. The ability to exercise such control over the electro-optic properties makes the KTN system particularly interesting for the storage of volume phase holograms via photorefractive effects. The linear electro-optic effect can be employed when the Nb/Ta ratio and crystal temperature are such that the system is in the ferroelectric tetragonal phase, and the quadratic electro-optic effect can be utilized when conditions correspond to the presence of the nonferroelectric cubic phase. Recent measurements using incoherent light have shown that the storage properties of KTN are very attractive in both cases.

In this work holographic techniques have been used to study photorefractive effects associated with quadratic electro-optic mechanisms in the cubic phase of KTN. An expression for the dependence of the refractive index change produced by external writing and by reading electric fields was derived, and the validity of the expression was examined by means of two-beam interference experiments. Additionally, the light-induced charge transport in KTN was investigated, and the sign of the dominant light-induced charge carriers was determined by means of beam coupling experiments carried out in the absence of an applied writing electric field.

1. Summary of paper: *Opt. Commun.* **35**, 45 (1980).

2. Philips Laboratories, Hamburg, Germany.
3. University of Osnabrück, Osnabrück, Germany.

RAMAN SCATTERING STUDIES OF THE IMPURITY-INDUCED FERROELECTRIC PHASE TRANSITION IN $KTaO_3$:Li[1]

R. L. Prater[2] L. L. Chase[2]
L. A. Boatner

A relatively recent review of the dynamics of phase transitions by Halperin and Varma[3] has served to stimulate increased interest in the related topic of the effects of impurities on phase transitions. Raman scattering and optical depolarization measurements were employed in investigations of the phase transition induced by the substitution of lithium for potassium in $KTaO_3$ to form $K_{1-x}Li_xTaO_3$. Lithium concentrations as high as 5.4 mol % were studied. At low concentrations $x \leq 0.004$, the intensities of the disorder-induced scattering features observed for pure $KTaO_3$ increase as the Li fraction increases. A low frequency feature, which was previously associated with a Li resonance mode, appears to be scattering from the coupled TA and TO branches due to disorder introduced by the lithium. For $x \gtrsim 0.01$, a clearly defined step in the optical depolarization is

observed at T_c, which increases rapidly with lithium concentration and reaches a value of T_c = 68 K at x = 0.054. The dependence on the polarization direction of the incident light indicates that a tetragonal or orthorhombic low-temperature phase is formed with ⟨100⟩ symmetry axes. New Raman-active phonons are observed near and below T_c. The anisotropy of the energy of the extraordinary phonon expected from polar modes is not observed in the unpoled samples. Poling can be accomplished by cooling the crystals through T_c with an applied electric field, after which the polar character of these phonons is observed. The lack of anisotropy in unpoled samples is the result of the presence of ferroelectric domains with diameters smaller than optical wavelengths. Additionally, the depolarization measurements imply domain sizes of at least a few thousand angstroms. These results clearly disagree with the previous claims that $K_{1-x}Li_xTaO_3$ is not ferroelectric for $x < 0.24$ and that the Li centers form a polar glass at low temperatures. Finally, the presence of the lithium impurities stiffens the TO branch at the zone center, and the ferroelectric phase results from an order-disorder transition of the off-center lithium ions.

1. Summary of paper: *Phys. Rev. B* **23**, 5904 (1981).
2. Indiana University, Bloomington, Ind.
3. B. I. Halperin and C. M. Varma, *Phys. Rev. B* **14**, 4030 (1976).

RAMAN SCATTERING STUDIES OF THE EFFECTS OF A SYMMETRY-BREAKING IMPURITY ON THE FERROELECTRIC PHASE TRANSITION IN $K_{1-x}Li_xTa_{1-y}Nb_yO_3$[1]

R. L. Prater[2] L. L. Chase[2]
L. A. Boatner

Raman spectroscopy and optical depolarization techniques have been employed in revealing the contrast between the low-temperature phases and the accompanying transitions when either lithium or niobium ions are included as substitutional impurities in the incipient ferroelectric $KTaO_3$. The Nb ions replace Ta in the cubic perovskite lattice; and for $0.008 \leq y \leq 0.06$ in the mixed crystal $KTa_{1-y}Nb_yO_3$, they induce a soft-mode-dominated transition to a trigonal ferroelectric phase where the transition temperature T_c depends on the Nb concentration. In contrast, Li ions, which substitute for K in the $K_{1-x}Li_xTaO_3$ lattice, induce a transition to a tetragonal ferroelectric phase where T_c increases with increasing Li concentration. The Raman spectra clearly show that the lowest transverse optic phonon increases in energy with increasing Li concentration both at the phase transition temperature and at 4.2 K. Therefore, this phase transition appears to have a predominantly order-disorder character with the Li ions occupying off-center positions near the K sites. The slow relaxation of the Li impurities between equivalent off-center positions combined with the large polarization of the lattice around the individual dipoles is apparently responsible for the unusual characteristics of the Li-induced phase transition.

An investigation of the properties of $KTaO_3$ containing the contrasting impurities Nb and Li (i.e., of the system $K_{1-x}Li_xTa_{1-y}Nb_yO_3$) has been carried out. A study of this type represented an opportunity for a direct experimental comparison of the effects of relaxing, symmetry-breaking defects on soft-mode phase transitions.

Raman scattering and optical depolarization measurements on $K_{1-x}Li_xTa_{1-y}Nb_yO_3$ with $y \leq 0.028$ and $x \leq 0.06$ show that lithium impurities destabilize the niobium-induced rhombohedral ferroelectric phase. With increasing x, the phase transition is altered from a soft-mode-dominated transition to a disorder-order transition in a tetragonal phase. The dependence of T_c on x disagrees with the predictions of classical mean-field theory.

1. Summary of paper: *Solid State Commun.* (in press).
2. Indiana University, Bloomington, Ind.

HIGH-TEMPERATURE MATERIALS

THE PREPARATION OF VC SINGLE CRYSTALS BY A FLOAT-ZONE TECHNIQUE

G. R. Gruzalski H. E. Harmon

Because of their high strengths and solidus temperatures, the Group IV and Group V transition metal monocarbides represent an important class of materials in high-temperature technology. In addition, these materials exhibit a host of other phenomena (e.g., variable stoichiometry, superlattice structure, and superconductivity) that have generated increasing interest in their fundamental

emical and physical properties. In spite of this erest, only a few investigators have produced single crystals of the transition metal carbides. Consequently, many of the data concerning these compounds have been obtained using sintered or cemented materials and, therefore, have been of limited utility. Since there is an obvious need for better quality well-characterized single crystals, several methods for producing them are currently being investigated. This summary describes the application of an rf float-zone technique to the growth of VC single crystals. The method described here is similar to that of Precht and Hollox.[1]

Hot-pressed rods 8 mm in diameter were made from a starting material of VC powder blended with 6, 10, or 14 wt % vanadium powder (both V and VC had a nominal purity of 99.8%). The rods were supplied by Cerac and were made using their powders. It was necessary to anneal the as-received rods at 1900°C for about 6 h in a vacuum to effect both outgassing and the dissolution of 200–300-μ inclusions, which were found by x-ray radiography and were tentatively identified as aggregates of vanadium. When the feed rods were not annealed, large chunks of material, several millimeters in dimension, were ejected as the liquid zone was advanced. A second technique for making feed rods was also pursued. In this approach, VC and V powders supplied by Cotronics Corporation and United Mineral and Chemical Corporation, respectively, were used. The rods were produced by blending the powders with a binder (both polyvinyl alcohol and polystyrene have been used) and then by loading the blended powders into Gouch tubing which was evacuated and isostatically pressed to about 50,000 psi at room temperature. The pressed rods were then sintered and diamond-ground to a 1/2-in. diameter. Although the rods made by this second approach have not been zone melted, it is anticipated that they will be superior to the Cerac hot-pressed rods.

Vanadium carbide single crystals were prepared in a Varian crystal growing furnace (MP type) using the feed rods supplied by Cerac. Figure 6.12 shows the chamber configuration after a typical growth run; note that an interface between the crystal and the original feed rod can be seen. The crystal feed rod specimen, originally two rods joined together, was held by Ta holders supported by boron nitride devices attached to water-cooled ainless steel rods. During the growth run the

ORNL-PHOTO 3709-81

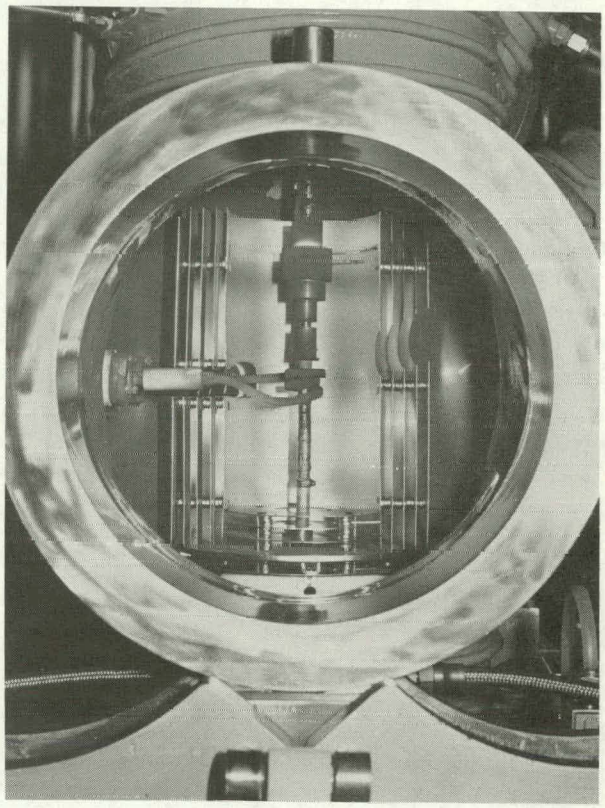

Fig. 6.12. Chamber configuration after the growth of a vanadium carbide single crystal.

chamber becomes heavily coated by decomposition products; hence, in Fig. 6.12 even the BN appears dark. The specimen was surrounded by tantalum heat shields, which are partially removed in Fig. 6.12, and the heat shields were supported by a mullite cylinder. The liquid zone was produced by passing rf current through an efficient lead structure (bus-bar type) and the three-turn coil shown, the ID of the center turn being about 1.3 cm. Several other coil configurations were tested.

The liquid zone was passed from the bottom to the top of the rods so that the liquid-crystal interface advanced at about 1.25 cm/h. The diameter of the resulting crystal was controlled by lowering the upper rod at a slightly faster rate than the lower rod. No afterheating was required. The chamber was pressurized with 5 atm of purified argon to alleviate problems associated with the high decomposition rates exhibited by these materials.

Five VC crystals, each with the nominal composition $VC_{0.83}$, were produced by the technique described above. The dislocation density of these crystals was found to be very low, with most of the dislocations confined to the subgrain boundaries. The crystals are about 5 cm long and, owing to narrow polycrystalline crusts of long grains which form along their peripheries, are only 6–7 mm in diameter. These parasitic grains, which are readily removed by spark cutting, are not actually detrimental since the outer region of the zoned crystal is often removed in any case, because both the oxygen and carbon concentrations are relatively high in this region.

1. W. Precht and G. E. Hollox, *J. Cryst. Growth* **3/4,** 818 (1968).

ELECTROLYTIC POLISHING OF VANADIUM MONOCARBIDES

G. R. Gruzalski

In order to study the optical properties of transition-metal carbide crystals, it is necessary to prepare high-quality flat specular surfaces. Since electrolytic polishing yields surfaces that are unworked and free from macroscopic steps and contamination, this technique was investigated as a means of preparing suitable surfaces on these materials. An electropolishing system consisting of a 5:1 mixture by volume of acetone-free, reagent-grade methanol and concentrated sulphuric acid yielded promising results for vanadium monocarbides polished at 200 K with stainless steel serving as a cathode.

Figure 6.13 shows the current-voltage relation for a $VC_{0.88}$ crystal in the above electrolyte. The shape of the curve is similar to that obtained for other metals and electrolytes, but the plateau region occurs at relatively low values of voltage and current density. In general, the polished surfaces are highly specular and exhibit large areas that appear featureless at 600× magnification. Portions of some surfaces, however, appear to be rough or two-phase-like. It is not clear at the present time whether these poorly polished regions are due to sample inhomogeneities or to an artifact of the electrolytic polishing procedures.

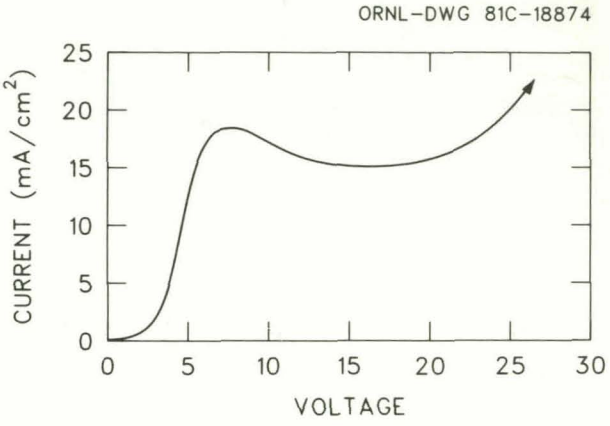

Fig. 6.13. Current-voltage relation for a $VC_{0.88}$ anode and stainless-steel cathode in a 5 to 1 solution of methanol to sulphuric acid, cooled to about 200 K.

ELECTRICAL PROPERTIES OF TRANSITION-METAL CARBIDES

G. R. Gruzalski T. W. Haywood[1]
F. A. Modine

Because the electrical conductivities of transition-metal monocarbides are especially interesting (e.g., they exhibit unusual temperature dependences similar to those of A15 compounds) and because they provide a convenient tool for specimen characterization, particularly with respect to stoichiometry and ordering, an apparatus has been designed and built for their measurement. The apparatus has been automated with a desk-top computer to facilitate rapid characterization on a routine basis, and the van der Pauw technique[2] has been employed because the samples often are flat disks having various irregular shapes.

Figure 6.14 shows the resistivity of two specimen disks as a function of temperature. The resistivity of the $TaC_{0.9}$ crystal has been used to interpret IR reflectance measurements.[3] By comparing the resistivity of the $VC_{0.88}$ specimen disk with that of other VC crystals with known compositions and thermal histories, it can be concluded that the present sample is the ordered compound V_8C_7 and that it is well annealed.

1. Summer faculty research participant from University of North Carolina, Wilmington, N. C.
2. L. J. van der Pauw, *Phil. Res. Rep.* **13,** 1 (1958).
3. F. A. Modine, R. W. Major, and G. R. Gruzalski, "Optical Reflectance of Tantalum Carbide," this report.

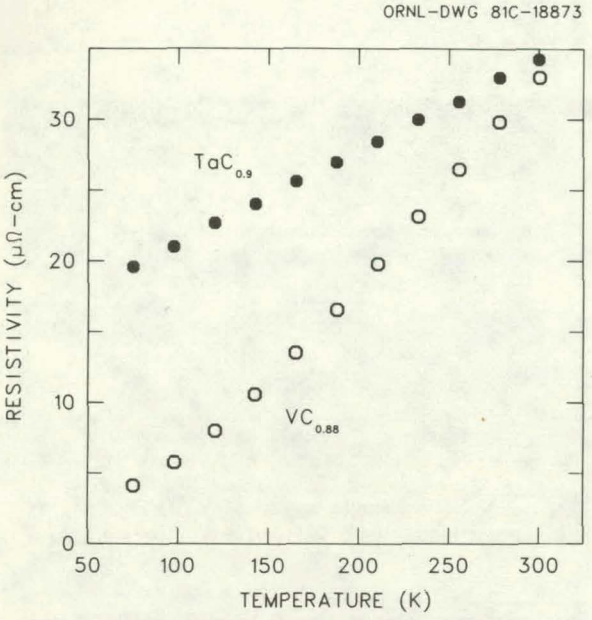

Fig. 6.14. The temperature dependence of the electrical resistivity of $TaC_{0.9}$ and $VC_{0.88}$.

DIFFUSION OF HYDROGEN AND DEUTERIUM INTO PURE AND DOPED $KTaO_3$ CRYSTALS

R. R. Gonzalez[1] L. A. Boatner
M. M. Abraham Y. Chen

Earlier measurements of the diffusion of hydrogen isotopes into $KTaO_3$ indicated that impurities can play an important role in determining the resulting hydrogen or deuterium uptake.[2] Accordingly, the diffusion of hydrogen and deuterium into single crystals of pure $KTaO_3$ and $KTaO_3$ doped with Fe, Ni, Cu, and Li has been investigated. Both hydrogen isotopes were introduced by heating the $KTaO_3$ crystals for 3 h at 1000°C in the presence of H_2O or D_2O vapor. The presence of H in the crystals as OH^- and OD^- was monitored using their infrared absorptions at 3472 and 2565 cm^{-1}, respectively. Broad optical absorption bands in crystals doped with Fe, Ni, Cu, and Li were observed to center at 2.8, 1.9, 1.8, and 1.9 eV, respectively. The H in crystals doped with varying concentrations of iron was studied using the 2.8 eV optical absorption and EPR techniques. Although no direct correlation between the OH^- or OD^- and the Fe^{3+} content was observed, the introduction of OH^- or OD^- was attended by a conversion of the local symmetry of the Fe^{3+} site from axial to cubic.

1. Guest scientist from Universidad Complutense, Madrid, Spain.

2. H. Engstrom, J. B. Bates, and L. A. Boatner, *J. Chem. Phys.* **73,** 1073 (1980).

INFRARED SPECTRA OF HYDROGEN ISOTOPES IN POTASSIUM TANTALATE[1]

H. Engstrom[2] J. B. Bates L. A. Boatner

The spectroscopic constants of OH^-, OD^-, and OT^- species in potassium tantalate $KTaO_3$ were determined from infrared absorption measurements on single crystals at 300 and 77 K using a Fourier transform spectrometer. Single crystals of $KTaO_3$ were grown by slowly cooling a molten mixture of Ta_2O_5 and K_2CO_3 which react to form $KTaO_3$ at 1450°C. Sharp absorption lines due to OH^- ions were readily apparent in as-grown crystals. These were probably introduced into the lattice by the reaction of $KTaO_3$ with atmospheric H_2O vapor during the crystal growth process.

After heating the crystals in D_2O or T_2O vapor at ~1000°C, sharp absorption lines due to OD^- and OT^-, respectively, were observed in the spectra. The peak positions and widths of the principal absorption bands of these species were measured at 77 K with a resolution of 0.5 cm^{-1}, and the results are listed in Table 6.2. By comparison of these results with the values observed for the same species in TiO_2[3] and Al_2O_3,[4] it can be seen that the peak positions are at higher wave numbers and the widths are much smaller in $KTaO_3$, indicating a weaker interaction between the hydroxyl ions and the $KTaO_3$ lattice. A weaker interaction is also indicated by the smaller anharmonic coefficients

Table 6.2. Peak positions ω and widths δ of the major absorption band of OH^-, OD^-, and OT^- ions in $KTaO_3$ from measurements at 77 K

	ω (cm^{-1})	δ (cm^{-1})
OH^-	3484.8 (± 0.1)	1.0 (± 0.1)
OD^-	2575.5	0.8
OT^-	2175.4	0.7

calculated from the frequencies observed in $KTaO_3$.

The intensity of the major hydroxyl absorption band and three weaker features at higher energies increased after treatment of as-grown crystals in H_2O at 1050°C. The total integrated intensity of these bands did not change after prolonged treatment beyond 2 h, suggesting that saturation is achieved rapidly as a result of the high diffusion rate of protons at this temperature. The weak infrared features, which grow at a faster rate with treatment than the principal absorption band, occur at 3488, 3495, and 3504 cm^{-1}. These bands are attributed to OH^- ions in different local environments which may be associated with impurities.

The importance of impurities in determining the saturation concentration of hydrogen-containing species in $KTaO_3$ was confirmed in this study by the observation that higher OH^- concentrations were found in regions of the same crystal which had higher concentrations of an unknown impurity. The addition of hydrogen to a lattice requires either the presence of a charge compensating impurity or a change of valence of one of the host ions of the lattice.

1. Summary of paper: *J. Chem. Phys.* **73,** 1073 (1980).
2. Present address: Sperry Univac, Santa Clara, Calif.
3. J. B. Bates and R. A. Perkins, *Phys. Rev. B* **16,** 3713 (1977).
4. H. Engstrom et al., *Phys. Rev. B* **21,** 2520 (1980).

CRYSTAL GROWTH OF A15 INTERMETALLIC COMPOUNDS

Y. K. Chang H. E. Harmon

The single crystals of V_3Si described previously[1] were grown from polycrystalline rods without the use of a seed. In order to obtain higher quality crystals with a predetermined orientation, V_3Si single crystals were grown by seeding from a high-quality V_3Si crystal chosen with a crystallographic axis lying close to a [100] orientation. An example of a seeded V_3Si crystal is shown in Fig. 6.15. This specimen is ~8 mm in diameter and was grown at a rate of 7 mm/h in an rf induction-heated float-zone furnace under a 207-kPa purified argon gas atmosphere with an oxygen content of 0.3 ppm.

ORNL-PHOTO 2451

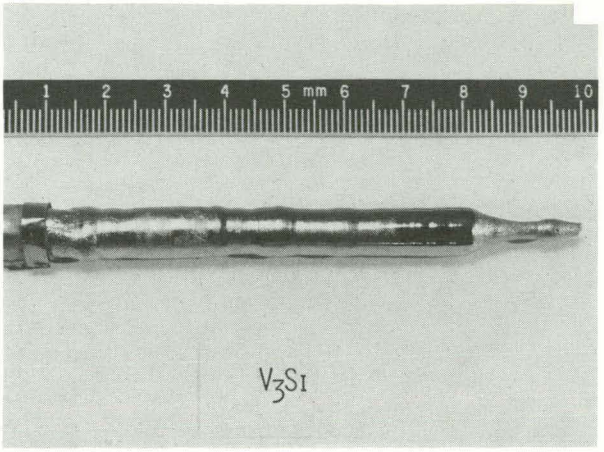

Fig. 6.15. Seeded single crystal of V_3Si. The long axis of the sample is parallel to a [100] crystallographic axis.

The zoned region was about 45 mm in length, and one single crystal was produced with a residual resistance ratio of ~40. Work on improving the crystal quality of V_3Ge and Nb_3Ge_{1-x} specimens is also currently in progress. A heavy crust formation over the zoned surface has complicated the growth of these materials. Using a scanning electron microscope with an energy-dispersive x-ray spectrometric mode, these crusts were identified as extraneous impurities that formed as crystallites on the main crystal surface.

1. Y. K. Chang and H. E. Harmon, *Solid State Div. Prog. Rep., Feb. 29, 1980,* ORNL-5640, p. 222.

SPECIAL MATERIALS

PREPARATION OF METAL AND ALLOY SINGLE CRYSTALS

Y. K. Chang H. E. Harmon

Recently, the success of a band structure calculation carried out for the Ag-Pd system has prompted a number of experimental investigations, including positron annihilation and photoemission studies, to verify the predicted band structure change near the Brillouin zone boundary when Ag is alloyed with Pd. A single crystal of pure Ag, 1.9 cm in diameter and 4 cm long, was successfully grown in a Bridgman-type vitreous carbon crucible. The loaded crucible was suspended in a quartz

tube in an argon atmosphere and was lowered through a long cylindrical induction coil at a rate of ~2.5 cm/h. The resulting single crystal is shown in Fig. 6.16. In order to grow single crystals of the Ag/Pd alloy, Pd metal with a purity better than 4 N was melted with Ag in an arc melter and then swaged to form a rod 6.35 mm in diameter. This rod was then chemically cleaned and zone refined in an electron-beam float-zone system at a rate of 20 mm/h under a dynamic vacuum of 2×10^{-7} torr. This technique resulted in the production of AgPd crystals with reduced diameters of ~4 mm.

ORNL-PHOTO 3990-81

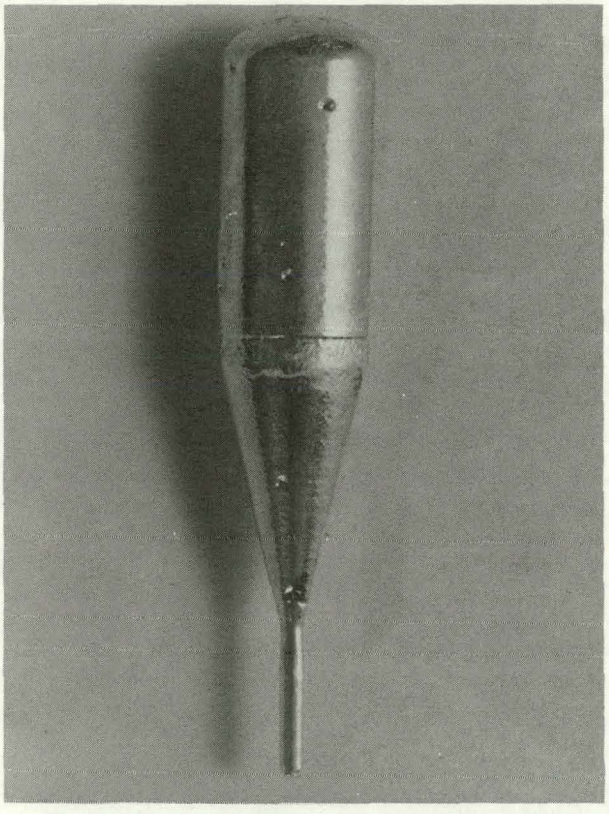

Fig. 6.16. Single crystal of Ag grown by the Bridgman technique in a vitreous carbon crucible.

ELECTROMIGRATION OF Cu IN Pb(Sn) ALLOYS

C.-K. Hu[1] H. B. Huntington[1]
G. R. Gruzalski

The transport of substitutional impurities in most metals occurs principally by a vacancy mechanism. Diffusivities of such impurities rarely differ from those of the hosts by more than an order of magnitude. In contrast with this behavior, however, the diffusivities of impurities having a substantial interstitial component are often many orders of magnitude greater than those exhibiting "normal" solute diffusion. These "fast diffusers" have been the subject of considerable study[2] with the most thoroughly investigated systems having Pb as a solvent and a noble metal or near-noble metal as a solute. These studies have shown that the diffusion process is quite complex, and the electromigration of many of these Pb alloys has been studied[3] extensively to obtain additional insight. As a continuation of these efforts and in an attempt to answer practical questions concerning the electromigration of impurities in different lead-tin solders, the electromigration of noble-metal and near-noble-metal solutes in Pb(Sn) alloys is being investigated. This report summarizes the initial efforts to measure the electromigration of Cu in dilute single-phase alloys of $Pb_{1-x}Sn_x$ ($0 \leq x \leq 0.12$).

The diffusivity of Cu in several alloys was studied using a tracer-sectioning technique to determine the minimum time in the electromigration experiments. These experiments were complicated by the short half-life of the Cu isotope (12.8 h for ^{64}Cu) and the low solubility of Cu in these alloys. The solubility problem was somewhat alleviated by using a source of high specific activity. The results already obtained show that a relatively small amount of Sn is sufficient to lower the Cu diffusivity markedly. For example, the ratio of the Cu diffusivity in a Pb(Sn) alloy to that in pure Pb is about 1:2 for a 50-ppm alloy at 230°C, and this ratio significantly decreases by either lowering the sample temperature or by raising the Sn content. The general pattern suggests that the activation energy for diffusion increases with increasing Sn concentration.

Using the steady-state technique, the electromigration of Cu in a 50-ppm Pb(Sn) alloy was measured. It was found that the effective charge number Z^* is approximately unity for a sample temperature of about 265°C.

---

1. Rensselaer Polytechnic Institute, Troy, N.Y.
2. This subject has been reviewed quite extensively by W. K. Warburton and D. Turnbull, p. 171 in *Diffusion in Solids Recent Developments,* ed. by A. S. Nowick and J. J. Burton, Academic Press, New York, 1975.

3. For example, see H. Nakajima and H. B. Huntington, *J. Phys. Chem. Solids* **42,** 171 (1981), and references therein.

AN EPR AND ENDOR INVESTIGATION OF THE $[F_{Li}]^\circ$ CENTER IN CaO[1]

M. M. Abraham
Y. Chen
D. N. Olson[2]
V. M. Orera[3]
T. M. Wilson[4]
R. F. Wood

A new paramagnetic color center, denoted by $[F_{Li}]^\circ$, has been found. The center has been observed in single crystals of CaO grown with Li impurities and consists of a single electron in a O^{2-} vacancy with a Li^+ ion replacing an adjacent Ca^{2+} ion (i.e., an F^+ center next to a Li-substitutional impurity). Therefore, this is the first paramagnetic electron-defect center possessing local electrical neutrality to be seen in the alkaline-earth-oxides. EPR and ENDOR measurements at both X- and K-bands yielded the following spin-Hamiltonian parameters at 4.2 K: $g_\parallel = 1.9993(2)$, $g_\perp = 2.0001(2)$, $A = \mp 9.01(1)$ MHz, $B = \mp 5.35(1)$ MHz, and $P \leqslant 0.005$ MHz. The hyperfine values are temperature dependent and were also measured at 77 and 150 K.

An oscilloscope display of the EPR signal at K-band with the ⟨100⟩ magnetic field parallel to a crystal ⟨100⟩ axis is shown in Fig. 6.17. Clearly visible are a large isotropic line and two sets of four lines. The former is due to the F^+ center, and the latter are attributed to the $[F_{Li}]^\circ$ center; they are due to the interaction of an electron at an O^{2-} vacancy with a $^7Li^+$ ion ($I = 3/2$) substituted for a Ca^{2+} ion in a nearest-neighbor site. The four-line set centered on the F^+ line has twice the amplitude of the four-line set displaced to higher fields, which suggests that the $[F_{Li}]^\circ$ center has an axial site symmetry oriented along a ⟨100⟩ direction of the crystal and that $g_\perp$ is the same as the isotropic g value of the F^+ center. This suggestion is further supported by the observed angular dependence.

Each of the EPR transitions, saturated in turn, produced ENDOR signals. The ENDOR transitions are shown in Fig. 6.18 for sites aligned parallel to the magnetic field. The magnetic field for each transition is indicated at the left of each trace in terms of the NMR proton frequencies. Counting from the low field line for the EPR transitions in Fig. 6.17, the second $\theta = 90°$ line and the first θ

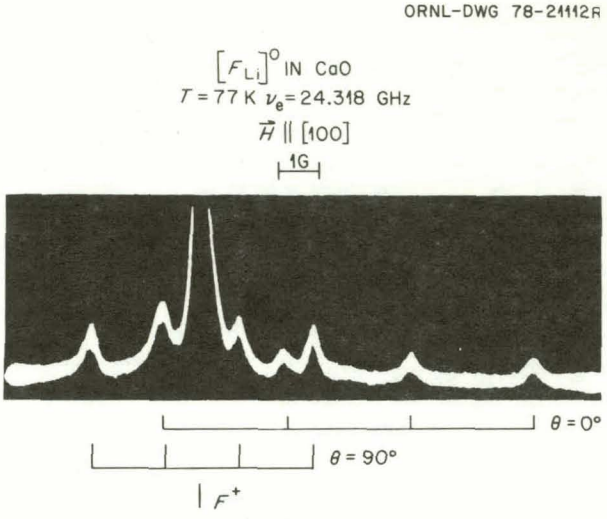

Fig. 6.17. EPR spectra of F^+ and $[F_{Li}]^\circ$ centers in CaO. The oscilloscope trace clearly shows two sets of four lines for the $[F_{Li}]^\circ$ center. One set, labeled $\theta = 0°$, arises when the field is along the axis of the center, while for the other set labeled $\theta = 90°$, the field is perpendicular to the axis. The isotropic F^+ centerline is located at the center of the $\theta = 90°$ set.

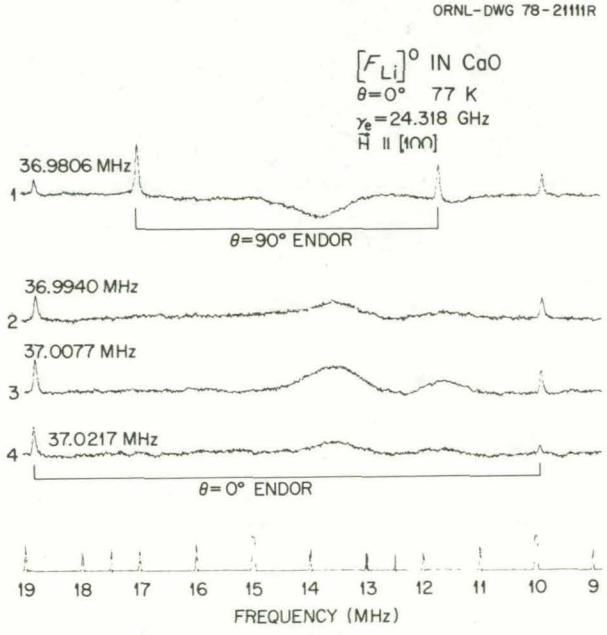

Fig. 6.18. ENDOR spectra of the $[F_{Li}]^\circ$ center in CaO with H parallel to the defect axis. Individual traces were taken on different hyperfine lines labelled progressively from 1 (low field) to 4 (high field). Applied magnetic fields are specified in terms of proton nuclear resonance frequency.

= 0° line can be seen to overlap. For this magnetic field, therefore, the ENDOR traces seen in Fig. 6.18 show evidence of both transitions.

The alignment of the ENDOR transitions, one above the other, at the same rf frequency in Fig. 6.18 is an indication that the quadrupole splitting factor $P = 3e^2qQ/4I(2I - 1)$ is very small. The data suggest that there is an outward relaxation of the lithium ion and probably of the other ions in the lattice, but there is no electric-field gradient.

---

1. Summary of paper: *Phys. Rev. B* **23,** 51 (1981).
2. Oak Ridge Associated Universities faculty research participant from St. Olaf College, Northfield, Minn.
3. Guest scientist from University of Zaragoza, Zaragoza, Spain.
4. Oak Ridge Associated Universities faculty research participant from Oklahoma State University, Stillwater.

THE GROWTH OF CRYSTALLINE Si SHEETS BY A LIQUID BED METHOD

Y. K. Chang L. A. Boatner

An inexpensive method for preparing thin, large-surface-area Si single crystals would represent a significant development in the solar photovoltaic field. An approach has been investigated in which molten Si is floated on a hot, liquid bed. The proper choice of the liquid bed material is, of course, the key to the possible success of this technique. Initially, BaF_2 was chosen as the liquid bed material due to its higher density relative to Si, lower melting point, and chemical inertness. The molten Si, however, does not spread uniformly over the top of molten BaF_2, and it forms an almost spherical body due to its large surface tension as compared to that of BaF_2. Based on these observations, a molten metallic substance was selected as the liquid bed material. Tin was chosen not only because it exhibits the above-mentioned properties but also because it has a low vapor pressure and is an inactive impurity in Si. Preliminary experiments have demonstrated that liquid tin is not an ideal molten-bed material. Further testing and an evaluation of lead as a possible molten-bed material are required.

7. Isotope Research Materials

The preparation of special chemical and physical forms of separated, high-purity isotopes is the task of the Isotope Research Materials Laboratory (IRML). Research samples using nearly all stable isotopes and many radioisotopes (especially the actinide elements) are made to customer specifications in support of research programs throughout the United States and in foreign countries. In addition to satisfying isotope research material requirements for DOE programs, IRML provides an international service of sample preparation supplying over 100 universities and commercial firms in more than 30 countries with samples unavailable from commercial sources. During the reporting period approximately 2700 samples were prepared for the international scientific community. Support for this work comes directly from sales of materials and services; therefore, IRML has an integral sales function with associated inventory and revenue-accounting operations. Research and development activities in IRML are funded by DOE through the Office of Basic Energy Sciences.

Technical functions of IRML can be categorized generally into materials research and development, inorganic chemical conversions, preparation of special physical material forms, radioisotope source preparations, purifications, single-crystal and epitaxial growth studies, and development of analytical techniques (usually nondestructive methods) that are compatible with characterization of thin film and other types of samples. From its inception, IRML has prepared particle accelerator targets; technologies of physical vapor deposition, chemical vapor deposition, mechanical rolling of metals, distillation of metals, metal reductions, arc melting, levitation melting, sintering, and other metallurgical and chemical processes are used to produce unique isotope-containing samples. Because of present-day interests in high-energy physics research, new technologies have been required to transform large (multigram) quantities of separated isotopes into thick, large-area target samples. In all operations, specific efforts to improve purity and to conserve isotope resources are of vital importance because the monetary value of isotopes consumed during a sample preparation may be many times the cost of assigned manpower and ancillary expense.

Procedures developed for handling stable isotope materials usually are equally applicable to radioisotope sample and source preparations. Adaptation of preparative methods to radioisotopes generally implies modification for remote operations (hot-cell enclosure of processing equipment) or at least glove-box operations required for personnel protection. Almost all of the above-noted operations have been adapted for radioisotope processing.

CHEMICAL COMPATIBILITY OF URANIUM AND PLUTONIUM CARBIDES WITH Cr-Fe-Ni ALLOYS

E. C. Beahm[1] C. A. Culpepper
W. S. Aaron

Fundamental studies associated with advanced fast breeder reactor fuels are being conducted in a cooperative effort with the Chemical Technology Division. Thermodynamic calculations and experimental phase studies are being used to determine the phases present in the interface, or reaction zone, between carbide fuel and the cladding alloy.

At 1273 K, the principal products in the reaction of uranium carbides with Cr-Fe-Ni alloys are $UNiC_2$ and the Laves phase $U(Fe,Ni,Cr)_2$. At 973 K, the principal products are UNi_5 and $(Cr,Fe)_7C_3$. At the lower temperature, reaction with uranium monocarbide is limited by the rate of formation of UNi_5. Liquid formation was observed in the UC-type 316 stainless steel system at 1292 ± 8 K and at 1351 ± 12 K in the UC-Inconel 718 system.

The compatibility studies have been expanded to include phase relations in the reaction products of mixed uranium/plutonium carbide fuel. Recent phase studies in our laboratory showed that up to 50% of the plutonium in hexagonal $PuNi_5$ may be replaced by uranium. However, no substitution of uranium by plutonium was detected in cubic UNi_5. Thus, in the fuel-clad interface of $(U_{\sim 0.8}Pu_{\sim 0.2})$ carbide with Cr-Fe-Ni alloys, we would expect a combination of either UNi_5 plus U-saturated $PuNi_5$ or UNi_5 plus (U,Pu) carbide containing more plutonium than the bulk fuel.

1. Chemical Technology Division, ORNL.

CHEMICAL THERMODYNAMICS AND PHASE EQUILIBRIA IN ACTINIDE-CARBON-OXYGEN-CONTAINING SYSTEMS

T. M. Besmann[1] C. A. Culpepper

High-temperature, chemical studies of the actinide-carbide-oxide systems associated with the preparation and use of advanced fast breeder reactor fuels are being conducted in a cooperative effort with personnel of the Chemical Technology Division. Thermodynamic calculations and experimental measurements are used to determine phase equilibria and chemical thermodynamic properties of actinide carbides and oxycarbides.

Measurements of CO pressures were made at constant temperatures to determine the equilibrium of $PuO_{1.5}$-$PuC_{1.5}$-C-CO. This work considerably extended the only previous data set and allowed the determination of thermodynamic data for $PuC_{1.5}$.

Measurements of CO pressure at constant temperature were begun to establish the equilibrium $(U,Pu)O_2$-$(U,Pu)C_{1.5}$-C-CO and to correlate composition and thermodynamic properties of $(U,Pu)C_{1.5}$.

1. Chemical Technology Division, ORNL.

TRITIUM SEPARATION FROM LIGHT AND HEAVY WATER BY BIPOLAR ELECTROLYSIS[1]

M. Petek D. W. Ramey
R. D. Taylor

Using multiple bipolar electrolytic separation of hydrogen isotopes with Pd–25% Ag electrodes, the mathematical feasibility of this method for tritium separation was shown and experimentally verified. Separation factors were measured on single bipolar electrodes and were found to be approximately equal to those associated with individual ordinary electrolytic systems. Multibipolar separations were experimentally achieved in single cascaded cells in which each bipolar electrode was of equal area to others in a series arrangement. Factors measured for multibipolar H-D separation were close to the values measured in single-stage cell measurements; for H-T separation, interstage leakage reduced the measured separation factor. However, in both cases separation of sufficient magnitude was achieved to show feasibility for real application to the extraction of tritium from large-volume systems at high current density.

1. Summary of paper: *J. Appl. Electrochem.* **11,** 477 (1981).

CUSTOM RESEARCH MATERIALS PREPARATIONS

W. S. Aaron
B. L. Byrum
K. B. Campbell
C. A. Culpepper
J. M. Dailey
W. B. Grisham
J. M. Lovegrove
T. C. Quinby
D. K. Thomas
L. A. Zevenbergen

As described in Table 7.1, a distribution of saleable special isotopic materials was prepared predominantly for the contractors of DOE during the past period. However, this skewed distribution is biased by the large number of radioisotope samples generally not allowed for sale to some foreign customers and by the materials required uniquely for accelerator devices present only in the United States (e.g., RTNS-II).[1] Although smaller in number, prepared, stable isotope research forms that were sold to foreign customers accounted for approximately 40% of the total revenues realized. Rather remarkably, the private sector of the United States provided an almost equal market to that of DOE contractors in terms of the total number of samples prepared using stable isotopes.

Of major importance to the entire separated isotopes program, the IRML processed nearly $900,000 of stable materials during this period. If equivalent valuation was applied to radioisotopes (particularly tritium and actinide materials), multimillion dollar quantities of these items were processed. Obviously, IRML contributed significantly to the distribution of separated isotopes on an international basis and, in particular, to the domestic research effort. This is a reasonable and expected result inasmuch as chemical and physical forming of separated isotopes is a costly and time-consuming activity when performed (if indeed it can be performed at all) on a local basis within the user's laboratory.

Of the 2647 samples prepared in this period, 433 samples were requested by ORNL research personnel. Of this quantity 288 were produced for the ORNL Instrumentation and Controls Division in their effort to develop an ultrasensitive flux monitoring fission chamber for the CRBR.

As in past reporting periods, conversion of isotope inventory forms (oxides, carbonates, chlorides, and nitrates) to elemental or other compound forms represented a major activity of IRML. These conversions were necessitated either to form the material into a physical shape needed to satisfy experimental conditions or to remove interferring nuclides which would preclude the attainment of meaningful experimental results. Most chemical conversions were performed by high-temperature chemistry (reduction-distillation or "bomb" reduction to metal), by electrodeposition, or by hydrogen reduction.

Outstanding examples of the importance of chemical conversions during this period were the reduction-distillation and casting of ^{25}Mg metal into a 5-cm by 5-cm block having a thickness of 1 cm and the preparation of 2 g of $^{246}Cm(\sim 70\%)$-^{244}Cm for fundamental equation-of-state measurements. It was also shown that ultrapure ^{241}Am metal could be produced by direct distillation from plutonium metal containing a minor ^{241}Pu content. Subsequently, the overall radiation level of the parent plutonium metal was significantly reduced, permitting it to be physically worked into useful forms without undue exposure to personnel. The by-product ^{241}Am metal was then cold-rolled into sheet stock for other target preparations; the purity of the ^{241}Am was the greatest produced by our laboratory because of the total absence of ^{243}Am. Two highly significant features of this process require comment: (1) impurity americium in plutonium metal can readily

Table 7.1. Enriched isotopic targets prepared by IRML

	Department of Energy contractors	U.S. colleges, universities, and private industries	Foreign customers	Total
Stable isotope sample preparations	293	274	155	722
Radioisotope sample preparations	1391	444	90	1925

be removed at far less cost than by using complex "wet" chemical processing and (2) the product ^{241}Am can be used to prepare ultrapure research samples.

The use of earlier developed and IRML-patented, ceramic powder forming technology to prepare both open and encapsulated samples of actinide oxides (for use in reactor dosimetry and other applications) was again of importance. However, generally the preparation of vanadium-encapsulated "wire" dosimeters decreased significantly because of the relatively few experiments being conducted at the Fast Flux Test Facility (FFTF) in this period. Ceramic wafers (~1 cm diam) were produced in relatively large quantities from NpO_2, PuO_2, and UO_2.

Finally, successful development of Cu-UO_2 cermets having ultrahigh uniformity of distribution of the UO_2 in the metal matrix (<1% variation) was performed to enable samples to be prepared in the near future for use in low-energy neutron experiments.

1. H. L. Adair et al., "Tritium Target Fabrication for the Rotating Target Neutron Source," this report.

US/UK HIGHER ACTINIDE IRRADIATIONS IN THE DOUNREAY PROTOTYPE FAST REACTOR

E. H. Kobisk D. K. Thomas
H. L. Adair B. L. Byrum
T. C. Quinby J. A. Setaro
J. M. Dailey D. W. Ramey
J. R. Gibson[1]

A cooperative US/UK research program was initiated some years ago to investigate the neutronic and irradiation behavior of higher actinides in fast breeder reactors. This program eventually involved ORNL, HEDL, and laboratories in the United Kingdom at Dounreay, Scotland, and Windscale, England. The test "fuel" pin(s) designed to observe actinide burnup rates and neutron cross section during irradiation in the Prototype Fast Reactor (PFR) at Dounreay contains three sections of actinide oxides (fuel pellets) in a normal fuel configuration and 21 actinide oxides (physics samples) encapsulated in vanadium. ORNL had specific responsibilities for selecting and providing the isotopes, for fabricating the fuel pellets, for fabricating the neutron dosimeters and physics samples, and for loading and seal-welding the fuel pin segments (with HEDL assistance). HEDL was responsible for test-pin design, pin fabrication, final assembly of pin sections, quality assurance, and shipping to the United Kingdom. ORNL responsibilities pertaining to test-pin preparation were successfully met by the middle of June 1981.

A major effort was required by several ORNL divisions to prepare and characterize both physics specimen and fuel pellet materials. The physics specimen materials were composed of milligram quantities of actinide oxide compounds that were encapsulated in 1.5-mm-diam vanadium capsules. The quantity of material contained in each capsule was accurately determined by using a substitution-weighing scheme that compared the weight of material loaded with standard weights as devised by the National Bureau of Standards. The amount of actinide material in each vanadium sample was, or will be, determined by using the compound weight together with isotopic and concentration analyses for each material. A total of 132 vanadium-encapsulated samples was prepared and loaded into three fuel pins for the physics specimen portion of the US/UK higher-actinide irradiation experiment.

Twenty-eight fuel pellets of each actinide fuel having dimensions 3.8 mm diam by 3.8 mm long were fabricated from $^{244}Cm_2O_3$, $^{241}Am_2O_3$, and a mixture of $^{244}Cm_2O_3$, $^{241}Am_2O_3$, and several lanthanide oxides. The high-density actinide oxide pellets were prepared by hot pressing fine powder produced in a urea precipitation process. Seven high-integrity pellets were prepared simultaneously in an ATJ graphite die (Fig. 7.1) by hot pressing carefully weighed powder at a temperature of 1575–1675 K. The integrity of the pellets was clearly demonstrated when 12 fuel pins, four each loaded with pellets prepared from the $^{244}Cm_2O_3$, $^{241}Am_2O_3$, and the mixture, were fabricated and found to be free of contamination after the loading process. Seven $^{244}Cm_2O_3$ pellets fabricated in a single pressing are shown in Fig. 7.2. Approximately 300 mg of ^{244}Cm is contained in each of the pellets shown in Fig. 7.2.

1. Plant and Equipment Division, ORNL.

ORNL-PHOTO 3768-81

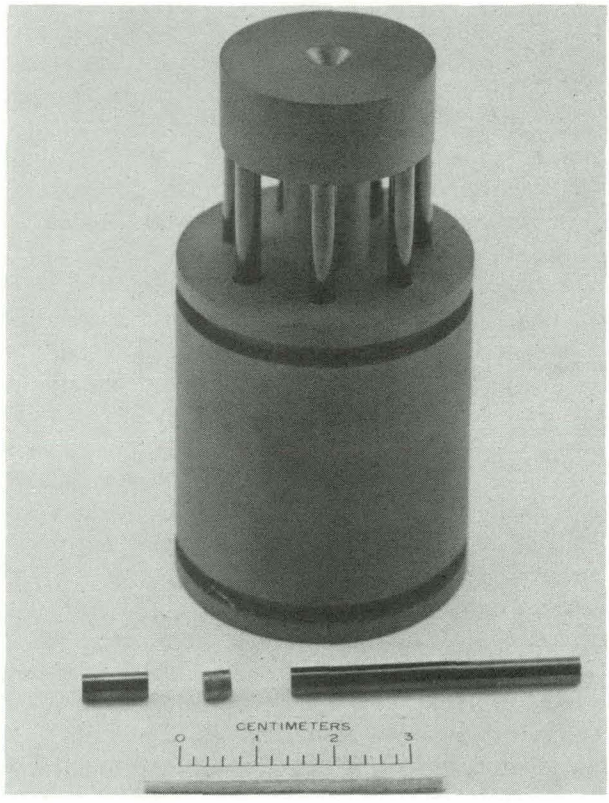

Fig. 7.1. ATJ graphite die and vitreous carbon rams used in pressing US/UK higher-actinide fuel pellets.

ORNL-PHOTO 3543-81

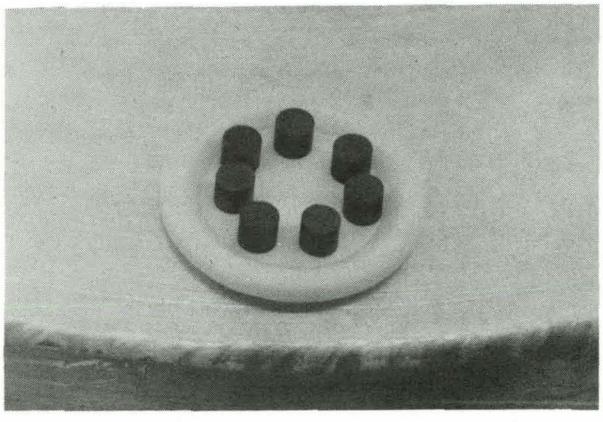

Fig. 7.2. $^{244}Cm_2O_3$ fuel pellets prepared in a single pressing operation.

$^{235}UO_2$ COATINGS FOR ULTRAHIGH SENSITIVE FISSION CHAMBER FOR THE CLINCH RIVER BREEDER REACTOR

B. L. Byrum J. M. Lovegrove
J. M. Dailey J. R. Gibson[1]
H. L. Adair

The Instrumentation and Controls Division of ORNL was requested to design and construct an ultrasensitive fission chamber that could be used to monitor the neutron flux during startup and operation of the Clinch River Breeder Reactor (CRBR). The major component of the proposed fission chamber was a set of approximately 300 curved aluminum substrates coated with approximately 2.0 mg/cm^2 of 93% enriched ^{235}U.

To obtain the best $^{235}UO_2$ coating possible, several techniques were experimentally studied and the resulting targets were examined under identical conditions. IRML prepared $^{235}UO_2$ deposits both by physical vapor deposition and by painting. The Instrumentation and Controls Division compared the resulting fission-fragment spectra from these deposits, as well as the spectra produced from electroplated deposits, during neutron bombardment. Fission fragments from the $^{235}UO_2$ deposits prepared by physical vapor deposition were shown to have a higher average energy and thus a better resolution. Deposits prepared by electroplating and painting produced a lower average fission-fragment energy that resulted from straggling fission fragments in the deposit layer. In addition, swipe tests revealed that the deposits prepared by physical vapor deposition were more adherent to the substrate. As a result of the tests, IRML was asked to prepare the $^{235}UO_2$ deposits for the CRBR fission chamber by physical vapor deposition.

The CRBR fission chamber required approximately 300 curved aluminum substrates to be coated on both the front and back surfaces with $^{235}UO_2$. The substrates were approximately 17 by 7 cm and curved such that the plates would fit in support ring grooves in the fission chamber spaced at approximately 6.1-cm intervals. Required tolerances associated with the UO_2 deposits were as follows:

1. Average coating thickness on any given plate was to be 2.1 ± 0.2 mg/cm^2.

Thickness of the coating on any given plate was to be 2.1 ± 0.3 mg/cm^2 at any given point on the coated surface.

A "ferris wheel" coating fixture was designed to cause both sides of the aluminum substrates to be coated during a single vapor deposition. The coating fixture permits 16 aluminum substrates to be coated on both surfaces by rotating each substrate on its own axis as the ferris wheel rotates simultaneously over the vapor source. The ferris wheel was installed in an oil diffusion-pumped, 61-cm-diam vacuum chamber as shown in Fig. 7.3. At the distance of closest approach, the aluminum substrates were approximately 30 cm above an electron-beam-heated evaporation source. Substrates rotated at approximately 75 rpm as the ferris wheel revolved over the vapor source at 25 rpm. Such movement permitted random orientation of the plates in the vapor beam. An evaporation time of 3 h and about 70 g of $^{235}UO_2$ were required to coat both surfaces of each set of 16 aluminum substrates with an average of 2.0 mg/cm^2 UO_2. The variation in uniformity across the substrate was ≤10%.

ORNL-PHOTO 4999-81

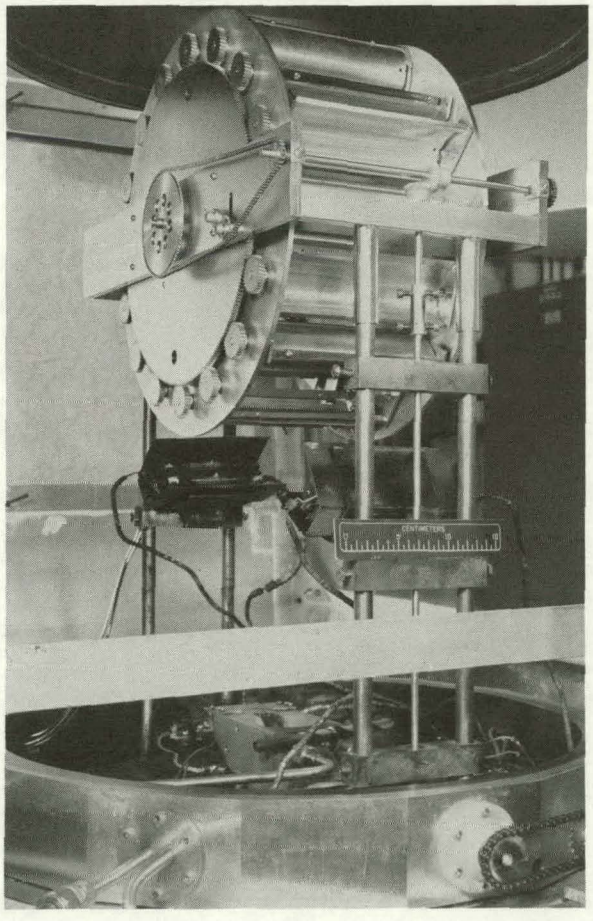

Fig. 7.3. $^{235}UO_2$ coating fixture installed in vacuum system.

1. Plant and Equipment Division, ORNL.

TRITIUM TARGET FABRICATION FOR THE ROTATING TARGET NEUTRON SOURCE[1]

H. L. Adair J. M. Dailey
B. L. Byrum D. W. Ramey

Since the inception of the LLNL program entitled "Rotating Target Neutron Source (RTNS)" in which high-flux neutron fields are generated by the $^3_1H(^2_1H, ^1_0n)^4_2He$ reaction, IRML has prepared the required tritium-containing targets. Originally, the RTNS program was conceived to provide monoenergetic 14.5 MeV neutrons with a flux of 10^{12}–10^{13} n/cm^2/s. The neutron field was used for biological experiments, materials damage studies, and a broad program involving users external to LLNL.

First-generation targets employed in the RTNS-I facility were 23 cm in diameter and contained approximately 4.4 × 10^7 MBq of tritium. These targets, when bombarded with a 20-mA D^+ beam at 400 keV, produced a source strength of 1 × 10^{12} n/cm^2/s. Increased interest in the use of such a neutron source for the study of fusion reactor materials and cancer therapy resulted in construction of two second-generation RTNS systems (RTNS-II) which can use 50-cm-diam targets that contain approximately 2.2 × 10^8 MBq of tritium. The design goal is that these targets (RTNS-II), when bombarded with a 150-mA D^+ beam at 400 keV, will produce a neutron flux of 1.2 × 10^{13} n/cm^2/s.

Development by IRML personnel of tritium target preparative techniques, equipment design, and construction have spanned a 20-year period. For the past five years, IRML has been preparing RTNS-type targets. In the later period several major substrate modifications have required changes in processing methods and equipment. Both the 23-cm-diam and 50-cm-diam targets presently are prepared by coating the targets with

approximately 3.5-mg/cm^2 titanium metal in an oil diffusion-pumped vacuum system that maintains a pressure level of $<2.7 \times 10^{-4}$ Pa during the titanium evaporation. A rod-fed, electron-beam-heated source is used to vaporize the titanium that is condensed on the rotating copper-alloy substrate. The substrate is heated to 673–723 K during the titanium coating to produce an adherent titanium-to-copper alloy substrate bond. The target is then placed in an all metal ion-pumped vacuum system to form subsequently the titanium tritide. Tritide formation is accomplished by pumping the system containing the titanium-coated target to $\leq 1.3 \times 10^{-6}$ Pa, heating the target to approximately 673 K, and exposing the target to a tritium gas pressure of 53.2 kPa that is generated by heating storage traps containing uranium tritide and uranium. Residual tritium that does not react with the titanium layer is sorbed back onto the storage traps. Resulting tritide targets, either 23-cm-diam or 50-cm-diam, are shipped to LLNL and mounted on the target assembly in the RTNS-II facility, a schematic view of which is shown in Fig. 7.4.

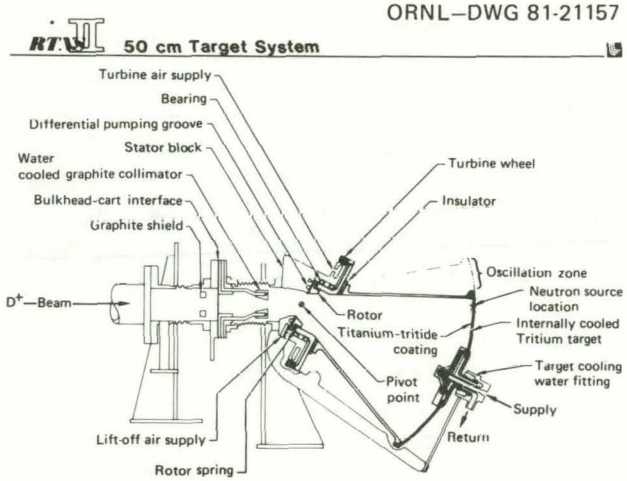

Fig. 7.4. Schematic of target assembly section in RTNS-II facility.

During the review period a total of forty-five 23-cm-diam targets and three 50-cm-diam targets has been prepared for the RTNS-II program. The first 50-cm-diam target is scheduled to be used at the RTNS-II facility in October 1981.

1. Summary of paper to be published.

PREPARATION OF HIGH-PURITY BERYLLIUM FOILS[1]

R. D. Taylor

One problem area involving beryllium fabrication technology is the preparation of thin foils (<25 μm) suitable for x-ray energy spectroscopy (XES) applications. Specific foil requirements are high purity (>99.8% Be) for x-ray transparency, vacuum tightness, and sufficient strength to withstand an indefinite number of cycles between 0 and 100 kPa differential pressure.

Prior researchers[2,3] have shown that dense, strong beryllium foils may be prepared by evaporation of beryllium onto heated (>775 K) copper substrates followed by dissolution of the copper in nitric acid; however, foil contamination arising from the copper substrate (~0.5 wt %) using this technique is unacceptable for XES applications.

Using a similar approach, a method has been investigated to minimize diffusion of copper into the evaporated beryllium deposit. Thin "barrier" films of molybdenum and/or silicon of varying thicknesses up to 0.5 μm were evaporated or sputtered onto copper substrates (0.13 mm thick) prior to beryllium vapor deposition. In this process the beryllium deposition system was evacuated to a base pressure of 1.3×10^{-4} Pa, and the substrate was heated to 825 K by backside radiation from quartz heat lamps. Beryllium was then evaporated onto the heated substrate at a deposition rate of 5 μm/min to a thickness of 7.5 μm, using a water-cooled electron beam gun (10 kV, 300 mA) located 25 cm above the substrate.

After cooling to room temperature, the copper substrate was dissolved in a 50% (by volume) HNO_3 solution. Light brushing under water served to remove any adherent residual film from the beryllium foil. Resulting beryllium foils were examined by optical microscopy for surface morphology and pinholes. A scanning electron microscope with an XES attachment was used for microstructural characterization and preliminary chemical analysis. Tube-excited x-ray fluorescence provided a more quantitative determination of elemental constituents.

The scanning electron micrograph of Fig. 7.5 shows the columnar grain growth characteristics of vapor-deposited beryllium; average grain diameter is 2.0 μm. Porosity and pinholes occurring in the foils are primarily attributable to contaminants on and roughness of the substrate surfaces. Chemical analysis of the foils showed a reduction of copper

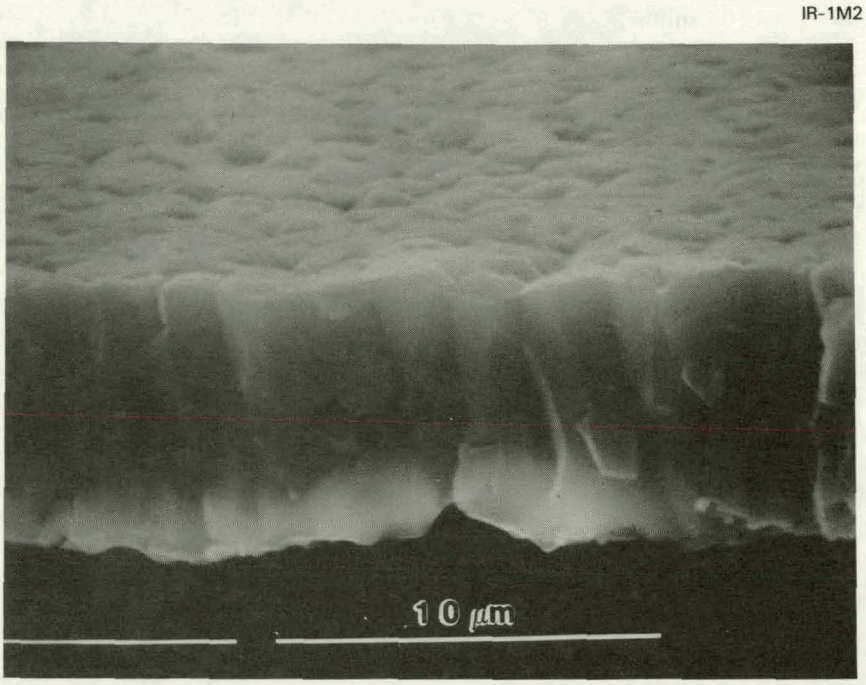

Fig. 7.5. Scanning electron micrograph of beryllium foil showing fracture cross section and surface texture.

content with increased thicknesses of barrier films. Molybdenum barrier films having thickness greater than 0.1 μm eliminated copper contamination, but the resultant molybdenum content exceeded 100 ppm and was, therefore, unacceptable. Silicon barrier films of thickness greater than 0.2 μm resulted in excessive residual stress in the beryllium deposit, as evidenced by curling of the foils after stripping.

Satisfactory results were obtained using a binary barrier consisting of 0.1 μm of Mo and 0.2 μm of Si on the Cu substrate. Copper and molybdenum levels in the resultant beryllium foil were determined to be less than 20 ppm each. Silicon content was less than 200 ppm, which is considered acceptable because of the small x-ray sorption cross section of silicon. Most of the silicon was present as shallow inclusions in the foil and may be reduced by sputter etching. The resultant foils exhibited some degree of residual stress, mostly because of the mismatch of the thermal expansion coefficients of the deposit and substrate. Preliminary work using nickel instead of copper as the primary substrate has shown a lesser degree of intrinsic foil stress.

1. Summary of paper to be published.
2. R. F. Bunshah and R. S. Juntz, *J. Vac. Sci. Technol.* **10,** 83 (1973).
3. G. Mah and C. W. Nordin, RFP-1814, Dow Chemical, Rocky Flats Division.

THIN METAL ENCAPSULATION OF FISSION FOILS AND OXIDE DISCS BY RESISTANCE WELDING[1]

T. C. Quinby

Development of a method for hermetic encapsulation of metal or oxide samples of actinide elements by diffusion bonding of thin metal shells has been successfully performed. Use of hydraulic pressure and heat generated by electric current resistance rapidly forms the circular (in this case)

bond. Double encapsulation was performed using concentric capsules sealed sequentially.

Several hundred neutron dosimeters were prepared by this method containing either a metal foil or a densified oxide disc. All copper or aluminum containers were leak checked by immersion in ethylene glycol under vacuum, and a rejection rate of less than 1% was achieved. Detection sensitivity of this leak test is considered to be 10^{-4}-cc/mi helium. Completed dosimeters were normall, radiographed to ascertain concentricity of the sample discs inside the shell containers.

1. Summary of paper to be published.

Publications and Papers

JOURNAL ARTICLES

M. M. Abraham, L. A. Boatner, T. C. Quinby, D. K. Thomas, and M. Rappaz, "Preparation and Compaction of Synthetic Monazite Powders," *Radioact. Waste Manage.* **1,** 181 (1980).

M. M. Abraham, L. A. Boatner, and M. Rappaz, "Novel Measurement of Hyperfine Interactions in Solids: $^{207}Pb^{3+}$ in YPO_4 and $LuPO_4$," *Phys. Rev. Lett.* **45,** 839 (1980).

M. M. Abraham, Y. Chen, D. N. Olson, V. M. Orera, T. M. Wilson, and R. F. Wood, "An EPR and ENDOR Investigation of the $[F_{Li}]^\circ$ Center in CaO," *Phys. Rev. B* **23,** 51 (1981).

M. J. Alguard, R. L. Swent, R. H. Pantell, S. Datz, J. H. Barrett, B. L. Berman, and S. D. Bloom, "Radiation from Channeled Leptons," *Nucl. Instrum. Methods* **170,** 7 (1980).

D. D. Allred, D. C. Booth, B. R. Appleton, P. D. Miller, C. D. Moak, J. P. F. Sellschop, C. W. White, and A. L. Wintenberg, "The Hydrogen Content of Multicomponent Amorphous Silicon Alloys by ^{19}F Nuclear Reaction Analysis," *IEEE Trans. Nucl. Sci.* **NS-28,** 1838 (1981).

G. D. Alton, J. B. Roberto, C. W. White, and R. A. Zuhr, "Design Features and Focal Properties of Simple Three Element Two- or Three-Dimensional Lens Systems for Decelerating Intense Ion Beams to Very Low Energies," *Nucl. Instrum. Methods* **177,** 273 (1980).

B. R. Appleton, E. J. Kelly, C. W. White, N. G. Thompson, and B. D. Lichter, "Evidence of Surface Migration and Formation of Catalytically 'Inactive' Pt in Corrosion Studies of Pt^+ Implanted Ti," *Nucl. Instrum. Methods* **182/183,** 991 (1981).

J. H. Barrett, B. R. Appleton, and O. W. Holland, "Role of Reversibility in Enhanced Ion Backscattering near 180° Scattering Angle," *Phys. Rev. B* **22,** 4180 (1980).

J. H. Barrett and D. P. Jackson, "Role of Correlations of Lattice Vibrations in Channeling," *Nucl. Instrum. Methods* **170,** 115 (1980).

J. B. Bates, Roger Frech, Herbert Engstrom, J. C. Wang, and T. Kaneda, "Infrared Absorption and Raman Scattering from H_2O in $Na_{1-x}Li_x$ Beta-Aluminas," *Solid State Ionics* **1,** 15 (1980).

J. B. Bates, T. Kaneda, J. C. Wang, and Herbert Engstrom, "Raman Scattering from NH_4^+ and ND_4^+ in Beta-Alumina," *J. Chem. Phys.* **73,** 1503 (1980).

G. W. Beall, L. A. Boatner, D. F. Mullica, and W. O. Milligan, "The Structure of Cerium Orthophosphate, A Synthetic Analog of Monazite," *J. Inorg. Nucl. Chem.* **43,** 101 (1981).

G. M. Begun, G. W. Beall, L. A. Boatner, and W. Gregor, "Raman Spectra of the Rare Earth Orthophosphates," *J. Raman Spectrosc.* **11,** 173 (1981).

A. I. Braginski, J. R. Gavaler, R. C. Kuznicki, B. R. Appleton, and C. W. White, "The Effect of Laser Annealing on the Critical Current Density in Nb_3Ge," *Appl. Phys. Lett.* **39,** 277 (1981).

P. J. Bray, S. A. Feller, G. E. Jellison, Jr., and Y. H. Yun, "B^{10} NMR Studies of the Structure of Bora Glasses," *J. Non-Cryst. Solids* **38/39,** 93 (1980).

J. W. Cable, "Temperature Dependence of the Spin Density Asymmetry in Ni," *Phys. Rev. B* **23,** 6168 (1981).

J. W. Cable and R. E. Parra, "Determination of the Pd-Gd Exchange Constant by Neutron Diffuse Scattering and the Pd Polarization in PdGd Alloys," *J. Magn. Magn. Mater.* **15-18,** 1165 (1980).

J. W. Cable, N. Wakabayashi, and R. M. Nicklow, "Temperature Dependence of the Magnetic Excitations in Gd," *J. Appl. Phys.* **52,** 2231 (1981).

Y. J. Chabal, R. J. Culbertson, L. C. Feldman, and J. E. Rowe, "Si(111):Ni Surface Studies by AES, UPS, LEED and Ion Scattering," *J. Vac. Sci. Technol.* **18,** 880 (1981).

Y. Chen, M. M. Abraham, J. L. Boldu, and V. M. Orera, "Current-Voltage Characteristics of Li-Doped MgO Oxidized at Elevated Temperatures," *J. de Phys.* (Paris) **C6,** 398 (1980).

Y. Chen, N. Dudney, J. Narayan, and V. M. Orera, "Subthreshold [Li]° Formation and Decoration of Strained Regions in Crystalline MgO," *Philos. Mag. A* **44,** 63 (1981).

Y. Chen, R. H. Kernohan, J. L. Boldu, M. M. Abraham, D. J. Eisenberg, and J. H. Crawford, "Enhancement of Electrical Conductivity in MgO due to Lithium Impurities," *Solid State Commun.* **33,** 441 (1980).

Y. Chen, E. Montesa, J. L. Boldu, and M. M. Abraham, "Neutron Irradiations in Oxidized Lithium-Doped MgO Crystals," *Phys. Rev. B* **24,** 5 (1981).

N. Cheung, R. J. Culbertson, L. C. Feldman, P. J. Silverman, K. W. West, and J. W. Mayer, "Ni on Si(111): Reactivity and Interface Structure," *Phys. Rev. Lett.* **45,** 120 (1980).

H. R. Child, "Small-Angle Neutron Scattering from Magnetic Correlations in $Fe_{0.7}Al_{0.3}$," *J. Appl. Phys.* **52,** 1732 (1981).

D. K. Christen, H. R. Kerchner, S. T. Sekula, and Y. K. Chang, "Observation of the Flux-Line Lattice in Superconducting V_3Si," *Physica B & C* **107,** 301 (1981).

W. H. Christie and C. W. White, "SIMS Depth Profiling Studies: The Effect of Laser Anncaling on the Distribution of Ion-Implanted Boron in Silicon," *Surf. Sci.* **100,** 43 (1980).

J. F. Cooke, "Temperature Dependent Dynamic Susceptibility Calculations for Itinerant Ferromagnets," *J. Appl. Phys.* **52,** 1640 (1981).

J. F. Cooke, J. W. Lynn, and H. L. Davis, "Calculations of the Dynamic Susceptibility of Nickel and Iron," *Phys. Rev. B* **21,** 4118 (1980).

R. J. Culbertson, L. C. Feldman, and P. J. Silverman, "Atomic Displacements in the Si(111)-(7×7) Surface," *Phys. Rev. Lett.* **45,** 2043 (1980).

R. J. Culbertson, L. C. Feldman, and P. J. Silverman, "Si(111)-(7×7) Surface Structure Using Ion Scattering," *J. Vac. Sci. Technol.* **18,** 871 (1981).

R. J. Culbertson, T. Sakurai, and G. H. Robertson, "Atom-Probe Field-Ion Microscopy of a Gallium Ion Beam from a Point Source," *J. Vac. Sci. Technol.* **17,** 203 (1980).

L. Darken, T. Raudorf, R. Trammell, R. Pehl, and J. Elliott, "Mechanism for Fast Neutron Damage of Ge(HP) Detectors," *Nucl. Instrum. Methods* **171,** 49 (1980).

L. Darken, R. Trammell, T. Raudorf, and R. Pehl, "Neutron Damage in Ge(HP) Coaxial Detectors," *IEEE Trans. Nucl. Sci.* **NS-28,** 572 (1981).

H. L. Davis and D. M. Zehner, "Structure of the Clean Re($10\bar{1}0$) Surface," *J. Vac. Sci. Technol.* **17,** 19 (1980).

pa Sarkar De, Uzi Landman, and Mark Rasolt, "Microscopic Theory of Thermal Desorption and Dissociation Processes Catalyzed by a Solid Surface," *Phys. Rev. B* **21,** 3256 (1980).

Herbert Engstrom, "Infrared Reflectivity and Transmissivity of Boron-Implanted, Laser-Annealed Silicon," *J. Appl. Phys.* **51,** 5245 (1980).

Herbert Engstrom and J. B. Bates, "Reply to Comments on 'Raman Scattering from Boron-Implanted Laser-Annealed Silicon,'" *J. Appl. Phys.* **52,** 4340 (1981).

Herbert Engstrom, J. B. Bates, and L. A. Boatner, "Infrared Spectra of Hydrogen Isotopes in Potassium Tantalate," *J. Chem. Phys.* **73,** 1073 (1980).

Herbert Engstrom, J. B. Bates, and J. C. Wang, "Non-Debye Capacitance in Single-Crystal Sodium Beta-Alumina," *Solid State Commun.* **35,** 543 (1980).

Herbert Engstrom, J. B. Bates, J. C. Wang, and M. M. Abraham, "Infrared Spectra of Hydrogen Isotopes in α-Al_2O_3," *Phys. Rev. B* **21,** 1520 (1980).

Herbert Engstrom and J. C. Wang, "Automated Multifrequency Measurements of the Complex Impedance of Fast Ion Conductors," *Solid State Ionics* **1,** 441 (1980).

G. P. Felcher, J. W. Cable, and J. L. Smith, "Magnetization Density in Ferromagnetic $TiBe_{1.8}Cu_{0.2}$," *Phys. Rev. Lett.* **45,** 751 (1980).

G. P. Felcher, J. W. Cable, J. Q. Zheng, J. B. Ketterson, and J. E. Hilliard, "Neutron Diffraction Analysis of a Compositionally Modulated Alloy of Nickel-Copper," *J. Magn. Magn. Mater.* **21,** L198 (1980).

G. E. Fish and H. R. Child, "Studies of Chemical Homogeneity and Magnetic Domain Walls in Fe-Based Metallic Glasses Using Small-Angle Neutron Scattering," *J. Appl. Phys.* **52,** 1880 (1981).

R. Frech, E. C. Wang, and J. B. Bates, "Thc I.R. and Raman Spectra of $CaCO_3$ (Aragonite)," *Spectrochim. Acta* **36A,** 915 (1980).

N. Fukuoka, H. Saito, and J. W. Cleland, "Substitution of Impurity Atoms by Self-Interstitials in Thermal Neutron Irradiated Germanium," *Jap. J. Appl. Phys.* **19,** 11 (1980).

D. J. W. Geldart and M. Rasolt, "Analytical Structure of the Wave-Number-Dependent Susceptibility of Many-Fermion Systems at Low Temperature and Long Wavelength. II," *Phys. Rev. B* **22,** 4079 (1980).

L. J. Gray and Theodore Kaplan, "A Self-Consistent Theory for Random Alloys with Short-Range Order," *Phys. Rev. B* **24,** 1872 (1981).

L. J. Groome, A. Teitsma, P. A. Egelstaff, and H. A. Mook, "An Experimental Study of the Two-Body Time Correlations in Gaseous Xenon," *J. Chem. Phys.* **73,** 1393 (1980).

G. R. Gruzalski, "On the Interstitial and Substitutional Distribution of Au Dissolved in Solid Pb," *Solid State Commun.* **34,** 539 (1980).

E. Gurmen, M. Chandrasekhar, P. E. Chumbley, H. D. Bale, D. A. Dolejsi, J. S. Lin, and P. W. Schmidt, "X-ray Scattering Study of the Critical Exponent η in Argon," *Phys. Rev. A* **22,** 170 (1980).

T. M. Hard, R. J. O'Brien, and T. B. Cook, "Pressure Dependence of Fluorescence and Photolytic Interferences in Laser Excited Detection of Hydroxyl Radical," *J. Appl. Phys.* **51,** 3459 (1980).

T. Hayhurst, G. Shalimoff, N. Edelstein, L. A. Boatner, and M. M. Abraham, "Optical Spectra and Zeeman Effect for Er^{3+} in $LuPO_4$ and $HfSiO_4$," *J. Chem. Phys.* **74,** 5449 (1981).

K.-M. Ho, B. N. Harmon, and S. H. Liu, "Surface-State Contribution to the Electroreflectance of Noble Metals," *Phys. Rev. Lett.* **44,** 1531 (1980).

W. Hodby, A. V. Lewis, C. Alexandrou, C. Schwab, and L. A. Boatner, "The Excitation by Light Pulses of Mechanical Vibrations in Solids," *Appl. Phys. Lett.* **36,** 736 (1980).

O. W. Holland, B. R. Appleton, and J. H. Barrett, "Enhanced Backscattering Near 180° for Energetic I in Solids," *IEEE Trans. Nucl. Sci.* **NS-28,** 1824 (1981).

W. R. Husinsky, "Impurity Studies in Fusion Devices Using Laser Fluorescence Spectroscopy," *J. Vac. Sci. Technol.* **18,** 1054 (1981).

Yoshikazu Ishikawa, Keisuke Tajima, Yasuhisa Noda, and Nobuyoshi Wakabayashi, "Magnetic Excitations in an Ordered Ferromagnetic Alloy Fe_3Pt," *J. Phys. Soc. Japan* **48,** 1097 (1980).

R. B. James and D. L. Smith, "Absorption of High-Intensity CO_2 Laser Light in p-type Semiconductors with Small Spin-Orbit Splittings," *J. Appl. Phys.* **52,** 4238 (1981).

R. B. James and D. L. Smith, "Calculation of 3-μm Probe Transmission in p-Ge Excited by a CO_2 Laser," *Solid State Commun.* **37,** 379 (1981).

R. B. James and D. L. Smith, "Dependence of the Saturation Intensity of p-type Germanium on Impurity Concentration and Residual Absorption at 10.59 μm," *Solid State Commun.* **33,** 395 (1980).

R. B. James and D. L. Smith, "Laser-Induced Changes in the Dispersive Properties of p-Ge due to Intervalence-Band Transitions," *Phys. Rev. B* **23,** 4044 (1981).

R. B. James and D. L. Smith, "Saturation Characteristics of p-type Semiconductors over the CO_2 Laser Spectrum," *J. Appl. Phys.* **51,** 2836 (1980).

R. B. James and D. L. Smith, "Saturation of Intervalence-Band Transitions in p-type Semiconductors," *Phys. Rev. B* **21,** 3502 (1980).

R. B. James and D. L. Smith, "Theoretical Description of the Intervalence-Band Photoconductivity of p-Ge at 10.6 μm," *Phys. Rev. B* **23,** 4049 (1981).

G. E. Jellison, Jr., F. A. Modine, C. W. White, R. F. Wood, and R. T. Young, "Optical Properties of Heavily Doped Silicon between 1.5 and 4.1 eV," *Phys. Rev. Lett.* **46,** 1414 (1981).

G. E. Jellison, Jr., G. L. Petersen, and P. C. Taylor, "Nuclear Quadrupole Resonance Studies of Amorphous, Orthorhombic, and Rhombohedral Arsenic," *Phys. Rev. B.* **22,** 3903 (1980).

D. R. Jennison, H. H. Madden, and D. M. Zehner, "Initial-State Screening Effects in Metal Auger Spectra: Be," *Phys. Rev. B* **21,** 430 (1980).

D. L. Johnson, B. N. Harmon, and S. H. Liu, "Self-Consistent Electronic Structure of the Refractory Metal ZrB_2, A Pseudo-Graphite Intercalation Compound," *J. Chem. Phys.* **73,** 1898 (1980).

L. M. Kahn, F. Perrot, and M. Rasolt, "Heat of Solution of Hydrogen in Aluminum," *Phys. Rev. B* **21,** 5594 (1980).

W. A. Kamitakahara, D. Khatamian, D. T. Peterson, and H. A. Mook, "Crystal Structure and Lattice Dynamics of $ThC_{0.063}$," *Phys. Rev. B* **21,** 4500 (1980).

Theodore Kaplan, P. L. Leath, L. J. Gray, and H. W. Diehl, "Self-Consistent Cluster Theory for Systems with Off-Diagonal Disorder," *Phys. Rev. B* **21,** 4230 (1980).

H. R. Kerchner, "The Statistical-Summation Theory of Weak Flux-Line Pins in Type II Superconductors," *Physica B & C* **107,** 463 (1981).

H. R. Kerchner, D. K. Christen, and S. T. Sekula, "Critical Fields H_c and H_{c2} of Superconducting Niobium," *Phys. Rev. B* **34,** 1200 (1981).

H. R. Kerchner, J. Narayan, D. K. Christen, and S. T. Sekula, "Fluxoid Pinning by Small Nitride Precipitates in Niobium," *Phys. Rev. Lett.* **44,** 1146 (1980).

J. Kirschner, R. Feder, and J. F. Wendelken, "Electron Spin Polarization in Energy and Angle-Resolved Photoemission from W(001): Experiment and Theory," *Phys. Rev. Lett.* **47,** 614 (1981).

S. Kobayashi and S. M. Ohr, "*In Situ* Fracture Experiments in bcc Metals," *Philos. Mag. A* **42,** 763 (1980).

S. Kobayashi and S. M. Ohr, "*In Situ* Observations of the Formation of Plastic Zone Ahead of a Crack Tip in Copper," *Scripta Met.* **15,** 343 (1981).

Y. Kuk, T. Sakurai, and R. J. Culbertson, "Optical Emission from Ga Ionization at a Field Emitter," *Appl. Phys. Lett.* **36,** 957 (1980).

L. A. Ladd, K. V. Ravi, and J. Narayan, "Ion-Implanted and Laser-Processed Solar Cells Made from EFG Ribbon," *J. Electrochem. Soc.* **80,** 122 (1980).

G. H. Lander, H. G. Smith, and N. Wakabayashi, "The Low-Temperature Phase Transition in Alpha-Uranium: An Old Problem Revisited," *J. Nucl. Mater.* **95,** 307 (1980).

B. C. Larson and J. F. Barhorst, "X-ray Study of Lattice Strain in Boron-Implanted Laser-Annealed Silicon," *J. Appl. Phys.* **51,** 3181 (1980).

B. C. Larson and W. Schmatz, "Huang Diffuse Scattering from Dislocation Loops," *Phys. Status Solidi B* **99,** 267 (1980).

S. S. Lau, B. Y. Tsaur, M. von Allmen, J. W. Mayer, B. Stritzker, C. W. White, and B. R. Appleton, "Ion-Beam Mixing of Metal-Semiconductor Eutectic Systems," *Nucl. Instrum. Methods* **182/183,** 97 (1981).

S. H. Liu, "Lattice Gas Model of the Metal-Electrolyte Interface," *Surf. Sci.* **101,** 49 (1980).

S. H. Liu, "Magnetic Excitations in Sinusoidally Modulated Spin Structures," *J. Magn. Magn. Mater.* **22,** 93 (1980).

S. H. Liu, "Spatial Inhomogeneity of the Electric Field at the Metal-Electrolyte Interface," *Surf. Sci.* **105,** 429 (1981).

S. H. Liu, "Spin Waves in Static Nonperiodic Structures," *J. Magn. Magn. Mater.* **15–18,** 1477 (1980).

S. H. Liu, B. N. Harmon, C. Stassis, and S. Symeonides, "Electronic Structure and Magnetic Properties of $CeSn_3$," *J. Magn. Magn. Mater.* **15–18,** 942 (1980).

D. H. Lowndes, C. Lin Hendel, R. Hendel, and G. W. Crabtree, "k-Dependence of the Conduction Electron-Local Moment Exchange Interaction in the Atomic and Covalent Mixing Limits," *Phys. Rev. Lett.* **44,** 1012 (1980).

Douglas H. Lowndes and R. F. Wood, "Time-Resolved Reflectivity during Pulsed-Laser Irradiation of GaAs," *Appl. Phys. Lett.* **38,** 971 (1981).

T.-M. Lu, S. R. Anderson, M. G. Lagally, and G.-C. Wang, "Quantitative Analysis of Step Densities Using a Two-Dimensional Random Probability Model," *J. Vac. Sci. Technol.* **17,** 207 (1980).

T.-M. Lu, M. G. Lagally, and G.-C. Wang, "The Effect of Instrumental Broadening on LEED Intensity-Energy Profiles," *Surf. Sci.* **104,** L229 (1981).

T.-M. Lu and G.-C. Wang, "Reconstructed Domains on a Stepped W(100) Surface," *Surf. Sci.* **107,** 139 (1981).

T.-M. Lu, G.-C. Wang, and M. G. Lagally, "Quantitative Island Size Determination in the Chemisorbed Layer W(110)p(2×1)-0, II. Theory," *Surf. Sci.* **108,** 494 (1981).

J. W. Lynn and H. A. Mook, "Temperature Dependence of the Dynamic Susceptibility of Nickel," *Phys. Rev. B* **23,** 198 (1981).

J. F. Marchiando, B. N. Harmon, and S. H. Liu, "Electronic Structure of Layered Compounds ZrCl, ZrBr, ScCl, and PtTe," *Physica* **99,** 259 (1980).

F. A. Modine and V. M. Orera, "Magneto-Optical Properties of Metallic Colloids in Insulators," *Phys. R B* **24,** 1159 (1981).

H. A. Mook, "Neutron Scattering Study of the Spin Dynamics of EuO," *J. Appl. Phys.* **52,** 2249 (1981).

H. A. Mook, "Temperature Dependence of the Spin Dynamics of EuO," *Phys. Rev. Lett.* **46,** 508 (1981).

H. A. Mook, M. B. Maple, Z. Fisk, and D. C. Johnston, "Magnetic Field Dependence of the Neutron Scattering from $ErRh_4B_4$," *Solid State Commun.* **36,** 287 (1980).

R. M. Moon, J. W. Cable, and Y. Shapira, "Neutron Scattering Evidence on Lifshitz Behavior in MnP," *J. Appl. Phys.* **52,** 2025 (1981).

R. M. Moon and W. C. Koehler, "New Evidence on the Magnetic Structure of Nd," *J. Magn. Magn. Mater.* **15–18,** 503 (1980).

M. Mostoller, H. Davis, and D. Zehner, "Skimming the Surface," *ORNL Review* **14,** 18 (1981).

J. Narayan, "Interface Instability and Cell Formation in Ion-Implanted and Laser-Annealed Silicon," *J. Appl. Phys.* **52,** 1289 (1981).

J. Narayan, "Ion Implantation Damage and Its Annealing Behavior," *J. Electrochem. Soc.* **80,** 1153 (1980).

J. Narayan, "Laser Annealing under the Oxide Layers in Silicon," *Appl. Phys. Lett.* **37,** 66 (1980).

J. Narayan, "Laser Processing of Materials," *J. Met.* **32,** 15 (1980).

J. Narayan and Y. Chen, "Characterization of Defects in Nickel-Doped MgO Crystals," *J. Appl. Phys.* **51,** 1242 (1980).

J. Narayan, Y. Chen, and R. M. Moon, "Nickel Colloids in Reduced Nickel-Doped Magnesium Oxide," *Phys. Rev. Lett.* **46,** 1491 (1981).

J. Narayan and V. N. Shukla, "Formation of Ohmic-Contacts in Semiconducting Oxides," *J. Appl. Phys.* **51,** 3444 (1980).

J. Narayan and C. W. White, "Melting Phenomenon and Properties of Defects Associated with Pulsed-Laser Irradiation," *Philos. Mag.* **43,** 1515 (1981).

R. M. Nicklow, W. P. Crummett, M. Mostoller, and R. F. Wood, "Neutron Scattering from Coupled Phonon-Impurity Modes in $KCl_{1-c}(KCN)_c$," *Phys. Rev. B* **22,** 3039 (1980).

R. M. Nicklow, M. Pomerantz, and Armin Segmuller, "Neutron Diffraction from Small Numbers of Langmuir-Blodgett Monolayers of Manganese Stearate," *Phys. Rev. B* **23,** 1081 (1981).

J. R. Noonan and H. L. Davis, "Limitations in Specular Beam LEED Analysis Due to Measurement of the Scattering Angle: Examples from a Study of Cu(110)," *Surf. Sci.* **99,** L424 (1980).

J. R. Noonan and H. L. Davis, "1979 LEED Analysis of the Cu(100)," *J. Vac. Sci. Technol.* **17,** 194 (1980).

O. S. Oen, "Redefined Scattering Cross Section in Monatomic Solids," *Nucl. Instrum. Methods* **170,** 383 (1980).

S. M. Ohr and S. Kobayashi, "*In Situ* Observation of Crack Propagation by Transmission Electron Microscopy," *J. Met.* **32,** 35 (1980).

D. N. Olson, V. M. Orera, Y. Chen, and M. M. Abraham, "Thermally Generated [Li]° Centers in CaO," *Phys. Rev. B* **21,** 1258 (1980).

R. Orlowski, L. A. Boatner, and E. Krätzig, "Photorefractive Effects in the Cubic Phase of Potassium Tantalate-Niobate," *Optics Commun.* **35,** 45 (1980).

V. M. Orera, Y. Chen, and M. M. Abraham, "Imprinting of Slip Bands in Mechanically Deformed MgO Crystals Using Lithium Impurities," *Philos. Mag. A* **41,** 431 (1980).

S. H. Overbury, W. Heiland, D. M. Zehner, S. Datz, and R. S. Thoe, "Investigation of the Structure of Au(110) Using Angle Resolved Low Energy K^+ Ion Backscattering," *Surf. Sci.* **109,** 239 (1981).

R. E. Parra and J. W. Cable, "Neutron Study of Magnetic-Moment Distribution in Ni-Pt Alloys," *Phys. Rev. B* **21,** 5494 (1980).

F. Perrot and M. Rasolt, "Energetics of Hydrogen in Aluminum," *Phys. Rev. B* **23,** 6534 (1981).

F. Perrot and M. Rasolt, "Hydrogen Impurity in Aluminum: Calculation of the Lattice Relaxation Energy," *Solid State Commun.* **36,** 579 (1980).

M. Petek, D. W. Ramey, and R. D. Taylor, "Tritium Separation from Light and Heavy Water by Bipolar Electrolysis," *J. Appl. Electrochem.* **11,** 477 (1981).

J. Petermann, R. M. Gohil, J. M. Schultz, R. W. Hendricks, and J. S. Lin, "Small-Angle X-ray Scattering from Polybutene-1 Films Crystallized from a Highly Extended Melt," *J. Mater. Sci.* **16,** 265 (1981).

G. L. Petersen, G. E. Jellison, Jr., and P. C. Taylor, "Pulsed NQR in Amorphous, Orthorhombic and Rhombohedral Arsenic," *J. Mol. Struct.* **58,** 263 (1980).

D. T. Pierce, R. J. Celotta, G.-C. Wang, and E. G. McRae, "Spin Dependence of Electronic Surface Resonance Scattering from W(100)," *Solid State Commun.* **39,** 1053 (1981).

R. L. Prater, L. L. Chase, and L. A. Boatner, "Raman Scattering Studies of the Impurity-Induced Ferroelectric Phase Transition in $KTaO_3$:Li," *Phys. Rev. B* **23,** 5904 (1981).

R. L. Prater, L. L. Chase, and L. A. Boatner, "Raman Scattering Studies of the Impurity-Induced Ferroelectric Phase Transition in $KTaO_3$:Nb," *Phys. Rev. B* **23,** 221 (1981).

P. P. Pronko, B. R. Appleton, O. W. Holland, and S. R. Wilson, "Near Surface Yield Enhancement in Narrow Acceptance 180° Elastic Scattering for He Ion in Noncrystalline and Polycrystalline Solids," *Nucl. Instrum. Methods* **170,** 227 (1980).

V. C. Rakhecha, G. H. Lander, A. J. Arko, and R. M. Moon, "Induced Magnetization Density in the 5f System UAl_2," *J. Appl. Phys.* **52,** 1636 (1981).

M. Rappaz, M. M. Abraham, J. O. Ramey, and L. A. Boatner, "EPR Spectroscopic Characterization of Gd^{3+} in the Monazite-Type Rare-Earth Orthophosphates: $LaPO_4$, $CePO_4$, $PrPO_4$, $NdPO_4$, $SmPO_4$, and $EuPO_4$," *Phys. Rev. B* **23,** 1012 (1981).

M. Rappaz, L. A. Boatner, and M. M. Abraham, "EPR Investigations of Gd^{3+} in Single Crystals and Powders of the Zircon-Structure Orthophosphates YPO_4, $ScPO_4$, and $LuPO_4$," *J. Chem. Phys.* **73,** 1095 (1980).

M. Rasolt and H. L. Davis, "Angular Terms in the Optical Potential: Effect on Photoemission from a Model (100) Surface of Aluminum," *Phys. Rev. B* **21,** 1445 (1980).

M. Rasolt and D. J. W. Geldart, "Wave-Vector Decomposition of the Exchange and Correlation Contributions to a Metallic Surface Energy," *Phys. Rev. B* **21,** 3158 (1980).

Mark Rasolt and Mark Mostoller, "Pair Potentials and Lattice Vibrations at Simple-Metal Surfaces," *Phys. Rev. B* **23,** 3774 (1981).

J. B. Roberto and M. T. Robinson, "A Measurement of the Transverse Range of (n,2n) Recoils in Au," *J. Appl. Phys.* **51,** 4589 (1980).

J. B. Roberto, R. A. Zuhr, and S. P. Withrow, "Surface Erosion in the Plasma Edge of ISX-B," *J. Nucl. Mater.* **93/94,** 146 (1980).

B. C. Sales, J. E. Turner, and M. B. Maple, "Sublimation Rate of Cobalt Near Its Curie Temperature," *Phys. Rev. Lett.* **44,** 586 (1980).

J. M. Schultz, J. Bentley, R. W. Hendricks, J. S. Lin, and J. Petermann, "Small-Angle X-ray and Electron Scattering from $(SN)_x$," *J. Appl. Phys.* **52,** 5389 (1981).

J. M. Schultz, J. S. Lin, R. W. Hendricks, R. R. Lagasse, and R. G. Kepler, "Temperature Dependent Small-Angle X-ray Scattering from Poly(vinylidene Fluoride)," *J. Appl. Phys.* **51,** 5508 (1980).

J. M. Schultz, J. S. Lin, R. W. Hendricks, J. Petermann, and R. M. Gohil, "Annealing of Polypropylene Films Crystallized from a Highly Extended Melt," *J. Polym. Sci., Polym. Phys. Ed.* **19,** 609 (1981).

B. Schweer, D. Rusbuldt, E. Hintz, J. B. Roberto, and W. R. Husinsky, "Measurement of the Density and Velocity Distribution of Neutral Fe in ISX-B by Laser Fluorescence Spectroscopy," *J. Nucl. Mater.* **93/94,** 357 (1980).

S. T. Sekula and J. R. Thompson, "Low-Temperature H-Ion Implantation in Aluminum," *Nucl. Instrum. Methods* **182/183,** 937 (1981).

S. T. Sekula and J. R. Thompson, "Variable-Temperature Ion-Implantation Cryostat," *Rev. Sci. Instrum.* **51,** 1618 (1980).

Harold G. Smith, "Phonons, Lattice Instabilities and Superconductivity," *Aust. J. Phys.* **33,** 861 (1980).

H. G. Smith and N. Wakabayashi, "Phonon Anomalies and Superconductivity in the hcp Metals Tc, Re, and Ru,"*Solid State Commun.* **39,** 371 (1981).

H. G. Smith, N. Wakabayashi, W. P. Crummett, R. M. Nicklow, G. H. Lander, and E. S. Fisher, "Observation of a Charge-Density Wave in α-U at Low Temperature," *Phys. Rev. Lett.* **44,** 1612 (1980).

E. Sonder, J. V. Spadaro, and R. A. Weeks, "Penetration of Surface Damage Resulting from Abrasion and Heating of MgO Crystals," *J. Am. Ceram. Soc.* **64,** C-65 (1981).

S. Spooner, H. R. Child, F. H. Hsu, E. R. Vance, and J. H. Smith, "Small-Angle Neutron Scattering and Positron Annihilation in Mn-Cu Alloys," *Phys. Status Solidi* **63,** 31 (1981).

C. Stassis, C.-K. Loong, J. Zarestky, O. D. McMasters, and R. M. Nicklow, "Lattice Dynamics of $CeSn_3$," *Solid State Commun.* **36,** 677 (1980); *Phys. Rev. B* **23,** 5128 (1981).

C. Stassis, C.-K. Loong, J. Zarestky, O. D. McMasters, and R. M. Nicklow, "Lattice Dynamics of $LaSn_3$," *Phys. Rev. B* **23,** 2227 (1981).

J. E. Turner, B. C. Sales, and M. B. Maple, "Oscillatory Oxidation of CO over a Platinum Catalyst," *Surf. Sci.* **103,** 54 (1981).

J. E. Turner, B. C. Sales, and M. B. Maple, "Oscillatory Oxidation of CO over Pd and Ir Catalysts," *Surf. Sci.* **109,** 591 (1981).

J. R. Thompson, S. T. Sekula, and Y. Chen, "Magnetic Properties of Ni in MgO; Ni^{+2} Ions and Magnetically Ordered Precipitates," *Physica B & C* **107,** 87 (1981).

B. van Bodegom, B. C. Larson, and H. A. Mook, "Diffuse X-ray and Inelastic Neutron Scattering Study of the Spin Peierl's Transition in N-Methyl-N-Ethyl-Morpholinium Bistetracyanoquinodimethane (MEM-$TCNQ_2$)," *Phys. Rev. B* **24,** 1520 (1981).

N. Wakabayashi, "Phonon Frequencies and Linewidths for Sm(Y)S," *Phys. Rev. B* **22,** 5833 (1980).

N. Wakabayashi, "Phonons in Transition Metals," *Comments Solid State Phys.* **10,** 11 (1981).

G.-C. Wang, R. J. Celotta, and D. T. Pierce, "Polarized Low Energy Electron Diffraction from W(100)," *Phys. Rev. B* **23,** 1761 (1981).

G.-C. Wang, D. T. Pierce, and R. J. Celotta, "Study of Temperature and Hydrogen Induced Reconstruction and Ordering of W(100) by Polarized Electron Scattering," *J. Vac. Sci. Technol.* **18,** 647 (1981).

J. C. Wang, "Local Fields near a Point-Charge Defect in Cubic Ionic Crystals," *Phys. Rev. B* **22,** 2725 (1980).

J. C. Wang, "On the Charge Compensation Mechanism in β-Alumina," *J. Chem. Phys.* **73,** 5786 (1980).

R. A. Weeks, J. Gastineau, and E. Sonder, "Distribution of Fe^{3+} in Iron-Doped MgO Single Crystals," *Phys. Status Solidi A* **61,** 265 (1980).

R. A. Weeks, R. H. Magruder, and D. L. Kinser, "The Effect of OH on UV Optical Absorption of Reduced GeO_2 Glasses," *J. Non-Cryst. Solids* **42,** 307 (1980).

R. A. Weeks, M. Nasrallah, S. Arafa, and A. Bishay, "Studies of Fusion Processes of Natural Glasses by Electron Magnetic Resonance Spectroscopy," *J. Non-Cryst. Solids* **38,** 129 (1980).

J. F. Wendelken, "The Chemisorption of Oxygen on Cu(110) Studied by EELS and LEED," *Surf. Sci.* **108,** 605 (1981).

S. A. Werner and J. W. Cable, "Neutron Scattering Experiments on the Magnetism in Cu-Mn Single Crystals," *J. Appl. Phys.* **52,** 1757 (1981).

C. W. White, B. R. Appleton, and S. R. Wilson, "Laser Annealing of Ion-Implanted Silicon," *IEEE Trans. Nucl. Sci.* **NS-28,** 1759 (1981).

C. W. White and W. H. Christie, "The Use of RBS and SIMS to Measure Dopant Profile Changes in Silicon Caused by Pulsed-Laser Annealing," *Solid State Technol.* **23,** 109 (1980).

G. D. Wignall, R. W. Hendricks, W. C. Koehler, J. S. Lin, M. P. Wai, E. L. Thomas, and R. S. Stein, "Measurements of Single Chain Form Factors by SANS from Polystyrene Containing High Concentrations of Labeled Molecules," *Polymer* **22,** 886 (1981).

S. R. Wilson, C. W. White, F. W. Young, Jr., B. R. Appleton, and J. Narayan, "Nonequilibrium Solubility and Segregation in Ion-Implanted, Laser-Annealed Silicon," *J. de Physique* **7,** C4-91 (1980).

S. P. Withrow, R. A. Zuhr, J. B. Roberto, B. R. Appleton, and M. T. Robinson, "Use of Radiation Damage Profiles in Silicon as a Measure of Plasma Particle Energies in Tokamaks," *J. Nucl. Mater.* **98,** 231 (1981).

R. F. Wood, "Influence of Carrier Diffusion on Melt-Front Penetration during Pulsed-Laser Annealing," *Appl. Phys. Lett.* **38,** 357 (1981).

R. F. Wood, "Model for Nonequilibrium Segregation during Pulsed-Laser Annealing," *Appl. Phys. Lett.* **37,** 302 (1980).

R. F. Wood and G. E. Giles, "Control of Melt-Front Velocity during Pulsed-Laser Annealing," *Appl. Phys. Lett.* **38,** 422 (1981).

R. F. Wood and G. E. Giles, "Macroscopic Theory of Pulsed-Laser Annealing: I. Model for Thermal Transport and Melting," *Phys. Rev. B* **23,** 2923 (1981).

R. F. Wood, J. R. Kirkpatrick, and G. E. Giles, "Macroscopic Theory of Pulsed-Laser Annealing: II. Dopant Diffusion and Segregation," *Phys. Rev. B* **23,** 5555 (1981).

R. F. Wood, R. T. Young, R. D. Westbrook, J. Narayan, J. W. Cleland, and W. H. Christie, "New Techniques for the Study and Control of Grain Boundary Effects," *Solar Cells* **1,** 381 (1980).

J. D. Woosley, C. Wood, E. Sonder, and R. A. Weeks, "Photoelectric Effects in Magnesium Aluminum Spinel," *Phys. Rev. B* **22,** 1065 (1980).

Y. Yamada, N. Wakabayashi, and R. M. Nicklow, "Neutron Diffuse Scattering in Magnetite due to Molecular Polarons," *Phys. Rev. B* **21,** 4642 (1980).

R. T. Young, M. C. Lu, R. D. Westbrook, and G. E. Jellison, Jr., "Effect of Lithium on the Electrica Properties of Grain Boundaries in Silicon," *Appl. Phys. Lett.* **38,** 628 (1981).

R. T. Young, R. F. Wood, W. H. Christie, and G. E. Jellison, Jr., "Substrate Heating and Emitter Dopant Effects in Laser-Annealed Solar Cells," *Appl. Phys. Lett.* **39,** 313 (1981).

R. T. Young, R. F. Wood, J. Narayan, C. W. White, and W. H. Christie, "Pulsed-Laser Techniques for Solar Cell Processing," *IEEE Trans. Electron Devices* **ED-27,** 807 (1980).

D. M. Zehner, J. R. Noonan, H. L. Davis, and C. W. White, "The Atomic Structure of Laser-Annealed Si(111)-(1×1)," *J. Vac. Sci. Technol.* **18,** 852 (1981).

D. M. Zehner, C. W. White, and G. W. Ownby, "Si and Ge (111) Surface Structures after Pulsed-Laser Annealing," *Appl. Phys. Lett* **37,** 456 (1980).

R. A. Zuhr, S. P. Withrow, and J. B. Roberto, "Deuterium and Impurity Deposition Profiles in the Plasma Edge of ISX-B," *J. Nucl. Mater.* **93/94,** 127 (1980).

BOOKS AND PROCEEDINGS

W. S. Aaron, E. H. Kobisk, and T. C. Quinby, "Development and Characterization of Cermet Forms for Radioactive Waste," p. 315 in *Scientific Basis for Nuclear Waste Management,* Vol. 2, Plenum Press, New York, 1980.

M. M. Abraham, L. A. Boatner, G. W. Beall, C. B. Finch, R. J. Floran, P. G. Huray, and M. Rappaz, "A Review of Research on Analogs of Monazite for the Isolation of Actinide Wastes," p. 144 in *Alternate Nuclear Waste Forms and Interactions in Geologic Media,* CONF-8005107, ed. by L. A. Boatner and G. C. Battle, Jr., U.S. Department of Energy, Washington, D.C., 1981.

M. M. Abraham, L. A. Boatner, and M. Rappaz, "EPR Investigations of Impurities in the Lanthanide Orthophosphates," p. 475 in *Nuclear and Electron Resonance Spectroscopies Applied to Materials Science,* Vol. 3, ed. by E. N. Kaufmann and G. K. Shenoy, North Holland, New York, 1981.

H. L. Adair, E. H. Kobisk, J. A. Setaro, T. C. Quinby, J. A. Carter, J. F. Emery, R. Walker, and J. Cooper, "Neutron Dosimeter Materials Development and Characterization," p. 1091 in *Proceedings of the Third ASTM-EURATOM Symposium on Reactor Dosimetry,* Vol. 2, EUR 6813 EN-FR, Luxembourg, Belgium, 1980.

M. J. Alguard, R. L. Swent, R. H. Pantell, S. Datz, J. H. Barrett, B. L. Berman, and S. D. Bloom, "Radiation from Channeled Leptons," p. 7 in *Proceedings of the 8th International Conference on Atomic Collisions in Solids,* ed. by D. P. Jackson, J. E. Robinson, and D. A. Thompson, North Holland, New York, 1980.

B. R. Appleton, "Ion Channeling Techniques for Defect and Surface Studies," p. 97 in *Defects in Semiconductors,* ed. by J. Narayan and T. Y. Tan, North Holland, New York, 1981.

B. R. Appleton, B. Stritzker, C. W. White, J. Narayan, J. Fletcher, O. Meyer, and S. S. Lau, "Laser Induced Defects and Materials Interactions in the V-Si System," p. 607 in *Laser and Electron-Beam Solid Interactions and Materials Processing,* ed. by J. F. Gibbons, L. D. Hess, and T. W. Sigmon, North Holland, New York, 1981.

B. R. Appleton, C. W. White, B. Stritzker, O. Meyer, J. R. Gavaler, A. I. Braginski, and M. Ashkin, "Ion Implantation and Laser Annealing of High T_c Superconducting Materials," p. 714 in *Laser and Electron Beam Processing of Materials,* ed. by C. W. White and P. S. Peercy, Academic Press, New York, 1980.

'. H. Barrett and D. P. Jackson, "Role of Correlations of Lattice Vibrations in Channeling," p. 115 in *Proceedings of the 8th International Conference on Atomic Collisions in Solids,* ed. by D. P. Jackson, J. E. Robinson, and D. A. Thompson, North Holland, New York, 1980.

L. A. Boatner, G. W. Beall, M. M. Abraham, C. B. Finch, P. G. Huray, and M. Rappaz, "Lanthanide Orthophosphates for the Primary Immobilization of Actinide Wastes," p. 411 in *Management of Alpha-Contaminated Wastes,* IAEA-SM 246/73, Vienna, Austria, 1981.

L. A. Boatner, G. W. Beall, M. M. Abraham, C. B. Finch, P. G. Huray, and M. Rappaz, "Monazite and Other Lanthanide Orthophosphates as Alternate Actinide Waste Forms," p. 289 in *Scientific Basis for Nuclear Waste Management,* Vol. 2, ed. by C. J. Northrup, Jr., Plenum Press, New York, 1980.

L. A. Boatner, M. M. Abraham, and M. Rappaz, "The Characterization of Nuclear Waste Forms by EPR Spectroscopy," p. 181 in *Scientific Basis for Nuclear Waste Management,* Vol. 3, ed. by J. G. Moore, Plenum Press, New York, 1981.

R. J. Celotta, D. T. Pierce, G.-C. Wang, S. D. Bader, and G. P. Felcher, "Surface Magnetism in Ni(110) as Studied by Polarized Electron Scattering," p. 1045 in *Proceedings of the Fourth International Conference on Solid Surfaces and the Third European Conference on Surface Science,* ed. by D. A. Degras and M. Costa, Vol. II, Societe Francaise du Vide, Paris, France, 1980.

R. R. Coltman, Jr., C. E. Klabunde, R. H. Kernohan, and C. J. Long, "Effects of Radiation at 5 K on Organic Insulators for Superconducting Magnets," p. 1694 in *Proceedings of the 8th Symposium on Engineering Problems of Fusion Research,* IEEE 79CH1441-5 NPS, New York, 1979.

S. Datz, J. H. Barrett, M. J. Alguard, R. L. Swent, R. H. Pantell, B. L. Berman, and S. D. Bloom, "Coherent Radiation from Correlated Collisions of Positrons with Si," p. 176 in *Proceedings Eleventh International Conference on Physics of Electronic and Atomic Collisions,* ed. by Society for Atomic Collision Research, North Holland, New York, 1979.

A. M. de Goër, B. Salce, and L. A. Boatner, "Low-Temperature Thermal Conductivity of $KTaO_3$ and KTN Single Crystals," p. 243 in *Phonon Scattering in Condensed Matter,* ed. by H. J. Maris, Plenum Press, New York, 1980.

G. P. Felcher, S. D. Bader, R. J. Celotta, D. T. Pierce, and G.-C. Wang, "Magnetic State at the Surface of a Ferromagnet by Polarized Electron Diffraction," p. 107 in *Proceedings of International Conference on Ordering in Two-Dimension,* ed. by S. K. Sinha, North Holland, New York, 1980.

L. C. Feldman, R. L. Kauffman, P. J. Silverman, I. Stensgaard, and R. A. Zuhr, "Surface Scattering of MeV $^{+}$He Ions from W(100) and Si(100) Single Crystals," p. 112 in *Proceedings VII International Conference on Atomic Collisions in Solids,* Vol. 2, ed. by Y. V. Bulgakov and A. F. Tulinov, Moscow State University Publishing House, Moscow, U.S.S.R., 1980.

J. Fletcher, J. Narayan, and D. H. Lowndes, "Analysis of Defects in Laser-Annealed Gallium Arsenide," p. 421 in *Defects in Semiconductors,* ed. by J. Narayan and T. Y. Tan, North Holland, New York, 1981.

J. Fletcher, J. Narayan, and O. W. Holland, "Studies of Defects and Solubility Limits in SPE Grown In- and Sb-Implanted Silicon," p. 295 in *Microscopy of Semiconducting Materials,* Vol. 60, Institute of Physics, London, 1981.

R. J. Floran, M. M. Abraham, L. A. Boatner, and M. Rappaz, "Geologic Stability of Monazite and Its Bearing on the Immobilization of Actinide Wastes," p. 507 in *Scientific Basis for Nuclear Waste Management,* Vol. 3, ed. by J. G. Moore, Plenum Press, New York, 1981.

R. J. Floran, M. Rappaz, M. M. Abraham, and L. A. Boatner, "Hot and Cold Pressing of (La,Ce)PO_4-Based Nuclear Waste Forms," p. 185 in *Alternate Nuclear Waste Forms and Interactions in Geologic Media,* CONF-8005107, ed. by L. A. Boatner and G. C. Battle, Jr., U.S. Department of Energy, Washington, D.C., 1981.

G. E. Giles, J. R. Kirkpatrick, and R. F. Wood, "Laser Annealing of Solar Cell Wafers," p. 1 *Proceedings of the 19th National Heat Transfer Conference of the American Society of Mechanical Engineers,* ASME Publication 80-HT-13, New York, 1980.

M. Hou and M. T. Robinson, "Computer Simulation of the Grazing Incidence Backscattering of Protons from a (110) Nickel Surface," p. 132 in *Proceedings VII International Conference on Atomic Collisions in Solids,* Vol. 2, ed. by Y. V. Bulgakov and A. F. Tulinov, Moscow State University Publishing House, Moscow, U.S.S.R., 1980.

J. A. Horton and W. A. Jesser, "Coarse Slip Processes and Crack Propagation in Irradiated Stainless Steel," p. 413 in *Effects of Radiation on Materials: 10th Conference,* ASTM STP 725, ed. by D. Kramer, H. R. Brager, and J. F. Perrin, American Society for Testing and Materials, Baltimore, Maryland, 1981.

F. H. Hsu and C. W. White, "Positron Annihilation in Ion-Implanted, Laser-Annealed Silicon," p. 461 in *Laser and Electron Beam Processing of Materials,* ed. by C. W. White and P. S. Peercy, Academic Press, New York, 1980.

G. E. Jellison, Jr., J. W. Cleland, and N. Fukuoka, "A Radiation-Resistant Substrate for a p^+-n-n^+ Solar Cell," p. 1398 in *Fourteenth IEEE Photovoltaic Specialists Conference-1980,* IEEE 80CH1508-1, New York, 1980.

G. E. Jellison, Jr., J. W. Cleland, and R. T. Young, "Transient Capacitance Studies of a Low-Lying Electron Trap in n-Type Silicon," p. 241 in *Defects in Semiconductors,* ed. by J. Narayan and T. Y. Tan, North Holland, New York, 1981.

G. E. Jellison, Jr., F. A. Modine, C. W. White, and R. T. Young, "Optical Absorption Measurements of Pure and Heavily Doped Silicon from 1.24 to 4.63 eV and the Effect on Solar Cell Performance," p. 1164 in *Fifteenth IEEE Photovoltaic Specialists Conference-1981,* IEEE 81CH1644-4, New York, 1981.

G. E. Jellison, Jr., R. T. Young, R. F. Wood, and A. Gat, "A Comparison between Pulsed and cw Laser Annealing for Solar Cell Applications," p. 15 in *Space Photovoltaic Research and Technology 1980,* NASA Conference Publication 2169, Washington, D.C., 1980.

K. L. Kelly, G. W. Beall, J. P. Young, and L. A. Boatner, "Valence States of Actinides in Synthetic Monazites," p. 189 in *Scientific Basis for Nuclear Waste Management,* Vol. 3, ed. by J. G. Moore, Plenum Press, New York, 1981.

H. R. Kerchner, D. K. Christen, S. T. Sekula, and P. Thorel, "Equilibrium Properties of the Fluxoid Lattice in Single-Crystal Niobium," p. 433 in *Superconductivity in d- and f-Band Metals,* ed. by H. Suhl and M. B. Maple, Academic Press, New York, 1980.

E. H. Kobisk, W. S. Aaron, T. C. Quinby, and D. W. Ramey, "High Level Waste Fixation in Cermet Form," p. 297 in *Alternate Nuclear Waste Forms and Interactions in Geologic Media,* CONF-8005107, ed. by L. A. Boatner and G. C. Battle, Jr., U.S. Department of Energy, Washington, D.C., 1981.

W. C. Koehler, R. W. Hendricks, H. R. Child, S. P. King, J. S. Lin, and G. D. Wignall, "The National Center for Small-Angle Scattering Research," p. 75 in *Proceedings of NATO Advanced Study Institute on Scattering Techniques Applied to Supra-molecular and Nonequilibrium Systems,* Vol. 73, ed. by S. H. Chen, B. Chu, and R. Nossal, Plenum Press, New York, 1981.

J. R. Kirkpatrick, G. E. Giles, Jr., and R. F. Wood, "Numerical Methods for the Analysis of Laser Annealing of Doped Semiconductor Wafers," p. 152 in *Heat Transfer and Thermal Control,* Vol. 78, AIAA Progress in Astronautics and Aeronautics Series, New York, 1980.

M. G. Lagally, T.-M. Lu, and G.-C. Wang, "Observations of Island Formation and Dissolution in Chemisorbed Layers by LEED," p. 113 in *Proceedings of International Conference on Ordering in Two Dimension,* ed. by S. K. Sinha, North Holland, New York, 1980.

C. Larson and J. F. Barhorst, "Diffuse X-ray Scattering for the Study of Defects in Silicon," p. 151 in *Defects in Semiconductors,* ed. by J. Narayan and T. Y. Tan, North Holland, New York, 1981.

S. H. Liu, "Electronic Structure of Rare Earth Systems," p. 121 in *The Science and Technology of Rare Earth Materials,* ed. by E. C. Subbarao and W. E. Wallace, Academic Press, New York, 1980.

S. H. Liu, C. Stassis, and K. A. Gschneidner, Jr., "Mixed Valent Properties of $CeSn_3$," p. 99 in *Valence Fluctuations in Solids,* ed. by L. M. Falicov, W. Hanke, and M. B. Maple, North Holland, New York, 1981.

D. H. Lowndes, "Waveshape Analysis in the dHvA Effect," p. 393 in *Electrons at the Fermi Surface,* ed. by M. Springford, Cambridge University Press, Cambridge, England, 1980.

Douglas H. Lowndes, J. W. Cleland, W. H. Christie, and R. E. Eby, "Pulsed Ruby Laser Annealing of Zn, Mg, Se, and Si Ion Implants in Semiconducting GaAs," p. 223 in *Laser and Electron-Beam Solid Interactions and Materials Processing,* Vol. 1, ed. by J. F. Gibbons, L. D. Hess, and T. W. Sigmon, North Holland, New York, 1981.

D. H. Lowndes, J. W. Cleland, J. Fletcher, J. Narayan, R. D. Westbrook, R. F. Wood, W. H. Christie, and R. E. Eby, "Pulsed-Laser Annealing of Ion-Implanted Semiconducting GaAs for Homojunction Solar Cells," p. 45 in *Fifteenth IEEE Photovoltaic Specialists Conference-1981,* IEEE 81CH1644-4, New York, 1981.

G. Maderlechner, R. Behrisch, B. M. U. Scherzer, and M. T. Robinson, "Sputtering Yield Calculations for Light Ions near Threshold Energies," p. 39 in *Proceedings VII International Conference on Atomic Collisions in Solids,* Vol. 2, ed. by Y. V. Bulgakov and A. F. Tulinov, Moscow State University Publishing House, Moscow, U.S.S.R., 1980.

H. A. Mook and F. Holtzberg, "Lattice Dynamics of the Intermediate Valence Compounds $Sm_{0.75}Y_{0.25}S$ and TmSe," p. 113 in *Valence Fluctuations in Solids,* ed. by L. M. Falicov, W. Hanke, and M. B. Maple, North Holland, New York, 1981.

H. A. Mook, W. C. Koehler, M. B. Maple, Z. Fisk, and D. C. Johnston, "Neutron Scattering Study of the Magnetic Transition in the Reentrant Superconductor $Ho_{0.6}Er_{0.4}Rh_4B_4$," p. 427 in *Superconductivity in d- and f-Band Metals,* ed. by H. Suhl and M. B. Maple, Academic Press, New York, 1980.

H. A. Mook, M. B. Maple, Z. Fisk, D. C. Johnston, and L. D. Woolf, "Neutron Scattering Studies of the Magnetic Transitions in the Ternary Alloy System $Er_{1-x}Ho_xRh_4B_4$," p. 179 in *Ternary Superconductors,* ed. by G. K. Shenoy, B. D. Dunlap, and F. Y. Fradin, North Holland, New York, 1981.

J. Narayan, "Characterization of Laser-Annealed Semiconductors," p. 302 in *38th Annual Proceedings of the Electron Microscopy Society of America,* ed. by G. W. Bailey, Claitor's Press, Baton Rouge, Louisiana, 1981.

J. Narayan, "Laser Processing of Semiconductors," p. 55 in *Lasers in Metallurgy,* ed. by K. Mukherjee and S. M. Copley, The Metallurgical Society of AIME, Warrendale, Pennsylvania, 1981.

J. Narayan, "Melting Phenomenon and Laser Annealing in Semiconductors," p. 101 in *Microscopy of Semiconducting Materials,* Vol. 60, Institute of Physics, London, 1981.

J. Narayan, "Structural Defects in Laser and Electron Beam Annealed Silicon," p. 397 in *Laser and Electron Beam Processing of Materials,* ed. by C. W. White and P. S. Peercy, Academic Press, New York, 1980.

J. Narayan and J. Fletcher, "Convection and Constitutional Supercooling Cells in Laser-Annealed Silicon," p. 431 in *Defects in Semiconductors,* ed. by J. Narayan and T. Y. Tan, North Holland, New York, 1981.

J. Narayan and J. Fletcher, "Radiation Damage and Its Annealing in Semiconductors," p. 191 in *Defects in Semiconductors,* ed. by J. Narayan and T. Y. Tan, North Holland, New York, 1981.

J. Narayan, J. Fletcher, B. R. Appleton, and W. H. Christie, "Enhanced Diffusion and Formation of Defects during Thermal Oxidation," p. 355 in *Defects in Semiconductors,* ed. by J. Narayan and T. Y. Tan, North Holland, New York, 1981.

J. Narayan, J. Fletcher, and R. E. Eby, "Melting and Laser Annealing in Semiconductors Using 0.485-μm and 0.195-μm Pulsed Lasers," p. 409 in *Defects in Semiconductors,* ed. by J. Narayan and T. Y. Tan, North Holland, New York, 1981.

J. Narayan, J. Fletcher, C. W. White, R. E. Eby, and W. H. Christie, "Melting Phenomenon and Laser Annealing in Semiconductors," p. 94 in *Proceedings of Conference on Lasers and Electro-Optics,* IEEE 81CH1655-0, New York, 1981.

J. Narayan and C. W. White, "Melting by Pulsed Laser Irradiation," p. 65 in *Laser and Electron Beam Processing of Materials,* ed. by C. W. White and P. S. Peercy, Academic Press, New York, 1980.

J. R. Noonan and H. L. Davis, "High Sensitivity LEED Analysis for Clean Metallic Surfaces," p. 1100 in *Proceedings of the Fourth International Conference on Solid Surfaces and the Third European Conference on Surface Science,* ed. by D. A. Degras and M. Costa, Vol. II, Societe Francaise du Vide, Paris, France, 1980.

O. S. Oen, "Redefined Scattering Cross Section in Monatomic Solids," p. 383 in *Proceedings of the 8th International Conference on Atomic Collisions in Solids,* ed. by D. P. Jackson, J. E. Robinson, and D. A. Thompson, North Holland, New York, 1980.

O. S. Oen, "Some Analytical Solutions to the Two Atom Blocking Model," p. 124 in *Proceedings VII International Conference on Atomic Collisions in Solids,* Vol. 2, ed. by Y. V. Bulgakov and A. F. Tulinov, Moscow State University Publishing House, Moscow, U.S.S.R., 1980.

D. T. Pierce, R. J. Celotta, and G.-C. Wang, "Spin-Polarized Electron Scattering Studies of W(100)," p. 1060 in *Proceedings of the Fourth International Conference on Solid Surfaces and the Third European Conference on Surface Science,* ed. by D. A. Degras and M. Costa, Vol. II, Societe Francaise du Vide, Paris, France, 1980.

F. E. Pinkerton, A. J. Sievers, J. W. Wilkens, M. B. Maple, and B. C. Sales, "An Optical Signature at meV Energies for Valence Fluctuation Compounds," p. 177 in *Valence Fluctuations in Solids,* ed. by L. M. Falicov, W. Hanke, and M. B. Maple, North Holland, New York, 1981.

M. Rappaz, L. A. Boatner, and M. M. Abraham, "The Application of EPR Spectroscopy to the Characterization of Crystalline Nuclear Waste Forms," p. 170 in *Alternate Nuclear Waste Forms and Interactions in Geologic Media,* CONF-8005107, ed. by L. A. Boatner and G. C. Battle, Jr., U.S. Department of Energy, Washington, D.C., 1981.

J. B. Roberto, "Light-Ion Sputtering Yields," chapter 7 in *Sputtering Caused by Plasma (Neutral Beam)–Surface Interactions,* ed. by M. Kaminsky and C. R. Finfgeld, CONF-790775, U.S. Department of Energy, Washington, D.C., 1979.

J. B. Roberto and M. T. Robinson, "A Measurement of the Transverse Range of (n,2n) Recoils in Au," p. 232 in *Proceedings VII International Conference on Atomic Collisions in Solids,* Vol. 2, ed. by Y. V. Bulgakov and A. F. Tulinov, Moscow State University Publishing House, Moscow, U.S.S.R., 1980.

Mark T. Robinson, "Theoretical Aspects of Monocrystal Sputtering," p. 73 in *Sputtering by Particle Bombardment I. Topics in Applied Physics,* Vol. 47, ed. by R. Behrisch, Springer-Verlag, Berlin, 1981.

H. G. Smith, N. Wakabayashi, W. P. Crummett, R. M. Nicklow, G. H. Lander, and E. S. Fisher, "Soft Modes and Lattice Instabilities in α-U," p. 143 in *Superconductivity in d- and f-Band Metals,* ed. by H. Suhl and M. B. Maple, Academic Press, New York, 1980.

N. G. Thompson, B. D. Lichter, B. R. Appleton, E. J. Kelly, and C. W. White, "Electrochemical Behavior of Titanium Implanted with Platinum," p. 181 in *Ion Implantation Metallurgy,* ed. by C. M. Preece and J. K. Hirvonen, The Metallurgical Society of AIME, Warrendale, Pennsylvania, 1980.

F. Wendelken, "The Adsorption and Coadsorption with CO of NO on Cu(110) Studied with EELS and LEED," p. 187 in *Proceedings of the Second International Conference on Vibrations at Surfaces,* Plenum Press, New York, 1981.

C. W. White, B. R. Appleton, B. Stritzker, D. M. Zehner, and S. R. Wilson, "Kinetic Effects and Mechanisms Limiting Substitutional Solubility in the Formation of Supersaturated Alloys by Pulsed-Laser Annealing," p. 59 in *Laser and Electron-Beam Solid Interactions and Materials Processing,* ed. by J. F. Gibbons, L. D. Hess, and T. W. Sigmon, North Holland, New York, 1981.

C. W. White, S. R. Wilson, B. R. Appleton, and J. Narayan, "Surface Segregation in Laser Annealing of Ion-Implanted Silicon," p. 124 in *Laser and Electron Beam Processing of Materials,* ed. by C. W. White and P. S. Peercy, Academic Press, New York, 1980.

C. W. White, S. R. Wilson, B. R. Appleton, F. W. Young, Jr., and J. Narayan, "Supersaturated Substitutional Alloys in Silicon Formed by Ion Implantation and Laser Annealing," p. 111 in *Laser and Electron Beam Processing of Materials,* ed. by C. W. White and P. S. Peercy, Academic Press, New York, 1980.

R. F. Wood, D. H. Lowndes, and W. H. Christie, "Pulsed-Laser Annealing of Ion-Implanted GaAs: Theory and Experiment," p. 231 in *Laser and Electron-Beam Solid Interactions and Materials Processing,* Vol. 1, ed. by J. F. Gibbons, L. D. Hess, and T. W. Sigmon, North Holland, New York, 1981.

R. F. Wood, J. C. Wang, G. E. Giles, and J. R. Kirkpatrick, "Macroscopic Theory of Pulsed-Laser Annealing," p. 37 in *Laser and Electron Beam Processing of Materials,* ed. by C. W. White and P. S. Peercy, Academic Press, New York, 1980.

R. F. Wood and R. T. Young, "Laser Processing for High-Efficiency Silicon Solar Cells," p. 688 in *Fourteenth IEEE Photovoltaic Specialists Conference-1980,* IEEE 80CH1508-1, New York, 1980.

R. T. Young, "Laser Techniques in Photovoltaic Application," p. 10 in *Proceedings of the First Republic of China Solar Cell Workshop,* Industrial Technology Research Institute, Taipei, Taiwan, 1980.

R. T. Young, G. E. Jellison, Jr., Y. K. Chang, M. C. Lu, and G. A. van der Leeden, "Effect of Lithium Diffusion Into Polycrystalline Si Solar Cells," p. 1316 in *Fifteenth IEEE Photovoltaic Specialists Conference-1981,* IEEE 81CH1644-4, New York, 1981.

R. T. Young and R. F. Wood, "Solar Cells from Ion-Implanted, Laser-Annealed Cast Polycrystalline Silicon," p. 214 in *Fourteenth IEEE Photovoltaic Specialists Conference-1980,* IEEE 80CH1508-1, New York, 1980.

R. T. Young, R. F. Wood, G. E. Jellison, Jr., and W. H. Christie, "Laser Processing for High Efficiency Solar Cells," p. 703 in *Third E. C. Photovoltaic Solar Energy Conference,* Reidel, Boston, Massachusetts, 1981.

R. T. Young, R. F. Wood, J. Narayan, and C. W. White, "Laser Processing of Polycrystalline Silicon Solar Cells," p. 651 in *Laser and Electron Beam Processing of Materials,* ed. by C. W. White and P. S. Peercy, Academic Press, New York, 1980.

R. T. Young, R. F. Wood, R. D. Westbrook, J. Narayan, and C. W. White, "Laser Techniques in Photovoltaic Research," p. 105 in *Proceedings of the Third High Efficiency and Radiation Damage Solar Cell Meeting,* NASA Conference Publication 2097, NASA-Lewis Research Center, Cleveland, Ohio, 1979.

D. M. Zehner, J. R. Noonan, H. L. Davis, C. W. White, and G. W. Ownby, "A LEED Investigation of (111) Oriented Si, Ge, and GaAs Surfaces Following Pulsed-Laser Irradiation," p. 111 in *Laser and Electron-Beam Solid Interactions and Materials Processing,* ed. by J. F. Gibbons, L. D. Hess, and T. W. Sigmon, North Holland, New York, 1981.

D. M. Zehner, C. W. White, and G. W. Ownby, "Silicon Surface Structure and Surface Impurities After Pulsed-Laser Annealing," p. 201 in *Laser and Electron Beam Processing of Materials,* ed. by C. W. White and P. S. Peercy, Academic Press, New York, 1980.

REPORTS ISSUED

W. S. Aaron, T. C. Quinby, E. H. Kobisk, and D. K. Thomas, *High Level Waste Program Progress Report for October 1, 1979, through December 31, 1979,* ORNL/TM-7253 (March 1980).

W. S. Aaron, T. C. Quinby, E. H. Kobisk, and D. K. Thomas, *High Level Waste Program Progress Report for January 1, 1980, through March 31, 1980,* ORNL/TM-7371 (May 1980).

W. S. Aaron, T. C. Quinby, E. H. Kobisk, D. W. Ramey, M. Petek, and D. K. Thomas, *High Level Waste Program Progress Report for April 1, 1980, through June 30, 1980,* ORNL/TM-7476 (August 1980).

W. S. Aaron, T. C. Quinby, E. H. Kobisk, D. W. Ramey, M. Petek, and D. K. Thomas, *High Level Waste Program Progress Report for July 1, 1980, through September 30, 1980,* ORNL/NFW-80/23 (October 1980).

E. H. Kobisk, T. C. Quinby, and W. S. Aaron, *Final Report on Cermet High-Level Waste Forms,* ORNL-5760 (August 1981).

R. F. Wood, D. H. Lowndes, and R. T. Young, *Applications of Laser Annealing and Laser-Induced Diffusion to Photovoltaic Conversion, Quarterly Progress Report No. 1, for the Period March 1–May 31, 1980,* ORNL/TM-7442 (July 1980).

R. F. Wood, D. H. Lowndes, and R. T. Young, *Applications of Laser Annealing and Laser-Induced Diffusion to Photovoltaic Conversion, Quarterly Progress Report No. 2, for the Period June 1–August 31, 1980,* ORNL/TM-7669 (January 1981).

R. F. Wood, D. H. Lowndes, and R. T. Young, *Applications of Laser Annealing and Laser-Induced Diffusion to Photovoltaic Conversion, Quarterly Progress Report No. 3, for the Period September 1–November 30, 1980,* ORNL/TM-7735 (March 1981).

THESES

O. W. Holland, "A Collisional Mechanism in the Ion-Solid Interaction Which Enhances Scattering Yields Near 180°," thesis submitted to the Graduate Council of North Texas State University in partial fulfillment of the requirements for the Ph.D. degree, November 1980.

PATENTS GRANTED

M. M. Abraham, Yok Chen, and Robert Kernohan, *Wide-Band-Gap, Alkaline-Earth-Oxide Semiconductor and Devices Utilizing Same,* U.S. Patent No. 4,264,914 (April 28, 1981).

J. Narayan, *Laser Method for Forming Low-Resistance Ohmic Contacts on Semiconducting Oxides,* U.S. Patent No. 4,261,764 (April 14, 1981).

PAPERS PRESENTED AT TECHNICAL MEETINGS

Indo-U.S. Conference on Science and Technology of Rare Earth Materials, Cochin, Kerala, March 3–8, 1980:

S. H. Liu, "Electronic Structure of Rare Earth Systems" (invited paper)

Third APS Topical Conference on High Temperature Plasma Diagnostics, Los Angeles, California, March 17–19, 1980:

J. B. Roberto, "Plasma Impurity Studies by Laser Fluorescence Copy" [*Bull. Am. Phys. Soc.* **25,** 688 (1980)] (invited paper)

International Conference on Single Electron Potentials in Solids, Yorktown Heights, New York, March 20–22, 1980:

M. Rasolt, "Non-Local Potential in Metals" (invited paper)

American Physical Society Meeting, New York, New York, March 24–28, 1980:

J. H. Barrett, "Mechanism for Enhanced Ion Backscattering Near 180°" [*Bull. Am. Phys. Soc.* **25,** 180 (1980)]

J. B. Bates, Roger Frech, Herbert Engstrom, J. C. Wang, and T. Kaneda, "Hydration of $Na_{1-x}Li_x$ Beta- and Beta″-Aluminas" [*Bull. Am. Phys. Soc.* **25,** 435 (1980)]

L. A. Boatner, G. W. Beall, M. M. Abraham, C. B. Finch, P. G. Huray, and M. Rappaz, "The Growth and Characterization of Actinide-Doped Lanthanide Orthophosphate Single Crystals" [*Bull. Am. Phys. Soc.* **25,** 186 (1980)]

G. M. Brown, J. B. Bates, and W. E. Brundage, "Structural Studies of K- and Ag-Beta″-Aluminas" [*Bull. Am. Phys. Soc.* **25,** 435 (1980)]

J. W. Cable, N. Wakabayashi, and R. M. Nicklow, "Temperature Dependence of the Magnetic Excitations in Gadolinium" [*Bull. Am. Phys. Soc.* **25,** 345 (1980)]

Y. Chen, N. Dudney, and V. M. Orera, "Subthreshold [Li]° Formation Induced by Mechanically Deformed Surfaces in MgO" [*Bull. Am. Phys. Soc.* **25,** 215 (1980)]

D. K. Christen, "Properties of the Flux-Line Lattice in Single-Crystal Niobium" [*Bull. Am. Phys. Soc.* **25,** 385 (1980)] (invited paper)

J. W. Cleland and N. Fukuoka, "Electrical Property Studies of Oxygen in Czochralski-Grown Neutron-Transmutation-Doped Silicon" [*Bull. Am. Phys. Soc.* **25,** 203 (1980)]

J. F. Cooke, "Temperature-Dependent Dynamic Susceptibility Calculations for Ferromagnetic Nickel" [*Bull. Am. Phys. Soc.* **25,** 183 (1980)]

R. J. Culbertson, L. C. Feldman, and P. J. Silverman, "Si(111) Surface Structure Using MeV Ion Scattering" [*Bull. Am. Phys. Soc.* **25,** 427 (1980)]

H. L. Davis and J. R. Noonan, "Structural Conclusion vs Nonstructural Parameters in LEED Analyses for Cu(100)" [*Bull. Am. Phys. Soc.* **25,** 328 (1980)]

Herbert Engstrom, J. B. Bates, L. A. Boatner, and J. C. Wang, "Infrared Spectra of Hydrogen Isotopes in Aluminum Oxide and Potassium Tantalate" [*Bull. Am. Phys. Soc.* **25,** 215 (1980)]

J. R. Gavaler, A. I. Braginski, M. Ashkin, B. R. Appleton, and C. W. White, "The Effect of Laser Annealing on Some High T_c A15 and B1 Superconducting Compounds" [*Bull. Am. Phys. Soc.* **25,** 332 (1980)]

K.-M. Ho, B. N. Harmon, and S. H. Liu, "Self-Consistent Calculation of the Electronic Structure of the Ag(110) Surface" [*Bull. Am. Phys. Soc.* **25,** 235 (1980)]

G. E. Jellison, Jr., and J. W. Cleland, "DLTS Studies of Oxygen-Cluster-Doped and Phosphorus-Doped Silicon Irradiated with 1.5 MeV Electrons" [*Bull. Am. Phys. Soc.* **25,** 291 (1980)]

L. H. Jenkins, M. Rasolt, and H. L. Davis, "Influences of Collective Excitations in Electron Spectroscopies" [*Bull. Am. Phys. Soc.* **25,** 237 (1980)]

W. A. Kamitakahara, D. Khatamian, D. T. Peterson, and H. A. Mook, "Neutron Scattering Study Hydrogen Diffusion in Thorium" [*Bull. Am. Phys. Soc.* **25,** 180 (1980)]

Theodore Kaplan, P. L. Leath, and L. J. Gray, "Self-Consistent Cluster Theory for Alloys with Off-Diagonal Disorder" [*Bull. Am. Phys. Soc.* **25,** 261 (1980)]

H. R. Kerchner and S. T. Sekula, "The Statistical Summation of Flux-Line Pins in the Weak-Pinning Limit" [*Bull. Am. Phys. Soc.* **25,** 413 (1980)]

C. E. Klabunde, J. M. Williams, and R. R. Coltman, Jr., "Fission Neutron Damage Production Efficiencies in Metals" [*Bull. Am. Phys. Soc.* **25,** 275 (1980)]

B. C. Larson and J. F. Barhorst, "Vacancy and Interstitial Loop Size Distributions in Irradiated Copper" [*Bull. Am. Phys. Soc.* **25,** 275 (1980)]

C.-K. Loong, C. Stassis, O. D. McMasters, and R. M. Nicklow, "Lattice Dynamics of $CeSn_3$" [*Bull. Am. Phys. Soc.* **25,** 343 (1980)]

H. A. Mook, "Lattice Dynamics of the Intermediate Valence Compound $Sm_{0.75}Y_{0.25}S$" [*Bull. Am. Phys. Soc.* **25,** 180 (1980)] (invited paper)

J. Narayan and Y. Chen, "Diffusion of Lithium Ions in Crystalline Magnesium Oxide" [*Bull. Am. Phys. Soc.* **25,** 216 (1980)]

J. Narayan, C. W. White, and B. R. Appleton, "Cell Formation in Ion-Implanted, Laser-Annealed Silicon" [*Bull. Am. Phys. Soc.* **25,** 203 (1980)]

R. M. Nicklow, "Neutron Scattering from Coupled Phonon-Complex Impurity Modes" [*Bull. Am. Phys. Soc.* **25,** 286 (1980)] (invited paper)

J. R. Noonan and H. L. Davis, "Normal Incidence LEED Analysis of the Clean Ag(110) Surface" [*Bull. Am. Phys. Soc.* **25,** 327 (1980)]

S. M. Ohr, "Electron Microscope Studies of Fracture" [*Bull. Am. Phys. Soc.* **25,** 371 (1980)] (invited paper)

S. H. Overbury, W. Heiland, D. M. Zehner, and S. Datz, "Angularly Resolved Low Energy K^+ Backscattering Spectra from the Reordered Au(110) Surface" [*Bull. Am. Phys. Soc.* **25,** 427 (1980)]

F. Perrot, L. M. Kahn, and M. Rasolt, "Heat of Solution of Hydrogen in Aluminum" [*Bull. Am. Phys. Soc.* **25,** 246 (1980)]

D. T. Pierce, R. J. Celotta, G.-C. Wang, and E. G. McRae, "Polarized Low-Energy Electron Diffraction Study of the Mechanism of Electron Reflection from W(100)" [*Bull. Am. Phys. Soc.* **25,** 328 (1980)]

J. Pinter, R. Vogel, C. Wood, J. Woosley, E. Sonder, and R. A. Weeks, "Thermoelectric Power Measurements on High Resistivity Materials" [*Bull. Am. Phys. Soc.* **25,** 438 (1980)]

D. B. Poker, B. R. Appleton, T. S. Noggle, and O. S. Oen, "Damage Production Rates of Ni Ions in Ni, Cu, and an Fe-Cr Alloy" [*Bull. Am. Phys. Soc.* **25,** 178 (1980)]

R. L. Prater, L. L. Chase, and L. A. Boatner, "Raman Scattering and Optical Depolarization Study of Ferroelectric Transitions Induced by Nb and Li in $KTaO_3$" [*Bull. Am. Phys. Soc.* **25,** 171 (1980)]

M. Rappaz, M. M. Abraham, J. O. Ramey, and L. A. Boatner, "EPR Investigations of Gd^{3+} in Monoclinic Lanthanide Orthophosphates" [*Bull. Am. Phys. Soc.* **25,** 244 (1980)]

M. Rasolt, G. Malmstrom, and D. J. W. Geldart, "Wave Vector Decomposition of the Exchange and Correlation Contributions to a Metallic Surface Energy" [*Bull. Am. Phys. Soc.* **25,** 292 (1980)]

J. M. Schultz, J. S. Lin, R. W. Hendricks, J. Petermann, and R. M. Gohil, "Annealing of Polypropylene Films Crystallized from a Highly Extended Melt" [*Bull. Am. Phys. Soc.* **25,** 351 (1980)]

H. G. Smith, N. Wakabayashi, Y. K. Chang, D. Lowndes, G. W. Webb, Z. Fisk, F. M. Mueller, and A. Arko, "Phonon Spectra in A15 Superconducting Compounds" [*Bull. Am. Phys. Soc.* **25,** 332 (1980)]

E. Sonder, J. E. Gastineau, and R. A. Weeks, "Distribution of Fe^{3+} Impurity in MgO Quenched from High Temperature" [*Bull. Am. Phys. Soc.* **25,** 215 (1980)]

C. Stassis, D. Arch, O. D. McMasters, and N. Wakabayashi, "Lattice Dynamics of hcp Hafnium" [*Bull. Am. Phys. Soc.* **25,** 417 (1980)]

Martin Ůlehla, "Gauge Fields and the Nature of the Ordered State" [*Bull. Am. Phys. Soc.* **25,** 277 (1980)]

J. R. Thompson and S. T. Sekula, "Low-Temperature Ion Implantation in Al" [*Bull. Am. Phys. Soc.* **25,** 433 (1980)]

N. Wakabayashi, "Charge Fluctuation Model of Phonons in Sm(Y)S" [*Bull. Am. Phys. Soc.* **25,** 343 (1980)]

G.-C. Wang, R. J. Celotta, and D. T. Pierce, "A Constant Momentum Transfer Average Study of PLEED from W(100)" [*Bull. Am. Phys. Soc.* **25,** 328 (1980)]

J. C. Wang, "On the Charge Compensation Problem in β-Alumina" [*Bull. Am. Phys. Soc.* **25,** 435 (1980)]

C. W. White, "Pulsed-Laser Annealing of Semiconductors" [*Bull. Am. Phys. Soc.* **25,** 225 (1980)] (invited paper)

R. F. Wood, "Model for Nonequilibrium Segregation during Pulsed-Laser Annealing" [*Bull. Am. Phys. Soc.* **25,** 312 (1980)]

D. M. Zehner, C. W. White, and G. W. Ownby, "LEED, AES Investigations of Semiconductor Surfaces Following Pulsed-Laser Annealing" [*Bull. Am. Phys. Soc.* **25,** 328 (1980)]

BES/DMS Workshop on Coal Structure and Related Properties, Gatlinburg, Tennessee, April 8–10, 1980:

J. S. Lin, "Research Techniques Applicable to Coal Studies: Small-Angle X-ray Scattering" (invited paper)

Fourth International Conference on Plasma-Surface Interactions in Controlled Fusion Devices, Garmisch-Partenkirchen, Federal Republic of Germany, April 21–25, 1980:

J. B. Roberto, R. A. Zuhr, and S. P. Withrow, "Surface Erosion in the Plasma Edge of ISX-B"

B. Schweer, D. Rusbuldt, E. Hintz, J. B. Roberto, and W. R. Husinsky, "Measurement of the Density and Velocity Distribution of Neutral Fe in ISX-B by Laser Fluorescence Spectroscopy"

R. A. Zuhr, S. P. Withrow, and J. B. Roberto, "Deuterium and Impurity Deposition Profiles in the Plasma Edge of ISX-B"

American Ceramic Society Eighty-Second Annual Meeting and Exposition, Chicago, Illinois, April 27–30, 1980:

W. S. Aaron, T. C. Quinby, E. H. Kobisk, and D. K. Thomas, "Radioactive Waste Isolation Using Cermets" [*Am. Ceram. Soc. Bull.* **59,** 392 (1980)]

M. M. Abraham, L. A. Boatner, T. C. Quinby, D. K. Thomas, and M. Rappaz, "Preparation and Compaction of Synthetic Monazite Powders" [*Am. Ceram. Soc. Bull.* **59,** 397 (1980)]

Y. Chen, N. Dudney, and V. M. Orera, "Effect of Mechanically Deformed Surfaces on [Li]° Colorization in Crystalline MgO" [*Am. Ceram. Soc. Bull.* **59,** 357 (1980)]

N. J. Dudney and R. L. Coble, "Galvanic Cell Measurements with Ionic Probes" [*Am. Ceram. So Bull.* **59,** 350 (1980)]

P. Moulton, A. Mooradian, Y. Chen, and M. M. Abraham, "A High-Power Tunable Laser Using MgO:Ni Crystal" [*Am. Ceram. Soc. Bull.* **59,** 350 (1980)]

R. A. Weeks, E. Sonder, and J. Narayan, "The Effect of Electric Fields and Field Reversal on Some Electrical Properties of MgO Single Crystals" [*Am. Ceram. Soc. Bull.* **59,** 350 (1980)]

American Nuclear Society Meeting on Tritium Technology in Fission, Fusion, and Isotopic Applications, Dayton, Ohio, April 29–May 1, 1980:

M. Petek, D. W. Ramey, R. D. Taylor, and E. H. Kobisk, "Tritium Separation from Light and Heavy Water by Bipolar Electrolysis"

1980 Spring Meeting of the Electrochemical Society, St. Louis, Missouri, May 11–16, 1980:

G. A. van der Leeden, R. M. Davis, and C. T. Chang, "The Recrystallization of Silicon on Graphite"

Workshop on Alternate Nuclear Waste Forms and Interactions in Geologic Media, Gatlinburg, Tennessee, May 13–15, 1980:

M. M. Abraham, L. A. Boatner, G. W. Beall, C. B. Finch, R. J. Floran, P. G. Huray, and M. Rappaz, "A Review of Research on Analogs of Monazite for the Isolation of Actinide Wastes" (invited paper)

R. J. Floran, M. Rappaz, M. M. Abraham, and L. A. Boatner, "Hot and Cold Pressing of $LaPO_4$-Based High-Level Waste Forms"

E. H. Kobisk, W. S. Aaron, T. C. Quinby, and D. W. Ramey, "High Level Waste Fixation in Cermet Form"

M. Rappaz, L. A. Boatner, and M. M. Abraham, "The Application of EPR Spectroscopy to the Characterization of Crystalline Nuclear Waste Forms"

Thin Film GaAs Solar Cell SERI Contractors' Review Meeting, Alexandria, Virginia, May 22–23, 1980:

Douglas H. Lowndes, Rosa T. Young, and Richard F. Wood, "Applications of Laser Annealing and Laser-Induced Diffusion to Photovoltaic Conversion"

International Conference on Ordering in Two Dimensions, Lake Geneva, Wisconsin, May 28–30, 1980:

Martin Úlehla, "Gauge Fields and Order"

Twenty-Fifth Annual Meeting of the American Section of the International Solar Energy Society, Phoenix, Arizona, June 2–6, 1980:

R. T. Young, G. E. Jellison, Jr., C. W. White, R. D. Westbrook, and A. Gat, "Comparison Between Pulsed- and cw Laser Annealing for Solar Cell Fabrication"

International Symposium on the Management of Alpha-Contaminated Wastes, Vienna, Austria, June 2–6, 1980:

L. A. Boatner, G. W. Beall, M. M. Abraham, C. B. Finch, R. J. Floran, P. G. Huray, and M. Rappaz, "Lanthanide Orthophosphates for the Primary Immobilization of Actinide Wastes"

Workshop on Plasma Edge Experiments and Modeling, Los Angeles, California, June 4–5, 1980:

J. B. Roberto, "Plasma Edge Experiments in ISX-B" (invited paper)

Tenth International Symposium on Effects of Radiation on Materials, Savannah, Georgia, June 3–5, 1980:

J. A. Horton and W. A. Jesser, "Coarse Slip Processes and Crack Propagation in Irradiated Stainless Steel"

First Republic of China Solar Cell Workshop, Taipei, Taiwan, June 5–6, 1980:

R. T. Young, "Laser Techniques in Photovoltaic Application" (invited paper)

American Nuclear Society Annual Meeting, Las Vegas, Nevada, June 8–12, 1980:

T. J. Hoffman, M. T. Robinson, H. L. Dodds, Jr., and D. K. Holmes, "Ion Penetration Distance Calculations with Multigroup Transport Computer Codes"

Polycrystalline Silicon Contractors' Review Meeting, Washington, D.C., June 11–13, 1980:

Rosa T. Young, Douglas H. Lowndes, and Richard F. Wood, "Applications of Laser Annealing and Laser-Induced Diffusion to Photovoltaic Conversion"

Fortieth Physical Electronics Conference, Ithaca, New York, June 16–18, 1980:

R. J. Culbertson, L. C. Feldman, and P. J. Silverman, "Si(111) Surface Structure Studies Using High Energy Ion Scattering"

Conference on Determination of Surface Structure by LEED, Yorktown Heights, New York, June 19–20, 1980:

H. L. Davis and J. R. Noonan, "Sensitivity of Structural Conclusions in LEED Analysis to Variation of Nonstructural Parameters"

J. R. Noonan and H. L. Davis, "Reliability of Contemporary Data Acquisition Techniques for LEED Analyses"

D. T. Pierce, R. J. Celotta, and G.-C. Wang, "What Can PLEED Contribute to Surface Structure Determinations"

International Conference on Dislocation Modeling of Physical Systems, Gainesville, Florida, June 22–27, 1980:

S.-J. Chang and S. M. Ohr, "A Model of BCS Cracks with a Dislocation-Free Zone"

Gordon Conference on Polymer Physics, New Hampton, Connecticut, June 23–27, 1980:

G. D. Wignall, "Recent Studies of Chain Conformation in Crystalline and Amorphous Polymers by SANS" (invited paper)

Gordon Research Conference on Diffusion in Solids, Andover, New Hampshire, July 7–11, 1980:

N. J. Dudney, J. B. Bates, G. M. Brown, J. C. Wang, B. C. Larson, and H. L. Engstrom, "Intercalation of Water in Lithium-Sodium Beta-Alumina"

Twelfth International Glass Congress, Albuquerque, New Mexico, July 9–12, 1980:

R. A. Weeks, M. Nasrallah, S. Arafa, and A. Bishay, "Studies of Fusion Processes of Natural Glasses by Electron Magnetic Resonance Spectroscopy"

AIAA Fifteenth Thermophysics Conference, Snowmass, Colorado, July 14–16, 1980:

J. R. Kirkpatrick, G. E. Giles, Jr., and R. F. Wood, "Numerical Methods for the Analysis of Laser Annealing of Doped Semiconductor Wafers"

IBMM-80 International Conference on Ion-Beam Modification of Materials, Albany, New York, July 14–18, 1980:

B. R. Appleton, E. J. Kelly, C. W. White, N. G. Thompson, and B. D. Lichter, "Corrosion Mechanisms Associated with Ti Surfaces Modified by Pt^+ Implantation"

S. S. Lau, B. Y. Tsaur, M. von Allmen, J. W. Mayer, B. Stritzker, C. W. White, and B. R. Appleton, "Ion-Beam Mixing of Metal-Semiconductor Eutectic Systems"

S. T. Sekula and J. R. Thompson, "Low-Temperature H-Ion Implantation in Aluminum"

Second Solid State Symposium on Electron Microscopy and Electron Paramagnetic Resonance, Galindo, Queretaro, Mexico, July 15–18, 1980:

M. M. Abraham, "Review of EPR Research on Analogs of Monazite for the Isolation of Actinide Waste" (invited paper)

L. A. Boatner, "A Review of Electron Paramagnetic Resonance Investigations of the Jahn-Teller Effect" (invited paper)

International Conference on Frontiers of Glass Science, Los Angeles, California, July 16–18, 1980:

R. A. Weeks, R. Magruder, and D. Kinser, "The Effect of OH on UV Optical Absorption of Reduced GeO_2 Glasses"

19th National Heat Transfer Conference of the American Society of Mechanical Engineers, Orlando, Florida, July 17–30, 1980:

G. E. Giles, J. R. Kirkpatrick, and R. F. Wood, "Laser Annealing of Solar Cell Wafers"

Gordon Research Conference on Particle-Solid Interactions, Andover, New Hampshire, July 21–25, 1980:

John H. Barrett, "Enhanced Backscattering near 180°" (invited paper)

R. J. Culbertson, "The Ni-Si(111) Interface" (invited paper)

O. S. Oen, "The Two-Atom Model in Ion Reversibility Studies"

M. T. Robinson, "Computer Simulation in the Binary Collision Approximation" (invited paper)

NATO Advanced Study Institute on Scattering Techniques Applied to Supra-Molecular and Nonequilibrium Systems, Wellesly, Massachusetts, August 3–15, 1980:

W. C. Koehler, R. W. Hendricks, H. R. Child, S. P. King, J. S. Lin, and G. D. Wignall, "The National Center for Small-Angle Scattering Research"

J. S. Lin, W. C. Koehler, R. W. Hendricks, and G. D. Wignall, "Research Applications of Small-Angle X-ray and Neutron Scattering"

American Crystallographic Association Summer Meeting, Calgary, Alberta, Canada, August 17–22, 1980:

J. E. Epperson, J. Faber, R. W. Hendricks, and J. S. Lin, "On the Decomposition and Ripening of a Ni-12.7 at. % Al Alloy"

American Chemical Society Symposium on Regional and National Facilities in Chemistry, Las Vegas, Nevada, August 24–29, 1980:

W. C. Koehler and R. W. Hendricks, "The National Center for Small-Angle Scattering Research"

Australian Physical Society Meeting, Melbourne, Australia, August 25–29, 1980:

H. G. Smith, "Phonons, Lattice Instabilities, and Superconductivity" (invited paper)

Third International Conference on Neutron-Transmutation-Doped Silicon, Frederikssund, Denmark, August 27–29, 1980:

J. W. Cleland and N. Fukuoka, "Electrical Property Studies of Oxygen in Czochralski-Grown Neutron-Transmutation-Doped Silicon"

Noboru Fukuoka and J. W. Cleland, "Optical Studies of Radiation Damage in Neutron-Transmutation-Doped Silicon"

Second International Conference on Vibrations at Surfaces, Namur, Belgium, September 10–12, 1980:

J. F. Wendelken, "The Adsorption and Co-Adsorption with CO of NO on Cu(110) Studied with ELS and LEED"

Joint U.S.-France Symposium on Small-Angle Neutron and X-ray Scattering, Strasbourg, France, September 16–19, 1980:

D. W. Schaefer, R. W. Hendricks, and J. S. Lin, "Static Correlations in Semidilute Solutions: Marginal Solvents"

G. D. Wignall, R. W. Hendricks, and W. C. Koehler, "Current Instrumentation Developments and Polymer Research at the United States National Center for Small-Angle Scattering Research" (invited paper)

Fourth International Conference on Solid Surfaces and the Third European Conference on Surface Science, Cannes, France, September 22–26, 1980:

R. J. Celotta, D. T. Pierce, G.-C. Wang, S. D. Bader, and G. P. Felcher, "Surface Magnetism in Ni(110) as Studied by Polarized Electron Scattering"

J. R. Noonan and H. L. Davis, "High Sensitivity LEED Analysis for Clean Metallic Surfaces"

D. T. Pierce, R. J. Celotta, and G.-C. Wang, "Spin-Polarized Electron Scattering Studies of W(100)"

Summer School on Neutron Scattering from Macromolecules, Kent, England, September 22–26, 1980:

G. D. Wignall, R. W. Hendricks, W. C. Koehler, and J. S. Lin, "The National Center for Small-Angle Scattering Research at Oak Ridge" (invited paper)

International Conference on Ternary Superconductors, Lake Geneva, Wisconsin, September 24–26, 1980:

H. A. Mook, M. B. Maple, Z. Fisk, D. C. Johnston, and L. D. Woolf, "Neutron Scattering Studies of the Magnetic Transitions in the Ternary Alloy System $Er_{1-x}Ho_xRh_4B_4$"

Conference of the Metallurgical Society of AIME, Pittsburgh, Pennsylvania, October 5–9, 1980:

J. W. Cable, "Atomic and Magnetic Moment Distributions in Transition Metal Alloys" (invited paper)

158th Meeting of the Electrochemical Society, Hollywood, Florida, October 5–10, 1980:

H. F. Bittner, J. T. Bell, C. W. White, and W. H. Christie, "Steam Oxidation of Laser-Annealed Incoloy 800"

Y. Chen and M. M. Abraham, "Thermochemically Induced Semiconductivity of Li-Doped MgO Crys tals"

J. W. Cleland and N. Fukuoka, "Annealing Studies of Czochralski-Grown Neutron-Transmutation-Doped Silicon"

J. Narayan, "Ion Implantation Damage and Its Annealing Behavior" (invited paper)

J. Narayan, J. Fletcher, and R. T. Young, "Laser Annealing of Dislocation Loops and Dislocations in Ion-Implanted and Thermally Annealed Silicon"

J. Narayan, J. Fletcher, and R. T. Young, "Laser Annealing of Residual Damage in Ion-Implanted, Thermally Annealed Silicon"

E. Sonder, J. Gastineau, T. G. Stratton, and R. A. Weeks, "The Use of Electron Resonance in the Study of Valence Changes and Impurity Aggregation in Dilute MgO:Fe"

R. D. Westbrook and R. T. Young, "Laser-Annealed Gaseous Discharge Implanted Silicon"

C. W. White, "Laser Annealing of Ion-Implanted Silicon" (invited paper)

S. R. Wilson, C. W. White, B. R. Appleton. J. Fletcher, and J. Narayan, "Thermal Annealing ^{75}As-Implanted <111> Si"

D. M. Zehner, C. W. White, and G. W. Ownby, "Investigation of Surfaces of Laser-Annealed Si Implanted with Fe or Cu"

Fifth International Conference on Small-Angle Scattering, Berlin, Federal Republic of Germany, October 6–10, 1980:

W. C. Koehler and R. W. Hendricks, "The United States National Center for Small-Angle Scattering Research"

P. LaBarbe, A. C. Wright, J. S. Lin, R. W. Hendricks, and J. Zarzycki, "SAXS and SANS Studies of Silica Glasses Prepared by Hot Pressing of Silica Gel"

S. M. Shapiro, C. R. Fincher, Jr., W. C. Koehler, and H. R. Child, "Inelastic and Elastic Small-Angle Neutron Scattering Studies of the Ferromagnetic-Spin Glass Alloy Fe_xCr_{1-x}"

Conference on Growth and Characterization of Crystalline Solids, Cairo, Egypt, October 11–12, 1980:

R. A. Weeks and E. Sonder, "Distribution of Iron Impurity in MgO Single Crystals" (invited paper)

1980 World Conference of the International Nuclear Target Development Society, Gatlinburg, Tennessee, October 13–16, 1980:

H. L. Adair, E. H. Kobisk, and B. L. Byrum, "Tritium Target Fabrication for the Rotating Target Neutron Source"

T. C. Quinby, "Thin Metal Encapsulation of Fission Foils and Oxide Discs by Resistance Welding"

R. D. Taylor, "Preparation of High Purity Beryllium Foils"

Twenty-Seventh National Vacuum Symposium, American Vacuum Society, Detroit, Michigan, October 14–17, 1980:

Y. J. Chabal, R. J. Culbertson, L. C. Feldman, and J. E. Rowe, "Si(111):Ni Surface Studies by Auger, Photoemission, LEED, and Ion Scattering"

R. J. Culbertson, L. C. Feldman, and R. J. Silverman, "Si(111)-(7×7) Surface Structure Using Ion Scattering"

W. R. Husinsky, "Impurity Studies in Fusion Devices Using Laser Fluorescence Spectroscopy" (invited paper)

G.-C. Wang, D. T. Pierce, and R. J. Celotta, "Study of Temperature and Hydrogen Induced Reconstruction and Reordering of W(100) by Polarized Electron Scattering"

D. M. Zehner, J. R. Noonan, H. L. Davis, and C. W. White, "The Atomic Structure of Laser-Annealed Si(111)-(1×1)"

Fourth High Efficiency and Radiation Damage Solar Cell Conference, Cleveland, Ohio, October 15–17, 1980:

G. E. Jellison, Jr., R. T. Young, R. F. Wood, and A. Gat, "A Comparison Between Pulsed- and cw Laser Annealing for Solar Cell Applications"

Midwest Section Meeting of the American Physical Society, Dayton, Ohio, October 17–18, 1980:

C. W. White, "Laser Annealing of Semiconductors" (invited paper)

Midwest Solid State Theory Symposium, Bloomington, Indiana, October 27–28, 1980:

S. H. Liu, "Contribution of Surface States to the Electroreflectance of Ag(110) Surface" (invited paper)

1980 Photovoltaic Solar Energy Conference, Cannes, France, October 27–31, 1980:

R. T. Young, R. F. Wood, G. E. Jellison, Jr., and W. H. Christie, "Laser Processing for High Efficiency Solar Cells"

First Annual Symposium and Equipment Exhibit, American Vacuum Society, Knoxville, Tennessee, October 28–30, 1980:

B. R. Appleton, "The Use of High Energy Ion Beams for Analysis of Surfaces and Solids" (invited paper)

J. B. Roberto, "Laser Spectroscopy of Neutral Particles in Fusion Research" (invited paper)

D. M. Zehner, "Surface Studies of Laser-Annealed Semiconductors" (invited paper)

Workshop on Artificial Superlattices, Urbana, Illinois, October 30–31, 1980:

G. P. Felcher and J. W. Cable, "Neutron Diffraction Investigation of Layered Coherent Structures"

Twentieth Science Week, Damascus, Syria, November 1–6, 1980:

R. A. Weeks, "Electron States of Glasses Used for Optical Waveguides" (invited paper)

R. A. Weeks, "Properties of Glasses for Use as Optical Waveguides" (invited paper)

Sixth Conference on the Applications of Accelerators in Research and Industry, Denton, Texas, November 3–5, 1980:

D. D. Allred, D. C. Booth, B. R. Appleton, P. D. Miller, C. D. Moak, J. P. F. Sellschop, C. W. White, and A. L. Wintenberg, "The Hydrogen Content of Multicomponent Amorphous Silicon Alloys by ^{19}F Nuclear Reaction Analysis"

O. W. Holland, B. R. Appleton, and J. H. Barrett, "Enhanced Backscattering Near 180° for Energetic Ions in Solids" (invited paper)

C. W. White, "Laser Annealing of Ion-Implanted Semiconductors" (invited paper)

Southeastern Section Meeting, American Physical Society, Chapel Hill, North Carolina, November 6–8 1980:

B. R. Appleton, "Ion Beam Analysis Techniques in Materials Research" (invited paper)

R. R. Coltman, Jr., and C. E. Klabunde, "The Resistance of Fusion Reactor Magnet Materials to Radiation: A Competition for the Role of 'Weakest Link'" [*Bull. Am. Phys. Soc.* **26,** 92 (1981)]

J. Narayan, "Laser Annealing of Semiconductors" (invited paper)

Sixteenth International Thermal Conductivity Conference, Chicago, Illinois, November 7–9, 1980:

C. L. Tsai, A. R. Moodenbaugh, M. Weinstock, and Y. Chen, "Thermal Conductivity of Damaged MgO"

American Physical Society Meeting, San Diego, California, November 10–14, 1980:

W. R. Husinsky, P. W. King, and J. B. Roberto, "Studies of Cr Impurities from a Limiter-Like Probe in ISX-B by Laser Fluorescence Spectroscopy" [*Bull. Am. Phys. Soc.* **25,** 977 (1980)]

J. B. Roberto, R. A. Zuhr, and S. P. Withrow, "Time-Resolved Measurements of Deuterium and Impurity Depositions in the Scrapeoff Layer of ISX-B" [*Bull. Am. Phys. Soc.* **25,** 977 (1980)]

S. P. Withrow, R. A. Zuhr, and J. B. Roberto, "D Fluxes During D To H Changeover in ISX-B" [*Bull. Am. Phys. Soc.* **25,** 977 (1980)]

R. A. Zuhr, R. E. Clausing, L. C. Emerson, L. Heatherly, W. R. Husinsky, P. W. King, R. A. Langley, J. B. Roberto, B. Schweer, J. E. Simpkins, and S. P. Withrow, "Summary of Surface Studies on ISX-B" [*Bull. Am. Phys. Soc.* **25,** 876 (1980)]

Twenty-Sixth Annual Conference on Magnetism and Magnetic Materials, Dallas, Texas, November 11–14, 1980:

J. W. Cable, N. Wakabayashi, and R. M. Nicklow, "Temperature Dependence of the Magnetic Excitations in Gd"

H. R. Child, "Small-Angle Neutron Scattering from Magnetic Correlation in $Fe_{0.7}Al_{0.3}$"

J. F. Cooke, "Temperature Dependent Dynamic Susceptibility Calculations for Itinerant Ferromagnets"

G. E. Fish and H. R. Child, "Studies of Chemical Homogeneity and Magnetic Domain Walls in Fe-Based Metallic Glasses Using Small-Angle Neutron Scattering"

H. A. Mook, "Neutron Scattering Study of the Spin Dynamics of EuO"

R. M. Moon, J. W. Cable, and Y. Shapira, "Neutron Scattering Evidence on Lifshitz Behavior in MnP"

R. M. Nicklow and N. Wakabayashi, "Neutron Scattering Investigations of Magnetic Excitations in Er Metal"

V. C. Rakhecha, G. H. Lander, A. J. Arko, and R. M. Moon, "Induced Magnetization Density in the 5f System UAL_2"

S. A. Werner and J. W. Cable, "Neutron Scattering Experiments on the Magnetism in Cu-Mn Single Crystal"

Materials Research Society Annual Meeting, Boston, Massachusetts, November 16–20, 1980:

M. M. Abraham, L. A. Boatner, and M. Rappaz, "EPR Investigations of Impurities in the Lanthanide Orthophosphates"

B. R. Appleton, "Ion Channeling Techniques for Defect Studies" (invited paper)

B. R. Appleton, B. Stritzker, C. W. White, J. Narayan, J. Fletcher, S. S. Lau, A. I. Braginski, and J. R. Gavaler, "Laser-Induced Materials Alterations in Superconducting Alloys"

L. A. Boatner, M. M. Abraham, and M. Rappaz, "The Characterization of Nuclear Waste Forms by EPR Spectroscopy"

R. J. Culbertson, "Interfacial Structure and Reactivity of Ni on Si(111)" (invited paper)

J. Fletcher, J. Narayan, and D. H. Lowndes, "Analysis of Defects in Laser-Annealed Gallium Arsenide"

R. J. Floran, M. M. Abraham, L. A. Boatner, and M. Rappaz, "Geologic Stability of Monazite and Its Bearing on Immobilization of Actinide Wastes"

G. E. Jellison, Jr., J. W. Cleland, and R. T. Young, "Transient Capacitance Studies of a Low-Lying Electron Trap in n-Type Silicon"

K. L. Kelly, G. W. Beall, J. P. Young, and L. A. Boatner, "Valence States of Actinides in Synthetic Monazites"

B. C. Larson and J. F. Barhorst, "Diffuse X-ray Scattering for the Study of Defect Clusters in Silicon" (invited paper)

Douglas H. Lowndes, J. W. Cleland, W. H. Christie, and R. E. Eby, "Pulsed-Ruby Laser Annealing of Zn, Mg, Se, and Si Ion Implants in Semiconducting GaAs"

J. Narayan and J. Fletcher, "Interface Instability and Cell Formation in Ion-Implanted, Laser-Annealed Silicon"

J. Narayan and J. Fletcher, "Radiation Damage and Its Annealing in Semiconductors" (invited paper)

S. M. Ohr and J. Narayan, "Studies of Fracture and Plastic Deformation in Silicon"

J. B. Roberto, "Low-Energy Hydrogen Interactions at Surfaces" (invited paper)

V. N. Shukla and J. Narayan, "Stability of Laser-Annealed Contacts in Barium Titanate"

C. W. White, B. R. Appleton, B. Stritzker, D. M. Zehner, and S. R. Wilson, "Kinetic Effects and Mechanisms Limiting Substitutional Solubility in the Formation of Supersaturated Alloys by Pulsed-Laser Annealing"

R. F. Wood, D. H. Lowndes, and W. H. Christie, "Pulsed-Laser Annealing of Ion-Implanted GaAs: Theory and Experiment"

D. M. Zehner, J. R. Noonan, H. L. Davis, C. W. White, and G. W. Ownby, "A LEED Investigation of (111) Oriented Si, Ge, and GaAs Surfaces Following Pulsed-Laser Irradiation"

Topical Polycrystalline Silicon Subcontractors' Review Meeting, Colorado Springs, Colorado, November 17, 1930:

R. T. Young and R. F. Wood, "Applications of Laser Annealing and Laser-Induced Diffusion to Photovoltaic Conversion"

1980 International Conference of the American Nuclear Society, Washington, D.C., November 17–21, 1980:

L. A. Boatner, M. M. Abraham, and M. Rappaz, "Analogues of Monazite for the Storage of Radioactive Wastes" (invited paper)

Department of Energy Workshop on Assessment of Insulators for Fusion Reactors, Gaithersburg, Maryland, December 2–3, 1980:

R. R. Coltman, Jr., and C. E. Klabunde, "Magnet Materials Studies in the Solid State Division, ORNL" (invited paper)

Fusion Power Coordinating Committee Meeting, Oak Ridge, Tennessee, December 9–11, 1980:

J. B. Roberto, "Plasma-Materials Interactions" (invited paper)

American Chemical Society Meeting, New Orleans, Louisiana, December 9–13, 1980:

P. G. Huray, S. E. Nave, M. B. Hoyt, J. R. Peterson, L. A. Boatner, M. M. Abraham, and M. Rappaz, "Mössbauer Studies of Actinide Orthophosphates"

G. D. Wignall, "Recent Studies of Chain Conformation in Crystalline and Amorphous Polymers by SANS" (invited paper)

International Conference on Valence Fluctuations in Solids, Santa Barbara, California, December 16–18, 1980:

H. A. Mook and F. Holtzberg, "Lattice Dynamics of the Intermediate Valence Compounds $Sm_{0.75}Y_{0.25}S$ and TmSe" (invited paper)

Gordon Research Conference on Electrochemistry, Ventura, California, January 26–30, 1981:

N. J. Dudney, J. B. Bates, G. M. Brown, J. C. Wang, B. C. Larson, and H. L. Engstrom, "Intercalation of H_2O in Li Beta-Alumina"

8th Annual Conference on the Physics of Compound Semiconductor Interfaces, Williamsburg, Virginia, January 27–29, 1981:

D. E. Eastman, P. Heiman, F. J. Himpsel, B. Reihl, D. M. Zehner, and C. W. White, "Electronic Properties of Highly Doped Si(111)-(1×1) Surfaces Prepared by Laser Annealing"

D. M. Zehner, C. W. White, G. W. Ownby, and B. R. Appleton, "Studies of Laser-Annealed GaAs (100), (110), and (111) Surfaces"

International Conference on Valence Fluctuations in Solids, Santa Barbara, California, January 27–30, 1981:

S. H. Liu, C. Stassis, and K. A. Gschneidner, Jr., "Mixed Valent Properties of $CeSn_3$" (invited paper)

RMIT International Workshop on Nonequilibrium Beam-Solid Interaction Processes, Philip Island, Australia, January 29–February 7, 1981:

B. R. Appleton, "Ion Beam and Pulsed-Laser Processing: Fundamentals and Applications" (invited paper)

B. R. Appleton, "Supersaturated Substitutional Alloys of Silicon Fabricated by Ion-Implantation Doping and Pulsed-Laser Annealing"

U.S.-Japan Workshop on Impurity Control, Divertors and Plasma-Wall Interactions, Princeton, New Jersey, February 2–5, 1981:

J. B. Roberto, "Plasma-Materials Interactions Research on ISX-B"

ıternational Seminar on Current and Future Developments in Microelectronics, Melbourne, Australia, ebruary 12, 1981:

B. R. Appleton, "New Methods of Materials Processing with Particular Emphasis on Solar Energy" (invited paper)

International Seminar on New Methods of Surface Processing of Materials, Melbourne, Australia, February 13, 1981:

B. R. Appleton, "Ion Beam and Laser-Induced Materials Interactions: Implications for Surface Treatment and Thin Film Reactions" (invited paper)

Fifth International Conference on Ion Beam Analysis, Sydney, Australia, February 16–20, 1981:

B. R. Appleton, J. H. Barrett, and O. W. Holland, "Enhanced 180° Scattering Effect in Surface Analysis by Positive Ion Channeling Spectroscopy" (invited paper)

Annual Meeting of the Metallurgical Society of AIME, Chicago, Illinois, February 23–26, 1981:

S.-J. Chang and S. M. Ohr, "Dislocation-Free Zone at the Crack Tip" [*J. Met.* **32,** 43 (1981)]

J. A. Horton and S. M. Ohr, "TEM Observations of Fracture in Aluminum" [*J. Met.* **32,** 43 (1981)]

J. Narayan, "Laser Processing of Semiconductors" [*J. Met.* **32,** 49 (1981)] (invited paper)

S. M. Ohr, "Direct Observation of Crack Tip Deformation" [*J. Met.* **32,** 74 (1981)] (invited paper)

Third American Physical Society Conference on Atomic Processes in High Temperature Plasma, Baton Rouge, Louisiana, February 25–27, 1981:

J. B. Roberto, "Laser Fluorescence Spectroscopy in Tokamak-Produced Plasmas" [*Bull. Am. Phys. Soc.* **26,** 811 (1981)] (invited paper)

German Physical Society Meeting, Muenster, Federal Republic of Germany, March 9–14, 1981:

E. Krätzig, L. A. Boatner, and R. Orlowski, "Storage of Holograms by Means of Quadratic Electro-Optical Effects"

American Physical Society Meeting, Phoenix, Arizona, March 16–20, 1981:

M. M. Abraham, L. A. Boatner, and M. Rappaz, "EPR of Rare Earth and Actinide Impurities in the Lanthanide Orthophosphates" [*Bull. Am. Phys. Soc.* **26,** 236 (1981)]

J. B. Bates, "Reaction and Properties of Water in the Beta- and Beta″-Aluminas" [*Bull. Am. Phys. Soc.* **26,** 370 (1981)] (invited paper)

L. A. Boatner, "Lanthanide Orthophosphates for the Primary Containment of High-Level Actinide Wastes" [*Bull. Am. Phys. Soc.* **26,** 401 (1981)] (invited paper)

A. I. Braginski, J. R. Gavaler, B. R. Appleton, and C. W. White, "The Effect of Laser Annealing on the Critical Current Density of Nb_3Ge" [*Bull. Am. Phys. Soc.* **26,** 479 (1981)]

J. W. Cable, "Temperature Dependence of the Spin Density Asymmetry in Nickel" [*Bull. Am. Phys. Soc.* **26,** 335 (1981)]

Y. Chen, J. Narayan, and K. L. Tsang, "Threshold Temperature for the Formation of Metallic Nickel Colloids in MgO Crystals" [*Bull. Am. Phys. Soc.* **26,** 268 (1981)]

D. K. Christen, H. R. Kerchner, S. T. Sekula, and Y. K. Chang, "Observation of a Flux-Line Lattice in Superconducting V_3Si" [*Bull. Am. Phys. Soc.* **26,** 479 (1981)]

J. F. Cooke, "Itinerant Electron Magnetism in Transition Metals" [*Bull. Am. Phys. Soc.* **26,** 333 (1981)] (invited paper)

R. J. Culbertson, L. C. Feldman, P. J. Silverman, and H. Boehm, "Ag(111) Surface Structure and t' Early Stages of Au Epitaxy" [*Bull. Am. Phys. Soc.* **26,** 226 (1981)]

H. L. Davis, J. R. Noonan, C. W. White, and D. M. Zehner, "Si(111)-(1×1) LEED—Comparison of Experimental and Calculated I-V Profiles" [*Bull. Am. Phys. Soc.* **26,** 350 (1981)]

Herbert Engstrom, J. B. Bates, W. E. Brundage, and J. C. Wang, "Ionic Conductivity in Naβ''-Alumina" [*Bull. Am. Phys. Soc.* **26,** 405 (1981)]

S. Epstein, R. J. Higgins, and D. H. Lowndes, "de Haas-van Alphen Studies of $LaAl_2$ Doped with Ce and Gd" [*Bull. Am. Phys. Soc.* **26,** 277 (1981)]

R. L. Fagaly, H. Weinstock, and Y. Chen, "Thermal Conductivity of Lithium-Doped MgO" [*Bull. Am. Phys. Soc.* **26,** 236 (1981)]

J. R. Gavaler, A. I. Braginski, B. R. Appleton, C. W. White, and J. M. Williams, "Critical Temperature of A15 Structure V-Si-C Films" [*Bull. Am. Phys. Soc.* **26,** 480 (1981)]

G. R. Gruzalski, Herbert Engstrom, and F. A. Modine, "Optical Properties of Transition Metal Carbides" [*Bull. Am. Phys. Soc.* **26,** 271 (1981)]

P. Heimann, F. J. Himpsel, B. Reihl, D. E. Eastman, C. W. White, and D. M. Zehner, "Electronic Structure of the Annealed Si(111) and Ge(111) Surfaces" [*Bull. Am. Phys. Soc.* **26,** 351 (1981)]

R. B. James and D. L. Smith, "Nonlinear Absorption of a CO_2 Probe Laser in p-Ge in the Presence of a High-Intensity Laser at 10.6 μm" [*Bull. Am. Phys. Soc.* **26,** 355 (1981)]

Theodore Kaplan and L. J. Gray, "A Self-Consistent Cluster Theory for Random Alloys with Short-Range Order" [*Bull. Am. Phys. Soc.* **26,** 454 (1981)]

H. R. Kerchner, D. K. Christen, and S. T. Sekula, "Elastic Instability of the Flux-Line Lattice in the Critical State" [*Bull. Am. Phys. Soc.* **26,** 244 (1981)]

W. C. Koehler, "The National Center for Small-Angle Scattering Research" [*Bull. Am. Phys. Soc.* **26,** 400 (1981)] (invited paper)

B. C. Larson, J. F. Barhorst, and T. S. Noggle, "Thermal Annealing of Dislocation Loops in Ion-Irradiated Copper" [*Bull. Am. Phys. Soc.* **26,** 349 (1981)]

S. H. Liu, C. Stassis, and K.-M. Ho, "Theory of LO Phonon Anomaly in hcp Transition Metals Ti, Zr, Hf, and Tc" [*Bull. Am. Phys. Soc.* **26,** 281 (1981)]

R. D. Lowde, R. M. Moon, B. Pagonis, C. H. Perry, and J. B. Sokoloff, "Polarized Neutron Studies of 'Forbidden Magnons' Well Below T_c in Nickel Alloy" [*Bull. Am. Phys. Soc.* **26,** 334 (1981)]

Douglas H. Lowndes, "Time-Resolved Reflectivity of GaAs during Pulsed-Ruby Laser Irradiation" [*Bull. Am. Phys. Soc.* **26,** 354 (1981)]

C. F. Majkrzak, G. Shirane, S. K. Satija, H. A. Mook, H. C. Hamaker, H. B. McKay, Z. Fisk, and M. B. Maple, "A Neutron Diffraction Study of the Magnetic Ordering in Superconducting $TmRh_4B_4$ and $NdRh_4B_4$" [*Bull. Am. Phys. Soc.* **26,** 277 (1981)]

F. A. Modine and V. M. Orera, "Magneto-Optical Properties of Metallic Colloids in Insulators" [*Bull. Am. Phys. Soc.* **26,** 298 (1981)]

R. M. Moon and B. Lebech, "Magnetic Susceptibility of the Cubic and Hexagonal Sites in Nd" [*Bull. Am. Phys. Soc.* **26,** 478 (1981)]

R. M. Moon and H. A. Mook, Jr., "Neutron Scattering Facilities at Oak Ridge National Laboratory" [*Bull. Am. Phys. Soc.* **26,** 399 (1981)] (invited paper)

Mark Mostoller and Mark Rasolt, "Pair Potentials at Simple Metal Surfaces" [*Bull. Am. Phys. Soc* **26,** 292 (1981)]

J. Narayan, Y. Chen, and R. M. Moon, "Nickel Colloids in Reduced Nickel-Doped Magnesium" [*Bull. Phys. Soc.* **26,** 268 (1981)]

R. M. Nicklow and N. Wakabayashi, "Magnetic Excitations in the Sinusoidally Modulated Spin Structure of Er" [*Bull. Am. Phys. Soc.* **26,** 468 (1981)]

J. R. Noonan and H. L. Davis, "LEED Analysis of Ag(110)-Second Interlayer Spacing Expansion" [*Bull. Am. Phys. Soc.* **26,** 224 (1981)]

S. M. Ohr, J. A. Horton, and S.-J. Chang, "Dislocation-Free-Zone Model of Fracture" [*Bull. Am. Phys. Soc.* **26,** 475 (1981)]

F. Perrot and M. Rasolt, "Energetics of Hydrogen in Aluminum" [*Bull. Am. Phys. Soc.* **26,** 336 (1981)]

R. L. Prater, L. L. Chase, and L. A. Boatner, "Demonstration of the Ferroelectric Nature of the Lithium-Induced Phase Transition in $KTaO_3$" [*Bull. Am. Phys. Soc.* **26,** 304 (1981)]

M. Rasolt and D. J. W. Geldart, "The Small and Large Wave Vector Behavior for the Nonuniform Electron Gas" [*Bull. Am. Phys. Soc.* **26,** 470 (1981)]

S. K. Sinha, H. A. Mook, D. G. Hinks, and G. W. Crabtree, "Study of the Coexistence between Superconductivity and Ferromagnetism in Single Crystal $ErRh_4B_4$" [*Bull. Am. Phys. Soc.* **26,** 277 (1981)]

D. L. Smith and R. B. James, "Laser-Induced Changes in the Dispersive Properties of p-Ge Due to Intervalence-Band Transitions" [*Bull. Am. Phys. Soc.* **26,** 353 (1981)]

Harold G. Smith, "Soft Modes and Charge Density Waves in Alpha-Uranium" [*Bull. Am. Phys. Soc.* **26,** 200 (1981)] (invited paper)

C. Stassis, J. Zarestky, C.-K. Loong, O. D. McMasters, and R. M. Nicklow, "Lattice Dynamics of $LaSn_3$" [*Bull. Am. Phys. Soc.* **26,** 281 (1981)]

N. Wakabayashi, "Phonon Spectra in Cu-Mn Alloys" [*Bull. Am. Phys. Soc.* **26,** 281 (1981)]

J. C. Wang, J. B. Bates, and Herbert Engstrom, "On The Non-Arrhenian Behavior in β''-Aluminas" [*Bull. Am. Phys. Soc.* **26,** 405 (1981)]

J. F. Wendelken and J. Kirschner, "Spin-Polarized Low-Energy Electron Diffraction Study of Oxygen Adsorption on Tungsten (001)" [*Bull. Am. Phys. Soc.* **26,** 225 (1981)]

C. W. White, D. M. Zehner, D. E. Eastman, P. Heimann, F. J. Himsel, and B. Reihl, "Photoelectron Spectroscopy of the Laser-Annealed Si(111)-(1×1) Surface" [*Bull. Am. Phys. Soc.* **26,** 350 (1981)]

C. Wood, J. Woosley, E. Sonder, and R. A. Weeks, "High-Temperature Seebeck Coefficient Measurements on Spinel" [*Bull. Am. Phys. Soc.* **26,** 386 (1981)]

R. F. Wood, "Macroscopic Models of Ultrarapid Crystallization" [*Bull. Am. Phys. Soc.* **26,** 329 (1981)] (invited paper)

D. M. Zehner, "Surface Properties of Laser-Annealed Semiconductors" [*Bull. Am. Phys. Soc.* **26,** 296 (1981)] (invited paper)

D. M. Zehner, C. W. White, P. Heimann, B. Reihl, and D. E. Eastman, "Laser Annealing of Ni(100) and Pt(100) Surfaces" [*Bull. Am. Phys. Soc.* **26,** 226 (1981)]

International Conference on Excited States and Multiresonant Nonlinear Optical Processes in Solids, Aussois, France, March 24–27, 1981:

R. B. James, D. L. Smith, and T. C. McGill, "Nonlinear Optical Properties of Semiconductors Induced by High-Intensity Infrared Light"

American Chemical Society Meeting, Atlanta, Georgia, March 29–April 3, 1981:

C. W. White and W. H. Christie, "The Use of RBS and SIMS to Investigate the Near-Surface Region of Laser-Annealed Semiconductors" (invited paper)

Fifth International Conference on Fracture, Cannes, France, March 29–April 3, 1981:

S. M. Ohr, S. Kobayashi, and S.-J. Chang, "Direct Observation of Dislocations in the Plastic Zone during Crack Propagation"

III-V Compound SERI Contractors' In-Depth Review Meeting, Raleigh, North Carolina, April 1, 1981:

D. H. Lowndes, R. T. Young, and R. F. Wood, "Applications of Laser Annealing and Laser-Induced Diffusion to Photovoltaic Conversion"

Application of Spectroscopy to Problems in Polymer Engineering and Science, Houston, Texas, April 5–9, 1981:

R. J. Samuels, G. D. Wignall, and H. R. Child, "Structural Characterization of Semicrystalline Polymer Blends by Small-Angle Neutron Scattering"

Second Microscopy of Semiconducting Materials Meeting, Oxford, England, April 6–10, 1981:

J. Fletcher and J. Narayan, "TEM Studies of Solid Phase Epitaxial Regrowth of Amorphous Layers in Ion-Implanted Silicon"

J. Fletcher, J. Narayan, and D. H. Lowndes, "TEM Studies of Defects in Laser-Annealed Gallium Arsenide"

J. Narayan, "Melting Phenomenon and Laser Annealing of Semiconductors" (invited paper)

International Topical Meeting on Advances in Mathematical Methods for the Solution of Nuclear Engineering Problems, Munich, Federal Republic of Germany, April 27–29, 1981:

T. J. Hoffman, H. L. Dodds, Jr., M. T. Robinson, and D. K. Holmes, "Charged Particle Calculations Using Boltzmann Transport Methods" (invited paper)

Seventeenth Annual Symposium of the American Vacuum Society, Albuquerque, New Mexico, April 28–30, 1981:

D. M. Zehner, "Characterization of Laser-Annealed Semiconductor Surfaces" (invited paper)

Eighty-Third American Ceramic Society Annual Meeting, Washington, D.C., May 3–6, 1981:

L. D. Bentsen, D. H. Hasselman, and Y. Chen, "Thermal Diffusivity of MgO Crystals Containing Ni^{2+} Ions and Metallic Ni Colloids" [*Am. Ceram. Soc. Bull.* **60,** 384 (1981)]

N. J. Dudney, J. B. Bates, and J. C. Wang, "Intercalation of Water into β-Alumina" [*Am. Ceram. Soc. Bull.* **60,** 360 (1981)]

P. LaBarbe, A. F. Wright, R. A. Weeks, J. S. Lin, R. W. Hendricks, and J. Zarzycki, "Small-Angle Neutron Scattering Studies of Magnetite Crystallization Process in Glasses of Different Silica and Iron Contents" [*Am. Ceram. Soc. Bull.* **60,** 355 (1981)]

R. Magruder, D. Kinser, and R. A. Weeks, "Dielectric and Optical Behavior of Irradiated GeO_2" [*Am. Ceram. Soc. Bull.* **60,** 412 (1981)]

E. Sonder, R. A. Weeks, and J. V. Spadaro, "Penetration of Surface Damage Resulting from Abrasion and Heating of MgO" [*Am. Ceram. Soc. Bull.* **60,** 384 (1981)]

›rkshop on the Interaction of Laser Radiation with Surfaces for Application to Microelectronics, Cam-dge, Massachusetts, May 4–5, 1981:

D. M. Zehner and C. W. White, "Surface Properties of Laser-Annealed Semiconductors" (invited paper)

Fifteenth IEEE Photovoltaic Specialists Conference, Kissimmee, Florida, May 12–15, 1981:

G. E. Jellison, Jr., F. A. Modine, C. W. White, and R. T. Young, "Optical Absorption Measurements of Pure and Heavily Doped Silicon from 1.24 to 4.63 eV and the Effect on Solar Cell Performance"

D. H. Lowndes, J. W. Cleland, J. Fletcher, J. Narayan, R. D. Westbrook, R. F. Wood, W. H. Christie, and R. E. Eby, "Pulsed-Laser Annealing of Ion-Implanted Semiconducting GaAs for Homojunction Solar Cells"

R. T. Young, G. E. Jellison, Jr., Y. K. Chang, M. C. Lu, and G. A. van der Leeden, "Effects of Lithium Diffusion into Polycrystalline Si Solar Cells"

International Conference on Fast Ionic Transport in Solids, Gatlinburg, Tennessee, May 18–22, 1981:

J. B. Bates, H. Engstrom, J. C. Wang, B. C. Larson, N. J. Dudney, and W. E. Brundage, "Composition, Ion-Ion Correlations, and Conductivity of Beta″-Alumina"

G. M. Brown, D. A. Schwinn, J. B. Bates, and W. E. Brundage, "Structures of Four Fast-Ion Conductors by Single-Crystal Neutron-Diffraction Analysis: Zn-Stabilized Naβ''-Alumina and Mg-Stabilized Na-, K-, and Agβ''-Aluminas"

N. J. Dudney, J. B. Bates, J. C. Wang, G. M. Brown, B. C. Larson, and H. Engstrom, "Intercalation of Water into Lithium β-Alumina"

B. C. Larson, J. B. Bates, N. J. Dudney, and J. F. Barhorst, "Effect of Hydration on Conduction Ion Correlations in Naβ''-Alumina"

J. C. Wang, J. B. Bates, N. J. Dudney, and H. Engstrom, "Study of β- and β''-Aluminas by Means of Potential Energy Calculations"

International Conference on Defects in Insulating Crystals, Riga, Salaspils, U.S.S.R., May 18–23, 1981:

R. F. Wood and T. M. Wilson, "Theoretical Calculations of the Electronic and Vibrational Structure of Point Defects in Ionic Crystals"

Second International Conference on Solid Films and Surfaces, College Park, Maryland. June 8–11, 1981:

John F. Wendelken, "A Study of Nitric Oxide Adsorption on Copper (100) and (110)"

Conference on Lasers and Electro-Optics, Washington, D.C., June 10–12, 1981:

B. R. Appleton, "Unique Materials Alterations Possible with Laser Annealing" (invited paper)

J. Narayan, J. Fletcher, C. W. White, R. E. Eby, and W. H. Christie, "Melting Phenomenon and Laser Annealing in Semiconductors"

S. R. Wilson, W. M. Paulson, and C. W. White, "CW and Pulsed-Laser Annealing of Polysilicon Films"

Polycrystalline Silicon Contractors' Review Meeting, Washington, D.C., June 17–19, 1981:

Rosa T. Young, R. F. Wood, G. A. van der Leeden, and D. H. Lowndes, "Applications of Laser Annealing and Laser-Induced Diffusion to Photovoltaic Conversion"

Electronics Materials Conference, Santa Barbara, California, June 24–26, 1981:

S. R. Wilson, W. M. Paulson, and C. W. White, "Comparison of Polysilicon Films Annealed with a CW or Pulsed Laser"

Forty-First Conference on Physical Electronics, Bozeman, Montana, June 19–July 1, 1981:

R. J. Culbertson, L. C. Feldman, P. J. Silverman, and R. Haight, "Hydrogen Adsorption on Si(111)-(7×7)"

J. R. Noonan and H. L. Davis, "Oxygen Induced Reconstruction of the Cu(100) Surface"

G.-C. Wang, D. M. Zehner, and H. C. Eaton, "Phase Transitions of Mo-5%Re(100) and Stepped W(100) Surfaces"

Ninth International Conference on Atomic Collisions in Solids, Lyon, France, July 6–10, 1981:

S. D. Bloom, D. C. Hamilton, B. L. Berman, M. J. Alguard, J. H. Barrett, Sheldon Datz, R. H. Pantell, and R. L. Swent, "Monte Carlo Calculations of Channeling Radiation"

Ordean S. Oen, "The Two-Atom Model in Enhanced Ion Backscattering Near 180° Scattering Angles"

Gordon Research Conference on Physical Metallurgy, Andover, New Hampshire, July 6–10, 1981:

S. M. Ohr, "Observations of Crack Tip Processes" (invited paper)

Gordon Research Conference on Point and Line Defects in Semiconductors, Plymouth, New Hampshire, July 13–17, 1981:

R. T. Young and Y. K. Chang, "Electrical and Structural Properties of Grain Boundary in Si"

International Symposium on Recent Theoretical (Computational) Developments in Atomic Collisions in Solids, Strasbourg, France, July 14–16, 1981:

Ordean S. Oen, "Ion Reversibility Studies in Solids Using the Two-Atom Scattering Model"

Fifth American Association for Crystal Growth International Conference on Vapor Growth and Epitaxy, Coronado, California, July 19–24, 1981:

L. A. Boatner, J. O. Ramey, C. B. Finch, and M. M. Abraham, "The Role of Crystal Growth in the Characterization of Nuclear Waste Forms"

C. W. White, "Laser Annealing of Ion-Implanted Semiconductors: Studies of Nonequilibrium Crystal Growth" (invited paper)

International Conference on Phase Transitions on Surfaces, Orono, Maine, August 3–7, 1981:

G.-C. Wang, D. M. Zehner, and H. C. Eaton, "Phase Transitions of Mo-5%Re(100) and Stepped W(100) Surfaces"

Second Topical Meeting on Fusion Reactor Materials, Seattle, Washington, August 10–12, 1981:

R. R. Coltman, Jr., and C. E. Klabunde, "Mechanical Strength of Low-Temperature-Irradiated Polyimides: A Five-to-Tenfold Improvement in Dose Resistance Over Epoxies"

J. A. Horton, S. M. Ohr, and W. A. Jesser, "TEM Observations of Crack Tip-Cavity Interactions"

V. Philipps, K. Sonnenberg, and J. M. Williams, "Diffusion of Helium in Nickel"

J. B. Roberto, R. C. Isler, S. Kasai, L. E. Murray, J. E. Simpkins, S. P. Withrow, and R. A. Zuhr "Hydrogen Recycling and Impurities during Isotopic Exchange in ISX-B"

Mark T. Robinson, "The Reflection of Low Energy Helium Atoms from Tungsten Surfaces"

R. A. Zuhr, J. B. Roberto, and S. P. Withrow, "Effects of Neutral Beam Injection and Gas Puffing on Deuterium and Impurity Levels in the Scrapeoff Layer of ISX-B"

International Symposium on the Physics of Solids under High Pressure, Bad Honnef, Federal Republic of Germany, August 10–14, 1981:

S. H. Liu, "Effects of Pressure on the Mixed-Valent Properties of Ce and Its Intermetallic Compounds" (invited paper)

Cryogenic Engineering Conference/International Cryogenic Materials Conference, San Diego, California, August 10–14, 1981:

A. Braginski, J. R. Gavaler, J. Dreggi, R. C. Kuznicki, M. D. Nakenow, B. R. Appleton, C. W. White, and J. M. Williams, "The Effect on the Critical Current Density of Nb_3Ge"

Symposium on Neutron Scattering, Argonne, Illinois, August 12–14, 1981:

W. C. Koehler, H. R. Child, R. W. Hendricks, J. S. Lin, and G. D. Wignall, "One Year's Experience with the ORNL-NSF National Facility for Small-Angle Neutron Scattering" (invited paper)

E. C. Trantham, H. E. Rorschach, J. C. Clegg, C. F. Hazelwood, and R. M. Nicklow, "QNS Measurements on Water in Biological and Model Systems"

Twelfth International Union of Crystallography, Ottawa, Canada, August 16–25, 1981:

J. E. Epperson, J. Faber, J. S. Lin, and R. W. Hendricks, "On the Decomposition of a Ni-12.5 at. % Al Alloy"

B. C. Larson, J. F. Barhorst, and S. S. Goldenberg, "X-ray Study of Near-Surface Strain in Implanted Silicon"

H. G. Smith, N. Wakabayashi, R. M. Nicklow, G. H. Lander, and E. S. Fisher, "The Modulated Structures of Uranium" (invited paper)

Fifth International Meeting on Ferroelectricity (IMG-5), University Park, Pennsylvania, August 17–22, 1981:

R. L. Prater, L. L. Chase, and L. A. Boatner, "Raman Scattering Studies of Ferroelectric Transitions Induced by Lithium and Niobium in $KTaO_3$"

Sixteenth International Conference on Low Temperature Physics, Los Angeles, California, August 19–25, 1981:

D. K. Christen, H. R. Kerchner, S. T. Sekula, and Y. K. Chang, "Observation of the Flux-Line Lattice in Superconducting V_3Si"

H. R. Kerchner, "The Satistical-Summation Theory of Weak Flux-Line Pins in Type II Superconductors"

S. K. Sinha, G. W. Crabtree, D. G. Hinks, and H. Mook, "Study of Coexistence of Ferromagnetism and Superconductivity in Single Crystal $ErRh_4B_4$"

J. R. Thompson, S. T. Sekula, and Y. Chen, "Magnetic Properties of Ni in MgO: Ni^{+2} Ions and Magnetically Ordered Precipitates"

L. D. Woolf, D. C. Johnston, H. A. Mook, W. C. Koehler, M. B. Maple, and Z. Fisk, "Interpretation of Specific Heat and Spontaneous Magnetization Anomalies at the Reentrant Superconducting-Ferromagnetic Transition in $(Ho_{0.6}Er_{0.4})Rh_4B_4$"

NATO Advanced Study Institute on Excitations in Disordered Systems, East Lansing, Michigan, Augı 23–September 4, 1981:

Theodore Kaplan and L. J. Gray, "Self-Consistent Approximations Beyond the CPA—Part II" (invited paper)

Seventh International Biophysics Congress and Third Pan American Biochemistry Congress, Mexico City, Mexico, August 23–28, 1981:

M. J. Zuckerman, M. Avignon, S. H. Liu, and D. A. Pink, "The Effect of Electrostatic Interactions on the Properties of Charged Lipid Membranes: A Theoretical Approach"

NATO Research Institute on Surface Modification and Alloying, Trevi, Italy, August 24–28, 1981:

C. W. White, "Nonequilibrium Crystal Growth during Laser Annealing"

C. W. White, "Semiconductor Surface Structures Resulting from Pulsed-Laser Irradiation" (invited paper)

C. W. White, B. C. Larson, and T. S. Noggle, "Time-Resolved X-ray Diffraction During Pulsed-Laser Annealing"

International Conference on Phonon Physics, Bloomington, Indiana, August 31–September 3, 1981:

B. Salce, A. M. de Goër, and L. A. Boatner, "Study of 'Pure' $KTaO_3$ and KTN Single Crystals by Thermal Conductivity Measurements to 50 mK"

Actinides Conference-1981, Pacific Grove, California, September 10–15, 1981:

M. M. Abraham, L. A. Boatner, and M. Rappaz, "EPR Investigations of ^{243}Cm, ^{244}Cm, and ^{238}U in $LuPO_4$ Single Crystals"

Actinide Workshop, Los Alamos, New Mexico, September 16–18, 1981:

S. H. Liu, "Excitons in f-Band Metals" (invited paper)

Seminars

SOLID STATE DIVISION SEMINARS AT ORNL

During this period D. M. Zehner served as Seminar Chairman March–August 1980; J. B. Bates, August 1980–June 1981; and F. A. Modine, June 1981–continuing. The following seminars were held:

"Relativistic Density Functional Theory and Some Applications,"[1] A. K. Rajagopal, Louisiana State University, Baton Rouge, Louisiana

"Properties of Magnetic Superconductors," J. W. Lynn, University of Maryland, College Park, Maryland

"Challenges and Opportunities in Ceramic Materials,"[2] D. W. Readey, Ohio State University, Columbus, Ohio

"The Thermodynamics of Solidification," J. Cahn, National Bureau of Standards, Washington, D.C.

"Development of Tuneable UV (Lyman-α) Lasers for Spectroscopy," R. Mahan, University of Maryland, College Park, Maryland

"High Purity Epitaxial INP as a Far-Infrared Detector," K. M. Lau, Rice University, Houston, Texas

"Iron Radio-Tracer Diffusion in Magnesium-Doped Aluminum Oxide," I. K. Lloyd, Massachusetts Institute of Technology, Cambridge, Massachusetts

"CO Dissociation on the Mo(100) Surface," S. Semancik, Brown University, Providence, Rhode Island

"Electronic Structure of Point Defects in Metals," P. H. Dederichs, Kernforschungsanlage, Jülich, Federal Republic of Germany

"Chemical Trends in Semiconductor Surface Structures," R. J. Meyer, Xerox Corporation, Rochester, New York

"Properties and Applications of Metal Hydrogen Systems for the Generation, Purification, and Storage of Hydrogen," H. Wenzl, Kernforschungsanlage, Jülich, Federal Republic of Germany

"Experimental Determination of Transport Properties of Magma at High Pressure and Temperature,"[2] H. S. Yoder, Jr., Geophysical Laboratory, Carnegie Institution, Washington, D.C.

"Device Physics of a Heavily Doped Region in PN Junction Si Solar Cell," M. A. Shibib, University of Florida, Gainesville, Florida

"Superconductivity, Stoichiometry, and Atomic Ordering in Nb_3Al," R. Flukiger, Kernforschungszentrum, Karlsruhe, Federal Republic of Germany

"The Calculation of Vacancy Formation and Self-Diffusion Energies in Simple Metals,"[1] R. Taylor, National Research Council, Ottawa, Canada

"Nucleation and Growth Studies of Crystallization in Glasses by Small-Angle Neutron Scattering,"[3] A. F. Wright, Institut Laue-Langevin, Grenoble, France

"Paramagnetic Point and Pair Defects in Perovskites," K. A. Müller, IBM, Zurich, Switzerland

"HVEM Studies of Helium Embrittlement in Stainless Steel," J. A. Horton, Y-12 Plant, Oak Rid Tennessee

"CuCl—A Few Facts and Ideas," G. Gilat, Technion, Haifa, Israel

"The One-Dimensional Classical Heisenberg Magnet with Anisotropic Interactions," J. M. Loveluck, Institut Laue-Langevin, Grenoble, France

"Formation of Silicides: Diffusion and Nucleation Control Kinetics," C. C. Peterson, University of Uppsala, Uppsala, Sweden

"Raman Measurement of Lattice Temperature During Pulsed-Laser Heating of Silicon," A. Compaan, Kansas State University, Manhattan, Kansas

"Energy and Electric Field Dependence of Si-SiO_2 Interface States by Optically Activated Admittance Measurements," T. C.-Y. Poon, Columbia University, New York, New York

"Accurate Spin-Dependent Electron Correlation Energies: Some Consequences in LSDA Calculations,"[1] S. H. Vosko, University of Toronto, Toronto, Canada

"What's Wrong with Laser Annealing," H. J. Leamy, Bell Laboratories, Murray Hill, New Jersey

"Temperature Dependence of the Haven Ratio in Beta-Alumina," H. Sato, Purdue University, West Lafayette, Indiana

"Channeling Studies of Si Interfaces," N. C. Cheung, California Institute of Technology, Pasadena, California

"Amorphous and Rare Earth Cobalt Magnets," E. C. Subbarao, India Institute of Technology, Kampur, India

"Ion Implantation—A Powerful Tool for the Production of Superconductors," B. W. Stritzker, Kernforschungsanlage, Jülich, Federal Republic of Germany

"Materials Problems in Fluidized Bed Combustion Systems,"[2] J. Stringer, Electric Power Research Institute, Palo Alto, California

"Hardening Mechanisms for Mechanical Properties, Superconductivity, and Ferromagnetism,"[4] P. Haasen, University of Göttingen, Göttingen, Federal Republic of Germany

"Neutron Small-Angle and Diffuse Scattering, a Powerful Tool for Materials Science," W. Schmatz, Kernforschungszentrum, Karlsruhe, Federal Republic of Germany

"Helium in Metals," W. F. Schilling, Kernforschungsanlage, Jülich, Federal Republic of Germany

"Ion-Beam Induced Mixing," W. Hofer, Max-Planck-Institut, Garching, Federal Republic of Germany

"An Integrated Approach to Desert Development," A. Bishay, American University in Cairo, Cairo, Egypt

"Hopping Conductivity and the Universal Dielectric Response," A. K. Jonscher, University of London, London, England

"Atomistic Modeling of Defects in Semiconductors," T. Y. Tan, IBM, Yorktown Heights, New York

"Photo-Ionization of Atomic Cesium," T. B. Cook III, Portland State University, Portland, Oregon

"A High-Efficiency, Low-Cost GaAs Solar Cell Program," D. Walsh, McGill University, Montreal, Canada

"The Rutherford Spallation Neutron Source: Current Status and Future Plans," S. W. Lovesey, Rutherford Laboratory, Oxford, England

"New Position-Sensitive Neutron Detector at Argonne National Laboratory," G. H. Lander, Argonne National Laboratory, Argonne, Illinois

"Aspects of the Ising Spin Glass Problem," J. A. Blackman, University of Reading, Reading, England

"Current Research Activities of the Laboratory Léon Brillouin," B. Farnoux, C.E.N., Saclay, France

"Monazite and Other Related Orthophosphates for the Primary Containment of Nuclear Waste," M. Rappaz, Solid State Division, ORNL

"Surface Phase Transformations; Molecular Dynamics of Epitaxial Crystallization and Melting," C. L. Cleveland, Georgia Institute of Technology, Atlanta, Georgia

"Resistivity of Metals: Exploring the Breakdown of Bloch-Boltzman Theory,"[1] P. B. Allen, State University of New York, Stony Brook, New York

"Micromechanics of Solids,"[1] T. Mura, Northwestern University, Evanston, Illinois

"Influence of the Electronic Structure of Complex Crystals on Metallic Properties: Theory and Application to Nb_3Sn,"[1] W. E. Pickett, Naval Research Laboratory, Washington, D.C.

"Ferromagnetism in Iron and Nickel,"[1] R. E. Prange, University of Maryland, College Park, Maryland

"Phase Diagrams, Gibbs' Free Energy and Their Applications," T. Lindemer, Chemical Technology Division, ORNL

"Auger Electron Spectroscopy and Solid Surface Chemistry," H. H. Madden, Sandia National Laboratories, Albuquerque, New Mexico

"Small-Angle Neutron Scattering Studies of Crystalline Polymers," D. G. H. Ballard, Imperial Chemical Industries, Runcorn, England

"Molecular Dynamical Calculations of Energy Transport in Solids,"[2] R. MacDonald, National Bureau of Standards, Washington, D.C.

"Artificial Intelligence: Is It Useful as a Research Tool?" C. K. Johnson, Chemistry Division, ORNL

"Recent Neutron Scattering Studies on the Diluted Heisenberg Ferromagnet System $Eu_xSr_{1-x}S$," W. Zinn, Kernforschungsanlage, Jülich, Federal Republic of Germany

"Diffusion of Point Defects—Interpretation of Neutron Scattering and Mössbauer Effect Studies," K. Schroeder, Kernforschungsanlage, Jülich, Federal Republic of Germany

"The Anderson Lattice Model for the Mixed Valent Crystal $CeSn_3$," S. H. Liu, Ames Laboratory, Iowa State University, Ames, Iowa

"Polarized Electrons and the Mysteries of Nickel," M. Campagna, Kernforschungsanlage, Jülich, Federal Republic of Germany

"Characteristic Properties of Mictomagnets (Spin Glasses)," P. A. Beck, University of Illinois, Urbana, Illinois

"Thermodynamics and Kinetics of Diffusion in High Defect Concentration Solids," R. A. McKee, Metals and Ceramics Division, ORNL

"Morphology of Amorphous Semiconductors," J. C. Phillips, Bell Laboratories, Murray Hill, New Jersey

"Structural Ceramic Research and Plans," V. J. Tennery, Metals and Ceramics Division, ORNL

"Advances in Magnetism," R. M. White, Xerox Corporation, Palo Alto, California

"Magnetic Excitations in Chromium and γ-MnCu Alloys," K. Mikke, Institute of Nuclear Research, Swierk, Poland

"The Oscillatory Oxidation of CO over a Platinum Catalyst," B. C. Sales, University of California, San Diego, California

"Atomic Positions at Crystal Surfaces Studied by MeV Ion Scattering," R. J. Culbertson, Bell Laboratories, Murray Hill, New Jersey

"Electronic Structure of Magnetic Impurities in FCC Metals," R. G. Zeller, Kernforschungsanlage, Jülich, Federal Republic of Germany

"Void Growth in Metals,"[1] J. W. Hutchinson, Harvard University, Cambridge, Massachusetts

"High Resolution Cathodoluminescence of Zinc Sulfide," S. H. Roberts, Bristol University, Bristol, England

"Local Environment Effects and Spin Glass States in Disordered Magnetic Alloys," J. S. Kouvel, University of Illinois, Chicago Circle, Illinois

"Correlation Theory of Static and Dynamic Properties of Multilevel Systems: A Generalization of the RPA Theory," P.-A. Lindgård, Risø National Laboratory, Roskilde, Denmark

"Kinetics of Order-Disorder Transitions in a Frustrated System," J. K. McCoy, Purdue University, Lafayette, Indiana

"Chemisorption Theory for Metallic Surfaces: Embedding Theory Based on Orbital Localization,"[1] J. L. Whitten, State University of New York, Stony Brook, New York

"Electron Localization: Fact and Theory,"[1] T. V. Ramakrishnan, Bell Laboratories, Murray Hill, New Jersey

"Excitation Behavior for Ce^{3+} Systems with Cogblin-Schrieffer Interaction," D. Yang, West Virginia University, Morgantown, West Virginia

"Advanced Nickel and Cobalt-Base Alloys for Gas Turbine Applications,"[2] N. S. Stoloff, Rensselaer Polytechnic Institute, Troy, New York

"Transport in Transition Metals," W. H. Butler, Metals and Ceramics Division, ORNL

"Critical Phenomena and Phase Transitions," P.-A. Lindgård, Risø National Laboratory, Roskilde, Denmark (Series of Lectures)

"Discrete Hydrodynamics: Transport Coefficients via Renormalization,"[1] P. B. Visscher, University of Alabama, University, Alabama

"The Relativistic KKR-CPA Method and Its Application to Au_xPt_{1-x} and Ni_xPt_{1-x},"[1] P. Weinberger, Technical University of Vienna, Vienna, Austria

"Electroreflectance of Noble Metal Surfaces," S. H. Liu, Ames Laboratory, Iowa State University, Ames, Iowa

"Mechanics and Petrology of Island Arc Volcanism,"[2] B. D. March, Johns Hopkins University, Baltimore, Maryland

"MgO as a Solvent—Conductivity; Diffusion; Reactions,"[2] W. D. Kingery, Massachusetts Institute of Technology, Cambridge, Massachusetts

"Research Opportunities in Amorphous Alloys," C. C. Koch, Metals and Ceramics Division, ORNL

"Soluble Ising Models on Crazy Lattices,"[1] R. B. Griffiths, Carnegie-Mellon University, Pittsburgh, Pennsylvania

"Surface Analysis by Spin-Polarized LEED," R. Feder, Universität Duisburg, Duisburg, Federal Republic of Germany

"Particle Size/Molecular Weight Distribution by Photon Correlation Spectroscopy,"[5] B. Chu, State University of New York, Stony Brook, New York

"Application of Diffuse-Elastic Neutron Scattering (DENS) to the Physics of Metallic Alloys," K. Werner, Kernforschungsanlage, Jülich, Federal Republic of Germany

"Instantaneous Dislocation Velocities in Metals," J. M. Galligan, University of Connecticut, Storrs, Connecticut

"The Pseudopotential Panacea," M. L. Cohen, University of California, Berkeley, California

"Diffusion Mechanisms in Transition Metal Oxides,"[2] N. Peterson, Argonne National Laboratory, Argonne, Illinois

"Computer Models of Crystal Growth,"[1] G. H. Gilmer, Bell Laboratories, Murray Hill, New Jersey

"*Ab Initio* Calculations of Superconducting Transition Temperatures and Some Mechanisms Limiting Tc's,"[1] H. Winter, Kernforschungszentrum, Karlsruhe, Federal Republic of Germany

"Interface Instability during Rapid Solidification," S. R. Coriell, National Bureau of Standards, Washington, D.C.

"Neutron Scattering Studies of the Ionic Motion in Fluorides," J. Kjems, Risø National Laboratory, Roskilde, Denmark

"Optical Studies of the Electronic and Dynamical Properties of Graphite Intercalation Compounds," P. Eklund, University of Kentucky, Lexington, Kentucky

"Light Ion-Atom Collision Processes and Uses at Lucas Heights," D. D. Cohen, AINSE, Lucas Heights, Australia

"Theory of Melting in Two and Three Dimensions,"[1] D. R. Nelson, Harvard University, Cambridge, Massachusetts

"Superconductivity and Magnetism of Ternary Rare Earth Compounds," B. Maple, University of California, La Jolla, California

"High-Temperature Alloys,"[2] E. R. Thompson, United Technologies Laboratories, Hartford, Connecticut

"Generalized Pseudo Atom and Its Application to Lattice Dynamics,"[1] M. Ball, University of Liverpool, Liverpool, England

"Theory of Photoemission from Random Alloys,"[1] D. Velický, Institute of Physics, Prague, Czechoslovakia

"Biological Applications of Small-Angle Scattering," V. R. Ramakrishnan, Yale University, New Haven, Connecticut

"Structural Investigations of Conducting Polymers by Neutron Scattering," M. Stamm, Kernforschungsanlage, Jülich, Federal Republic of Germany

"A Microscopic Mechanism for the Formation of Excited Sputtered Molecular Ions," K. Snowden, Universität Osnabruck, Osnabruck, Federal Republic of Germany

"Inelastic Gamma-Ray Scattering from V_3Si," Monash University, Clayton, Victoria, Australia

"Use of High Resolution Electron Microscopy in Materials Science," S. Amelinckx, Studiecentrum voor Kernenergie, Mol, Belgium

"STEM and Microanalysis," A. Howie, Cavendish Laboratory, University of Cambridge, England

"Description of Reactive and Inelastic Molecular Collisions,"[1] J. Linderburg, Aarhus University, Aarhus, Denmark

"Small-Angle Neutron Scattering from High-Impact Polystyrene," O. A. Pringle, University of Missouri, Columbia, Missouri

"Itinerant Magnetic Systems in the Disordered State,"[1] S. H. Liu, Solid State Division, ORNL

"Bonding Geometry of Hydrogen on W(110) Studied by Electron Energy Loss Spectroscopy," N. J. DiNardo, University of Pennsylvania, Philadelphia, Pennsylvania

"Coherent Inelastic Neutron Scattering from Polycrystals," U. Buchenau, Kernforschungsanlage, Jülich, Federal Republic of Germany

"The Effect of Beam Broadening on X-ray Microchemical Analysis in Scanning Transmission Electron Microscopy (STEM)," M. E. Twigg, University of Illinois, Urbana, Illinois

"Some Recent Neutron Scattering Studies at Risø," H. B. Moller, Risø National Laboratory, Roskilde, Denmark

"Electron Energy Loss Study of Optical Properties," A. B. Ray, Cornell University, Ithaca, New York

"Lattice Dynamics of Naphthalene and Anthracene and Their Pressure and Temperature Dependence," B. Dorner, Institut Laue-Langevin, Grenoble, France

"Fracture Mechanics for Fracture Tough Materials," S. J. Burns, University of Rochester, Rochester, New York

"Electronic Structure of A15 Compounds: The Role of Chains," W. Weber, Kernforschungszentrum, Karlsruhe, Federal Republic of Germany

"Equilibrium, Small-Signal, and Transient Space Charge Effects in Solids and Liquids," J. R. Macdonald, University of North Carolina, Chapel Hill, North Carolina

"Vacuum Physics for the 1980s,"[4] P. J. Hobson, National Research Council of Canada, Ottawa, Canada

"Determination of Residual Stresses in the Interior of Technical Parts by Means of Neutron Diffraction," L. A. Pintschovius, Kernforschungszentrum, Karlsruhe, Federal Republic of Germany

---

[1]Metals and Ceramics Division and Solid State Division Joint Theoretical Seminar.
[2]High-Temperature Materials Seminar Series.
[3]Sponsored by ORNL-NSF National Center for Small-Angle Scattering Research.
[4]Sponsored jointly by Metals and Ceramics Division and Solid State Division.
[5]Sponsored jointly by Chemistry Division and Solid State Division.

LECTURES AND SEMINARS

Lectures and seminars presented by Division members during the period covered by this report included the following:

M. M. Abraham—National University of Mexico, Galindo, Queretaro, Mexico, "Review of EPR Research on Analogs of Monazite for the Isolation of Actinide Waste"; University of South Carolina, Columbia, South Carolina, University of Kansas, Lawrence, Kansas, Oklahoma State University, Stillwater, Oklahoma, University of Texas, Arlington, Texas, Texas Christian University, Fort Worth, Texas, University of Georgia, Athens, Georgia, and College of William and Mary, Williamsburg, Virginia, "Application of EPR to the Characterization of Radioactive Waste Forms"; College of William and Mary, Williamsburg, Virginia, "Methods of Electron Nuclear Double Resonance"

B. R. Appleton—Vanderbilt University, Nashville, Tennessee, "Ion Implantation Doping for New Materials Modifications"; University of North Carolina, Chapel Hill, North Carolina, "Ion Beam and Laser Techniques in Materials Research"; Minerals Physics Branch, CSIRO, North Ryde, Australia, "Ion Beam Analysis Techniques"; National Measurements Laboratory, CSIRO, North Ryde, Australia, "Materials Processing by Ion Implantation and Pulsed-Laser Annealing"

H. Barrett—Chalk River Nuclear Laboratory, Chalk River, Ontario, Canada, "Role of Reversibility in Enhanced Ion Backscattering Near 180° Scattering Angle"

J. B. Bates—University of Kentucky, Lexington, Kentucky, "Fast Ion Transport in Solid Electrolytes" (ACS Lecture) and "Fast Ion Transport in the Alkali Metal Aluminates"

L. A. Boatner—Lawrence Livermore National Laboratory, Livermore, California, Rice University, Houston, Texas, Emory University, Atlanta, Georgia, and McGill University, Montreal, Canada, "Analogs of Monazite as an Alternate Nuclear Waste Form"; University of Alabama, Birmingham, Alabama, and Virginia Military Institute, Lexington, Virginia, "The Growth of Single Crystals and Their Applications in Solid State Physics"

Y. Chen—University of North Carolina, Chapel Hill, North Carolina, "Positive and Negative Decoration of Strained Regions in MgO Crystals Using Lithium Impurities"; National Taiwan University, Taipei, Taiwan, "Nickel Colloids in Reduced Nickel-Doped Magnesium Oxide"

J. F. Cooke—University of Cincinnati, Cincinnati, Ohio, "Itinerant Electron Magnetism in Transition Metal Systems"

R. J. Culbertson—Pennsylvania State University, University Park, Pennsylvania, and Cleveland State University, Cleveland, Ohio, "Applications of MeV He^+ Scattering to the Study of Silicon Surface Structures"; Sandia National Laboratories, Albuquerque, New Mexico, "Atom Displacements at Crystal Surfaces Using MeV Ion Scattering"; Bell Laboratories, Murray Hill, New Jersey, "Si(111): Study of the (7×7), Ni-Stabilized (1×1)" and "Au-Ag(111) Epitaxy and Au/Ag/Au/Ag . . . , Layered Structures"

H. L. Davis—Louisiana State University, Baton Rouge, Louisiana, "Nonstructural Parameters Used in Modeling Electron Diffraction" and "Surface Crystallography via LEED"

G. R. Gruzalski—Metals and Ceramics Division, ORNL, "Transition-Metal Carbide Research in the Solid State Division"; University of Nebraska, Lincoln, Nebraska, "The Optical Properties of the Group IV and Group V Transition Metal Carbides"; University of Illinois, Urbana, Illinois, "Transition-Metal Carbide Research at ORNL"

R. B. James—Cornell University, Ithaca, New York, Los Alamos National Laboratory, Los Alamos, New Mexico, and Lawrence Livermore National Laboratory, Livermore, California, "Theory of Nonlinear Infrared Absorption in p-type Germanium"; Texas Instruments Central Research Laboratory, Dallas, Texas, and Research Triangle Institute, Research Triangle Park, North Carolina, "Saturation of Intervalence-Band Transitions in p-type Semiconductors"; IBM Corporation, Yorktown Heights, New York, and Rockwell International Science Center, Thousand Oaks, California, "Nonlinear Optical Properties Associated with Free Carriers in Group IV Semiconductors"; General Motors Research Laboratories, Warren, Michigan, and The Aerospace Corporation, El Segundo, California, "Nonlinear Optical Properties of Semiconductors Induced by CO_2 Laser Light"

G. E. Jellison, Jr.—Oak Ridge Associated Universities, Oak Ridge, Tennessee, "Photovoltaics for Energy Conversion"

W. C. Koehler—Institut Laue-Langevin, Grenoble, France, and Risø National Laboratory, Roskilde, Denmark, "Small-Angle Scattering Research at the ORNL-NSF 30-m Facility"; C.E.N., Saclay, France, "The Magnetic Structures of Nd—Chapter II"

J. S. Lin—State University of New York, Stony Brook, New York, "Small-Angle X-ray and Neutron Scattering—Techniques and Applications"; University of Delaware, Newark, Delaware, "Small-Angle X-ray and Neutron Scattering: Applications in Chemical and Energy Engineering"; Case Western Reserve University, Cleveland, Ohio, "National Facility for Small-Angle Scattering Research"

S. H. Liu—National Taiwan University, Taipei, Taiwan, "New Developments in the Theory of Transitic Metal Magnetism"; National Tsinghwa University, Hsinchu, Taiwan, "Introduction to the Intermedia.. Valence Phenomena"; National Central University, Chungli, Taiwan, "The f-Band Problem"; Free University, Berlin, Federal Republic of Germany, "Theory of Itinerant Magnetic Systems in the Disordered State," "Electronic and Magnetic Properties of the Mixed Valent Compound $CeSn_3$," "Spin Waves in Modulated and Disordered Spin Systems," "Electroreflectance of Ag(110) Surface," and "Lattice Gas Model for the Metal-Electrolyte Interface"; Technical University, Vienna, Austria, "A Unified Theory for Itinerant Magnetic Metals"; Argonne National Laboratory, Argonne, Illinois, "Electronic and Magnetic Properties of the Mixed-Valent Compound $CeSn_3$"

D. H. Lowndes—United Technologies Laboratories, East Hartford, Connecticut, "Pulsed-Laser Processing and Time-Resolved Behavior of Gallium Arsenide"; McGill University, Montreal, Quebec, Canada, and University of Sherbrooke, Sherbrooke, Quebec, Canada, "Pulsed-Laser Processing of Semiconductors"

J. Narayan—The National Microelectronics Research Center, Grenoble, France, "Melting Phenomena and Laser Annealing in Semiconductors," "Mechanisms of Crystallization and Solubility Limits During Solid- and Liquid-Phase-Epitaxial Growth," and "Annealing of Defects in Semiconductors"; Atomic Energy Research Establishment, Harwell, England, "Metal Colloids in MgO"

R. M. Nicklow—Rice University, Houston, Texas, "Neutron Scattering Studies of Phonon-Defect Interactions"

J. R. Noonan—ETH, Zurich, Switzerland, "Investigation of the Laser-Irradiated Si(111)- and Ge(111)-(1×1) Surfaces by LEED Intensity Analysis"; University of Alabama, Tuscaloosa, Alabama, "Techniques for Surface Analysis"

O. S. Oen—University of Alabama, Tuscaloosa, Alabama, "Computer Simulation of the Reflection of Hydrogen and the Sputtering of Hydrogen from Metal Hydrides"; Max-Planck-Institut für Plasmaphysik, Garching bei München, Federal Republic of Germany, "Ion Reversibility Studies in Solids Using the Two-Atom Scattering Model"

S. M. Ohr—Columbia University, New York, New York, "Electron Microscope Studies of Crack Tip Deformation"; University of Connecticut, Storrs, Connecticut, and Massachusetts Institute of Technology, Cambridge, Massachusetts, "Electron Microscope Observation of Crack Propagation"; Georgia Institute of Technology, Atlanta, Georgia, "*In Situ* Electron Microscope Observations of Crack Propagation in Solids"; Kernforschungsanlage, Jülich, Federal Republic of Germany, "Direct Observation of Crack Propagation"; Kernforschungszentrum, Karlsruhe, Federal Republic of Germany, and Max-Planck-Institut für Metallforschung, Stuttgart, Federal Republic of Germany, "Electron Microscope Studies of Fracture"

D. B. Poker—Clemson University, Clemson, South Carolina, "The High- and Low-Temperature Release of Ion-Implanted Helium from Nickel"

M. Rasolt—Stockholm Institute of Technology, Stockolm, Sweden, "The Optical Potential in Electron Surface Spectroscopy"; University of Lund, Lund, Sweden, "Exchange and Correlation Contributions in Nonuniform Electron Systems"; Chalmers Technical Institute, Gothenburg, Sweden, "Electron Interactions in Metallic Surfaces"; Louisiana State University, Baton Rouge, Louisiana, "Ground State Energy of Interacting Nonuniform Electronic Systems: I and II"; Tulane University, New Orleans, Louisiana, "The Electron-Hole Droplet in Si and Ge"

J. B. Roberto—Max-Planck-Institut für Plasmaphysik, Garching bei München, Federal Republic of Germany, and UKAEA Culham Laboratory, Abingdon, England, "Surface Erosion, Deuterium Trapping, Impurity Deposition, and Laser Fluorescence Measurements in ISX-B"; Kernforschungsanlage, Jülich, Federal Republic of Germany, "Plasma-Surface Studies in Tokamaks Using Surface Probes"

C. Sales—University of Oregon, Eugene, Oregon, and Iowa State University, Ames, Iowa, "Oscillatory Surface Reactions: The Oxidation of CO over a Pt Catalyst"; Lawrence Livermore National Laboratory, Livermore, California, and E. I. duPont de Nemours, Wilmington, Delaware, "The Oscillatory Oxidation of CO over a Pt Catalyst"; Xerox Corporation, Palo Alto, California, "The Oscillatory Oxidation of CO over Pt, Pd, and Ir Catalysts"

S. T. Sekula—Clemson University, Clemson, South Carolina, "Low-Temperature Ion Implantation and Superconductivity"

J. R. Thompson—University of Tennessee, Knoxville, Tennessee, "Low-Temperature Research on Superconductivity and Magnetism"

G.-C. Wang—Princeton University, Princeton, New Jersey, "LEED Studies of Surfaces: Defects, Phase Transitions, and Magnetic Properties"

J. C. Wang—Wake Forest University, Winston-Salem, North Carolina, "Fast Ion Transport in Beta-Alumina"

R. A. Weeks—Auburn University, Auburn, Alabama, "Electric Field Effects on the Electrical Conductivity of Some Insulating Solids"; Sandia National Laboratories, Albuquerque, New Mexico, "Precipitation of Impurities in Insulating Crystals by Electric Fields"; Los Alamos National Laboratory, Los Alamos, New Mexico, "Electric Field Effects on Some Insulating Solids"; National Research Center of Egypt, Cairo, Egypt, "Role of Materials Science in Future Electricity-Generating Technologies"; American University in Cairo, Cairo, Egypt, "Electron States of Wide-Band-Gap Glass Forming Oxides: I and II" and "Effect of Impurities on the Conductivity of MgO Single Crystals"; Ain Shams University, Cairo, Egypt, "Effect of Electric Fields on the Conductivity of Some Wide-Band-Gap Oxide Single Crystals"; University of Damascus, Damascus, Syria, "Introduction to Defects in Crystals and Their Electron States" and "Role of Materials Science in Future Electricity-Generating Technologies" (Series of Eight Lectures); University of Jordan, Amman, Jordan, "Role of Materials Science in Future Electricity-Generating Technologies" and "Thermal Electric Breakdown in Some Wide-Band-Gap Oxides"; University of Clausthal-Zellerfeld, Clausthal-Zellerfeld, Federal Republic of Germany, "Fusion Processes of Some Natural Glasses"; Ecole Polytechnique Federale de Lausanne, Lausanne, Switzerland, "Some Electrical Properties of Some Wide-Band-Gap Oxide Single Crystals"

J. F. Wendelken—Chalmers University of Technology, Gothenborg, Sweden, Kernforschungsanlage, Jülich, Federal Republic of Germany, Max-Planck-Institut für Plasmaphysik, Garching bei München, Federal Republic of Germany, University of York, Heslington, England, and Daresbury Laboratory, Daresbury, England, "The Adsorption of Oxygen and Nitric Oxide on Copper(110) Studied with Electron Energy Loss Spectroscopy and Low-Energy Electron Diffraction"; University of Cambridge, Cambridge, England, "Current Topics in Electron Scattering from Surfaces"

C. W. White—Motorola, Inc., Phoenix, Arizona, Rice University, Houston, Texas, Kernforschungsanlage, Jülich, Federal Republic of Germany, "Laser Annealing of Ion-Implanted Silicon"; IBM Thomas J. Watson Research Center, Yorktown Heights, New York, "Pulsed-Laser Annealing of Ion-Implanted Silicon"; Massachusetts Institute of Technology, Cambridge, Massachusetts, "Laser Annealing of Ion-Implanted Silicon; Studies of Nonequilibrium Crystal Growth"; FOM Institute, Amsterdam, the Netherlands, "Recent Laser Annealing Results: Semiconductor Surface Structures and Time-Resolved X-ray Diffraction"

G. D. Wignall—National Bureau of Standards, Washington, D.C., "Some Artifacts and Experimental Constraints in SANS Studies of Polymers"; Exxon Corporate Research Laboratories, Linden, New Jersey, "Small-Angle Scattering Studies of Polymers, Blends, and Oilshales"; Tennessee Eastman Company, Kingsport, Tennessee, "Current Polymer Research at Oak Ridge by Small-Angle Neutron Scattering"; Bell Laboratories, Murray Hill, New Jersey, "Recent Studies of Chain Configuration in Polymers by Small-Angle Neutron Scattering"

R. F. Wood—Eastman Kodak Research Laboratories, Rochester, New York, Washington University, St. Louis, Missouri, and Arizona State University, Tempe, Arizona, "Laser Processing of Semiconductor Devices" (IEEE Electron Devices Society Lectures)

R. T. Young—University of Rome, Rome, Italy, and Catholic University, Leuven, Belgium, "Laser Annealing of Ion-Implanted Si and Its Application to Photovoltaic Research"

R. A. Zuhr—Fusion Energy Division, ORNL, "Accelerator-Based Techniques for Plasma Studies"

Scientific Professional Activities

W. S. Aaron	Member, Program Committee, Conference on the Leachability of Radioactive Solids, Gatlinburg, Tennessee, 1980
M. M. Abraham	Member, Editorial Board, *KINAM Revista de Fisica* Member, Organizing Committee and Session Chairman, Workshop on Alternate Nuclear Waste Forms and Interactions in Geologic Media, Gatlinburg, Tennessee, 1980 Lecturer, ORAU Traveling Lecture Program, 1980–1981
B. R. Appleton	Member, Editorial Board, *Nuclear Science Applications* Co-Chairman, Materials Research Society Symposium on Laser and Electron Beam Interactions with Solids (to be held in 1981) Member, Fusion Program Committee, ORNL Chairman, Committee on Near-Surface Modifications, ORNL Member, ASTM Subcommittee on Energetic Ion Analysis Chairman, Particle-Solid Interactions Gordon Research Conference, Andover, New Hampshire, 1980 Participant, BES/DMS Workshop on Coal Structure and Properties, Gatlinburg, Tennessee, 1980 Participant, International Workshop on Accelerator Related Atomic and Molecular Science, New London, New Hampshire, 1980 Participant, Industrial Research Institute Management Study Group Adjunct Professor, Department of Physics, North Texas State University, Denton, Texas Guest Scientist, Australian Atomic Energy Commission, Lucas Heights, Australia, January–May, 1981 Guest Lecturer, International Seminar on Current and Future Developments in Microelectronics, RMIT, Melbourne, Australia, 1981 Guest Lecturer, International Seminar on New Methods of Surface Processing of Materials, RMIT, Melbourne, Australia, 1981 Participant, International Workshop on Nonequilibrium Beam-Solid Interaction Processes, Philip Island, Australia, 1981
J. H. Barrett	Adjunct Professor, Department of Physics, North Texas State University, Denton, Texas Member, Ph.D. Thesis Committee, Department of Physics, North Texas State University, Denton, Texas
J. B. Bates	Co-Chairman, International Conference on Fast Ionic Transport in Solids, Gatlinburg, Tennessee, 1981 Associate Editor, *Solid State Ionics* Lecturer, ORAU Traveling Lecture Program, 1980–1981 Member, Ad Hoc Committee on Energy Storage, ORNL Member, High Temperature Materials Laboratory Committee, ORNL

L. A. Boatner	Member, Seed Money Proposal Review Committee, ORNL Member, World's Fair Committee, ORNL Lecturer, ORAU Traveling Lecture Program, 1979–1980 Member, High Temperature Materials Laboratory Committee, ORNL General Chairman and Editor of Proceedings, Workshop on Alternate Nuclear Waste Forms and Interactions in Geologic Media, Gatlinburg, Tennessee, 1980 Participant, Workshop on Irradiation Effects in Nuclear Waste Forms, Seattle, Washington, 1980 Panel Member, DOE/Argonne Workshop on Comparative Leaching of Radioactive Waste Forms, Argonne, Illinois, 1980 Member, Program Committee, Materials Research Society Symposium on the Scientific Basis for Nuclear Waste Management, Boston, Massachusetts, 1980 General Co-Chairman, Materials Research Society Annual Meeting (to be held in 1982) Member, Program Committee, Materials Research Society Symposium on the Scientific Basis for Nuclear Waste Management (to be held in 1982)
Y. K. Chang	Guest Scientist, Kernforschungsanlage, Jülich, Federal Republic of Germany, 1981–1982
Y. Chen	Member, Program Committee, Symposium on Coal, American Physical Society Member, Graduate School Doctoral Committee, Department of Physics, University of Alabama, Birmingham, Alabama Member, Program Committee, and Session Chairman, Conference on the Chemistry and Physics of Coal Utilization, Morgantown, West Virginia, 1980
H. R. Child	Lecturer, ORAU Traveling Lecture Program, 1980–1981
J. W. Cleland	Session Co-Chairman, 158th Meeting of the Electrochemical Society, Hollywood, Florida, 1980 Member, Advisory Committee, Fourth International Conference on Neutron Doping (to be held in 1982)
R. R. Coltman	Adjunct Professor, Department of Physics and Astronomy, Clemson University, Clemson, South Carolina
J. F. Cooke	Lecturer, ORAU Traveling Lecture Program, 1980-1981
H. L. Davis	Member, Organizing and Program Committee, and Session Chairman, Conference on Determination of Surface Structure by LEED, Yorktown Heights, New York, 1980 Co-Chairman, First Annual Symposium and Equipment Exhibit of the Tennessee Valley Chapter of the American Vacuum Society, Knoxville, Tennessee, 1980 Member, Local Committee, Physical Electronics Conference (to be held in 1982)
N. J. Dudney	Member, Local Committee, International Conference on Fast Ionic Transport in Solids, Gatlinburg, Tennessee, 1981
R. B. James	Recipient, Eugene P. Wigner Fellowship, 1981
G. E. Jellison, Jr.	Referee, Polycrystalline Contractors' Review Meeting, Washington, D.C., 1980
L. H. Jenkins	Member, General Committee, Physical Electronics Conference Session Chairman, Physical Electronics Conference, Ithaca, New York, 1980 Session Chairman, Physical Electronics Conference, Bozeman, Montana, 1981 Participant, NSLS Users' Meeting, Brookhaven National Laboratory, Upton, New York, 1981 Member, Wigner Fellowship Committee, ORNL Member, Ph.D. Recruiting Steering Committee, ORNL

H. Kobisk	President, International Nuclear Target Development Society, 1981–1982 Chairman of the Board, International Nuclear Target Development Society Chairman, World Conference of the International Nuclear Target Development Society, Gatlinburg, Tennessee, 1980
W. C. Koehler	Director, ORNL-NSF National Center for Small-Angle Scattering Research Member, Editorial Advisory Board, *Journal of Magnetism and Magnetic Materials* Member, Editorial Advisory Board, *Magnetism Letters*
J. S. Lin	Faculty Member, Department of Chemical, Metallurgical, and Polymer Engineering, The University of Tennessee, Knoxville, Tennessee Participant, BES/DMS Workshop on Coal Structure and Related Properties, Gatlinburg, Tennessee, 1980
S. H. Liu	Session Chairman, International Symposium on the Physics of Solids under High Pressure, Bad Honnef, Federal Republic of Germany, 1981 Member, Program Review Committee, Lawrence Berkeley Laboratory, 1980–1982 Participant, Actinide Workshop, Los Alamos, New Mexico, 1981
D. H. Lowndes	Member, Users' Advisory Committee, Francis Bitter National Magnet Laboratory, Massachusetts Institute of Technology, Cambridge, Massachusetts Member, Ph.D. Dissertation Committee, University of Oregon, Eugene, Oregon ORNL On-Site Senior Thesis Research Advisor, Kalamazoo College, Kalamazoo, Michigan Member, National Science Foundation Review Committee for Scientific Proposals Participant, SERI Program Review Meetings on Si and GaAs Solar Cell Technology, 1980–1981
F. A. Modine	Member, ORNL Evaluation Team, Proposal for Advanced Metal Oxide Varistor Concepts Coordinator, ORNL Seed Money Program, 1979–1980 Member, ORNL Exploratory Studies Review Committee, 1979–1980 Secretary, ORNL Research Committee, 1979–1980
H. A. Mook	Member, Program Advisory Committee, International Conference on Ternary Superconductors, Lake Geneva, Wisconsin, 1980 Secretary, ORNL Neutron Scattering Users' Group
R. M. Moon	Member, Commission on Electron Charge, Spin, and Momentum Densities, International Union of Crystallography Member, Evaluation Panel for the Center for Materials Research, National Bureau of Standards Member, Organizing Committee, U.S.-Japan Cooperative Program on Neutron Scattering
J. Narayan	Co-Editor, *Defects in Semiconductors*, North Holland, New York, 1981 Chairman, Program Committee, Conference on Lasers and Electro-Optics Symposium on Laser Annealing and Materials Processing, Washington, D.C., 1981 Chairman, Materials Research Society Symposium on Laser and Electron-Beam Interactions with Solids: Fundamentals and Applications (to be held in 1982) Chairman and Organizer, Materials Research Society Symposium on Defects in Semiconductors, Boston, Massachusetts, 1980

R. M. Nicklow	Member, Organizing Committee, U.S.-Japan Cooperative Program on Neu Scattering
J. R. Noonan	Chairman, Tennessee Valley Chapter, American Vacuum Society, 1981
O. S. Oen	Lecturer, ORAU Traveling Lecture Program, 1979–1980 Session Chairman, International Symposium on Recent Theoretical (Computational) Developments on Atomic Collisions in Solids, Strasbourg, France, 1981
S. M. Ohr	Member, Chemistry and Physics of Metals Committee, the Metallurgical Society of AIME Member, Nuclear Metallurgy Committee, the Metallurgical Society of AIME Member, Nuclear Metallurgy Committee, Materials Science Division, American Society for Metals Lecturer, ORAU Traveling Lecture Program, 1980–1981 Symposium Chairman, the Metallurgical Society of AIME Symposium on Physical and Chemical Properties of Coal (to be held in 1982) Participant, BES/DMS Coal Structure and Properties Meeting, Gatlinburg, Tennessee, 1980
M. Rasolt	Session Chairman, American Physical Society Meeting, Phoenix, Arizona, 1981 Guest Scientist, University of Paris XI, Orsay, France, April–May, 1980
J. B. Roberto	Technical Secretary, DOE Basic Energy Sciences Assessment Co-Chairman, International Program Committee, Fifth International Conference on Plasma Surface Interactions in Controlled Fusion Devices (to be held in 1982) Member, Editorial Advisory Board, *Journal of Nuclear Materials* Member, Plasma-Materials Interactions Task Group, DOE Coordinator, U.S. Participation in the TEXTOR (FRG) Tokamak Program, Edge Flux and Recycling Measurements, DOE Key Person, U.S.-Japan Fusion Cooperative Program, Exchange BL-15, DOE Participant, Sixth TEXTOR Executive Committee Meeting, Jülich, Federal Republic of Germany, 1981 Participant, U.S.-Japan Workshop on Impurity Control, Divertors, and Plasma-Wall Interactions, Princeton, New Jersey, 1981 Experimental Working Group Chairman, Workshop on Plasma Edge Experiments and Modeling, Los Angeles, California, 1980
M. T. Robinson	Western Hemisphere Editor, *Radiation Effects* Participant, DOE Workshop on Plasma Edge Experiments and Modeling, Los Angeles, California, 1980 Participant, DOE Workshop on Irradiation Effects in Nuclear Waste Forms, Seattle, Washington, 1981 Member, Future Technology Subcommittee, ORNL Computer Steering Committee, 1980–1981
J. A. Setaro	Member, Organizing Committee, World Conference of the International Nuclear Target Development Society, Gatlinburg, Tennessee, 1980
H. G. Smith	Member, International Advisory Board, Fourth Conference on the Superconductivity in the d- and f-Band Metals, Karlsruhe, Federal Republic of Germany (to be held in 1982)
E. Sonder	Member, Advisory Board, *Diffusion and Defects Data* (Nonmetals)
G.-C. Wang	Secretary, Tennessee Valley Chapter, American Vacuum Society, 1981

C. Wang	Member, Local Committee, International Conference on Fast Ionic Transport in Solids, Gatlinburg, Tennessee, 1981
R. A. Weeks	Adjunct Professor, Department of Materials Science and Mechanical Engineering, Vanderbilt University, Nashville, Tennessee Adjunct Professor, Department of Geology, University of Pennsylvania, Philadelphia, Pennsylvania Member, Editorial Committee, *Journal of the American Ceramic Society* Member, Editorial Board, *Egyptian Journal of Solid State Science* Session Chairman, Frontiers of Glass Science Conference, Los Angeles, California, 1980 Recipient, Fulbright Short-Term Lectureship in Middle East, 1980 Professor Invitè, Ecole Polytechnique Federale, Lausanne, Switzerland, January–July, 1981 Lecturer, ORAU Traveling Lecture Program, 1979–1980
J. F. Wendelken	Guest Scientist, Kernforschungsanlage, Jülich, Federal Republic of Germany, 1979–1980
R. D. Westbrook	Member, ASTM Committee F-1 on Electronics Member, Semiconductor Equipment and Materials Institute Solar GaAs and Substrate Committee
C. W. White	Member, Organizing Committee, Materials Research Society Symposium on Laser and Electron-Beam Solid Interactions and Materials Processing, Boston, Massachusetts, 1980 Co-Editor, *Laser and Electron Beam Processing of Materials,* Academic Press, New York, 1980 Chairman, Program Committee, Materials Research Society Annual Meeting (to be held in 1981) Participant, DOE Research Task Force Meeting on Molten Carbonate Fuel Cell Materials, Argonne, Illinois, 1981 Chairman and Organizer, Conference on Lasers and Electro-Optics Symposium on Laser Annealing and Materials Processing, Washington, D.C., 1981 Participant, NATO Research Institute on Surface Modification and Alloying, Trevi, Italy, 1981 Member, 1981 Von Hipple Award Committee, Materials Research Society
G. D. Wignall	Lecturer, ORAU Traveling Lecture Program, 1980–1981 Adjunct Professor, Department of Polymer and Chemical Engineering, The University of Tennessee, Knoxville, Tennessee
M. K. Wilkinson	Member, Solid State Sciences Committee of the National Research Council Member, Executive Committee, Division of Condensed Matter Physics, American Physical Society Member, Advisory Committee, Division of Materials Research, National Science Foundation Member, Evaluation Panel for NSF Materials Research Laboratory Site Visits Member, Advisory Panel for the Solid State Sciences Committee of the National Research Council Adjunct Professor, School of Physics, Georgia Institute of Technology, Atlanta, Georgia Member, Program Advisory Committee, National Synchrotron Light Source, Brookhaven National Laboratory Secretary, Organizing Committee, International Conference on Magnetism (to be held in 1985) Member, Advisory Committee, Department of Physics, University of Georgia Consultant, DOE Neutron Scattering Review Panel

	Member, ORNL Committee on Quality in Research
	Member, International Advisory Panel, Conference on the Neutron and Its Applicat (to be held in 1982)
	Member, Organizing Committee, U.S.-Japan Cooperative Program on Neutron Scattering
S. P. Withrow	Member, Ph.D. Recruiting Committee, ORNL
R. F. Wood	National Lecturer, IEEE Electron Devices Society, 1980–1981
	Vice-Chairman, International Organizing Committee, and Session Chairman, International Conference on Defects in Insulating Crystals, Riga, Salaspils, U.S.S.R., 1981
	Editor, Solid State Physics, *Computer Physics Communications*, North Holland, New York
	Symposium Co-Chairman, Electrochemical Society Symposium on Annealing of Semiconductors, Hollywood, Florida, 1980
	Member, Professional Education Resource Committee, ORNL
	Member, Polycrystalline Silicon Program Review Panel, Solar Energy Research Institute
	Participant, DOE Workshop on Basic Research Needs and Opportunities on Interfaces in Solar Materials, Denver, Colorado, 1980
	Participant, SERI Program Review Meetings on Si and GaAs Solar Cell Technology, 1980–1981
F. W. Young, Jr.	Member, Executive Committee, American Association of Crystal Growth
	Member, Editorial Board, *Topics in Crystal Growth*
	Member, Program Committee, Intense Pulsed Neutron Source-I, Argonne National Laboratory
	Member, Visiting Committee, Materials Science Center, Cornell University
	Participant, DOE/DMS Workshop on the Effects of Irradiation on the Structure and Properties of Materials, Aspen, Colorado, 1981
	Participant, COMAT Workshop on Rapid Solidification Technology, Washington, D.C., 1981
	Member, Advisory Committee, International Conference on Neutron Irradiation Effects (to be held in 1981)
R. T. Young	Lecturer, ORAU Traveling Lecture Program, 1979–1980
	Participant, SERI Program Review Meetings on Si and GaAs Solar Cell Technology, 1980-1981
	Symposium Co-Chairman, Electrochemical Society Symposium on Annealing of Semiconductors, Hollywood, Florida, 1980
	Member, Polycrystalline Silicon Program Review Panel, Solar Energy Research Institute
D. M. Zehner	Member, ORNL Graduate Fellow Selection Panel
	Member, ASTM E-42 Committee on Surface Analysis
R. A. Zuhr	Participant, DOE Workshop on Nonmagnetic Divertors, Boston, Massachusetts, 1980
	Member, Plasma Materials Interaction Task Group, DOE

Personnel Changes

New Staff Members

A. Scientific Staff
- J. A. Blackman, University of Reading, Reading, England
- T. B. Cook III, Portland State University, Portland, Oregon
- R. J. Culbertson, Bell Laboratories, Murray Hill, New Jersey
- L. S. Darken, EG&G ORTEC, Oak Ridge, Tennessee
- J. Fletcher, Oxford University, Oxford, England
- G. R. Gruzalski, Harvard University, Cambridge, Massachusetts
- O. W. Holland, North Texas State University, Denton, Texas
- J. A. Horton, Development Division, Y-12 Plant, Oak Ridge, Tennessee
- R. B. James, California Institute of Technology, Pasadena, California
- S. H. Liu, Ames Laboratory/Iowa State University, Ames, Iowa
- F. A. Modine, transferred from Program Planning and Analysis Office, Central Management Offices (completion of temporary assignment)
- M. Rappaz, Ecole Polytechnique Institut, Lausanne, Switzerland
- B. C. Sales, University of California at San Diego, La Jolla, California
- G. A. van der Leeden, Poly Solar, Inc., Garland, Texas
- G.-C. Wang, National Bureau of Standards, Washington, D.C.

B. Administrative and Technical Staff
- T. L. Collins, Senior Laboratory Technician (transferred from Industrial Safety and Applied Health Physics Division)
- D. L. Cordts, Secretary
- L. C. Cunningham, Secretary
- D. L. Slagle, Senior Secretary (transferred from Central Management Offices)

Staff Transfers and Terminations

A. Scientific Staff
- J. A. Blackman (completion of temporary assignment)
- H. L. Engstrom (voluntary resignation)
- J. Fletcher (deceased)
- W. R. Husinsky (completion of temporary assignment)
- S. Kobayashi (voluntary resignation)
- P. R. Kuehn (retirement)
- M. Rappaz (completion of temporary assignment)
- M. V. K. Ulehla (voluntary resignation)
- N. Wakabayashi (voluntary resignation)

B. Administrative and Technical Staff
- G. C. Battle, Information Center Analyst (transfer to Information Division)
- W. E. Busby, Senior Engineering Draftsman (retirement)
- D. L. Cordts, Secretary (voluntary resignation)
- F. A. Kocur, Administrative Assistant (retirement)

Guest Assignments

A. Scientific Staff
- G. M. Beardsley, Millsaps College, Jackson, Mississippi
- N. Bjerre, Aarhus University, Aarhus, Denmark
- P. Burlet, Centre National de la Recherche Scientifique, Grenoble, France
- G. Dolling, Atomic Energy of Canada Limited, Chalk River, Ontario, Canada
- E. R. Dullni, University of Bochum, Bochum, Federal Republic of Germany
- D. Frischke, University of Munich, Munich, Federal Republic of Germany
- R. R. Gonzalez, Universidad Complutense, Madrid, Spain
- P. A. Lindgard, Risø National Laboratory, Roskilde, Denmark
- C.-K. Loong, Ames Laboratory/Iowa State University, Ames, Iowa
- H. Naramoto, Japan Atomic Energy Research Institute, Tokai-mura, Japan
- L. A. R. Pintschovius, Kernforschungszentrum, Karlsruhe, Federal Republic of Germany
- A. K. Rai, Universal Energy Systems, Kettering, Ohio
- C. K. Saw, Ames Laboratory/Iowa State University, Ames, Iowa
- H. B. Schweer, Kernforschungsanlage, Jülich, Federal Republic of Germany
- G. S. Smith, Ames Laboratory/Iowa State University, Ames, Iowa
- B. W. Stritzker, Kernforschungsanlage, Jülich, Federal Republic of Germany
- K. Werner, Kernforschungsanlage, Jülich, Federal Republic of Germany
- C. E. Young, Argonne National Laboratory, Argonne, Illinois
- J. Zarestky, Ames Laboratory/Iowa State University, Ames, Iowa

B. Graduate Students
- O. W. Holland, North Texas State University, Denton, Texas
- J. R. Martinelli, Vanderbilt University, Nashville, Tennessee
- K.-L. Tsang, University of Alabama, Birmingham, Alabama

C. Great Lakes College Association Science Program
- S. M. Casey, Knox College, Galesburg, Illinois
- D. J. Crary, Earlham College, Richmond, Indiana
- R. D. Esman, Kalamazoo College, Kalamazoo, Michigan
- M. R. Holland, Kalamazoo College, Kalamazoo, Michigan

Summer Assignments

A. Scientific Staff
- S. J. Burns, University of Rochester, Rochester, New York
- A. M. Castets, Centre National de la Recherche Scientifique, Grenoble, France
- J. R. Clem, Ames Laboratory/Iowa State University, Ames, Iowa

K. E. Clements, Auburn University, Auburn, Alabama
W. L. Clinton, Georgetown University, Washington, D.C.
P. Coleman, Princeton University, Princeton, New Jersey
T. W. Haywood, University of North Carolina, Wilmington, North Carolina
B. Hennion, Centre National de la Recherche Scientifique, Grenoble, France
R. W. Johnson, University of Southwestern Louisiana, Lafayette, Louisiana
F. Jona, State University of New York, Stony Brook, New York
R. M. Jones, Tuskegee Institute, Tuskegee, Alabama
P. L. Leath, Rutgers University, New Brunswick, New Jersey
R. W. Major, University of Richmond, Richmond, Virginia
R. L. Mills, Ohio State University, Columbus, Ohio
A. K. Rajagopal, Louisiana State University, Baton Rouge, Louisiana
H. Sato, Purdue University, West Lafayette, Indiana
S. Suehiro, Kyoto University, Kyoto, Japan
N. G. Thompson, Vanderbilt University, Nashville, Tennessee
S. Y. Tong, University of Wisconsin, Milwaukee, Wisconsin
G. T. Trammell, Rice University, Houston, Texas
S. A. Werner, University of Missouri, Columbia, Missouri
G. Zaccai, Centre National de la Recherche Scientifique, Grenoble, France

B. Administrative and Technical Staff
M. E. Guthrie, Tennessee Wesleyan College, Athens, Tennessee
R. S. Speas, Oak Ridge High School Faculty, Oak Ridge, Tennessee
S. E. Wright, The University of Tennessee, Knoxville, Tennessee

C. ORAU-University Faculty
H. C. Eaton, Tennessee Technological University, Cookeville, Tennessee
J. Kasichainula, Tennessee Technological University, Cookeville, Tennessee
M. C. Lu, Walters State Community College, Morristown, Tennessee

D. ORAU-Undergraduate Research Trainees
K. Brister, Sonoma State University, Rohnert Park, California
S. C. Corbato, Rice University, Houston, Texas
S. S. Goldenberg, University of North Carolina, Chapel Hill, North Carolina
J. V. Spadaro, Stockton State College, Union, New Jersey

SOLID STATE DIVISION
PROGRAMMATIC MANPOWER DISTRIBUTION
FY 1981

Programs	Staff (person-years)	Guests (person-years)	Total (person-years)
KC 02 02 DOE Basic Energy Sciences (Materials Sciences)	73.0	9.0	82.0
AT 15 30 DOE Fusion (Magnetic Fusion)	5.0	1.0	6.0
Work for others			
Solar Energy Research Institute	2.0	0	2.0
National Science Foundation	4.0	1.5	5.5
Sales (Isotope Research Materials Laboratory)	12.0	0	12.0
Total	96.0	11.5	107.5

SOLID STATE DIVISION

SEPTEMBER 30, 1981

M. K. WILKINSON, DIRECTOR
D. L. SLAGLE, SECRETARY
F. W. YOUNG, JR., ASSOC. DIRECTOR*
S. L. EVANS, SECRETARY*

SPECIAL STAFF ASSIGNMENTS
P. H. GREEN, AFFIRMATIVE ACTION COORDINATOR*
W. S. AARON, QUALITY ASSURANCE COORDINATOR*
J. A. SETARO, RADIATION SAFETY OFFICER*
D. L. SMALLEY, FINANCE OFFICER[2]

ADMINISTRATION, ENGINEERING, MAINTENANCE
P. H. GREEN*
W. E. BUSBY
B. J. COPELAND
J. R. GIBSON[1]
J. E. WEIDLEY[1]

SOLID STATE THEORY
J. F. COOKE*
V. G. HENDRIX, SECRETARY

- **DEFECTS AND ALLOYS**
  R. F. WOOD*
  T. KAPLAN
  M. E. MOSTOLLER
- **RADIATION EFFECTS**
  M. T. ROBINSON
  J. H. BARRETT
  O. S. OEN
- **MAGNETISM AND SURFACES**
  H. L. DAVIS
  J. F. COOKE*
  S. H. LIU
  M. RASOLT

CRYSTAL PHYSICS
R. M. MOON*
R. L. BURRELL, SECRETARY
M. A. GILLESPIE, SECRETARY
I. M. BARKER, SECRETARY*

- **NEUTRON DIFFRACTION**
  J. W. CABLE
  H. R. CHILD
  W. C. KOEHLER*
  R. M. MOON*
  J. L. SELLERS
  K. WERNER[3]
- **NEUTRON SPECTROMETRY**
  R. M. NICKLOW
  T. L. COLLINS
  S. P. KING[4]
  H. A. MOOK
  H. G. SMITH
- **ORNL-NSF-DOE SAS CENTER**
  W. C. KOEHLER*
  P. BURLET[3]
  J. S. LIN
  G. D. WIGNALL
- **SUPERCONDUCTIVITY**
  S. T. SEKULA
  D. K. CHRISTEN
  H. R. KERCHNER
  J. R. THOMPSON[4]
- **AMES LABORATORY NEUTRON SCATTERING**
  J. L. ZARESTKY[5]
  C. K. LOONG[5]
  C. K. SAW[5]
  G. S. SMITH[5]

CERAMICS AND SURFACES
L. H. JENKINS*
A. M. KEESEE, SECRETARY
L. S. TYLER, SECRETARY

- **SURFACE PHYSICS**
  D. M. ZEHNER
  L. H. JENKINS*
  J. R. NOONAN
  G. W. OWNBY
  G. C. WANG
  J. F. WENDELKEN
- **HIGH TEMPERATURE CERAMICS**
  F. A. MODINE
  Y. CHEN
  R. R. GONZALEZ[3]
  J. R. MARTINELLI[6]
  E. SONDER
  K. L. TSANG[6]
  R. A. WEEKS
- **OPTICAL AND MAGNETIC SPECTROSCOPY**
  J. B. BATES
  S. M. CASEY[7]
  N. J. DUDNEY
  J. C. WANG
- **CRYSTAL GROWTH AND CHARACTERIZATION**
  L. A. BOATNER
  M. M. ABRAHAM
  W. E. BRUNDAGE
  Y. K. CHANG
  G. R. GRUZALSKI
  H. E. HARMON
  J. O. RAMEY
  B. C. SALES

PARTICLE-SOLID INTERACTIONS
B. R. APPLETON*
S. E. HIMES, SECRETARY
S. L. EVANS, SECRETARY*

- **ION-SOLID INTERACTIONS**
  B. R. APPLETON*
  G. M. BEARDSLEY[3]
  N. J. CULBERTSON
  O. W. HOLLAND
  J. L. MOORE
  H. NARAMOTO[3]
  T. S. NOGGLE*
  O. E. SCHOW III
  C. W. WHITE
  J. M. WILLIAMS
  S. P. WITHROW*
- **PLASMA MATERIALS INTERACTIONS**
  J. B. ROBERTO
  T. B. COOK
  E. R. DULLNI[3]
  S. P. WITHROW*
  C. E. YOUNG[3]
  R. A. ZUHR
- **X-RAY DIFFRACTION AND ELECTRON MICROSCOPY**
  B. C. LARSON
  J. F. BARHORST
  G. W. BOGGS
  J. NARAYAN
  T. S. NOGGLE*
  A. K. RAI[3]
- **FRACTURE**
  S. M. OHR
  T. C. ESTES
  J. A. HORTON

RESEARCH MATERIALS
F. W. YOUNG, JR.*
J. T. LUCK, SECRETARY
I. M. BARKER, SECRETARY*

- **PHOTOVOLTAIC MATERIALS**
  R. F. WOOD*
  J. W. CLELAND
  L. S. DARKEN
  P. H. FLEMING
  R. B. JAMES[8]
  G. E. JELLISON, JR.
  D. H. LOWNDES
  G. VAN DER LEEDEN
  R. D. WESTBROOK
  R. T. YOUNG
- **RADIATION EFFECTS IN METALS**
  R. R. COLTMAN, JR.
  C. E. KLABUNDE
  D. B. POKER
- **ISOTOPE RESEARCH MATERIALS LABORATORY**
  E. H. KOBISK*
  B. A. CAYLOR, SECRETARY

  ISOTOPE RESEARCH MATERIALS
  H. L. ADAIR*

  ISOTOPE MATERIALS R&D
  W. S. AARON*
  C. A. CULPEPPER*
  P. R. KUEHN
  M. PETEK

  SAMPLE PREPARATION
  H. L. ADAIR*
  B. L. BYRUM
  K. B. CAMPBELL
  W. B. GRISHAM
  L. A. ZEVENBERGEN

  REACTOR DOSIMETRY
  J. A. SETARO*
  J. M. DAILEY
  J. M. LOVEGROVE

  SPECIAL PROJECTS
  E. H. KOBISK*
  W. S. AARON*
  C. A. CULPEPPER*
  T. C. QUINBY
  D. W. RAMEY
  R. D. TAYLOR
  D. K. THOMAS

ULTIPLE CAPACITY
LANT AND EQUIPMENT DIVISION
NANCE AND MATERIALS DIVISION
UEST SCIENTIST
ART-TIME EMPLOYMENT
N ASSIGNMENT FROM AMES LABORATORY
RADUATE STUDENT
LCA SCIENCE STUDENT
MO – WIGNER FELLOW

THIS PAGE

WAS INTENTIONALLY

LEFT BLANK

ORNL-5850
Special Distribution

INTERNAL DISTRIBUTION

1. W. S. Aaron
2. M. M. Abraham
3. H. L. Adair
4. E. D. Aebischer
5–9. B. R. Appleton
10. S. I. Auerbach
11. J. F. Barhorst
12. I. M. Barker
13. J. H. Barrett
14. J. B. Bates
15. G. E. Beardsley
16. E. E. Bloom
17. L. A. Boatner
18. C. W. Boggs
19. W. E. Brundage
20. W. D. Burch
21. R. L. Burrell
22. B. L. Byrum
23. J. W. Cable
24. K. B. Campbell
25. R. S. Carlsmith
26. B. A. Caylor
27. S.-J. Chang
28. Y. K. Chang
29. Y. Chen
30. H. R. Child
31. D. K. Christen
32. B. R. Clark
33. G. W. Clark
34. J. W. Cleland
35. T. L. Collins
36. R. R. Coltman, Jr.
37. T. B. Cook III
38–42. J. F. Cooke
43. B. J. Copeland
44. R. J. Culbertson
45. C. A. Culpepper
46. L. C. Cunningham
47. J. M. Dailey
48. L. S. Darken
49. H. L. Davis
50. N. J. Dudney
51. T. C. Estes
52. S. L. Evans
53. P. H. Fleming
54. W. Fulkerson
55. M. A. Gillespie
56. P. H. Green
57. W. B. Grisham
58. G. R. Gruzalski
59. H. E. Harmon
60. V. G. Hendrix
61. R. F. Hibbs
62. S. E. Himes
63. O. W. Holland
64. J. A. Horton
65. R. B. James
66. D. W. Jared
67. G. E. Jellison, Jr.
68–72. L. H. Jenkins
73. S. Kaplan
74. T. Kaplan
75. S. V. Kaye
76. A. M. Keesee
77. H. R. Kerchner
78. S. P. King
79. C. E. Klabunde
80. E. H. Kobisk
81. W. C. Koehler
82. E. H. Krieg
83. B. C. Larson
84. J. S. Lin
85. S. H. Liu
86. C.-K. Loong
87. J. M. Lovegrove
88. D. H. Lowndes
89. J. T. Luck
90. B. K. Lyon
91. F. C. Maienschein
92. L. K. Mansur
93. J. R. Martinelli
94. C. J. McHargue
95. L. E. McNeese
96. C. D. Moak
97. F. A. Modine
98. H. A. Mook
99–103. R. M. Moon
104. J. L. Moore
105. M. E. Mostoller
106. H. Naramoto
107. J. Narayan
108. R. M. Nicklow
109. T. S. Noggle
110. J. R. Noonan

111. O. S. Oen
112. S. M. Ohr
113. G. E. Oliphant
114. G. W. Ownby
115. M. Petek
116. J. J. Pinajian
117. D. B. Poker
118. H. Postma
119. T. C. Quinby
120. V. C. Ramakrishnan
121. D. W. Ramey
122. J. O. Ramey
123. M. Rasolt
124. C. R. Richmond
125. J. B. Roberto
126. M. T. Robinson
127. M. W. Rosenthal
128. T. H. Row
129. B. C. Sales
130. C. K. Saw
131. O. E. Schow III
132. S. T. Sekula
133. J. L. Sellers
134. J. A. Setaro
135. W. D. Shults
136. D. L. Slagle
137. G. S. Smith
138. H. G. Smith
139. K. W. Sommerfeld
140. E. Sonder
141. S. Spooner
142. J. O. Stiegler
143. J. H. Swanks
144. R. D. Taylor
145. D. K. Thomas
146. J. R. Thompson
147. K. L. Tsang
148. D. B. Trauger
149. L. S. Tyler
150. G. van der Leeden
151. G.-C. Wang
152. J. C. Wang
153. R. A. Weeks
154. J. F. Wendelken
155. K. Werner
156. R. D. Westbrook
157. C. W. White
158. G. D. Wignall
159–233. M. K. Wilkinson
234. J. M. Williams
235. S. P. Withrow
236. R. F. Wood
237. C. E. Young
238–242. F. W. Young, Jr.
243. R. T. Young
244. J. L. Zarestky
245. D. M. Zehner
246. A. Zucker
247. R. A. Zuhr
248. Biology Library
249–250. Central Research Library
251. ORNL–Y-12 Technical Library Document Reference Section
252–253. Laboratory Records Department
254. Laboratory Records, ORNL R.C.

EXTERNAL DISTRIBUTION

255. Dr. S. Amelinckx, SCK/CEN, B2400, Mol, Belgium
256. Dr. R. T. Arnold, Department of Physics, University of Mississippi, University, MS 38677
257. Dr. K. J. Bachmann, School of Physical and Mathematical Sciences, North Carolina State University, Box 5247, Raleigh, NC 27650
258. Dr. R. W. Balluffi, Department of Materials Science and Engineering, Massachusetts Institute of Technology, 77 Massachusetts Avenue, Cambridge, MA 02139
259. Dr. H. Behrens, Zentralstelle für Atomkernergie-Dokumentation, 7514 Eggnestein-Leopoldshafen, Kernforschungszentrum, Federal Republic of Germany
260. Dr. Rainer Behrisch, Max-Planck-Institut für Plasmaphysik, 8046 Garching/München, Federal Republic of Germany
261. Prof. K. Bennemann, Institute of Theoretical Physics, Free University Berlin, Arnimallee 3, 1000 Berlin 33, Federal Republic of Germany

262. Bibliotheque, Institut Max von Laue-Paul Langevin, 156X Centre de Tri, 38042 Grenoble, Cedex, France
263. Dr. T. H. Blewitt, Materials Science Division, Argonne National Laboratory, 9700 South Cass Avenue, Argonne, IL 60439
264. Dr. N. Bloembergen, Gordon McKay Laboratory, 9 Oxford Street, Cambridge, MA 02138
265. Dr. M. Blume, Brookhaven National Laboratory, Upton, NY 11973
266. Dr. J. L. Boldu, Instituto de Física, Universidad Nacional Autonoma de Mexico, Apartado Postal 20-364, Mexico 20, D.F.
267. Dr. A. I. Braginski, Research and Development Center, Westinghouse Electric Corporation, Churchill Borough, Pittsburgh, PA 15235
268. Dr. William F. Brinkman, Bell Laboratories, 600 Mountain Avenue, Murray Hill, NJ 07974
269. Dr. F. Brown, Solid State Science Branch, Chemistry and Materials Division, Chalk River Nuclear Laboratories, Chalk River, Ontario, Canada
270. Dr. F. C. Brown, Department of Physics, University of Illinois, Urbana, IL 61801
271. Dr. Walter Brown, Room IE452, Bell Laboratories, 600 Mountain Avenue, Murray Hill, NJ 07974
272. Dr. R. Bullough, Atomic Energy Research Establishment, Harwell, Didcot, Oxon., OX11 ORA, England
273. Dr. John Burnett, Division of Chemical Sciences, Office of Basic Energy Sciences, Office of Energy Research, Department of Energy, Washington, DC 20545
274. Dr. W. J. L. Buyers, Atomic Energy of Canada Limited, Chalk River, Ontario, Canada
275. Dr. N. Cabrera, Departmento de Física Fundamental, Facultad de Ciencias, Universidad Autonoma de Madrid, Canto Blanco, Madrid, Spain
276. Prof. Ray W. Carpenter, Center for Solid State Science, Arizona State University, Tempe, AZ 85281
277. Dr. R. L. Chaplin, Department of Physics, Clemson University, Clemson, SC 29631
278. Dr. Andre Chatelain, Lab. Phys. Exp., Federal Institute of Technology, 33 av. Cour, 1007 Lausanne, Switzerland
279. Dr. W. J. Choyke, Research and Development Center, Westinghouse Electric Corporation, Churchill Borough, Pittsburgh, PA 15235
280. Dr. Wei-Kan Chu, Department of Physics, University of North Carolina, Chapel Hill, NC 27514
281. Dr. Mui Fatt Chung, Physics Department, University of Singapore, Bukit Timah Road, Singapore 10
282. Dr. C. B. Clark, Department of Physics, University of North Carolina, Greensboro, NC 27412
283. Dr. G. J. Clark, T. J. Watson Research Center, International Business Machines Corporation, P.O. Box 218, Yorktown Heights, NY 10598
284. Prof. Marvin Cohen, Department of Physics, University of California, Berkeley, CA 94720
285. Dr. Morrel Cohen, Exxon Research and Engineering Company, Linden, NJ 07036
286. Dr. W. Dale Compton, Vice President-Research, Ford Motor Company, P.O. Box 1603, Dearborn, MI 48121
287. Dr. L. R. Cooper, Code 427, Office of Naval Research, Arlington, VA 22217
288. Dr. J. W. Corbett, Physics Department, State University of New York at Albany, Albany, NY 12222
289. Dr. J. H. Crawford, Jr., Department of Physics and Astronomy, University of North Carolina, Chapel Hill, NC 27514
290. Dr. J. C. Crespi, Comision Nacional de Energia Atomica, Avenida del Libertador 8250, Buenos Aires 1429, Argentina

291. Mr. Floyd L. Culler, Jr., Electric Power Research Institute, 3412 Hillview Avenue, Palo Alto, CA 94303
292. Dr. Lubomir David, Director, Departamento de Fisica Nuclear, Instituto Venezolano de Investigaciones Cientificas (IVIC), Apartado 1827, Caracas 101, Venezuela
293. Prof. Dr. P. H. Dederichs, Institut für Festkörperforschung der Kernforschungsanlage Jülich GmbH, Postfach 1913, D-5170 Jülich 1, Federal Republic of Germany
294. Dr. J. Diehl, Max-Planck-Institut für Metallforschung, Institut für Werkstoffwissenschaften, Sestrasse 92/BRD, D-7000 Stuttgart 1, Federal Republic of Germany
295. Dr. J. Dienes, Department of Physics, Brookhaven National Laboratory, Upton, NY 11973
296. Prof. H.-D. Dietze, Institut für Theoretische Physik C, RWTH Aachen, 51 Aachen, Federal Republic of Germany
297. Dr. G. Dolling, Atomic Energy of Canada Limited, Chalk River, Ontario, Canada
298. Dr. D. G. Doran, Hanford Engineering Development Laboratory, P.O. Box 1970, Richland, WA 99352
299. Dr. M. Dresselhaus, Electrical Engineering Department, Massachusetts Institute of Technology, Cambridge, MA 02139
300. Dr. B. Dreyfus, Chef du DRF-G, Centre d'Études Nucléaires de Grenoble, 85X, 38041 Grenoble, Cedex, France
301. Dr. C. B. Duke, Xerox Corporation, Xerox Square 114, Rochester, NY 14644
302. Dr. Dean E. Eastman, T. J. Watson Research Center, International Business Machines Corporation, P.O. Box 218, Yorktown Heights, NY 10598
303. Dr. H. C. Eaton, Department of Mechanical Engineering, Louisiana State University, Baton Rouge, LA 70803
304. Dr. Norman Edelstein, Building 70-A, Room 1149, Lawrence Berkeley Laboratory, Berkeley, CA 94720
305. Dr. H. Ehrenreich, Division of Engineering and Applied Physics, Harvard University, Cambridge, MA 02138
306. Dr. F. H. Eisen, Electronics Research Center, Rockwell International, Thousand Oaks, CA 91320
307. Prof. T. L. Estle, Physics Department, Rice University, Houston, TX 77001
308. Dr. C. Peter Flynn, Director, Materials Research Laboratory, University of Illinois, Urbana, IL 61801
309. Dr. F. Y. Fradin, Argonne National Laboratory, Science Building 212, 9700 South Cass Avenue, Argonne, IL 60439
310. Prof. Dr. W. Frank, Max-Planck-Institut für Metallforschung, Institut für Physik, Busnauer Strasse 171, 7 Stuttgart 80, Federal Republic of Germany
311. Dr. Roger Frech, Department of Chemistry, University of Oklahoma, Norman, OK 73019
312. Prof. Arthur Freeman, Physics Department, Northwestern University, Evanston, IL 60201
313. Dr. J. Friedel, Physique des Solides, Université Paris Sud, 91405 Orsay, France
314. Dr. A. T. Fromhold, Department of Physics, Auburn University, Auburn, AL 36830
315. Dr. N. Fukuoka, Department of Physics, College of General Education, Osaka University, Toyonaka, Osaka 560, Japan
316. Dr. B. N. Ganguly, Systems Analysis Area/W-147, Xerox Corporation, Webster, NY 14580
317. Dr. W. B. Gauster, Physical Research Division 8347, Sandia National Laboratories, Livermore, CA 94550
318. Dr. J. R. Gavaler, Research and Development Center, Westinghouse Electric Corporation, Churchill Borough, Pittsburgh, PA 15235

319. Dr. H. A. Gersch, School of Physics, Georgia Institute of Technology, Atlanta, GA 30332
320. Dr. J. F. Gibbons, Electronics Engineering Laboratory, Stanford University, Palo Alto, CA 94305
321. Dr. A. N. Goland, Physics Department, 510-B, Brookhaven National Laboratory, Upton, NY 11973
322. Dr. M. Guinan, Lawrence Livermore National Laboratory, P.O. Box 808, Livermore, CA 94550
323. Dr. B. Henderson, Department of Pure and Applied Physics, Physical Laboratory, Trinity College, Dublin 2, Ireland
324. Dr. T. J. Hicks, Department of Physics, Monash University, Clayton, Victoria, Australia 3168
325. Dr. J. K. Hiroven, Code 5215D, Naval Research Laboratory, Washington, DC 20390
326. Dr. J. W. Hodby, University of Oxford, Clarendon Laboratory, Oxford OX1 3PU, England
327. Dr. P. H. Holloway, Department of Materials Sciences and Engineering, University of Florida, Gainesville, FL 32601
328. Dr. H. H. Hopkins, Jr., Rockwell International, Atomics International Division, Rockwell-Hanford Operations, P.O. Box 800, Richland, WA 99352
329. Dr. J. C. Houmann, Risø National Laboratory, DK-4000 Roskilde, Denmark
330. Dr. Marc Hou, Physique des Surfaces, Faculté des Sciences, Université Libre de Bruxelles, Campus de la Plaine (C.P. 234), Boulevard de Triomphe, B-1050 Bruxelles, Belgium
331. Dr. A. E. Hughes, Materials Development Division B552, Atomic Energy Research Establishment, Harwell, Didcot, Oxon., OX11 ORA, England
332. Dr. Louis C. Ianniello, Director, Division of Materials Sciences, Office of Basic Energy Sciences, Office of Energy Research, Department of Energy, Washington, DC 20545
333. Dr. Tadao Iwata, Division of Physics, Japan Atomic Energy Research Institute, Tokai-mura, Ibaraki-ken 319-11, Japan
334. Dr. P. K. Iyengar, Director, Physics and Metallurgy Groups, Bhabha Atomic Research Centre, Trombay, Bombay 400 085, India
335. Dr. W. A. Kamitakahara, Department of Physics, Iowa State University, Ames, IA 50010
336. Dr. D. W. Kammer, Department of Physics, Albion College, Albion, MI 49224
337. Dr. J. S. Kane, Deputy Director, Office of Energy Research, Department of Energy, Washington, DC 20545
338. Dr. T. Kaneda, Research Laboratories Tokyo, Fuji Photo Film Company, Ltd., Asakashi, Saitamaken, 351 Japan
339. Dr. Fred Keller, Department of Physics, Clemson University, Clemson, SC 29631
340. Dr. Q. H. Khan, N.P.D., PINSTECH, P.O. Nilore, Rawalpindi, Pakistan
341. Dr. D. L. Kinser, Department of Materials Science, Vanderbilt University, Nashville, TN 37235
342. Dr. J. S. Koehler, Physics Department, University of Illinois, Urbana, IL 61801
343. Dr. Eckhard Krätzig, Physics Department, University of Osnabrück, Postfach 4469, 45 Osnabrück, Federal Republic of Germany
344. Dr. R. H. Kropschot, Associate Director for Basic Energy Sciences, Office of Energy Research, Department of Energy, Washington, DC 20545
345. Prof. J Kübler, Institut für Festkörperphysik, Technische Hochschule Darmstadt, Hochschulstrasse 2, D-6100 Darmstadt, Federal Republic of Germany
346. Dr. Ad Lagendijk, Universitaire Instelling Antwerpen, Department Natuurkunde, Universiteitsplein 1, 2610 Wilrijk, Belgium

347. Dr. G. H. Lander, Argonne National Laboratory, 9700 South Cass Avenue, Argonne, IL 60439
348. Dr. S. S. Lau, California Institute of Technology, Pasadena, CA 91125
349. Dr. H. P. Leighly, Department of Metallurgical and Nuclear Engineering, University of Missouri–Rolla, Rolla, MO 65401
350. Dr. F. Li Aravena, Comision Chilena de Energia Nuclear, Los Jesuitas 645, Casilla 188D, Santiago, Chile
351. Librarian, Building 465, Atomic Energy Research Establishment, Harwell, Didcot, Oxon., OX11 ORA, England
352. The Librarian, Department of Physics, University of Islamabad, P.O. Box 1090, Islamabad, Pakistan
353. Dr. A. B. Lidiard, Theoretical Physics Division, Building 8.9, Atomic Energy Research Establishment, Harwell, Didcot, Oxon., OX11 ORA, England
354. Dr. W. M. Lomer, Director, UKAEA Culham Laboratory, Abingdon, Oxon., OX14 3DB, England
355. Dr. Stephen Lovesey, Rutherford Laboratory, Chilton, Didcot, Oxon., OX11 OQX, England
356. Dr. G. Lucovsky, Department of Physics, North Carolina State University, Raleigh, NC 27650
357. Prof. Dr. H.-O. Lutz, Fakultat für Physik, Universität Bielefeld, P.O. Box 8640, D-4800 Bielefeld 1, Federal Republic of Germany
358. Dr. J. W. Lynn, Department of Physics, University of Maryland, College Park, MD 20742
359. Dr. C. W. Magee, RCA Laboratories, Princeton, NJ 08540
360. Dr. R. W. Major, Department of Physics, University of Richmond, Richmond, VA 23173
361. Dr. W. C. Mallard, Physics Department, Georgia State University, Atlanta, GA 30303
362. Dr. P. M. Marcus, T. J. Watson Research Center, International Business Machines Corporation, P.O. Box 218, Yorktown Heights, NY 10598
363. Dr. J. W. Meyer, Department of Materials Sciences, Cornell University, Ithaca, NY 14853
364. Dr. A. Merlini, Physics Division, C.C.R. EURATOM, 21020 Ispra (Varese), Italy
365. Dr. J. L. Merz, Department of Electrical Engineering, University of California, Santa Barbara, CA 93106
366. Dr. Joseph B. Milstein, Photovoltaic Program Office, Solar Energy Research Institute, 1617 Cole Boulevard, Golden, CO 80401
367. Dr. J. W. Mitchell, Department of Physics, University of Virginia, Charlottesville, VA 22901
368. Dr. E. Munoz P, Instituto de Física, Universidad Nacional Autonoma de Mexico, Apartado Postal 20-364, Mexico 20, D.F.
369. Dr. R. B. Murray, University of Delaware, Newark, DE 19711
370. Dr. Taki Negas, Solid State Chemistry, Ceramic, Glass, and Solid State Science Division, Building 223, Room B-220, National Bureau of Standards, Washington, DC 20234
371. Dr. M. A. Nicolet, Department of Electrical Engineering, California Institute of Technology, Pasadena, CA 91125
372. Dr. L. H. Nosanow, Head, Condensed Matter Materials Section, Division of Materials Research, National Science Foundation, Washington, DC 20550
373. Dr. A. S. Nowick, Columbia University, 1146 S. W. Mudd Building, New York, NY 10027
374. Oak Ridge Associated Universities, MERT Division Library, P.O. Box 117, Oak Ridge, TN 37830

375. Office of Assistant Manager for Energy Research and Development, Department of Energy, Oak Ridge Operations Office, Oak Ridge, TN 37830
376–455. Office of Information Services, Oak Ridge Associated Universities, P.O. Box 117, Oak Ridge, TN 37830
456. Dr. D. N. Olson, Department of Physics, St. Olaf College, Northfield, MN 55057
457. Dr. V. M. Orera, Departamento de Física Fundamental, Facultad de Ciencias, Universidad de Zaragoza, Zaragoza-6, Spain
458. Dr. A. W. Overhauser, Department of Physics, Purdue University, West Lafayette, IN 47907
459. Dr. Arthur Papc, Centre de Recherches Nucléaire, 67037 Strasbourg, Cedex, France
460. Dr. Robert L. Park, Director, Center for Materials Research, University of Maryland, College Park, MD 20742
461. Dr. P. S. Peercy, Division 5112, Sandia National Laboratories, Albuquerque, NM 87115
462. Dr. Hans Peisl, Sektion Physik, Universitat München, Geschwister-Scholl-Platz 1, 8000 München 22, Federal Republic of Germany
463. Physics/Optics/Astronomy Library, 374 Bausch and Lomb Building, University of Rochester, Rochester, NY 14627
464. Dr. Elliott Pierce, Director, Division of Chemical Sciences, Office of Basic Energy Sciences, Office of Energy Research, Department of Energy, Washington, DC 20545
465. Dr. T. Pinkston, Department of Physics and Astronomy, Vanderbilt University, Nashville, TN 37240
466. Dr. Lothar A. R. Pintschovius, Kernforschungszentrum Karlsruhe GmbH, Postfach 3640, D-7500 Karlsruhe 1, Federal Republic of Germany
467. Dr. E. W. Plummer, Department of Physics, University of Pennsylvania, Philadelphia, PA 19104
468. Dr. J. M. Poate, Bell Laboratories, 600 Mountain Avenue, Murray Hill, NJ 07974
469. Dr. P. P. Pronko, Universal Energy Systems, 3195 Plainfield Road, Dayton, OH 45432
470. Dr. Y. Quéré, Centre d'Études Nucléaires de Fontenay-aux-Roses, B.P. No. 6, 92260 Fontenay-aux-Roses (Seine), France
471. Dr. R. A. Reynolds, Defense Advanced Research Projects Agency, Materials Sciences Office, 1400 Wilson Boulevard, Arlington, VA 22209
472. Dr. R. W. Reynolds, General Research Corporation, 307 Winn Drive, Huntsville, AL 35807
473. Dr. James R. Rice, Division of Engineering, Brown University, Providence, RI 02912
474. Dr. E. Rimini, Istituto di Struttura della Materia, Dell Universita, 57 Corso Italia, I95129 Catania, Italy
475. Dr. T. Riste, Institutt for Atomenergi, P.O. Box 40, 2007 Kjeller, Norway
476. Dr. J. E. Rives, Department of Physics, University of Georgia, Athens, GA 30602
477. Dr. C. A. Rotter, Department of Physics, West Virginia University, Morgantown, WV 26506
478. Dr. J. M. Rowe, Reactor Radiation Division, National Bureau of Standards, Washington, DC 20234
479. Dr. F. W. Saris, FOM Institute, P.O. Box 41883, 1009 DB Amsterdam, The Netherlands
480. Dr. H. Sato, Materials Engineering School, Purdue University, West Lafayette, IN 47907
481. Dr. William R. Savage, Department of Physics and Astronomy, University of Iowa, Iowa City, IA 52242
482. Dr. Kurt Scharnberg, Institut für Angewandte, Universität Hamburg, Jungiusstrasse 11, D-2000 Hamburg 36, Federal Republic of Germany
483. Dr. W. Schilling, Institut für Festkörperforschung der Kernforschungsanlage der Jülich GmbH, Postfach 1913, D-5170 Jülich 1, Federal Republic of Germany

484. Prof. Dr. W. Schmatz, Kernforschungszentrum Karlsruhe GmbH, Institut für Angewandte Kernphysik 1, Postfach 3640, D-7500 Karlsruhe, Federal Republic of Germany
485. Dr. W. Schnepple, EG&G, Energy Measurements Group, Santa Barbara Operations, 130 Robin Hill Road, Goleta, CA 93017
486. Prof. R. Schuttler, I.N.S.A. Service Informatique, Avenue de Rangueil, F-31077 Toulouse, Cedex, France
487. Dr. H.-B. Schweer, Institut für Festkörperforschung der Kernforschungsanlage Jülich GmbH, Postfach 1913, D-5170 Jülich 1, Federal Republic of Germany
488. Prof. Dr. A. Seeger, Max-Planck-Institut für Metallforschung, Institut für Physik, Heisenbergstrasse 1, Postfach 800665, D-7000 Stuttgart 80, Federal Republic of Germany
489. Dr. David N. Seidman, Department of Materials Science and Engineering, Bard Hall, Cornell University, Ithaca, NY 14850
490. Dr. G. Shirane, Brookhaven National Laboratory, Upton, NY 11973
491. Dr. C. G. Shull, Department of Physics, Massachusetts Institute of Technology, Cambridge, MA 02139
492. Dr. W. A. Sibley, Assistant Vice President for Research, 101 Whitehurst Hall, Oklahoma State University, Stillwater, OK 74078
493. Dr. R. H. Silsbee, Clark Hall, Physics Department, Cornell University, Ithaca, NY 14853
494. Prof. Dr. T. Springer, Directeur, Institut Max von Laue-Paul Langevin, Avenue des Martyrs, 38042 Grenoble, Cedex, France
495. Dr. C. Stassis, Physics Department, Iowa State University, Ames, IA 50011
496. Dr. D. K. Stevens, Deputy Associate Director for Basic Energy Sciences, Office of Energy Research, Department of Energy, Mail Station G-256, Washington, DC 20545
497. Dr. J. R. Stevenson, Acting Vice President for Academic Affairs, Georgia Institute of Technology, Atlanta, GA 30332
498. Prof. R. Street, Vice-Chancellor, The University of Western Australia, Nedlands, Australia 6009
499. Dr. B. G. Streetman, Department of Electrical Engineering, University of Illinois, Urbana, IL 61801
500. Dr. B. W. Stritzker, Institut für Festkörperforschung der Kernforschungsanlage Jülich GmbH, Postfach 1913, D-5170 Jülich 1, Federal Republic of Germany
501. Dr. Thomas Surek, Photovoltaic Program Office, Solar Energy Research Institute, 1617 Cole Boulevard, Golden, CO 80401
502. Dr. M. L. Swanson, Chalk River Nuclear Laboratories, Chalk River, Ontario, Canada KOJ 1JO
503. Dr. F. J. E. Tasset, Institute Max von Laue-Paul Langevin, 156X Centre de Tri, 38042 Grenoble, Cedex, France
504. Dr. D. O. Thompson, Ames Laboratory, Iowa State University, Ames, IA 50010
505. Dr. M. W. Thompson, University of East Anglia, Norwich Norfolk NR4 7TJ, England
506. Dr. J. O. Thomson, Department of Physics, The University of Tennessee, Knoxville, TN 37917
507. Dr. H. T. Tohver, Department of Physics, University of Alabama, Birmingham, AL 35233
508. Dr. G. T. Trammell, Department of Physics, Rice University, Houston, TX 77001
509. Dr. J. G. Traylor, Buena Vista College, Storm Lake, IA 50588
510. Dr. James B. Trice, Program Manager, General Electric AEP, Room 7246, C7, P.O. Box 8661, Philadelphia, PA 19101
511. Dr. B. Y. Tsaur, Steele Laboratory, Mail Code 116-81, California Institute of Technology, Pasadena, CA 91125

512. Dr. K. N. Tu, T. J. Watson Research Center, International Business Machines Corporation, P.O. Box 218, Yorktown Heights, NY 10598
513. Prof. David Turnbull, Division of Applied Sciences, Harvard University, Cambridge, MA 02138
514. Universidade Federal de Minas Gerais, ICEX-Depto de Física, Servico de Documentacão, 30.000—Belo Horizonte—MG—Brazil
515. Dr. W. P. Unruh, Department of Physics, University of Kansas, Lawrence, KS 66044
516. Dr. P. D. Vashishta, Solid State Sciences Division, Argonne National Laboratory, 9700 South Cass Avenue, Argonne, IL 60439
517. Dr. W. E. Vehse, Department of Physics, University of West Virginia, Morgantown, WV 26506
518. Dr. H. Verbeek, Max-Planck-Institut für Plasmaphysik, D-8046 Garching, Federal Republic of Germany
519. Dr. Donald L. Vieth, Chief, Materials and Radiation Effects Branch, Division of Development and Technology, Office of Fusion Energy, Office of Energy Research, Department of Energy, Washington, DC 20545
520. Dr. P. R. Vijayaraghavan, Nuclear Physics Division, Bhabha Atomic Research Centre, Trombay, Bombay 400 085, India
521. Dr. G. Vogl, Hahn-Meitner-Institut für Kernforschung Berlin GmbH, Glienicker Strasse 100, D-1000 Berlin 39, Federal Republic of Germany
522. Dr. F. L. Vook, Solid State Sciences, Org. 5100, Sandia National Laboratories, Albuquerque, NM 87185
523. Dr. N. Wakabayashi, Keio University, Yokohama, Japan
524. Prof. David Walsh, Department of Physics, Ernest Rutherford Physics Building, McGill University, 3600 University Street, Montreal PQ, H3A 2TB, Canada
525. Prof. George D. Watkins, Sherman Fairchild Lab. 161, Lehigh University, Bethlehem, PA 18015
526. Dr. M. S. Webster, Department of Physics and Astronomy, Vanderbilt University, Nashville, TN 37203
527. Dr. M. S. Wechsler, Department of Metallurgy, Iowa State University, Ames, IA 50010
528. Dr. A. M. Weinberg, Director, Institute for Energy Analysis, Oak Ridge Associated Universities, Oak Ridge, TN 37830
529. Dr. H. F. Wenzl, Institut für Festkörperforschung der Kernforschungsanlage Jülich GmbH, Postfach 1913, D-5170 Jülich 1, Federal Republic of Germany
530. Prof. S. Werner, Department of Physics, University of Missouri, Columbia, MO 65201
531. Dr. C. W. Wert, Head, Department of Metallurgy and Mining Engineering, University of Illinois, Urbana, IL 61801
532. Dr. A. R. Williams, T. J. Watson Research Center, International Business Machines Corporation, P.O. Box 218, Yorktown Heights, NY 10598
533. Dr. W. Williams, Materials Research Laboratory, University of Illinois, Urbana, IL 61801
534. Dr. S. R. Wilson, Semiconductor Group, Motorola, Inc., Mail Drop B-132, 5006 East McDowell, Phoenix, AZ 85008
535. Dr. T. M. Wilson, Department of Physics, Oklahoma State University, Stillwater, OK 74078
536–543. Dr. R. R. Winters, Director, Oak Ridge Science Semester, GLCA, Denison University, Main Street, Granville, OH 43023
544. Dr. Mark C. Wittels, Division of Materials Sciences, Office of Basic Energy Sciences, Office of Energy Research, Mail Station G-256, Department of Energy, Washington, DC 20545

545. Prof. Dr. H. Wollenberger, Hahn-Meitner-Institut für Kernforschung Berlin GmbH, Glienicker Strasse 100, D-1000 Berlin 39, Federal Republic of Germany
546. Dr. R. A. Young, School of Physics, Georgia Institute of Technology, Atlanta, GA 30332
547. Dr. Solomon Zwerdling, Northeast Solar Energy Center, 70 Memorial Drive, Cambridge, MA 02142
548–574. Technical Information Center, Department of Energy, Oak Ridge, TN 37830

*U.S. GOVERNMENT PRINTING OFFICE: 1981-546-067/429